

University of Huddersfield Repository

Tunes, Matheus A.

Transmission Electron Microscopy Study of Radiation Damage in Potential Nuclear Materials

Original Citation

Tunes, Matheus A. (2020) Transmission Electron Microscopy Study of Radiation Damage in Potential Nuclear Materials. Doctoral thesis, University of Huddersfield.

This version is available at http://eprints.hud.ac.uk/id/eprint/35253/

The University Repository is a digital collection of the research output of the University, available on Open Access. Copyright and Moral Rights for the items on this site are retained by the individual author and/or other copyright owners. Users may access full items free of charge; copies of full text items generally can be reproduced, displayed or performed and given to third parties in any format or medium for personal research or study, educational or not-for-profit purposes without prior permission or charge, provided:

- The authors, title and full bibliographic details is credited in any copy;
- A hyperlink and/or URL is included for the original metadata page; and
- The content is not changed in any way.

For more information, including our policy and submission procedure, please contact the Repository Team at: E.mailbox@hud.ac.uk.

http://eprints.hud.ac.uk/

A Transmission Electron Microscopy Study of Radiation Damage in Potential Nuclear Materials

Matheus Araujo Tunes
BSc MSc MInstP

Revised Version

April 14, 2020

A Transmission Electron Microscopy Study of Radiation Damage in Potential Nuclear Materials

Matheus Araujo Tunes
Ion Beam Centre
School of Computing and Engineering
University of Huddersfield

Submitted in partial fulfilment of the requirements of the degree of
Doctor of Philosophy

United Kingdom
2019

Funding acknowledgement

Funding for this doctoral research was provided by Professor Stephen E. Donnelly, director of the Ion Beam Centre at the University of Huddersfield, United Kingdom, and partially supported through the ASTRO Fellowship, a United States Department of Energy workforce development program implemented at Oak Ridge National Laboratory through the Oak Ridge Institute for Science and Education under contract DE-AC05-06OR23100.

Declaration

I hereby declare that the research work presented in this thesis is my own and other published works on the topics herein discussed have been referenced appropriately. The phase diagrams presented in the Chapter 6 were obtained using the software ThermoCalc in a scientific collaboration with Prof. Dr. rer. nat. Claudio G. Schön at University of São Paulo. The analytical characterisation of the Ti-based MAX phases presented in section 4.4.2.1 was performed with the support of Mr. Luigi Cattini at Montanuniversität Leoben.

Copyright statement

- The author of this thesis (including any appendices and/or schedules to this thesis) owns any copyright in it (the "copyright") and he has given the University of Huddersfield the right to use such copyright for any administrative, promotional, educational and/or teaching purposes.
- Copies of this thesis, either in full or in extracts, may be made only in accordance with the regulations of the University Library. Details of these regulations may be obtained from the Librarian. This page must form part of any such copies made.
- The ownership of any patents, designs, trademarks and any and all other intellectual property rights except for the copyright (the "intellectual property rights") and any reproductions of copyright works, for example graphs and tables ("reproductions"), which may be described in this thesis, may not be owned by the author and may be owned by third parties. Such intellectual property rights and reproductions cannot and must not be made available for use without the prior written permission of the owner(s) of the relevant Intellectual Property Rights and/or Reproductions.

Statement of publications arising during this doctoral research

The following publications are from my doctoral research period (2015–2019) in the Ion Beam Centre at the University of Huddersfield and in the Materials Science and Technology Division at the Oak Ridge National Laboratory. The publications marked with † are directly related with the scientific research reported in this thesis.

Peer-Reviewed International Scientific Papers

† 1. **M.A. TUNES**, G. GREAVES, T.M. KREMMER, V.M. VISHNYAKOV, P.D. EDMONDSON, S.E. DONNELLY, S. POGATSCHER and C.G. SCHON. Thermodynamics of an austenitic stainless steel (AISI-348) under in situ TEM heavy ion irradiation. **Acta Materialia**, 179, 360-371, Elsevier, 2019.
Contribution of the candidate: I performed most of the research and wrote the entire manuscript with minor input and editorial changes from my co-authors.

† 2. **M.A. TUNES**, V.M. VISHNYAKOV, O. CAMARA, G. GREAVES, P.D. EDMONDSON, Y. ZHANG and S.E. DONNELLY. A candidate accident tolerant fuel system based on a highly concentrated alloy thin film. **Materials Today Energy**, 12, 356-362, Elsevier, 2019.
Contribution of the candidate: I performed all the research and wrote the entire manuscript with minor input and editorial changes from my co-authors.

† 3. **M.A. TUNES**, G. GREAVES and C.G. SCHÖN. Radiation-induced precipitation with concurrent bubbles formation in an austenitic stainless steel (AISI-348). **Materialia**, 7, 100408, Elsevier, 2019.
Contribution of the candidate: I performed all the research and wrote the entire manuscript with minor input and editorial changes from my co-authors.

† 4. **M.A. TUNES**, H. LE, G. GREAVES, C.G. SCHON, H. BEI, Y. ZHANG, P.D. EDMONDSON and S.E. DONNELLY. Investigating sluggish diffusion in a concen-

trated solid solution alloy using ion irradiation with in situ TEM. **Intermetallics**, 110, 106461, Elsevier, 2019.
Contribution of the candidate: I performed all the research and wrote the entire manuscript with minor input and editorial changes from my co-authors.

5. O. CAMARA, **M.A. TUNES**, G. GREAVES, A.H. MIR, S.E. DONNELLY and J.A. HINKS. Understanding Amorphization Mechanisms Using Ion Irradiation and 3D Damage Reconstruction. **Ultramicroscopy**, 207, 112838, Elsevier, 2019.
Contribution of the candidate: This publication was the result of a collaboration in which I performed 100% of the computational research including active contribution to the discussion of the results as well as editing changes in the manuscript.

6. Y. ZHANG, **M.A. TUNES**, M.L. CRESPILLO, F. ZHANG, W.L. BOLDMAN, P.D. RACK, L. JIANG, C. XU, G. GREAVES, S.E. DONNELLY, L. WANG, and W.J. WEBER. Thermal Stability and Irradiation Response of Nanocrystalline CoCrCuFeNi High-entropy Alloy. Invited article for **Nanotechnology**, 30, 294004, IOP Publishing, 2019.
Contribution of the candidate: This publication was the result of a collaboration in which I performed 50% of the experimental research and I wrote around of 20% of the manuscript.

7. G. GREAVES, A.H. MIR, R.W. HARRISON, **M.A. TUNES**, S.E. DONNELLY and J.A. HINKS. New Microscope and Ion Accelerators for Materials Investigations (MIAMI-2) System at the University of Huddersfield. **Nuclear Instruments & Methods in Physics Research A**, 931, 37-43, Elsevier, 2019.
Contribution of the candidate: I have implemented an automatic interface system of the MIAMI-2 dosimeters with LabView. This has been performed in collaboration with a master student (W. Zhang) co-supervised by me. Additionally, I have performed the analytical characterisation of the irradiated material reported in the paper.

† 8. **M.A. TUNES**, R.W. HARRISON, S.E. DONNELLY and P.D. EDMONDSON. A Transmission Electron Microscopy study of the neutron-irradiation response of Ti-based MAX phases at high temperatures. **Acta Materialia**, 169, 237-247, Elsevier, 2019.
Contribution of the candidate: I performed all the research and wrote the entire manuscript with minor input and editorial changes from my co-authors.

† 9. **M.A. TUNES** and V.M. VISHNYAKOV. Microstructural origins of the high

mechanical damage tolerance of NbTaMoW refractory high-entropy alloy thin films. **Materials & Design**, 170, 107692, Elsevier, 2019.
Contribution of the candidate: I performed all the characterisation research and wrote the entire manuscript with minor input and editorial changes from my co-author which was responsible for the synthesis of the studied material.

10. V.O. DOS SANTOS, **M.A. TUNES**, L.T.F. ELENO, C.G. SCHON and K.W. RICHTER. Experimental investigation of phase equilibria in the Nb-Ni-Si refractory alloy system at 1073 K. **Scripta Materialia**, 164, 96-10, Elsevier, 2019.
Contribution of the candidate: This is the second paper derived from my master research at the University of Sao Paulo (2013–2015).

† 11. **M.A. TUNES**, F.C. SILVA, O. CAMARA, C.G. SCHON, J.C. SAGAS, L.C. FONTANA, S.E. DONNELLY, G. GREAVES AND P.D. EDMONDSON. Energetic particle irradiation study of TiN coatings: are these films appropriate for accident tolerant fuels? **Journal of Nuclear Materials**, 512, 239-245, Elsevier, 2019.
Contribution of the candidate: I performed all the research and wrote the entire manuscript with minor input and editorial changes from my co-authors.

12. **M.A. TUNES**, C.M. SILVA and P.D. EDMONDSON. Site specific dependencies of hydrogen concentrations in zirconium hydrides. **Scripta Materialia**, 158, 136-140, Elsevier, 2019.
Contribution of the candidate: I performed all the research and wrote the entire manuscript with minor input and editorial changes from my co-authors.

13. I. HANIF, O. CAMARA, **M.A. TUNES**, R.W. HARRISON, G. GREAVES, S.E. DONNELLY and J.A. HINKS. Ion-Beam-Induced Bending of Semiconductor Nanowires. **Nanotechnology**, 29(33), 3355701, IOP Publishing, 2018.
Contribution of the candidate: This publication was the result of a collaboration in which I performed 90% of the computational research including active contribution to the discussion of the results as well as editorial changes in the manuscript.

14. O. CAMARA, I. HANIF, **M.A. TUNES**, R.W. HARRISON, G. GREAVES, S.E. DONNELLY and J.A. HINKS. Shape Modification of Germanium Nanowires during Ion Irradiation and Subsequent Solid-Phase Epitaxial Growth **Advanced Materials Interfaces**, 1800276, Wiley-VHC, 2018.
Contribution of the candidate: This publication was the result of a collaboration in which I performed 90% of the computational research including active contribution to the discussion of the results as well as editorial changes in the manuscript.

† 15. **M.A. TUNES**, V.M. VISHNYAKOV and S.E. DONNELLY. Synthesis and characterisation of high-entropy alloy thin films as candidates for coating nuclear fuel cladding alloys. **Thin Solid Films**, 649C, pp. 115-120. Elsevier, 2018.
Contribution of the candidate: I performed all the research and wrote the entire manuscript with minor input and editorial changes from my co-authors.

16. **M.A. TUNES**, R.W. HARRISON, G. GREAVES and S.E. DONNELLY. Effect of He implantation on the microstructure of Zircaloy-4 using in-situ TEM. **Journal of Nuclear Materials**, 493, 230-238. Elsevier, 2017.
Contribution of the candidate: I performed all the research and wrote the entire manuscript with minor input and editorial changes from my co-authors.

17. O. CAMARA, I. HANIF, **M.A. TUNES**, R.W. HARRISON, G. GREAVES, S.E. DONNELLY and J.A. HINKS. Effects of temperature on the ion-induced bending of germanium and silicon nanowires. **Materials Research Express**, 4(7), 075056. IOP Publishing, 2017.
Contribution of the candidate: This publication was the result of a collaboration in which I performed 90% of the computational research including active contribution to the discussion of the results as well as editorial changes in the manuscript.

18. **M.A. TUNES**, C.R.E. DE OLIVEIRA and C.G. SCHON. Multi-objective optimization of a compact pressurized water nuclear reactor computational model for biological shielding design using innovative materials. **Nuclear Engineering and Design**, 313, 20-28, Elsevier, 2017.
Contribution of the candidate: This is the first paper derived from my master research at the University of Sao Paulo (2013–2015).

Peer-Reviewed Papers and Abstracts at International Conferences

1. F.C. da SILVA, **M.A. TUNES**, J.C. SAGAS, C.G. SCHON. Influence of substrate stiffness and of PVD parameters on the microstructure and tension fracture characteristics of TiN thin films. Procedia Structural Integrity 13, 2018, 658-663.

2. V.O. SANTOS, **M.A. TUNES**, M.S. JAEGER, L.T.F. ELENO, C.G. SCHON. Experimental Assessment of the Nb-Ni-Si System, in Discussion Meeting on Thermodynamics of Alloys TOFA, 2016, Santos, Brazil, vol. 1, Q11.

3. **M.A. TUNES**, S.R. SALINAS, C.G. SCHON. The non-extensive spinodal line: solution of the problem in the Bethe approximation, in Discussion Meeting on Thermodynamics of Alloys TOFA, 2016, Santos, Brazil, vol. 1, Q12.

4. **M.A. TUNES**, R.W. HARRISON, G. GREAVES, J.A. HINKS and S.E. DONNELLY. An *in-situ* irradiation study of the Zircaloy-4 under 6 keV Helium ions. Universities Nuclear Technology Forum, 2016, University of Sheffield - United Kingdom.

5. † **M.A. TUNES**, R.W. HARRISON, G. GREAVES, J.A. HINKS and S.E. DONNELLY. The effect of 6 keV Helium implantation on the microstructure of zirconium alloys. Winter-school in Calculus of Variations in Physics and Materials Science at Julius-Maximilians-Universität Würzburg, 2016, Germany.

6. S.E. DONNELLY, J.H. EVANS, **M.A. TUNES**, G. GRAEVES, R.W.HARRISON and J.A. HINKS. Inert gas bubbles super-lattices in ion-irradiated metals. IBMM2016 20th International Conference on Ion Beam Modification Of Materials, 2016, New Zealand.

7. R.W. HARRISON, **M.A. TUNES**, G. GREAVES, J.A. HINKS and S.E. DONNELLY. Impact of He Concentration on the Microstructure of W Using TEM with In Situ Ion Irradiation. 2017 TMS Annual Meeting & Exhibition. Symposium: Microstructural Processes in Irradiated Materials. San Diego, California, 2017, United States of America.

8. O. CAMARA, G. GREAVES, R.W. HARRISON, **M.A. TUNES**, J.A. HINKS, I. HANIF and S.E. DONNELLY. Ion-induced bending of germanium and silicon nanowires at high temperature. EUROMAT 2017. Symposium: Deposition and nanostructuring assisted by ion and laser irradiation, Thessaloniki, 2017, Greece.

† 9. **M.A. TUNES**, V.M. VISHNYAKOV, J.A. HINKS and S.E. DONNELLY. Irradiation behaviour of high-entropy alloy thin films for coating nuclear fuel claddings. EUROMAT 2017. Symposium: Nuclear Materials – Fuel cladding, Thessaloniki, 2017, Greece.

10. V.O. DOS SANTOS, C.G. SCHON, L.T.F. ELENO, **M.A. TUNES** and M. JAEGER. Experimental assessment of the Nb-Ni-Si system. XVI SBPMAT. Symposium G: Analysis and Modification of Materials with Electron and Ion Beams,

Gramado, Rio Grande do Sul, 2017, Brazil.

† 11. S.E. DONNELLY, **M.A. TUNES** and V.M. VISHNYAKOV. Radiation resistance of High-Entropy Thin Films deposited on Zircaloy-4: prospective ATF research at MIAMI facilities. Materials Research Society Fall Meeting and Exhibit (MRS 2017), Boston - Massachusetts, 2017, United States of America.

† 12. **M.A. TUNES**, P.D. EDMONDSON, V.M. VISHNYAKOV and S.E. DONNELLY. The microstructural evolution of austenitic stainless steels under in situ TEM heavy ion irradiation. Innovation in Materials for Extreme Environments (IMEE 2018), University of Huddersfield Conference, 2017, United Kingdom.

† 13. **M.A. TUNES**, P.D. EDMONDSON, S.E. DONNELLY and V.M. VISHNYAKOV. Advanced concentrated solid solution alloy thin film as protective coatings of zirconium alloys. Composite Materials Congress (CMC2018), Sweden.

† 14. **M.A. TUNES**, S.E. DONNELLY and P.D. EDMONDSON. Microstrutural evolutions of ion and neutron radiation damage in MAX Phases alloys – Can ion beams emulate neutron damage?, Materials Science and Technology 2018 (MST18), United States of America.

† 15. **M.A. TUNES**, P.D. EDMONDSON, V.M. VISHNYAKOV and S.E. DONNELLY. The microstructural evolution of austenitic stainless steels under in situ TEM heavy ion irradiation. The 5th Workshop on TEM with in situ irradiation (WOTWISI-5-2018), University of Huddersfield, United Kingdom.

16. O. CAMARA, I. HANIF, **M.A. TUNES**, R.W. HARRISON, G. GREAVES, S.E. DONNELY and J.A. HINKS. Controlling the shape of germanium nanowires via ion irradiation and temperature. The 5th Workshop on TEM with in situ irradiation (WOTWISI-5-2018), University of Huddersfield, United Kingdom.

† 17. **M.A. TUNES**, P.D.EDMONDSON and S.E. DONNELLY. Comparison of high-temperature neutron and ion irradiation of Ti-based max Phases. 21st International Conference on Ion Beam Modification of Materials (IBMM 2018), San Antonio, United States of America.

† 18. **M.A. TUNES**, A.H. MIR, G.GREAVES and P.D. EDMONDSON. High-Temperature ion and neutron irradiation of Ti_3SiC_2 and Ti_2AlC. International workshop on MAX phases for harsh environments (2018), Poitiers, France.

† 19. **M.A. TUNES**, S.E. DONNELLY and P.D. EDMONDSON. High Temperature Radiation Response of Ti-based M_nAX_{n-1} Phases. 43rd International Conference and Exposition on Advanced Ceramics and Composites (2019), Florida, United States of America.

Technical Reports

† 1. **M.A. TUNES**, G. GREAVES, A.H. MIR, S.E. DONNELLY and P.D. EDMONDSON. Further evidence on the radiation tolerance of Ti-based nanolayered MAX Phases. Fusion Materials Semi-annual Progress Report, U.S. Department of Energy Office for Fusion Energy Science, DOE/ER-0313, vol 64, pp.133-134, 2018.

† 2. **M.A. TUNES** and P.D. EDMONDSON. High-temperature neutron-irradiation of Ti-based $M_{n+1}AX_n$ Phases. Bi-annual report for the Materials Science and Technology Division at the Oak Ridge National Laboratory, U.S. Department of Energy, 2018.

† 3. **M.A. TUNES** and P.D. EDMONDSON, V.M. VISHNYAKOV and S. E. DONNELLY. Displacement Damage and Self-Healing in High-Entropy Alloys: a TEM with in situ ion irradiation study. ORNL Fusion Materials FY2017, Oak Ridge National Laboratory, ORNL/TM-2017/732, U.S. Department of Energy, 2017.

† 4. P.D. EDMONDSON, **M.A. TUNES**, R. W. HARRISON, G. GREAVES, J. A. HINKS and S. E. DONNELLY. Preliminary assessment of the irradiation behaviour of the FeCrMnNi high-entropy alloy for nuclear applications. ORNL Fusion Materials FY2016, Oak Ridge National Laboratory, ORNL/TM-2016/685, U.S. Department of Energy, 2016.

Not Patented or Registered Softwares

1. **M.A. TUNES**, G. GREAVES, J. A. HINKS and S. E. DONNELLY. IDRAGON: a set of MATLAB scripts coupled with SRIM2013 for ion beam damage profile analysis of nanowires, 2016.

2. **M.A. TUNES**, G. GREAVES and O. CAMARA. IDRAGON Cascades for 3D Damage Reconstruction, 2019.

Prizes and Honours

Certificate of Excellence: for first place in the student poster competition at the University of Huddersfield Materials Forum. Institute for Materials Research and Engineering, 2017, United Kingdom.

ASTRO Fellowship: academic merit-based fellowship to carry out research at the Oak Ridge National Laboratory, 2017-2018, United States of America.

Contents

List of Figures **I**

List of Tables **XVII**

Acknowledgements **XIX**

Abbreviations **XXII**

Abstract **XXIV**

1 Introduction **1**

2 Background and Literature Review **7**

2.1 The materials: definitions and properties 7

2.1.1 Multicomponent alloy systems 7

2.1.1.1 Steel and its variants 8

2.1.1.1.1 Definition and classification 8

2.1.1.1.2 Atomic structures of Fe, steels and their phases 9

2.1.1.1.3 Stainless steels and applications 11

2.1.1.2 High-entropy alloys 13

2.1.1.2.1 Historical context for the emergence of high-entropy alloys 13

2.1.1.2.2 Ideal solid solutions and binary systems . . 15

2.1.1.2.3 Real solid solutions 16

2.1.1.2.4 The concept of high-entropy alloy 17

2.1.1.2.5 The core effects of high-entropy alloys . . . 18

2.1.1.2.6 Recent theoretical developments on the theory of HEAs: configurational entropy and sluggish diffusion. 21

2.1.2 Nanolayered materials 21

2.1.2.1 $M_{n+1}AX_n$ phases 22

2.1.2.1.1 Historical context . . . 22
2.1.2.1.2 Definition . . . 22
2.1.2.1.3 Classification . . . 22
2.1.2.1.4 Properties and potential applications . . . 23
2.2 Principles of radiation damage in solids . . . 26
2.2.1 Primary events of radiation damage . . . 27
2.2.1.1 Ions colliding with solids . . . 29
2.2.1.1.1 Computational methods and ion implantation 30
2.2.1.2 Neutrons colliding with solids . . . 31
2.2.1.2.1 Neutron-induced nuclear reactions and impurity damage . . . 33
2.2.1.3 Kinchin-Pease model . . . 33
2.2.1.4 The Norgett–Robinson–Torrens displacement model and the definition of displacements-per-atom . . . 34
2.2.1.5 Collision cascades and thermal spikes . . . 35
2.2.2 Radiation-induced point and extended defects . . . 37
2.2.2.1 Vacancies and voids . . . 37
2.2.2.2 Interstitials . . . 38
2.2.2.2.1 Clusters of interstitials . . . 39
2.2.2.3 Vacancy-interstitial pairs and recombination (or recovery) . . . 39
2.2.2.4 Impurity damage: gas bubbles . . . 40
2.2.2.4.1 Impact of bubble nucleation on mechanical properties of nuclear materials . . . 42
2.2.2.5 Black-spots and dislocation loops . . . 43
2.2.2.5.1 Impact on the mechanical properties of metals and alloys . . . 44
2.2.2.6 Stacking faults . . . 47
2.2.2.7 Radiation-assisted atomic migration: elemental segregation . . . 47
2.3 Methodologies for radiation damage investigation in solids . . . 49
2.3.1 Neutron irradiation using materials testing reactors . . . 49
2.3.2 Ion irradiation using particle accelerators . . . 50
2.3.3 Electron irradiation . . . 52
2.3.4 Critical comparison between methodologies . . . 52
2.4 Review of radiation damage in multicomponent alloys and MAX phases 56
2.4.1 Austenitic stainless steels . . . 56
2.4.1.1 Damage microstructure under neutron irradiation . . 56
2.4.1.2 Damage microstructure under ion irradiation . . . 60

2.4.1.3 The austenitic stainless steel AISI-348 61
2.4.2 High-entropy alloys 65
2.4.3 $M_{n+1}AX_n$ phases 69
2.4.3.1 Ion irradiation effects 69
2.4.3.2 Neutron irradiation effects 71
2.5 Next generation of nuclear materials and primary thesis goals 72

3 Experimental Techniques and Methodology 76
3.1 Materials synthesis 77
3.1.1 Production of austenitic stainless steels and the AISI-348 steel 77
3.1.2 Synthesis of the FeCrMnNi HEA 77
3.1.3 Production of MAX phases 78
3.1.4 Synthesis of thin solid films 79
3.2 Sample preparation techniques 80
3.2.1 Electro-chemical jet-polishing 81
3.2.2 Focused ion beam 82
3.3 Transmission Electron Microscopy 84
3.3.1 The equipment 85
3.3.1.1 An electron gun 85
3.3.1.2 Magnetic lenses 87
3.3.1.2.1 Spherical (C_S) and chromatic aberrations (C_3) 87
3.3.1.2.2 Astigmatism and stigmators 87
3.3.1.3 Deflectors 88
3.3.1.4 Condenser and objective lenses 88
3.3.1.5 Intermediate lenses 88
3.3.1.6 Projectors 88
3.3.1.7 Condenser, objective and intermediate apertures . . 88
3.3.1.8 Specimen stage 89
3.3.1.9 Specimen holders 89
3.3.1.10 Electron image capture methods and post-imaging analsysis 90
3.3.2 The imaging techniques: the interaction between electrons and matter 90
3.3.2.1 Elastic scattering 90
3.3.2.1.1 Atomic-scattering factor in crystalline solids 90
3.3.2.1.2 Bragg's law 91
3.3.2.2 Inelastic scattering 92
3.3.2.3 Diffraction patterns and Kikuchi lines 93

3.3.2.4 Amplitude contrast . . . 93
3.3.2.4.1 Mass-thickness . . . 93
3.3.2.4.2 Diffraction contrast . . . 93
3.3.2.4.3 Many-beam and two-beam conditions . . . 94
3.3.2.4.4 Weak-beam . . . 95
3.3.2.5 Phase contrast and Fresnel contrast . . . 95
3.3.2.6 Scanning Transmission Electron Microscopy . . . 95
3.3.3 TEMs used for the work reported in this thesis . . . 97
3.4 Ion irradiation *in situ* within a TEM . . . 97
3.4.1 MIAMI-1 . . . 98
3.4.1.1 Capabilities . . . 98
3.4.1.2 Ion source . . . 98
3.4.1.3 Ion beam transport and monitoring . . . 99
3.4.1.4 Coupling within a TEM . . . 99
3.4.1.5 Dosimetry . . . 100
3.4.2 MIAMI-2 . . . 100
3.4.2.1 Capabilities . . . 101
3.4.2.2 Ion source . . . 102
3.4.2.3 Ion beam transport and monitoring . . . 102
3.4.2.4 Coupling within a TEM . . . 102
3.4.2.5 Dosimetry . . . 102
3.4.3 Stopping and range of ions in matter . . . 104
3.4.3.1 The Monte Carlo algorithm in SRIM . . . 104
3.4.3.2 Fluence-to-dpa conversion . . . 105
3.5 Neutron irradiations at the High Flux Isotope Reactor . . . 106
3.6 Sample characterisation techniques . . . 107
3.6.1 Scanning Electron Microscopy . . . 107
3.6.2 Energy dispersive X-ray spectroscopy . . . 109
3.6.2.1 EDX in MAX Phases . . . 110
3.6.3 Multivariate statistical analysis . . . 110
3.6.4 Electron energy loss spectroscopy . . . 112
3.6.4.1 Energy-Filtered Transmission Electron Microscopy . 113
3.6.4.2 Thickness measurements using EELS and EFTEM . 113
3.7 Thermodynamic calculations with CALPHAD . . . 114

4 Pre-irradiation characterisation of the multicomponent alloys and the Ti-based MAX phases 116
4.1 Introduction . . . 116
4.2 Austenitic stainless steel: AISI-348 . . . 116

4.2.1 Microstructural characterisation . . . 118
4.2.1.1 Scanning electron microscopy . . . 118
4.2.1.2 Transmission electron microscopy . . . 119
4.2.2 Analytical characterisation . . . 122
4.2.2.1 Qualitative characterisation of the Nb(C,N) nanoparticles using EFTEM . . . 122
4.2.2.2 Qualitative and quantitative characterisation of the Nb(C,N) nanoparticles using STEM-EDX . . . 123
4.2.2.3 Elemental composition of the alloy . . . 125
4.3 The FeCrMnNi quaternary high-entropy alloy . . . 127
4.3.1 Microstructural characterisation . . . 127
4.3.1.1 Scanning electron microscopy . . . 127
4.3.1.2 Transmission electron microscopy . . . 127
4.3.2 Analytical characterisation . . . 128
4.3.2.1 Elemental composition of the alloy . . . 128
4.4 The Ti-based MAX phases . . . 130
4.4.1 Microstructural characterisation . . . 131
4.4.1.1 Scanning electron microscopy . . . 131
4.4.1.2 Transmission electron microscopy . . . 132
4.4.2 Analytical characterisation . . . 133
4.4.2.1 Elemental composition of the Ti-based MAX phases 133
4.5 Summary and comparison of the materials and alloys under investigation . . . 137

5 Investigating the reduced mobility of irradiation-induced defects of highly concentrated multicomponent alloys 140
5.1 Introduction and background . . . 140
5.2 Design of the experiment . . . 141
5.3 Light ion irradiation at low temperatures and subsequent annealing . 142
5.4 Heavy ion irradiation at low temperatures and subsequent annealing . 147
5.5 The influence of Nb(C,N) nanoparticles on the microstructure of the AISI-348 steel under irradiation . . . 151
5.6 Discussion . . . 154
5.6.1 Sequential quantitative data on bubble sizes and areal densities 154
5.6.2 Inert gas bubble size analysis: matrix phases, interfaces and thermal annealing . . . 156
5.6.3 The relationship between inert gas bubbles nucleation and growth in the irradiated multicomponent metallic alloys . . . 160
5.7 Summary and conclusions . . . 162

6 Comparison of phase stability under irradiation of AISI-348 steel and FeCrMnNi HEA 164
6.1 Introduction and background . . . 164
6.2 Low-energy heavy ion irradiation . . . 165
6.2.1 Design of the experiment . . . 166
6.2.2 Low, moderate and high temperatures regimes . . . 166
6.2.2.1 Irradiations at 293 K . . . 166
6.2.2.2 Irradiations at 573 K . . . 168
6.2.2.3 Irradiations at 873 K . . . 172
6.2.2.4 Irradiations at 1073 K . . . 174
6.2.2.5 Discussion . . . 185
6.2.2.5.1 Stability of the AISI-348 steel and the HEA matrix phases at low and moderate temperatures . . . 185
6.2.2.5.2 Radiation-induced precipitation and formation of the α' phase and accelerated aging at high temperatures . . . 189
6.3 Medium-energy heavy ion irradiation . . . 192
6.3.1 Design of the experiment . . . 193
6.3.2 Low and moderate temperatures regimes . . . 194
6.3.2.1 Irradiations at 298 K . . . 194
6.3.2.2 Irradiations at 573 K . . . 194
6.3.2.3 Discussion . . . 194
6.4 Thermodynamics of alloys, degradation mechanisms and accelerated damage in MIAMI experiments . . . 198
6.5 Summary and conclusions . . . 201

7 Synthesis, characterisation and radiation resistance of high-entropy alloy thin film coatings 203
7.1 Preface and motivations . . . 203
7.2 Objectives and perspectives of the research reported in this chapter . 204
7.3 Synthesis and characterisation of the HEATF on Si substrates . . . 206
7.3.1 Deposition conditions and methodology . . . 206
7.3.2 Results . . . 207
7.3.3 Discussion . . . 211
7.3.3.1 The nucleation and growth dynamics and the thermodynamics of HEATFs . . . 211
7.3.3.2 Twinning and surface roughening . . . 213
7.3.4 Conclusions . . . 214

7.4 Synthesis and characterisation of the HEATF on Zircaloy-4^{TM} 214
7.4.1 Deposition and methods 215
7.4.2 Characterisation at the mesoscale 215
7.4.3 Characterisation at the nanoscale 218
7.4.4 Discussion 218
7.5 Radiation resistance of the HEATF deposited on Zircaloy-4^{TM} 221
7.5.1 The design of the experiment 221
7.5.2 Results and discussion 222
7.5.2.1 Microstructural response of the HEATF/Zircaloy-4^{TM} system under *in situ* TEM heavy ion irradiation 222
7.5.2.2 Microstructural response of the TiN thin film under *in situ* TEM heavy ion irradiation 225
7.5.2.3 Quantitative comparison between the radiation response of HEATF and TiN coatings 227
7.6 Conclusions and perspectives for HEATFs in the accident tolerant fuels technology 231

8 Neutron and heavy-ion irradiation effects on Ti-based MAX phases 233
8.1 Introduction and background 233
8.2 Neutron irradiation effects in Ti-based MAX phases at high temperatures 235
8.2.1 Materials and Methods 235
8.2.2 Results and discussion on the neutron irradiation response of Ti-based MAX phases 236
8.2.2.1 Pre-existing defects in the pristine microstructures . 237
8.2.2.2 Black-spots 239
8.2.2.3 Stacking faults 241
8.2.2.4 Cavities 242
8.2.2.5 Dislocation loops, lines and networks 244
8.2.2.6 Phase instabilities, recrystallisation and precipitation 249
8.2.3 Discussion of the effects of neutron irradiation on the Ti-based MAX phases and directions for future work 250
8.3 Heavy-ion irradiation effects at high temperatures 252
8.3.1 Materials and methods 253
8.3.2 Results 254
8.3.2.1 MAX phase decomposition upon thermal annealing at 1273 K 254
8.3.2.2 Comparison of the MAX phases results with the Ti and Al under heavy ion irradiation 260

8.3.2.3 Neutron and heavy ion irradiated MAX phases . . . 263
8.3.3 Discussion: contribution of this research and future directions 264
8.4 Conclusions . . . 265

9 Summary and Conclusions **267**
9.1 Summary . . . 268
9.2 Conclusions . . . 269
9.3 Recommendations for further research work . . . 270

Bibliography **273**

List of Figures

2.1 The crystal structures for (a) α–Fe, the body-centred cubic phase and (b) γ–Fe, the face-centred cubic. 10

2.2 The atomic structure of an austenitic stainless steel solid solution. Cr atoms are substitutional due to their atomic radius similarity with Fe whilst C atoms are interstitials. 11

2.3 The Fe-Cr phase diagram. (Reproduced from H. Bhadeshia and R. Honeycombe [32]) 12

2.4 Schematic entropy and Gibbs free energy curves for binary solid solutions. The maximum of the entropy curve is reached when x_B is equal x_A or 0.5 wt.%. Additionally, the minimum in the Gibbs free energy is lower as T increases: HEAs are supposed to be even more stable at high temperatures. 16

2.5 A quaternary equiatomic alloy system (a) before mixing and (b) after mixing to compose a HEA solid solution. 19

2.6 Schematic illustration of the severe lattice distortion concept. The atomic mismatch between the solutes causes a distortion within the crystal structure. 20

2.7 The unit cell of the Ti_3SiC_2 MAX phase. 23

2.8 Stress-strain cycles for (a) Ti_3SiC_2 and (b) Ti_2AlC showing their hysteretic and nonlinear elastic behaviour. Figure (a) shows how the nonlinear elastic behaviour changes with different grain sizes. In figure (b), the samples had similar grain sizes, but different densities. (Reproduced from Barsoum *et al.* [110]) 25

2.9 The collision between two bodies. Modified from [22]. 27

2.10 Representation of the contributions of both electronic and nuclear stopping powers as functions of energy for self-ion irradiations. Modified from [147]. 29

2.11 Collision cascades generated in Fe irradiated with several 134 keV Xe ions: (a) depth view and (b) transverse view. Calculations were performed using the SRIM2013Pro Monte Carlo code [148]. 30

2.12 Inelastic (a) and elastic (b) neutron scattering cross-section data for the Fe-56 isotope. Plots produced from the JEFF nuclear database [162]. 32
2.13 He bubbles formed in the microstructure of β–Zr during 6 keV He implantation at 1148 K. (Reproduced from [217]) 41
2.14 Dislocation loops and black-spots in neutron-irradiated copper at a fluence of 6.7×10^{17} n· cm^{-2} at 308 K. (Scanned from the original article by Silcox and Hirsch (1959) [223]). 43
2.15 The curves of engineering stress-strain obtained with irradiated 300-series stainless steels (extracted and adapted from Garner *et al.* [242, 243]): (a) AISI-316 irradiated in the HFIR around 373 K and tested at room temperature, (b) AISI-316 irradiated in the HFIR around 623 K and tested at 561 K and (c) EC316LN steel irradiated around 373 K in the LANSCE spallation source with mixed neutron and protons spectrum and tested at room temperature. The graph in (d) shows the contribution of different types of irradiation-induced defects to embrittlement of 300-series stainless steels as a function of the tensile testing temperature (extracted and adapted from Pawel *et al. apud* Garner [243]). 45
2.16 Irradiation temperature versus damage rate diagram which illustrates the region where RIS significantly occurs for austenitic stainless steels. (Modified from [272].) 48
2.17 Morphologies of defect cascades for different types of energetic particles with same incident energy (1 MeV) into a pure Ni target. $\bar{T}$ represents the average energy which is transferred to a PKA and ϵ is defined as the efficiency of producing point defects available to migrate and affect RIS and RIP effects. Extracted from Was *et al.* [286]. 53
2.18 (a) Radiation-induced voids (light contrast) and $M_{23}C_6$ precipitates (dark contrast) formed in an austenitic stainless steel neutron-irradiated at 653 K up to 21.7 dpa (reproduced from [301]) and (b) dark-field TEM micrograph showing voids, dislocation lines and networks in an neutron-irradiated austenitic stainless steel up to 15 dpa at 743 K (reproduced from [302]). Micrograph (c) shows the formation of the G-phase under neutron irradiation up to 11 dpa at 723 K for an austenitic stainless steel (reproduced from [303]). Note: the scale bar in (c) also applies to (b). 58

2.19 Comparison between neutron and proton irradiation on AISI-316 steel samples showing: (a) the profiles of RIS for Cr, Ni and Si measured on a grain boundary and (b) the evolution of the yield strength (assessed via hardness and shear punch tests) as a function of the irradiation dose. (Adapted and extracted from Was *et al.* [319]). 61
2.20 Tensile testing carried out in AISI-348 steel samples after neutron irradiation in the ATR showing the (a) yield strength, (b) ultimate tensile strength, (c) total elongation and (d) uniform elongation all as a function of the fluence. (Extracted and plotted from Beeston *et al.* [321]) 62
2.21 The AISI-348 steel microstructure after irradiation up to 39 dpa (2.55×10^{22} n·cm^{-2}) at 623 K showing the presence of voids (or He bubbles) and the G-phase (niobium-nickel-silicide): (a) underfocus and (b) overfocus TEM micrographs in bright-field. The inset in (b) is the diffraction pattern of the area showing Debye-Scherrer rings corresponding to the precipitates. (Adapted from Thomas and Beeston [322]) 63
2.22 The effects of neutron irradiation on the FeCrMnNi HEA showing the microstructures of the alloy at (a) 0.1 and (b) 1 dpa. The diffraction pattern inset in (a) reveals no precipitation of secondary phases. The mechanical response of the alloy to neutron irradiation showing (a) the tensile curves and (b) the measured hardness. (Extracted and adapted from Li *et al.* [339]) 66

3.1 The ion beam sputter-deposition system in the Ion Beam Centre at the University of Huddersfield [376]. 80
3.2 The TenuPol-5 jet electro-polishing station at the MIAMI facility: A is the station controller, B the cold stage vessel, C the electro-polishing unit and D the sample holder. 81
3.3 A 3 mm disk of the AISI-348 steel electro-polished in the TenuPol-5 system. 82
3.4 Focused ion beam steps to produce TEM samples of the HEA: (a) sample as received, (b-c) milling and thinning, (d-f) the sample is cleaved from the cross sectional cut, (g) attaching to the TEM grid by depositing C and (h) making it electron transparent using the ion beam. 83
3.5 A cross-sectional profile of a common TEM. (Reproduced from [384].) 89
3.6 Modes of imaging using diffraction contrast: (a) bright-field (BFTEM) and (b) dark-field (DFTEM). (Modified from [388]) 94

3.7 Typical ray diagram in STEM microscopes. (Adapted from [389].) . . 96
3.8 The MIAMI-1 facility schematics. (Reproduced from [393].) 99
3.9 The MIAMI-1 final deflection system [393] (left) and the JEOL JEM 2000FX TEM. 100
3.10 Overview of the MIAMI-2 facility. (Courtesy of Dr J.A. Hinks.) . . . 101
3.11 The MIAMI-2 facility schematics. (Courtesy of Dr. J.A. Hinks) . . . 103
3.12 The mixing magnet and the beam section that allows the ion beam coupling with the microscope. (Courtesy of Dr. J.A. Hinks.) 103
3.13 The profile of neutron fluxes at HFIR when the reactor core operates at 85 MW. Fluxes of the order of 10^{15} neutrons·cm^{-2}·s^{-1} can be achieved. Source: ORNL *apud* Wikipedia [397]. 106
3.14 The several effects of the electron beam interaction with the specimen within a SEM is exhibited in (a) and (b) showing that the occurrence of these effects is a function of the electron beam depth of penetration, *i.e.* the energy of the incident beam and the material under analysis. 108
3.15 Demonstration of MVSA refinement of STEM-EDX maps acquired from a neutron-irradiated steel. Note: These figures are an adaption from a work authored by Burke, Watanabe, Williams and Hyde in 2006 [408]. 111
3.16 Thickness map obtained with a typical sample using the EFTEM capabilities in the Hitachi H-9500. The calibration bar (top right) exhibit the values for thickness in nanometres after conversion using equation 3.13. 114

4.1 SEM-BSE micrograph of the AISI-348 steel microstructure as-received after electro-polishing. 118
4.2 BFTEM micrographs of the AISI-348 showing a set of images (a) at focus, (b-c) under- and over-focused, respectively, with a defocus degree of ±1000 nm. Note: the scale marker in (a) also applies to (b) and (c). 119
4.3 (a) The microstructure of the steel (and (b) its diffraction pattern) with a Nb(C,N) particle, (c) a BFTEM image with the selected-area aperture in and (d) the corresponding diffraction pattern of a region containing twins in the microstructure of the AISI-348 steel as-received. 121
4.4 EFTEM analysis of the Nb(C,N) nanoparticles. Limitations of the EFTEM technique in the Hitachi H-9500 impair the detection of elements like C and N. 123
4.5 STEM-EDX analysis of the Nb(C,N) nanoparticles. 124

4.6 EDX spectrum of the AISI-348. The quantification is shown in table 4.3. . . . 125
4.7 SEM-BSE micrograph of the FeCrMnNi HEA after synthesis and heat treatment. Courtesy of Professor Steve J. Zinkle (UT/ORNL) [338]. . 128
4.8 BFTEM micrographs of the FeCrMnNi HEA showing (a–c) a set of images taken at, under- and over-focus, respectively. The defocus (b) and (c) was 800 nm. The diffraction pattern (d) corresponds to the region selected by the SAED aperture indicated in (c). The BFTEM micrograph (e) shows part of the matrix free of annealing twins. The figure in (f) shows that when the matrix is selected without twins, the DP (g) does not exhibit satellite spots. Note: the scale marker in (a) also applies to (b) and (c). . . . 129
4.9 EDX spectrum of the FeCrMnNi HEA. The quantification is shown in table 4.5. . . . 130
4.10 The microstructures of the Ti_2AlC (a) and the Ti_3SiC_2 (b) at the microscale. The red squares indicate the area where the EDX analyses (section 4.4.2) have been carried out. Note: the scale marker in (a) also applies to (b). . . . 131
4.11 The microstructure of both Ti-based $M_{n+1}AX_n$ at the nanoscale. Micrographs (a) and (b) show the Ti_2AlC while (c) and (d) show the Ti_3SiC_2. . . . 132
4.12 EDX spectrum of the Ti-based $M_{n+1}AX_n$ phases. The quantification for both materials are shown in the tables 4.6 and 4.7. . . . 134
4.13 The EDX qualitative characterisation of the dark grey and stoichiometric MAX phases present in both Ti_3SiC_2 (top) and Ti_2AlC (bottom) microstructures. . . . 135
4.14 SEM-BSE elemental EDX mapping of both Ti_3SiC_2 (top) and Ti_2AlC (bottom). . . . 136

5.1 (a) The implantation depth; (b) the distributions of vacancies per Ångström-ion from SRIM for 6 keV He and 134 keV Xe ions and (c) the fluence-to-dpa conversion. . . . 141
5.2 A set of sequential micrographs showing the microstructural evolution of the (a-d) FeCrMnNi HEA and the (e-h) AISI-348 steel as function of dose for light ion irradiations using 6 keV He at 298 K. Note: the scale marker in (a) applies to (b-d) and the scale marker in (e) applies to (f-h). All micrographs were recorded with an objective lens underfocus of 1000 nm. . . . 143

5.3 BFTEM micrographs of the FeCrMnNi HEA (a) before irradiation and (b–c) after 6 keV He irradiation up to 4 dpa and (d) following subsequent annealing at 673 K. The inset in micrograph (d) is a diffraction pattern taken of that area. Note: the scale marker in (c) also applies to (d); the micrograph in (a) was recorded with an objective lens underfocus of 1500 nm whilst micrographs (b–e) were recorded with an objective lens underfocus of 1000 nm. 144
5.4 BFTEM micrographs of the AISI-348 steel (a) before irradiation, (b) after 6 keV He irradiation to 4 dpa and (c–d) after subsequent annealing at 673 K. Note: the scale marker in (a) also applies to (c) and the scale marker in (b) also applies to (d); all micrographs in the figure were recorded with an objective lens underfocus of 1000 nm. . . 145
5.5 BFTEM micrographs of the AISI-348 steel irradiated with 6 keV He to 4 dpa (a) before annealing and (b) after annealing at 673 K. The BFTEM micrographs (c) and (d) show the microstructure of the steel in another area with He bubbles trapped at grain boundaries. Note: the scale marker in (a) also applies to (b) and the scale marker in (c) also applies to (d); all micrographs in the figure were recorded with an objective lens underfocus of 1000 nm. 146
5.6 A set of sequential micrographs showing the microstructural evolution of (a-d) the FeCrMnNi HEA and (e-h) the AISI-348 steel as a function of dose for heavy ion irradiation using 134 keV Xe at 298 K. Note: the scale marker in (a) applies to (b-d) and the scale marker in (e) applies to (f-h). All micrographs were recorded with an objective lens underfocus of 1000 nm. 148
5.7 BFTEM micrographs of the FeCrMnNi HEA (a) before irradiation and (b–c) after 134 keV Xe irradiation to 4 dpa. The BFTEM micrograph (d) shows the FeCrMnNi HEA at 4 dpa after subsequent annealing at 673 K. The inset in (d) is the diffraction pattern taken of that area after the irradiation and annealing. Note: the scale marker in (a) also applies to (b) and the scale marker in (c) also applies to (d); all micrographs in the figure were recorded with an objective lens underfocus of 1000 nm. 149

5.8 BFTEM micrographs of the AISI-348 (a) before irradiation and (b–c) after 134 keV Xe irradiation up to 4 dpa. The BFTEM micrographs (e–g) show the damage microstructure of the AISI-348 after 4 dpa and subsequent annealing at 673 K. Note: the scale marker in (a) also applies to (b) and (e). The scale marker in (c) also applies to (f); all micrographs were recorded with an objective lens underfocus of 1000 nm. 150
5.9 BFTEM micrographs of the AISI-348 microstructure showing (a–b) He bubbles trapped at the Nb(C,N) nanoparticle interfaces after 4 dpa and subsequent annealing. The BFTEM micrograph in (c) shows the presence of nanometre-sized secondary phases around a Nb(C,N) nanoparticle formed after 134 keV Xe irradiation to 4 dpa and subsequent annealing and the micrograph in (d) also shows that in some Nb(C,N) nanoparticles, Xe bubbles were observed at the nanoparticle interface. All micrographs in the figure were recorded with an objective lens underfocus of ≈ 1000 nm. Note: the scale bar in (d) also applies to (c). 152
5.10 (a) The BFTEM micrograph shows the SAED aperture around a Nb(C,N) nanoparticle in the austenite matrix after heavy ion irradiation (134 keV Xe) to 4 dpa and subsequent annealing. (b) Shows the diffraction pattern corresponding to (a). DFTEM micrograph in (c) shows the presence of small crystallites around the Nb(C,N) particles resulting from the precipitation of secondary (nanometre-sized) phases. 153
5.11 Average bubble sizes (diameter) as a function of dose and after irradiation and thermal annealing for (a) 6 keV He and (b) 134 keV Xe ion irradiations. Note: the data presented in graph (a) is from Kalchenko *et al.* [445]. 155
5.12 Average areal densities of bubbles as a function of dose and after irradiation and thermal annealing for (a) 6 keV He and (b) 134 keV Xe ion irradiations. Note: the data presented in graph (a) is from Kalchenko *et al.* [445]. 156
5.13 The size (diameter) distribution of He bubbles in the matrix of the (a) FeCrMnNi HEA and (b) AISI-348 after 4 dpa and subsequent annealing to 673 K. 157
5.14 The size (diameter) distribution of He bubbles at interfaces in the (a) FeCrMnNi HEA and (b) AISI-348 after 4 dpa and subsequent annealing to 673 K. 158

5.15 The size (diameter) distribution of Xe bubbles in the matrix of (a) the FeCrMnNi HEA and (b) AISI-348 steel after 4 dpa and subsequent annealing to 673 K. 158
5.16 The size (diameter) distribution of Xe bubbles at interfaces of (a) the FeCrMnNi HEA and (b) AISI-348 steel after 4 dpa and subsequent annealing to a temperature of 673 K. 159
5.17 Trends resulting from the size analysis of He and Xe bubbles at interfaces and in the matrix for both the FeCrMnNi HEA and AISI-348 after irradiation up to 4 dpa with (a–b) He and (c–d) Xe including subsequent annealing to 673 K. 159

6.1 (a) The implantation depth, (b) the distributions of vacancies per Ångström-ion and (c) the fluence-to-dpa conversion for 30 keV Xe ions into the FeCrMnNi HEA and the AISI-348 steel calculated using the SRIM code. Calculations were carried out with 5000 ions in the "quick" calculation mode using the Kinchin-Pease model. 165
6.2 Microstructural evolution of the (a–c) FeCrMnNi HEA and (d–f) the AISI-348 steel under low-energy heavy ion irradiation at 293 K. Notes: scale bar in (a) applies to all micrographs in the figure. All micrographs were underfocused (≈1000 nm) and the contrast of micrographs (d–f) was slightly enhanced. The purple circles in figures (b–c) show the annihilation of black-dots in the FeCrMnNi HEA and the yellow arrows in figures (e–f) show the nucleation and evolution of precipitates in the AISI-348 steel. 167
6.3 Low-energy heavy ion irradiation at 293 K to higher doses, 21 dpa, show that (c) precipitates are observed in the matrix phase of the AISI-348 whilst (a-b) the HEA matrix is still single-phase with the twins (satellite spots in the DP at (a) highlighted with a blue circle) which are better visualised in the DFTEM micrograph (b). Note: all micrographs were underfocused (≈1000 nm). 169
6.4 Microstructural evolution of (a–c) the FeCrMnNi HEA and (d–f) the AISI-348 under low-energy heavy ion irradiation at 573 K. Note: scale bar in (a) applies to all micrographs in the figure. Images are underfocused (≈1000 nm). 170

6.5 Low-energy heavy ion irradiations at 573 K, showing the microstructure of (a) the FeCrMnNi HEA with some Xe bubbles at higher fluences, 6.8×10^{16} ions·cm^{-2} (25 dpa) and (b) the AISI-348 steel showing that the austenite phase was decomposed at 5.1×10^{16} ions·cm^{-2} (19 dpa). (c) At a fluence of 1.0×10^{17} ions·cm^{-2} (37 dpa), bubble growth and precipitation are observed to occur in the AISI-348 steel and (d) black-spots evolve to a maximum size of 20 nm (at 21 dpa). The same was not observed to occur in the FeCrMnNi HEA. Note: (a–b) are underfocused to ≈1000 nm; the insets in (c) and (d) are defocused by ± 300 nm and ± 1000 nm, respectively. 171
6.6 Microstructural evolution of (a–d) the FeCrMnNi HEA and (e–h) the AISI-348 steel under low-energy heavy ion irradiation at 873 K. Note: scale bar in (a) applies to all micrographs in the figure and all images are underfocused by ≈1000 nm. 173
6.7 The microstructures of (a–b) the FeCrMnNi HEA and (c–d) the AISI-348 steel irradiated to 4.2×10^{16} ions·cm^{-2} (15 dpa) at 873 K. Dark grey zones have been observed to form in both alloys at these dose levels which suggests the occurrence of RIS and the formation of precipitates. Note: The underfocused micrographs (b) and (c) were taken with an underfocus of ≈1000 nm and 1600 nm, respectively, and the scale marker in (a) applies to all micrographs in the figure. The arrows indicate the areas of RIS. 174
6.8 The microstructure of the FeCrMnNi HEA after annealing at 1073 K for 10 minutes. 175
6.9 Low-magnification images of microstructural evolution of the austenite phase under 30 keV Xe irradiation at 1073 K. BFTEM micrograph shows (a) the microstructure after 30 minutes of annealing at 1073 K and (b–d) the subsequent microstructural evolution under irradiation up to 10 dpa. Note: the scale bar in (a) applies to all micrographs in the figure. 176
6.10 Post-irradiation screening of the AISI-348 steel after 1.3×10^{17} ions·cm^{-2} (46 dpa) at 1073 K: (a) and (b) are low and high-magnifications BFTEM micrographs, respectively, (c) selected-area diffraction pattern corresponding to the inset shown in (b) and (d) is the simulated DP from CrystalMaker with the Badjuk *et al.* dataset [454] used to index the new phase that formed under the present irradiation conditions. 177

6.11 Quantitative data for the new BCC phase (α'-phase) that nucleated and grew in the AISI-348 steel matrix under 30 keV Xe ion irradiation at 1073 K showing: (a) the average diameter and (b) volumetric density. Note: results are compared with atom probe tomography data published by Briggs *et al.* [455] on neutron-irradiated FeCrAl alloys (composition in wt.%); error in sizes and density were not provided (or were to small to be detected in the plots) by Briggs *et al.* in their paper. 178
6.12 A set of sequential BFTEM micrographs showing the real-time evolution of nanometre-sized precipitates in the austenite matrix of the AISI-348 steel at 1073 K. Note: the scale bar in the micrograph at 0 dpa applies to all images in the figure. 179
6.13 Formation of nanometre-sized precipitates in the AISI-348 steel before irradiation and after annealing at 1073 K (a) and after 30 keV Xe irradiation up to 17 dpa at 1073 K (b). Note: The scale bar in (a) also applies to (b). 180
6.14 (a) Average precipitate diameter and (b) average volumetric density as a function of the irradiated dose for accelerated ageing due to heavy ion irradiation in two austenitic stainless steels: the AISI-348 steel (this work) monitored *in situ* within the TEM during irradiation and HR3C steel (Jin *et al.* [456]) investigated with ion irradiation followed by *ex situ* TEM. 180
6.15 Low-magnification STEM-EDX mapping of the AISI-348 steel irradiated to 1.3×10^{17} ions·cm^{-2} (46 dpa) at 1073 K. Note: the solid circles show the α'-phase and the dashed circles show the Nb(C,N) nanoparticles. 182
6.16 High-magnification STEM-EDX mapping of the AISI-348 irradiated to 1.1×10^{17} ions·cm^{-2} (40 dpa) at 1073 K. RIP occurs in the austenite matrix and also around the Nb(C,N) nanoparticles. The size of the precipitates is around 40 nm. 183
6.17 TEM characterisation of the $M_{23}C_6$ precipitates: the micrograph (a) is a selected-area diffraction pattern taken from the area shown in the inset in (b) which is a DFTEM micrograph using the (004) reflection. The fluence was around of 1.3×10^{17} ions·cm^{-2} (46 dpa). 184

6.18 Post-irradiation MVSA analysis obtained from the STEM-EDX maps in figure 6.15 at 46 dpa. The amplitude map in (a) and its respective (a1) EDX spectrum represents the austenite phase depleted in Cr after irradiation. Similarly, the amplitude maps in (b) and (c) and their respective EDX spectra (b1) and (c1) show the Cr-rich α'-phase and the Nb(C,N) phase, the latter existing before irradiation. 185
6.19 Estimation of area phase fractions for the (a-b) Cr-rich α' at 46 dpa and (c-d) τ-$M_{23}C_6$ precipitates at 17 dpa. Note: The micrographs (b) and (d) are the images treated (known as threshold images) with the ImageJ software to estimate the area phase fraction. 186
6.20 Equilibrium phase diagrams for the AISI-348 steel calculated using Thermo-calc® [415]. The molar fraction of the phases present in the steel system in the temperature range 500 to 2000 K is shown in (a) and (b) is a zoomed-region from the bottom part of the phase diagram (a) evidencing the presence of Nb(C,N) and $M_{23}C_6$ precipitates as minor phases. Elemental compositions of the γ-Fe (austenite, the matrix phase) and the Cr-rich α' phases are shown in (c) and (d), respectively. 190
6.21 (a) The implantation profile, (b) the distributions of vacancies per Ångström-ion and (c) the fluence-to-dpa conversion for 300 keV Xe ions into the FeCrMnNi HEA and the AISI-348 steel calculated using the SRIM code. Calculations were carried out with 5000 ions in the "quick" calculation mode using the Kinchin-Pease model. 193
6.22 The microstructure of (a) the AISI-348 steel and (b) the FeCrMnNi HEA at a fluence of 3.9×10^{16} ions·cm^{-2} (123 dpa) at 298 K. The micrographs (c) and (d) were taken in other regions of the sample with (c) the Nb(C,N) nanoparticle where Xe bubbles are observed to grow at the interfaces. Note: the scale marker in (a) applies to all micrographs in the figure. All micrographs were taken at an underfocus of 1000 nm. 195
6.23 The microstructure of the (a) AISI-348 and the (b) FeCrMnNi HEA at a fluence of 4.4×10^{16} ions·cm^{-2} (140 dpa) at 573 K. Note: the scale marker in (a) also applies to (b). All micrographs were taken at an underfocus of 1000 nm. 196
6.24 Collision cascades profile comparison between 30 and 300 keV Xe ions in the FeCrMnNi HEA (same applies for the AISI-348). The figures are displaying the transport of five Xe ions into the alloys. Note: blue dots represent the recoils and red dots are the PKAs. 197

7.1 A HEATF lamella attached to a Mo TEM grid during the FIB sample preparation. Note: micrograph taken with SEM-BSE. 207
7.2 The NETF microstructure at the nanoscale. The circle in (a) represents the selected area corresponding to the diffraction pattern in (b). 208
7.3 Several BFTEM micrographs showing the microstructure of the NETF from 0 to 10° x-axis tilt. Note: the dashed region in (a) represents the area analysed to compose image 7.4. 209
7.4 (a) The grain pattern of the NETF constructed from the BFTEM micrographs taken in the tilting range of 0–10°. The dark field TEM micrographs (b) and (c) show the microstructure of the NETFs at 0 and 10°, respectively. 210
7.5 The microstructure of the HEATF showing (a) BFTEM micrograph and (b) the corresponding diffraction pattern. (c) The DFTEM micrograph showing the presence of larger grains when compared with the NETF (around 100 nm). The BFTEM micrographs (d-e) show the planar defects in the HEATF. 210
7.6 Histograms of the grain sizes measured from the microstructures of both NETF and HEATF as-deposited. The average grain size for the NETF and HEATF are 26.6±1.3 and 109.4±10.7 nm, respectively. The HEATF has bigger grains, but the dispersion of sizes is also larger than the NETF. 212
7.7 Speckled contrast in underfocused bright field TEM micrographs due to surface roughening in both (a) NETF and (b) HEATF. The micrographs were recorded with an objective lens underfocus of 0.95 μm. Note: the scale bar in (a) also applies to (b). 213
7.8 SEM-BSE micrographs showing (a) the microstructure of the Zircaloy-4^{TM} substrate before the deposition and (b) the FeCrMnNi HEATF after deposition on the Zircaloy-4^{TM} substrate. Small changes in the BSE contrast after deposition as shown in (b) are attributed to different crystallographic orientations of the substrate as shown in (a). . 216
7.9 SEM-BSE elemental map of the FeCrMnNi HEATF as deposited on the Zircaloy-4^{TM} substrate. These elemental maps are showing uniformity in the distribution of coating elements on the substrate: no secondary phase was detected at this scale. 217
7.10 EDX spectrum of the FeCrMnNi HEATF as deposited on the Zircaloy-4^{TM} substrate. The elemental quantification is shown in table 7.3. . . 218

7.11 BFTEM micrographs of the FeCrMnNi HEATF deposited on Zircaloy-4^{TM} (a) at focus and (b) underfocused (1 μm) showing porosity in the oxide layer. The micrographs show the three-layer structure with the Zircaloy-4^{TM} substrate, the oxide layer and the FeCrMnNi HEATF. . 219
7.12 (a) BFTEM micrograph of the HEATF microstructure. (b) Diffraction pattern taken in the region of the interface between the HEATF and the Zircaloy-4^{TM} substrate as shown in the inset in (a). The diffraction pattern contains the Zircaloy-4^{TM} reflection spots, the HEATF reflection spots and the amorphous Zr oxide ring. The BFTEM and DFTEM micrographs (c) and (d), respectively, show the presence of planar defects in the thin film. Note: the underfocus degree in (a) and (c) was 1000 nm. 220
7.13 (a) The implantation and (b) damage profiles for the FeCrMnNi HEATF and the Zircaloy-4^{TM} for the 134 keV Xe ion irradiation. . . 222
7.14 The microstructural evolution of the FeCrMnNi HEATF and the Zircaloy-4^{TM} substrate monitored *in situ* within the TEM from (a) 0 dpa to (d) 15.4 dpa. Note: all the micrographs in the figure are underfocused (1 μm) and the scale bar in (a) also applies to (b-d). . . 223
7.15 EFTEM micrographs of the post-irradiated FeCrMnNi HEATF deposited on the Zircaloy-4^{TM} substrate at the end of the irradiation experiment at 15.4 dpa. 224
7.16 The microstructural evolution of the TiN thin film monitored *in situ* within the TEM and irradiated at similar conditions to the FeCrMnNi HEATF. Note: all micrographs in the figure are underfocused ($\approx$ 1 μm) and the scale marker in (a) applies to all micrographs in the figure. 226
7.17 EFTEM micrographs of the TiN thin films irradiated to 6.2 dpa showing Ti segregation. Results were further confirmed by STEM-EDX analysis of the same irradiated lamella. The bottom figure is the multivariate statistical analysis (MVSA): (a) the EDX spectrum corresponding to the (b) spectral image. The spectral image (b) in combination with the EDX spectrum in (a) indicates the presence of Ti within Xe bubbles after 6.2 dpa of irradiation. 227
7.18 *In situ* TEM monitoring of Xe bubble nucleation and growth (a-c) in the HEATF and (d-f) in the TiN as a result of the heavy ion irradiations reported in this section. All micrographs in the figure were recorded with an objective lens underfocus of $\approx$ 1000 nm Note: scale bar in (a) also applies to (b-c) and the scale bar in (d) also applies to (e-f). 229

7.19 Histograms of sizes (diameter) of Xe bubbles as a function of the irradiated dose in (a) TiN and (b) HEATF coatings. 230
7.20 (a) Average Xe bubbles diameter and (b) average areal density of Xe bubbles as a function of the irradiation dose for TiN and HEATF coatings. 230

8.1 The ternary phase diagrams in the isothermal section of 1273 K and 1 atm for the systems (a) Ti–Si–C [441] (b) and Ti–Al–C [439]. (Adapted from references [441] and [439].) 234
8.2 The crystal structures of (a) Ti_2AlC and (b) Ti_3SiC_2 visualised using CrystalMaker with data available in the literature [429, 430]. Both materials have a hexagonal-compact crystal structure. The laminated nature of the materials is clearly visible. 236
8.3 BFTEM micrographs of the pristine Ti-based MAX phases recorded at room temperature showing (a) the presence of some black-spots and (b) artefacts resembling TiH in the Ti_2AlC; (c) a dislocation network viewed at the basal zone axis in the Ti_3SiC_2 and (d) black-spots concentrated in a secondary phase. The micrograph (e) shows pre-existing cavities in one Ti_3SiC_2 grain. Note: micrograph (e) has been recorded with the objective lens underfocused by $\approx$ 1000 nm whilst micrographs (a–d) are in focus. 238
8.4 (a) A BFTEM micrograph of the Ti_2AlC at 2 dpa showing black-spot damage and (b–c) DFTEM micrographs at 2 and 10 dpa, respectively, showing the evolution of the black-spots as a function of the dose. The areal density of black-spots has increased on going from 2 to 10 dpa. (d) and (f) BFTEM micrographs of Ti_3SiC_2 at 2 and 10 dpa, respectively, showing that black-spot damage is preferentially concentrated within the secondary particles (SiC and TiC). (e) Black-spot damage in the Ti_3SiC_2 close to grain-boundaries of the matrix phase (seen only at 2 dpa). Note: the scale marker in (a) also applies to (b–c). 240
8.5 Long stacking faults observed parallel to the [0001] zone axis in Ti_3AlC_2 neutron irradiated to 2 dpa at 1273 K. 241
8.6 BFTEM micrographs showing cavities in Ti_2AlC at (a) 2 dpa and (b) 10 dpa. (c) Ti_2AlC at higher magnification showing the presence of small voids and black-spots. Ti_3SiC_2 at (d) 2 dpa and (e) 10 dpa showing voids in the matrix and along grain boundaries. Note: the defocus for (a–d) was 300 nm and for (e) was 1000 nm. 243

8.7 (a-b) Dislocation loops observed in the Ti_2AlC at 2 dpa and (e–f) at 10 dpa; (c–d) in the Ti_3SiC_2 at 2 dpa and (g–h) at 10 dpa. The Burgers vector analysis indicated that these are <a> loops constrained within basal planes. Note: the scale marker displayed in (a) applies to all micrographs in the figure. 245
8.8 (a) A high-resolution TEM micrograph of a dislocation loop in neutron irradiated Ti_3SiC_2 at 2 dpa and (b) a Fourier filtered image from the micrograph (a) showing the interstitial nature of the loop. The micrograph in (a) was taken at focus, without an objective aperture and looking down the $[\bar{1}2\bar{1}0]$ direction. Note: the scale marker in (a) also applies to (b). 246
8.9 BFTEM micrograph taken along the basal zone axis [0001] (a) Ti_3SiC_2 at 2 dpa; (b) Ti_3SiC_2 at 10 dpa; (c) Ti_2AlC at 2 dpa; and (d) Ti_2AlC at 10 dpa. Note: the scale marker in (a) applies to all micrographs in the figure. 247
8.10 Quantitative data for dislocation loops obtained from this work in both the Ti_2AlC and the Ti_3SiC_2 at 2 and 10 dpa neutron-irradiated at 1273 K and from data available in the literature reported by Tallman *et al.* [356] for both Ti_3SiC_2 and Ti_3AlC_2 at 1.6 and 3.4 dpa neutron-irradiated at 1008 K: (a) loop sizes and (b) areal densities. . 248
8.11 The microstructure of (a–c) Ti_2AlC and (d–f) Ti_3SiC_2 at 10 dpa where irradiation-induced phases have been detected. Note: the yellow arrows in the inset in (b) show the spots where a satellite spot (from the precipitates) was observed. 251
8.12 (a) The implantation and (b) damage profiles for 700 keV Kr ions into Ti_2AlC and Ti_3SiC_2, calculated from SRIM [148]. 253
8.13 The microstructure of the Ti_3SiC_2 (a) before and (b) during *in situ* TEM annealing at around 1073 K. The microstructure of Ti_2AlC (c) before and (d) during *in situ* TEM annealing at around 1273 K. Note: scale bar in (a) also applies to (b) and scale bar in (c) also applies to (d). 255
8.14 BFTEM and DFTEM characterisation of the Ti_3SiC_2 after 2 hours of *in situ* TEM annealing at 1273 K. DFTEM micrograph 1 shows pre-existing defects in the Ti_3SiC_2 whereas micrographs 2-3 show the presence of secondary phases after annealing. 256
8.15 EFTEM characterisation of the Ti_3SiC_2 matrix phase decomposition after *in situ* TEM annealing for 2 hours at 1273 K showing small embryos that nucleated upon annealing and the EFTEM analysis indicated they are enriched in Si. 258

8.16 BFTEM images of cross-section specimens of (left) Ti_2AlC and (right) Ti_3SiC_2 after neutron irradiation to 2 dpa at 1273 K. The decomposition layer can be clearly seen in both materials. 259
8.17 Comparison of heavy ion irradiation of Ti, Al, Ti_2AlC and Ti_3SiC_2. . 261
8.18 Cavities observed in the pure Ti and Al at around 1 and 2.7 dpa, respectively. 262
8.19 Diffraction patterns of the Ti-based MAX phases before and after heavy ion irradiation up to 5 dpa. No significant alterations were observed. 262
8.20 A single experimental case where a direct comparison with the neutron- and heavy-ion irradiated Ti_2AlC exhibited led similar damage microstructures. 263

List of Tables

2.1 Thermodynamic potentials and microstructure systems in alloys. (Adapted from [55].) 19
2.2 Comparison between neutron and ion irradiation methodologies. . . . 55

3.1 Materials and alloys used in this doctoral research. 76
3.2 Nominal composition of the AISI-348 steel [359]. 78

4.1 Nominal composition of the AISI-348 steel [359]. 117
4.2 The elemental composition of the Nb(C,N) nanoparticles measured using STEM-EDX. 124
4.3 The elemental composition of the austenitic stainless steel AISI-348 measured by SEM-EDX (the error is ±5% for each value). 125
4.4 The elemental composition of the austenitic stainless steel AISI-348 measured by ICP-OES (the error is ±1% for each value). 126
4.5 The elemental composition of the FeCrMnNi HEA measured by SEM-EDX (the error is ±5% for each value). 130
4.6 The elemental composition of the Ti_2AlC measured by SEM-EDX (error is 5% of each value). 133
4.7 The elemental composition of the Ti_3SiC_2 measured by SEM-EDX (error is 5% of each value). 134
4.8 The elemental composition of the dark grey phase present in the Ti_3SiC_2 measured by SEM-EDX (error is 4% of each value). 135
4.9 The elemental composition of the dark grey phase present in the Ti_2AlC measured by SEM-EDX (error is 4% of each value). 136
4.10 A comparison of the materials studied in this doctorate work. 139

5.1 The number of vacancies generated by one ion collision (SRIM calculation statistical error is ≈ 3% using 5000 ions for the calculations). . 142

6.1 Low-energy heavy ion irradiation effects in the FeCrMnNi HEA and the AISI-348 (in the dose range 0-50 dpa)*. 188

7.1 The elemental composition of the FeCrMnNi HEATF measured by SEM-EDX. 207
7.2 The elemental composition of the Zircaloy-4^{TM} prior to deposition as measured by SEM-EDX. 217
7.3 The elemental composition of the HEATF on Zircaloy-4^{TM} after deposition and measured by SEM-EDX. 217

8.1 Areal density and average size of dislocation loops obtained in this work. 249

Acknowledgements

This is Oscar Wilde, an Irish genius:

"I choose my friends not by their skin or other archetype, but by the pupil.
They have to have questioning shine and unsettled tone.
I'm not interested in the good spirits or the ones with bad habits.
I'll stick with the ones that are made of me being crazy and blessed.
From them, I don't want an answer, I want to be reviewed.
I want them to bring me doubts and fears and to tolerate the worst of me."

I dedicate my PhD thesis to my beloved Pamela for her eternal patience and comprehension and by supporting me in the most difficult moments.

The scientific work present in this doctorate thesis was performed with incommensurable help and patience of good friends and collaborators. For them, I would like to express my deepest gratitude:

Firstly, I must thank Prof. Stephen E. Donnelly my dear supervisor who has opened the doors of his beautiful country and powerful laboratory for a fuzzy and non-linear student like me. And also thank you, Prof., for teaching me your precious wisdom and restless desire for the scientific truth. Also to Dr. Jonathan A. Hinks (MIAMI team research leader) for the opportunity to work as a PhD student at the MIAMI facilities and for your friendship during my whole PhD journey.

I don't have many words to describe how much Dr. Philip D. Edmondson have helped my during this doctorate research, but I can say that it was a real honour to have worked and collaborated with him. Dr. Edmondson is a extremely competent scientist in condensed-matter and materials physics and one of the bests scientists in electron microscopy and radiation damage that I ever saw and with whom I am still learning quite a lot. Thank you very much Phil, for your co-supervision, friendship and for allowing this research to be performed through our scientific partnership and I am sorry to have spent a lot of your research money.

I would like to express my deepest gratitude to a friend, scientific partner and co-supervisor, Dr. Graeme Greaves, one of the bests experimental physicists that I have worked with and the best man in measurements in England, for his accurate ability of correcting and guiding me and my friend Osmane Camara.

For their scientific support, co-supervision and friendship throughout my PhD journey, I would like to thank Prof. Vladimir Vishnyakov for the scientific partnership and personal friendship. I would like to express my deepest gratitude for you, your patience, support and guidance throughout my research. I will never forget our moments in the laboratory during the synthesis of our thin solid films. Also, thank you very much for being there when I needed you the most: you put me back on track several times. In my scientific life, I will carry with myself your brave and diamond spirit.

Thanks to the IBC-EMMA research fellows: Dr. Robert Harrison for teaching me the precious art of specimen preparation and advanced TEM techniques and for his close co-supervision of my scientific projects, Dr. Anamul Mir Haq Jeri for his infinite wisdom and support, Dr. Emily Aradi for her patience with me and also by very useful discussions on many aspects of materials sciences and scientific writing.

My big friend Osmane Camara: I would like to say thank you very much for all your friendship and help in my research. We have passed through countless setbacks, but we did it! Thanks also goes for the IBC-MIAMI PhD students team, Benjamin Clay, Hoang Le, Jacob Lewis-Fell, Mohammed Imtyaz Uddin, Italo Oyarzabal (UFRGS), Mohammed Hussein and Waleed Muftahby all their support, friendship and numerous joint collaborations. It was a real honour to work with all of you guys!

I have also to express my deepest gratitude to my friends at the Oak Ridge National Laboratory: Dr. José Arregui-Mena, Quinlan Smith and Dr. Chad Parish for their support and countless hours that they have helped me with inserting radiological activated samples into electron microscopes. Bill Cummings for the radiological protection training and his friendship. Stephanie G. Melton for all the help and Dr. Keith J. Leonard for the unique opportunity that I had to carry out part of this research work in his MSTD division. Also to Prof. Yanwen Zhang for the opportunity and honour to have let me work on her ongoing projects in nanocrystalline HEAs.

To Prof. Claudio Schön (EPUSP) and Prof. Cassiano R. E. de Oliveira (UNM) for their friendship and for believing in me throughout the early stages of my scientific career. I will be eternally grateful and proud of my scientific origins. Thanks also goes to some very special people: Prof. Francisco T. Degasperi (FATEC-SP), Prof. Ana R. Blak (IFUSP) and to Profs. Manfredo Tabacniks, Nemitala Added and Andre Bohomoletz from IFUSP. Also, very specially I would like to thank Maria E. R. Paiva and Aylton Paiva to partially fund my travel tickets when I moved to England.

I also would like to thank Professors Stefan Pogatscher, Helmut Antrekowitsch and Peter Uggowittzer at Montanuniversität Leoben by their support on my research work, friendship and by their infinite knowledge and wisdom. I am so honoured to

have the opportunity to work with you.

Thanks also goes to all the School of Computing and Engineering Research Administration staff for all their effective and fast academic support during my research period at the University of Huddersfield: Chris Sentence, Liz Rees, Nicola Williams, Sharon Forster, Lili Gilston and Gwen Wood.

To my parents Alice C. Quoos and Jose R. Tunes including my brother Eduardo A. Tunes Neto for their emotional support and dedication to me throughout my whole life. Also to Arnaldo Forner, Emily Forner and Zenite Martins Forner, for the friendship and patience. This thesis is specially dedicated *In memoriam* to Prof. Kenya Moore de Almeida Dias da Cunha and Prof. George Carter.

Abbreviations

AISI - American Iron and Steel Institute
AGR - Advanced Gas-cooled Reactor
BCC - Body-Centred Cubic
BSE - Backscattered Electrons
BFTEM - Bright-Field TEM
BWR - Boiling Water Reactor
DBTT - Ductile-Brittle Transition Temperature
DFT - Density Functional Theory
DFTEM - Dark-Field TEM
DOE - (The U.S.) Department of Energy
EBSD - Electron Backscatter Diffraction
EDX - Energy-Dispersive X-ray Spectroscopy
EELS - Electron Energy Loss Spectroscopy
EP - Electropolishing
FCC - Face-Centred Cubic
FIB - Focused Ion Beam
HCP - Hexagonal Close Packed
HAZ - Heat-Affected Zones
HEA - High-Entropy Alloy
HEATF - High-Entropy Alloy Thin Film
HFIR - High-Flux Isotope Reactor
IASCC - Irradiation-Assisted Stress Corrosion Cracking
IBSD - Ion Beam Sputter-Deposition
IMR - Institute for Materials Research
ICP-OES - Inductively Coupled Plasma Optical Emission Spectrometry
LAMDA - Low Activation Materials Development and Analysis Laboratory
MD - Molecular Dynamics
MIAMI - Microscope and Ion Accelerators for Materials Investigations
MTR - Materials Testing Reactor
MVSA - Multivariate Statistical Analysis
ONRL - Oak Ridge National Laboratory

ORAU - Oak Ridge Associated Universities
PAM - Plasma Arc Melting
PKA - Primary Knock-on Atom
PWR - Pressurized Water Reactor
RIP - Radiation-Induced Precipitation
RIPT - Radiation-Induced Phase Transformation
RIS - Radiation-Induced Segregation
SAED - Selected-Area Electron Diffraction
SEM - Scanning Electron Microscope
SF(T) - Stacking Fault (Tetrahedra)
SGTE - Scientific Group Thermodata Europe
SIA - Self-Interstitial Atom
SRIM - Stopping and Range of Ions on Matter
STEM - Scanning Transmission Electron Microscopy (& Microscope)
TEM - Transmission Electron Microscopy (& Microscope)
TWR - Travelling-Wave Reactor
UoH - University of Huddersfield
UT - University of Tennessee

Abstract

A study of the radiation response of two classes of prospective materials for future generations of nuclear reactors is presented in this thesis. These materials are highly concentrated alloys – commonly known as High-Entropy Alloys (HEAs) – and the Ti-based $M_{n+1}AX_n$ phase ternary carbides. Ion irradiation *in situ* within a Transmission Electron Microscope (TEM) was used to investigate the effects of energetic particle irradiation on these materials. This methodology allowed the real-time monitoring of the microstructural evolution of the studied materials whilst under irradiation over a wide variety of dose and temperature conditions of relevance to nuclear technology.

To shed light on the core effects responsible for enhanced radiation resistance in HEAs, such as the sluggish mobility of atomic defects and the superior thermodynamic stability, a quaternary HEA, FeCrMnNi, was selected for investigation. For this purpose, experiments with the FeCrMnNi HEA were directly compared with a conventional nuclear structural material, the austenitic stainless steel grade 348, which is an Fe-based alloy containing Cr, Ni and Mn as major alloying elements. The stainless steel 348 has the same elements as the HEA in solid-solution, but not in equiatomic composition: thus it can be considered as a "low-entropy" version of the FeCrMnNi HEA. It was shown that the sluggish diffusion property played only a minor rule in suppressing the nucleation and growth of He and Xe bubbles under irradiation. However, under heavy ion irradiation, the phase stability of the HEA was observed to be superior to its low-entropy counterpart, the steel, in the temperature range from 298 to 573 K: at higher irradiation temperatures both alloys displayed similar radiation responses. The results suggest (for the alloys investigated in this work) that the relationship between the key high-entropy core effects and superior radiation tolerance of HEAs is limited to low and moderate temperatures.

Following the results with the bulk FeCrMnNi HEA and given the possibility of designing radiation tolerant structural nuclear materials by tuning the elemental composition, High-Entropy Alloy Thin Films (HEATF) within the quaternary metallic system FeCrMnNi were developed through the technique of ion beam sputter-deposition. A complete synthesis and characterisation investigation was firstly performed on Si wafer substrates in order to demonstrate the feasibility of

depositing equiatomic metallic thin films within the FeCrMnNi system. Then, these thin films were deposited onto Zircaloy-4^{TM} substrates and their radiation tolerance was assessed under medium-energy, heavy ion irradiation *in situ* within a TEM. By comparing the radiation response of the HEATF with titanium nitride (a material currently under consideration for coating Zr alloys) using the ion irradiation with *in situ* TEM technique, it was found that the HEATF possessed superior radiation tolerance and this alloy is thus proposed in this thesis as an alternative to ceramic coatings in the context of the accident tolerant fuels programme.

An extensive study of the neutron and ion irradiation responses of two Ti-based MAX phases is also presented. Firstly, an electron-microscopy post-irradiation study on the Ti_3SiC_2 and Ti_2AlC MAX phases irradiated with neutrons in the High-Flux Isotope Reactor (HFIR) at high temperatures (1273 K) is presented. This study, which was carried out up to 10 dpa, revealed a complex chain of radiation damage effects: from perfect basal dislocation loops to irradiation-induced segregation with formation of secondary phases. The heavy ion irradiation with *in situ* TEM methodology was utilised to explore possible experimental comparisons between ion and neutron irradiation of these materials. *In situ* TEM annealing was also performed to investigate the thermal stability of both Ti_3SiC_2 and Ti_2AlC MAX phases at high temperatures and, under the studied conditions, these materials in a form of electron-transparent lamellae were found decompose at temperatures around of 1273 K.

The results obtained with all the materials studied led to the major conclusion that there is a strong connection between the thermodynamics of materials and their radiation tolerance. Due to the possibility of tuning the elemental composition of metallic alloys with the aim of optimising the key core effects of high-entropy systems, the outcomes of this thesis indicate that these metallic alloys can be considered promising candidates for future generations of nuclear reactors operating at moderate temperatures. Ion irradiation with the *in situ* TEM methodology is thus shown to be fast and efficient for triaging innovative candidate materials for use in nuclear reactors.

"High authorities tell us that new sources of power, vastly more important than any we yet know, will surely be discovered. Nuclear energy is incomparably greater than the molecular energy which we use today. The discovery and control of such sources of power would cause changes in human affairs incomparably greater than those produced by the steam-engine four generations ago. Materials thirty times stronger than the best steel would create engines fit to bridle the new forms of power."

Sir Winston Leonard Spencer-Churchill
KG OM CH TD PC DL FRS RA
Prime Minister of the United Kingdom
Part of "Fifty years hence", a chapter of Thoughts and Adventures, 1932.

Chapter 1

Introduction

Social and economic advances in our modern society are associated with the fast development of new products and technologies that are directly derived from the progress of science. The fast growth of modern economies has triggered several concerns over sustainability, a concept that aims at to mitigate the deleterious anthropogenic effects on the earth. Since the beginning of civilisation, one field of science that has inspired the development of a technological and sustainable world and at the same time, delivered products and innovation to everybody, is materials science [1]. Historians categorise the early stages of human civilisation by man's ability to work with metals for producing tools. The historical ages were, therefore, subdivided and named after the specific materials that humans dominated at the time, and extracted and explored for their own comfort and survival: the Stone Age, the Bronze Age and the Iron Age [2]. Human progress is therefore linked with our ability to work with materials.

Nowadays, the intensive pace of economic growth in both developed and underdeveloped countries requires maximum industrial performance and productivity to support the emergence of new commercial technologies and such goals have set new paradigms for the development of innovative materials. The immediate consequences of these demands were evident in many material developments in our industries in the 20th century and today: materials that allowed miniaturisation of semiconductor devices [3]; the production of lightweight and resistant alloys for aerospace, new aircraft designs and the automotive industry [4]; new metamaterials for optical devices such as high-power lasers [5]; metallic alloys with enhanced strength and fatigue resistance [6]; super hard refractory ceramics for extreme environments [7]; and single-layered nanomaterials, like graphene [8, 9], whose potential commercial applications are yet to be realised.

Synthesis and production of conventional and innovative materials, either on laboratory or industrial scales, often require a deep basic understanding of their properties and microstructures aiming at establishing the limits for a particular

application. Standardised procedures for testing, evaluating and analysing the materials behaviour under a wide set of environmental conditions is also of concern in both science and industry. To address such challenges, materials scientists resort to microstructural analysis with powerful microscopes as the physical, chemical and mechanical properties of a material are directly related to its microstructure at the atomic level. A synthetic material can be broadly defined as "*a substance (or compound) intended for a practical purpose*" [2]. From this point of view, it is necessary to investigate the effects of a such practical purposes on the microstructure of a material prior to its commercialisation. This is a mandatory requirement in order to ensure that, under operational (either normal or accident) conditions, the material does not fail as this could be at the expense of human lives. One particular part of our economy that has revolutionised human comprehension of material sciences is the energy industry.

The advent of new technologies (like electric cars) and the constant population growth will exponentially increase the worldwide demand for electricity over the next decade [10]. In the United Kingdom, for example, policymakers have alerted the government that the minimum level of infrastructure investment to supply electricity for Britain by 2020 is around £264 bn [11]. At the same time, due to international agreements, governments will have to invest in clean energy solutions that do not damage the environment with pollutant gases, like carbon dioxide (CO_2), which are the cause of the greenhouse effect. The solution calls for the development of "green" or renewable energy sources. Hydroelectric, solar, wind, geothermal, biomass waste and biofuels are the most common renewable energy sources because they play a major rule in reducing greenhouse gas emissions. When renewable energy sources are introduced into the energy matrix of a country, it has been reported that the demand for fossil fuels is significantly reduced [12]. Although green energy sources are an alternative to increase global electric power generation, they are subject to seasonal variations like weather conditions, drought periods and agricultural priorities. Such problems may jeopardise their use on a large scale in a future world that depends even more on electric energy for the well-being and comfort of its citizens or even in strategic situations involving national and global security. These problems have been the motivation of several ongoing international research projects involving materials science with the objective to increase electric energy generation efficiency, storage and reliability.

An alternative to supply the increasing demand of electric power generation with reliable baseload over time is nuclear energy through fission power. The question as to whether nuclear energy can be considered renewable is still a subject of strong debate by scientists in academia and policymakers around the globe. Major arguments in favour lie in the fact that nuclear reactors do not generate greenhouse gas emis-

sions and therefore should be included in the list of renewable energy sources [13]. On the other hand, the element uranium, the main fuel source for fission power, is a finite natural resource [14] while renewable sources by definition uses indefinite natural sources, like wind and sunlight. However, modern breeder reactors can reprocess uranium and this has been considered a strong argument in favour of categorising nuclear energy as renewable [15]. Additionally, compared to other renewable energy sources, nuclear energy has the highest achievable energy density (kWh/kg): for a Light-Water Reactor (LWR) with 3.5% of enriched U-235, the energy density is 960 MWh/kg while for natural gases, biodiesel oil and hydroelectric power the numbers are around 13.8, 11.7 and 0.0003 kWh/kg, respectively [13, 16].

Concerns regarding the use of nuclear energy are in the safety aspects and radioactive waste generation. The safe operation of a nuclear reactor is dependent on the choice of materials that compose the entire nuclear installation, from the nuclear core to the shielding. It is also determined by the interaction of these materials with the nuclear reactor environment and with the possible occurrence of external events within or nearby the installation site, such as tornadoes, earthquakes and tsunamis [17, 18]. Due to engineering project criteria and by the force of national and international standardised licensing regulations, prior its utilisation in a nuclear installation, a material or alloy must be exhaustively tested in a wide variety of normal operating conditions and in accident conditions [19]. The general guidelines and properties of interest that a material or alloy need to have in order to be used in a nuclear reactor structure can be summarised as follows [20, 21]:

- **Mechanical strength:** This is the property that will limit how much a material will be able to resist external loads and stresses during operation. In a light-water reactor, for example, the nuclear fuel rods are subject to high axial stresses; they should not plastically deform in a such way that they may get stuck or crack in the core.

- **Ductility:** The ability of a material to deform elastically and/or plastically under stress conditions. If the stress conditions exceed the yield strength, the material should plastically deform within certain limits that do not compromise the operation (e.g. fracture and release of radioactive material into the coolant circuits).

- **Structural integrity:** The ability of a material to retain its mechanical properties during both normal operation and under accident conditions. Materials that suffer phase transformations when the core temperature raises, for example, should be avoided.

- **Machinability and formability:** The ease of manufacturing pieces, such

as plates and rods that will be components of a bigger structure. Materials that are able to be welded are also of great interest. Lamination, cutting and milling are common processes to make nuclear structural materials, therefore, they may also have to lend themselves to such manufacturing processes.

- **Corrosion and oxidation:** When in contact with corrosive fluids and other substances, such as coolant liquids and nuclear fuels, materials cannot exhibit strong degradation due to oxidation and corrosion. This is an important parameter to take into consideration. Temperature plays a major role in such corrosion properties. Oxidation and corrosion may change a whole list of properties in certain materials or can even cause their chemical dissolution which could result in a serious nuclear accident.

- **Heat transfer and thermal stability:** A nuclear reactor is a thermodynamic machine. A nuclear-fuel cladding alloy, for example, will have to exhibit good heat transfer properties in order to transfer the heat generated in-core to the coolant with maximum efficiency.

- **Compatibility:** A paramount requirement for designing a nuclear reactor is that the materials have to be compatible with each other. For example, it is well-known to be challenging to weld Al and Fe. No one will select these materials to compose a nuclear-fuel cladding rod system where Fe is the rod material and Al the material for the welded rod cap.

- **Costs and availability:** Selecting materials for a nuclear installation is a challenge where costs and availability are major limiting factors. It is well-known that the generation of nuclear energy is expensive. For example, Ir is a metal with excellent corrosion resistance and high mechanical strength including good heat transfer capabilities, however, it is one of the most expensive and rare metals on earth. Therefore, expensive and rare materials are unlikely to be used in nuclear installations.

- **Neutron capture and activation:** During the operation of a nuclear reactor, the nuclear fission events will generate neutrons in-core with a broad and specific energy spectrum. Certain materials absorb neutrons and this will induce transmutations. Transmuted elements are often sources of radioactivity. For nuclear-fuel cladding materials, this should be avoided as much as possible by selecting appropriated materials that are (preferably) transparent to neutrons in their energy range (0.025 eV to 10 MeV). Biological shielding materials, for example, need to reduce the effective dose outside the shielding. Otherwise, workers may be exposed to high radiation exposure levels that may cause illness and death.

- **Stability under particle irradiation exposure (radiation damage):** The neutrons generated in-core are energetic particles which may cause atomic displacements of atoms in a material. The process is known as radiation damage and it may induce undesirable effects in nuclear materials, such as swelling, embrittlement and irradiation-assisted stress corrosion cracking [21–24]. Physical properties like electric resistivity and thermal conductivity may also significantly change under neutron exposure for certain materials [22]. Therefore, materials with high radiation resistance are preferred and this aspect has been considered a topic of paramount interest and importance for nuclear technologists worldwide.

The reliability of nuclear power depends on the performance of structural materials whose degradation and failure may be caused by several aspects of the environment within a nuclear reactor. In particular, conventional nuclear fuel-cladding systems are subjected to high neutron fluxes with a broad energy spectrum. In this context, the topic of radiation damage in materials is considered a key parameter in the design of nuclear reactors as it affects all the aforementioned properties.

During the last century, improved fundamental understanding of irradiation-induced damage in nuclear materials has led to the development of conventional multicomponent alloys, in particular zirconium alloys [25] and stainless steels [26], whose performance, to date, is responsible for the worldwide success of nuclear power as a safe, large-scale source of electricity. The displacement of lattice atoms may induce permanent microstructural defects under in-service conditions giving rise to a damaged material with degraded mechanical properties. Upon the development of sustainable and improved nuclear power plants (so-called Generation IV) that could operate for several decades without refuelling and with low radioactive waste production, the major challenge is the design of accident-tolerant fuel (ATF) materials that can also sustain structural integrity over long-term exposure to both particle irradiation and corrosive environments [21, 27].

Displacements-per-atom or dpa is the scientific unit to express the damage caused by energetic particles in a material. It quantifies how many times on average a lattice atom has been displaced. 10 dpa means that on average lattice atoms have been displaced from their positions 10 times. Future innovative nuclear reactor designs like the Travelling-Wave Reactor (TWR) are currently being designed to sustain damage levels in the range of 200 to 500 dpa [21, 28] while in a commercial LWR, the damage level is around 2 dpa per three years of continuous operation [24, 29]. Radiation damage is also a huge concern within the context of nuclear fusion reactors as they generate neutrons with energies of approximately 14.1 MeV, and may develop damage levels of around 150–200 dpa. A consensus has been established within the nuclear technology community that conventional materials, *i.e.* the ones that have

already been used in LWRs and fast reactors, such as zirconium alloys and austenitic stainless steels, will not be used in advanced nuclear reactors [23].

The effects of particle irradiation on materials that have been recently considered candidates for the next generation of fission nuclear reactors and for fusion reactors is the main subject of this doctoral research. A systematic multidisciplinary study is presented which sheds light on the main mechanisms of radiation damage in an innovative quaternary High-Entropy Alloy (or HEA), FeCrMnNi. The radiation effects observed to occur in the HEA were then compared with those in an austenitic stainless steel – AISI-348 – that was irradiated under very similar conditions. This stainless steel is a conventional nuclear-grade alloy that has already been used as cladding for ceramic nuclear fuel in LWRs and fast-fission reactors worldwide and it contains the same four elements, FeCrMnNi, as major alloying elements [26]. The methodology used in this work, to study the radiation resistance of both materials, was ion irradiation *in situ* within a Transmission Electron Microscopy (TEM). This methodology allowed the real-time observation of radiation effects in both materials: the HEA and the stainless steel. Another class of candidate materials that is under consideration for use in the next fleet of generation IV nuclear reactors was also investigated during this doctoral research: two Ti-based $M_{n+1}AX_n$ phases, Ti_3SiC_2 and Ti_2AlC, where a comparison study between neutron and ion irradiation effects has been carried out. For the HEAs, the outcome of this work is to suggest that the deposition of High-Entropy Alloy Thin Films (HEATFs) on conventional nuclear-fuel cladding alloys with the aim of enhancing their radiation and corrosion resistance could be an alternative to be further explored on new potential materials within the scope of accident tolerant fuels. Regarding the Ti-based MAX phases, the results of this work introduce new datasets for the nuclear materials community, including a first-time characterisation of neutron irradiation induced defects up to 10 dpa and results from comprehensive ion irradiation *in situ* within a TEM at high temperatures. On the MAX phases research, both thermal and radiation stability of Ti-based MAX phases were investigated and the major conclusions are that both Ti_3SiC_2 and Ti_2AlC may not be as stable as previously expected.

Chapter 2

Background and Literature Review

This chapter presents a literature review of the materials and alloys that are the subject of this thesis. The current accepted definitions and main properties of the multicomponent alloy systems (HEAs and stainless steels) and the nanolayered ternary carbides (the Ti-based $M_{n+1}AX_n$ phases) will be introduced. This will be followed by an exploration of the main concepts of radiation effects in solids, with a focus on reported results regarding the effects of particle irradiation (both neutrons and ions) on the microstructures of the FeCrMnNi HEA, the austenitic stainless steel 348 and the Ti-based $M_{n+1}AX_n$ phases.

2.1 The materials: definitions and properties

2.1.1 Multicomponent alloy systems

In classical metallurgy, conventional alloys are those based on a single element which will dictate the main properties of a mixed alloy system [30]. In order to enhance certain properties of an element, such as its mechanical strength or corrosion resistance, in general two or three major alloying elements are added to create a solid solution and this procedure will result in a binary or ternary alloy system. For example, commercial aluminium alloys have been categorised according to their major alloying components. For an aluminium alloy that belongs to the 2xxx group, copper is the major solute and it confers superior mechanical properties (when compared to unalloyed Al or the 1xxx group) while the group 4xxx is dedicated to Al-Si alloys that are characterised by low melting points and low densities which allow applications in the manufacture of automotive and aerospace parts [31]. Complexity arises when several minor alloying elements are added into the solid solution. The definition of conventional multicomponent alloys covers all alloys with one base element and two

or more major alloying elements including several other minor alloying elements [32, 33].

Major and minor alloying elements are distinguishable by their elemental composition within a system, although the boundaries for such classification will vary for each system. As an example, the alloy IMI834 is a Ti-based multicomponent alloy for aircraft engine applications [34]. According to its specifications [35], Al, Sn, Zr, Nb, Mo and Si are alloyed with Ti. For this particular case, Al, Sn, Zr and Mo are the major alloying elements with nominal compositions of 5.5, 4, 4 and 1 in weight percent (wt.%), respectively. At the atomic level, major solutes can replace lattice atoms in substitutional sites. Mo and Si with 0.3 and 0.5 wt.%, respectively, are the minor elements. Despite the fact that major solutes play a role in enhancing physical and chemical properties, from the point of view of thermodynamics, they also define which phases a system retains after processing and whether they are stable. Minor alloying elements have similar effects, but depending on the system, the addition of specific elements as minor interstitial solutes will induce changes in the final microstructure, such as promoting or suppressing precipitation [32], grain refinement [36], stability of phases [37] and improving corrosion properties [30]. In some circumstances, minor elements can also be considered impurities of a system. Among the diverse and wide variety of multicomponent alloys, commercial stainless steels and most recently the high-entropy alloys are of paramount importance for metallurgy due to their suitable sets of properties for several technological applications. For these reasons, the metallurgy of steels and high-entropy alloys will be introduced in the next section.

2.1.1.1 Steel and its variants

2.1.1.1.1 Definition and classification

Steels can be defined as Fe-based multicomponent alloys. A wide variety of alloy systems with specific properties can be designed by accurately alloying Fe with other elements such as C, Si, Mn, Cr, Ni and Mo. Steels can be categorised by their alloying elements (elemental composition) and/or by the properties of the final product as a consequence of the mixing [32, 38, 39]. Exceptions in this definition are for cast iron, white and grey cast irons and silicon cast iron, which are characterised by the presence or addition of Si and C in Fe, but in very high quantities. Although they are Fe-based alloys with intrinsic poor malleability properties, they are not technically considered to be steels. The same to crude iron – an intermediate Fe-based product that is a by product of Fe ores – that also have additional elements in their compositions, but cannot be considered steels [39–42].

Low carbon steels are the most common form of Fe-based alloys. The term “low carbon” is due to the fact that this element is the only intentional alloying element

in the ferritic matrix, although in low concentrations [39]. Elements such as P and S can be detected as undesirable impurities and their content are often reduced. General applications for low carbon steels are in civil engineering, the naval industry and in the fabrication of tubes and sheets. [39, 43].

High-strength low alloy (HSLA) steels are those in which the alloying elements (including carbon) are added within very narrow and accurate tolerances. These alloying elements are often Al, Ti and Nb which control the microstructure of the steel during thermo-mechanical processing. These steels often require specific heat treatments after forming [44, 45]. HSLAs are widely used in the automotive industry [46].

High-alloy steel is a wide category where the alloying elements are added into Fe in large quantities, typically 2–20 wt.%. They are well known by their unique set of properties such as high mechanical strength, high fracture and fatigue resistance and include suitable corrosion, oxidation and high-temperature properties [30, 39, 43, 46]. Additionally, the alloying elements are added in a controlled manner with low margins of error which allows complete control of the microstructure and phases in the system. High-alloy steels can be used in extreme conditions, *e.g.* high-temperature and corrosive environments (stainless steels), such as oil and gas pipes, and in the nuclear, aerospace and defence industries [32].

2.1.1.1.2 Atomic structures of Fe, steels and their phases

At the atomic level, the Fe atoms are arranged in a periodic crystal structure or lattice. Depending on both temperature and pressure, the element Fe can exhibit different crystal structures, known as the phases and often designated by Greek letters. At low temperatures there is the body-centred cubic (BCC) ferrite, or α–Fe, but above 1184 K, Fe starts to suffer recrystallisation forming a face-centred cubic (FCC) phase, austenite or γ–Fe. Heating up to around 1673 K, δ–Fe is formed with a BCC structure. Above 1809 K, the δ–Fe melts. Upon cooling, the phases are formed according to their designated temperatures and due to the fact that they have completely different crystal structures, their physical and chemical properties are also different [32, 39].

As steels are not pure Fe, the addition of alloying elements results in different atomic structures. The process of alloying is governed by the Hume-Rothery rules. This set of rules will dictate whether or not a specific element can be dissolved in the crystal structure of Fe, becoming a solute in solid solution. The four rules can be stated as follows [47]:

1. The difference in the atomic radii of the solute and the solvent should be less than or equal to 15%;

2. Solute and solvent must belong to the same crystallographic group;

3. Solubility can be determined by analysing the valency. When both valencies of solute and solvent are the same, complete solubility will occur; and

4. Solute and solvent should have similar electro-negativities.

In the case where solutes and solvent have similar atomic radii, the solute atoms will occupy substitutional positions within the Fe lattice. The product is considered to be a substitutional solid solution. Cr, Mn and Ni are all substitutional solutes, for example. When solutes are smaller than the lattice base-element, like C and N, they will occupy interstitial lattice sites [33].

The octahedral interstitial inter-spaces are larger for the γ–Fe than for those in the α-Fe phase. Due to this, it is easier to dissolve small atoms in the γ–Fe. The addition of more solute atoms in a given crystal structure will induce lattice deformations. This will help limit the solubility, but upon increasing the temperature, the lattice atoms will oscillate around their equilibrium positions with a higher amplitude and frequency, thus increasing the lattice parameter and also the lattice atomic inter-spaces. The result is a direct relationship between solubility and temperature in steels [32, 39, 43, 48].

In the thermodynamics of alloys, the relationship between solubility and temperature is regulated by the Gibbs free energy and entropy. Under fixed compositions, and in the limit of diluted solutions as is the case of interstitial solutes in metals, the

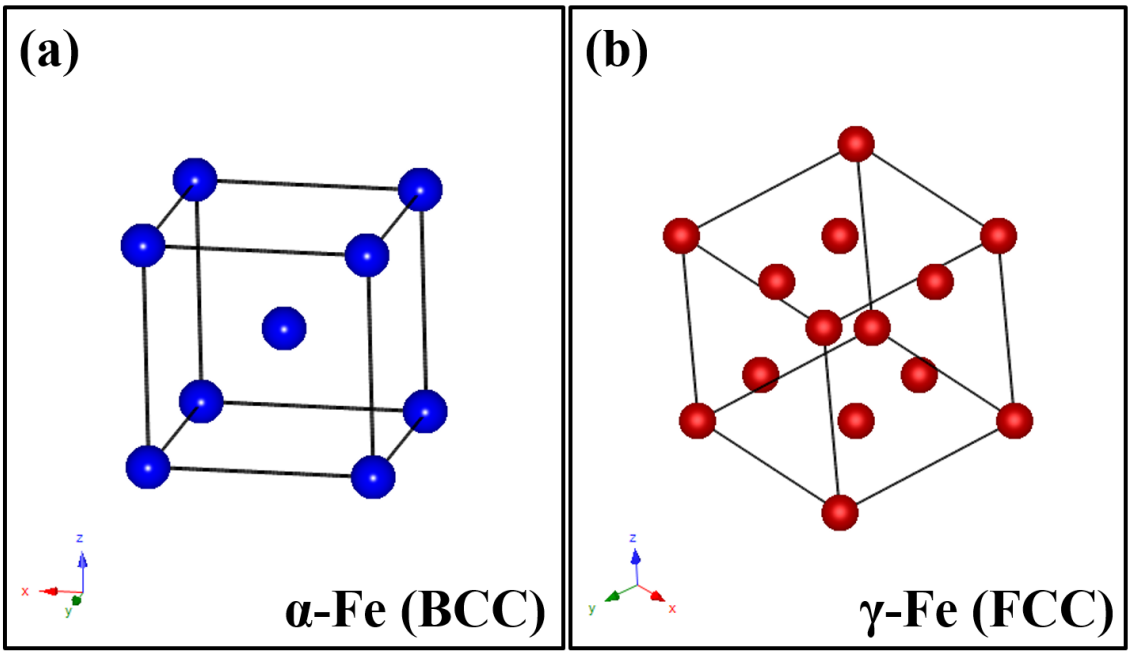

Figure 2.1: The crystal structures for (a) α–Fe, the body-centred cubic phase and (b) γ–Fe, the face-centred cubic.

configurational contribution to entropy is mostly constant, and hence, the increase in solubility with temperature should be attributed to the vibrational entropy [49], in accordance with the atomistic picture described above. Additionally, the continuous insertion of alloying elements into α–Fe, for example, may induce (or suppress) phase transformations under certain conditions. That is the case when Cr, Ni, Mn, C and N are added to Fe to form an austenitic stainless steel (with a FCC structure as depicted in figure 2.2) [50–52].

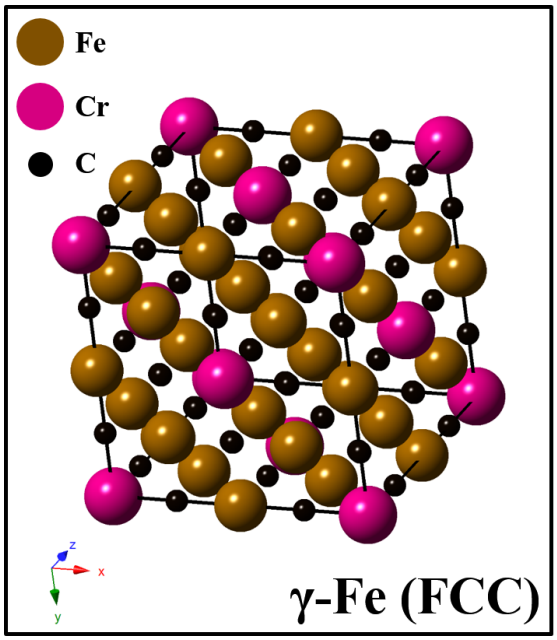

Figure 2.2: The atomic structure of an austenitic stainless steel solid solution. Cr atoms are substitutional due to their atomic radius similarity with Fe whilst C atoms are interstitials.

When the solubility limit for a solute is exceeded, the solute will tend to combine with other elements in its surroundings, thus forming their own local crystal structure alongside the matrix phase. This secondary crystal structure is composed of small crystallites that grow with the addition of more alloying elements. This phenomenon is known as precipitation [30, 53]. For steels, the most common precipitates are carbides which are formed when C does not enter into solid solution with the Fe lattice and starts to combine with other solute elements depending on the thermodynamic activity of the precipitate system [39, 53]. The presence of a secondary phase often degrades mechanical properties as it hinders the movement of defects, therefore, limiting the ability of the alloy to plastically deform.

2.1.1.1.3 Stainless steels and applications

In the case of high-alloy steels, three classifications are used to distinguish commercial alloys and their respective phases [54]. Ferritic stainless steels are those with

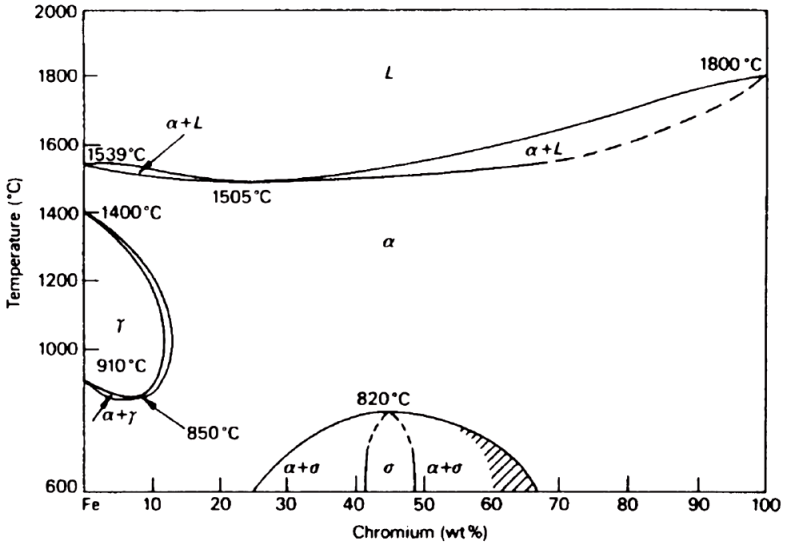

Figure 2.3: The Fe-Cr phase diagram. (Reproduced from H. Bhadeshia and R. Honeycombe [32])

BCC (the ferrite phase or α–Fe) and very low C content. The level of Cr in solid solution varies between 10.5 and 18 wt.%. They possess good ductility and mechanical strength, but moderate to low mechanical, oxidation and corrosion resistances at high temperatures [39].

The first stainless steels developed for cutlery and general tools are of martensitic phase. With high C content, around 0.1 and 1.2 wt.%, and Cr between 12 and 18 wt.%, martensitic stainless steels are considered heat treatable and such thermal treatments allow the manipulation of several properties including ductility and mechanical strength. Tempering martensitic stainless steels makes them useful for applications in the aerospace and nuclear industries. The martensitic phase is retained upon rapid cooling the austenitic phase at high temperatures. Martensitic stainless steels posses a BCC structure: it is considered a diffusionless and displacive (without atomic diffusion) phase transformation and it is activated by stress [32].

Austenitic stainless steels, the third type of stainless steels, comprise around 80% of worldwide steel production [53]. The austenitic phase is of face-centred cubic (γ–Fe) crystal structure which can be achieved by adding Ni to the Fe-Cr solid solution in certain proportions. Both Ni and Cr are substitutional alloying elements in Fe. In order to improve the stabilisation of the γ–Fe phase at room temperature, either interstitial elements such as C or substitutional such as Mn, Mo, Co, Ti, Nb, V, W, Cu and Al are used and these may also improve the microstructure and mechanical properties. Austenitic steels posses high temperature, oxidation and corrosion resistance and due to their suitable properties, they have been applied in several different types of industry from nuclear to oil and gas [32, 43, 53]. Their commercial classification is the AISI 300 series where the most widely used alloys

are AISI-304 and AISI-316.

Metallurgists and materials scientists often look at phase diagrams to analyse the different phases that will be present in a multicomponent alloy system as a function of the composition of alloying elements. The phase diagram is a type of chart showing the thermodynamic phases which (co)exist in equilibrium under certain conditions, such as temperature, pressure and composition. The Fe-Cr phase diagram, which guides the industrial production of stainless steels, is presented in figure 2.3 [32]. The ferrite phase (α–Fe) is the dominant phase for moderate and high Cr contents, but a loop can be seen when the Cr composition is around 15 wt.% in the temperature range from 1673 to 1123 K. This loop is known as the γ–Fe loop and this is the region of interest for producing stainless steels with the austenite structure. Minor alloying elements such as C and N act so as to increase the size of the γ–Fe loop allowing the accommodation of higher Cr concentrations in the FCC structure. Major alloying elements, such as Ni and Mn, also promote an increase in the size of the γ–Fe loop.

2.1.1.2 High-entropy alloys

2.1.1.2.1 Historical context for the emergence of high-entropy alloys

There are many ways to create or synthesize a new material. Conventionally, this involves the use of the phase diagram for developing terminal solid-solutions, i.e. alloys with a base element and major/minor alloying elements, as in the case of stainless steels discussed above (figure 2.3). The second step is to use certain alloying additions to cast and produce the material. This recipe has led to the development of many engineering materials with suitable and interesting properties, but this concept of alloying has its limitations because, for example, the phase retained may not be thermodynamically stable and precipitation of secondary phases may even occur inadvertently. Recently, in materials science and metallurgy, HEAs have become a new alloying concept, a new paradigm beyond terminal solid solution. The innovative concept involves making multicomponent alloys with equiatomic composition of the alloying elements [55].

The first scientist to assess the benefits of producing multicomponent high-entropy alloys beyond the conventional alloying procedure was the German metallurgist Karl Franz Achard [56]. Achard studied several alloys with five to seven elements in equiatomic proportions. In his book, *Recherches sur les Propriétés des Alliages Métallique* published in Berlin around 1788, he studied 900 alloys made from 11 elements and all those systems were made by choosing equiatomic compositions. Unfortunately, Achard's work was largely ignored by the scientists of his time as the book was written in the French language since the funding came from Frederick the Great who wanted to impress the French government with German

science at that time [55].

Four hundred years after Achard's work, Brian Cantor was the first scientist to note that no work had been carried out on alloys with several components in equiatomic compositions [57, 58] and he was the first also to point out that multicomponent HEAs could overcome some limitations of binary and ternary alloy systems.

In 1981 Cantor's group had investigated the system $Fe_{20}Cr_{20}Ni_{20}Mn_{20}Co_{20}$ which forms a single FCC solid solution phase solidifying dendritically at these equiatomic compositions (op. cit. in [55]). Between 1980 and 2000 no paper was published regarding these multicomponent equiatomic alloys, but in 2004 Cantor's group came up again with a better description of the work carried out in the 80s, coining the term "concentrated solid solution multicomponent alloys" as a new alloying concept [57–60].

In parallel with Cantor's work, Jien-Wei Yeh's research group in China carried out research on the high-entropy mixing factor as an important effect in reducing the number of phases in high order equiatomic alloys. The creation of the name "High-Entropy Alloys" is attributed to Yeh and also three of the four core effects of these alloys (discussed further below) were for the first time investigated by this group [61–63]. Regarding HEAs and their characteristics, the major outcomes of Yeh's work are: (a) the dendritic structure in the HEAs was seen in the as-cast structure, (b) these alloys in general can achieve high hardness level (590–890 HV) and (c) small additions of boron led to some increase in hardness.

The theoretical and computational design of these alloys was carried out by Srinivasa Ranganatthan, who spent a long time studying different ways to visualize these high-order phase diagrams. His investigations were into HEAs, although focused on computational thermodynamics [64]. He published a work, *Alloyed pleasures: multimetallic cocktails* [65], where he introduced three new potential research areas for alloys in metallurgy: bulk metallic glases, superelastic and superplastic alloys often known as "gum metals" [66] and the HEAs [67].

High-entropy alloys have interesting properties to be explored as a nuclear material and for general applications as well. These properties are based on five metallurgic concepts: performance, composition, modelling, microstructure and processing. It is reported that in terms of performance the HEAs have high strength at room and elevated temperatures, good wear and corrosion resistance and can be applied as diffusional barriers [55]. They can be cast using plasma arc melting furnaces with equiatomic (or near equiatomic) compositions. The microstructure of the HEAs is a single-phase solid solution (either FCC or BCC), ordered precipitates or metallic glass "cocktails" and some researchers have been exploring the possibility of mod-

elling [55] these alloys using CALPHAD[1] and *ab initio* methods [68, 69], Monte Carlo simulations [70, 71] and Molecular Dynamics [72–76]. In order to assess the irradiation behaviour of the HEAs, firstly, it is necessary to define the HEAs as materials, exploring their four core effects and explain what is the main difference between them and conventional terminal solid solution alloys.

2.1.1.2.2 Ideal solid solutions and binary systems

Following the Hume-Rothery rules, the interaction between different atoms is regulated by the laws of thermodynamics. In this sense, a competition between entropy and enthalpy of mixing affects the solubility of an alloy system with two or more components. When the enthalpy of mixing (ΔH_{mix}) is less than zero, it is expected that an attractive interaction occurs between the atoms: this leads to an ordered solid solution. For values higher than zero, a repulsive interaction occurs leading to clustering and segregation; when the value is approximately zero, disordered solid solutions are formed [47]. The Gibbs free energy of an alloy system (ΔG_{mix}) is defined as:

$$\Delta G_{mix} = \Delta H_{mix} - T\Delta S_{mix} \tag{2.1}$$

Where H and S are respectively the enthalpy and entropy of mixing. In this sense, the simplest type of mixing to treat first is when $\Delta H_{mix} = 0$. For this approximation, the resultant solid solution is ideal and the free energy on mixing is only due to variations in entropy:

$$\Delta G_{mix} = -T\Delta S_{mix} \tag{2.2}$$

In statistical mechanics the entropy is strongly related to randomness: the famous Boltzmann equation $S = k \ln \omega$, where k is Boltzmann's constant and ω is a measure of randomness in terms of the configurational sites where an atom may be positioned in a lattice. For substitutional solid solutions (binary systems) with molar concentrations of x_A and x_B for each alloying element [33]:

$$\omega = \frac{(N_A + N_B)!}{N_A! N_B!} \tag{2.3}$$

where N_a is the Avogadro's number for 1 mol of solutions and $N_A = x_A N_a$ and $N_B = x_B N_b$ are the number of atoms of A and B in a given configurational state. Using Stirling's approximation ($\ln n! = n \ln n - n$), the Boltzmann equation and equation 2.3, the entropy of mixing for an ideal solid solution is:

[1] CALPHAD is a commercial software package in which is possible to draw phase diagrams using multiple algorithms.

$$\Delta S_{mix} = -nR(x_A \ln x_A + x_B \ln x_B) \tag{2.4}$$

where $x_A + x_B = 1$ and R the universal gas constant. The stability of phases and ordered mixing are thus regulated by the Gibbs free energy (ΔG_{mix}) and as x_A and x_B are smaller than 1, the entropy is a positive term (entropy increases on mixing). The Gibbs free energy is, therefore, for a binary alloy system given by:

$$\Delta G_{mix} = RT(x_A \ln x_A + x_B \ln x_B) \tag{2.5}$$

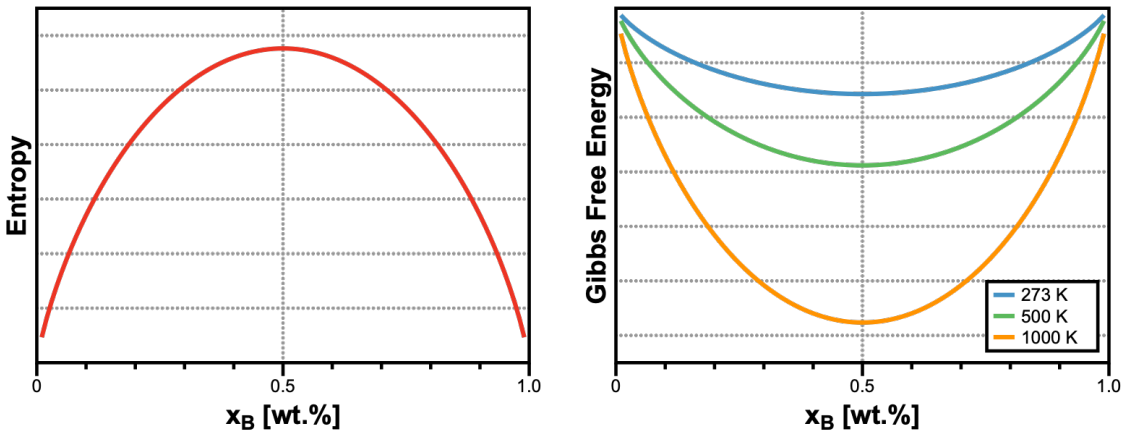

Figure 2.4: Schematic entropy and Gibbs free energy curves for binary solid solutions. The maximum of the entropy curve is reached when x_B is equal x_A or 0.5 wt.%. Additionally, the minimum in the Gibbs free energy is lower as T increases: HEAs are supposed to be even more stable at high temperatures.

In a terminal solid solution alloy, the concentration of the second (or third) alloy component is situated at the extremity of an axis in the phase diagram (*e.g.* Zr-1.5Sn wt.%). Upon increasing the composition of the alloying elements, intermetallic compounds and ordered solid solutions can be formed. When the Gibbs free energy reaches a minimum value, it is expected that the atoms A and B are in equilibrium and the solid solution formed is stable. In the case of regular and high-order solid solutions the enthalpy has to be taken in account for these calculations above [33].

2.1.1.2.3 Real solid solutions

The concept of an ideal solid solution is an oversimplified explanation of the reality of metallic alloys. In the latter case, where the enthalpy of mixing is not zero (*i.e.* $\Delta H_{mix} \neq 0$), the equation 2.5 does not accurately represent the relationship and effects between the Gibbs free energy with the composition of its constituents and temperature of a certain alloy system. For this, the random solid solution picture to represent the thermodynamic equilibrium of an alloy is not correct and the use

of equation 2.5 to estimate the Gibbs free energy of the system will lead to a value which is not the lowest free energy.

In real solid solutions, the actual arrangement of atoms will be established by means of a synergistic combination between a certain state of entropy (or randomness) and the lowest possible internal energy of the system: with this, the minimum free energy will be attained [33].

For example, the internal energy of a binary system can be reduced when the number of atomic bonds between A and B is increased. In this case, the solid solution is known as ordered substitutional. In the case where strong chemical bonding occurs between the constituents leading to a phase with defined stoichiometry and ordered crystal structure, it is said that an intermetallic solid solution will form. When the number of bonds is increased between the pairs A–A and B–B, there will be a tendency for clustering, thus the formation of A- and B-rich regions within the alloy. In addition, due to the increasing contribution of entropy upon increasing the temperature, the degrees of clustering and ordering will decrease accordingly [33].

Both ordered substitutional and clustering solutions will occur when the atomic mismatch between A and B is small. When the size difference between A and B is significant, a strain energy component of the enthalpy will be dominant over the chemical term. For real solid solutions with large atomic mismatch between the constituents, interstitial solid solutions are formed as they will be most energetically favourable [33].

The relationship between composition variation and Gibbs free energy in real solid solutions can be very complex and the curve in figure 2.4(b) does not represent this case. This relationship can also vary to each studied system considering the different types of alloys *i.e.* ordered substitutional, intermetallic phase, clustering or interstitial solid solutions [33].

2.1.1.2.4 The concept of high-entropy alloy

When mixing is carried out with binary, ternary or even quaternary systems, the question arises as to whether it is possible to obtain solid solution phases in the centre of the phase diagrams (*i.e.* at the equiatomic condition). This is the core question of the HEAs.

Cantor and Yeh independently made the observation that the entropy of mixing for a binary system has a maximum when the compositions are equiatomic (or near-equiatomic) [58, 61]. This is not a conventional approach to making alloys. At the same time when the entropy of mixing is maximum, the configurational entropy increases with the number of elements in a system: these facts were found to play a major rule in the kinetics of phase formation, lattice strain and other properties of a multicomponent and equiatomic alloy system [76].

In classical thermodynamics, the Gibbs phase rule estimates the number of possible phases (P) that can form at thermodynamic equilibrium in a multicomponent alloy. The rule states that the sum of P with the number of degrees of freedom (F) has to be equal to the number of alloying elements (C) plus 2.

$$F + P = C + 2 \tag{2.6}$$

In equation 2.6, the degrees of freedom represent the number of independent intensive variables that completely determine the thermodynamic state of a certain system. Intensive variables in thermodynamics are parameters such as temperature, pressure and chemical potential which do not depend on the size of the system [77].

In equilibrium, binary, ternary, quaternary and quinary systems cannot have more than three, four, five, and six phases, respectively. But the number of phases observed in alloys following the high entropy effect is significantly fewer than the maximum number of phases expected by the Gibbs phase rule: this strongly suggests that the large configurational and mixing entropies enhances the mutual solubility in order to form single solid solution phases even if the diffusion in these high-order systems is supposed to be strongly limited due the large number of different elements [55]. However, the reasons for this are not yet well understood [59].

The definition of the HEAs is straightforward and arises as a new alloy concept in metallurgy and materials sciences: it is a class of alloys with multiple elements, in general four or more, all in equiatomic proportions [61]. Due to the equiatomic composition, these materials are also known as highly concentrated solid solution alloys. Minor elements with concentrations less than 5% are accepted in the definition. These minor additions, for example C and N, are often reported to enhance some properties of the alloy as recently investigated by Cheng *et al.* and Hsueh *et al.* [78, 79].

A basic principle is that at equiatomic compositions, the high configurational mixing entropy is dominant and it is responsible for the enhancement of their stability at high temperatures by lowering the Gibbs free energy, thus improving the phase stability of a solid solution [55, 80, 81]. This allows HEAs to be easily manipulated, analysed, synthesized and processed with good control of the microstructure and mechanical properties.

2.1.1.2.5 The core effects of high-entropy alloys

The HEAs have four core effects [63] that are responsible for their microstructure and behaviour: (A) high-entropy effect, (B) severe lattice distortion, (C) sluggish diffusion and (D) cocktail effects [61]. These core effects constitute the main differences between HEAs and conventional alloy systems, such as stainless steels.

Table 2.1: Thermodynamic potentials and microstructure systems in alloys. (Adapted from [55].)

Thermodynamic States	Elemental Phases	Compounds	Intermediate Phases	Random Solid Solutions
ΔH_{mix}	≈ 0	Large negative	Medium negative	Slightly negative
ΔS_{mix}	≈ 0	≈ 0	Medium	$\Delta S_{mix} = -x \sum_{i=1}^{n} \ln x_i$
ΔG_{mix}	≈ 0	Large negative	Medium negative	Slightly negative

(A) High-entropy effect In order to understand the effect of high-entropy, firstly, the mixing enthalpy (ΔH_{mix}) for a multicomponent system can be calculated as described by Takeuchi, Inoue and de Boer [82, 83]:

$$\Delta H_{mix} = 4 \sum_{i=1, j \neq i}^{n} \Delta H^{mix}_{<ij>} x_i x_j + \sum_{k} \Delta H^{trans}_{k} x_k \tag{2.7}$$

Where x_k is the mole fraction of the k component in the multicomponent system, the term $\Delta H^{mix}_{<ij>}$ is the enthalpy (per mole) of mixing and the term $\Delta H^{trans}_{<k>}$ is the transformation enthalpy of the k component. The system is defined by the indices $i - j$ in the solid state.

Remembering the Gibbs free energy of mixing, equation (2.1), it is clear that increasing the number of components in a system would lower the Gibbs free energy as the entropy increases with the number of elements. For any alloy system, due to the second law of thermodynamics, the most stable state is that in which the Gibbs free energy is the lowest possible leading to three possible states: solid solution, intermetallic or elemental phases. Stability here means that the alloy microstructure tends to retain its properties and morphology without significant modification upon the action of external driving forces.

Looking at table 2.1, it is notable that the high-entropy effect is evident in the formation of random solid solutions (figure 2.5): increasing the number of elements n, the high-entropy effect is responsible for lowering the Gibbs free energy and a stable compound arises. The high entropy effect promotes the random solid solution state rather than the ordered state, since it would be more stable thermodynamically.

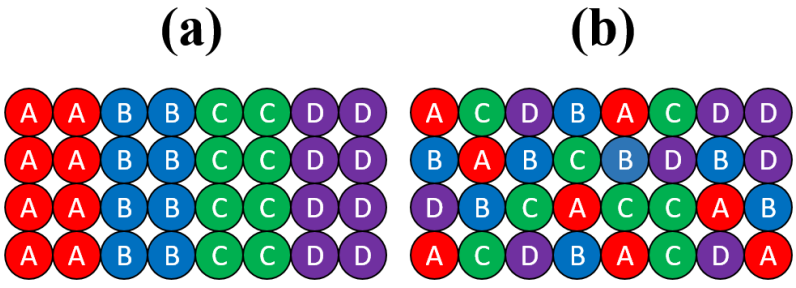

Figure 2.5: A quaternary equiatomic alloy system (a) before mixing and (b) after mixing to compose a HEA solid solution.

(B) Severe lattice distortion In a HEA the multicomponent matrix of each solid solution phase is a whole-solute matrix. Every atom is surrounded by different atoms and it suffers from a wide range of lattice stresses and strains mainly due the atomic size mismatch. This leads to the formation of an "average lattice" as assessed by X-ray diffraction measurements (XRD) [55, 84].

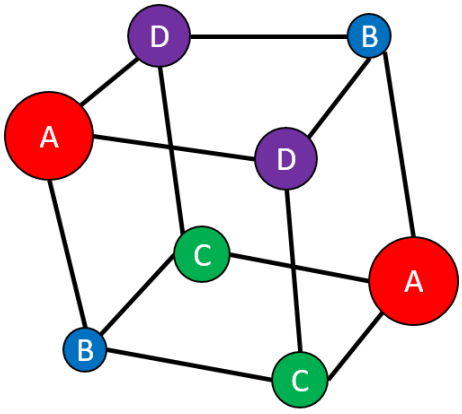

Figure 2.6: Schematic illustration of the severe lattice distortion concept. The atomic mismatch between the solutes causes a distortion within the crystal structure.

These lattice distortions arise for a number of reasons: (i) atomic size mismatch, (ii) differences in the binding energy and (iii) different crystalline structures. Also recent measurements have indicated that this effect is responsible for the enhancement of the hardness and strength of the HEAs [85].

Regarding the X-ray diffraction patterns, such irregularities in the lattice may affect the Miller planes modifying the shape of its peaks. They may also cause an electron scattering effect reducing the electrical and thermal conductivities [55].

(C) Sluggish diffusion As a HEA in a random solid solution state is a mixture of different atoms, slow (or sluggish) diffusion and high activation energy are expected due to the large fluctuation of lattice potential energy. From recent reports, it is expected that sluggish diffusion may affect phase nucleation, nucleation and growth, the creep resistance and the response to energetic particle irradiation [68, 69, 86–90]. As this core-effect will be investigated in this research work, further discussion will be presented in chapters 5 and 6.

(D) Cocktail effect This concept in HEAs is attributed to a paper from Ranganathan [64] and has caught the imagination of scientists in this area by means of *Gedankenexperiment*[2]: the multicomponent matrix of a HEA could be regarded as a cocktail of metallic elements. Due to processing and elemental composition deviations (*e.g.* the incorporation of a minor alloying element in small quantities),

[2]Term from German language used to express imaginary or hypothetical experiments.

multiple solid solution phases can form in an HEA system. Each new phase formed is considered an HEA by itself and this "cocktail effect" has been reported to enhance several properties of these alloys. Yeh *et al.* [55, 91] studied the system CoCrCuFeAl and found that two HEA phases were observed in the system (an FCC and a BCC phase) when the Al content was increased from 15 to 35 at.%. He also showed that the hardness of the dual-phase HEA alloy increased by 300% when the Al content was 15 at.%. These results were also later confirmed by Varvenne *et al.* [92].

2.1.1.2.6 Recent theoretical developments on the theory of HEAs: configurational entropy and sluggish diffusion.

Early in 2018, a paper written by researchers at the University of São Paulo (Brazil) and Texas A&M at College Station (USA) led by C.G. Schön, shed light on the theoretical possibility of the configurational entropy having a very small (or even zero) influence on phase transformations and stability for HEAs [68]. It was theoretically shown by means of *ab initio* calculations that the relevant factor behind the observed single phase stability for these alloys is the strong competition between alloying elements due to interatomic forces within the disordered state. The authors proposed that the phase stabilisation in HEAs is probably caused by configurational frustration instead of configurational entropy; however the conclusions of the authors are based on the computational study of only one HEA system: VNbTaMoW [68, 69].

Within the context of condensed matter physics, frustration happens when atoms have a tendency to occupy non-trivial positions within a lattice due to conflicting interatomic forces. The conflict between different interatomic potentials is a competition where each potential favours a certain structure. The result is a very complex disordered structure even when formed at higher temperatures (the case of HEAs). In materials science and condensed matter physics, examples of such frustration phenomena extend from amorphous to ferromagnetic materials [93–98]. Additionally, the authors are not supportive of the idea of sluggish diffusion.

Such recent developments, therefore, demonstrate that the theory of high-entropy alloys is still under development. Experimental evidence is needed to test the computational results provided by Schön and his co-authors [68, 69].

2.1.2 Nanolayered materials

With their development driven by advances in reactive hot pressing techniques, nanolayered materials can now be artificially produced with accurate control of both elemental composition and final microstructure. The result is the emergence of an entire new class set of materials with unique properties and specific applications in

engineering, nanotechnology and industry. Additionally, nanolayered materials have also set a wide variety of new challenges of scientific interest [99]. In this section, the definitions and properties of the $M_{n+1}AX_n$ phases are discussed.

2.1.2.1 $M_{n+1}AX_n$ phases

2.1.2.1.1 Historical context

Carbides and nitrides were the subject of intense research during the 1960s and 1970s. Nowotny summarised in 1971 the work performed at that time on the so-called *H-Phasen* [100–103], or Hägg Phases, which consisted of a series of ternary carbides and nitrides with Si, Ge and Sn mixed with transition metals that exhibited an interesting and unique set of properties [104]. Researchers at that time catalogued almost thirty ternary carbides and nitrides which were of a similar chemistry following a specific formation rule: M_2AX with M_2X layers intercalated with "A" early transition metals [105]. The history of the Hägg Phases changed completely upon the discovery of a new Ti-based carbide, the Ti_3SiC_2 that was produced using reactive hot pressing techniques, and was considered incredibly soft when compared to other carbides [106]. In 1996, Barsoum *et al.* reproduced the results from the 1960s and again synthesized the Ti_3SiC_2 concluding that ternary carbides and nitrides formed with the association of a early transition metal, C and/or N with "A" elements were, in fact, an entirely new class of materials: the $M_{n+1}AX_n$ phases. In Barsoum's words *"since 1996 (...) we have embarked on an ambitious program whose goal is to synthesis and characterise all the $M_{n+1}AX_n$ phases"* [105].

2.1.2.1.2 Definition

$M_{n+1}AX_n$ phases, or simply MAX phases, are a class of multilayered materials that have been attracting the attention of researchers and scientists due to their unique set of properties and potential applicability in the nuclear industry, particularly in fusion reactors. They are distinguishable from other multicomponent materials due to their unique crystal structure and by a specific mixing rule. MAX phases can be defined as the set of layered and hexagonal carbides and nitrides that can be made by mixing a transition metal (M), an element (A) from the 13 and 14 groups of the periodic table with C or N (X). Crystallographically, C and N occupy the interstitial positions, i.e. the octahedral sites of a M_6X crystal structure while the A-atoms are accommodated at the centre of the interatomic spaces of M atoms [107, 108]. A typical MAX phase unit cell structure, that of Ti_3SiC_2, is presented in figure 2.7.

2.1.2.1.3 Classification

The classification of MAX phases is performed by looking at the number (n) of M layers in the unit cell structure. For example, MAX phases with $n = 2$ belong

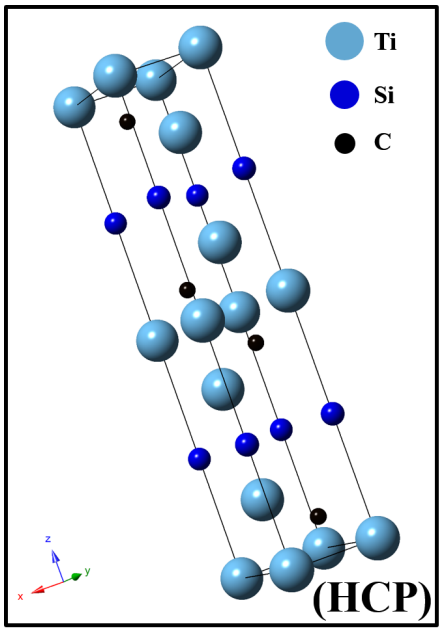

Figure 2.7: The unit cell of the Ti_3SiC_2 MAX phase.

to the group 211, while when $n = 3$, the classification group is 312. To date, the list of known MAX phases extends to $n = 4$, or the group 413 phases, where Ti_4AlN_3, Nb_4AlC_3 and Ta_4AlC_3 are representatives of this group [108]. It has been reported that the most studied groups are the 211 and 312 where the most common M elements are V, Ti, Zr, Cr, Nb, Ta and Hf including the A elements Al, P, S, Ga, Ge, Si, Cd, As, Tl and Pb.

2.1.2.1.4 Properties and potential applications

The nanolayered nature is responsible for most of the properties exhibited by the MAX phases. As with conventional binary and ternary carbides and nitrides, MAX phases exhibit strong stiffness, good thermal and electrical conductivity, low thermal expansion and are highly resistant to chemical attack and oxidation processes [109–111]. However, some small differences between the mechanical properties of MAX phases compared to conventional ceramics have been found to be critical in certain applications. Compared with TiN where the hardness is around 15–25 GPa, MAX phases are softer, with hardness generally around 2–8 GPa. On the other hand, MAX phases are harder than, for example, ferritic stainless steels with yield strength approximately 45 MPa. Due to the fact that MAX phases are softer than most of the available ceramics, they are readily machinable, less brittle and thermal shock resistant [105, 110]. The properties and characteristics of MAX phases have been recently reviewed by Barsoum and Radovic [110] and are summarised below.

Atomic bonding Experimental, theoretical and computation simulations have been recently used to assess the atomic bonding structure of MAX phases. The current understanding is that the atomic bonding in MAX phases is a unique combination of metallic, covalent and ionic [112–117]. Orbital hybridisation between the p levels of the X elements and the d levels of the M atoms has been reported to lead to strong covalent bonding [110] when compared with MX ceramics (e.g. TiC). Hybridisation also occurs between the p and d orbitals of A and M atoms, respectively. Specifically for the 211 group with Al and C, it has been reported that a net charge transfer occurs from the Al to the C atoms [116]. Due to similarities in atomic bonding, the MAX phases share a number of common properties across a wide variety of known compounds in their groups [110].

Microstructural defects in MAX phases Compared with conventional ceramic compounds, MAX phases have been characterised as having pseudo-ductility at higher temperatures due to the activation of a few basal slip systems, but at lower temperatures the brittle nature is restored [109, 118]. Regarding the response of MAX phases to external stress, results indicate that only basal plane dislocations (*i.e.* constrained to slip within the basal plane) contribute to the mechanical deformation of such materials, although this statement is based on reports from the most studied MAX phase so far, Ti_3SiC_2. According to Barsoum *et al.* [110], there is no indication that twins or non-basal dislocations participate in deformation processes in MAX phases. Further work is needed to assess whether non-basal plane dislocations can also contribute to the mechanical deformation of such materials [110].

With respect to the nature of the dislocations, conventional TEM characterisation has indicated that basal plane dislocations in Ti_3SiC_2 have a Burgers vector of $\vec{b} = 1/3[11\bar{2}0]$ with mixed edge and screw behaviour [119, 120]. The interaction between dislocations, which plays a major role during deformation processes is also of concern. It has been reported that the dislocations can arrange themselves into arrays, forming low- and high-angle grain boundaries either parallel or normal to the basal planes [110].

Elastic properties MAX phases have slightly lower hardness than most of the conventional ceramics: for polycrystalline MAX phases the Vickers hardness values were reported to be in the range of 2-8 GPa [110]. However, compared with metals, for example, Ti_3SiC_2 is three times harder than pure Ti [110, 121]. Some mechanical properties such as shear modulus and Young's modulus are generally of the order of GPa (comparable with MX ceramics). The MAX phases studied in this work – Ti_2AlC and Ti_3SiC_2 – have a shear modulus of 118 and 139 GPa and a Young's

modulus of 277 and 339-343 GPa, respectively [110]. Among the wide variety of different MAX phases, those with Pb and Sn are generally less stiff than when the element is Al or Si. The elastic properties of MAX phases have been recently reviewed by Barsoum *et al.* [110]. In general, stoichiometry is influential in many elastic properties of the MAX phases. This indicates that such materials could, in principle, be engineered for specific applications where stiffness and hardness are major requirements.

Hysteretic and nonlinear elastic behaviour MAX phases exhibit an unusual nonlinear hysteretic elastic behaviour meaning that the cycles of loading (either compression or tension) are reversible and very dependent on grain size and density [110, 122]. A model of subcritical Kink Bands (KB) has been proposed to address such experimental observations and indicates that shear and normal stresses are required to start interaction between dislocations which then contribute to nucleation of a KB. Upon removing the load, the KB shrinks, which is in agreement with the observed reversible nonlinear elastic behaviour, although nucleation and growth of KBs in MAX phases is not yet completely understood [110, 123, 124]. Typical stress-strain curves showing the hysteretic and nonlinear elastic behaviour of two Ti-based MAX phases are shown in figure 2.8.

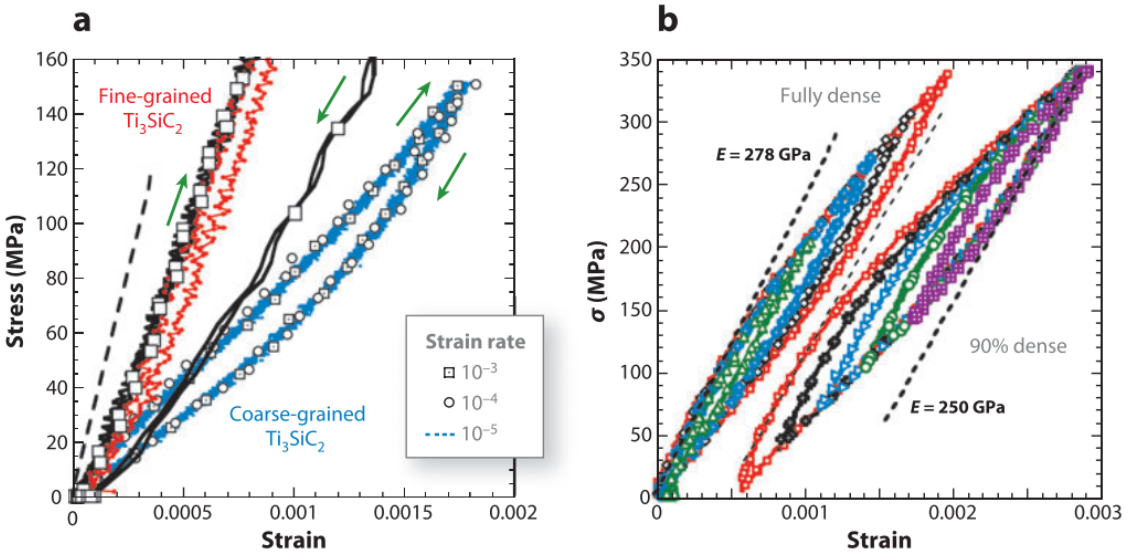

Figure 2.8: Stress-strain cycles for (a) Ti_3SiC_2 and (b) Ti_2AlC showing their hysteretic and nonlinear elastic behaviour. Figure (a) shows how the nonlinear elastic behaviour changes with different grain sizes. In figure (b), the samples had similar grain sizes, but different densities. (Reproduced from Barsoum *et al.* [110])

Room and high temperature plastic behaviour As MAX phases are of hexagonal-compact nature, when slip through basal planes is allowed, the mechani-

cal deformation of MAX phases at room temperature is regulated by the formation of classic shear bands: a behaviour that resembles a metal-like compound and for this reason, some MAX phases are known as ductile carbides [125]. It is important to note here that shear bands can be defined as distortions in a material (usually ductile materials) when part of a grain rotates towards another orientation in order to accommodate the applied load [126]. Conversely, when the external load is parallel to the direction of the slip planes (a case where dislocation glide is limited or does not occur), KBs are observed to form. For the latter case, delamination of individual grains is also reported to occur [110]. However, KBs have been attributed to the suppressed delamination behaviour of some MAX phases [125]. Coarse-grained MAX phases of the 211 group have been reported to not fail suddenly during tensile experiments: a phenomenon that occurs for most conventional ceramics [110].

At higher temperatures, all MAX phases suffer brittle-to-plastic transformations (BPT) [110, 127–129]. Ti_3SiC_2, for example, exhibits strong brittle behaviour at lower temperature while it can be plastic at higher temperature [130]. The BPT transition temperature for most of the Al-containing MAX phases and the Ti_3SiC_2 are in the range of 1273-1373 K [110].

Potential of MAX phases for application in nuclear technology All the properties discussed above mean that MAX phases are included in the list of possible suitable candidate materials for structural components in future nuclear reactors [131]. The elastic behaviour, the stability of the matrix and the complex atomic bonding structure constitute a unique set of properties that nowadays, is under investigation in order to assess how particle irradiation environments affect these properties and the microstructure of the materials. Although several MAX phases systems based on Hf [132], Zr [133–135] and Zr-Nb [136] have been proposed for application within the nuclear technology, the literature review on the effects of energetic particle irradiation on MAX phases will be presented in section 2.4.3 and it is focused on Ti-based MAX phases due to the relevance of these materials for this thesis.

2.2 Principles of radiation damage in solids

This section will discuss the main physical effects of particle radiation on the structure of solids. The physics that regulates the interaction between an energetic particle and a lattice atom can be described through ballistic processes, e.g. momentum transfer, interatomic forces and their potentials. This section has been primarily based on the detailed treatise on *"Defects and Radiation Damage in Metals"* written by M.W. Thompson in 1969 at the University of Sussex [22], but modern

concepts and references are introduced when appropriate.

2.2.1 Primary events of radiation damage

When an energetic particle impinges on a crystalline solid, collision events can take place. If the energy transferred by the incident particle is high enough, a lattice atom recoils from its crystal site. The recoil creates a vacancy (i.e. the absence of an atom), and the recoiled atom is now considered an interstitial within the crystal lattice. In other words, upon displacing an atom from its crystalline position, an energetic particle can induce the formation of an interstitial-vacancy pair (also known as a Frenkel-pair). The simplistic view of radiation damage in solids, is therefore, a two-body collision phenomenon. Upon increasing the energy, the process involves multiple binary collisions and the multiple recoils of lattice atoms will be distributed in a cascade of defects. A cascade of defects can also be caused by the impact of a single energetic particle with a crystalline solid [137, 138].

The interaction between an energetic particle (with mass M_1 and with initial velocity v_1) and a lattice atom (with mass M_2 and initial velocity v_2) can be described by the conservation laws of momentum and energy. Let us first assume that the lattice atom is not initially at rest, but it has some velocity v_2 (general case). The interaction can be described with respect to the centre-of-gravity of the system (G), as shown in figure 2.9. Momentum and energy conservation laws give, respectively:

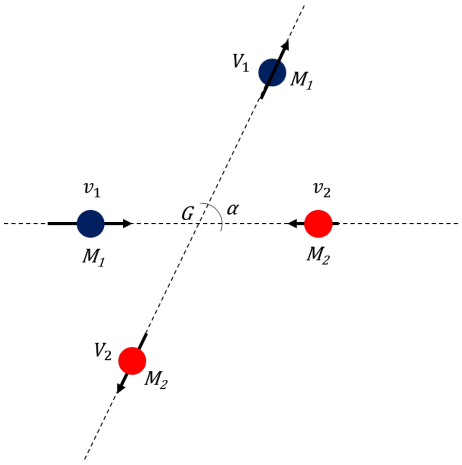

Figure 2.9: The collision between two bodies. Modified from [22].

$$M_1 v_1 + M_2 v_2 = M_1 V_1 + M_2 V_2 \tag{2.8}$$

$$M_1 v_1^2 + M_2 v_2^2 = M_1 V_1^2 + M_2 V_2^2 \tag{2.9}$$

The left terms in equations 2.8 and 2.9 are known quantities before the collision

event. The velocities of bodies V_1 and V_2 after the collision are the quantities of interest and they can be calculated, with the coordinates and velocity (v_g) of centre-of-mass taken as reference.

$$V_2^2 = 2(1 - \cos\alpha)\frac{M_1^2 v_g^2}{(M_1 + M_2)^2} \tag{2.10}$$

Using equation 2.10, the relationship between the energies before (E_i) and after (E_f) the collision can be expressed as:

$$E_f = \Gamma E_i \sin^2\left(\frac{\alpha}{2}\right) \tag{2.11}$$

where the parameter Γ is:

$$\Gamma = \frac{4M_1 M_2}{(M_1 + M_2)^2} \tag{2.12}$$

A head-on collision happens when $\alpha = \pi$. This is a case where there is maximum energy transfer between the bodies. When $\alpha = 0$, no scattering occurs.

Such calculations are important to define how much energy will be transferred to an atom as a result of an energetic particle collision. For a given combination of particle and substrate, there is a minimum incident particle energy, E_{min}, at which damage will occur. This is expressed by:

$$E_{min} = \frac{E_d}{\Gamma} \tag{2.13}$$

The average energy that must be transferred to a lattice atom to displace it from its crystalline position is known as the displacement energy, denoted by E_d. For metals like Fe, Cr, Ni and Mn (alloying elements of stainless steels), the E_d is approximately 40 eV [139, 140].

For collisions between neutrons/ions and atoms at the energies of interest in the current work, the classical mechanics approach described here is valid. In the case of electron irradiations, a relativistic treatment may be necessary [22]. The physical interactions between energetic charged particles or neutrons and solid targets have been extensively studied in theoretical physics and a detailed description involves complex interatomic forces and potentials. Such theoretical investigations of energetic particles interacting with atoms in solids started early in the 1900s with Niels Bohr and collaborators [141, 142]. The nature of the incident particle and the interatomic forces regulating such interactions are of paramount importance to describe the radiation damage events with accuracy, but in this section focus will be given to the phenomenological aspect of the damage events, rather than the theoretical aspect.

2.2.1.1 Ions colliding with solids

As an energetic particle travels within a solid, a significant reduction of its kinetic energy is expected to occur as a function of the path travelled. Energy is transferred to the lattice atoms by elastic or inelastic scattering. Eventually, the energetic ion irreversibly loses kinetic energy and stops within the material [143–145]. In physics, stopping power is the ability of a material to decelerate an energetic particle and it is a function of the particle's energy. The linear stopping power – for example – is defined by the rate of energy loss per length travelled [143, 146]:

$$S(E) = -\frac{dE}{dx} \tag{2.14}$$

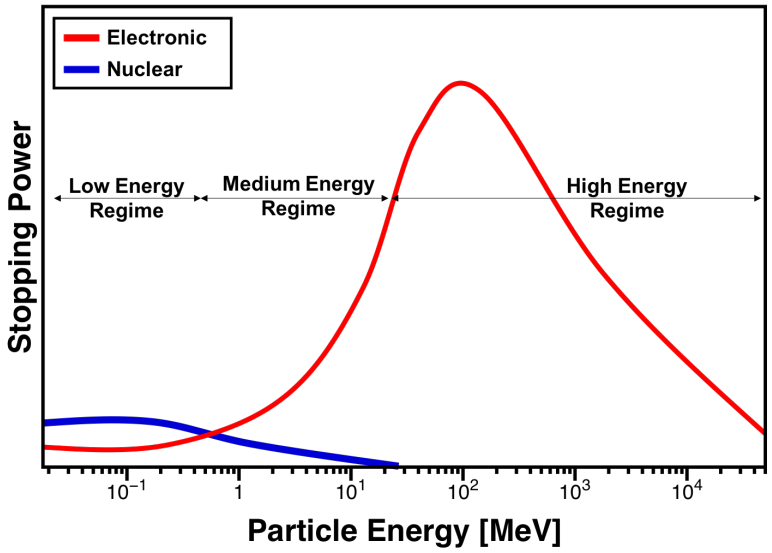

Figure 2.10: Representation of the contributions of both electronic and nuclear stopping powers as functions of energy for self-ion irradiations. Modified from [147].

It has been reported that, for heavy and light ions with low energies (in the order of keV), nuclear binary elastic collisions are predominant and the energy loss is due to elastic scattering [22]. In this case, the collision process involves a stationary lattice atom and an incident energetic ion. The energy loss process in this case is known as nuclear stopping [143–145]. For light ions with medium to high energies (MeV to GeV), the slowing down process is dominated by inelastic processes involving interactions between the electron clouds of the target atom and ion travelling within the solid. The energy loss process in this case is known as electronic stopping [143, 146]. The energy ranges for which the nuclear and electronic stopping powers are dominant are shown in figure 2.10.

For the purposes of studying radiation damage in materials by using ion implanters and accelerators, the nuclear stopping is the most important mechanism of ion energy loss. In the experiments reported in this thesis (30-300 keV), the nuclear

stopping is, therefore, dominant and the collisions between the incident energetic ions and the lattice atoms are treated as binary elastic collisions.

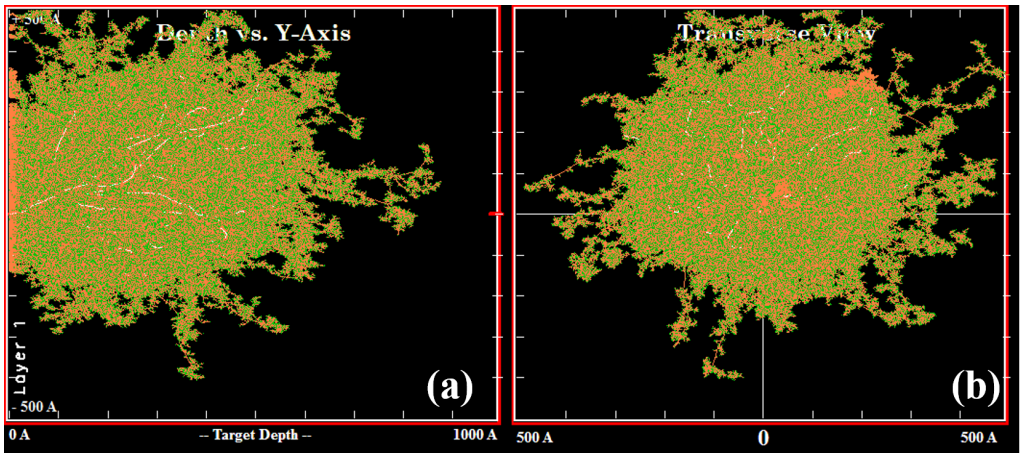

Figure 2.11: Collision cascades generated in Fe irradiated with several 134 keV Xe ions: (a) depth view and (b) transverse view. Calculations were performed using the SRIM2013Pro Monte Carlo code [148].

If the energy transfer from the ion at the moment of the collision is higher than the displacement energy of the lattice atom, the latter will be displaced from its lattice position creating a so-called primary knock-on atom (or PKA). Through a nuclear collision, a displaced lattice atom (interstitial) is formed and a vacancy is created at the original lattice site. If the energy of the displaced atom is high enough, it may impact another lattice atom causing its displacement. This is known as the knock-on effect and it may trigger several lattice displacements creating a chain of collisions known as displacement cascade (as shown in figure 2.11). There is also a case where an already displaced lattice atom collides with another atom displacing it from its site, but itself comes to rest in that position. When this happens, the phenomenon is known as a replacement collision [149].

2.2.1.1.1 Computational methods and ion implantation

Nuclear and electronic stopping powers for ions in matter can be determined either by means of scattering experiments in ion accelerators, such as the Rutherford Backscattering technique [150–152], or can also be calculated by means of Monte Carlo simulations [153]. One of the most popular Monte Carlo codes for calculating ion implantation ranges and radiation damage is the Stopping and Range of Ions in Matter or SRIM [148]. Generally, prior to the design of an ion irradiation experiment, scientists resort to computation techniques and software such as SRIM to predict implantation depths, distribution of damage, ion straggling for a wide variety of materials.

In order to simulate the ion collisions with atoms in a solid, the statistical algorithm in SRIM allocates several variables input by the user. These variables include,

for example, the ion energy, mass, angle of incidence and thickness of the solid target. As SRIM uses a Monte Carlo algorithm, the accuracy of the results depends on the number of ion collisions simulated. SRIM output data has been extensively benchmarked with real experiments and cross-checked with other algorithms. Ziegler *et al.* reported that in 2010 [148], the potentials used within the SRIM code were accurately benchmarked along with 27.000 experimental data points and by this, it is a widely accepted tool by the entire ion beam community [140, 154, 155].

2.2.1.2 Neutrons colliding with solids

A neutron is a subatomic particle with zero-charge and the interactions between energetic neutrons and the crystal lattice are different than for charged ions [156, 157]. Nuclear reactions of concern to nuclear reactor technology can generate neutrons with a broad energy spectrum [158]. The interaction between neutrons and structural materials in a nuclear reactor is the core of nuclear materials research and radiation damage [22, 159].

Elastic collisions are the most important type of interaction for radiation damage. The energy domain of typical elastic collisions (treated as "hard-spheres") between neutrons and matter is within 0.5–20 MeV and this is the energy range where radiation damage via displacements of atoms from their lattice positions may occur in structural nuclear materials. In nuclear reactors, Watt reported in 1952 that the average and maximum energies for fission neutrons from both ^{235}U and ^{239}Pu are 0.7 and 2 MeV, respectively [160].

At lower energies, thermal neutrons with energies around 0.025 eV are likely to be captured (inelastic collision) by nuclei resulting into either transmutation or activation reactions [161]. After transmutation, the released atoms may have a high kinetic energy. By this reason, transmutation products and neutrons generated through nuclear reactions can also generate radiation damage via elastic interactions. Inelastic collisions and transmutations can also change the local chemical composition of the materials in a nuclear reactor.

The interaction between energetic neutrons and matter is described by means of nuclear cross-sections which are physical quantities that estimates the probability of elastic and inelastic scattering, absorption and other types of nuclear reaction that can be triggered by these neutral particles. Ex- and in-core materials for nuclear reactors are primarily chosen by looking at their neutron absorption (inelastic) cross-sections. The lower the neutron absorption cross-section for a certain material, the lower will be the probability for neutrons of that energy to be absorbed by the nuclei of the material, and therefore produce intense damage from transmutation products and recoils. A material that absorbs neutrons is not recommended to be used as a nuclear fuel cladding material as it can penalise its neutron efficiency.

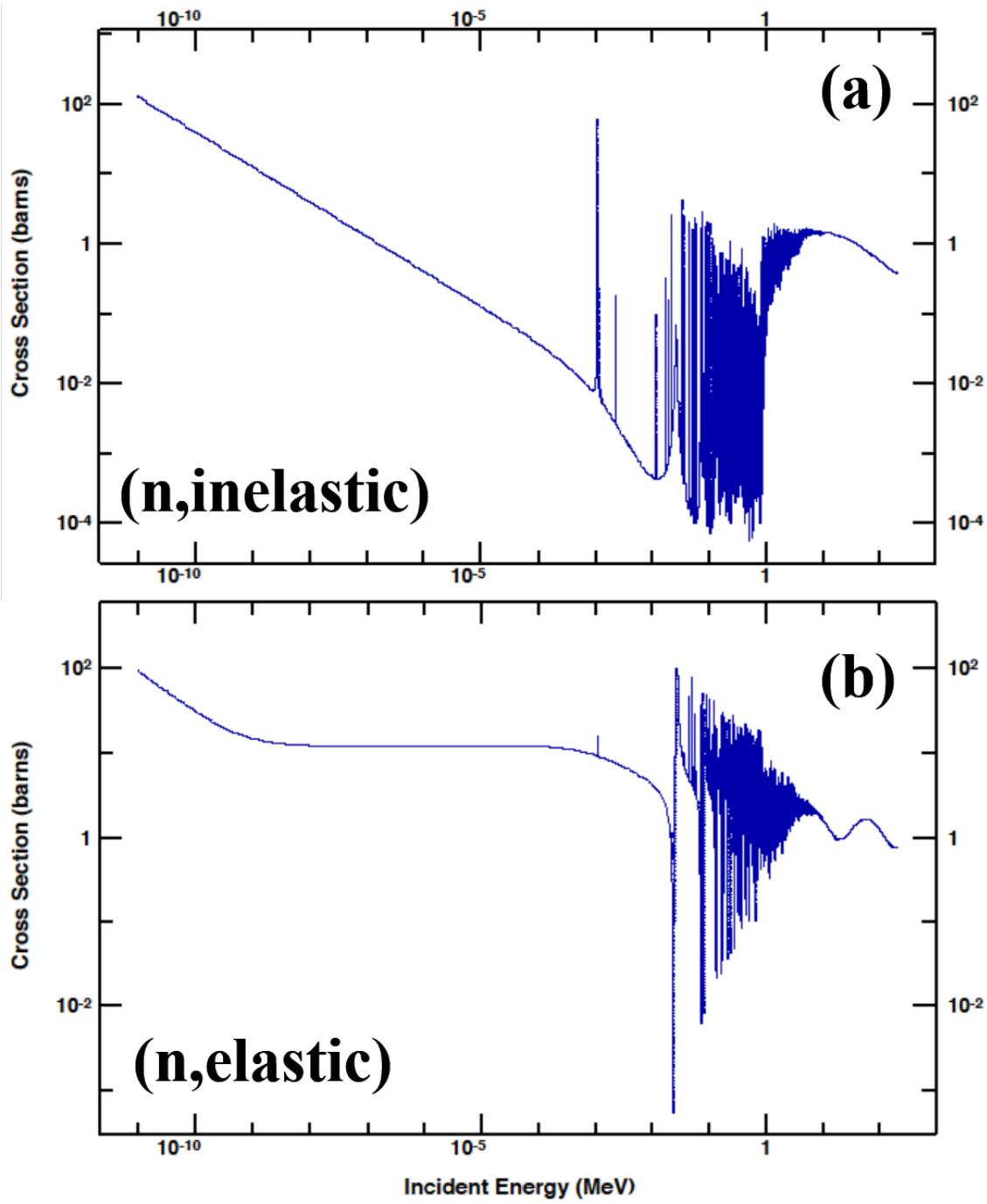

Figure 2.12: Inelastic (a) and elastic (b) neutron scattering cross-section data for the Fe-56 isotope. Plots produced from the JEFF nuclear database [162].

In nuclear physics, cross-sections are expressed by the unit barn, where 1 barn is equal to 10^{-24} cm^2. Cross-sections can vary with incident neutron energy and temperature. As an example, the inelastic and elastic cross-sections for iron (isotope Fe–56) – as a function of the neutron energy – are showed in figure 2.12 [162].

2.2.1.2.1 Neutron-induced nuclear reactions and impurity damage

Three nuclear reactions are of particular importance for the study of radiation damage in solids because of their relevance within the context of the performance of structural materials as well as the reliability and safe operation of a nuclear installation.

Lattice atoms can absorb neutrons which may induce transmutation to a lighter element. Alpha particles (α) can be emitted during such reactions. This type of reaction is known as (n,α) and it may occur for a wide variety of elements exposed to thermal neutrons, i.e. with energies around 0.025 eV. Alpha particles may be considered as ionising radiation and their effects on biological systems have been already catalogued [163]. In materials, alpha particles accumulate as He atoms and can induce the precipitation of bubbles, degrading the mechanical properties of such materials by means of an effect known as helium embrittlement [164, 165]. A similar transmutation reaction (n,p) produces protons which accumulate as H atoms and may lead to the nucleation and growth of H bubbles as well as formation of metal hydrides.

The third nuclear reaction of relevance is the (n,γ) reaction in which a neutron is absorbed by the nucleus of an element inducing its activation. The element transforms into an unstable isotope emitting γ–rays. This form of ionising radiation is highly energetic and can induce biological transformations in living systems [166]. As stated earlier, elements that undergo neutron absorption and become sources for γ–rays are generally avoided in nuclear installations, although γ–rays can be attenuated and/or absorbed by shielding elements [167]. For radiation damage in structural materials, γ–rays are not of practical importance, however they may induce an effect known as gamma heating which has been reported to damage the crystal structure of diamond [168] and silicon [169].

2.2.1.3 Kinchin-Pease model

Kinchin and Pease, working at the Atomic Energy Research Establishment at Harwell in the United Kingdom, developed a model to describe the events of radiation damage in solids [160]. Their assumptions are firstly based on the fact that primary knock-on atoms do not have sufficient energy to travel very large distances before coming to rest in an interstitial position and, secondly, due to the fact that vacancies and interstitials can recombine. Kinchin and Pease aspired to answer the following

question: what is the number of displaced lattice atoms induced by the collisions with PKAs? Kinchin and Pease derived an equation where the number of displaced atoms in a monoatomic crystal is a function of the PKA energy, *i.e.*:

$$N_d = 0.4\frac{\bar{E}}{E_d} \tag{2.15}$$

Where $\bar{E}$ is the initial energy of the PKA and E_d is the displacement energy. Equation 2.15 is valid only, of course, when $\bar{E} > 2E_d$. The constant 0.4 was introduced later by Sigmund [170] and corrects the Kinchin-Pease model to compensate the effect of electronic energy loss.

In the case of irradiation with neutrons, Watt showed in 1952 that the fission neutrons produced in a nuclear reactor from ^{235}U and ^{239}U have an average energy of around 2 MeV and a peak at approximately 0.7 MeV [171]. Assuming that the hard-sphere model of collisions is adequate to describe irradiation with (fast) neutrons, the number of recoiled atoms is:

$$N(E)dE = \frac{dE}{E_{max}} \tag{2.16}$$

Where $E_{max} = \Gamma E$ is from the equation that describes a head-on collision (eq. 2.11). Regarding the number of displaced atoms, this was found to be a function of the mass of the PKA [160]. For heavy elements, the number of displaced atoms is simply [172]:

$$N_d = \frac{E_{max}}{4E_d} \tag{2.17}$$

The ionisation limit (L_c) has to be taken in account for lighter elements as the PKA lose all the excess energy in ionisation processes. Therefore equation (2.17) is slightly modified to:

$$N_d = \left(2 - \frac{L_c}{E_{max}}\right)\frac{L_c}{4E_d} \tag{2.18}$$

In summary, heavy nuclei can take up less recoil energy and light nuclei can receive more recoil energy, but lose at a greater proportion due to ionisation processes. Kinchin and Pease reported that for elements such as Fe, neutrons with an average energy of 2 MeV produce a maximum (peak) number of displacements. [160].

2.2.1.4 The Norgett–Robinson–Torrens displacement model and the definition of displacements-per-atom

According to Nordlung *et al.* [173], the KP model established the foundations of an early model to calculate the number of displacements by using kinetic energy

transfer considerations and the material-specific threshold displacement energy. As an evolution to the KP model, Norgett–Robinson–Torrens introduced a model of displacement damage [174, 175] which allowed the estimation of the number of displacements-per-atom (dpa) collision as a function of a given PKA energy [140].

The concept of dpa is the average number of times in which a lattice atom is displaced from its lattice site during irradiation. In this way, 10 dpa means that a lattice atom was displaced from its lattice position 10 times on average during irradiation, for example.

The Norgett–Robinson–Torrens (NRT) model states that the number of displacements (N_d) is a function of a damage energy (T_d) which is the available kinetic energy that could be used to generate displacements. For a single ion, for example, the damage energy is simply the difference between the total ion energy and energy lost via electronic interactions (ionization) [173]. The number of displacements is then calculated according the NRT model as:

$$N_d(T_d) = \begin{cases} 0 & \text{if } T_d < E_d, \\ 1 & \text{if } E_d < T_d < \frac{2E_d}{0.8}, \\ \dfrac{0.8T_d}{2E_d} & \text{if } \frac{2E_d}{0.8} < T_d < \infty \end{cases} \tag{2.19}$$

Nordlung *et al.* [173] emphasises that the NRT model is essentially the KP model (see equation 2.15) with the kinetic energy term substituted by T_d in order to consider the electronic interaction effects. In addition, the factor 0.8 was introduced to take into account "more realistic" interatomic potentials [173].

Equation 2.19 can be used to estimate the number of vacancies (from the number of displacements) produced by a PKA. The damage energy can be calculated using commercial software such as the Monte Carlo code SRIM-2013. The complete description of the algorithm and the limitations of the code can be found elsewhere [145, 148]. In this thesis, the procedure to estimate the dpa based on a certain fluence (measured during MIAMI experiments) and using the code SRIM-2013 will be discussed in detail later in section 3.4.3.2.

2.2.1.5 Collision cascades and thermal spikes

In a nuclear reactor and also in ion accelerator irradiation, the primary knock-on atoms have energies in the order of a few hundred keV which is higher than the displacement energy for most metals, *i.e.* 40 eV. Due to the high energies involved, a single PKA can trigger several other collisions that will displace more lattice atoms. The process can be viewed as a collision cascade.

For an energetic particle impinging in a solid, a large amount of energy may be

deposited in a very small volume which can be considered melted for short period of time [160, 176]. This is a different concept known as thermal spike (or displacement spike) and it was proposed by Brinkmann in 1954 [159]. Within the cascade, a spike can create a large number of defects and theoretical approach to describe collision cascades have been proposed since the early years of nuclear technology [137, 159, 177].

Ishino *et al.* observed in 1983, by means of heavy ion irradiations *in situ* in a TEM, by monitoring the sizes of surviving cascade-induced defects such as clusters. The authors concluded, that the size of damage cascades in Au targets was a function of the ion energy, while the shape of the cascade could be changed with both the mass and energy of the incident ions [176]. The same authors reported the observation of small clusters of defects constantly appearing and disappearing in Ni as the irradiation was monitored: this was attributed to the formation of a "cascade image" according to the authors, but obviously this is a cascade image after the collapse of the cascade as the time resolution of the Japanese system was 30 ms [176]. Some of the clusters remained in the microstructure after the irradiation and exhibited diffraction contrast within the TEM [178, 179]. Such clusters were also reported to occur in other materials, Au, Ag and $AuCu_3$ [180, 181]. The same type of defects were reported by Merkle *et al.* in Au samples damaged in a nuclear reactor by fission fragments [182]. All these reported defects were attributed to the collapse of the damage cascade when Frenkel-pairs undergo into recombination, but not all the defects are able to annihilate and thus may form clusters. Within the cascade, recombination occurs within timescales around pico to nanoseconds [183], making it impossible to image the cascade in a TEM. However, the cascade can be studied by investigating the formation of such defect clusters which is thought to be a direct result of the so-called cascade collapse.

Observing the damage microstructure of Au with the TEM with an *in situ* heavy ion irradiation facility, Muroga *et al.* [184] and Ishino *et al.* [176] observed that temperature plays a major rule in the evolution of defects after the cascade collapse. In the temperature range from 120 to 470 K, both the structure surviving damage did not change. When thermal annealing of defects started to occur, at around 470 K, the cascades evolved to extended defects such as vacancy clusters, loops as well as stacking fault tetrahedra. An interesting point made by these authors for experiments at moderate temperature (470 K) is the fact that formation of extended defects occurred rapidly. This indicated that the time-frame of radiation damage events was shorter than the limits of experimental detection (≈30 ms). At higher temperatures, the number of defects was observed to increase proportionally with increasing temperature.

On the other hand, the thermal spikes can raise the local temperature of the

target material up to 1000 K, but for very short time-frames, 10^{-11} s [159, 185]. Donnelly *et al.* also reported that thermal spikes caused local melting of Au, In, Pb and Ag under Xe ion irradiation which led to the formation of craters and holes within the materials [137].

2.2.2 Radiation-induced point and extended defects

The effects of the radiation on solids is to create defects in the microstructure of the materials. An overview of radiation-induced defects in solids will be presented in this section. Although some of the radiation-induced defects were briefly presented in the previous sections, detailed description of their formation, characterisation in the microscope and influence on the performance of the materials will also be introduced in this section. When defects are formed in a material by its exposure to energetic particles, the effects on its mechanical, thermal and electrical properties are, in general, detrimental. The characterisation of damage microstructures and the mechanisms behind their formation is of paramount importance for nuclear engineering. Before use as a structural material in a nuclear reactor, a material has to be tested in a wide variety of conditions [186]. Ion irradiation using ion accelerators and neutron irradiation in materials testing reactors (MTRs) are methodologies to investigate the effects of irradiation on solids. Post-irradiation characterisation is often carried out with electron microscopes and by mechanical testing.

2.2.2.1 Vacancies and voids

A vacancy it is the simplest form of crystal defect (a point defect). The necessary (thermal) energy to form a vacancy within a solid can be derived assuming that to displace an atom from its lattice position, one needs to break all its interatomic bonds. The energy to form a vacancy, U_f^v is [22]:

$$U_f^v \approx L_s \tag{2.20}$$

Where the L_s is the latent heat of sublimation per atom and is on the order of a few eV for most solids. Vacancies can be thermally activated and start to diffuse throughout the crystal lattice. When a vacancy encounters another vacancy, a divacancy may be formed. A void is formed upon the agglomeration of several vacancies. Supposing that a vacancy cluster, *i.e.* a void, has a spherical shape, the energy necessary for its formation is approximately:

$$U_f^v \approx 4\pi r_a^2 \gamma \tag{2.21}$$

The parameter γ is the surface energy per unit area and r_a the radius of the

small void. For most metals with $\gamma \approx 0.1\text{eV}\cdot\text{Å}^{-1}$ and $r_a = 1.5\text{Å}$, the formation energy has been reported to be of around $U_f^v \approx 2$ eV [22]. Thompson commented that such a value will be overestimated as the collapse of a cavity under surface tension is neglected in the derivation process of equation (2.20) [22]: the effective potential energy of the crystal with defects will be reduced by the relaxation caused by strains associated with the formation of vacancies and for this reason, U_f^v will be smaller.

Formation of voids in metals and alloys has been associated with embrittlement which causes degradation not only of the mechanical properties [187, 188], but also the thermal and electrical conductivities [189]. Voids are also influential in the occurrence of cracks in steels subjected to irradiation [190].

Upon increasing the temperature of a metal, vacancies start to diffuse throughout the crystal lattice [191, 192] and their activation energy for migration as well as the enthalpy of formation can both be estimated by means of positron annihilation in pulse heating experiments [193]. Radioactive tracers have also been employed to measure the activation energies of vacancies of several elements since the 1950s [194, 195]. The migration energy for vacancies can be as low as 0.02 eV for sodium [196] and as high as 3.2 eV for graphite [197], however the latter is not a consensus value.

Vacancies exist naturally in crystals (equilibrium vacancies), but they can of course be produced by collisions with energetic particles. In the case of the formation of vacancies as a result of irradiation, the required energy to be transferred to a lattice atom to displace it from its equilibrium position within the lattice is around 40 eV [139]. Upon displacing atoms from their lattice positions as a result of elastic collisions, vacancies and interstitials are created. This process is different from the formation of thermal vacancies. The nucleation and growth of radiation-induced voids in nuclear materials is often associated with swelling and porosity: both of which are very detrimental to mechanical properties and the safe operation of nuclear fuel rods [198–200].

2.2.2.2 Interstitials

After a knock-on collision, the displaced lattice atom can initially be in an interstitial position within the crystal lattice. This interstitial atom will cause local lattice distortion, and consequently, a large increase in the repulsive energy.

Three types of interstitial atoms have been reported to occur in crystal structures. A *dumb-bell* interstitial is the case where two atoms form a pair on a interstitial site. For face-centred cubic structures, when the interstitial occupies the largest open space within the lattice, it is said that it is a *body-centred* interstitial. The last case, a long chain of interstitials atoms aligned, is known as *crowdion* and it is formed in a close-packed crystallographic direction where long-relaxations are possible [22].

When an interstitial atom is of the same type as the crystal lattice atoms, it is considered to be a *self-interstitial atom* or SIA. Upon ion implantation, different elements can come to rest in lattice positions, either in substitutional or interstitial positions. Similarly, if the ion is the same element as the crystal lattice atom, the process is known as *self-ion implantation*. SIAs can be produced by irradiation/implantation, plastic deformation or thermal equilibrium at elevated temperatures. Within the context of radiation damage in solids, SIAs undergo strong elastic interactions which may be influential in radiation-related effects like void-swelling, radiation-assisted creep and degradation of mechanical properties. Due to their strong elastic interactions, there is also a great tendency for SIAs to form clusters [201].

As in the case of vacancies, interstitial atoms can be activated to migrate within the crystal lattice. Studying copper, Johnson and Brown were able to estimate the minimum energy for *dumb-bell* migration in 0.05 eV [202]. Thompson noted that for *crowdions* and *body-centred* interstitials, migration energies were approximately the same as for *dumb-bells*. Regarding the formation energies for interstitials, values have been reported to be higher than for vacancies, due to elastic stress fields: for example, Wirth *et al.* reported that the formation energies for dumbell, crowdion and vacancies in α-Fe are 4.87, 4.91 and 1.83 eV, respectively [203].

2.2.2.2.1 Clusters of interstitials

Clusters of interstitials may form during the collapse of a collision cascade. After the energetic impact, the highly disturbed region may undergo a fast relaxation and the short-range fast diffusion that happens during the thermal spike may allow interstitials to diffuse, and meet each other forming agglomerates [159]. By means of MD calculations in heavy metals, Nordlund reported that a high-density melted zone formed during the thermal spike which suffers fast recrystallisation and creates very large interstitial clusters [204]. Molecular dynamics simulations have also indicated that the number of interstitial clusters increases with the cascade energy for Fe [205]. With respect to the size of the clusters, MD simulations also indicate that the number of defects (both interstitial and vacancies) is a direct function of the PKA energy and temperature [206], although these processes are very dependent on the target materials and their properties.

2.2.2.3 Vacancy-interstitial pairs and recombination (or recovery)

The collision of an energetic particle with a crystal lattice generates an equal number of vacancies and interstitials. An interstitial atom has a strong strain field associated with it. In the case of a vacancy, such field is of opposite sign, therefore, there is strong interaction between vacancies and interstitials. For this reason, a close

Frenkel pair is viewed as a type of single defect. As both defects can be activated and start to migrate, they can also interact and recombine. Recombination of vacancy-interstitial pairs leads to the annihilation of both point defects.

Annihilation of point defects has been reported to occur in a wide variety of conditions within the field of research of nuclear materials [207–210]. The damage recovery in metals and ceramics can be monitored by measuring some properties before and after irradiation and on annealing, such as electrical resistivity [211] and elastic parameters [212].

2.2.2.4 Impurity damage: gas bubbles

The defects that are produced or generated due to the displacement of lattice atoms are known as *displacement damage*. But inside a nuclear reactor, energetic neutrons may also induce transmutation of atoms by means of nuclear reactions. The transmuted elements are foreign atoms within a crystal lattice structure, and upon diffusion, they will interact with vacancies and interstitials which may eventually lead to clustering.

When the nuclei are inert gases, such as He from (n,α) nuclear reactions, the occurrence of clustering will most likely result in the nucleation of inert gas bubbles within the microstructure [137, 213–215]. The same process also happens from (n,p) nuclear reactions which may lead to the formation of H bubbles. Bubbles are part of an entire class of irradiation-induced defects known as *impurity damage* [22]. In a solid with mobile vacancies, there will be a tendency for bubbles to grow or shrink. Bubbles can also migrate and coalesce. The equilibrium condition for a inert gas filled bubble in a solid is reached when the rates of arrival and departure of vacancies are exactly the same. At equilibrium, a inert gas bubble does not grow or shrink.

A reasonable approximation from experimental observations is the assumption that a inert gas bubble in a solid presents a spherical shape and both volume V and surface area a are a function of its radius r,

$$V = \frac{4}{3}\pi r^3, a = 4\pi r^2 \tag{2.22}$$

Upon irradiation, the departure and/or arrival of vacancies results in small changes in the radius r and this can be expressed as infinitesimal alterations in both V and a, expressed by:

$$dV = 4\pi r^2 dr, da = 8\pi r dr \tag{2.23}$$

As a bubble can be understood to be a thermodynamic system, during its expansion the pressure drives the work done by the system, pdv, and the surface energy, γ, increases by γda. The equilibrium condition under which the bubble does not

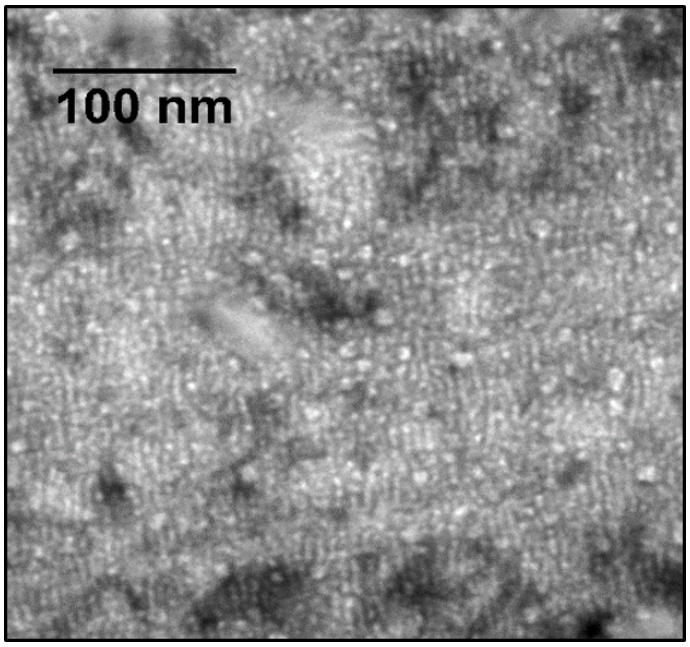

Figure 2.13: He bubbles formed in the microstructure of β–Zr during 6 keV He implantation at 1148 K. (Reproduced from [217])

grow or shrink, is therefore a trade-off between the work done by the pressure and the surface created by such work, mathematically expressed by the condition:

$$pdV = \gamma da \tag{2.24}$$

Substituting (2.22) into (2.23) results in:

$$pdV = \gamma da \rightarrow p4\pi r^2 dr = \gamma 8\pi r dr \Longrightarrow p = \frac{2\gamma}{r} \tag{2.25}$$

The equation (4) shows that for small radii, the pressure tends to be high, but the process is linear with the surface energy. Donnelly [214] reviewed calculations for both density and pressure of He gas bubbles in several metals. He reported that for Fe, He bubbles with radii of 1, 2 and 3 nm have pressures around 39, 19 and 13 kbar, respectively, thus confirming that with increasing size, gas bubbles have lower internal pressures.

There has been some debate in the literature on how to properly identify under- and over-pressurised bubbles with electron microscopy. Mitchell *et al.* [216] carried out 40 keV Xe implantation of β-Sn and observed the formation of small ($\approx$ 2-3 nm) and large ($\approx$ 20 nm) Xe bubbles. Through calculations using equation 2.25 and an appropriate equation of state, the authors have showed that the small bubbles were at equilibrium whilst larger ones, could be considered under-pressurised with respect to the calculated equilibrium pressure. However, the contrast within the TEM was indistinguishable for both types of bubbles.

Ultraviolet (UV) spectroscopy was used to investigate the pressures in He bubbles in metals. Upon increasing the implantation content from 1.45 to 3.1 at.% of He in Al, blue shift was observed in the UV spectra from small bubbles at lower fluences implying high pressures [218]. In the case of over-pressurised bubbles, reports also indicate that due to a strong stress field at their interfaces, it is sometimes possible to distinguish them using diffraction contrast within a TEM [219].

2.2.2.4.1 Impact of bubble nucleation on mechanical properties of nuclear materials

The nucleation and growth of inert gas bubbles in nuclear reactor materials is often associated with an effect known as swelling. Inert gases are insoluble in metals, and for this reason, a bubble can be viewed as a precipitate that upon nucleation, increases the volume of a material. Using the theory of bubbles and equations of state for several inert gases, Barnes derived a model to express the total swelling of any metal containing bubbles within its microstructure [220]:

$$\frac{\Delta V}{V} = \frac{mkT}{2\gamma} r \tag{2.26}$$

Where k is the Boltzmann constant, T the temperature of the irradiation (or annealing), r the average radius of the bubbles, m the amount of gas in moles contained in the bubbles and γ the surface energy of the material. For a fixed temperature, the swelling increases upon increasing the size of the bubbles. Barnes noted that his model has limitations on the assumption that the gas within the bubbles obeys the perfect gas law, therefore, it is a valid model for big bubbles (in the range of 20–50 nm) at equilibrium conditions. Additionally, it also assumes that: (i) bubbles are of spherical shape (which is not true for all metals), (ii) deviations in the average size is not large, (iii) surface diffusion dictates the migration of bubbles and (iv) there is no re-dissolution of the gas into the crystal lattice (*i.e.* the model does not apply for H, N and O) [220].

Within a nuclear reactor, swelling is a huge concern. For example, α-U, the nuclear fuel base material, swells around 3% at 723 K when the enrichment level is at 30% at a burn-up[3] level of 0.18% [221]. A nuclear reactor project needs to take swelling into consideration when designing the whole fuel assembly. If a control or nuclear fuel rod swells severely, it can get stuck in the thermohydraulic channel which could trigger a nuclear accident.

Inert gas bubbles also act as obstacles for dislocation motion within a crystal causing another effect that may severely degrade the mechanical properties of nuclear materials embrittlement. For austenitic stainless steels, it has been reported that

[3]Percentage of U atoms that undergo fission.

He bubbles along the grain boundaries were responsible for reducing the ductility of the steel significantly, thus leading to accelerated inter-granular fracture during tensile testing of the irradiated alloy [165].

2.2.2.5 Black-spots and dislocation loops

Methods for the analysis of neutron and ion irradiated materials were developed in the United Kingdom late in the 1950s by some pioneers in the field of electron microscopy of metals such as Hirsch [222] and Silcox [223] at the Cavendish Laboratory in Cambridge and Barnes [224], Mazey and Smallman [225] at the Harwell Laboratories [22]. Hirsch summarised this pioneering research in a review paper in 1980s [226].

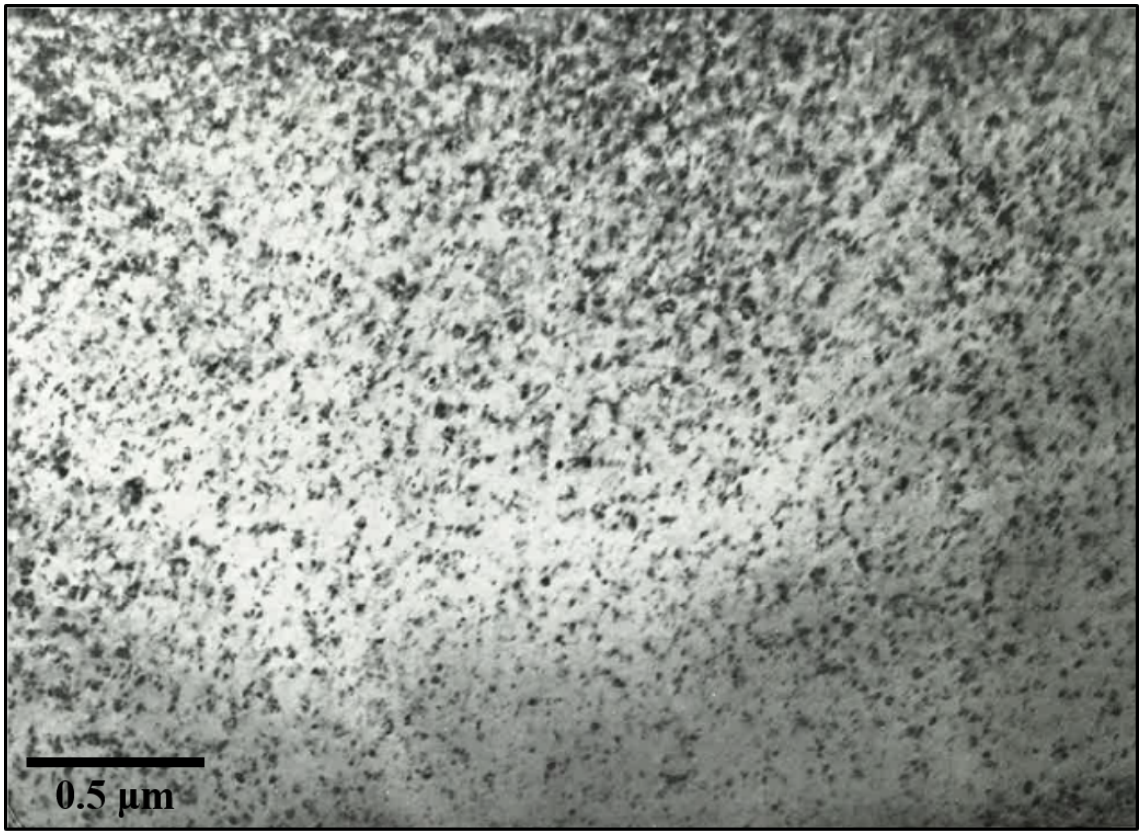

Figure 2.14: Dislocation loops and black-spots in neutron-irradiated copper at a fluence of 6.7×10^{17} n$\cdot$ cm^{-2} at 308 K. (Scanned from the original article by Silcox and Hirsch (1959) [223]).

By analysing neutron-irradiated Cu samples in an electron microscope in 1959, Silcox and Hirsch reported the observation of small black-spots with an average diameter of 7.5 nm at a dose of 6.7×10^{17}n$\cdot$cm^{-2} at 308 K as shown in figure 2.14. Some of these black-spots were resolved to be dislocation loops and exhibited strong strain fields in their surroundings. After analysing additional samples at a higher fluence, 5.6×10^{18}n$\cdot$cm^{-2}, the black-spots were seen to have clearly evolved into big-

ger dislocation loops with an average diameter of 15 nm. The formation of such small black-spots and dislocation loops in neutron-irradiated Cu was attributed to the collapse of the displacement cascade which forms vacancy clusters that upon growth, may evolve to dislocation loops. Radiation hardening, for these authors, related to the (areal) density of dislocation loops and black-spots formed under irradiation, however, upon annealing some of these defects were observed to annihilate [223].

Dislocation loops and black-spots in irradiated materials were observed to exhibit diffraction contrast. Tilting electron-transparent specimens within the electron microscope showed that their contrast changed and this has been attributed to the effect of strain fields caused by these defects within the lattice [222, 226]. The term "loop" was due to the fact that, upon tilting, such defects exhibited an elliptical annular shape [22].

Smallman and Westmacott also observed the formation of dislocation loops and black-spots in quenched, neutron- and ion-irradiated Al specimens. For this metal, neutron irradiation at room temperature gave rise to no defects. Upon increasing the irradiation temperature, defects were visible within a TEM, thus suggesting that the mobility of point defects such as interstitials and vacancies plays a major role in the formation of dislocation loops and black-spots [224, 227].

In general, the evolution of black-spots and dislocation loops in a wide variety of irradiated metals and ceramics can be summarised as follows: (i) the sizes increase upon increasing both the irradiation temperature and dose, (ii) the areal density in the TEM increases with the dose, but can decrease with temperature (due to recovery), and (iii) their nature is associated with events of the displacement cascade and migration of vacancies and interstitials [228–233].

2.2.2.5.1 Impact on the mechanical properties of metals and alloys

Formation of black-spots and dislocation loops in metals and alloys exposed to energetic particle irradiation is often associated with a hardening phenomenon which strongly affects their elasto-plastic properties. An expanded review on the effects of radiation damage on mechanical properties of materials goes beyond the scope of this thesis, but complete and detailed reports can be found elsewhere [234].

Makin and Manthorpe carried out tensile measurements on neutron-irradiated Cu and showed that the formation of black-spots and dislocation loops strongly increased the yield stress compared with the pristine samples. The measurements indicated that, as the irradiation dose increased, the metal lost its ability to plastically deform. The material became brittle, and this effect is known as irradiation hardening [235]. As studied by Blewitt in 1962, the yield stress of Cu increases upon increasing both the irradiation dose and temperature [236]. This observation was

also later confirmed by Diehl, Leitz and Schilling [237].

Seeger proposed an explanation of the irradiation hardening effect. He suggested that the presence of damage zones due to the displacement cascades, prevented the free movement of dislocations which explained the increase in the yield stress [238–240]. Possible ways for a dislocation loop to overcome the potential barrier for free movement within a damaged region would be the application of external stresses or by means of thermal activation. The application of the Seeger model was successful for a wide variety of irradiated materials and alloys, although the model has been improved with additional experiments over the years [241].

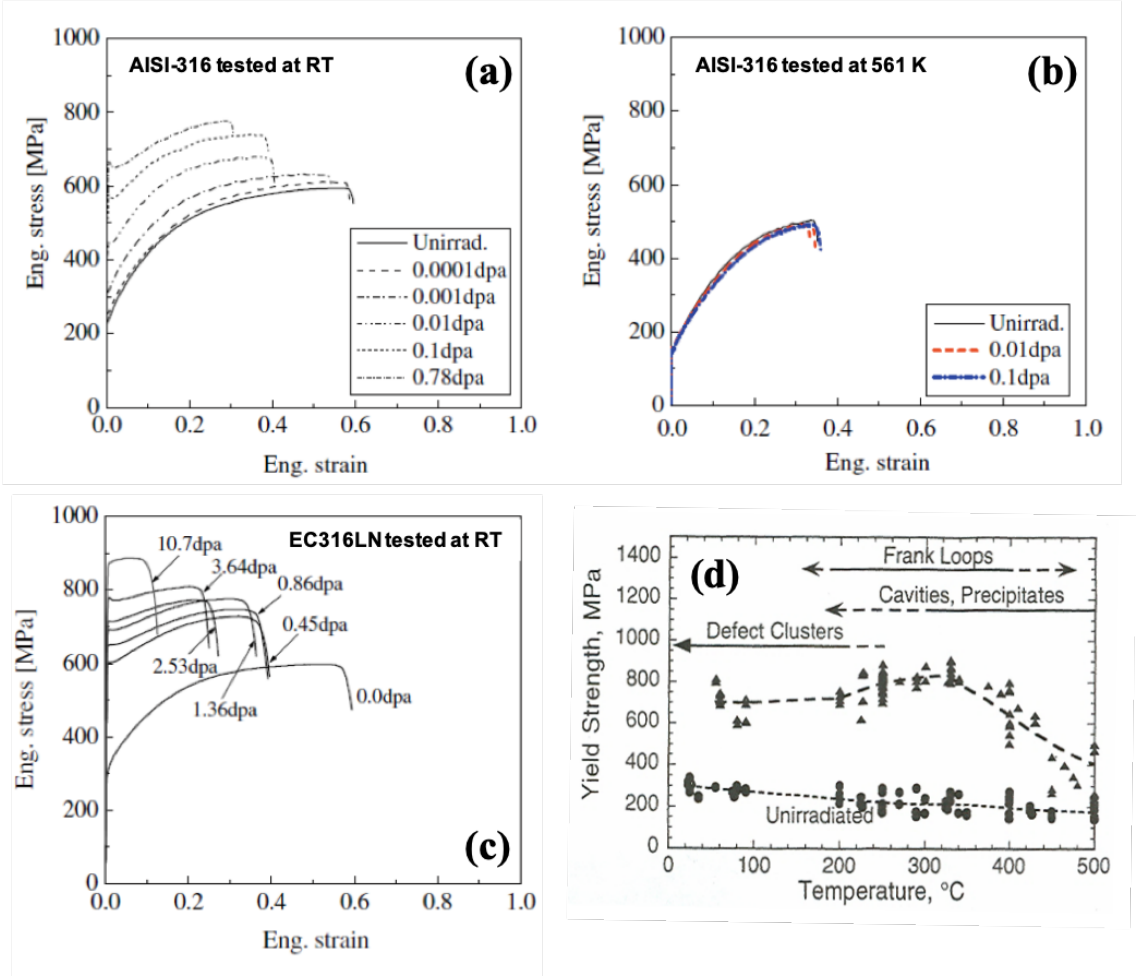

Figure 2.15: The curves of engineering stress-strain obtained with irradiated 300-series stainless steels (extracted and adapted from Garner *et al.* [242, 243]): (a) AISI-316 irradiated in the HFIR around 373 K and tested at room temperature, (b) AISI-316 irradiated in the HFIR around 623 K and tested at 561 K and (c) EC316LN steel irradiated around 373 K in the LANSCE spallation source with mixed neutron and protons spectrum and tested at room temperature. The graph in (d) shows the contribution of different types of irradiation-induced defects to embrittlement of 300-series stainless steels as a function of the tensile testing temperature (extracted and adapted from Pawel *et al. apud* Garner [243]).

Garner *et al.* [242] performed tensile testing on neutron-irradiated samples of

the AISI-316 alloy in order to investigate the interaction of irradiation-induced defects with moving dislocations by means of assessing the mechanical properties. The irradiation was performed in the HFIR. When the AISI-316 and the EC316LN steels were irradiated around 373 K and mechanically tested at room temperature, it was observed that the yield strength increased upon increasing the dose as shown in figures 2.15(a) and 2.15(c): as noted by Garner [243], the increase of the yield strength saturates at dose levels around 10 dpa following a similar observed saturation of irradiation-induced defects on a microstructural level. When the yield strength increases upon irradiation, the alloy loses its initial ductility and becomes more brittle. Conversely, concentration of irradiation-induced defects is expected to decrease when the irradiations are carried out at higher temperatures as shown in figure 2.15(b) for the AISI-316 steel: in this case, as the dose increases, the engineering stress-strain curve from the irradiated samples is very similar to that of the unirradiated sample.

Pawel *et al.* (*apud* Garner [243]) carried out detailed microstructural characterisation along with tensile testing on AISI-316 samples under irradiation in order to identify the contribution of different types of irradiation-induced defects to the embrittlement effect. In figure 2.15(d) one can see that defect clusters (black-spots) are dominant over the low temperature regime whilst cavities and Frank loops contribute to a "peak strengthening" (saturation) around 573 K. When radiation-induced segregation becomes significant at temperatures around 623 K, the yield strength increases even more as a result of the formation of nanometre-sized precipitates under irradiation. For temperatures higher than 773 K, the yield strength decreases as the saturation of irradiation-induced defects also decreases. Fast recombination of point-defects plays a major role when metallic alloys are irradiated at high temperatures [242, 243], thus reducing the formation of extended defects.

The irradiation also affects the fracture toughness of metallic alloys. Observing the effects of irradiation on Nb – a ductile metal – it was found that the formation of dislocation loops and black-spots was also associated with brittle fracture upon application of stress at low temperatures. This was associated to an important mechanism known as the ductile-brittle transition [244]. The temperature at which it occurs is known as the ductile-brittle transition temperature (DBTT). In steels, the irradiation increases the DBTT to above room temperature [245] and as a result, the chances of brittle fracture considerably increases as the alloy becomes less ductile [246]. This phenomenon is also widely studied outside the nuclear technology field. By etching fracture surfaces of pure and single-crystal Si, the DBTT was reported very sharp and to occur in a very narrow temperature range, less than 263 K [247]: at the transition temperature, Samuels and Roberts reported that the samples fractured in a brittle manner, but in a fracture stress 80% greater than a "base level".

This effect was associated with the high concentration of dislocations around the front of cracks [247, 248]. In ferritic steels the DBTT was reported to vary with both microstructure and strain-rate, however, in general, it is centred around of 223 to 273 K [249]. This phenomenon is still the subject of intense research materials science [250].

2.2.2.6 Stacking faults

The accumulation of vacancies and interstitials in clusters can also result in the formation of another type of defect known as a stacking fault (SF) [251–255]. A SF is considered a crystallographic disorder of the stacking sequence: a planar defect. For example, in an hexagonal close-packed (HCP) crystal structure, the stacking sequence is ABABABABA. If the stacking sequence is disordered, *i.e.* the atoms in the first layer are not placed right under the atoms in the first layer, the sequence becomes ABCABCABC which is the close-packed direction of FCC crystals [111]. When this happens, a SF is observed in a HCP crystal [256]. Both temperature and local composition affect the stacking fault formation energy [225, 248, 257]. As in the case for the other types of radiation-induced defects discussed above, SFs have been also reported to affect the mechanical properties of materials [258].

2.2.2.7 Radiation-assisted atomic migration: elemental segregation

The generation of Frenkel-pairs caused by the displacement cascade can significantly change the local thermodynamic equilibrium of a material. This is particularly important for those materials and alloys whose matrix phase is in a metastable/unstable condition. The large number of vacancies and interstitials produced by multiple atomic collisions and displacement cascades will result in a non-equilibrium process where the local composition of the target material will be changed by means of the irradiation-assisted diffusion of these point defects. Such assisted diffusion of defects will induce the segregation of atoms of the target material to sinks, preferentially at grain boundaries. This effect is known as Radiation-Induced Segregation (RIS) [177, 259–269].

RIS is a phenomenon that occurs significantly at specific dose levels and temperatures. RIS occurs predominantly for multicomponent alloys. Recovery and annihilation, segregation and recombination will compete and RIS only dominates at specific doses and temperatures depending on the target material. Thermodynamic potentials and activities between alloying elements and the interaction with the vacancies and interstitials migrating within the microstructure will define which portion of the alloy composition is going to change [270, 271]. In austenitic stainless steels, Wiedersich-Okamoto-Lam-Bruemmer developed an asymptotic model in

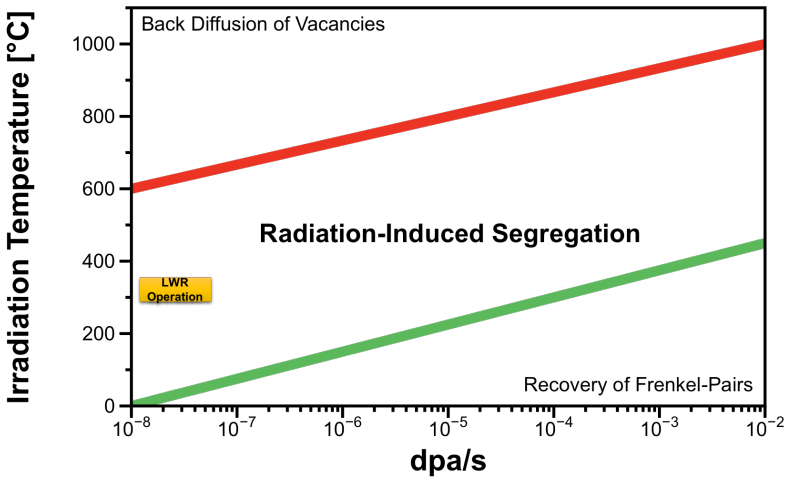

Figure 2.16: Irradiation temperature versus damage rate diagram which illustrates the region where RIS significantly occurs for austenitic stainless steels. (Modified from [272].)

which RIS is a function of the dose rate and the irradiation temperature as shown in figure 2.16: in-between back diffusion of vacancies and recovery of Frenkel-pairs, RIS can occur in austenitic stainless steels when subjected to energetic particle irradiation [271–273].

Attempts have been made to explain RIS based on the Inverse Kirkendall (IK) effect [273]. In materials science, the Kirkendall effect occurs in a diffusion couple made two different materials A and B: as the flux of A and B atoms are different, a vacancy flux will occur in the couple in order to balance the interdiffusion of both elements [191]. In the case of IK, when a vacancy flux is pre-existing in a material (often generated by external actions *e.g.* irradiation), the interdiffusion of A and B will be affected [191, 274]. To model RIS, Perks *et al.* assumed the IK effect and solved the equation describing the balance of point defects in an austenitic stainless steel (Fe–Cr–Ni) in a foil with one grain boundary [275]. The Perks model was further modified by Allen *et al.* [276] to take into account the local atomic configuration as well as to better accommodate both dose and temperature in irradiated austenitic steels. According to Wharry *et al.* [277], the Perks model and its modification by Allen *et al.* have described with accuracy some experimental results on RIS for such steels. Phase transformations and precipitation induced by irradiation are common consequences of RIS in multicomponent alloys [272].

2.3 Methodologies for radiation damage investigation in solids

As described in section 2.2, the study of radiation damage consists (at a fundamental level) of inducing atomic lattice displacements in materials as a result of energetic particle collisions followed by appropriate post-irradiation characterisation techniques to assess the effects of such energetic collisions from either a microstructural or mechanical perspectives. Often, three experimental methodologies are used to carry out investigations of radiation damage effects within the scope of nuclear materials: neutron, ion and electron irradiations. In this section, such radiation damage techniques are briefly reviewed and a critical comparative framework on their similarities and differences is outlined.

2.3.1 Neutron irradiation using materials testing reactors

In order to generate a high flux of neutrons that allow the investigation of radiation damage within reasonable times, a materials testing reactor is required. An MTR is a special type of high-power research nuclear reactor designed to operate an intense flux of neutron radiation that can be used to investigate the effects of energetic neutral particle irradiation in materials [278]. These reactors can operate with different neutron fluxes at different in- and ex-core positions, thus allowing radiation effects research to be conducted with different intensities as well as for a wide range of purposes such as structural materials, materials for cooling systems and also radiation shielding materials [279].

The methodology of investigating the effects of energetic neutron irradiation within MTRs consists of irradiating the materials within the reactor and post-analysing them in radiological laboratories (often known as "hot laboratories") as the exposure to neutron fluxes can induce transmutation nuclear reactions where the initial material can become a source of ionising radiation.

Currently, there is a limited availability of MTRs worldwide [280]. The United States has only two MTRs that can generate radiation damage at a maximum rate of 8 dpa·year^{-1} [280]. Conversely, the BOR-60 nuclear reactor in Russia is capable of irradiating materials with dose rates from 5 to 26 dpa·year^{-1} with an average neutron energy from 40 to 350 keV depending on the irradiation position with respect to the reactor's core [280, 281].

According to Was *et al.* [280, 282], MTRs are not capable of producing radiation damage doses faster than those already generated in commercial nuclear reactors which poses a challenge to discover and study – in advance – some problems associated with radiation damage effects in structural materials during the enve-

lope of normal operation of commercial reactors. In addition, due to the high costs associated with the operation of MTRs and the high radioactivity levels observed in materials after neutron irradiation, the use of MTRs faces several challenges to support the accelerated discovery of new materials for the nuclear industry [280, 282]. Despite these facts, to be considered safe for use in a commercial reactor by regulatory agencies, nuclear materials must be tested in MTRs in a wide variety of conditions to receive licensing.

2.3.2 Ion irradiation using particle accelerators

Historically, the use of ion beams to investigate the effects of energetic particle irradiation in materials is in the origin of the nuclear reactor technology. As mentioned in section 2.2, several historic studies performed with ion beams in the 1960s identified (before MTRs) how energetic irradiation modifies the microstructure of a material at a fundamental level. In contrast with nuclear reactions promoted by neutrons in an MTR, the interaction between an energetic incident ion with matter is mediated mainly via screened Coulomb interactions which are also capable of displacing lattice atoms from their positions.

Ions can be generated and accelerated to very high speeds in particle accelerators and there are numerous advantages on the use of ion beams to study radiation damage when compared to MTRs. Firstly, the damage rates can be many orders of magnitude higher than MTRs meaning that high doses can be achieved in hours or days instead of years or even decades in MTRs [280, 282]. This is particularly important to investigate potential nuclear materials within the context of generation IV reactors which are currently in the design process to operate up to doses in the order of 200-500 dpa [280, 282]. Secondly, ion beams induce negligible (proton irradiation) or no (heavy ion irradiation) atomic transmutation resulting in samples that are not radiological activated [280, 282]. The latter implies that post-irradiation characterisation of ion beam irradiated samples do not require the use of hot laboratories which significantly reduces the costs associated with such characterisation. Thirdly, ion irradiation allows experiments to be performed with careful control of temperature, damage rate and levels when compared with MTRs. In addition, the possibility of combining two or more ion beams in a single ion irradiation experiment allow the investigation of displacement damage generation with either pre-implantation or concurrent implantation of impurity damage for example to study inert gas bubbles nucleation and growth (caused by transmutation in a nuclear reactor as described in section 2.2.1.2.1) [280, 282].

Despite the advantages, the study of radiation damage with ion beam technology faces several challenges. One of the major challenges according to Was *et al.* [280,

282], involves the acceleration of damage in materials as the dose rates involved in ion irradiation experiments are significantly higher than in MTRs and commercial nuclear reactors. By this, the response of the microstructure to such accelerated damage rates must be considered when using ion beams [280, 282]. Mansur developed a theoretical invariance theory to address the accelerated damage rates achieved in ion beam irradiation when compared with reactor-like conditions [283–285]. In his model, Mansur stated that changes of microstructural processes during irradiation in a reactor, such as radiation-induced segregation and void nucleation and growth, can be investigated similarly with ion beams by an appropriate selection of irradiation variables. For both RIS and void formation, Was *et al.* observed that the high damage rates in an accelerator can be compensated for by increasing the temperature of the material, in order to achieve similar conditions of those experienced in a nuclear reactor [283–285]. In this sense, high damage rates imply fast annihilation of vacancy-interstitial pairs through recombination and an increase in the irradiation temperature could compensate this effect by promoting either loss of point defects to sinks or their capture by extended defects [283–285]. Such differences in damage rates by ion beams and nuclear reactors indicate that extended defects will nucleate at different damage levels, although to date, the existing number of computational and theoretical works to guide such comparisons remains limited [283–285]. Despite these differences, recent validation studies on austenitic stainless steels with proton irradiation at 633 K steels were found to replicate similar neutron irradiated microstructures at 548 K [280]: the size of dislocation loops as well as Ni, Si and Cr segregation profiles generated due to proton irradiation match remarkably well with neutron irradiations at lower temperatures point out the validity of the theoretical approach developed by Mansur to emulate neutron irradiation with ions [283–285].

On the use of ion beams to investigate the effects of radiation damage in materials using a microstructural perspective, two methodologies can be used: (1) materials can be irradiated using accelerators and then samples are produced after irradiation in order to carry out *ex situ* post-characterisation with existing microscopy methods (such as TEM, SEM and AFM); (2) materials can be irradiated in ion accelerators *in situ* within a TEM which allows the real-time monitoring of the microstructural response to irradiation and its evolution as a function of several irradiation parameters such as dose and temperature. In the work reported in this thesis, the methodology of ion irradiation with *in situ* TEM is used and proposed as a technique to rapidly investigate potential nuclear materials under extreme irradiation conditions.

2.3.3 Electron irradiation

Electrons are also used to investigate the effects of irradiation in materials. For example, high-voltage TEMs can produce electron beams with energies around 1 MeV and allow irradiation experiments to be performed *in situ* [286]. One of the major differences between ion, neutron and electron irradiations lie in the morphological aspects of the displacement cascades. This can be schematically viewed in figure 2.17 [286] in which different energetic particles with same incident energy (1 MeV) into a pure Ni target. Whilst neutrons and ions can generate dense defect cascades with high potential of recombination, electrons can induce the generation of a few Frenkel pairs with a low probability of recombination [286]. This implies that electron irradiation has a higher capability of producing a low-population of "freely migrating" point defects that can significantly affect processes such as radiation-induced segregation and void growth [286]. Electron beam irradiation has been successfully applied in different types of nuclear materials, such as graphite [287], as a surrogate for neutron irradiation and also to simulate the effects of lengthy and expensive neutron irradiations.

2.3.4 Critical comparison between methodologies

It is evident that ion irradiation cannot fully replace neutron irradiation when licensing new materials for nuclear technology is a primary concern. However, ion irradiation can be used as an alternative tool to investigate the effects of energetic particle irradiation in materials at a fundamental level. For example, if a material is observed to fail to sustain its microstructural integrity under ion irradiation, it could be discarded for future irradiations in an MTR, thus saving enormous time, research funding and efforts.

At the same time, ion irradiation methodologies are now evolving to cope with complicated damage rates and temperature transients that structural materials can experience whilst in commercial nuclear reactors. Even proton irradiation with *in situ* corrosion has been investigated thus allowing synergistic processes to be investigated whilst under irradiation [288]. By this, the number of studies that are aimed to compare neutron irradiated with ion irradiated microstructures of the same material has increased considerably in the past few years [280, 282]. This emphasises the current use and future improvements of ion beam technology as a predictive tool for radiation damage effects in materials under reactor-like emulated conditions. In addition, the possibility of observing the microstructure of a material whilst under ion irradiation – as allowed via ion irradiation with *in situ* TEM techniques – can be viewed as an even more useful experimental methodology for fast screening of potential nuclear materials as several experiments can be carried out in a matter of

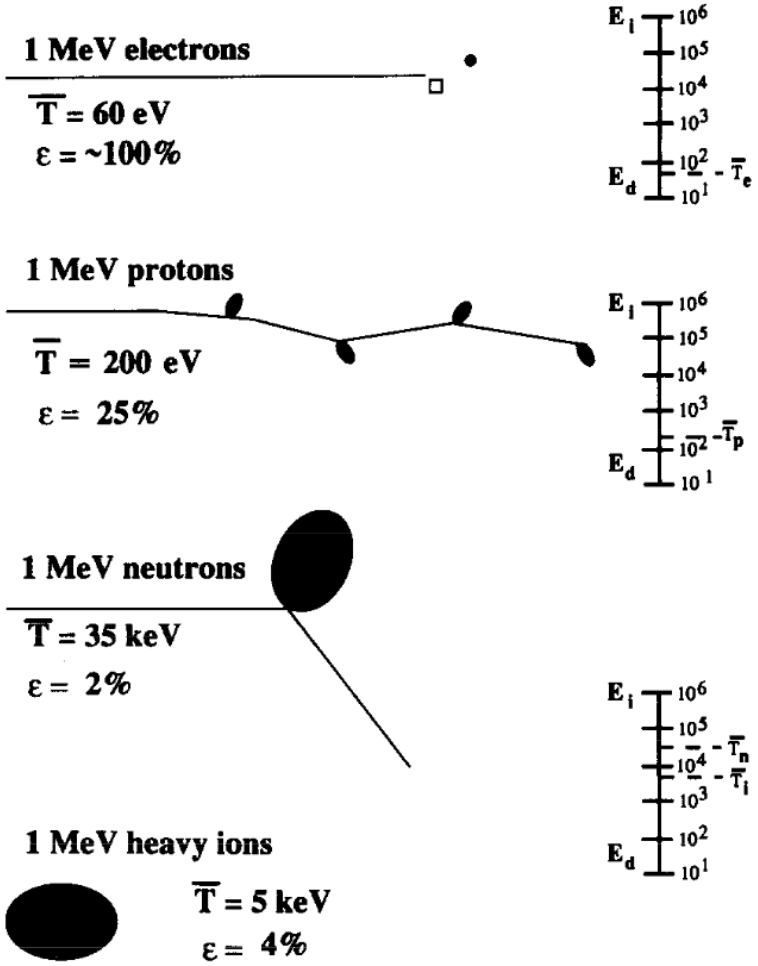

Figure 2.17: Morphologies of defect cascades for different types of energetic particles with same incident energy (1 MeV) into a pure Ni target. $\bar{T}$ represents the average energy which is transferred to a PKA and ϵ is defined as the efficiency of producing point defects available to migrate and affect RIS and RIP effects. Extracted from Was *et al.* [286].

hours. A general comparison between neutron and ion irradiation methodologies is presented in table 2.2.

Table 2.2: Comparison between neutron and ion irradiation methodologies.

	Neutron Irradiation	**Ion irradiation with *ex situ* TEM**	**Ion irradiation with *in situ* TEM**	**Electron Irradiation**
Negligible or no sample activation	No	Yes	Yes	Yes
Damage rates reported	2-20 dpa/year in MTRs	1 dpa/min, but it can be lower or higher depending on ion fluxes and target materials		1 dpa/min for 1 MeV electrons
Experimental planning timeframe	Years	Hours		Hours
Costs associated with irradiation and post-irradiation characterisation	Millions of dollars per experiment	Approx. 1-5 thousand dollars per experiment		$<$ 1 thousand dollars, higher or lower depending on the instrument
Irradiation depth	Neutron has no charge leading to high penetration depths	Stopping power calculations required (*e.g.* SRIM)		Electronic stopping calculations required (*e.g.* CASINO)
Real-time nanoscale microstructural evolution under irradiation	No	No	Yes	Yes

2.4 Review of radiation damage in multicomponent alloys and MAX phases

This section reviews radiation effects in the materials and alloys investigated during this PhD research. The focus here is on the effects of energetic particle irradiation on the microstructures of the materials, although the impact of the defect generation on the physical and chemical properties will also be discussed where appropriate.

A review on the effects of irradiation in austenitic stainless steels is firstly presented with focus on the AISI-348 steel which will be irradiated in this thesis and the results will be compared with the FeCrMnNi HEA. This comparison is justified as the steel has the same elements as the HEA in solid-solution, but not in equiatomic composition, therefore, it can be considered a "low-entropy" version of the FeCrMnNi HEA. This comparison is also aimed at revealing whether the core-effects of HEAs are responsible for superior radiation tolerance. Then, the state-of-the-art on the radiation response of HEAs will be reviewed in subsection 2.4.2. The last subsection 2.4.3 contain a detailed review on the effects of energetic irradiation of the Ti-based MAX phases.

2.4.1 Austenitic stainless steels

The effect of energetic particle irradiation on austenitic stainless steels has been recently reviewed by Garner [243] and in the 1990s by Lucas [289]. Among the diverse number of austenitic stainless steels commercially available, the alloys grades 304 and 316 have been subjected to several studies within the scope of nuclear engineering due to their importance for advanced gas cooled reactors (AGRs) in the United Kingdom and LWRs in the United States [243, 290].

In general, upon exposure in nuclear reactor conditions, the austenite phase (γ–Fe) undergoes several microstructural modifications. Such effects have been attributed to the fact that the γ–Fe phase corresponds to a metastable thermodynamic state inherited from processing and the large cooling rates which follow it [291]. These irradiation-induced microstructural alterations produce a final damage microstructure with new phases that are not commonly found in equilibrium phase diagrams [243].

2.4.1.1 Damage microstructure under neutron irradiation

The generation and survival of vacancies and interstitials in austenitic steels due to neutron collisions in a reactor are dependent on the irradiation temperature. For most commercial AGRs, the operational temperature (coolant outlet temperature) is around 913 K while for structural components in LWRs, the temperature is around

600 K. The generation, migration and recombination of point defects will be strongly enhanced by the irradiation at these temperatures.

In such stainless steels, interstitials generally diffuse faster than vacancies, although under irradiation, both processes are accelerated [243, 292, 293]. The fast diffusion of interstitials promotes the agglomeration, nucleation and growth of black-spots, dislocation loops and dislocation networks that are in one- (except disloscation networks) or two-dimensions [294]. The formation of such two-dimensional defects strongly affects the mechanical properties of the austenitic steels. It has been reported that the yield strength, for example, increases by around 75% upon increasing the neutron fluence from 10^{17} to 10^{18} n·cm^{-2}. Ductile stainless steel thus becomes hard and brittle after irradiation [243, 295, 296].

Regarding the diffusion of vacancies under irradiation, their agglomeration causes the nucleation of voids, and in combination with He generated through (n,α) and H from (n,p) nuclear reactions, the nucleation of inert gas bubbles has been reported [214]. For austenitic stainless steels, the transmutation gives rise to the transformation of Mn to Fe, Cr to V and B to Li and then He [243]. Alloying elements like Ni undergo (n,α) reactions for neutron irradiation with an energy range of 6 to 20 MeV, therefore contributing to the formation of bubbles [295, 297–300].

The damage caused by (n,α) nuclear reactions can be estimated using a ratio known as the He/dpa, *i.e.* the concentration of He generated per dpa. Alpha particles from transmutation reactions have high energy ($\approx$ 5 MeV), thus they are also considered sources of displacement damage. According to Garner [243], in austenitic steels (Fe-Cr-Ni), alpha particles generated via transmutation of ^{59}Ni are responsible for 95% of the damage associated with transmutation. The reason is the high probability (cross-sections) of (n,α) and (n,p) reactions for ^{56}Ni and its isotopes. In comparison, for fusion reactors the He/dpa ratio will be around 3-10 appm He/dpa. In LWRs the ratio is approximately 15 appm He/dpa and for fast reactors, 0.1-0.3 appm He/dpa [304–306]. The continuous He generation and its association with vacancies induces the formation of He bubbles within the γ–Fe phase: thus, alpha particles also causes impurity damage. The migration and/or nucleation of He bubbles at the grain boundaries of the austenite phase has been associated with a process known as irradiation-assisted stress corrosion cracking (IASCC) where intra-granular cracks may occur in the steel as result of the embrittlement effect caused by the He bubbles in the microstructure [243, 307].

The enhanced production and migration of point defects have also been associated with elemental segregation in these steels. The consequence is the formation of radiation-induced phases that sometimes, for certain alloys within the 300-series class, are not present in the equilibrium phase diagram [293, 308]. The formation of non-equilibrium phases (rather than thermodynamically expected phases) within

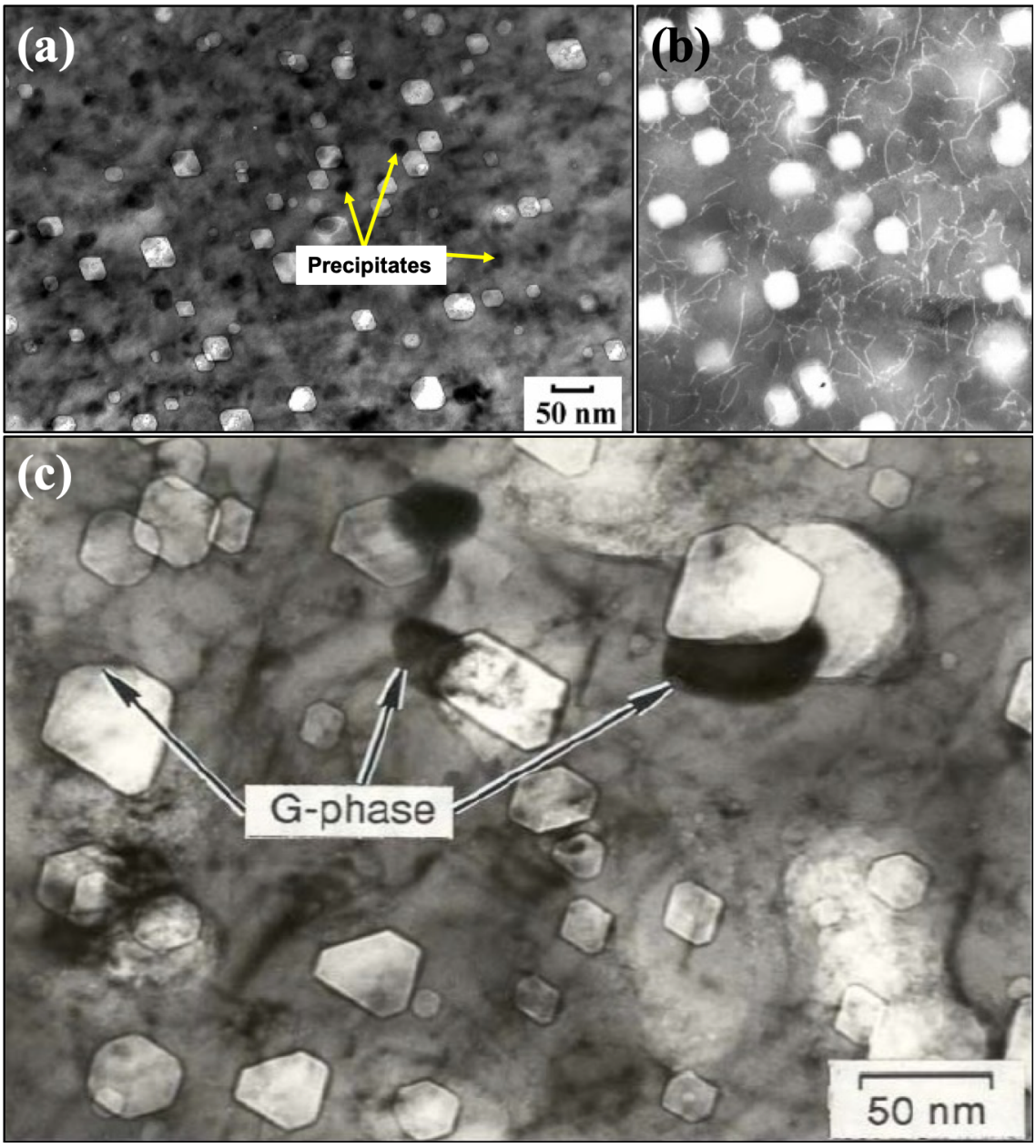

Figure 2.18: (a) Radiation-induced voids (light contrast) and $M_{23}C_6$ precipitates (dark contrast) formed in an austenitic stainless steel neutron-irradiated at 653 K up to 21.7 dpa (reproduced from [301]) and (b) dark-field TEM micrograph showing voids, dislocation lines and networks in an neutron-irradiated austenitic stainless steel up to 15 dpa at 743 K (reproduced from [302]). Micrograph (c) shows the formation of the G-phase under neutron irradiation up to 11 dpa at 723 K for an austenitic stainless steel (reproduced from [303]). Note: the scale bar in (c) also applies to (b).

the austenite matrix as a result of irradiation can be attributed to the favourable thermodynamic conditions that can be attained by means of the introduction of point defects in excess (resulting in enhanced solid-state diffusion via vacancies, but also interstitials) and the huge amount of energy which is stored in the lattice as a result of the irradiation.

In order to explain such segregation, diffusional models have been proposed. At low to moderate irradiation temperatures, in the range of 473 to 823 K, a super-saturation of vacancies and interstitials is expected under irradiation. The excess of vacancies, for example, accelerates all diffusional processes related to this type of defect. Due to such diffusion, solutes can bind with vacancies or interstitials. Such binding induces a flux of alloying elements throughout the microstructure due to differences in the concentration gradients of defects which will result in segregation. This is known as the solute-drag model. For some elements like as P, Si and N, this model has been observed to agree with experimental observations [243, 271].

A more complex model was derived from the inverse Kinkendall effect [269]. In this case, each solute is considered to have its own elemental diffusivity and by means of vacancy exchange, elemental segregation occurs (preferentially) for the solute species which has the slower diffusion coefficient. Segregation is observed to occur primarily at sinks, such as grain boundaries and precipitates. Experiments indicate that among the alloying elements in austenitic stainless steels, Ni is the most prone to segregate as $D_{Cr} > D_{Fe} > D_{Ni}$ [309].

A large number of phases have been reported to form in the AISI-316 in irradiation environments: Ni_3Si (γ'), G-phase ($M_6Si_{16}Ni_7$), needle-like phosphides, $M_{23}C_6$ (τ-carbide) and M_6C precipitates [303]. Very often, the radiation-induced phases differ from the phases formed during thermal ageing with respect to microstructure, composition and nucleation dynamics [243, 303]. The damage microstructures of some austenitic stainless steels showing voids, secondary phases and displacement damage are exhibited in figure 2.18(a-c), extracted and reproduced from multiple sources [301–303, 310].

When the microstructure of an austenitic stainless steel changes under irradiation, its initial mechanical and thermal properties also change which may pose a deep concern for the nuclear industry. In general, materials for nuclear reactors and installations should be as stable as possible. In designing a structural material component, nuclear materials scientists try to find the best material to fit an appropriate envelope of conditions for its application aiming at mitigating possible failures. For this reason, austenitic steels are still applicable in the nuclear industry, but the nuclear fuel rods claddings made from these alloys have limited lifetimes (three years in general for LWRs) and are often changed during the nuclear reactor core refuelling.

2.4.1.2 Damage microstructure under ion irradiation

Neutron irradiation experiments are often carried out in specific MTRs. Due to the costs and long times associated with such experiments, ion irradiation is an alternative to explore the effects of irradiation on materials and alloys. The methodology of using ion irradiation prior to testing a new austenitic steel under neutron irradiation can be justified using the argument that, if the new material does not exhibit good radiation resistance under ion implantation, it can almost certainly be discarded as needing testing in a MTR. However, some authors have argued that ion irradiation often produces "artefacts" such as very high displacement damage and ionisation rates, primary knock-on atom energies different than those generated by neutrons, C contamination that make it difficult to compare ion and neutron induced damage [311]. It is clear that ion irradiation cannot entirely reproduce and/or replace neutron irradiation experiments and nor will it fill the validation requirements from regulatory agencies for the use of materials in reactors, but it can be used for first screening of a certain material prior sending it for expensive experiments at MTRs [29]. Therefore, it should be noted that the roots of the radiation damage research are back in the late 1950s when ion irradiation experiments on Cu, Al and Au targets were used to explore the effects of energetic particle irradiation on crystal structures. Much of the knowledge in the field of radiation damage are due to pioneering studies with ion beams [22, 226].

Several works have been focused on the ion irradiation resistance of 300-series stainless steels. Both AISI-304 and 316 have been irradiated with 160 keV Fe ions up to 5 dpa at 573 K and the authors reported the observation of black-spots, dislocation loops and lines and networks. The results were in good agreement with published data on neutron irradiation of the same alloys [243, 303, 312]. Another study with AISI-316L and a prototypic FeCrNi alloy, both austenitic stainless steels, investigated the ion irradiation behaviour *in situ* within a TEM at 773 K with 4 MeV Au ions [313]. The authors reported the formation of black spots as well as dense networks of dislocations and voids. The mean sizes of the loops exhibited a saturation behaviour upon increasing the dpa: similarly to the case of neutron irradiations [313]. Void swelling in two austenitic steels, Fe-15Cr-15Ni and Fe-25Cr-15Ni, has been observed after irradiation with 2 MeV Fe at 873 K [314]. Void swelling is a concern in neutron irradiated materials and it has been demonstrated that this also can be studied using self-ion irradiation.

Similarly, a self-ion irradiation study using Fe ions with an energy of 10 MeV analysed the irradiated microstructure of AISI-316 at 573 K. Atom probe tomography (APT) imaging of the irradiated material revealed the occurrence of radiation-induced segregation similiar to that seen in neutron irradiation experiments. Si and

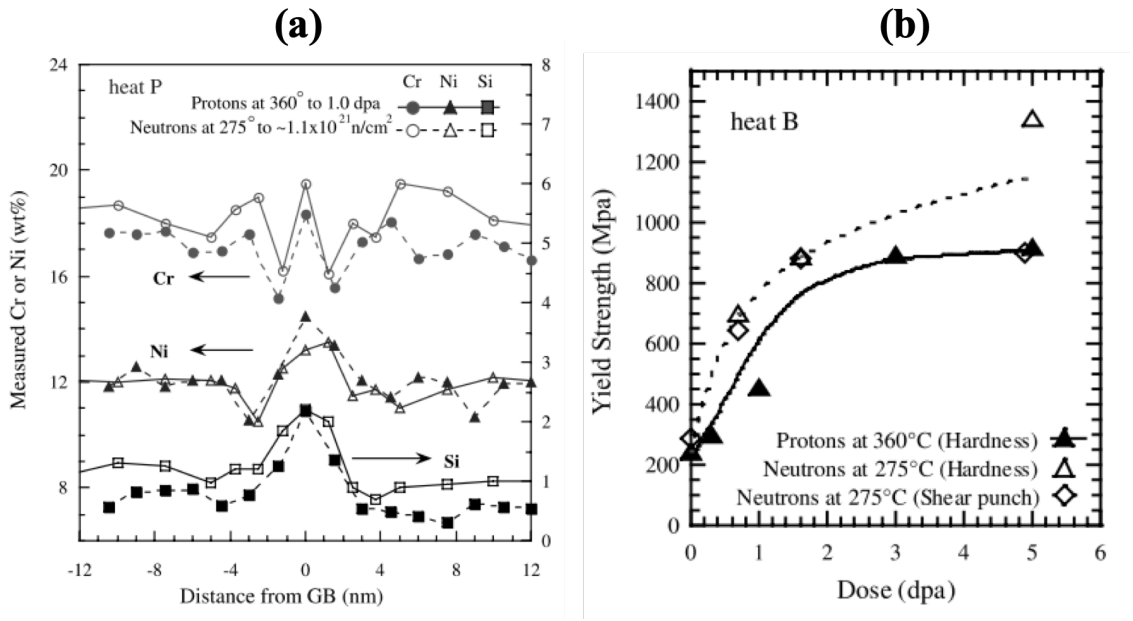

Figure 2.19: Comparison between neutron and proton irradiation on AISI-316 steel samples showing: (a) the profiles of RIS for Cr, Ni and Si measured on a grain boundary and (b) the evolution of the yield strength (assessed via hardness and shear punch tests) as a function of the irradiation dose. (Adapted and extracted from Was *et al.* [319]).

Ni were observed to segregate at grain boundaries [315]. These authors also compared their results with neutron irradiation data and found good agreement with previous reports for this alloy. Solute segregation in austenitic stainless steels has also been observed under electron irradiation [316], and under He [317] and proton irradiation [318].

In some specific austenitic stainless steels, ion irradiation has been used as a technique to replicate or emulate neutron irradiation. Was *et al.* [319] carried out a detailed investigation on the validation of neutron irradiation by using energetic proton beams on AISI-316 steel samples. As shown in figure 2.19, the profile of radiation-induced segregation of Cr, Ni and Si as well as the evolution of the yield strength upon increasing the dose for both neutrons and protons were found to be in excellent agreement. It was proposed that when using protons to emulate neutron irradiation on austenitic stainless steels, it is necessary to slightly increase the irradiation temperature in order to attain similar diffusion kinetics aiming at compensating the higher damage yield promoted by protons.

2.4.1.3 The austenitic stainless steel AISI-348

The AISI categorises the stainless steel 348 as an Fe-based alloy with 19Cr-11Ni-2Mn (wt.%) fully austenitic at room and high temperatures [320]. The AISI-348 belongs to the 300 series of steels and it is similar to the widely used AISI-316. The

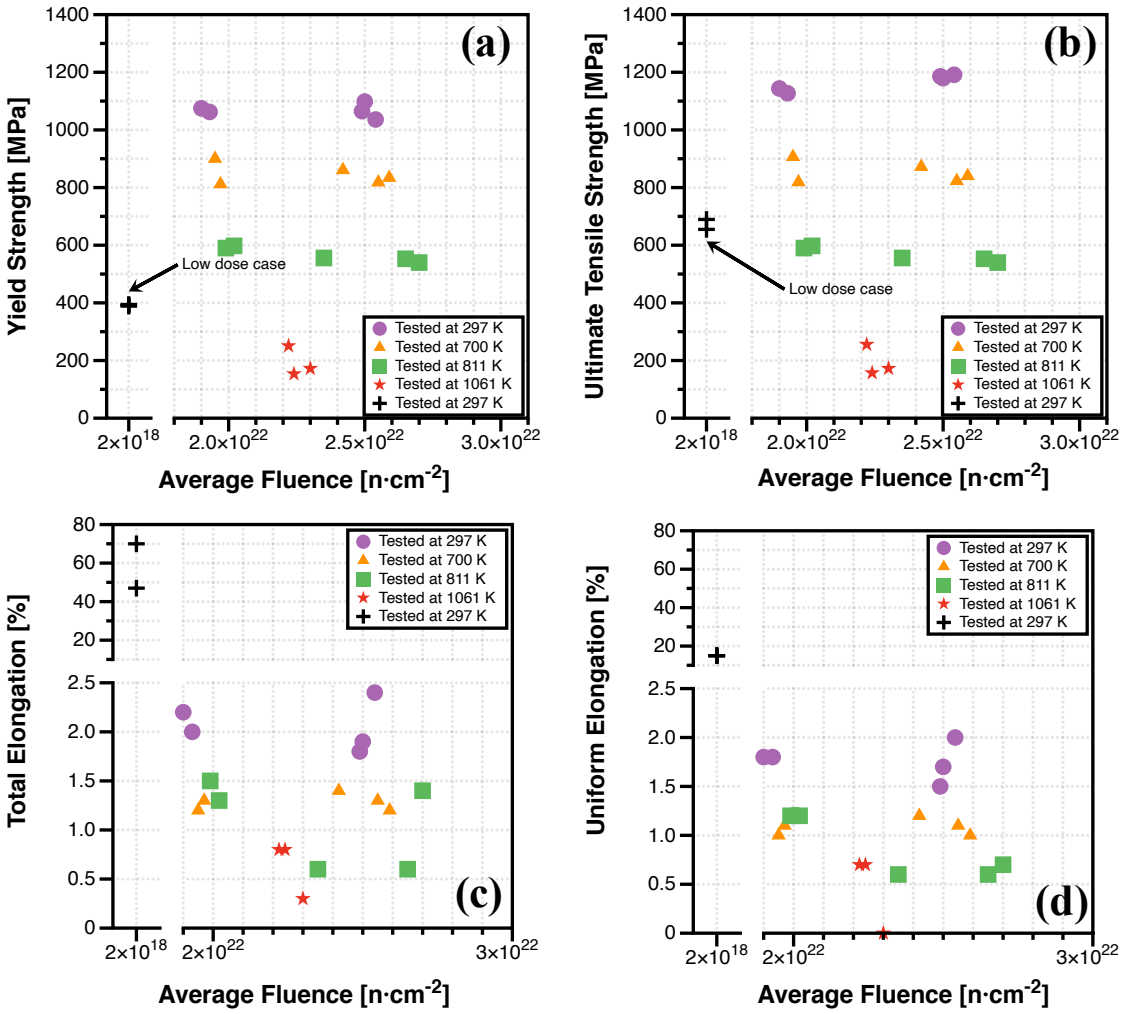

Figure 2.20: Tensile testing carried out in AISI-348 steel samples after neutron irradiation in the ATR showing the (a) yield strength, (b) ultimate tensile strength, (c) total elongation and (d) uniform elongation all as a function of the fluence. (Extracted and plotted from Beeston *et al.* [321])

differences lie in the presence of the elements Nb and Ta in minor concentrations, that are added into the AISI-348 to capture C from solid solution thus enhancing the corrosion properties of the steel by avoiding the formation of $M_{23}C_6$ carbides, observed to nucleate preferentially at grain boundaries and which are often associated with intergranular stress corrosion cracking [32, 43].

AISI-348 has excellent corrosion and mechanical properties for applications at high temperatures, generally above 950 K, making the steel suitable for use in aero-engines, turbochargers and in oil and gas pipelines [323]. The improved corrosion resistance made this steel a potential candidate for structural components in nuclear reactors. At the beginning of LWR technologies in 1960s, AISI-348 was applied as the nuclear fuel cladding material in the Yankee Rowe (USA) nuclear reactor [26], but its use was phased out upon the discovery of irradiation-assisted stress corrosion cracking in nuclear grade stainless steels in the 1980s and because of the advent of

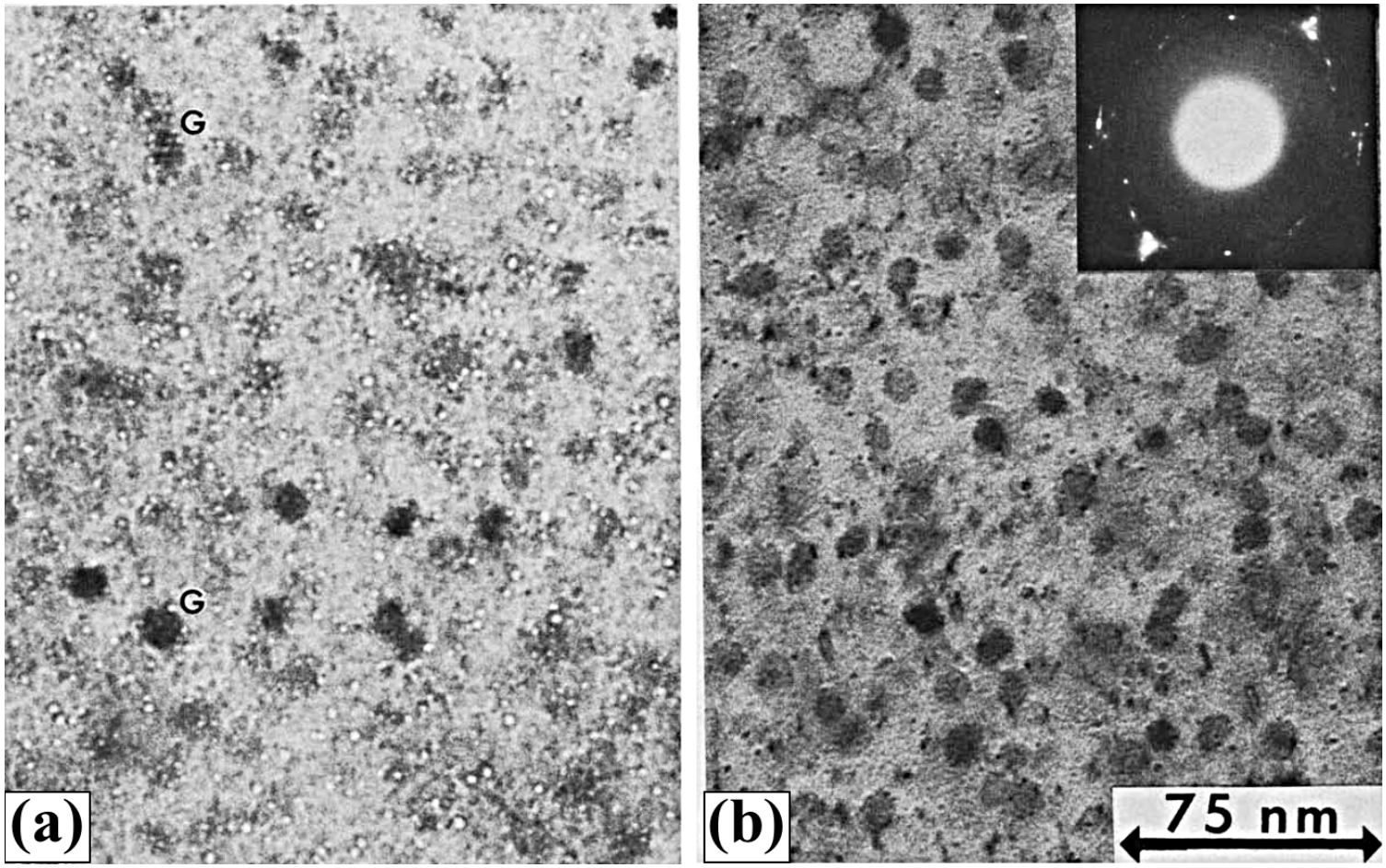

Figure 2.21: The AISI-348 steel microstructure after irradiation up to 39 dpa (2.55×10^{22} n·cm^{-2}) at 623 K showing the presence of voids (or He bubbles) and the G-phase (niobium-nickel-silicide): (a) underfocus and (b) overfocus TEM micrographs in bright-field. The inset in (b) is the diffraction pattern of the area showing Debye-Scherrer rings corresponding to the precipitates. (Adapted from Thomas and Beeston [322])

Zr alloys which gave better neutron efficiency (lower thermal neutrons absorption cross-section) for LWRs. Recently, some authors revisited austenitic stainless steels for possible applications in LWRs instead of Zr alloys in which the corrosion at high temperature produces hydrogen gas during a loss of coolant accident (LOCA) [324].

According to Garner *et al.* radiation resistance data for AISI-348 at high doses are scarce and are not available in the scientific literature [325]. The majority of the available data is regarding lower neutron exposure levels [326–328]. Although there are substantial neutron and ion irradiation data for AISI-316 which is a very similar steel to the AISI-348, literature screening reveals that there is no published work regarding the effects of ion irradiation and *in situ* TEM ion irradiation in the latter alloy.

On the limited dataset for neutron irradiation on AISI-348, Beeston *et al.* [329] analysed samples of this steel that were irradiated in the Advanced Test Reactor (ATR) up to a peak neutron fluence of 2.8×10^{22} n·cm^{-2} in the temperature range of 623 to 652 K. The post-irradiation characterisation was carried out by assessing the mechanical properties of the steel with tensile testing at different temperatures: the results are presented in figure 2.20(a-b). It is possible to note that neutron irradiation significantly changed the mechanical parameters such as yield strength (YS) and ultimate tensile strength (UTS). The irradiation increases the value of both parameters when tested in the temperature range from 297 to 811 K. At the same time, the increase in US and UTS implied in a significant reduction in both total and uniform elongations leading to the conclusion that neutron irradiation caused an aggressive embrittlement on the AISI-348 steel.

Aiming at further investigating the origins of such pronounced embrittlement effect on the AISI-348 steel under neutron irradiation, Thomas and Beeston [322] carried out post-irradiation characterisation of the same ATR-irradiated samples in a TEM. As shown in figure 2.21, the authors found voids and He bubbles from Ni transmutation (although indistinguishable within the TEM) both with average sizes around 1-2 nm. Nanometre-sized precipitates at a dose of 39 dpa corresponding to a fluence of 2.6×10^{22} n·cm^{-2} were also detected with a TEM. The authors carried out X-ray microanalysis with a 20 nm convergent electron probe in a STEM and identified qualitatively that these precipitates could be the niobium-nickel-silicide known as G-phase. They also reported a large amount of spurious X-rays, leading to inconclusive results regarding the nature (elemental composition and stoichiometry) of the irradiation-induced precipitates, although diffraction pattern indexing also was positive to the G-phase identification. Energy dispersive X-ray spectroscopy or any other quantification were absent in the paper. Therefore, it was concluded that the presence of voids, He bubbles and precipitates – formed as a result of the neutron irradiation – contributed to the severe embrittlement effect of the AISI-348

steel [322].

Due to the presence of Ni in the AISI-348, the exposure to neutron irradiation induces the generation of alpha particles by means of the nuclear reaction (n,α) and nucleation of He bubbles may occur. As inert gas bubbles pose obstacles to the motion of dislocations, the steel will then experience significant loss of ductility due to an irradiation-induced embrittlement effect [330]. This was confirmed by Thomas and Beeston [322] in AISI-348 steel samples irradiated in the ATR. For conventional LWRs operating with austenitic stainless steels, 1100 appm of He has been measured after three years of in-service operation and recent calculations indicate that after 18.5 years of exposure, a concentration of around 22000 appm is expected due to the ^{59}Ni transmutation reaction [243]. These facts are the motivation behind the study of inert gas behaviour in this austenitic stainless steel.

In addition to the data on the AISI-348 steel, post-irradiation examination of AISI-316 and AISI 347 steels have led to the conclusion that irradiation induces the segregation of alloying elements which manifests in the formation of new phases [325], similar to the effect observed by Thomas and Beeston [322]. The neutron irradiation may also induce the formation of carbides and Ni- and Si-rich precipitation [331]. This segregation may degrade significantly the mechanical properties of the steel by modifying the original austenite matrix phase.

2.4.2 High-entropy alloys

Early reports on the radiation resistance of HEAs were published by groups in Japan [332]. Egami *et al.* published a paper in 2013 on the radiation resistance calculated by means of computer simulations in equiatomic systems containing Nb, Zr and Hf [333]: the results clearly showed that high stresses at the atomic level are responsible for accommodating the radiation damage better than in conventional multicomponent alloys. Later experimental work using MeV electron irradiation has shown that this system can sustain its single solid solution phase and also structural stability (*i.e.* no amorphisation or phase transformations) under ion irradiation up to 10 dpa [334].

A five-component HEA, CoCrCuFeNi, was tested in Osaka, Japan by the group of Takeshi Nagase via electron beam irradiations in a ultra-high voltage in a Hitachi H-3000 electron microscope [335]. The results were similar to the previous results at with Nb-Zr-Hf [332–334]: the FCC solid solution showed high phase stability over 40 dpa at both 298 and 773 K, but the role of irradiation energy, dose and temperature in these high-entropy alloys remains not well understood.

A small number of other HEA systems have been studied by the group of S. J. Zinkle at the University of Tennessee and Oak Ridge National Laboratory. The

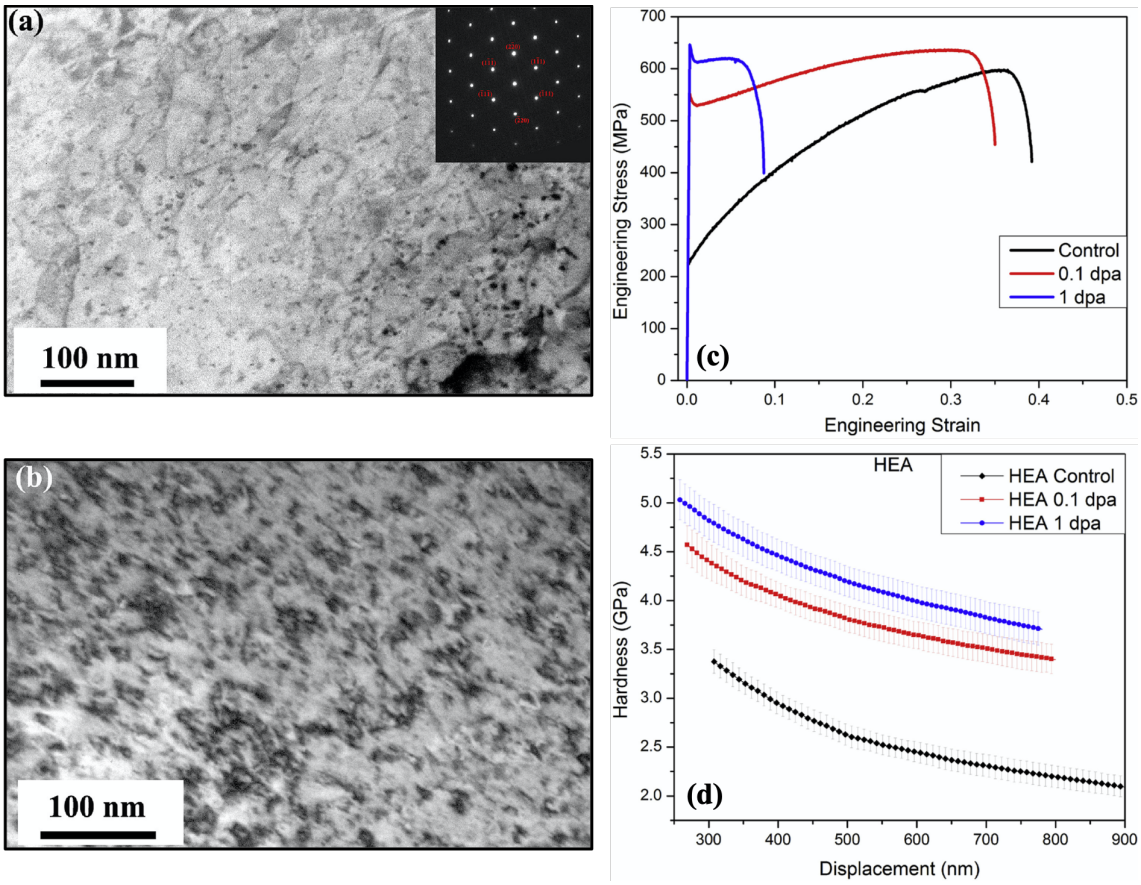

Figure 2.22: The effects of neutron irradiation on the FeCrMnNi HEA showing the microstructures of the alloy at (a) 0.1 and (b) 1 dpa. The diffraction pattern inset in (a) reveals no precipitation of secondary phases. The mechanical response of the alloy to neutron irradiation showing (a) the tensile curves and (b) the measured hardness. (Extracted and adapted from Li *et al.* [339])

system Fe-28Ni-27Mn-18Cr (wt%) was irradiated in 2013 with 3 MeV Ni ions [336], to temperatures from 293 to 793 K and different dose levels of 1 and 10 dpa. The hardness was observed to increase quickly at room temperature when the dose increased. Voids were not observed to form under these irradiation conditions. In later works on the same alloy also under ion irradiation [337, 338], these authors reported that Cr accumulates while Ni depletes at grain boundaries at higher temperatures, thus possibly contributing to the irradiation-induced embrittlement of the alloy. In comparison with the austenitic steel Fe-Cr-Ni, Zinkle *et al.* concluded that this HEA system appears to exhibit a very different behaviour under irradiation that needed to be better explored [337, 338].

The mechanisms of damage generation in HEAs were investigated by Granberg *et al.*[75] using 3 MeV Au ion irradiation of the equiatomic alloy NiCoCr. In combination with molecular dynamics simulations the authors showed that defect clusters and interstitial-type dislocation loops started to form in the HEA at around 0.1 dpa, but due to reduced defect mobility, the loops did not grow under prolonged irradi-

ation. Some important contributions to the understanding of the radiation damage resistance in these alloys was made by Lu *et al.* [340]. Comparing the irradiation behaviour of pure Ni with that of the equiatomic alloys NiCo, NiFe and NiCoFeCr, the authors proposed that both reduced defect mobility and energy dissipation were key factors in mitigating damage production and accumulation in HEAs [340]. A high-fluence He implantation study was carried out on the alloy NiCoFeCr showing that He precipitated into bubbles. Due to the observation of small bubble sizes, the authors concluded that somehow this HEA has a higher resistance to He bubble formation when compared with pure Ni and steels [341].

The five-component system $Al_xCoCrFeNi$ has also been studied under 3 MeV Au ion irradiation and it was shown that upon increasing the Al content, the system suffered phase transformation from FCC to a duplex microstructure with both FCC and BCC phases. Under irradiation, the BCC phase was responsible for the observed irradiation-induced swelling, although this increase was not as high as for conventional alloys under similar conditions (50 dpa at 298 K) [342]. An APT study of the system $Al_{0.1}CoCrFeNi$ showed irradiation-induced defects such as dislocation loops and lines, stacking faults, but no void formation. The same study demonstrated that upon increasing the irradiation temperature, radiation-induced segregation occurred by means of enrichment of Ni and Co solutes at defect boundaries as well as depletion of Fe and Cr in the same regions [343].

Xia *et.al.* indicated in a recent review paper (in mid-2015) on effects of radiation in HEAs that there is no work in the scientific literature on neutron irradiation response on these new alloys [344]. However, in mid-2019 Li *et al.* published the first neutron irradiation report of a HEA: the FeCrMnNi [339]. Samples of the FeCrMnNi HEA were irradiated at the HFIR up to a maximum dose of 1 dpa at 333 K. The main findings of this study were [339]:

1. Post-irradiation characterisation carried out in a TEM and with X-ray diffraction showed that the FeCrMnNi HEA matrix phase, *i.e.* the random FCC solid solution, was stable up to 1 dpa. Neither RIS nor RIP was detected at such dose. Black-spots and small dislocation loops were observed to increase in size and density from 0.1 to 1 dpa (although the authors have not provided quantification) as shown in figure 2.22(a) and 2.22(b).

2. Post-irradiation characterisation carried out with tensile testing revealed that the mechanical response of the FeCrMnNi HEA – in terms of changes in properties like hardness, strength and ductility as a result of neutron irradiation – was found to be very similar to the response of conventional austenitic stainless steels. This results can be seen in figures 2.22(c) and 2.22(d).

3. The irradiation hardening was found to be completely annealed at a temperature around of 923 K.

4. Measured changes in resistivity of the FeCrMnNi HEA were larger than in austenitic stainless steels and the authors suggested that such large increase in resistivity is probably due to changes in the disordering of the random solid solution as no phase transformations, RIP or RIS were observed.

As the HEAs are a recent class of new alloy systems, the research necessary to assess their capabilities as a new class of nuclear materials is at an early stage. The state-of-the-art on the response of HEAs to both ion and neutron irradiation can be summarised in the following major points:

1. Ion irradiation works, mainly with heavy ions, have indicated superior radiation damage resistance of HEAs when compared with other multicomponent alloys such as stainless steels. This superiority was mainly assessed by analysing defect formation at a microstructural level, changes in the mechanical properties and stability of the random solid solution matrix phase after irradiation [334, 335, 338, 340, 343, 345, 346].

2. The most recent (and so far unique) neutron irradiation study on the FeCrMnNi HEA has shown that the response of the alloy – as irradiated at 333 K up to 1 dpa at the HFIR – is very similar to the response observed in austenitic stainless steels [339]. This study has offered a different perspective to the results obtained with previous (heavy) ion irradiation works as mentioned in the item above.

3. Most notably, the nucleation and growth of voids as well as manifestation of the RIS and RIP effects were both significantly suppressed in HEAs when compared with other materials [338, 340, 343, 345].

4. Although some studies claim the some of the HEA core-effects (introduced in section 2.1.1.2) such as the sluggish diffusion can act in order to suppress solid-state diffusion under irradiation, thus limiting nucleation and growth of voids and bubbles for example [340, 346, 347], recent computational studies have show that the sluggish diffusion property ceases at high temperatures [343].

Many additional studies will thus be needed and this is one of the main subjects of this thesis. Additionally, comparative studies between HEAs and conventional nuclear materials such as Zr alloys and austenitic stainless steels have special importance in order that these new materials gain acceptance in this area of technology

as well as to probe whether the core-effects promoted by the (close to) equiatomic condition are responsible for a superior radiation tolerance. This will be one of the main research goals of this present thesis on such alloys.

2.4.3 $M_{n+1}AX_n$ phases

As a recent class of candidate materials for the next generation of nuclear reactor, the number of works addressing the radiation resistance of MAX phases is somehow limited. Ti_3AlC_2, Ti_2AlC and the Ti_3SiC_2 are the most studied materials so far. This section is divided into sections on both ion and neutron irradiations effects on MAX phases.

2.4.3.1 Ion irradiation effects

Early reports on the irradiation resistance of Ti_3AlC_2 and Ti_3SiC_2 were made by Whittle *et al.* [348]. The authors investigated the irradiation resistance of such MAX phases at the Intermediate Voltage Electron Microscopy (IVEM)-Tandem Facility at the Argonne National Laboratory. The *in situ* TEM ion irradiations were performed using 1 MeV Kr^{2+} at 50 and 300 K and 1 MeV Xe^{2+} at 300 K. The authors observed only minor evidence of amorphisation for both materials at around 25 dpa and suggested that if amorphisation occurs, it would be for doses higher than 100 dpa [348].

The irradiation resistance of Ti_3SiC_2 has been also investigated with *ex situ* 2 MeV I^{2+} ion irradiation and grazing incident x-ray diffraction by Zhang *et al.* [349]. After irradiation, microcracks were observed at grain boundaries and at 10.3 dpa, strong evidence for phase decomposition was reported from analysis of the XRD spectra. The Ti-carbide phase, TiC, was observed to nucleate after high doses. Post-irradiation annealing in the temperature range of 773–1073 K yielded evidence for recrystallisation of both the Ti_3SiC_2 and TiC phases [349].

A set of MAX phases – $(Ti,Zr)_3(Si,Al)C_2$ system – was irradiated with 95 MeV Xe^{+} ions up to 16.6 dpa by Marion *et al.* [350]. After the irradiation, the authors reported that the hardness had increased for all materials as confirmed by nanoidentation measurements, but a plateau was observed at around 3.2 dpa which indicated supersaturation of radiation damage defects, although no TEM was performed on the irradiated materials to support this statement. No amorphisation was observed under the irradiation conditions. The authors also analysed the radiation resistance of secondary phases, TiC and ZrC, which had not amorphised under the irradiations, thus concluding that these secondary phases are also resistant to irradiation [350].

Liu *et al.* [351] investigated the effects of Kr and Xe ion irradiation in a quaternary MAX phase: $Ti_3Si_{0.9}Al_{0.1}C_2$. XRD measurements indicated a large increase in

the lattice parameter of the α-phase (c-expansion) in this MAX phase. Annealing at both 573 and 773 K resulted in a modified microstructure contrast and partial recovery of radiation induced defects was noted by Marion *et al.* [350] who also reported a complete recovery of defects upon annealing.

Anisotropic swelling (c-expansion and a-contraction) observed in the irradiated Ti_3SiC_2 under 74 MeV Kr and 92 MeV Xe ion irradiations which resulted in an increase of the hardness. Although no amorphisation was observed, the authors reported defects in the microstructure that led to the loss of the nanolamellar structure [352]. The same behaviour was later observed by Clark *et al.* [353] with 5.8 MeV Ni^+ ion irradiation in the range of 673–973 K between 10–30 dpa.

The effects of ion irradiation on the MAX phases, to date, can be summarised as follows [348–352]:

1. No significant amorphisation for doses less than 100 dpa has been observed, although further studies at very high doses ($>$ 100 dpa) are still pending;

2. Dynamic recovery of radiation defects occurs at high irradiation temperatures and with post-irradiation annealing, but the mechanisms behind such recovery are not well understood;

3. There is strong evidence that some MAX phases containing Al suffer significant phase decomposition under irradiation;

4. Little or no dependence of damage evolution with dose, and saturation at doses around 3 dpa;

5. Fewer radiation damage effects upon increasing the irradiation temperature suggests an enhanced defect recombination capability or "self-healing" effect which deserves further investigation;

6. Anisotropic swelling and hardening have been detected under a wide variety of irradiation conditions and the MAX phases containing Al exhibiting significantly more damage when compared with their Si counterpart; and

7. Ion irradiation experiments on MAX phases suggest that Ti_3SiC_2 exhibited the best radiation resistance among all the MAX phases studied.

With respect to ion irradiation, a reduced number of works were addressed to the overall effects of irradiation on Ti-based MAX phases and specifically few TEM works on the damage microstructure in these materials.

2.4.3.2 Neutron irradiation effects

A limited number of papers on neutron irradiation effects on MAX phases were published by Tallman and Barsoum *et al.* at Drexel University using nuclear reactors at MIT and Idaho National Laboratory.

Ti_3SiC_2, Ti_3AlC_2, Ti_2AlC and Ti_2AlN were irradiated with neutrons up to 0.1 dpa at both 633 and 968 K. Post-irradiation characterisation was performed using XRD and electrical resistivity measurements. The $Ti_3(Si,Al)C_2$ suffered phase decomposition into TiC whilst the Ti_2AlN decomposed into TiN. The electrical resistivity at room temperature increased by one order of magnitude for the MAX phases irradiated at 633 K. At 968 K, the electrical resistivity increased by around only 25% suggesting that these materials exhibit recovery of radiation-induced defects for temperatures as low as 968 K. There was no signs of amorphisation in any MAX phases analysed. Tallman *et al.* concluded that both Ti_2AlC and Ti_3SiC_2 were the most promising candidates for nuclear applications [354].

Later in 2016, Tallman *et al.* investigated the damage microstructures of both Ti_3SiC_2 and Ti_2AlC up to 0.1 dpa at 633 and 968 K and up to 0.4 dpa at 633 K [355]. The authors report on the observation of black-spots in both materials at 0.1 dpa and 0.4 dpa at 633 K and small basal dislocation loops at 0.1 dpa for the irradiation at 633 K. Analysis also revealed extensive micro-cracks in the Ti_2AlC which were not present in the Ti_3SiC_2. The secondary phases, TiC and Al_2O_3, exhibited worse radiation resistance than their parent MAX phases. The authors concluded that the Ti_3SiC_2 was better than its Al counterpart for nuclear applications [355].

A study of the neutron radiation behaviour of Ti_3SiC_2 and Ti_3AlC_2 was conducted in 2017 for the temperature range of 394–1321 K and doses of 0.14, 1.6 and 3.4 dpa [356]. Black-spots were observed in both materials and for the samples irradiated up to 3.4 dpa at 1008 K, basal dislocation loops and stacking faults were observed. The authors also reported extensive cavity formation for the irradiations up to 3.4 dpa at 1321 K, but smaller grains with sizes around of 3–5 μm were observed to be damage free. It was suggested that the A-layers of these MAX phases considerably enhanced the irradiation resistance of these materials [357], but these assumptions need to be supported by further research. The consensus however is that the Ti_3SiC_2 is the more promising candidate material for nuclear applications up to 3.4 dpa and temperatures around 973 K [356].

2.5 Next generation of nuclear materials and primary thesis goals

Throughout the literature review chapter it has been shown that MAX phases and high-entropy alloys are currently attracting the attention of both materials science and nuclear technology communities with the aim of investigating the possibility of applying these materials in the next generation of nuclear reactors. Nevertheless, the existing dataset on the radiation response of both classes of materials can be considered limited in a wide variety of aspects. With respect to these limited datasets, it is important to highlight:

- The major requirements delineating the selection of materials for the next generation of nuclear reactors lie on the demonstration of their phase stability in irradiation, corrosive and oxidative environments (including coolant compatibility) and high temperature exposure. In addition to such conditions, the materials will need to demonstrate stability under abnormal operational conditions like those experienced during nuclear accidents caused by either internal or external events.

- It is also of paramount importance that such materials are capable of preserving their initial set of properties and microstructural integrity at very high irradiation doses: between 50-200 dpa.

- The number of ion irradiation studies on the radiation response of high-entropy alloys has been observed to increase rapidly over the past 5 years. Most of these studies – using *ex situ* TEM ion irradiation techniques – have identified that the HEAs may have superior radiation resistance when compared to conventional multicomponent alloys such as stainless steels. Conversely, a recent neutron irradiation investigation on the FeCrMnNi HEA has shown that its radiation response – in terms of changes in mechanical properties and microstructural defects – was very similar to austenitic stainless steels.

- The majority of the ion irradiation studies do not directly compare the HEAs with conventional multicomponent alloys under the same irradiation conditions. These comparisons are often carried out qualitatively and are based on previous works published on conventional alloys.

- A limited number of computational studies have indicated that some of the core-effects of HEA such as sluggish-diffusion and high-entropy are responsible for the experimentally-observed superior radiation tolerance. However, the number of studies targeting directly these core-effects under irradiation is

still scarce. A more direct assessment on the influence of such core-effects in suppressing the development of radiation damage is also pending experimental confirmation.

- The number of studies on the neutron irradiation resistance of Ti-based MAX phases is also very limited. These studies were performed by the same research group. So far, the Ti-based MAX phases were only screened under neutron irradiation at very low doses and within a limited temperature range.

- Amorphisation has not so far been observed for Ti-based MAX phases irradiated with low dose neutron irradiation. Although some Ti-based MAX phases were reported to decompose to Ti-rich carbides and nitrides under neutron irradiation up to 0.1 dpa.

- With respect to ion irradiation, the Ti-based MAX phases were observed to preserve their matrix phase at very high doses (up to 100 dpa). Reports also indicate that Al-containing Ti-based MAX phases are more prone to decomposition under irradiation than the Si-containing ones.

- Some ion irradiation works have also identified that the MAX phases may have a high capability of self-healing for irradiation-induced defects. Recent modelling suggested that fast diffusion through the A-layers may play a major role on such high defect recombination capability.

- A lack of studies on the matrix phase stability of such Ti-based MAX phases upon neutron, ion irradiation or high temperature exposure was noted, in particularly for those providing analysis at a nanoscale level with electron-microscopy methods.

The lack of studies using the *in situ* TEM ion irradiation technique on both MAX phases and HEAs was also detected. This can be understood as the number of facilities or laboratories worldwide that are capable of performing such experiments is fairly limited, with only one in UK (*i.e.* MIAMI facilities). This technique is important not only by allowing the real-time monitoring and evolution of the microstructure of potential nuclear materials as a function of important parameters such as dose and irradiation temperature, but it can also provide a fast and reliable way for quick comparisons between many different materials. As a result, the research reported in this thesis will focus on the use of this technique to address the radiation resistance of MAX phases and HEAs and at the same time, it will propose the use of this technique to triaging potential nuclear materials before their testing in complex and expensive MTRs.

Given the items above as well as the literature screening presented in this chapter, the primary goals of the research reported in this thesis on potential nuclear materials can be summarised as follows:

- The FeCrMnNi HEA bulk alloy was selected to be studied in this thesis. Due to the enormous similarities of this alloy with austenitic stainless steels, the AISI-348 steel was also selected to be used as a comparable material for most the experiments that will be carried out with the HEA. The lack of irradiation studies with this austenitic stainless steel was also mentioned in section 2.4.1.3.

- The existing constitutive hypothesis and core-effects of HEAs will be targeted using the *in situ* TEM ion irradiation technique. In particular, the possible influence of the sluggish diffusion and high-entropy core-effects on the radiation resistance and phase stability of the FeCrMnNi HEA will be investigated in two different chapters (chapters 5 and 6). Direct comparison of the irradiation effects with the AISI-348 steel will be provided.

- The radiation resistance of the FeCrMnNi in a form of thin solid films will be also investigated. The importance here is to provide new irradiation data for innovative coating materials that could be considered as candidate materials for further testing within the scope of the accident tolerant fuels programme.

- As many of the HEAs investigated by previous authors were produced using plasma vapour deposition techniques, in order to evaluate the effects of ion irradiation on such equiatomic thin solid films, a complete and detailed study on the synthesis of the FeCrMnNi HEA thin films using ion-beam sputtered deposition will be carried out for the first time. The radiation resistance of the equiatomic thin solid film will be assessed with comparison with a conventional thin film – the titanium nitride – that was recently proposed as a candidate coating material for accident tolerant fuels.

- The Ti-based MAX phases were also selected to be subjected to investigation in this thesis due to their potential radiation tolerance as detected by previous works. On this topic, it will be carried out in this thesis, a neutron irradiation study on two select Ti-based MAX phases irradiated in the HFIR at 1273 K up to 10 dpa. A complete microstructural characterisation using TEM is shown for this irradiation conditions.

- Regarding the Ti-based MAX phases, an attempt to replicate the results obtained with neutron irradiation in the HFIR by using the *in situ* TEM ion irradiation methodology in MIAMI facilities will also be performed. Existing trends on the radiation response of these Ti-based MAX phases such as high

phase stability under either irradiation or high temperature exposure as well as absence of amorphisation will be targeted in the present study.

Chapter 3

Experimental Techniques and Methodology

This chapter is dedicated to the experimental techniques and the scientific methodology that are the basis of this doctoral research. Section 3.1 explores methods for the synthesis of the materials studied in this research, although some of the materials and alloys were obtained by means of scientific collaborations with Oak Ridge National Laboratory (USA) and the University of São Paulo (Brazil) as shown in table 3.1. Section 3.2 addresses the sample preparation methods for electron microscopy. Transmission electron microscopy and ion irradiation *in situ* within a TEM performed at the Microscope and Ion Accelerator for Materials Investigations (MIAMI) facilities are the core techniques of the present research and will be described in detail in sections 3.3 and 3.4, respectively. Section 3.5 briefly describes the use of the HFIR for the neutron irradiations carried out on the Ti-based MAX phases. In order to further analyse the results from both the ion and neutron irradiations, sample characterisation techniques are introduced in section 3.6.

Table 3.1: Materials and alloys used in this doctoral research.

Material	**Synthesis Technique**	**Provenance**
FeCrMnNi HEA	Plasma Arc Melting	Oak Ridge National Laboratory
AISI-348	Commercial steel production routes	FOPIL-Sandvik
MAX Phases	Reactive Hot Pressing	Oak Ridge National Laboratory
HEA Thin Films	Ion Beam Sputter-Deposition	Developed in this research work

3.1 Materials synthesis

3.1.1 Production of austenitic stainless steels and the AISI-348 steel

The first step in the production of steels is the mining of Fe minerals. After the extraction of the Fe minerals, the industrial routes for stainless steel production involve four major transformation stages: (a) ore treatment, (b) reduction, (c) steel fabrication and (d) refinement. The elemental enrichment of Fe can be achieved through the ore treatment by means of chemical separation and reaction processes. In the last step of steel refining, a wide variety of steels, such as austenitic stainless steels, can be obtained by means of accurate addition of alloying elements such as Cr, Mn, Ni, Co, Cu and C. Final stages often require heat treatments aimed at achieving certain mechanical and specific physico-chemical properties such as corrosion and oxidation resistance [32, 39].

In the research reported in this thesis, the radiation response of the austenitic stainless steel AISI-348 was studied and compared with the FeCrMnNi bulk HEA as its major alloying elements are Cr, Mn and Ni, although not in equiatomic composition. This steel was obtained in collaboration with University of São Paulo and it was redistributed by the company FOPIL, but produced by Sandvik. The AISI-348 steel is a commercial evolution from the AISI-347 and the only difference between them is that in the AISI-348, the maximum allowed Ta content is usually less than 0.10 wt.% whilst in the AISI-347, the Ta content can be 10 times the C content [358]: both steels are Nb-stabilised and their mechanical properties can be considered identical. The additions on Nb in the AISI-300 steel series is performed in order to maximise the resistance of oxidation and corrosion of the austenite matrix [32, 53].The nominal composition of this steel is shown in table 3.2.

The AISI-348 steel that was used in this work was solution-annealed at 1313 K followed by air-cooling. Hot-rolling was performed in order to obtain a fully equiaxed grain microstructure. The complete details of the thermo-mechanical processing were not provided by the manufacturer. The AISI-348 samples used throughout the research work reported in this thesis were not subjected to any kind of additional heat-treatment, thermo-mechanical processing or deformation: the samples of the steel were used in its as-received condition. A complete characterisation of the AISI-348 before irradiation is shown in section 4.2.

3.1.2 Synthesis of the FeCrMnNi HEA

The FeCrMnNi high-entropy bulk alloy studied in the work reported in this thesis was produced at Oak Ridge National Laboratory using a standard plasma arc-

Table 3.2: Nominal composition of the AISI-348 steel [359].

Element	Composition [wt.%]
Fe	Balance
Cr	17.00-19.00
Ni	9.00-13.00
Mn	2.00 (max)
C	0.08 (max)
P	0.045 (max)
S	0.030 (max)
Si	1.00 (max)
Ta	0.10 (max)
Nb	10×C (min)
Co	0.20 (max)

melting furnace and complete details on the metallurgy of alloy synthesis using such methods can be found elsewhere [30, 32, 360–363].

The alloying elements close to equimolar proportions were initially put into a refractory ceramic crucible. The crucible was placed inside the plasma arc furnace where thermodynamic reactions occur upon heating to the melting temperatures of the alloying elements. After casting, the produced bar was homogenised at 1573 K for 48 h followed by subsequent cold rolling and recrystallised 1173 K for 4 h in a vacuum furnace in order to achieve a complete equiaxed microstructure. The average grain sizes after cold rolling was measured to be approximately 35 μm. The synthesis of FeCrMnNi HEA is also described in a recent work from ORNL [338]. The alloy as-received had nominal composition of 27Fe-18Cr-27Mn-28Ni (wt.%) and it was characterised by ORNL to be single-phase face-centred cubic as determined by X-ray diffraction [338]. Earlier attempts to produce a 25Fe-25Cr-25Mn-25Ni (wt.%) have not resulted in a single-phase HEA as reported by Kumar *et al.* [338]. A complete microstructural characterisation of the FeCrMnNi HEA as-received is shown in section 4.3. In the work reported in this thesis, the FeCrMnNi bulk HEA was used in its pristine form, *i.e.* neither further heat-treatment nor thermo-mechanical processing was performed.

3.1.3 Production of MAX phases

Conventional routes to synthesize ceramic compounds include a final processing stage which is aimed at increasing the compound strength by eliminating free surfaces (reducing the surface energy) of the powder raw material. The concept of reducing the surface energy of ceramic powders at very high temperatures is known as sintering or firing. During this process, as the materials are kept at high temperatures (but below the melting point), atomic diffusion takes place and reduces

the initial porosity. The elimination of pores and the subsequent creation of strong inter-particle bonds result in the increased strength of the material. As the atomic mobility is proportional to the exponential of the inverse temperature, and considering that reaching the high temperatures needed to promote diffusion in the high melting point ceramic compounds is difficult, sintering is often carried out for long periods of times. As an example, sintering of alumina (Al_2O_3) was reported to take around 10 hours at 1973 K to complete [364, 365].

An alternative technique which is able to eliminate the long times and reduce the very high temperatures required by sintering, and that at the same time produce good quality and denser ceramic parts, is known as reactive hot pressing (RHP). The RHP technique was developed in the early 1960s as a method to produce stronger clay products [366, 367]. It consists of applying pressure to powdered materials at moderate-to-high temperatures (higher than the recrystallisation temperature of the studied system). During the process, the materials that are subjected to high hydrostatic loads at high temperatures often undergo in decomposition/dissociation reactions (thus the term 'reactive') or polymorphic phase transformations [368]. After the process, the final product has its strength considerably enhanced. In the case of alumina, RHP gives after a shorter time the same strength levels as the conventional sintering process: 20 minutes under pressures around 96.5 MPa and temperatures as low as 973 K.

The MAX phases studied in this work were obtained by Oak Ridge National Laboratory and were synthesized by the Reactive Hot Pressing technique at the company 3-ONE-2 LCC. The compound Ti_2AlC, for example, was produced by pouring pre-reacted powders of the material into a graphite die, which was subsequent hot pressed for 4 hours at around 1500 K with uniaxial stresses in the order of 40 MPa [353]. Similar synthesis routes have been reported for Ti_3SiC_2 [369] and several other MAX phases [370–372]

3.1.4 Synthesis of thin solid films

The sputter-deposition of thin films involves three major steps [373]: (i) the transport of alloying or coating materials towards the substrate, (ii) adsorption and diffusion of the sputtered coating elements on the substrate with nucleation and growth of small embryos and (iii) the rearrangement of the coating atoms into their final positions driven by bulk and surface diffusional processes. The final microstructure of the deposited thin films will be strongly dependent on the deposition temperature as shown in detailed studies conducted by Thornton [373, 374] and Movchan *et al.* [375].

In the work reported in this thesis, high-entropy alloy thin films (HEATF) from

the quaternary system FeCrMnNi were produced using the technique of ion beam sputter-deposition (IBSD) which is a type of physical vapour deposition (PVD) [374].

Ar^+ ions with an energy of a 1.25 keV are used to induce sputtering of elemental targets towards a specific substrate. Deposition is controlled using magnetic fields to focus and deflect the ion beam. Sputtered atoms are deposited without significant implantation into the substrate. The substrate was not intentionally heated during the deposition experiments, although this temperature was monitored with a thermocouple to be in the range from 350 to 400 K. In addition, during the deposition experiments, the substrate was grounded and no bias potential was applied. The IBSD system used in this work is shown in figure 3.1.

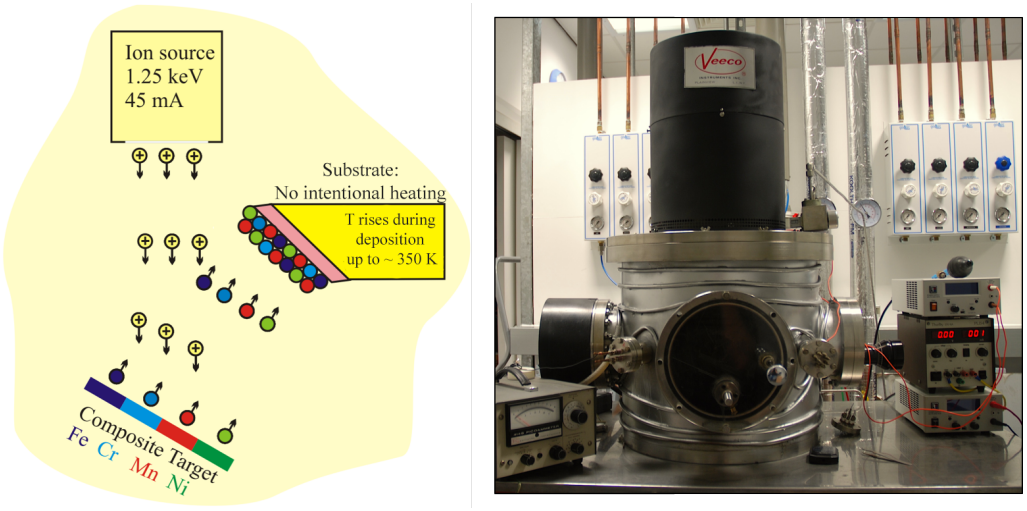

Figure 3.1: The ion beam sputter-deposition system in the Ion Beam Centre at the University of Huddersfield [376].

In chapter 7, a detailed report on the synthesis, characterisation and radiation resistance of these HEATFs is presented. In this chapter, an study on the feasibility of depositing equiatomic metallic thin films from the quaternary system FeCrMnNi on pure Si substrates is firstly presented. Then, the development of FeCrMnNi HEATFs on a Zr alloy substrate is demonstrated and the radiation resistance of the HEATF/Zr alloy system is assessed by using the technique of *in situ* TEM ion irradiation.

3.2 Sample preparation techniques

To image materials in a TEM, samples have to be electron transparent. This requires that the thickness of the sample has to be on the order of 100 nm. In order to prepare TEM samples of the materials studied in this work, two sample preparation methods were used: focused ion beam (FIB) milling and electro-polishing (EP). Despite the

ballistic nature of FIB and the electro-chemical nature of EP, a major difference between these two techniques is that in the former, the electron transparent area is smaller than the latter. In this section, these sample preparation methods are described in further detail.

3.2.1 Electro-chemical jet-polishing

Electro-chemical jet-polishing (EJP) can be defined as a physico-chemical technique that through the application of an electric current in a material which is subjected to a temperature-controlled set of electrolyte, a material removal process takes place [377]. Such removal occurs as a result of the interaction between the ions of the electrolyte and the surface of the materials. The removal rate can be controlled by changing electropolishing parameters, such as temperature of the electrolyte and the electric current. The ability to control accurately the removal of material makes EJP techniques very useful to fast produce electron transparent layers for electron microscopy.

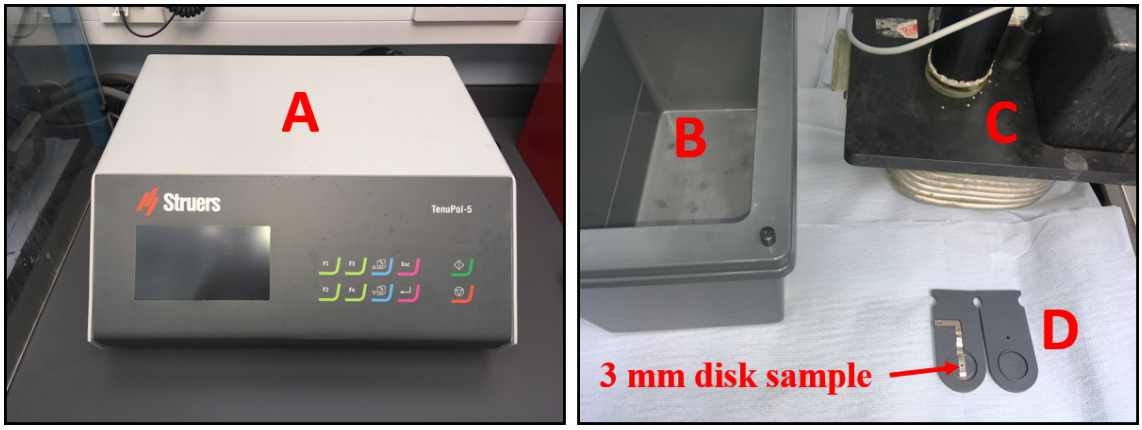

Figure 3.2: The TenuPol-5 jet electro-polishing station at the MIAMI facility: A is the station controller, B the cold stage vessel, C the electro-polishing unit and D the sample holder.

Prior to electro-polishing the AISI-348 samples, the alloys were subjected to several sessions of mechanical polishing and grinding in order to reduce their thicknesses to ≈0.10 mm. At this stage, SiC grinding papers with grits between 120 and 1200 μm were used. There is a water flow onto the SiC papers during the mechanical grinding stage to cool, lubricate and removal of debris. When the specimen thickness has reached the required value, a set of diamond papers (from 8 to 1 μm grit size) are used to polish the surface further. From the mechanical polished alloy samples, 3 mm disk are punched using a conventional Gatan mechanical punch.

For electro-polishing, a Struers TenuPol-5 EJP system was used (figure 3.2). The 3 mm disk is placed in a sample holder and inserted into a temperature-controlled

vessel. For the EP of the AISI-348 stainless steel, in particular, a modified recipe from reference [378] was employed for this TenuPol-5 EJP system: (a) the electrolyte was 10% $HClO_4$, 90% CH_3OH, (b) the bath temperature was 233 K, (c) the flow rate was set to 30 and (d) a potential of 20 V was applied to the sample. With these conditions, the electro-polishing was performed under constant current of 90 mA until perforation and the samples were washed thoroughly in pure methanol and dried in air. When perforation occurs, an annular region around the hole is electron transparent (often over a radial distance in the order of microns) and the sample is ready for TEM. A typical 3 mm disk after EP is shown in figure 3.3.

3.2.2 Focused ion beam

The FeCrMnNi high-entropy alloy sample was obtained from the Oak Ridge National Laboratory and due to the limited availability of the material, the Focused Ion Beam (FIB) technique was used to produce electron transparent samples instead of electro-polishing as FIB requires much smaller quantities of material.

A FIB instrument consists of a liquid metal ion source (LMIS) operating with an ion column at high vacuum ($\approx 10^{-6}$ Pa). In the LMIS, Ga is melted and flows over the surface of a fine W tip. This enables Ga ions to be extracted from a very small region of the tip and thus focused to micrometre beam spots. In a FIB, the energies of the ion beam are in the range of 5 to 30 keV. By scanning and rastering the fine beam spot, Ga ions are then used to sputter target atoms in order to fabricate electron transparent samples [379].

A conventional procedure to produce good quality electron transparent samples with FIB has been described by Giannuzzi *et al.* and it has been adopted in the work reported in this thesis [380]. The first step in producing a TEM specimen using

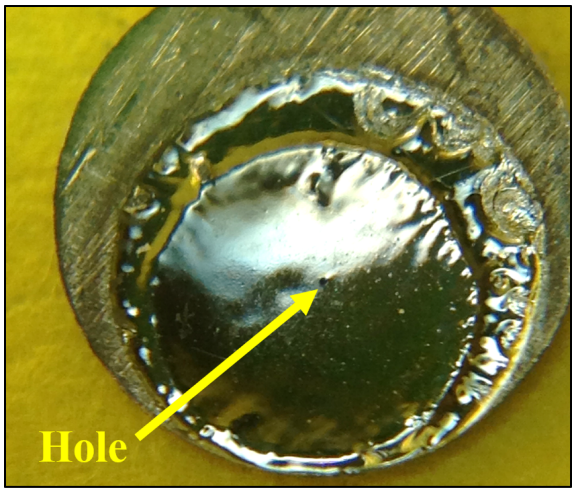

Figure 3.3: A 3 mm disk of the AISI-348 steel electro-polished in the TenuPol-5 system.

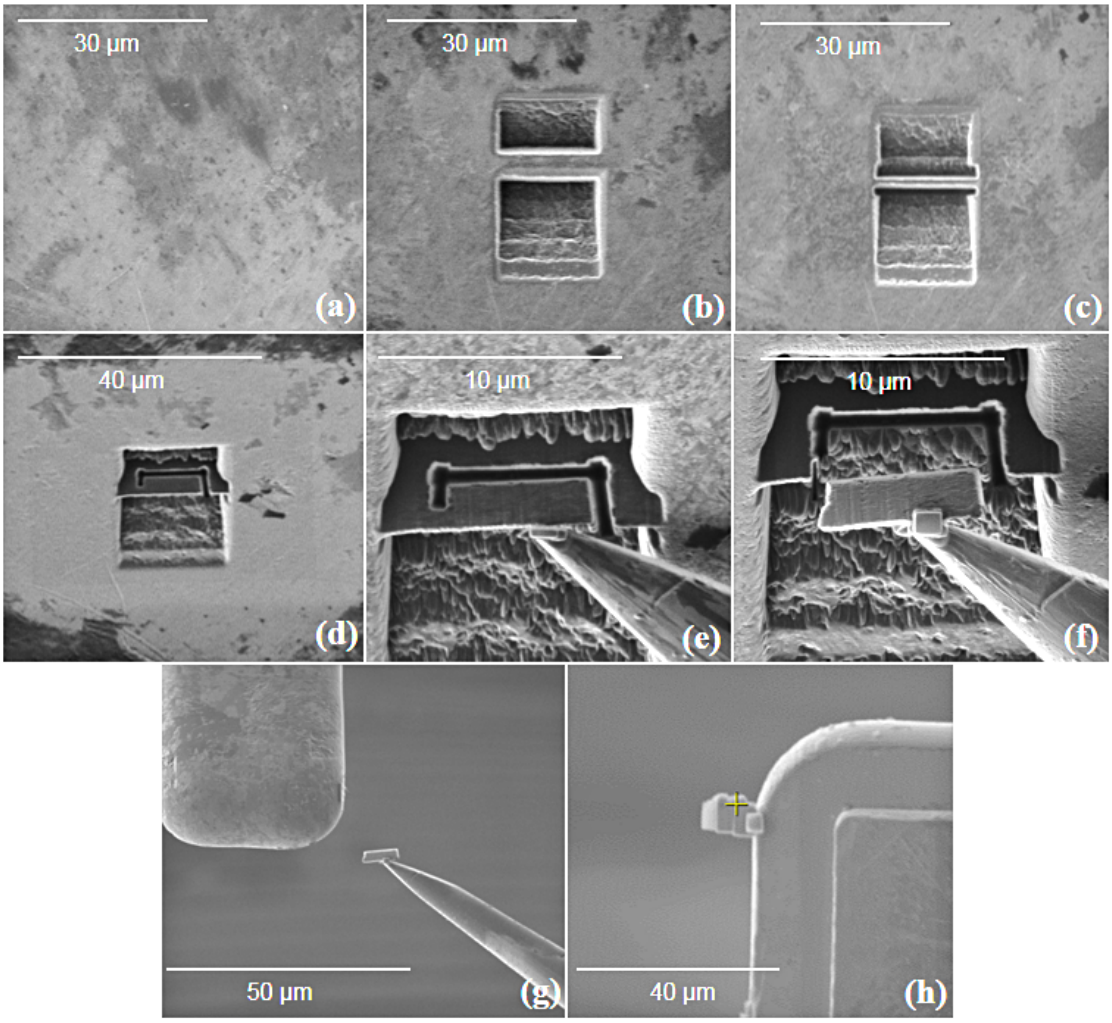

Figure 3.4: Focused ion beam steps to produce TEM samples of the HEA: (a) sample as received, (b-c) milling and thinning, (d-f) the sample is cleaved from the cross sectional cut, (g) attaching to the TEM grid by depositing C and (h) making it electron transparent using the ion beam.

the FIB technique was to make a cross sectional cut using the Ga ion beam. Two rectangular trenches were milled in order to leave a thin slice of the HEA (figure 3.4b) between the trenches. After the milling, the same procedure was repeated to make the slice thinner, as can be seen in figure 3.4c. The sample was cleaved (figure 3.4d) from the selected region and attached to the probe using C deposition (figure 3.4e). After attachment, the sample was removed from the milled cross section (figure 3.4f) by withdrawing the probe. The final steps consisted of attaching the sample to the TEM grid (figure 3.4g) and selecting a region for further milling to electron transparency using the ion beam. The whole process is shown in figure 3.4. Focused ion beam is a powerful technique for producing TEM samples and has been used since the seventies with particular developments in materials science in the 1980s [381]. Necessary precautions were taken to avoid FIB damage in the specimens, such as pre-coating lamellae with Pt and C top-layers and reducing the ion beam energy during the final polishing steps.

In the work reported in this thesis, the FIB technique has been used to produce TEM samples for the FeCrMnNi HEA, the high-entropy entropy thin films, the AISI-348 steel and the Ti-based MAX phases.

3.3 Transmission Electron Microscopy

In a transmission electron microscope, an electron beam is focused on a thin, electron-transparent sample. Then electrons are produced using thermionic emission where a cathode made of a tungsten filament (or LaB_6 crystal) is heated up until electrons are emitted from the surface by overcoming the potential-energy barrier. Electrons can also be generated via field emission: in this method, high negative potential is applied in an electrode inducing a strong potential gradient at its surface. By this, electrons are emitted from the surface. After emission, either by thermionic or field emission, electrons are accelerated to an energy in the range of 60–300 keV [382].

After the electron gun stage, the area of the specimen which is illuminated and the brightness are controlled using the condenser lens system and apertures. After the condenser system, the electrons are transmitted through a specimen and undergo into scattering. Those electrons scattered by the sample are focused by the objective lens and form a diffraction pattern in the back focal plane where electrons scattered through the same angle are focused. Then, electrons emerging from the same point of the sample are focused and an image is formed in the image plane. This first image can be magnified using the intermediate and then the projector lenses. Nowadays, images and videos can be recorded using charged-coupled devices (CCDs), but this procedure was carried out in the past using photographic films [382, 383].

The spherical aberration of the objective lens is not negligible and it is thus necessary to use small objective apertures to work only with paraxial beams. Bright-field (BF) images are generated by scattered electrons using the objective aperture in order to allow only the direct beam to pass. Conversely, dark-field (DF) images are produced when the unscattered beam is blocked by the diaphragm whilst one or more scattered diffracted beams are allowed to pass though the objective aperture. DF images are very useful to detect planar defects, precipitates and stacking faults [382, 383].

Transmission electron microscopy has become one of the most widely used techniques in materials sciences due to its suitability for the microstructural characterisation of a wide range of materials. Despite the fact that TEM can provide direct observation of materials at the nanoscale, analytical techniques can also be used to obtain chemical and physical information from electronic excitations caused by the interaction of the electron beam with the sample. Due to the importance of conventional and analytical TEM methods for this project, the next section will describe the principles of microscope operation as well as its components and capabilities in more detail.

3.3.1 The equipment

A TEM consists of a tall structure with an electron gun on the top which together with of a set of magnetic lenses and apertures, can generate and manipulate an electron beam for the purposes of imaging [382–384]. This will be described in some detail in this section.

3.3.1.1 An electron gun

The first step to produce, control and manipulate an electron beam within a TEM is to extract electrons from a source. Two different types of electron sources are used in TEMs: thermionic and field-emission. The basic difference between these two type of sources is that field-emission provides more monochromatic electrons, *i.e.* electrons with well defined energies without significant dispersion. Thermionic sources are either W filaments or LaB_6 crystals. Field-emission guns or FEGs are usually made of W crystals sharpened to a tip with radius of around 100 nm [382–384].

The physical principle of thermionic sources can be summarised as follows. The material is heated to a high temperature which gives sufficient energy for the electrons to overcome a natural energy barrier that prevents them from escaping from the surface. This natural barrier is known as the work function, denoted by Greek letter Φ. The physics of thermionic emission is described by Richardson's law [385]:

$$J = AT^2 \exp -\frac{\Phi}{kT} \tag{3.1}$$

Where J is the current density of the extracted electrons, T is temperature to overcome the barrier Φ and A and k are known as the Richardson's and Boltzmann's constants, respectively. The work function of W filaments is around of 4.5 eV, compared to 2.4 eV for LaB_6 crystals. Although the current density increases with temperature, the process is limited by the melting point of the filament which for W is around 3660 K. Evaporation and oxidation of filaments can also further limit their lifetime [382–385].

In the case of FEGs, the physical principle relies on the fact that in the region of a nanometre-sized tip, the electric field can be very high [386]. On the application of an electric potential (V) at a tip of radius r, the electric field is:

$$E = \frac{V}{r} \tag{3.2}$$

When the potential is applied to the tip (or needle), the work function is lowered and the electrons start to tunnel out of the material. A FEG source requires ultra-high vacuum conditions for operation as its surface has to be in a pristine condition for the field emission to occur. In this case, the FEG is normally referred to as a cold FEG. A so-called hot FEG can be operated under poorer vacuum conditions as heat is applied to the tip enhancing the electron emission by giving the material some thermal energy as well as inducing desorption of contaminants from the tip. In this latter case, the electrons do not undergo a quantum tunnelling effect. Deposition of zirconium oxide is often made on the surface of the needle in order to lower the work function, thus improving the extraction of electrons. The hot FEGs are also known as Schottky FEGs [383].

A major distinction between different sources is the brightness of the beam: the electron current density per unit solid angle. At 100 keV, thermionic sources have brightnesses in the order of 10^{10} to 10^{11} A/m^{2}sr, FEG sources are much higher: 10^{12} to 10^{13} A/m^{2}sr [382–384].

In the research reported in this thesis, the electron guns used in the TEMs employ thermionic sources and are known as triodes. A Wehnelt cylinder and a grounded anode with centre aperture are the two other parts of the triode. The Wehnelt cylinder acts as an electrostatic lens and the anode aperture is aligned with the W filament or LaB_6 crystal-tip. The cathode is attached to a high-voltage power supply and the thermionic emission starts upon application of an acceleration potential, generally between 100 to 300 kV, which heats the filament. A microscope with a thermionic source normally operates in near-saturated filament conditions. Operation above saturation significantly reduces the source lifetime [382–384].

3.3.1.2 Magnetic lenses

Electromagnetic lenses are used within TEMs to control the electron beam path in a similar way to optical lenses in an optical microscope. Magnetic lenses are used rather than electrostatic due to their higher reliability, better aberration properties and the absence of electrical breakdowns. The magnetic field is produced when an electric current flows through Cu coils. By varying the electric current, the strength of the magnetic field can be changed. Magnetic lenses suffer from spherical aberration, chromatic aberration and astigmatism [383].

These lenses are generally manufactured as cylindrically-symmetrical soft iron polepieces with embedded copper coils. The electron beam travels through a bore path on the axis of the cylindrical lens. The term "soft iron" means that the material does not retain the magnetic field upon removal of the voltage to the coils of the electromagnetic lens and it is an important requirement to mitigate problems such as aberration and astigmatism. The magnetic lenses are cooled with water to help provide stability to the magnetic field as upon increasing the temperature, the resistivity of the Cu coils changes significantly [383].

3.3.1.2.1 Spherical (C_S) and chromatic aberrations (C_3)

Spherical aberration occurs when the magnetic field fails to focus off axis electrons to a single point thus limiting the resolution. This type of aberration is stronger for the electrons that are away from the optical axis and often produces a degraded image [383, 384].

Chromatic aberration occurs when electrons of different wavelengths are focused at different points. Their energies within the TEM should therefore be as monochromatic as possible. Chromatic aberration is thus due to the energy dispersion of electrons in the TEM and it can be exacerbated by scattering effects in thicker samples [383, 384].

3.3.1.2.2 Astigmatism and stigmators

The astigmatism in TEMs is often associated with asymmetries in the soft-iron polepieces as well as the presence of contaminants along the beam path, e.g. on the apertures. Upon charging, these contaminants will deflect the electron beam slightly. The astigmatism in TEMs can be corrected by the use of stigmators which are magnetic coils that correct the electron beam path. The stigmators are particularly useful when working with magnetic samples [383, 384].

3.3.1.3 Deflectors

Magnetic coils are also used within the TEM to tilt and shift the electron beam in order to optimise the alignment. The beam shift and tilt are also essential for carrying out BFTEM, DFTEM microscopy and to record diffraction patterns. In scanning transmission electron microscopes (STEM) the deflectors are also used to scan and raster the electron beam over a sample in a similar way to that in scanning electron microscopes.

3.3.1.4 Condenser and objective lenses

After extraction from the gun, the condenser lenses are used to illuminate the specimen with the electron beam. The condenser lens system will also focus the beam on the specimen. The objective lens will then: focus the electron beam when they exit the specimen and start magnifying the image. Near to the objective lens within the TEM column, a so-called "cold finger" is used to trap possible contaminants and thus improve the vacuum in the vicinity of the specimen. It consists of an anticontaminant Cu surface that must be cooled with liquid nitrogen so contaminants will condense onto it.

3.3.1.5 Intermediate lenses

Between the objective and projector lenses, an intermediate lens system works to adjust the electron beam on either a diffraction pattern or electron image into the projector lens. The intermediate lens system magnifies the focused diffraction pattern or TEM image on the object plane of the projector lens system.

3.3.1.6 Projectors

This is the final stage of the imaging system. The projectors takes the magnified image (in the object plane) and transfer it to the back focal plane. The image is projected in a fluorescent screen, thus allowing the microscopist to see an image from the specimen. This system magnifies the image from the intermediate lenses even further.

3.3.1.7 Condenser, objective and intermediate apertures

The TEM has a set of apertures with the primary aim of limiting the electron beam collection angle (β). The objective lens aperture, for example, controls the illumination, resolution, depths of field and focus, the angular resolution of the diffraction pattern and the image contrast. The condenser aperture limits the size of the electron beam on the specimen which helps to control the illumination intensity

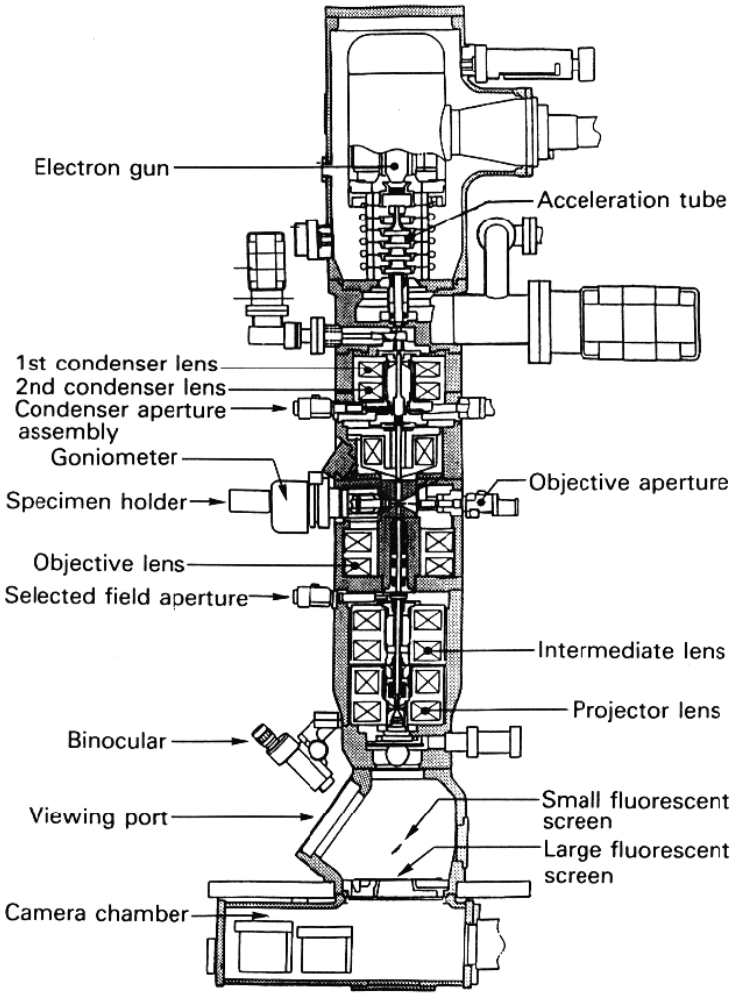

Figure 3.5: A cross-sectional profile of a common TEM. (Reproduced from [384].)

on the specimen as well as to reduce spherical aberration effects. The intermediate aperture, or selected-area electron diffraction (SAED) aperture, can be used to select specific areas within the specimen for electron diffraction.

3.3.1.8 Specimen stage

At the specimen stage, a high precision motorised goniometer can be used to align the specimen to specific crystal orientations with respect to the electron beam. With the goniometer, specimens can be accurately tilted generally over tens of degrees with precision in the order of 0.1°.

3.3.1.9 Specimen holders

Different types of experiments can be carried out using a TEM. For conventional TEM imaging, single and double tilt holders are used and the main difference is that in the latter, the user has access to an azimuthal tilt angle (axis at right angles to the

main tilt axis provided by the goniometer) which can be particularly important for dislocation analysis ($\vec{b}\cdot\vec{g}$ conditions), for example. It is also possible to have heating holders that allow annealing studies of specimens up to very high temperatures. Similarly, cold holders are those where the specimen is kept at temperatures between room temperature and liquid nitrogen or liquid helium temperatures. Straining holders also allow the dynamic study of the effects of mechanical stress on samples.

3.3.1.10 Electron image capture methods and post-imaging analsysis

With the advent of charged-coupled devices (CCDs), the specimen image generated from the electron beam within the TEM can be recorded digitally with very high resolutions. The cameras are inserted below the projector lens. In the past, photonegative films were used to record images and *in situ* TEM experiments were recorded by coupling the microscope with a camera and a television [383]. During this project, two CCDs were used to collect images from MIAMI experiments: a Gatan Orius digital camera with 4 megapixels up to 30 fps (MIAMI-1) and a Gatan OneView digital camera with 16 megapixels and up to 300 fps video (MIAMI-2).

TEM images recorded during *in situ* experiments were analysed using the ImageJ software. For videos, the applications iMovie and FFmpeg were also used. The latter allows the extraction of image frames and saved in different image formats.

3.3.2 The imaging techniques: the interaction between electrons and matter

When the electron beam is incident on the specimen within a TEM, scattering effects will occur which will induce modifications in its amplitude and phase that will depend intrinsically on the nature of the studied specimen. Therefore, the electron scattering phenomenon plays a fundamental role in the imaging in a TEM and this is the subject of this section.

3.3.2.1 Elastic scattering

If an electron wave is scattered by an atom (or a solid) without losing energy, the process is known as elastic scattering. As the wavelength of the electrons is in the same order of magnitude of the lattice spacing in crystalline solids, diffraction will occur. The physical interaction between the electron waves and the crystalline solids will be mediated by the "strength or power" of an atom to scatter electrons: the atomic-scattering factor.

3.3.2.1.1 Atomic-scattering factor in crystalline solids

The scattering cross section $\sigma(\theta)$ is the probability of an electron to be scattered by an atom as a function of the scattering angle (θ). Thus, the differential scattering cross section per unit of solid angle (Ω) is:

$$\frac{d\sigma(\theta)}{d\Omega} \tag{3.3}$$

This express the proportion of the incident intensity that will suffer scattering by an atom per unit of solid angle. This intensity can be linked with the atomic-scattering factor, $f(\theta)$, which express how capable an atom is to promoting scattering of electrons at an angle θ [387]:

$$\frac{d\sigma(\theta)}{d\Omega} = |f(\theta)|^2 \tag{3.4}$$

In a crystalline solid, the atomic-scattering factor is a sum of the contribution of each atom to the scattering process at its specific lattice position, *i.e.*:

$$F(\theta) = \sum_n f_n(\theta) \exp(i\psi_n) \tag{3.5}$$

Where ψ_n is the phase angle at the atom n and $f_n(\theta)$ is the contribution of an atom n within the lattice to the scattering process. The dot product of the scattered wavenumber in the reciprocal lattice, $\vec{K} = (ha^*, kb^*, lc^*)$, with the position of each n atom within the lattice, *i.e.* $\vec{r_n} = (u_n a, v_n b, w_n c)$ gives the phase angle [387]:

$$\psi_n = 2\pi(u_n h + v_n k + w_n l) \tag{3.6}$$

Where h, k and l are the Miller indices; a, b and c the lattice parameters (the reciprocal ones are a^*, b^* and c^*); and u_n, v_n and w_n are the specific positions of the n-atoms within the lattice. In this way, the structure factor for a solid crystal can be expressed as:

$$F(\theta) = \sum_n f_n(\theta) \exp[i2\pi(u_n h + v_n k + w_n l)] \tag{3.7}$$

Therefore, the structure factor of a crystal will dictate the intensity (strength) of any hkl reflection within a TEM as well as which reflections will be allowed in a certain crystallographic system [387].

3.3.2.1.2 Bragg's law

The electron beam inside the TEM can be regarded as monoenergetic (or monochromatic) although it actually has a small energy spread. The diffraction of the electron waves in a crystalline solid is described by Bragg's law which relates the wavelength

(λ) of a planar wave (the beam) with a scattering angle θ_B and the lattice spacing d of the crystal (specimen) to be analysed:

$$n\lambda = 2d\sin\theta_B \tag{3.8}$$

Where n is the order of diffraction. When this law is applied to analyse cubic systems, like the AISI-348 and the FeCrMnNi HEA in this thesis, the lattice spacing becomes:

$$d = \frac{a}{\sqrt{h^2 + k^2 + l^2}} \tag{3.9}$$

For this case, the indices h, k and l are the Miller indices for a specific crystal plane. Bragg's law can be viewed as a mirror-like physical process: the crystal planes of a specimen behaves like an atomic mirror and for this reason, a diffracted beam within a TEM is known as a reflection. These coherent reflections are considered a type of elastic scattering of the electron beam where no energy transfer occurs. Incoherent elastic scattering may also occur and this is associated with a change in the phase of the incident beam wave and will be discussed later.

Within a TEM, diffraction can occur without exactly satisfying Bragg's law [383, 387]. By this, a deviation parameter $\vec{s_g}$ is introduced to take into account how far the diffraction conditions are from the exact mathematical condition (*i.e.* $2d\sin\theta_B$) [383]. $\vec{K}$ is the diffraction vector when the Bragg's condition is satisfied the diffraction vector. The difference between $\vec{K}$ and the deviation parameter $\vec{s_g}$ is:

$$\vec{g} = \vec{K} - \vec{s_g} \tag{3.10}$$

The vector $\vec{g}$ is the diffraction condition in a TEM when $\vec{s_g}$ is higher or smaller than θ_B. The exact Bragg condition exists when $\vec{s_g} = 0$.

3.3.2.2 Inelastic scattering

During inelastic scattering events, the incident electron beam transfers energy and momentum to the specimen and this is associated with losses of the initial electron beam energy. Inelastic events are particularly important for the identification of elements (*i.e.* analytical TEM techniques) as the losses may be characteristic for different elements in the periodic table. These losses are also associated with the excitation of plasmons which are collective oscillations of valence electrons and the energy loss associated with plasmon excitations is lower than for shell-ionisation processes [383, 384].

3.3.2.3 Diffraction patterns and Kikuchi lines

In a TEM, a diffraction pattern can be formed when there is coherent elastic scattering of electrons by a crystalline specimen. Each spot of the diffraction pattern is a reflection $\vec{g}$ corresponding to a specific set of atomic planes. Unlike the electrons which form a crystalline diffraction pattern, incoherent elastically-scattered electrons do not share a common direction and phase, but they can still be diffracted by any set of planes they intersected at the Bragg angle θ_B. As a result, the diffraction of incoherent elastically-scattered electrons will form a so-called Kossel cone and the intersection of such a cone with the plane where the TEM diffraction pattern is formed (back focal plane) will result in the formation of a parabolic line known as a Kikuchi line [383, 387].

3.3.2.4 Amplitude contrast

Due to scattering effects of the initial beam, the electron wave can have both its amplitude and phase changed after passing through the specimen. Such modifications of the electron wave are give rise to contrast mechanisms within a TEM. The amplitude contrast is related to variations in the atomic density or in the thickness of the electron transparent specimen and the most common mechanisms are mass-thickness and diffraction contrast.

3.3.2.4.1 Mass-thickness

The scattering interaction between charged particles with matter is governed by the Rutherford cross section which is a function of the atomic number and the thickness of the material. Inelastic scattering processes give rise to so called mass-thickness contrast. In this case, darker contrast (more electron scattering) is related to higher Z elements and thicker regions whilst lighter contrast is associated with elements of lower Z or thinner regions. In the context of non-crystalline materials, for example, mass-thickness has paramount importance as the TEM final image will have no contrast arising from diffraction effects.

3.3.2.4.2 Diffraction contrast

For crystalline materials, Bragg's law may be satisfied and intensity changes in the image may occur as a result of so-called "diffraction contrast".

In BFTEM, the diffracted waves are intercepted by the objective aperture allowing only the transmitted beam (*i.e.* not diffracted) to form an image. For example, for specific crystallographic orientations, small crystallites satisfying the Bragg's

law will be seen to have strong dark contrast when under bright-field conditions. In the DFTEM, the objective aperture will be placed around the diffracted reflection and then, some of those small crystallites will appear bright. The electron beam configuration for BF and DFTEM is shown in figure 3.6.

If the electron transparent specimen is bent, dark lines or bands will be visible under bright-field conditions and, similarly bright in dark-field. These lines are known as bend contours and they exhibit strong intensity in both BF and DF when Bragg conditions are satisfied.

In the context of both crystalline and amorphous materials, the generation of diffraction patterns (DP) due to the interaction between the electron beam with the specimen are of particular importance for a TEM user, not only for characterisation purposes, but also for selecting the desired type of imaging within the TEM. The generation of an image in a TEM is then dependent on the specimen diffraction pattern and the operational conditions defined by the microscopist.

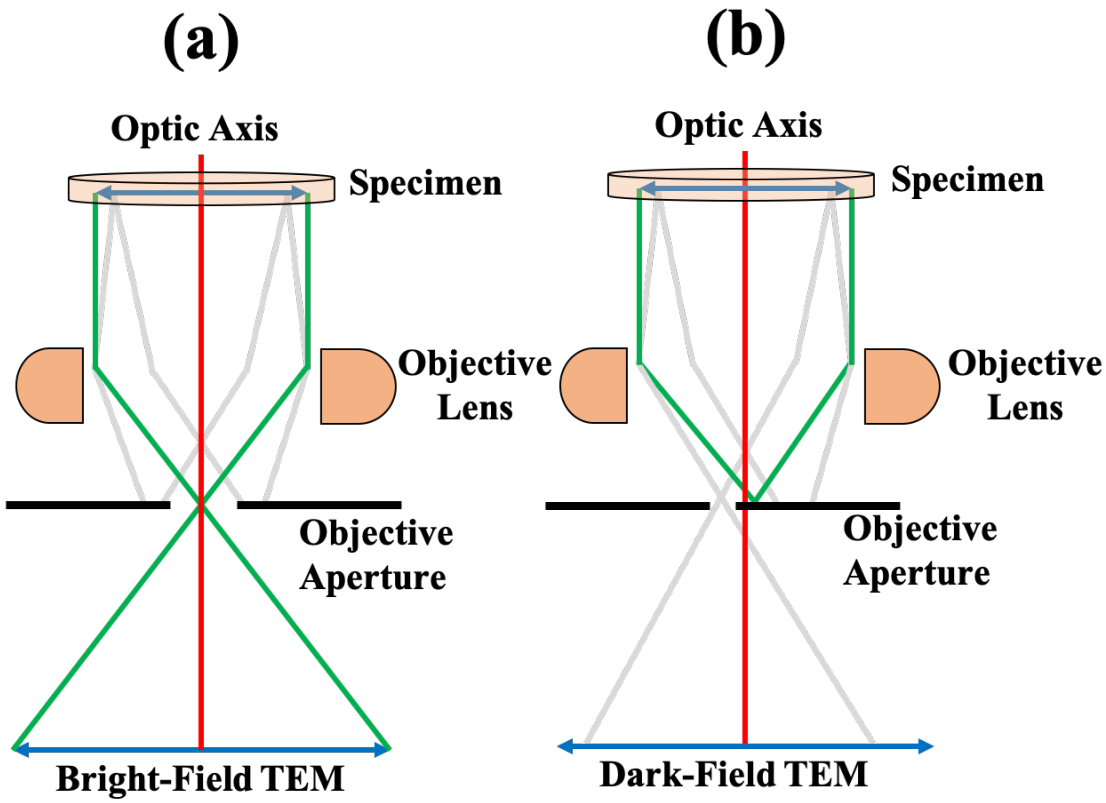

Figure 3.6: Modes of imaging using diffraction contrast: (a) bright-field (BFTEM) and (b) dark-field (DFTEM). (Modified from [388])

3.3.2.4.3 Many-beam and two-beam conditions

The many-beam condition occurs when a group of reflections characteristic of a specific crystal zone are excited. When the specimen is aligned and tilted to exhibit such characteristic set of reflections uniformly illuminated, it is said that the crystal is at down-zone.

The two-beam condition (or two-beam approximation) is achieved when two strong diffracted beams are observable in the diffraction pattern. One is the transmitted beam and the second is a reflected beam from one specific set of lattice planes. This method allows, for example, the characterisation of dislocations in bright-field. This can be achieved by tilting the specimen around a specific zone axis in order to find a two-beam beam condition where the inner product of the Burgers vector ($\vec{b}$) with the excited reflection ($\vec{g}$) is $\vec{b} \cdot \vec{g} > 0$. This is visibility condition in dislocation analysis. Often, a set of four of more two-beam conditions are necessary unequivocally determine the Burgers vector [248, 383, 387].

3.3.2.4.4 Weak-beam

For weak-beam dark-field (WBDF) imaging, the sample is tilted with the purposes of exciting large-order reflections (3th order or more) which are of low intensity (weak). This is often carried out after a two-beam condition is established. WBDF is particularly useful for imaging dislocations. This is because under weak-beam conditions most of the crystallographic planes in the specimen are tilted away from the Bragg condition, but due to strain fields, the dislocation core satisfy the Bragg condition.

3.3.2.5 Phase contrast and Fresnel contrast

Phase contrast occurs when transmitted and diffracted waves with different phases emerge from a specimen. Such phase differences give rise to an interference pattern. By defocusing the electron beam (in combination with spherical aberration), phase contrast can be converted to amplitude contrast which, for example, allows the characterisation of several types of radiation damage defects in materials, in particular voids and bubbles (known as Fresnel contrast). A particular feature of phase-contrast imaging technique is that it can provide spatial resolutions on the order of 0.1 nanometre, therefore allowing the capture of high-resolution TEM (HRTEM) images so called lattice imaging [383].

3.3.2.6 Scanning Transmission Electron Microscopy

STEM is a mode of operation for a TEM. In the STEM operational mode, a focused electron beam is used to scan and raster over the specimen in similar way to a

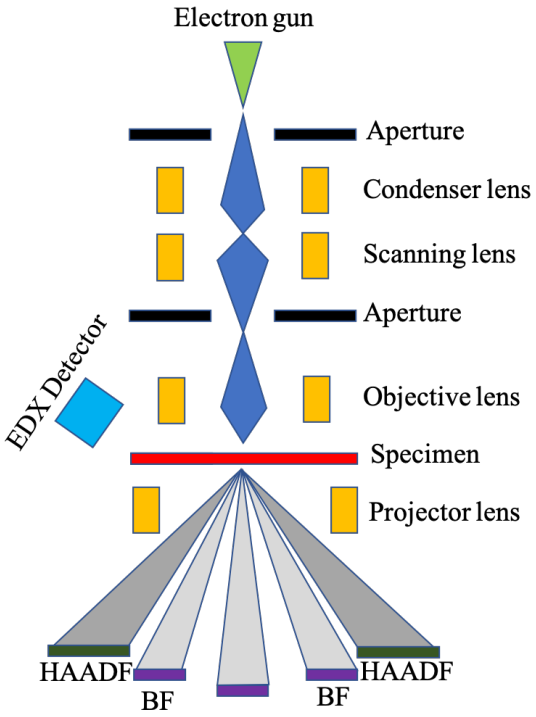

Figure 3.7: Typical ray diagram in STEM microscopes. (Adapted from [389].)

television-style pattern [384, 389]. A set of STEM detectors are inserted after the specimen to detect the transmitted electrons during the raster pattern. A typical ray diagram of STEMs is shown in figure 3.7. In this way, several different signals can be obtained from the specimen which are processed separately, such as X-rays, secondary and backscattered electrons.

STEMs are particularly useful within the context of analytical TEM characterisation. The emitted X-rays during the scan of the electron beam over the specimen can be acquired and used to compose an elemental chemical map (a fingerprint) of the sample if an EDX spectroscopy detector is used to collect such emitted X-rays. Similarly, electron energy loss spectroscopy (EELS) can be performed by means of a coupled EELS spectrometer with the STEM mode of operation. EDX mapping and EELS will be further discussed in the next section as they have been used for characterisation of radiation-induced damage effects in the samples during this work.

Another particularity of STEM operation is the ability of using incoherent elastic scattered electrons to form high-angle annular dark-field (HAADF) images. Also known as Z-contrast images, HAADF images may provide high resolution images of atom columns [384].

3.3.3 TEMs used for the work reported in this thesis

At the University of Huddersfield, a JEOL 3010 operating at 300 kV with a LaB_6 filament was used to carry out post-irradiation characterisation of samples. The two TEMs with *in situ* ion irradiation at the MIAMI facilities are a JEOL 2000FX operating at 200 kV with a W filament and a Hitachi H9500 operating at 300 keV with a LaB_6 filament. These were used to monitor in real-time the effects of ion irradiation on the materials used during the work reported in this thesis.

During the six-month internship period at the Oak Ridge National Laboratory, a JEOL 2100F high-resolution TEM operating at 200 keV with a Schottky Field-Emission Gun was used for post-irradiation characterisation. An FEI Talos STEM microscope with a FEG filament operating at 200 kV was used for analytical characterisation of irradiated samples.

In collaboration with the University of Limerick, a FEI Titan STEM/TEM microscope was used to produce HRTEM images as well as to analytically quantify some irradiated samples from MIAMI. In the results chapters, when appropriate, it will be specified which microscope was used to produce a certain set of results.

3.4 Ion irradiation *in situ* within a TEM

The technique of ion irradiation *in situ* within a transmission electron microscope was firstly reported in 1961 at the T.I. Research Laboratories in Hinxton Hall at Cambridge (UK) by Pashley, Presland and Menter [390]. They observed the formation of small black spots in BF images of Au and concluded that such defects were caused by the impact of negative ions which were not identified. Later, Parsons *et al.* investigated whether these ions were produced during oxidation of the W filament in the poorer vacuum conditions, indicating that these ions were probably O^- [391]. The surprising real-time observation of radiation-induced defects in a material led Pashley *et al.* to conclude that this technique could be of paramount importance for the field of nuclear materials and technology [392].

The experiments carried out by Pashley *et al.* were attributed to a faulty electron gun and did not result from the use of a dedicated instrument for *in situ* TEM with ion irradiation. The first TEM coupled with an ion accelerator was reported by Thackery, Nelson and Sansom at the Atomic Energy Research Establishment (AERE) at Harwell (UK) late in the 1960s. It consisted of a JEOL JEM-6A TEM operating at 100 kV coupled with an ion implanter with acceleration energies from 30 to 140 keV [392–394].

Although theoretically the technique itself is of low complexity, according to Hinks [392] in 2009, there were only 11 facilities around the world dedicated to ion

irradiation *in situ* within TEMs. Although, this class of experiments does not replace either *ex situ* ion irradiation techniques or neutron irradiations: the *in situ* monitoring of radiation effects in a TEM can provide new insights into the mechanisms of damage production, thus contributing to the understanding of the potential performance of many nuclear materials under irradiation and complementing the other techniques.

The University of Huddersfield currently hosts two *in situ* TEMs with ion accelerators: the MIAMI-1 and -2 facilities whose capabilities and operational details will be given in this section. In the current research, the *in situ* TEM ion irradiation technique was used to investigate the effects of energetic particle irradiation on high-entropy alloys, the AISI-348 steel, MAX phases and HEATFs.

3.4.1 MIAMI-1

The Microscope and Ion Accelerator for Materials Investigations, MIAMI-1, is one of a small number of facilities coupling an ion accelerator with a TEM. This allows the dynamic investigation of the microstructural evolution of different materials whilst being irradiated under many different conditions. The MIAMI-1 facility at Huddersfield is able to accelerate ions initially up to 10 keV with an addition acceleration stage up to 100 keV after a bending and mass-selecting magnet. Ion beam current measurements are carried out by means of skimming apertures along the ion beam line. The MIAMI-1 project started in March 2007 and some first experiments were conducted in 2009 by Hinks [393] in the research group of S.E. Donnelly.

3.4.1.1 Capabilities

The MIAMI-1 facility is capable of running a wide variety of inert gas ion beams routinely within the energy range from 2 to 100 keV with fluxes in the range from 10^{10} to 10^{14} ions·cm^{-2}·s^{-1}. The ion implanter is coupled with a JEOL JEM-2000FX TEM operating with energies between 80–200 keV with images and videos recorded using a Gatan Orius digital camera with 4 megapixels. The facility also has a set of different specimen holders including double-tilt with heating (up to 1273 K), single-tilt with heating (up to 1573 K), straining and cooling (to 100 K). Although a detailed description of the system was published elsewhere [393], the mechanisms that allow the *in situ* TEM with ion irradiation will be briefly described here.

3.4.1.2 Ion source

The generation of ions in MIAMI-1 is achieved by a Colutron G-2 ion source that is capable of extracting ions (singly-charged) with energies from 0.5 to 10 keV. Beam

deflectors and stigmators, an einzel lens and a Wien filter contribute to the first stage of beam alignment and optimisation.

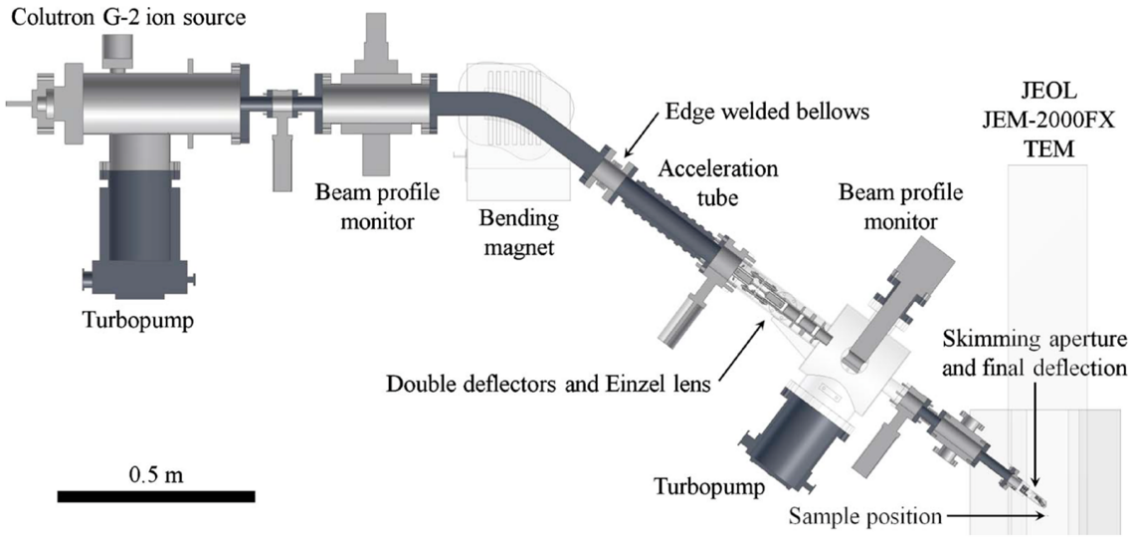

Figure 3.8: The MIAMI-1 facility schematics. (Reproduced from [393].)

3.4.1.3 Ion beam transport and monitoring

As the ion accelerator column is initially perpendicular to the TEM column, a bending magnet is used both to deflect the ion beam at an angle of 37° and to provide mass selection. After the generation of the ions at the source and acceleration towards the TEM, the beam is transported through a post-acceleration tube with the purpose of accelerating the ions further to yield an energy in the range of 10–100 keV. This post-acceleration tube is made of nine electrodes separated by ceramic spacers and connected to a resistor chain. After the acceleration tube an einzel lens and double deflectors serve to focus and accurately align the ion beam. The final stage consists of electrostatic deflectors (horizontal and vertical) for final alignment of the ion beam onto the sample position within the TEM. The overall schematic of the MIAMI-1 system is shown in figure 3.8 [393].

In order to monitor the ion beam from extraction to the final deflection stages, two National Electrostatic Corporation beam profile monitors are installed on main panel of MIAMI-1. These monitor the beam profile after the ion source and before the sample position.

3.4.1.4 Coupling within a TEM

In order to couple the ion accelerator with the JEOL JEM-2000FX TEM, a small modification in the standard microscope section was carried out between the condenser and objective systems as showed in the figure 3.9.

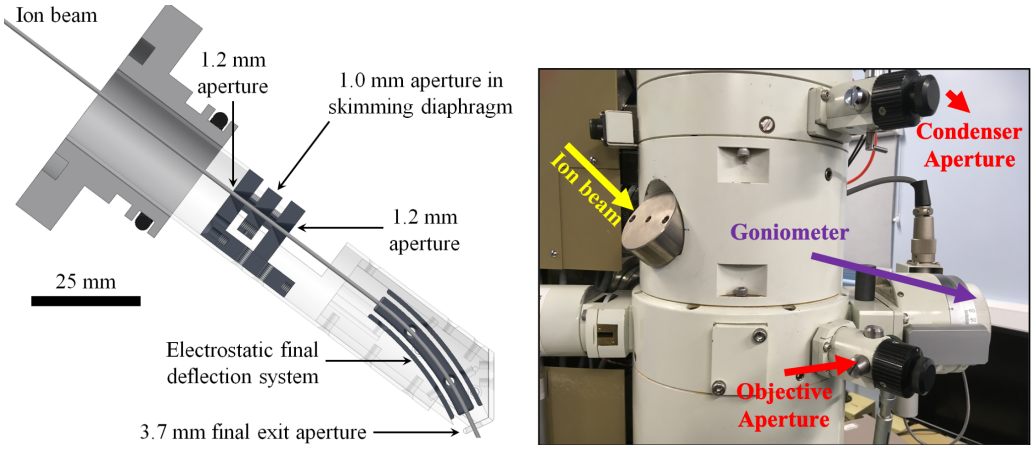

Figure 3.9: The MIAMI-1 final deflection system [393] (left) and the JEOL JEM 2000FX TEM.

3.4.1.5 Dosimetry

MIAMI-1 has a dosimetry system that allows precise and accurate current (ion flux) measurement at the specimen position. Before the final deflection system, a skimming diaphragm system is used to measure the ion beam current: a set of 1 and 1.2 mm apertures are placed in the skimming diaphragm in order to deliver a well-aligned ion beam to the final deflection system. The skimmers also allow fluctuations in ion beam current to be measured during ion irradiation experiments.

After the final deflection system, the current at the specimen position is measured using a current metering rod (CMR). The CMR is a device (resembling a specimen rod) that can measure both the electron and ion beam currents. Its design comprises metal plates with insulators in between. The measured currents are displayed using Keithley model 6485 picoammeters. With the measured values after stabilisation, current-to-flux conversion is performed based on previous calibrations: 1 nA corresponds to 4.8×10^{14} ions·cm^{-2}·s^{-1}. The CMR is a unique, in-house designed and developed dosimetry system.

3.4.2 MIAMI-2

The MIAMI-2 facility was commissioned in late 2016 and officially inaugurated in early 2018. It provides the possibility of irradiation at higher energies, *i.e.* from 5 to 350 keV, for most elements. The MIAMI-2 facility is installed over two floors as shown in figure 3.10. The first floor has the accelerator hall where the ion beam is produced and accelerated and a beamline hall for ion beam transport in the medium-energy ion beam line. On the ground floor, a second low-energy (second) ion beamline, the transmission electron microscope and the computer-control for the whole instrument (figure 3.10) are installed. The capabilities and detailed specifica-

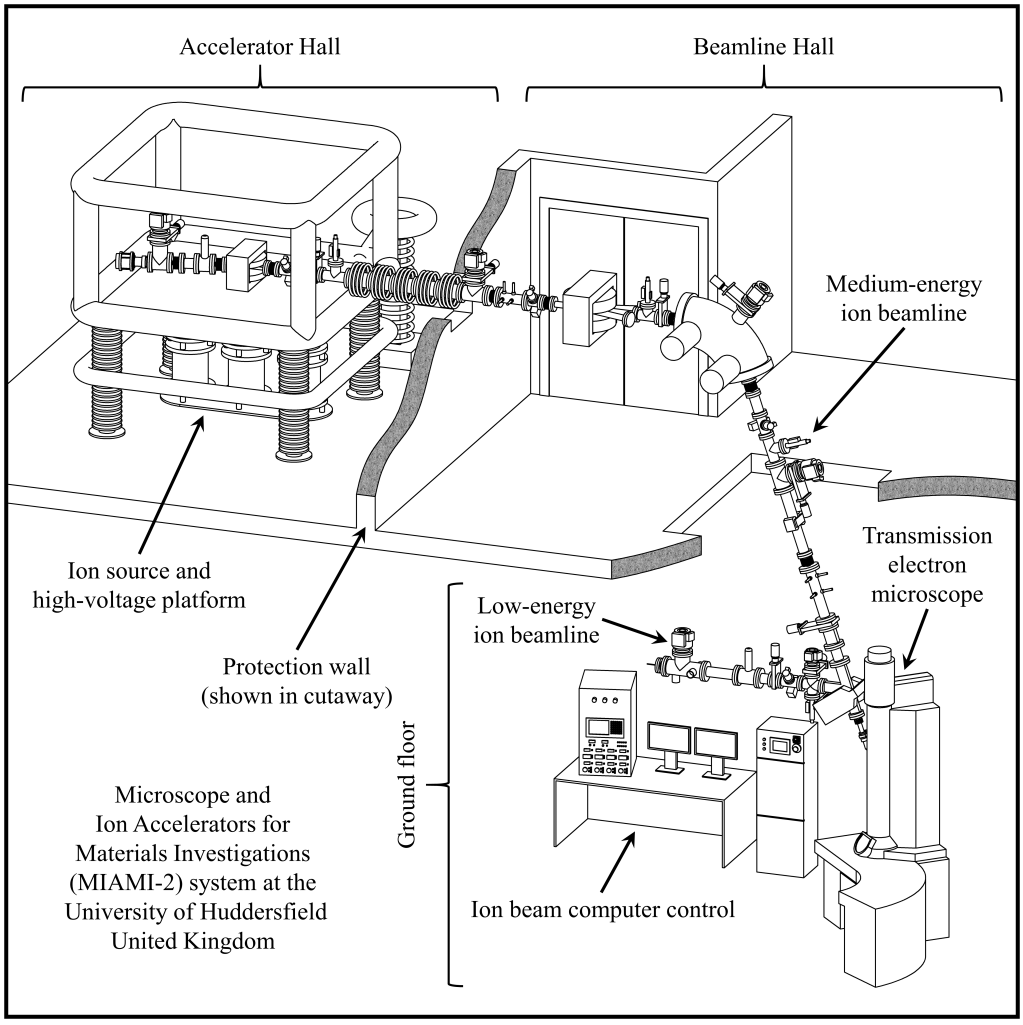

Figure 3.10: Overview of the MIAMI-2 facility. (Courtesy of Dr J.A. Hinks.)

tion of the MIAMI-2 facility will be described here.

3.4.2.1 Capabilities

The MIAMI-2 facility has two ion beams: a medium-energy ion beamline with acceleration voltages between 5 to 350 kV and the angle of the ion beam with respect to the electron beam within the TEM is 18.7°. The second is a low-energy ion beam line for H and He species with an energy range of 1 to 20 kV. The two ion beams are combined into the same trajectory before entering the TEM. This is a Hitachi H-9500 operating at energies between 60 to 300 keV and has a resolution of 0.14 nm with a LaB_6 filament. The microscope is equipped with a Gatan Model 1095 OneView camera with 4k resolution (*i.e.* 4096 x 4096 pixels) for imaging, a Gatan Model 693 GIF Quantum SE camera for energy-filtered TEM (EFTEM) with a resolution of 0.25 eV at zero loss and a Bruker Quantax 400 with XFlash 6T-60 energy-dispersive X-ray spectroscopy (EDX) detector. MIAMI-2 also has a wide range of sample holders which allow experiments at low and high temperatures as

well as double tilt and tomography holders.

3.4.2.2 Ion source

In the accelerator hall, a Danfysik 921A ion source operating at around 30 kV is used to produce the ion beam. This specific ion source allows the possibility of mounting a metal disk inside the discharge chamber in order to sputter metal atoms and produce ions from most metals. After the sputtering process, the atoms are ionised and mixed with the discharged plasma and therefore the extracted ion beam has a large proportion of metal ions [395].

3.4.2.3 Ion beam transport and monitoring

The medium-energy beamline includes an electromagnet and slit system before the acceleration stage that allow mass selection of the required species. The acceleration lens can provide potentials up to 320 kV and a Faraday cup is used to monitor the beam profile and current. Electrostatic quadrupole lenses are used at this stage for beam focusing. The next stage involves deflecting the ion beam through an angle of 71.3° towards the TEM where a second Faraday cup allows beam monitoring. Additional alignment and focusing of the ion beam at this stage is further provided by quadrupole lenses, and magnetic and electrostatic steerers. The low-energy beamline has a Colutron G-2 ion gun and its alignment, beam profile monitoring and optimisation is quite similar to those in MIAMI-1. The two beams are aligned prior to entering the TEM using a mixing magnet. The overall schematic of the MIAMI-2 facility are shown in figure 3.11.

3.4.2.4 Coupling within a TEM

Hitachi engineers added a new section into the TEM column to allow the coupling of the ion beams with the TEM as shown in figure 3.12. The mixed ion beams hit the specimen position at an angle of 18.7° with respect to the electron beam.

3.4.2.5 Dosimetry

The dosimetry in MIAMI-2 is performed with CMRs in a similar way to the MIAMI-1 facility. The current measured at the CMR can be converted to flux by using previous calibrations. For this case, 1 nA corresponds to 4×10^{14} ions·cm^{-2}·s^{-1}. For heavy ions such as Xe at 30 keV the fluxes are on the order of 3×10^{13} ions·cm^{-2}·s^{-1}. For lighter ions, such as 6 keV He, the flux can be on the order of 2×10^{14} ions·cm^{-2}·s^{-1}. Recently, successful dual-ion irradiation experiments have been carried out by mixing 10 keV He with 200 keV Kr ions.

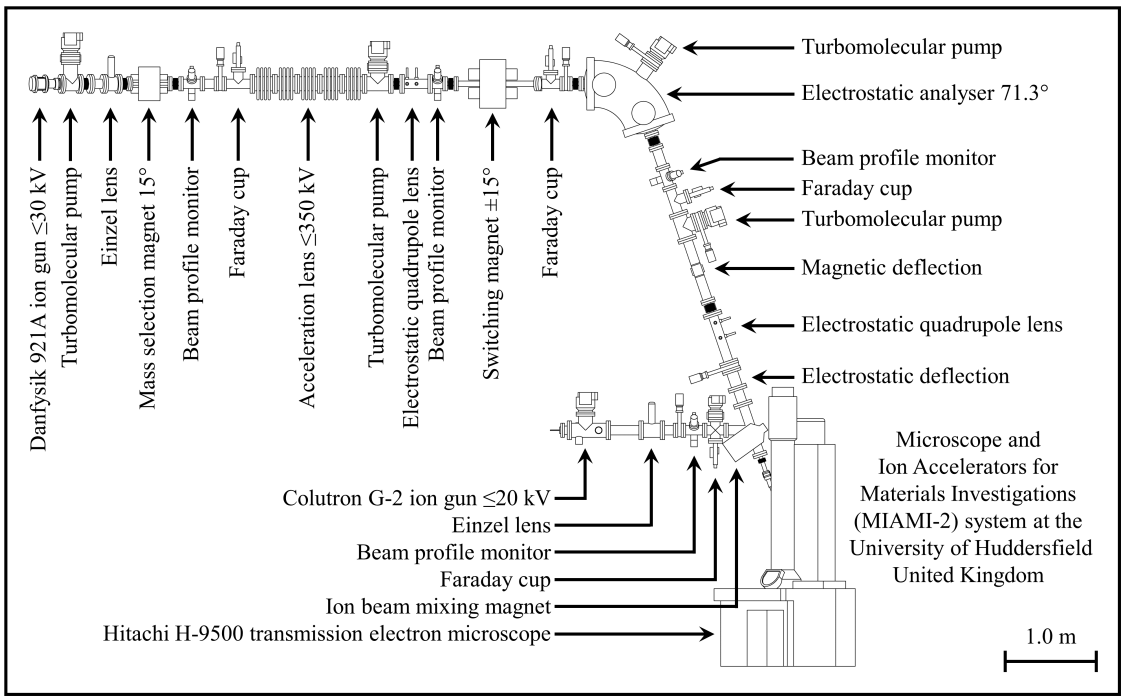

Figure 3.11: The MIAMI-2 facility schematics. (Courtesy of Dr. J.A. Hinks)

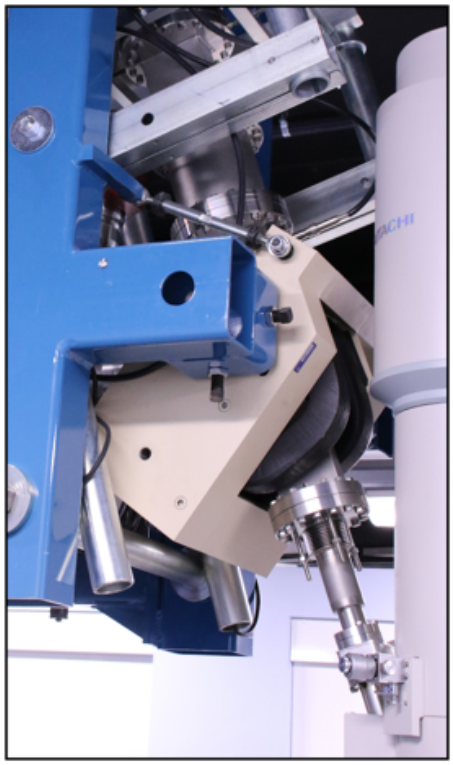

Figure 3.12: The mixing magnet and the beam section that allows the ion beam coupling with the microscope. (Courtesy of Dr. J.A. Hinks.)

3.4.3 Stopping and range of ions in matter

Prior to conducting ion irradiation experiments at the MIAMI facilities, calculations with the Stopping and Range of Ions in Matter (SRIM) Monte Carlo code are performed in order to estimate physical parameters such as implantation depth, and distribution of vacancies and interstitials. The SRIM Monte Carlo code is a standard software package widely used by the ion beam community. SRIM is benchmarked with real physical experiments [148]. It is based on a hard-sphere binary collision model which has been discussed in the section 2.2.1.1. The code is able to calculate a number of different parameters such as within the energy range from 10 eV to 2 GeV [145, 148].

The SRIM interface allows the user to change a set of variables, including the ion species, the ion energy, the incident angle, the target elements including multilayer structure, lattice energy, surface binding energy, number of ions and type of calculation. The code does not simulate the crystal structure of a material: it simply approximates binary collisions between impinging ions and target atoms at 0 K [148, 396]. The code also features several modes of calculations, however during this project, the "ion distribution and quick calculation of damage" mode has been used as it allows fluence-to-dpa conversion without overestimating the calculated vacancy concentration [140].

3.4.3.1 The Monte Carlo algorithm in SRIM

The SRIM code uses the Monte Carlo method which was developed in late 1930s by S. Ulam and N. Metropolis [153] and it consists of uniformly distributing the collisions along a random-walk flight path of incident energetic particles and estimating the recoiled atoms (*i.e.* the displaced target atoms) generated as a result of these collisions. By definition, if the transferred energy from the ion to the target atom is higher than its displacement energy (E_d), this target atom is displaced thus becoming a primary knock-on atom. For a first collision between an ion and a target atom, SRIM calculates an impact parameter to define whether displacement will occur. Glancing angle collisions are ignored. A PKA will be followed until it reaches an energy cut-off (E_f) that varies for each element in the periodic table (e.g. 2 eV for Si). For energies bellow the cut-off, the transported atom or ion will come to rest within the target layer. SRIM also calculates the number of vacancies, interstitials and replacement collisions. The latter occur when a vacancy is immediately annihilated by a displaced atom.

Aiming at improving the computational efficiency, the SRIM algorithm for the high energy regime (E >100 keV) is modified by the introduction of a free flight path parameter and the mean interatomic spacing parameter. In this case of high

energy ions, the collisions that do not generate displacements are ignored [148, 396].

3.4.3.2 Fluence-to-dpa conversion

Displacements-per-atom or dpa is a measure of the average number of times that a lattice atom is displaced from its equilibrium position. SRIM does not calculate and/or estimate the either flux of particles or fluence (flux integrated over time): these are experimental parameters from the ion irradiation experiments. However, SRIM calculates the number of generated vacancies per ion using the Kinchin-Pease model in the quick mode of calculation [160] which allows a direct conversion from experimental fluence to dpa. Recently, a standard procedure to convert fluence-to-dpa has been proposed by Stoller *et al.* aiming at comparing the dpa from neutron irradiation and ion irradiation experiments [140]. This procedure has been used for all experiments during the current research project. Additionally, throughout this thesis, the calculated dpa values are an average of the damage over the specimen thicknesses.

For fluence-to-dpa conversion based on Stoller *et al.* [140], "quick calculation of damage" mode of SRIM is used as it does not overestimate the number of generated vacancies. This procedure was developed based on recent results from detailed molecular dynamics calculations. The recipe is described as follows:

1. The displacement energy for each element of the target materials is selected from the ASTM E521 tabulation [139] where 40 eV is applicable for most metals.

2. The lattice and surface binding energies are set to zero.

3. The damage energy is calculated using the following equation, $T_d = E_i^P + E_T^P$, where E_i^P is the beam energy lost to the production of phonons and E_T^P is the target atom energy lost to phonons. This information can be found in the `PHONONS.txt` output file of SRIM.

4. Using the calculated T_d, the number of displacements (ν_{NRT}) is calculated using the Norgett-Robinson-Torrens (NRT) displacement model in which:

$$\nu_{NRT} = 0.8\frac{T_{dam}}{2E_d} \tag{3.11}$$

5. With the calculated number of displacements, the direct fluence (Φ) to dpa conversion is given by:

$$\Phi = \frac{\text{dpa} \cdot t \cdot N}{\nu_{NRT}} \tag{3.12}$$

Where t is the assumed (or measured) thickness of the sample and N the atomic density of the material. Throughout this thesis, the SRIM calculations as well as the conversion from fluence to dpa will be given at the beginning of each results chapter. For the calculations performed in this project, step 3 was found to produce on average the same number of vacancies per ion as the value exhibited in the "calculation parameters" section in the SRIM main graphical interface.

3.5 Neutron irradiations at the High Flux Isotope Reactor

In the research reported in this thesis in chapter 8, neutron irradiations of Ti-based MAX phases have been carried out in the HFIR at the Oak Ridge National Laboratory in the United States.

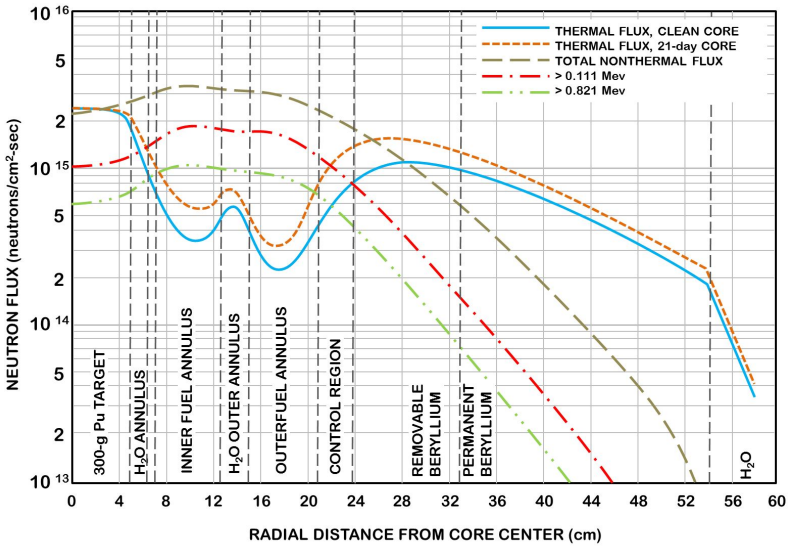

Figure 3.13: The profile of neutron fluxes at HFIR when the reactor core operates at 85 MW. Fluxes of the order of 10^{15} neutrons·cm^{-2}·s^{-1} can be achieved. Source: ORNL *apud* Wikipedia [397].

The HFIR is a nuclear research reactor that currently operates at 85 MW and is considered the highest neutron flux source for research available in the US [397]. The reactor went critical for the first time in 1965 and to date, it has been used as a multipurpose platform for scientific research in several areas of knowledge including condensed matter physics, materials science, nuclear fuels and nuclear fusion energy [REF]. The reactor also serves for radioisotope production for either medical imaging or cancer treatment [397].

HFIR is cooled and moderated with light-water and it uses highly enriched uranium-235 (at an enrichment level of 93%) as nuclear fuel [397]. Specifically,

the nuclear fuel is of cermet-type: U_3O_8-Al alloy 6061 [398–400]. When operating continuously at 85 MW, the average core lifetime (cycle) of HFIR is reported to be 23 days [397]. The reactor concept is based on beryllium reflectors that establishes a "flux trap" which consists of an annular region of nuclear fuel surrounding a moderating region with no nuclear fuel. At the centre of the non-fuelled region, a very high neutron flux can be achieved. Holes within the reflectors and at the peripheral positions of the core are used to either irradiate samples or for the production of radioisotopes [397–399]. A profile of neutron fluxes as a function of distance from the HFIRs core is shown in figure 3.13.

The irradiation capsules and sample holders for materials research are designed and operated by ORNL personnel who are also responsible for dosimetry calculations of dose rates and accumulated doses. In the research reported in this thesis, the Ti-based MAX phases were irradiated at the HFIR at 1273 K and at two different doses: 2 and 10 dpa calculated with the NRT model from their respective fluences, 2×10^{21} and 1×10^{22} n·cm^{-2}. Complete thermal histories during irradiation were not provided by ORNL. After irradiation in the HFIR, the samples are safely stored in radiation-shielded containers in order to wait for activity reduction. When the activity levels are sufficiently low, following ORNL internal protocols, samples are sent to the Low Activation Materials Design and Analysis (LAMDA) laboratory for post-irradiation analysis in "hot" electron microscopes (SEM, FIBs and TEMs) where the research with Ti-based MAX phases herein reported was performed.

3.6 Sample characterisation techniques

In combination with the major technique of ion irradiation *in situ* in a TEM, a set of analytical techniques has also been used in this project with the aim of better understanding radiation damage effects in the materials under investigation. This section will introduce these analytical techniques and describe how they were used for the purposes of post-irradiation characterisation. A typical example from the literature will be provided in order to illustrate the application of newer techniques, for example the multivariate statistical analysis in subsection 3.6.3.

3.6.1 Scanning Electron Microscopy

Instead of analysing the transmitted electrons through electron transparent specimens, an SEM generates images by scanning an electron beam over a sample and measuring non-transmitted electrons. As in the case of TEM, the physical interactions of the electron beam with the specimen generate a set of signals that can be used for both imaging and analytical characterisation (as shown in figure 3.14).

According to D. Joy, around 90% of the scientific literature on SEM and its applications lie in the imaging of surface topography as it is particularly useful for analysing the surface microstructure of materials with good accuracy at the mesoscale [401]. Surface topography analysis offers: detection of the presence of secondary phases, surface details (e.g. roughness, blisters etc.) and compositional variations on the different phases [402, 403]. In recent decades, due to with the introduction of FEGs with higher brightness (than W filaments) in SEMs has allowed the determination of crystallographic orientation of grains by means of analysing electron backscattering patterns: a technique known as EBSD. The information from EBSD patterns is represented by the three Euler angles that define a certain crystal orientation, thus resulting in the formation of an image which is a map of

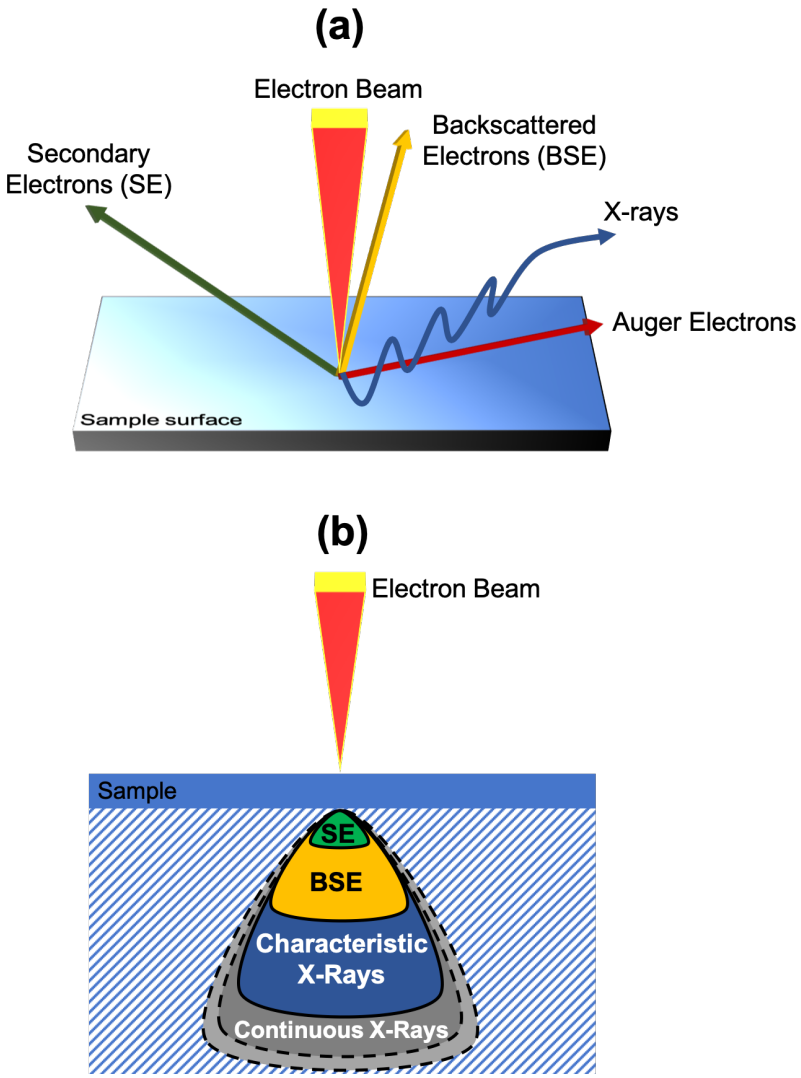

Figure 3.14: The several effects of the electron beam interaction with the specimen within a SEM is exhibited in (a) and (b) showing that the occurrence of these effects is a function of the electron beam depth of penetration, *i.e.* the energy of the incident beam and the material under analysis.

grain orientation. These maps have been used over the last century for several purposes including, for example, the study of texture in materials [404, 405].

A typical SEM operates with electron beam energies from 2 to 30 keV. Upon increasing the energy, the electron beam penetrates deeper in the sample. Higher electron beam energies are also associated with multiple scattering effects which may affect the overall quality of images in specific cases. Typical physical interactions of the electron beam with the specimen result in secondary electrons (SE), backscattered electrons (BSE), characteristic X-rays (photons), Auger electrons and cathodoluminescence (which is the emission of photons within the visible wavelength range). The emission of characteristic X-rays is particularly useful for elemental composition determination and will be more fully described in subsection 3.6.2. SE and BSE images are used for imaging purposes with the later being useful to distinguish between different elements within the material: backscattered electrons from heavier elements will appear with darker contrast [401, 404].

3.6.2 Energy dispersive X-ray spectroscopy

The EDX (or EDS) technique consists of analysing the X-rays which emerge from the sample due to the interaction with high energetic electron beams. The incident electrons can promote electrons from inner shells to another shell and when an electron from an outer shell decays, to fill the gap, an X-ray is emitted with an energy equivalent to the energy difference between the two levels [406].

An EDX system has four main components: (a) an excitation source which is the electron beam within a SEM or TEM, (b) the X-ray detector, (c) a pulse analyser processor and (d) the computer instrumentation for data processing. With the energy dispersive spectrometer coupled to a TEM or SEM, the number and the energy of X-rays emitted from such interactions can be recorded. The energy of the X-rays is the characteristic energy between the energy levels of an element and therefore, these EDX measurements give a detailed quantitative report of the sample's elemental composition.

Important protocols for EDX spectroscopy experiments are the mathematical methods for elemental quantification. These routines are incorporated into most EDX systems and are treated as standardless quantification methods in analysis. Among the wide variety of methods, the most common is known as ZAF: the letters Z, A and F stand for correction factors for the calculated concentrations based on their corresponding intensities of the peaks. The production (Z), absorption (A) and enhancement of the characteristic radiation (F) are thus taken in account within the EDX analysis [407].

In the work reported in this thesis, an FEI Quanta 300i SEM-FEG with a coupled

EDX detector from Oxford Instruments was used for the pre- and post-irradiation characterisation of the HEA and the AISI-348. The accuracy of this system is defined by the statistics of X-ray counts. For major alloying elements, the relative error is in the order of 1%. For minor elements, the minimum detectable amount is about 1000 appm in the composition. This SEM is located in the School of Applied Sciences at the University of Huddersfield. In addition, for the MAX phases imaging, a Tescan MIRA3 was used in the Low Activation Materials Development and Analysis laboratory (LAMDA) at Oak Ridge National Laboratory. Pre-calibration of the EDX detectors was carried out using stoichiometric SiC samples for C and pure Cu for metals.

3.6.2.1 EDX in MAX Phases

In order to perform EDX measurements in the Ti-based MAX phases investigated in this thesis, both Ti_3SiC_2 and Ti_2AlC samples were plasma cleaned in a Femto low-pressure plasma system (Diener GmbH) for 15 minutes prior insertion in the SEM. This was a necessary step aiming at reducing possible sources of C contamination on the specimens.

3.6.3 Multivariate statistical analysis

The advent of probe-forming analytical electron microscopes (AEM) operating field emission guns has allowed the acquisition of spectral EDX imaging with an average spatial resolution in the order of 1-2 nm [408]. These elemental maps can provide qualitative information on the distributions of elements in an electron-transparent sample, but such techniques are limited when quantitative information on possible different phases in a multicomponent system and the presence of minor elements in such phases are major concerns. Refinement of conventional analytical STEM-EDX methods has been recently revolutionised by using statistical methods that are capable of deconvolving spectral signals aiming at finding correlation between the distribution of elements over a wide variety of multicomponent alloy samples.

By using a statistical technique known as Principal Component Analysis (PCA), Watanabe *et al.* [409] demonstrated the viability of detecting minor elements with accuracy on the order of 1 wt.% when examining STEM-EDX imaging with spatial resolution around (less than) 5 nm. PCA algorithms in this context – a type of multivariate statistical analysis (or MVSA) – use orthogonal transformations in order to convert a series of possibly-correlated variables into linearly uncorrelated variables which are known as principal components [410, 411]. The application of PCA algorithms on STEM-EDX spectral images as shown by Watanabe *et al.* [409], demonstrated that STEM-EDX maps can be refined to reveal and identify

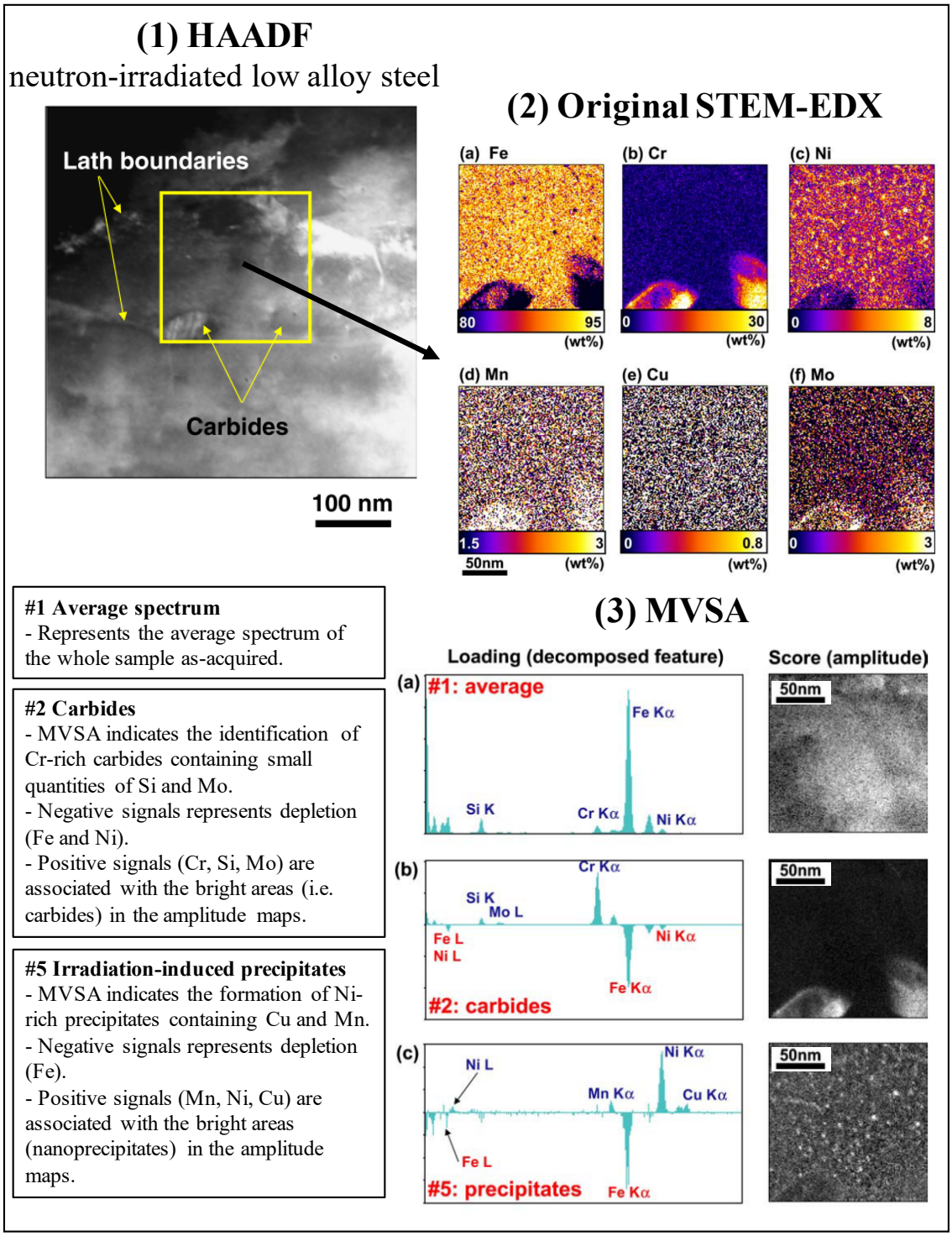

Figure 3.15: Demonstration of MVSA refinement of STEM-EDX maps acquired from a neutron-irradiated steel. Note: These figures are an adaption from a work authored by Burke, Watanabe, Williams and Hyde in 2006 [408].

any statistically significant features in complex alloys (such as nano-precipitation and the elements present in them) as well as reducing the noise arising from the measurements.

A typical example of the application of MVSA methods in a neutron-irradiated low alloy steel is shown in figure 3.15 that was adapted from a reference paper by Burke, Watanabe, Williams and Hyde in 2006 [408]. A HAADF micrograph of a region of interest (ROI) containing carbides is shown in the figure 3.15(1). A set of STEM-EDX maps were acquired from the ROI and as can be observed in figure 3.15(2): the images reveal the presence of nanometre-sized Ni precipitates, however, the Mn, Cu and Mo elemental maps do not indicate the presence of these elements within the nano-precipitates regions. The use of MVSA, figure 3.15(3a-3c) allowed the decomposition of the average EDX signal from the whole sample (figure 3.15(3a)) into the detection of two different phases: (figure 3.15(3b)) Cr-rich carbides containing Si and Mo, but depleted in Fe and Ni and (figure 3.15(3c)) Ni-rich precipitates containing Cu and Mn but depleted in Fe. The application of MVSA methods on STEM-EDX maps as demonstrated by Burke *et al.* [408] has shown that the irradiation-induced precipitates are not pure Ni (as initially indicated by the set of STEM-EDX maps in figure 3.15(2)), but also contain Cu and Mn. In addition, as observed in figure 3.15(3), the MVSA-EDX processed spectra can be use to plot an amplitude map which represents the different phases in the neutron-irradiated alloy.

MVSA has been used in the work reported in this thesis in order to provide more accurate quantification of STEM-EDX mapping of irradiation-assisted secondary phases observed to form in the AISI-348 steel. These results will be shown in chapter 6, subsection 6.2.2.4.

3.6.4 Electron energy loss spectroscopy

The interaction between the electron beam of a TEM with a specimen produces a broad electron energy distribution that can be used to extract useful physical and chemical information about the material studied. The electron beam in a TEM has a defined energy typically within the range of 60 to 300 keV. In this energy range, the electrons undergo a wide variety of interactions, but specifically the information on the their loss of energy in passing through the specimen can be used for the purposes of spectroscopy: EELS.

Three components are required to perform EELS: (a) source of electrons, (b) an electron transparent sample and (c) a magnetic spectrometer to analyse the energy of the scattered electrons.

The output of an EELS experiment is a spectrum of the transmitted signal in-

tensity as a function of energy losses for all electrons within the angular distribution limited by the entrance aperture to the spectrometer. A zero-loss peak (ZLP) is observed at $E = 0$ and represents those electrons which have passed through the specimen without losing energy (*i.e.* elastically scattered electrons or unscattered).

Inelastically scattered electrons are the remaining part of the spectrum: these have suffered a loss of energy due to their interactions with the sample. These interactions include phonon excitations, electron inter-band transitions, plasmon excitations (collective oscillations of electrons), inner shell ionisations and the emission of Cherenkov radiation. Particularly, the inner shell ionisations can be used to determine the elemental composition of the sample. Additionally, the integration of the low-loss region can quickly provide quantitative measurements of the thickness of a region.

During this work, a Gatan 666 PEELS system within a JEOL JEM-3010FX TEM was used. The EELS system is from Gatan and the full-width at half maximum (FWHM) of the ZLP recorded with this instrument is in the range of 2–4 eV. Additionally, the new EELS capabilities at MIAMI-2 with the Hitachi H-9500 TEM have also been used. For this latter case, a Gatan EELS system featuring a Gatan imaging filter (GIF) with a Quantum SE detector is coupled with the Hitachi TEM. The ZLP FWHM in this case is 2.2 eV.

3.6.4.1 Energy-Filtered Transmission Electron Microscopy

The information from EELS spectra can also be used to produce qualitative elemental maps in a similar way to EDX. EFTEM images are formed based on the specific electron energy loss in the area of analysis in an electron transparent specimen.

In order to carry out EFTEM, an EELS spectrometer is used. An energy slit filters a defined energy range that allows the detection of specific ionisation edges and the generation of qualitative elemental maps. EFTEM reported in this thesis used a GIF with a Quantum SE camera on the Hitachi H9500 TEM. This technique was also used to compare the results obtained with STEM-EDX analysis of irradiations of the AISI-348 and the thin films.

3.6.4.2 Thickness measurements using EELS and EFTEM

EELS and EFTEM were used to estimate the thicknesses of the samples prior to *in situ* ion irradiation within the TEM. In this technique, a ratio between the intensities of the zero-loss (I_0) and the inelastic scattered (I_t) electron beams is estimated from a sample region [412]. By estimating such a ratio, the thickness (t) of the TEM electron-transparent sample is related to the mean free path (λ) of electrons (at a specific energy) within a specific material:

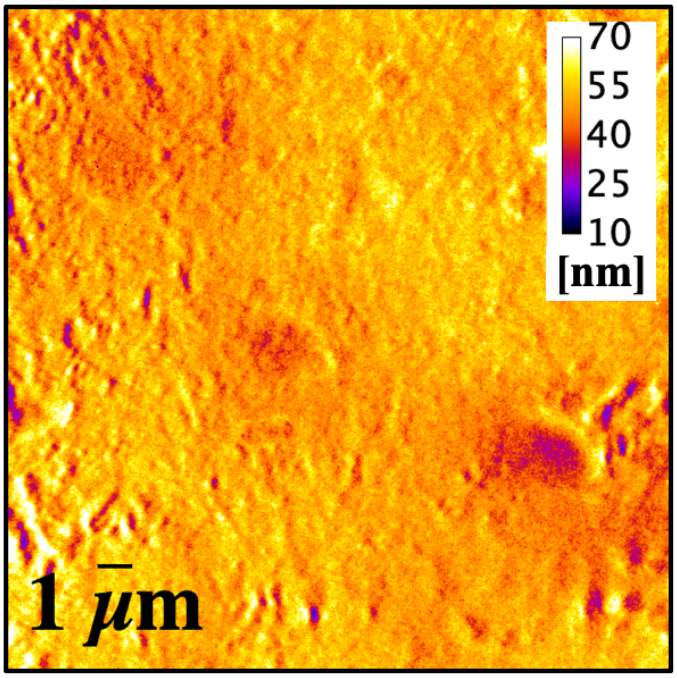

Figure 3.16: Thickness map obtained with a typical sample using the EFTEM capabilities in the Hitachi H-9500. The calibration bar (top right) exhibit the values for thickness in nanometres after conversion using equation 3.13.

$$\frac{t}{\lambda} = -\ln \frac{I_0}{I_t} \tag{3.13}$$

Using data available in the literature for the mean free path of 300 keV electrons into Fe (different values are reported in literature, but are in the range of $\lambda \approx$100–200 nm [413]) as an approximation, the thicknesses of the samples was estimated to be in the range of 60 to 120 nm. For the SRIM calculations, the thicknesses of the samples were measured to be $\approx$ 70 nm as the t/λ ratios were measured in the EFTEM to be around 0.5. When the samples were found to be thicker, additional thinning was performed. However, more accurate measurements of the mean free path in complex multicomponent alloys would be required in order to accurately estimate such thicknesses.

3.7 Thermodynamic calculations with CALPHAD

The CALPHAD method designate a series of procedures designed to calculate phase diagrams based on thermodynamic models. The CALPHAD methods include not only the software used for minimising the free energy of a set of phases described by thermodynamic models, but also to protocols on how to derive these models and how to obtain model parameters based on experimental data. In general a system is defined by the components included in the calculation, the model parameters

are read from published databases, and a dedicated software (e.g. Thermo-calc®) obtains the solution corresponding to the minimum of the free energy of a set of phases corresponding to a given set of thermodynamic state functions (T, P and so on) [414, 415].

In the research reported in the chapter 6, the CALPHAD method was used to calculate the equilibrium phase diagrams of the AISI-348 steel. For these thermodynamic calculations, the SGTE Solid Solution 2.0 database (SSOL2) was used. In order to model the multicomponent system of the AISI-348 steel, the elements Fe–C–Cr-Ni–Mn–Si–Nb were chosen along with the A1_FCC, A2_BCC, LIQUID, $M_{23}C_6$ and SIGMA phases. The first two phases are described with two sub-sets. In the first sub-set of the A1_FCC phase, the γ-Fe phase is represented by a highly defective interstitial sublattice whilst the second subset is an interstitial sublattice fully occupied with C, thus corresponding to the Nb carbides. With respect to the A2_BCC, the two sub-sets are represented by either the Fe-rich and the Cr-rich ferritic phases. For the thermodynamic modelling of the AISI-348 steel reported in this thesis, the composition of the steel as reported in subsection 4.2.2.3 was used.

Chapter 4

Pre-irradiation characterisation of the multicomponent alloys and the Ti-based MAX phases

4.1 Introduction

The austenitic stainless steel grade 348 and the high-entropy alloy investigated in this research project are part of the same multicomponent thermodynamic system: the quaternary alloy FeCrMnNi. In order to qualitatively and quantitatively explore the similarities and differences between these two alloys, a full characterisation study was carried out prior to irradiation at the MIAMI facilities. This characterisation methodology included conventional microstructural analysis and analytical quantification within electron microscopes (both SEM and TEM). The same methodology was also used to characterise the Ti-based MAX phases: Ti_3SiC_2 and the Ti_2AlC. A discussion of the results is presented and previously published data in the scientific literature is used to confirm and reflect on the results obtained.

4.2 Austenitic stainless steel: AISI-348

As discussed in section 2.1.1.1, stainless steels comprises a specific class of Fe-based alloys in which Cr and Ni are added into solid solution as major alloying elements. The word stainless refers to the capability of these alloys to resist stains that can be due to discolouration, loss of mass or corrosion [32]. The main reason why these alloys are resistant to stains is the formation of a superficial layer of oxides (known as passivation layer), thus protecting the bulk material from possible chemical and physical reactions with the environment. These steels are categorised according to the major alloying elements and crystal structure. The latter refers to the case where

Table 4.1: Nominal composition of the AISI-348 steel [359].

Element	**Composition [wt.%]**
Fe	Balance
Cr	17.00-19.00
Ni	9.00-13.00
Mn	2.00 (max)
C	0.08 (max)
P	0.045 (max)
S	0.030 (max)
Si	1.00 (max)
Ta	0.10 (max)
Nb	10×C (min)
Co	0.20 (max)

the stainless steel is austenitic (FCC), ferritic (BCC) or martensitic (BCC), or even a mixture of these phases. The AISI 300 series is the designation for austenitic stainless steels, often with Cr, Ni and Mn as major solutes.

Before commencing the irradiation experiments on the austenitic stainless steel 348, this material was characterised in its pristine (*i.e.* as-received) condition. Pieces of this steel were provided in collaboration with the University of São Paulo and were obtained from steel tubes redistributed by the FOPIL company [416], but manufactured by Sandvik. The AISI-348 steel was solution-annealed at 1313 K. Following the solution-annealing heat treatment, the AISI-348 steel was air-cooled (in the case of Nb-stabilised steels, according to Padilha *et al.* [417] water-quenching is not needed and air cooling is sufficient to avoid sensitization of the steel) and hot-rolled. Complete details of the thermo-mechanical history of this steel were not provided by the manufacturer and the nominal composition of this steel is shown in table 3.2.

The main reasons for selecting the AISI-348 are: (i) the high relevance of austenitic steels within the context of nuclear reactor technology, mainly in backbone fleet of the British Advanced Gas-cooled Reactors (AGRs) [418]; and (ii) the lack of data regarding the behaviour of the AISI-348 under energetic particle exposure [325]. Additionally, as the major constituents of this steel are Fe, Cr, Mn and Ni, a useful comparison on its radiation response with the FeCrMnNi quaternary HEA will be made. For all the experiments reported in this thesis, the AISI-348 steel samples were used as-received (referred as pristine throughout the thesis), *i.e.* neither further heat-treatment nor cold-working was performed.

4.2.1 Microstructural characterisation

In order to analyse the microstructure of the AISI-348, EJP was performed as described in section 3.2.1. This step was necessary both to reveal the grains in the alloy and to prepare electron-transparent samples for TEM. The microstructural analysis was performed at the mesoscale with SEM and at the nanoscale with TEM.

4.2.1.1 Scanning electron microscopy

At the mesoscale, the microstructure of the AISI-348 consists of equiaxed grains with sizes from 10 to 50 μm as shown in the backscattered electron (SEM-BSE) micrograph in figure 4.1(a).

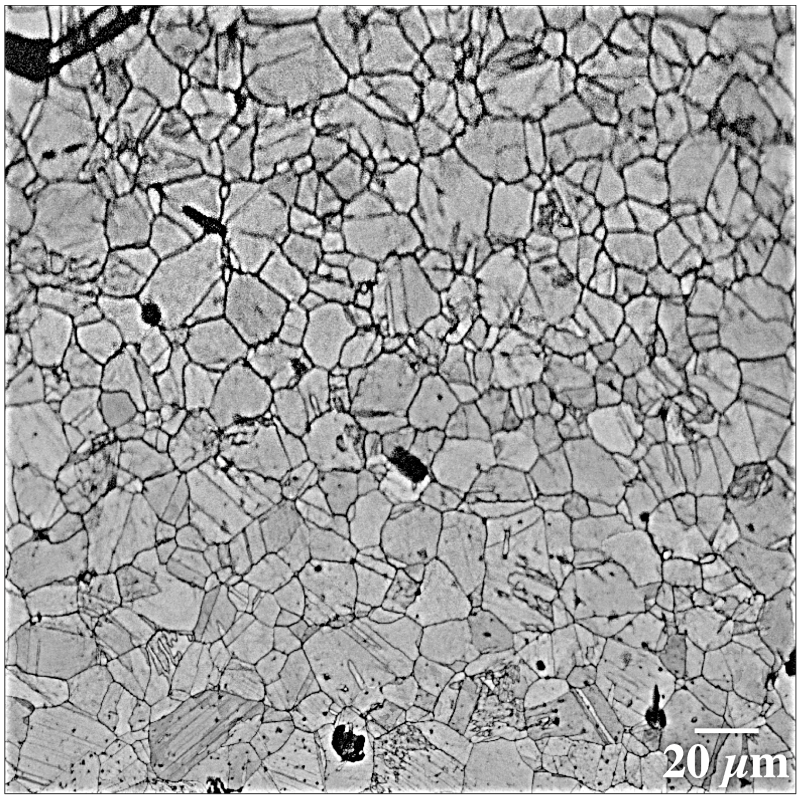

Figure 4.1: SEM-BSE micrograph of the AISI-348 steel microstructure as-received after electro-polishing.

The origin of equiaxed grains in austenitic stainless steels is attributed to dynamic recrystallisation processes during high temperature rolling at around 1273 K [419]. In addition, as dynamic recrystallisation encompasses the simultaneous nucleation and growth of austenite grains during the deformation at high temperatures, the matrix experiences a certain degree of grain refinement. Hot rolling is used by steel manufacturers as a commercial route for the production of flat steel and it also introduces some degree of work-hardening into these alloys [420].

Figure 4.1(a) shows that the AISI-348 is an austenite matrix free of precipitation.

This indicates that after hot rolling and recrystallisation, the stainless steel was cooled from high temperatures in a way that prevents substitutional atom diffusion: a required condition for precipitation [32, 421, 422]. An austenite matrix free of precipitates indicates that the austenitisation (*i.e.* the transformation of ferrite to austenite) is complete. For the AISI-300 austenitic steel series, such precipitates have been reported in the scientific literature to be $M_{23}C_6$ where M is a substitutional solute (*e.g.* either Cr or Mn). At the mesoscale and when the austenitisation is not complete, such precipitates are found as residual carbides along grain boundaries which may give rise to inter-granular stress corrosion cracking [32, 421, 422]. The black regions observed in the austenite matrix in figure 4.1(a) are holes/craters (pitting) as a consequence of the sample preparation method (electro-polishing).

4.2.1.2 Transmission electron microscopy

At the atomic scale, the AISI-348 steel contains some defects such as dislocations introduced by metalworking processes such as hot rolling. The BFTEM micrograph in figure 4.2(a) shows the austenite grains and a twin. Under- and over-focused micrographs, figures 4.2(b-c), reveal no sign of surface roughening or cavities in the pristine steel.

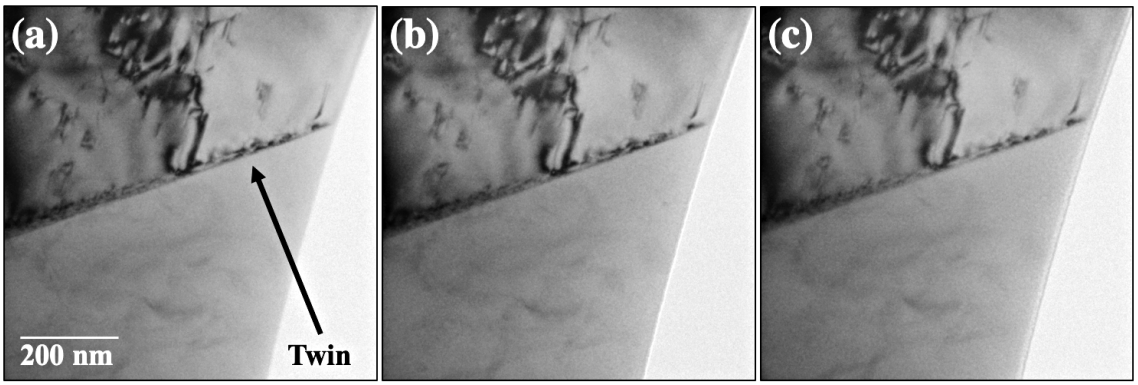

Figure 4.2: BFTEM micrographs of the AISI-348 showing a set of images (a) at focus, (b-c) under- and over-focused, respectively, with a defocus degree of ±1000 nm. Note: the scale marker in (a) also applies to (b) and (c).

A reduced number of twins are observed in the steel in its pristine condition after electropolishing and electron diffraction has been used for characterisation as shown in the micrographs 4.3(c)-(d). Twins can readily form in FCC matrices during heat treatment due to the low stacking fault formation energy which has a dependency on the local composition [32, 423]. These twins (known as annealing twins) arise from the thermo-mechacnial processing of the material and share the same crystallographic structure as the parent matrix (austenite): when using the SAED aperture and electron diffraction, satellite spots can be observed in the diffraction pattern

(figure 4.3(d)). Morphologically, annealing twins are indistinguishable from martensite plates, but the latter can be characterised with electron diffraction as it is of BCC structure. However, in this work martensite plates have not been detected in TEM specimens of the AISI-348 in a pristine condition after electro-polishing.

An important property of austenitic stainless steels is their superior corrosion resistance at higher temperatures compared with low-alloy or ferritic-martensitic steels. This can be achieved by the addition of small amounts of specific alloying elements such as Nb, W, Ta and V. Upon the incorporation of these minor alloying elements, there will be a tendency for the formation of carbides (and also carbonitrides) typically as rounded inclusions in the austenitic matrix [32, 39]. The removal of carbon from solid-solution is the mechanism behind the high corrosion resistance of the 300 series austenitic stainless steels.

Rounded nano-particles of Nb(C,N)[1] have been observed throughout the AISI-348 steel as shown in figure 4.3(a). In bright-field, the Nb(C,N) particles in the AISI-348 are of dark contrast and are often found in twinned regions or along the whole grain (trans-granular). These carbides may also have some Ta content as the chemical separation of Ta-Nb is often reported to be difficult to achieve in totality [424]. Nitrogen is another minor alloying element in 300-series steels which can be also incorporated into the Nb(C,N) structure and by this, sometimes these nano-particles are referred as Nb(C,N).

The mechanism for the nucleation of Nb(C,N) has been studied by Silcock *et al.* [425]. The rounded-shape is a result of the growth of pre-existing stacking faults due to climb of Frank partials followed by the continuous segregation (or incorporation) of Nb and C. A governing factor for the nucleation and growth of Nb(C,N) particles in austenitic stainless steels is, therefore, a matrix with a low stacking-fault energy.

The observation of Nb(C,N) particles also reveals some information about the synthesis of this austenitic stainless steel. The formation of Nb(C,N) in 300-series steels indicates that the material was subjected to high-temperature solution treatment at temperatures around 1473 K followed by rapid cooling to room temperature [32]. Rapid cooling is often necessary to avoid the formation of $M_{23}C_6$ precipitates (sensitisation) of the austenite matrix [32], although Padilha *et al.* commented that quenching is not needed in Nb-stabilised austenitic steels and only air-cooling is sufficient to prevent sensitisation. This is also consistent with the equiaxed grain microstructure as showed by the SEM-BSE micrograph in figure 4.1(a). Crystallographically, Nb(C,N) has an NaCl crystal structure which is FCC and may form and evolve within the stoichiometric range of $Nb(C,N)_{x-1}$ where x is higher than 0.6 %at [32]. Another important observation from the TEM screening is that the

[1]Sometimes, the Nb(C,N) are also referred in literature as simply NbC: throughout this thesis the Nb(C,N) terminology will be used.

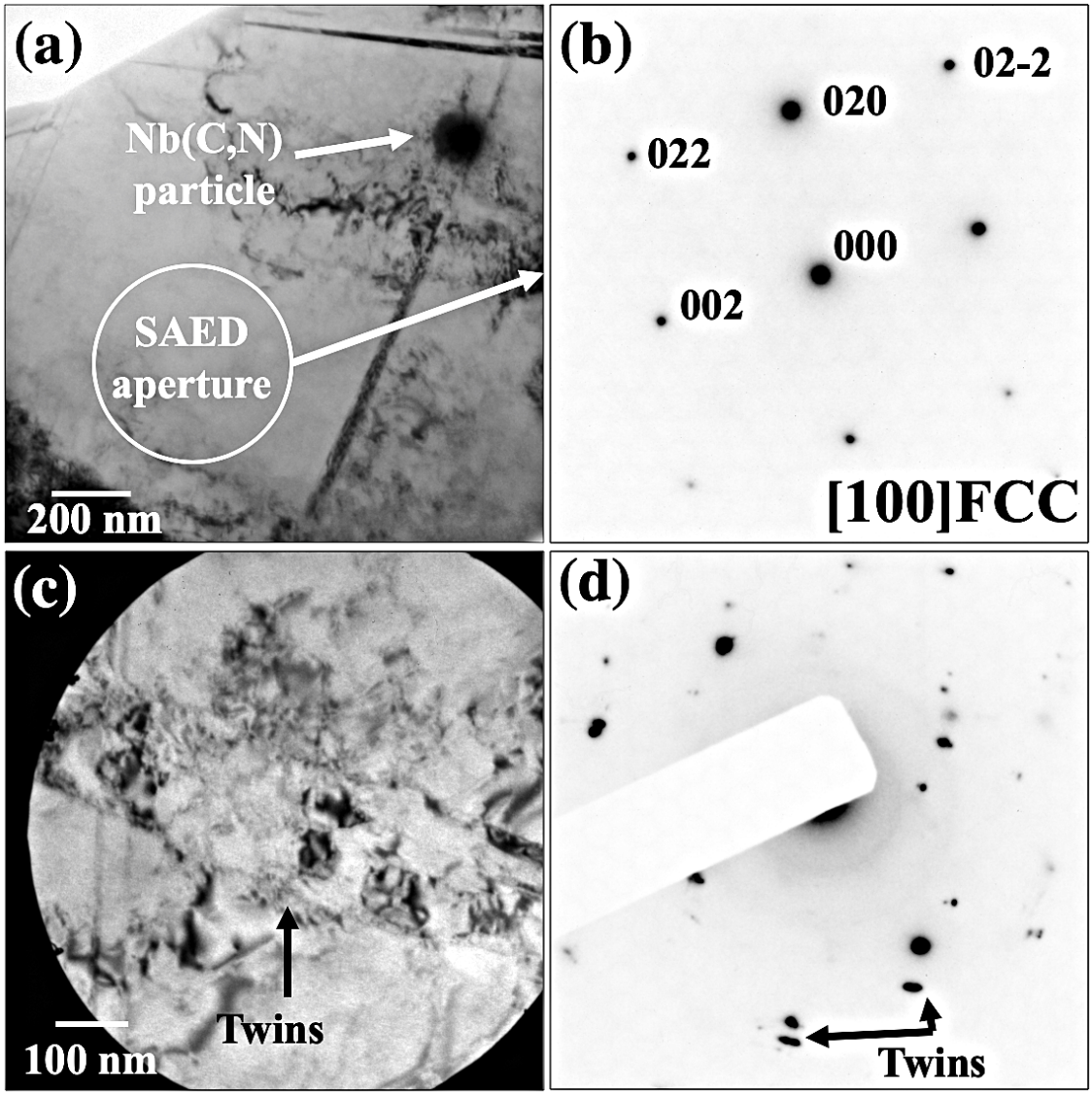

Figure 4.3: (a) The microstructure of the steel (and (b) its diffraction pattern) with a Nb(C,N) particle, (c) a BFTEM image with the selected-area aperture in and (d) the corresponding diffraction pattern of a region containing twins in the microstructure of the AISI-348 steel as-received.

austenite matrix was free of $M_{23}C_6$ precipitates.

The microstructural features identified by electron microscopy (both SEM and TEM) indicate that the AISI-348 was subjected to high temperature solution treatment with the purpose of stabilisation/normalisation of the austenite phase followed by hot rolling aiming at achieving a microstructure consisting of equiaxed grains.

4.2.2 Analytical characterisation

The electron microscopes have also been used to analytically characterise the AISI-348 samples. This section presents the results of EFTEM and STEM-EDX of the rounded-shape Nb(C,N) particles as well as determination of the elemental composition of the austenitic steel measured by EDX and compared with the quantitative analysis by Inductively Coupled Plasma Optical Emission Spectrometry (ICP-OES) provided by the steel manufacturer.

4.2.2.1 Qualitative characterisation of the Nb(C,N) nanoparticles using EFTEM

An electron transparent sample of the AISI-348 was used for elemental mapping of the austenite grains containing Nb(C,N) nanoparticles by means of EFTEM. Figure 4.4 shows both a BFTEM micrograph of the austenite with a Nb(C,N) particle and a set of elemental maps for Fe, Cr, Ni, Mn, Nb and C. It is clear that the blackround region, believed to be the Nb(C,N), indeed exhibits Nb enrichment and C build up (at the interface of the nanoparticle) whereas the other elements, around the nanoparticle region, are observed to be depleted. For the EFTEM analysis the following edges have been used: Fe L_3 =708 eV, Cr L_3 =575 eV, Ni L_3 =855 eV, Mn L_3=640 eV, C K=284 eV and Nb L_3 =2371 eV. N mapping exhibited no significant number of counts (very low signal-to-noise) and therefore was not included in figure 4.4. Therefore, identifying the presence of Nb with EFTEM confirms that the rounded particles are Nb nanoparticles.

In these measurements, C manifests only an enrichment around the particle and the signal–to–noise ratio in regions of the matrix is much reduced, but this can be explained by the fact that the AISI-348 is a low C steel, *i.e.* the content for this element in the alloy is expected to be lower than 0.1% by weight. The low C content in the alloy and the non-stoichiometric nature of the Nb(C,N) precipitates will limit the ability of EFTEM to accurately map the element C within the Nb precipitates. Nevertheless, the observed C build up at one side of the interface of the Nb particle is another indicative that in this alloy, the small addition of Nb contributes to the removal C from the austenite matrix: a requirement to improve the corrosion resistance in austenitic steels. Although the EFTEM mapping mode does not provide

quantification of the alloying elements, the signals from each element can be qualitatively related with their composition. In this way, the fractional composition of the austenite matrix is in the following order (from high to low): Fe > Cr > Ni > Mn.

4.2.2.2 Qualitative and quantitative characterisation of the Nb(C,N) nanoparticles using STEM-EDX

In order to further characterise the Nb(C,N) nanoparticles and to clarify the inconsistencies observed during the EFTEM analysis presented in subsection 4.2.2.1, *i.e.* the lack of signal for C and N around the Nb region, an experiment using the STEM-EDX capabilities of a FEI Talos F200X was performed in a pristine sample of the AISI-348 steel.

Figure 4.5 shows two micrographs acquired using the high-angle annular dark-field (HAADF) and the bright-field (BF-STEM) detectors along with a series of elemental maps (spectral images) acquired during 91 min of exposure. The major alloying elements of the AISI-348 steel – Fe, Cr, Mn and Ni – and also the minor alloying elements – Nb, C, N and Ta – were successfully detected. From the set of spectral images shown in figure 4.5, it can be noticed that the rounded Nb regions have an enrichment of C and N, thus confirming the presence of Nb(C,N) nanoparticles in the AISI-348 steel. The images also show a small content of Ta within the Nb(C,N) nanoparticle. Therefore, the data obtained using STEM-EDX elucidates the fact that the EFTEM technique (in the Hitachi H9500 in MIAMI-2) is not accurate in detecting elements such as C and N within the Nb(C,N) nanoparticles due to signal-to-noise issues. The longer exposure times during the STEM-EDX mapping and the high spatial resolution of the Thermo Fisher Talos S/TEM enables a more accurate identification of the Nb(C,N) nanoparticles.

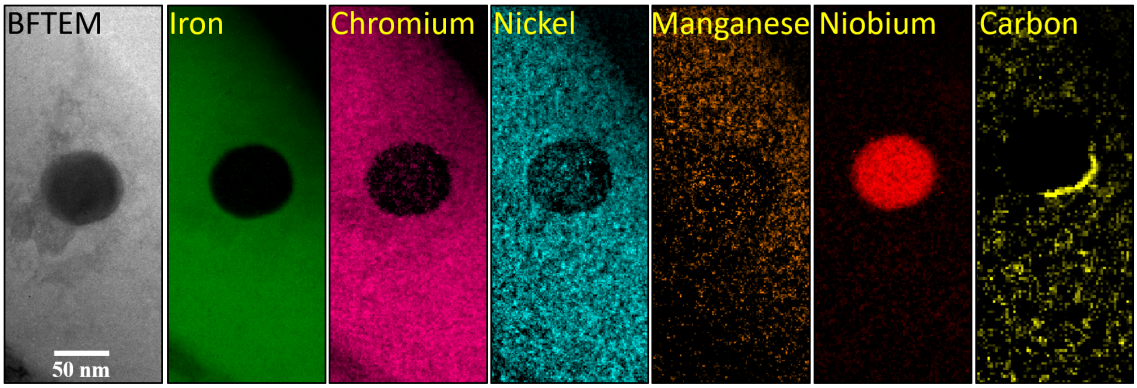

Figure 4.4: EFTEM analysis of the Nb(C,N) nanoparticles. Limitations of the EFTEM technique in the Hitachi H-9500 impair the detection of elements like C and N.

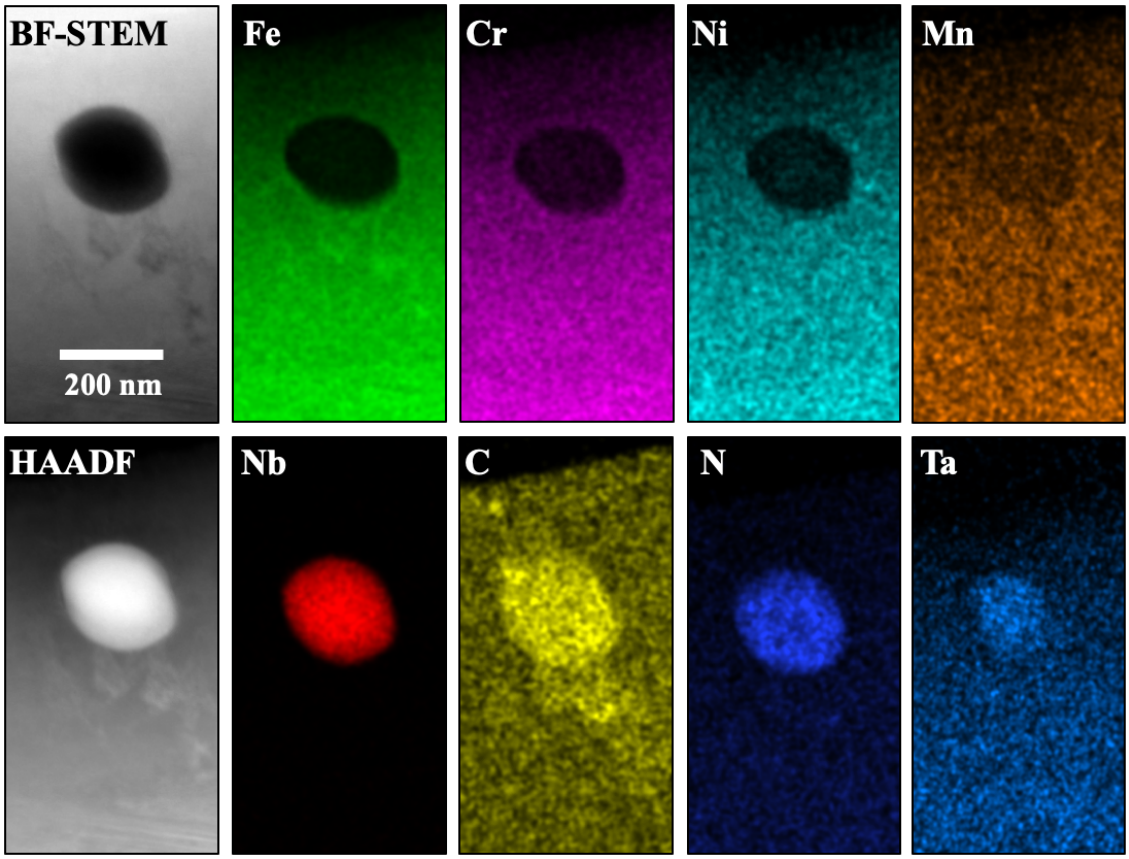

Figure 4.5: STEM-EDX analysis of the Nb(C,N) nanoparticles.

Table 4.2: The elemental composition of the Nb(C,N) nanoparticles measured using STEM-EDX.

Element	**Composition [at.%]**
C	32.9±5.2
N	20.8±5.3
Cr	1.5±0.3
Mn	0.08±0.02
Fe	3.9±0.8
Ni	0.34±0.07
Nb	40.4±8.2
Ta	0.08±0.2

By selecting the region around the Nb(C,N), it was possible to carry out an elemental quantification of the nanoparticle. For this, the Brown-Powell empirical ionization cross-section was used within the Thermo Fisher Velox software. Table 4.2 shows the atomic composition of the elements detected only around the Nb(C,N) nanoparticle characterised in figure 4.5. The low content of Fe, Cr, Mn and Ni is attributed to the matrix: as the experiment was carried out in an electron-transparent lamella, a small signal from the austenite matrix is detected in the same region of the Nb(C,N) nanoparticle. The atomic ratio between C and Nb was calculated to be 0.82 and it is in agreement with values reported previously in the literature [426–428], although these carbonitrides are considered highly non-stoichiometric.

4.2.2.3 Elemental composition of the alloy

SEM-EDX was used to quantify the elemental composition of the AISI-348. Using an electron beam of 30 keV energy, the EDX spectrum of the AISI-348 is shown in figure 4.6. Using the ZAF standardless quantification method [407] embedded in the INCA software from Oxford Instruments, the elemental composition of the AISI-348 was estimated as shown at table 4.3.

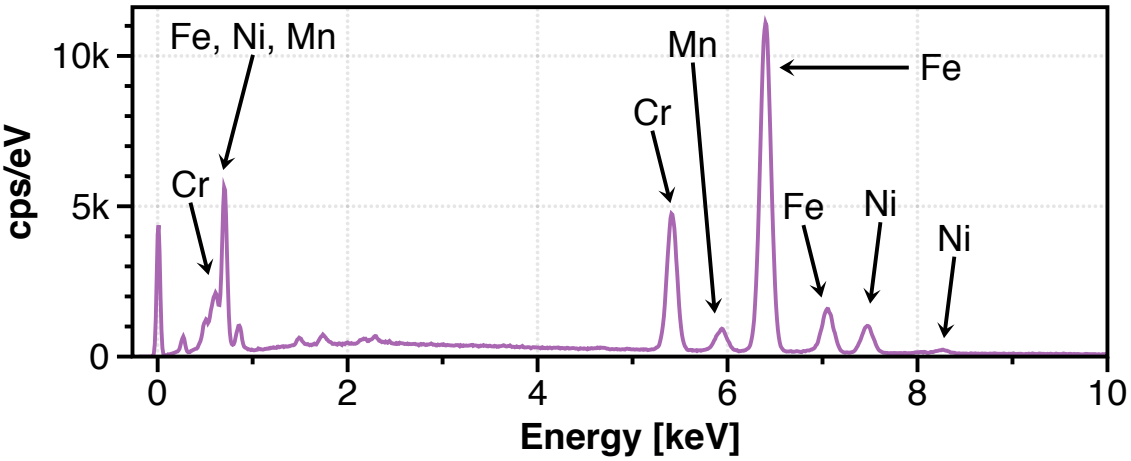

Figure 4.6: EDX spectrum of the AISI-348. The quantification is shown in table 4.3.

Table 4.3: The elemental composition of the austenitic stainless steel AISI-348 measured by SEM-EDX (the error is ±5% for each value).

Element	Composition [wt.%]
Fe	71.44
Cr	18.08
Ni	9.38
Mn	1.10

From table 4.3, the ZAF quantification shows that the AISI-348 is an Fe-based

alloy with Cr, Ni and Mn as major alloying elements. Elements like C and N have not been included in this quantification as EDX is known to be insensitive to light elements and thus inaccurate in its measurement of trace quantities. For comparison, the elemental composition of this steel as measured by the manufacturer using ICP-OES, is presented in table 4.4. Although the accuracy of ICP-OES elementally to quantify both the major and minor alloying elements in the steel is higher than that of EDX, both techniques are in good agreement within the error margins. The elemental quantification from EDX also agrees qualitatively with the EFTEM measurements presented in figure 4.4.

Table 4.4: The elemental composition of the austenitic stainless steel AISI-348 measured by ICP-OES (the error is ±1% for each value).

Element	**Composition [wt.%]**
C	0.037
S	<0.001
P	0.002
Ni	9.47
Si	0.36
Mn	1.81
Cr	17.50
Co	<0.001
B	<0.008
Ta	0.003
Nb	0.32
Fe	70.48

In terms of physical metallurgy of stainless steels, the AISI-348 is inserted in the class of iron-chromium-nickel (Fe-Cr-Ni) steels. The Fe-Cr binary system has a ferritic structure which is BCC. The retention of the FCC austenite at room temperature is guaranteed by the addition of Ni in a weight content higher than 8%. When Ni is added into Fe-Cr binary system, the austenite loop (known as γ-phase loop) is considerably expanded in the Fe-Cr phase diagram and the austenite phase will exist at room temperature. Small additions of manganese also contributes to the austenite phase formation and retention. Carbon is also an austenite former and it contributes to its stabilisation by acting as an interstitial strengthener [32, 39]. From the ICP-OES analysis the C content in the AISI-348 is as low as 0.037 in wt.%. Keeping the C content low in this steel is of paramount importance for its corrosion resistance and the Nb addition also contributes in removing the C from the austenite solid solution.

4.3 The FeCrMnNi quaternary high-entropy alloy

A FeCrMnNi high-entropy alloy produced by the technique of Plasma Arc Melting was received from Oak Ridge National Laboratory. After casting, the alloy was homogenised at 1473 K for approximately 48 hours. Cold rolling was used for strengthening and shaping the alloy as-cast that was subsequently subjected to heat treatment at 1173 K for 4 hours in a vacuum furnace [338]. The characterisation of FeCrMnNi HEA as received from ORNL has been performed using conventional and analytical electron microscopy techniques and this is described in the following sections.

4.3.1 Microstructural characterisation

In order to assess the microstructure of the FeCrMnNi high-entropy alloy, the material as received from ORNL was subjected to mechanical grinding using SiC papers from grit 180 to 1600. After grinding, the alloy was polished with diamond lapping films (down to a grit size of 1 μm). During polishing, diamond compound paste (fine grit with 2–4 μm of grit size) was also used as an abrasive. Due to the limited availability of the material, focused ion beam was used to produce TEM specimens.

4.3.1.1 Scanning electron microscopy

The microstructure of the FeCrMnNi high-entropy alloy is composed of equiaxed grains with sizes from 15 to 50 μm as shown in figure 4.7. The average grain size is around 35 μm as reported by the ORNL group that produced the alloy [338]. A single-phase microstructure can be observed and some annealing twins are visible within some grains (small transgranular lines/planes).

The black regions observed in the figure 4.7 are holes probably introduced during the polishing. If these were precipitates, after mechanical grinding and polishing, they would have the same z-topography as the matrix and under these imaging conditions, these would not be imaged as black features with white fringes. An equiaxed microstructure is characteristic of a heat-treated material (as mentioned in section 4.2.1.1 in the case of austenitic stainless steels) and it is also an indication that recrystallisation has occurred as expected.

4.3.1.2 Transmission electron microscopy

At the nanoscale, the FeCrMnNi high-entropy alloy exhibited large annealing twins that were characterised by selected-area diffraction as shown in figure 4.8(a–d). Under and over-focused micrographs in figure 4.8 show no voids or surface roughening

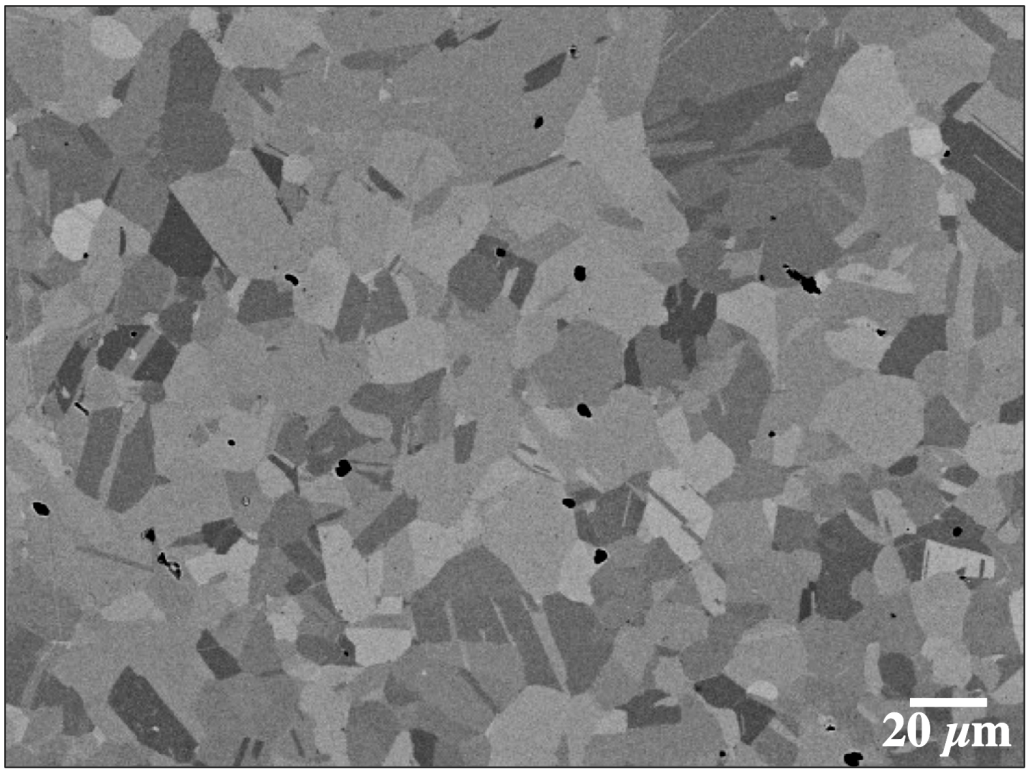

Figure 4.7: SEM-BSE micrograph of the FeCrMnNi HEA after synthesis and heat treatment. Courtesy of Professor Steve J. Zinkle (UT/ORNL) [338].

in the pristine material. When the SAED aperture is placed in areas without the annealing twins, the diffraction pattern does not exhibit the satellite spots as can be seen in micrographs 4.8(f–g). Therefore, such twins follow the FCC structure of the parent phase, *i.e.* the HEA matrix. Dislocation lines, characteristic of heat treated and mechanically deformed microstructures, are shown in the figure 4.8(e).

TEM thus reveals that the FeCrMnNi HEA consists of a single-phase FCC structure with annealing twins. The microstructure was free of any form of precipitation and/or secondary phases. The presence of large annealing twins also indicates that this quaternary thermodynamic system has a low energy for stacking fault formation [423]. The absence of precipitation indicates that all the alloying elements were in solid solution in a single phase microstructure as expected according to current understanding of highly concentrated alloys [55].

4.3.2 Analytical characterisation

4.3.2.1 Elemental composition of the alloy

Energy dispersive X-ray spectroscopy was used to characterise the alloy as received from ORNL. The spectrum in the figure 4.9 presents an average of data from five different areas of the FeCrMnNi HEA. The curves were acquired using the point and area analyser routines in the software INCA from Oxford Instruments.

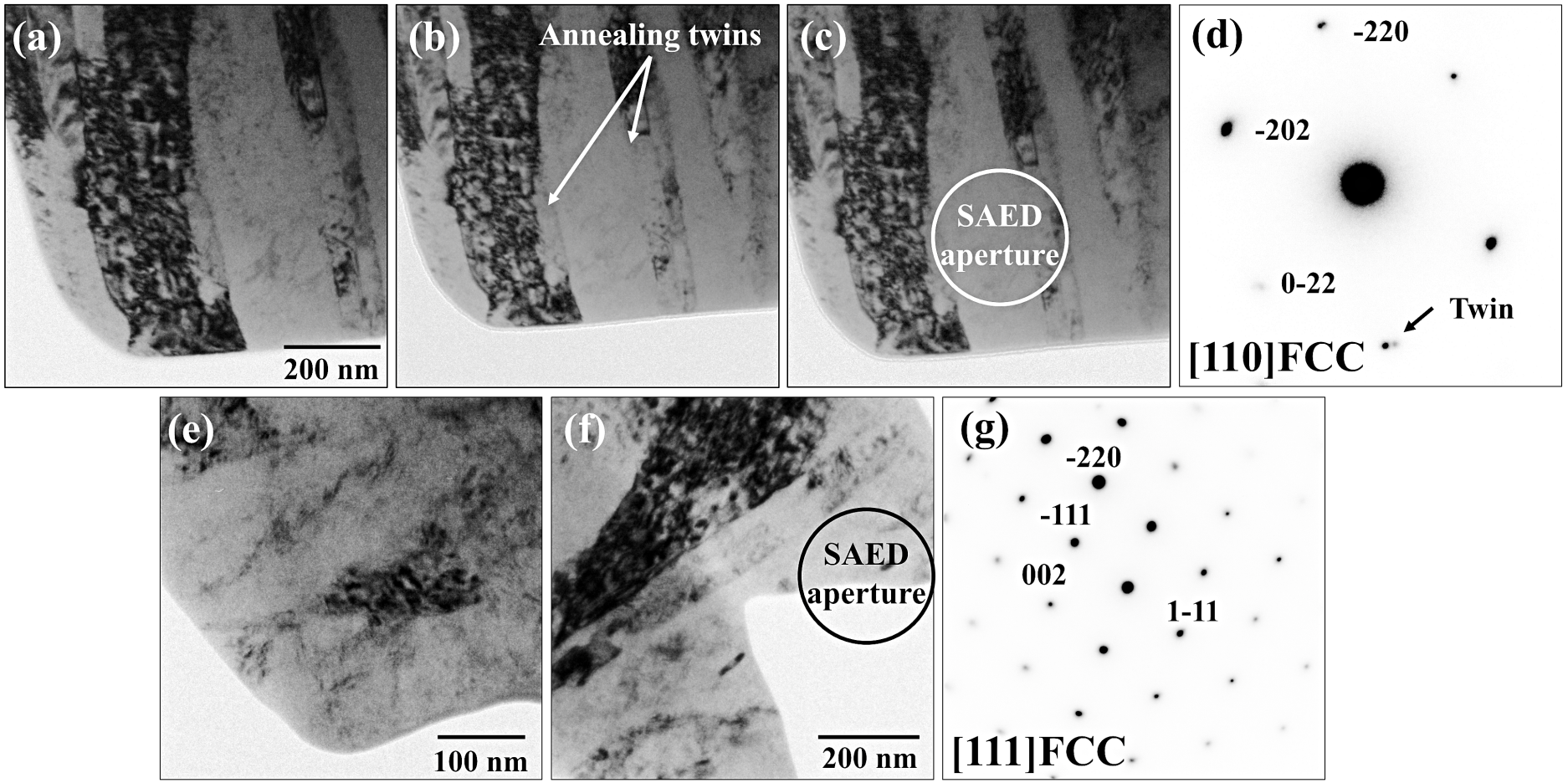

Figure 4.8: BFTEM micrographs of the FeCrMnNi HEA showing (a–c) a set of images taken at, under- and over-focus, respectively. The defocus (b) and (c) was 800 nm. The diffraction pattern (d) corresponds to the region selected by the SAED aperture indicated in (c). The BFTEM micrograph (e) shows part of the matrix free of annealing twins. The figure in (f) shows that when the matrix is selected without twins, the DP (g) does not exhibit satellite spots. Note: the scale marker in (a) also applies to (b) and (c).

From the spectrum in figure 4.9 and using a quantification algorithm (based on the ZAF method) embedded in the INCA software, the elemental composition of the alloy was estimated and this is shown in table 4.5 with an error of ±5% on each value.

Table 4.5: The elemental composition of the FeCrMnNi HEA measured by SEM-EDX (the error is ±5% for each value).

Element	**Composition [wt.%]**
Fe	26.8±1.3
Cr	18.40±0.9
Ni	27.50±1.4
Mn	27.30±1.4

High-entropy alloys should contain elements in near equiatomic proportions which poses a practical challenge for a metallurgist. Regarding the FeCrMnNi HEA, exploratory studies at Oak Ridge National Laboratory have indicated that when the alloy was synthesised precisely at the equiatomic condition, it was not a single phase product [338], thus violating the main tenet of HEA theory, *i.e.* a highly concentrated alloy at (or close to) equimolar composition should be a single-phase random solid solution. This problem was overcome by slightly decreasing the Cr content in the quaternary system and for this reason, the composition seen in table 4.5 shows that Cr is a little depleted compared to the other elements.

4.4 The Ti-based MAX phases

The radiation resistance of two Ti-based MAX phases was studied in this work: Ti_2AlC (a) and Ti_3SiC_2. Both materials were provided by Oak Ridge National

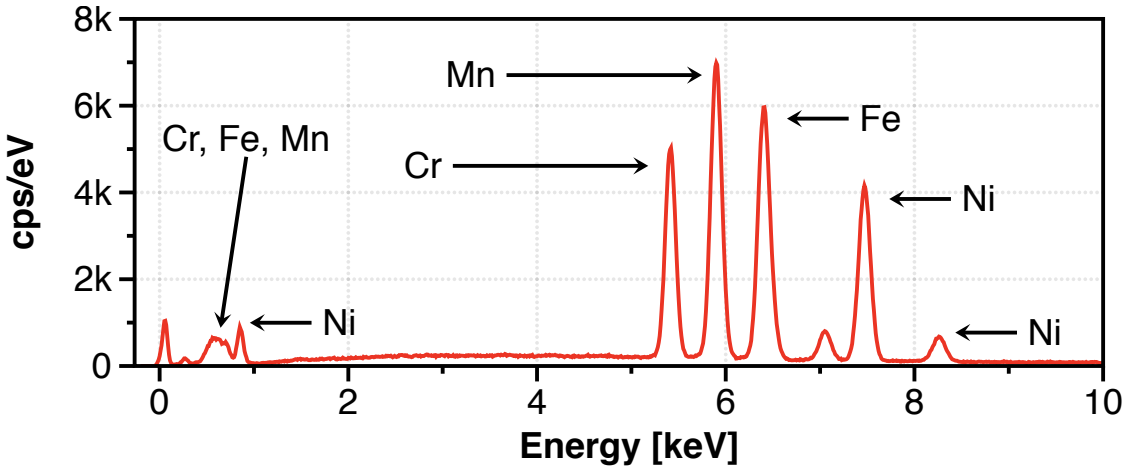

Figure 4.9: EDX spectrum of the FeCrMnNi HEA. The quantification is shown in table 4.5.

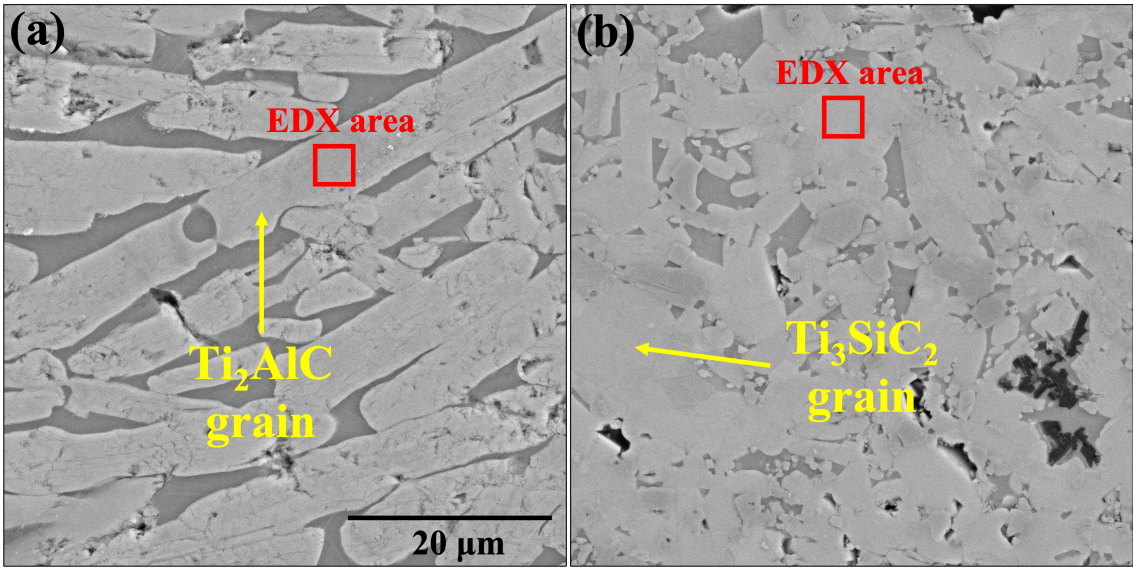

Figure 4.10: The microstructures of the Ti_2AlC (a) and the Ti_3SiC_2 (b) at the microscale. The red squares indicate the area where the EDX analyses (section 4.4.2) have been carried out. Note: the scale marker in (a) also applies to (b).

Laboratory, but synthesised by the Philadelphia-based company 3-ONE-2. The method used for the production of these MAX phases was reactive hot pressing as described in section 3.1.3. As in the case of the austenitic stainless steel AISI-348 and the FeCrMnNi HEA, the MAX phases were also characterised by conventional and analytical electron microscopy techniques.

4.4.1 Microstructural characterisation

Samples were mechanically ground with SiC sheets with grits from 180 to 1600 and subsequent polished with diamond lapping films (down to a grit size of 1 μm) and a compound diamond paste solution as an abrasive. Following this process, the surface of the samples were mirror-like. Both transmission and scanning electron microscopy were used to assess the microstructure at the micro and nanoscales. Electron-transparent lamellae for TEM were produced used the FIB technique. Analytical characterisation was performed in a SEM with an EDX detector.

4.4.1.1 Scanning electron microscopy

The microstructures at the microscale of the Ti_2AlC (a) and the Ti_3SiC_2 MAX phases are shown in figures 4.10(a) and 4.10(b), respectively. Both Ti_2AlC and Ti_3SiC_2 exhibit a grain structure with lamellar or lath-shaped grains, *i.e.* preferentially elongated in one direction. By analysing the microstructure of the Ti_3SiC_2, the grains appear to be bigger than in the Ti_2AlC case.

Another important aspect of the Ti-based MAX phases microstructures was re-

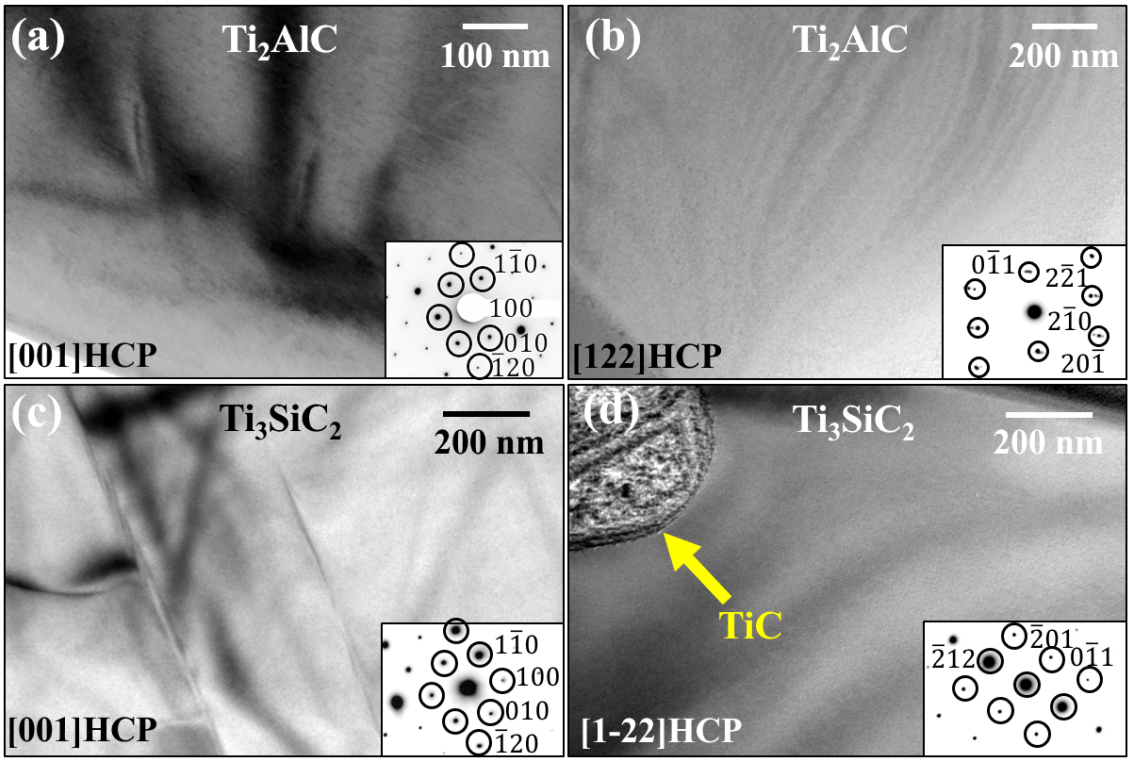

Figure 4.11: The microstructure of both Ti-based $M_{n+1}AX_n$ at the nanoscale. Micrographs (a) and (b) show the Ti_2AlC while (c) and (d) show the Ti_3SiC_2.

vealed through the contrast of the backscattered electrons in the SEM. In both micrographs in figure 4.10, the presence of two different phases is clearly seen: a lighter grey which are the MAX phase grains and a dark grey phase. The identification of both phases will be given in the analytical characterisation section 4.4.2; however the electron-transparent lamellae prepared in this research from these bulk materials were always lifted-out from the lighter grey grains corresponding to the MAX phase regions.

4.4.1.2 Transmission electron microscopy

At the nano scale, the microstructure of the Ti_2AlC (a) and the Ti_3SiC_2 consisted of large grains without noticeable defects such as dislocation loops and voids as shown in figure 4.11(a–d). Both MAX phases were characterised as having a hexagonal HCP crystal structure by indexing the diffraction patterns inset in figure 4.11 with data available in the literature [429, 430]. Figure 4.11 presents micrographs recorded with the electron beam along the basal direction (4.11a and c) and other zone axes (4.11d–e).

As shown in figure 4.11(d), the Ti_3SiC_2 included secondary particles which have been previously reported to be TiC (when the particle has a rounded shape) or SiC (when the particle has an angular shape) [431]. The formation of such inclusions was

associated with sample preparation methods by Morgiel *et al.* [431], although the existence of TiC and SiC compounds in the phase diagrams of the ternary system Ti–Si–C indicate that these phases can be formed by diffusional mechanisms during reactive hot pressing at high temperatures [432–434].

TiC and SiC inclusions in conventional ceramics are associated with the occurrence of microcracks in their boundaries with the matrix phase. This is for two main reasons: (i) an increase in the internal stresses within the matrix promoted by the thermal or elastic expansion of the secondary particles and (ii) the accumulation of defects along their grain boundaries. The microcracks are thus a result of the reduced ductility (high hardness) of the ceramic matrix phase [435, 436].

In this work no microcracks were observed for the inclusions present in the Ti_3SiC_2. This can be explained by the fact that the MAX phases have lower hardness compared to conventional ceramics and as reported extensively in the scientific literature as described in section 2.1.2.1.4.

4.4.2 Analytical characterisation

The analytical characterisation of both Ti-based MAX phases has been carried out using EDX within the SEM. The major aims were: (i) to quantify the elemental composition of the MAX phases by analysing the light grey grains as identified in figure 4.10(a) and 4.10(b); and (ii) to quantify the elemental composition of the matrix phase by analysing the dark grey grains in the same electron micrographs.

4.4.2.1 Elemental composition of the Ti-based MAX phases

The EDX spectra of the Ti_3SiC2 and the Ti_2AlC MAX phases are shown in figure 4.12. The areas in both MAX phases where the spectra were recorded are indicated by red squares in figures 4.10(a) and 4.10(b). By means of the Cliff-Lorimer quantification method within the AZTec software, the elemental composition of the two MAX phases is presented in tables 4.6 and 4.7.

Table 4.6: The elemental composition of the Ti_2AlC measured by SEM-EDX (error is 5% of each value).

Element	**Measured [wt.%]**	**Expected [wt.%]**	**Measured [at.%]**	**Expected [at.%]**
Ti	70.3	71.0	45.6	50.0
Al	15.6	20.0	18.0	25.0
C	14.0	9.0	36.3	25.0

The major difference in the EDX spectra from the two MAX phases is the differentiation of the Al ($K\alpha = 1.49$ keV) and Si ($K\alpha = 1.74$ keV) peaks as expected. Both spectra are overlapping apart from in the regions where the Al and Si peaks were detected.

Table 4.7: The elemental composition of the Ti_3SiC_2 measured by SEM-EDX (error is 5% of each value).

Element	Measured [wt.%]	Expected [wt.%]	Measured [at.%]	Expected [at.%]
Ti	69.8	73.5	43.1	50.0
Si	12.4	14.3	13.1	17.0
C	17.8	12.2	43.8	33.0

Regarding the elemental composition quantification for both materials, the observed deviations from an ideal elemental composition of 321 and 211 MAX phases can be attributed to the limitations of the EDX technique: mainly in correctly identifying and quantifying the element C. The quantitative estimation of C may include a systematic error strongly influenced by the presence of impurities and carbonaceous contaminants, for example, the vacuum chamber and walls of the scanning electron microscope and in the surface of the sample (hydrocarbons). Additionally, the electron beam in the SEM can induce the deposition of C on the surfaces of the MAX phases, thus strongly affecting the quantification of the results [437]. Therefore, this present EDX analysis showed that the C detection in both MAX phases is overestimated (by around of 12 at.%).

However, when the element C is removed from the quantification algorithm within the SEM-EDX software, for example, the atomic percentages of the Ti and Al in the Ti_2AlC are estimated to be 64.55 and 35.45 ($\approx$*i.e.* 2:1 with an error of $\pm$ 3%), respectively. The same was observed in the Ti_3SiC_2 where the percentages of Ti and Si were estimated to be 74.30 and 25.70 ($\approx$*i.e.* 3:1 with an error of $\pm$ 10%), respectively. The analytical characterisation of MAX phases by the measuring the ratio between the metal and its "A" element is often reported in the literature as the analytical characterisation procedure for such ternary carbides [438]. As commented

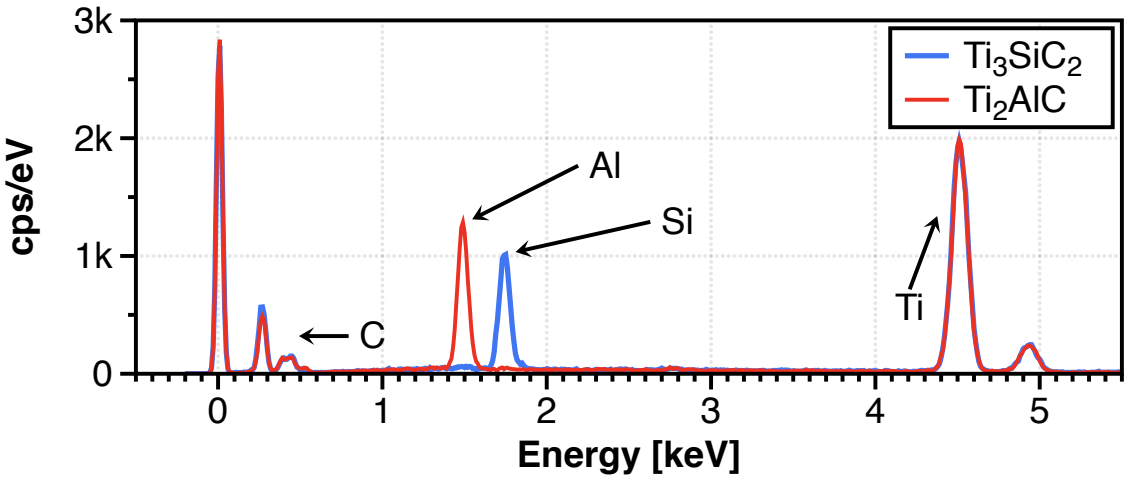

Figure 4.12: EDX spectrum of the Ti-based $M_{n+1}AX_n$ phases. The quantification for both materials are shown in the tables 4.6 and 4.7.

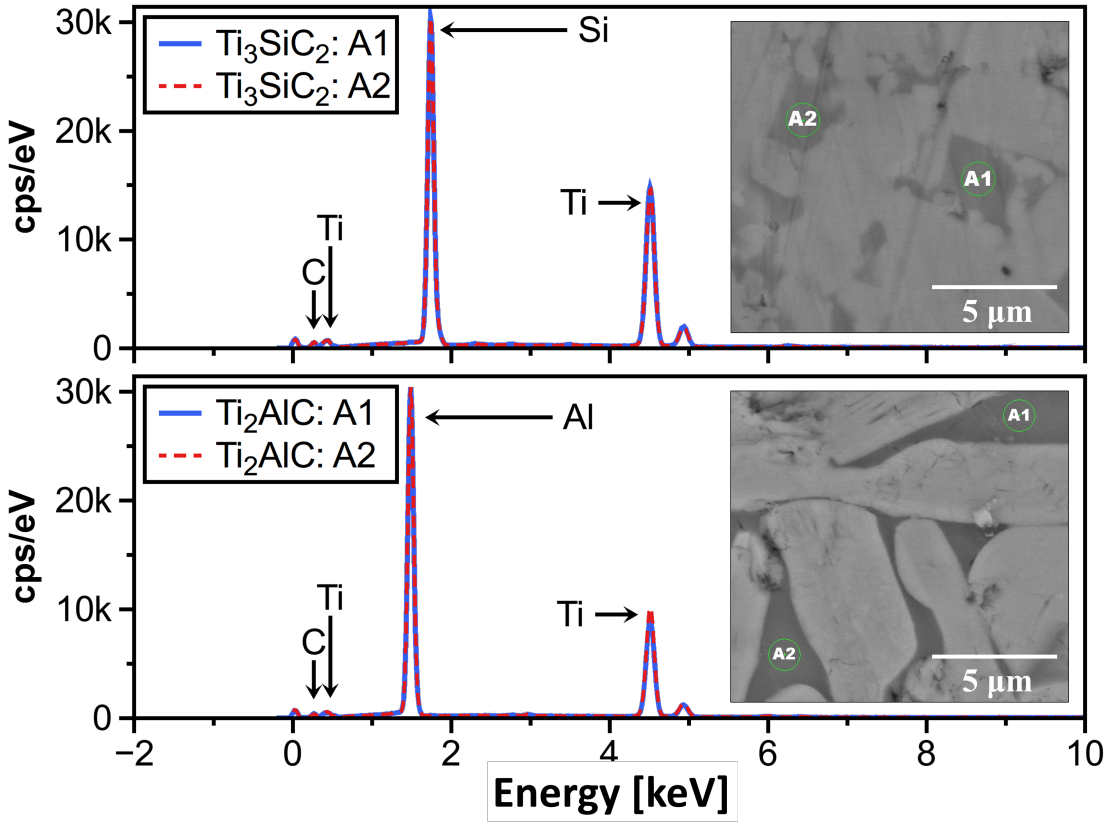

Figure 4.13: The EDX qualitative characterisation of the dark grey and stoichiometric MAX phases present in both Ti_3SiC_2 (top) and Ti_2AlC (bottom) microstructures.

by Burr *et al.* *"C (...) precludes precise quantification by EDX"* [438].

The regions where dark grey phases are observed in the microstructure of both MAX phases were also analysed by EDX as shown in figure 4.13. From an analysis of two different areas as indicated in the insets in figure 4.13, it was possible to conclude that in the case of the Ti_3SiC_2, the phase is likely to be a titanium silicide whereas for the Ti_2AlC, the dark phase was characterised as a titanium aluminide. The elemental quantification for both dark phases in the Ti_3SiC_2 and the Ti_2AlC are shown in tables 4.8 and 4.9, respectively.

Elemental mapping carried out using SEM-EDX has also indicated qualitatively the same results obtained by the elemental quantification of such silicides and alu-

Table 4.8: The elemental composition of the dark grey phase present in the Ti_3SiC_2 measured by SEM-EDX (error is 4% of each value).

Element	**Composition - A1 [wt.%]**	**Composition - A2 [wt.%]**
Ti	49.23	48.46
Si	39.00	39.11
C	11.77	12.43

Table 4.9: The elemental composition of the dark grey phase present in the Ti_2AlC measured by SEM-EDX (error is 4% of each value).

Element	Composition - A1 [wt.%]	Composition - A2 [wt.%]
Ti	40.14	42.93
Al	48.78	48.11
C	11.08	8.96

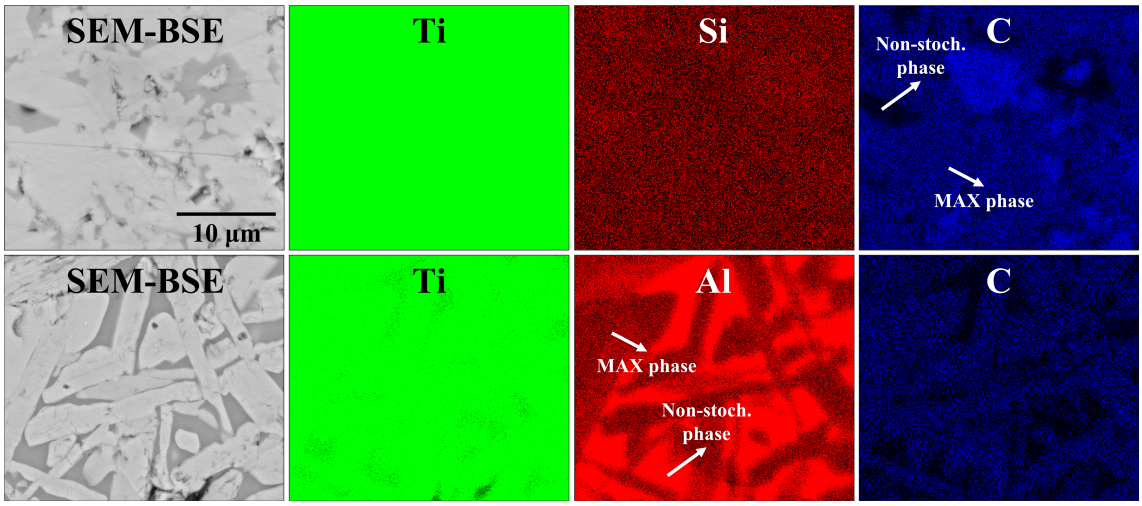

Figure 4.14: SEM-BSE elemental EDX mapping of both Ti_3SiC_2 (top) and Ti_2AlC (bottom).

minides, as shown in figure 4.14, although the phase fraction of the Ti_3SiC_2 was higher compared with its respective silicide whereas for the Ti_2AlC, a considerable phase fraction of aluminides has been identified. The formation of such titanium aluminides and silicides has been already predicted through phase diagrams and thermodynamic calculations for both ternary systems: Ti–Si–C and Ti–Al–C [432–434, 439].

Ti aluminides and silicides are known as intermetallics and can be defined as a class of ordered solid-solution compounds, exhibiting metallic bonding and with well-defined crystal structure and stoichiometry [440].

The existence of two phases – a MAX phase and an intermetallic phase – in the microstructures above suggests that at high temperatures and under high pressures during the reactive hot pressing, these phases compete synergistically to nucleate and grow. Experiments performed by Sambasivan *et al.* have indicated that the stabilisation of both Ti silicides and Ti_3SiC_2 is dictated by the dynamics of C incorporation at high temperatures and pressures [441]. Additionally, calculations using density functional theory have indicated that the formation energy of MAX phases is very similiar to that of their intermetallic counterparts suggesting that the competition for nucleation, growth and stabilisation between these phases is high [442].

The results from the analytical characterisation also indicate that EDX is not an accurate technique to measure the composition of such MAX phases, as multiples sources of C contamination in the SEM (possibly including the deposition of carbonaceous materials on the surfaces of the MAX phases via electron beam induced deposition) and the limitations of this technique in quantifying light elements are major concerns.

4.5 Summary and comparison of the materials and alloys under investigation

From the pre-irradiation characterisation of the materials under investigation in the work presented in this chapter, it can be noted that the austenitic stainless steel AISI-348 and the FeCrMnNi HEA are very similar metallic alloy systems. The same crystalline structure, microstructural morphology (equiaxed grains), atomic densities (see table 4.10) and twins can be found in both alloys, but at the atomic scale, twinning was more prone to occur in the FeCrMnNi HEA. Two major differences can be noted between these alloys: the presence of nanometre-sized Nb(C,N) particles in the AISI-348 and the different elemental compositions.

An irradiation study of these two alloy systems will be performed to probe whether the FeCrMnNi HEA possesses superior radiation tolerance when compared with conventional AISI-348 steel. The main methodology of this ion irradiation study consists of subjecting both alloys to the same ion irradiation parameters such as energy, dose and temperature whilst providing real-time microstructural analysis of the materials using *in situ* TEM. As described in the literature review in chapter 2, the lack of irradiation data on these metallic alloys in the scientific literature shows that the new data obtained by this research work will contribute guiding future neutron irradiation studies and help determine the suitability of this HEA (and also the AISI-348) for nuclear applications.

As exhibited by the electron microscopy characterisation, apart from stoichiometry and the "A" element, the two Ti-based MAX phases are similar. For both of them, the production route is RHP and the final crystal structures are the same: HCP. In the Ti_3SiC_2, nanometre-sized secondary TiC or SiC particles were identified at the atomic scale. Secondary phases were not present of the Ti_2AlC at the nanoscale. The radiation resistance will also be a major topic of the current work, however the aim in this case is to compare the ion irradiated microstructures at the MIAMI facilities with neutron irradiated microstructures at the High Flux Isotope Reactor. The TEM characterisation of neutron-irradiated MAX Phases was performed at Oak Ridge National Laboratory during a six month academic fellowship

awarded by the U.S. Department of Energy/Oak Ridge Associated Universities. A comparison (not exhaustive) of the properties of the materials used in the present research is presented in table 4.10.

Table 4.10: A comparison of the materials studied in this doctorate work.

	AISI-348	**FeCrMnNi HEA**	**Ti_3SiC_2**	**Ti_2AlC**
Crystal Structure	FCC	FCC	HCP	HCP
Microstructure Morphology	Equiaxed Grains (with twins)		Widmanstätten Structure	
Melting Point [K]	1673–1723 [32, 39]	1673–1723†	Dissociation at around of 1673 K [110]	
Presence of secondary phases	Nb(C,N)	–	(Ti,Si)C^{ξ} [431]	–
Density [g·cm^{-3}]	8.0 [32, 39]	8.0 [338]	4.5 [110]	4.1 [110]
Atomic Density $\times 10^{22}$ [atoms·cm^{-3}]‡	8.69	8.70	8.30	7.33
Base Element (Alloying Elements)	Fe-based (Cr, Ni, Mn)	Equiatomic	Ti-based (Si, C)	Ti-based (Al, C)

† Experimental data not available

‡ Calculated using SRIM-2013.

ξ Reported by Morgiel *et al.* [431] and confirmed in this doctorate work.

Chapter 5

Investigating the reduced mobility of irradiation-induced defects of highly concentrated multicomponent alloys

5.1 Introduction and background

Recent research has shown that in multicomponent alloys, the elemental composition is a key parameter in reducing the deleterious effect of energetic particle radiation. In highly concentrated multicomponent alloys, including the HEAs, the disordered state (*i.e.* a random solid solution) was observed to have a strong influence on both the defect formation energies and potential barriers for atomic diffusion [87, 340].

This complex state of microstructural disorder at the atomic level in combination with the reduced mobility of defects and the high energy of defect formation are believed to modify positively the irradiation-induced defect energetics in these alloys, thus contributing to its superior radiation tolerance. However, the atomistic mechanisms behind such resistance are still largely unclear [75, 87, 443]. The properties of highly concentrated alloys (including HEAs) and their characteristic radiation response were introduced in sections 2.1.1.2 and 2.4.2.

In order to investigate the effects of reduced mobility of irradiation-induced defects in HEAs, the FeCrMnNi HEA and the austenitic stainless steel AISI-348 were subjected to light and heavy ion irradiation under identical conditions and their microstructural responses were monitored *in situ* in a TEM at the MIAMI facilities. The nucleation and growth of He and Xe bubbles during irradiation and subsequent annealing were then analysed and the results will be presented in this chapter the focus of which is the generation and evolution of impurity damage.

As shown in the previous chapter, both multicomponent alloys are identical from a microstructural the point of view, with the elemental composition being the only major difference. An important question to be tested here is whether under similar irradiation and annealing conditions, the bubbles in the microstructure of HEA grow as much as in the austenitic stainless steel, therefore shedding light on the possible reduced mobility of vacancies and interstitials in the HEA.

5.2 Design of the experiment

Electron-transparent samples of both FeCrMnNi HEA and AISI-348 steel were irradiated in separate experiments with a light ion, 6 keV He^+ and a heavy ion, 134 keV Xe^+. The fluxes for these two irradiations were fixed, respectively, at: 2.35×10^{13} and 2.40×10^{12} ions·cm^{-2}·s^{-1}. The energies of the light and the heavy ions were selected to match both the implanted ion range and the damage profile as closely as possible as exhibited in figures 5.1(a) and 5.1(b). The number of vacancies generated by a single ion collision is nearly two orders of magnitude higher for the heavy ion irradiation according to calculations using the Monte Carlo code SRIM (see table 5.1). The fluence-to-dpa conversions for these experiments were performed following the procedure described in the section 3.4.3.2 and are exhibited in figure 5.1(c). In the two experiments, the alloys were irradiated up to a dose of 4 dpa corresponding to fluences of 1.69×10^{17} for 6 keV He and 2.74×10^{15} ions·cm^{-2} for 134 keV Xe using 70 nm (as indicated by elastic scattering measurements performed with EELS) as the approximate thicknesses of the lamellae.

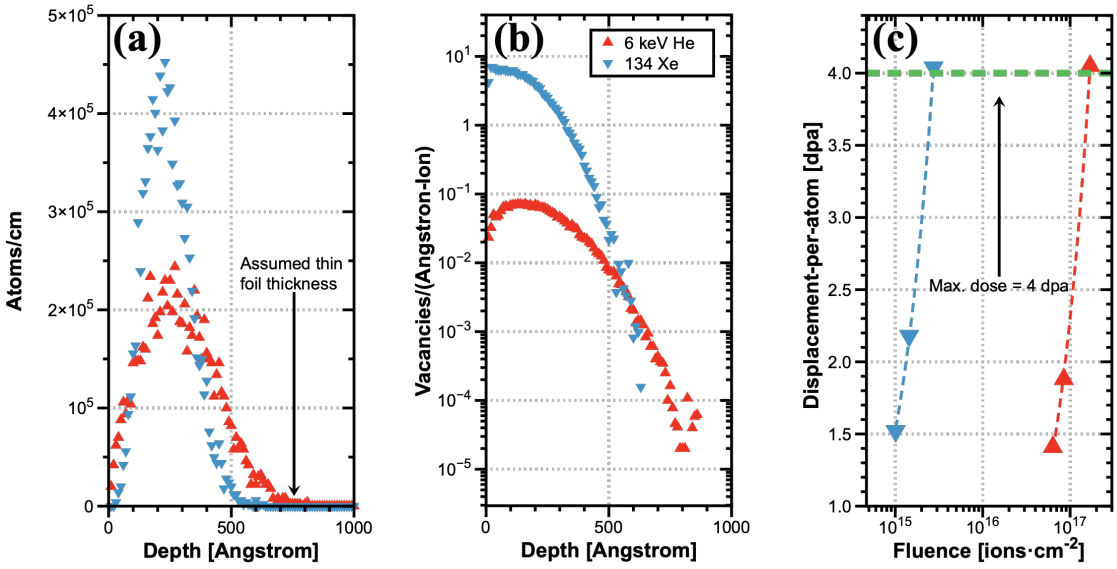

Figure 5.1: (a) The implantation depth; (b) the distributions of vacancies per Ångström-ion from SRIM for 6 keV He and 134 keV Xe ions and (c) the fluence-to-dpa conversion.

Table 5.1: The number of vacancies generated by one ion collision (SRIM calculation statistical error is ≈ 3% using 5000 ions for the calculations).

	6 keV He	**134 keV Xe**
AISI-348	13.4	907.5
FeCrMnNi HEA	13.3	910.4

The irradiations were carried out at room temperature in order to minimise the effects of thermal diffusion. After irradiation up to 4 dpa, the alloys were subjected to 30 minutes of annealing at 673 K using a Gatan double-tilt heating holder and their microstructural evolution was monitored *in situ* in the TEM by means of a Gatan OneView digital camera with 16 megapixels and up to 300 fps video. Inert gas bubbles were observed in bright-field mode with the objective lens underfocused by 1000 nm. After irradiation and subsequent annealing, the diameters of He and Xe bubbles were measured using the software ImageJ by following protocols already reported in the literature [217, 444].

5.3 Light ion irradiation at low temperatures and subsequent annealing

A set of sequential electron-micrographs that exhibits the microstructural evolution of the FeCrMnNi HEA and the AISI-348 steel as a function of dose (from 0 to 4 dpa) for 6 keV He irradiations at room temperature (298 K) is shown in figure 5.2.

The microstructure of the FeCrMnNi HEA under 6 keV He irradiation is also shown in the set of BFTEM micrographs in figure 5.3. The microstructure before irradiation is shown in the underfocused BFTEM micrograph in figure 5.3(a). During the irradiation, He bubbles were firstly noticeable at a fluence of around 7.1×10^{16} ions·cm^{-2} corresponding to ≈ 1.5 dpa as shown in figure 5.2(b). After the irradiation, He bubbles were observed throughout the matrix and also trapped at interfaces as shown in the BFTEM micrographs in figure 5.3(b) and 5.3(c). Subsequent annealing at 673 K resulted in the growth of He bubbles preferentially at interfaces as shown in figure 5.3(d). The inset in figure 5.3(d) is the diffraction pattern of that area after irradiation and annealing which confirms that neither amorphisation nor phase decomposition were seen in the HEA microstructure.

Similarly, the pristine microstructure of the AISI-348 is presented in figure 5.4(a). At a fluence of around 3.7×10^{16} ions·cm^{-2}, corresponding to 0.83 dpa, He bubbles became observable in the matrix as shown in figure 5.2(f). Figure 5.4(b) shows the AISI-348 with He bubbles in the matrix. In these experiments, He bubbles were not observed to be trapped at the annealing-induced twin interfaces as shown in figure

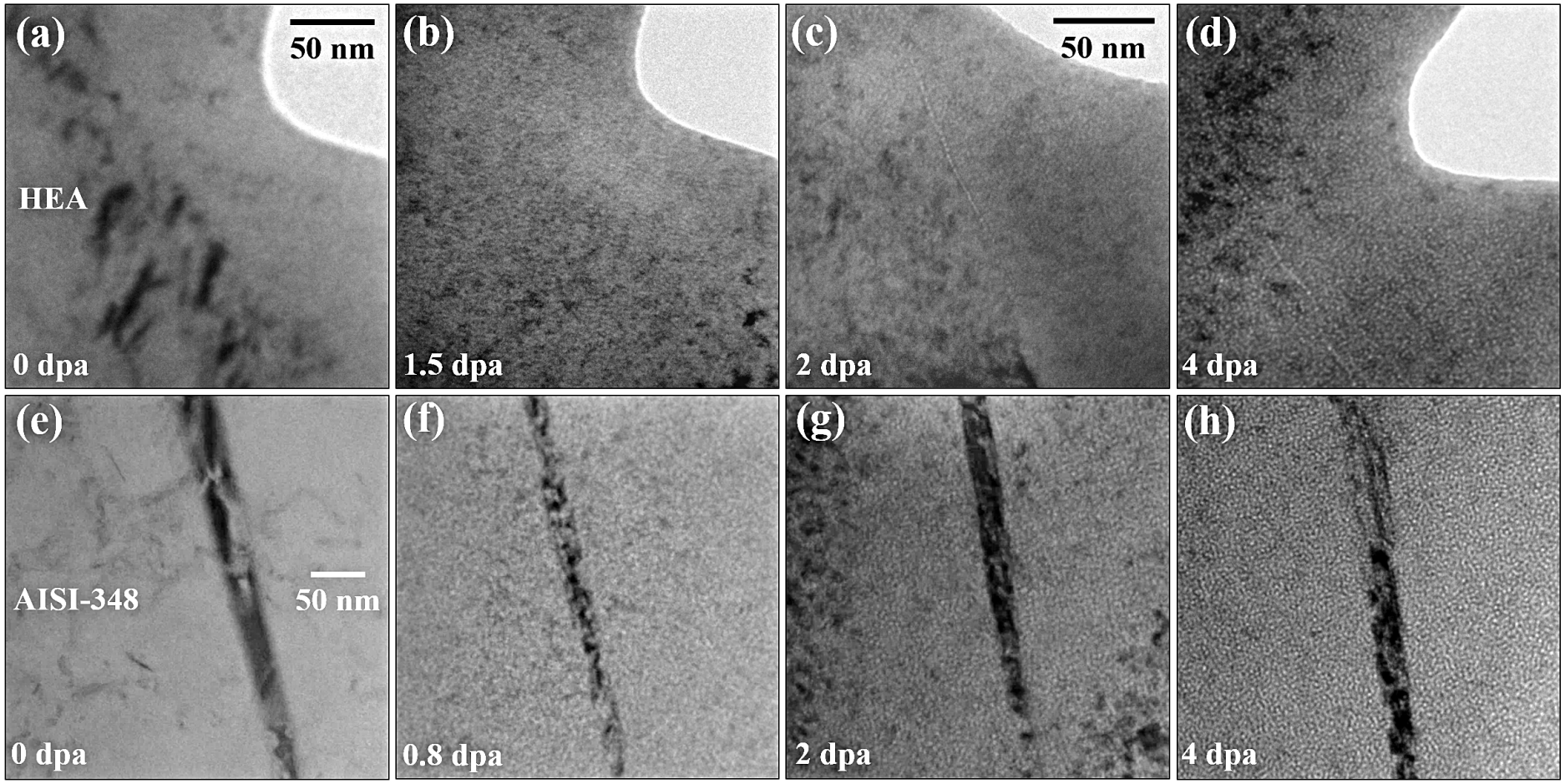

Figure 5.2: A set of sequential micrographs showing the microstructural evolution of the (a-d) FeCrMnNi HEA and the (e-h) AISI-348 steel as function of dose for light ion irradiations using 6 keV He at 298 K. Note: the scale marker in (a) applies to (b-d) and the scale marker in (e) applies to (f-h). All micrographs were recorded with an objective lens underfocus of 1000 nm.

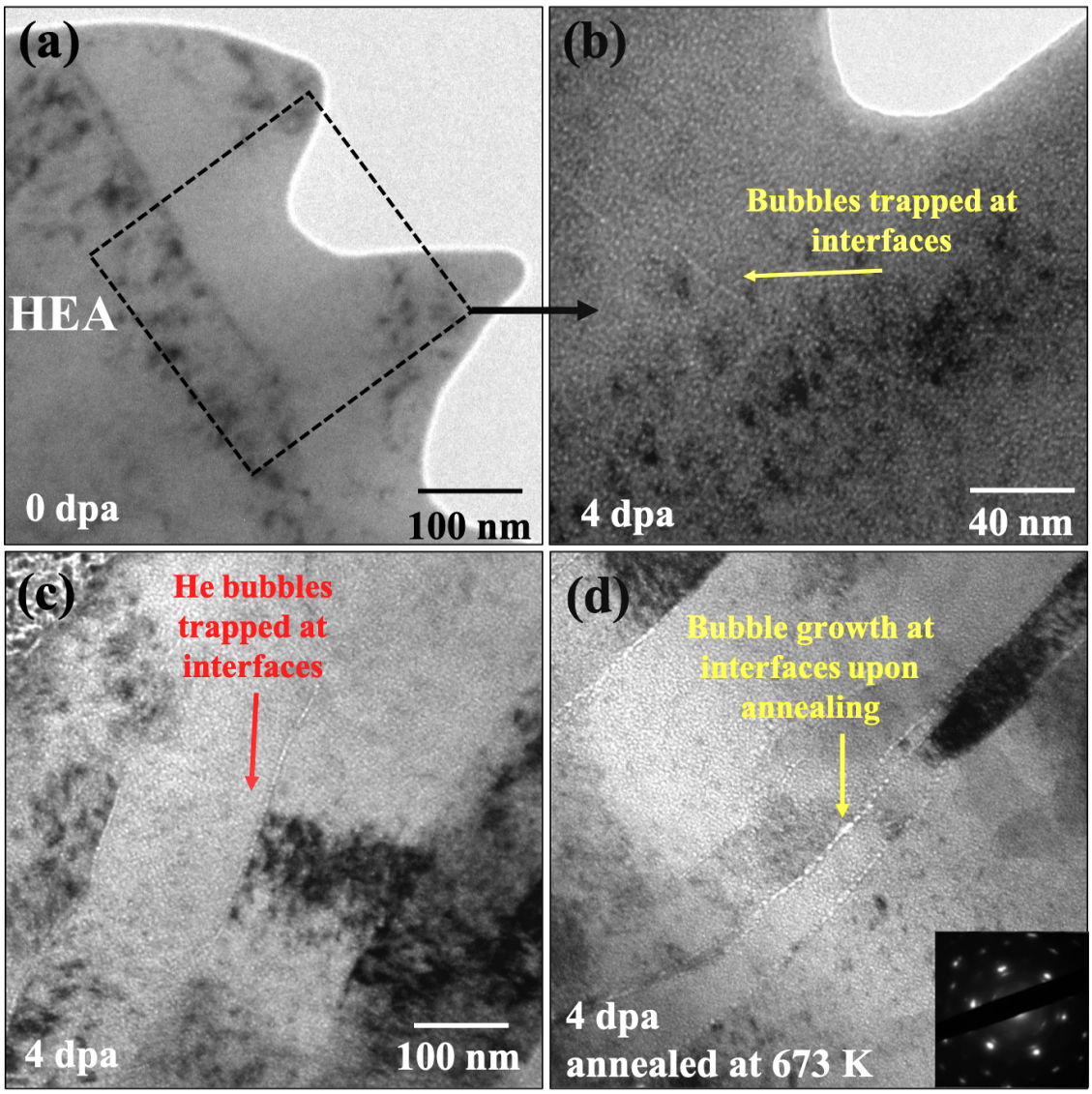

Figure 5.3: BFTEM micrographs of the FeCrMnNi HEA (a) before irradiation and (b–c) after 6 keV He irradiation up to 4 dpa and (d) following subsequent annealing at 673 K. The inset in micrograph (d) is a diffraction pattern taken of that area. Note: the scale marker in (c) also applies to (d); the micrograph in (a) was recorded with an objective lens underfocus of 1500 nm whilst micrographs (b–e) were recorded with an objective lens underfocus of 1000 nm.

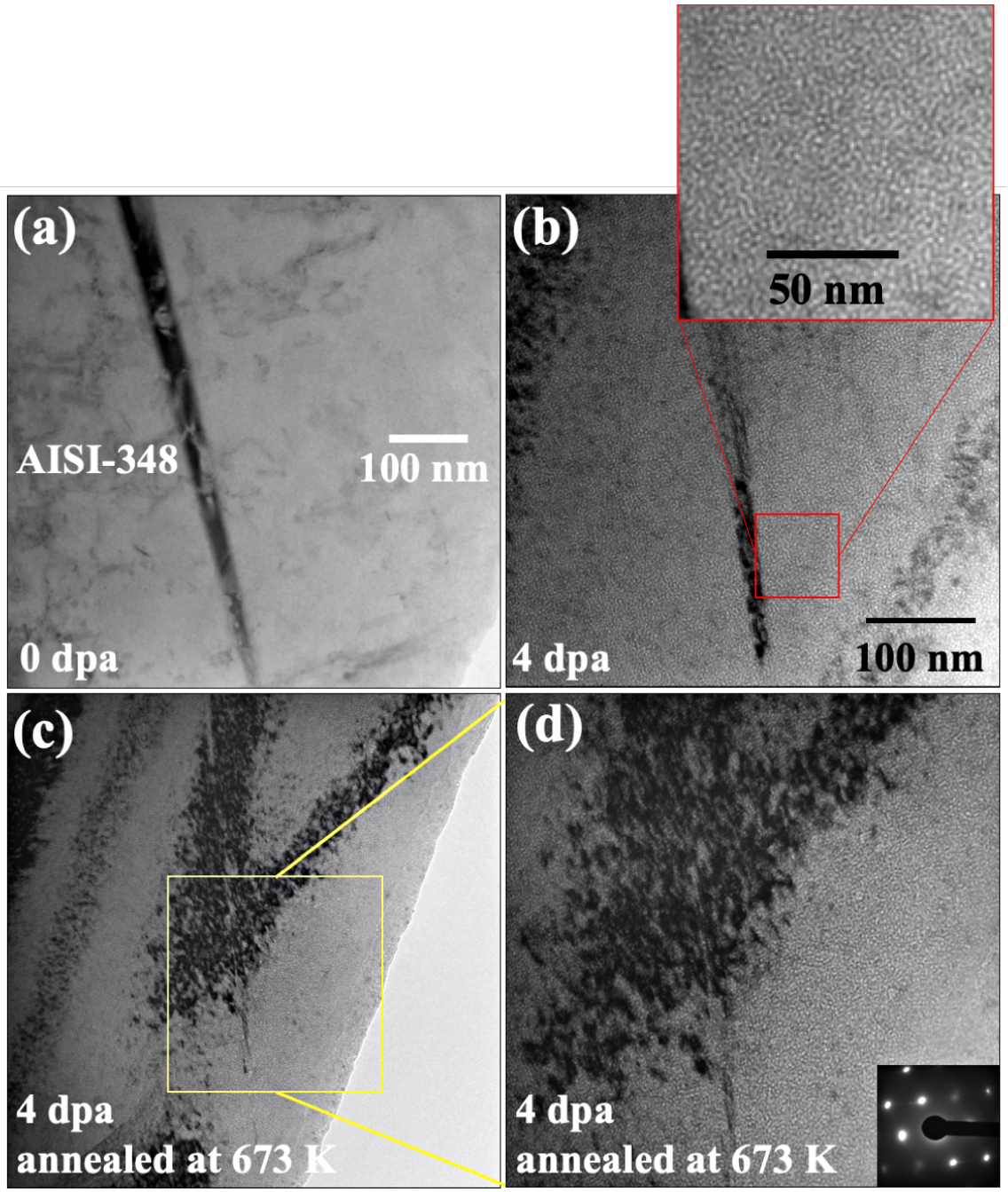

Figure 5.4: BFTEM micrographs of the AISI-348 steel (a) before irradiation, (b) after 6 keV He irradiation to 4 dpa and (c–d) after subsequent annealing at 673 K. Note: the scale marker in (a) also applies to (c) and the scale marker in (b) also applies to (d); all micrographs in the figure were recorded with an objective lens underfocus of 1000 nm.

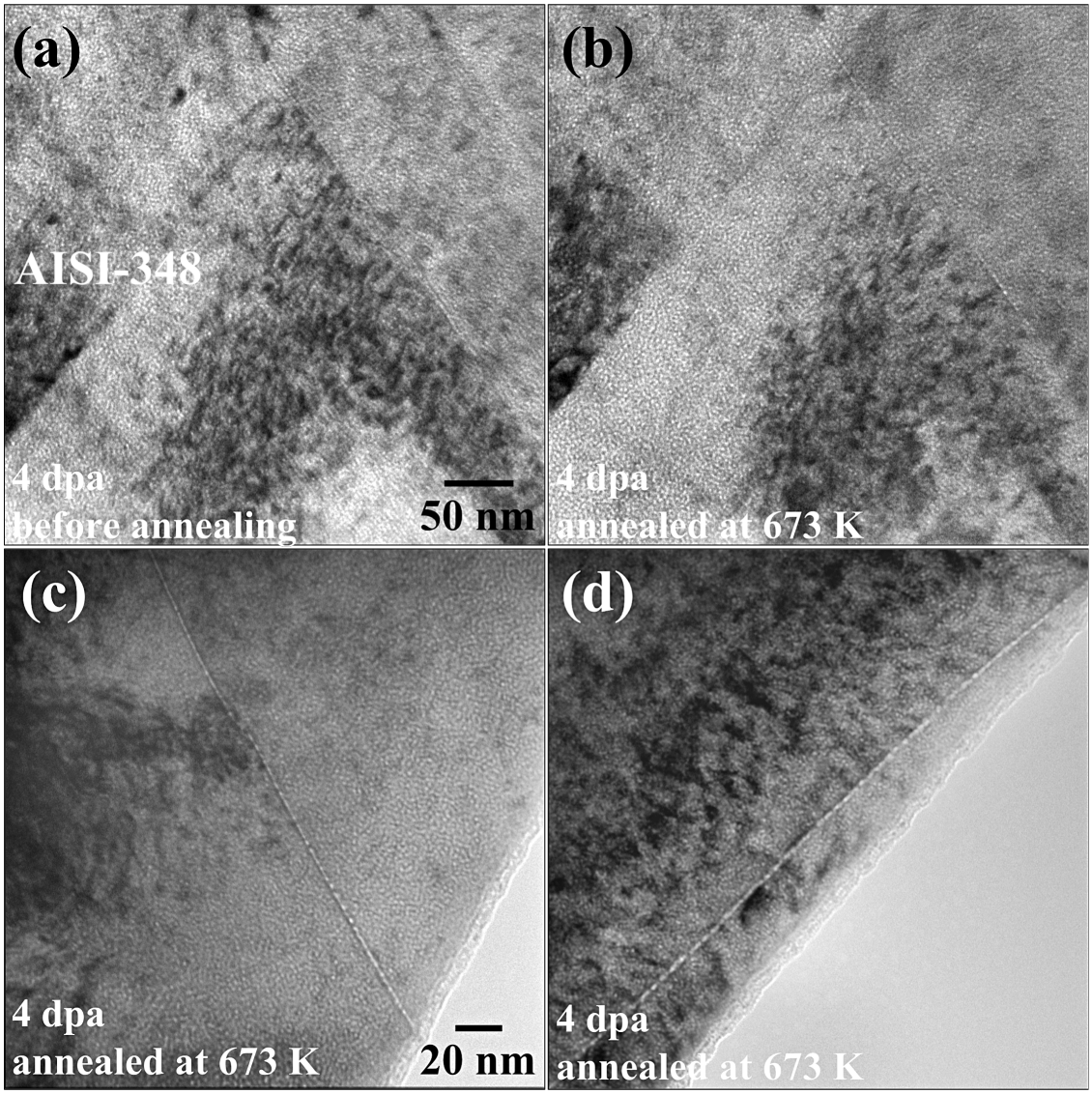

Figure 5.5: BFTEM micrographs of the AISI-348 steel irradiated with 6 keV He to 4 dpa (a) before annealing and (b) after annealing at 673 K. The BFTEM micrographs (c) and (d) show the microstructure of the steel in another area with He bubbles trapped at grain boundaries. Note: the scale marker in (a) also applies to (b) and the scale marker in (c) also applies to (d); all micrographs in the figure were recorded with an objective lens underfocus of 1000 nm.

5.4(b). Subsequent annealing at 673 K showed that the He bubbles were more likely to grow in the steel matrix, as shown in figure 5.4(c–d). The diffraction pattern inset in figure 5.4(d) shows that the steel has suffered neither amorphisation (as expected for metallic alloys) nor phase transformation under the experimental conditions in this experiment.

He bubbles were also observed to be trapped at the austenite grain boundaries at 4 dpa as shown in figure 5.5(a) and after subsequent annealing, they appeared with brighter contrast as exhibited in figures 5.5(b–d). In both experiments, 6 keV He irradiation of the FeCrMnNi HEA and the AISI-348 up to 4 dpa and after subsequent annealing, the electron beam has not exerted any noticiable influence on the nucleation and growth of the inert gas bubbles. This was confirmed by screening areas that were not under constant electron beam exposure whilst under ion irradiation.

As confirmed by the diffraction patterns taken after irradiation and annealing, the FeCrMnNi HEA and the AISI-348 retained their initial crystalline structures (*i.e.* phase decomposition has not occured). Regarding the 6 keV He irradiation, in summary, the results indicate that He bubbles tend to grow preferentially at the interfaces in the HEA case whilst in the austenitic stainless steel, this was not observed. The quantitative size distribution analysis will be presented in the discussion section of this chapter.

5.4 Heavy ion irradiation at low temperatures and subsequent annealing

Similarly, a set of sequential electron-micrographs that exhibits the microstructural evolution of the FeCrMnNi HEA and the AISI-348 steel as a function of dose (from 0 to 4 dpa) for 134 keV Xe irradiations at room temperature (298 K) is shown in figure 5.6.

The pristine microstructure of the FeCrMnNi HEA before irradiation with 134 keV Xe ions is shown in figure 5.7(a). Xe bubbles became observable in the HEA at around 4.8×10^{14} ions·cm^{-2} which corresponds to 0.7 dpa as shown in micrograph 5.6(b). After 4 dpa, post-irradiation analysis showed that Xe bubbles were present at interfaces and throughout the matrix as shown in figure 5.7(b–c).

Extended annealing at 673 K did not result in significant differences from the microstructure at 4 dpa at room temperature (figure 5.7(d)). The inset in figure 5.7(d) is the diffraction pattern of the FeCrMnNi HEA after irradiation and annealing: no amorphisation or phase decomposition were observed.

The AISI-348 microstructure before 134 keV Xe irradiation is shown in the un-

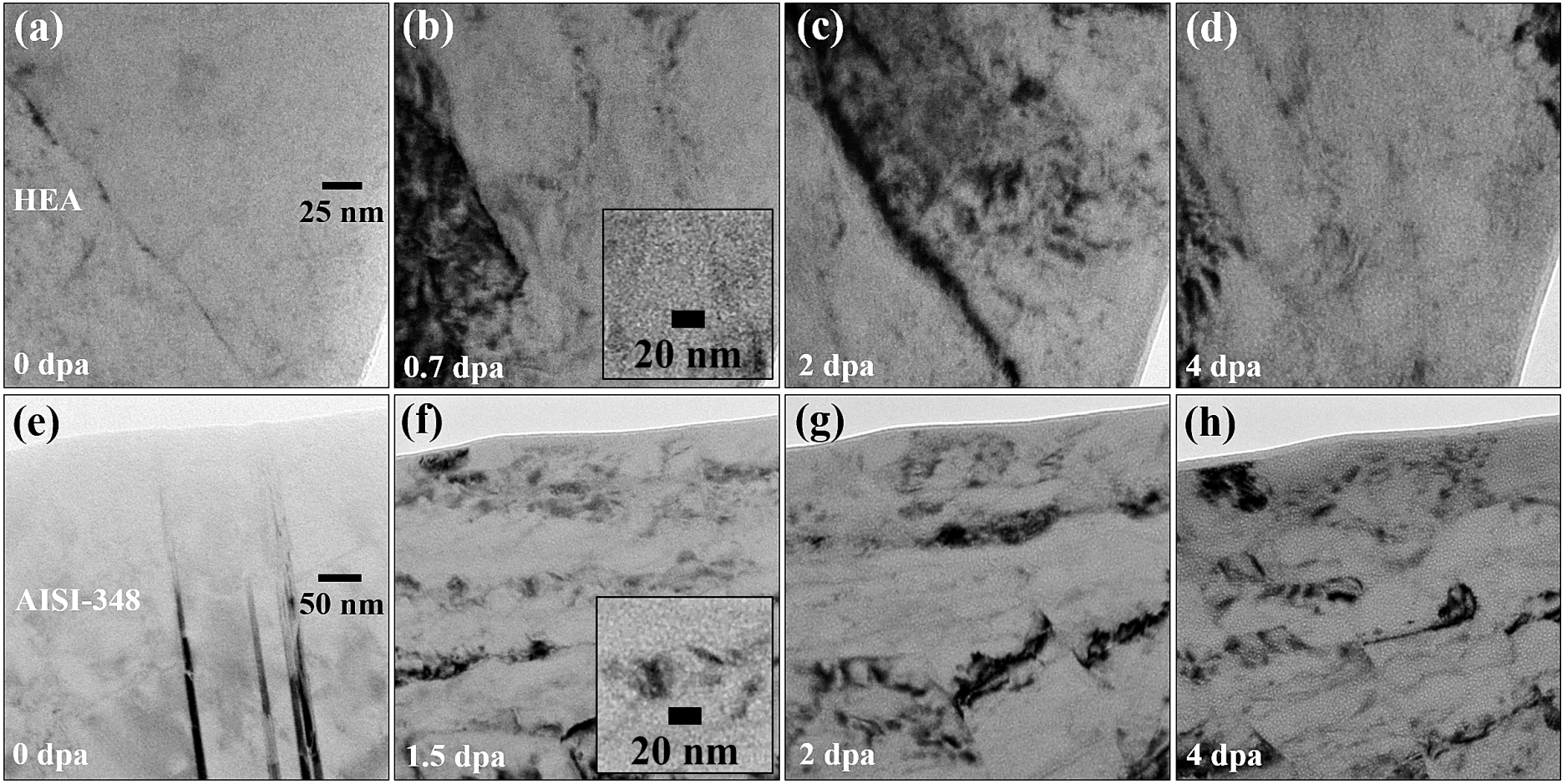

Figure 5.6: A set of sequential micrographs showing the microstructural evolution of (a-d) the FeCrMnNi HEA and (e-h) the AISI-348 steel as a function of dose for heavy ion irradiation using 134 keV Xe at 298 K. Note: the scale marker in (a) applies to (b-d) and the scale marker in (e) applies to (f-h). All micrographs were recorded with an objective lens underfocus of 1000 nm.

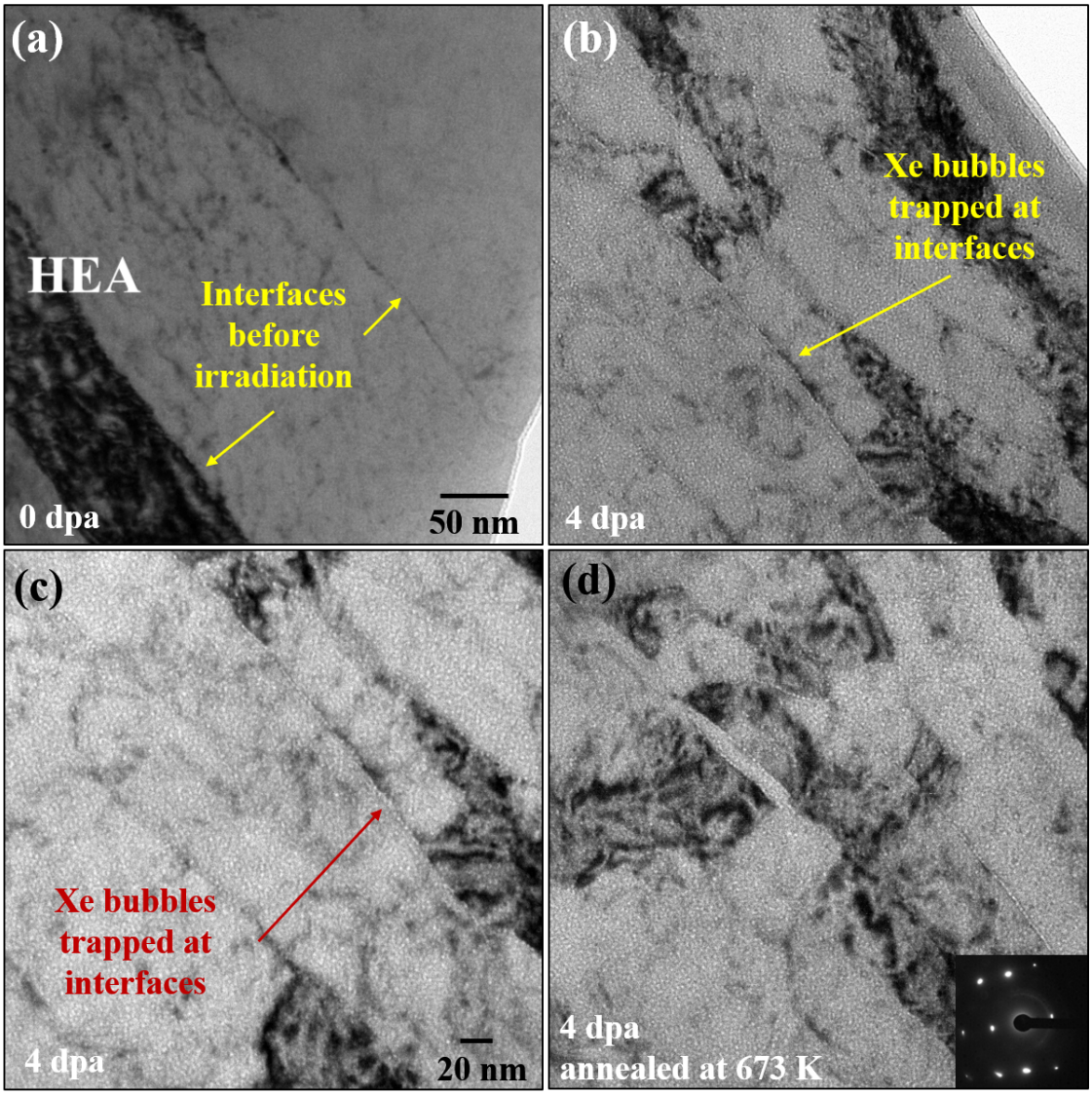

Figure 5.7: BFTEM micrographs of the FeCrMnNi HEA (a) before irradiation and (b–c) after 134 keV Xe irradiation to 4 dpa. The BFTEM micrograph (d) shows the FeCrMnNi HEA at 4 dpa after subsequent annealing at 673 K. The inset in (d) is the diffraction pattern taken of that area after the irradiation and annealing. Note: the scale marker in (a) also applies to (b) and the scale marker in (c) also applies to (d); all micrographs in the figure were recorded with an objective lens underfocus of 1000 nm.

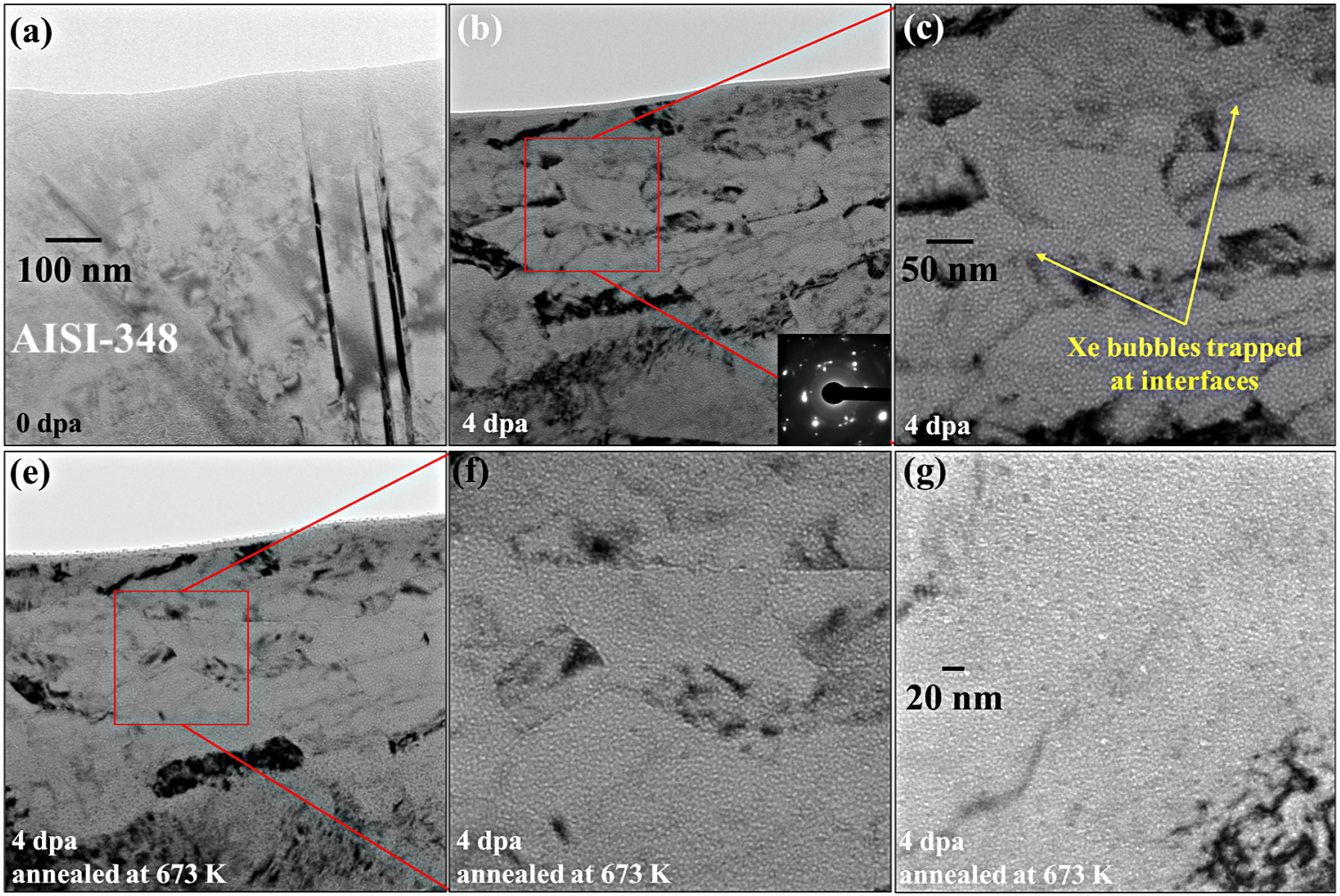

Figure 5.8: BFTEM micrographs of the AISI-348 (a) before irradiation and (b–c) after 134 keV Xe irradiation up to 4 dpa. The BFTEM micrographs (e–g) show the damage microstructure of the AISI-348 after 4 dpa and subsequent annealing at 673 K. Note: the scale marker in (a) also applies to (b) and (e). The scale marker in (c) also applies to (f); all micrographs were recorded with an objective lens underfocus of 1000 nm.

derfocused micrograph in figure 5.8(a). Xe bubbles became observable in the steel matrix at a fluence of around 1.0×10^{15} ions·cm^{-2} corresponding to 1.5 dpa as shown in the micrograph in figure 5.6(f). After 4 dpa, Xe bubbles could be seen in the matrix and also at the interfaces as seen in figure 5.8(b–c). After subsequent annealing at 673 K, figures 5.8(e–f) show Xe bubbles both in the matrix and at the interfaces (grain boundaries). As revealed in figure 5.8(g) taken at a higher magnification, Xe bubbles were observed to grow during annealing preferentially in the matrix.

5.5 The influence of Nb(C,N) nanoparticles on the microstructure of the AISI-348 steel under irradiation

Nb(C,N) nanoparticles are observed throughout the AISI-348 austenite matrix phase before irradiation (section 4.2.2.1). During the light and heavy ion irradiations, He and Xe bubbles were observed at the Nb(C,N) nanoparticle boundaries with the austenite matrix. The BFTEM micrographs in figure 5.9(a–b) show He bubbles at the Nb(C,N) nanoparticle boundaries in the AISI-348 after 4 dpa of 6 keV He irradiation and subsequent annealing at 673 K.

With respect to the heavy ion irradiations, Xe bubbles were also observed to nucleate at the Nb(C,N) boundaries as shown in figure 5.9(d). As shown in figure 5.9(c), small crystallites with sizes of around 30 nm became observable in the surroundings of some Nb(C,N) nanoparticles after 134 keV Xe irradiation up to 4 dpa and subsequent annealing at 673 K. Under bright-field conditions such crystallites are of dark contrast and by underfocusing the electron beam, their boundaries can be delineated.

By placing the selected-area diffraction aperture around the Nb(C,N) nanoparticle in the micrograph shown in figure 5.10(a), a diffraction pattern of that area was obtained and revealed the presence of continuous rings thus confirming the existence of small nanocrystals as exhibited in figure 5.10(b). DFTEM has revealed these nanocrystals appear to be precipitates as a result of the ion irradiation and annealing (figure 5.10(c)).

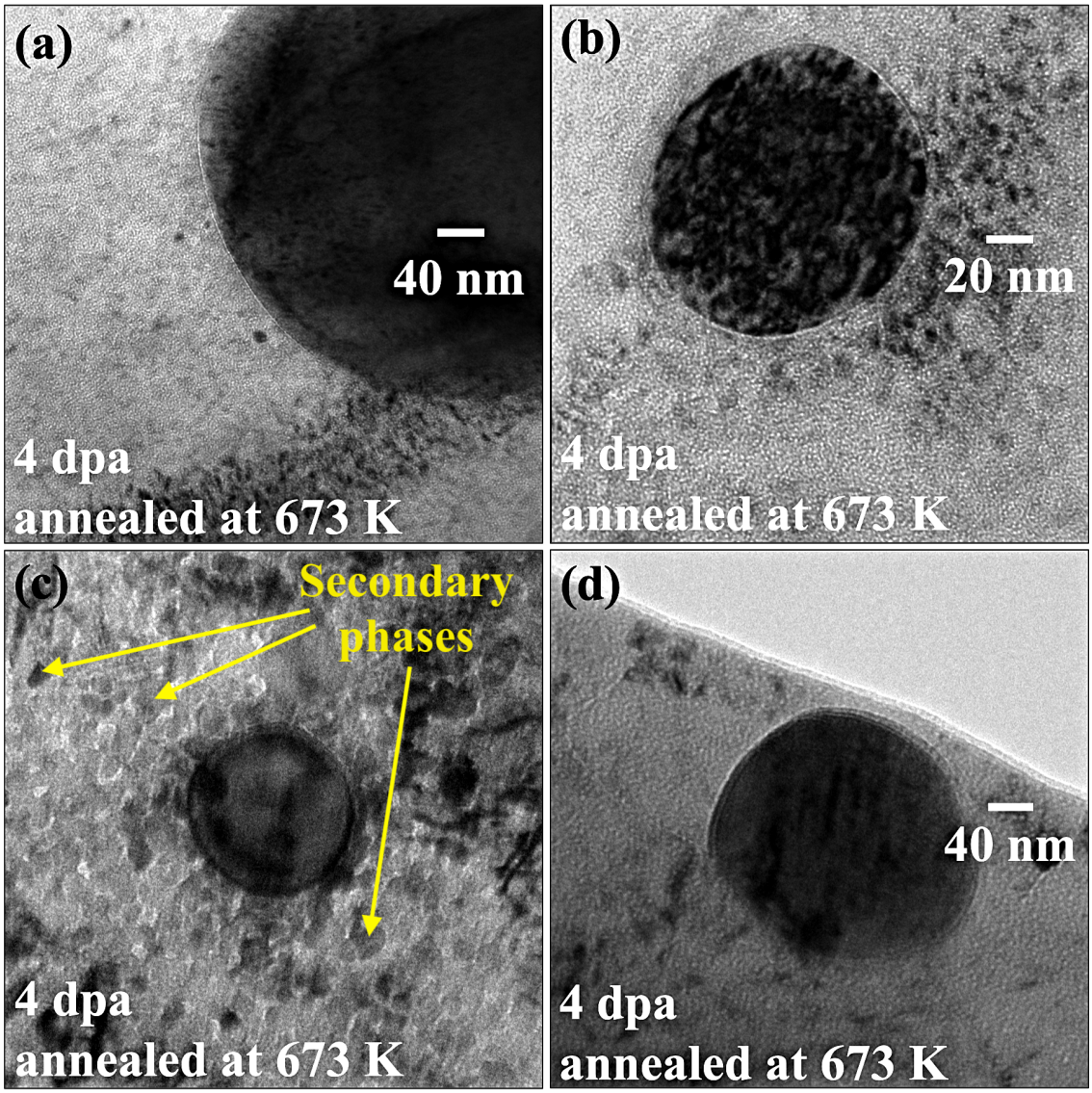

Figure 5.9: BFTEM micrographs of the AISI-348 microstructure showing (a–b) He bubbles trapped at the Nb(C,N) nanoparticle interfaces after 4 dpa and subsequent annealing. The BFTEM micrograph in (c) shows the presence of nanometre-sized secondary phases around a Nb(C,N) nanoparticle formed after 134 keV Xe irradiation to 4 dpa and subsequent annealing and the micrograph in (d) also shows that in some Nb(C,N) nanoparticles, Xe bubbles were observed at the nanoparticle interface. All micrographs in the figure were recorded with an objective lens underfocus of $\approx$ 1000 nm. Note: the scale bar in (d) also applies to (c).

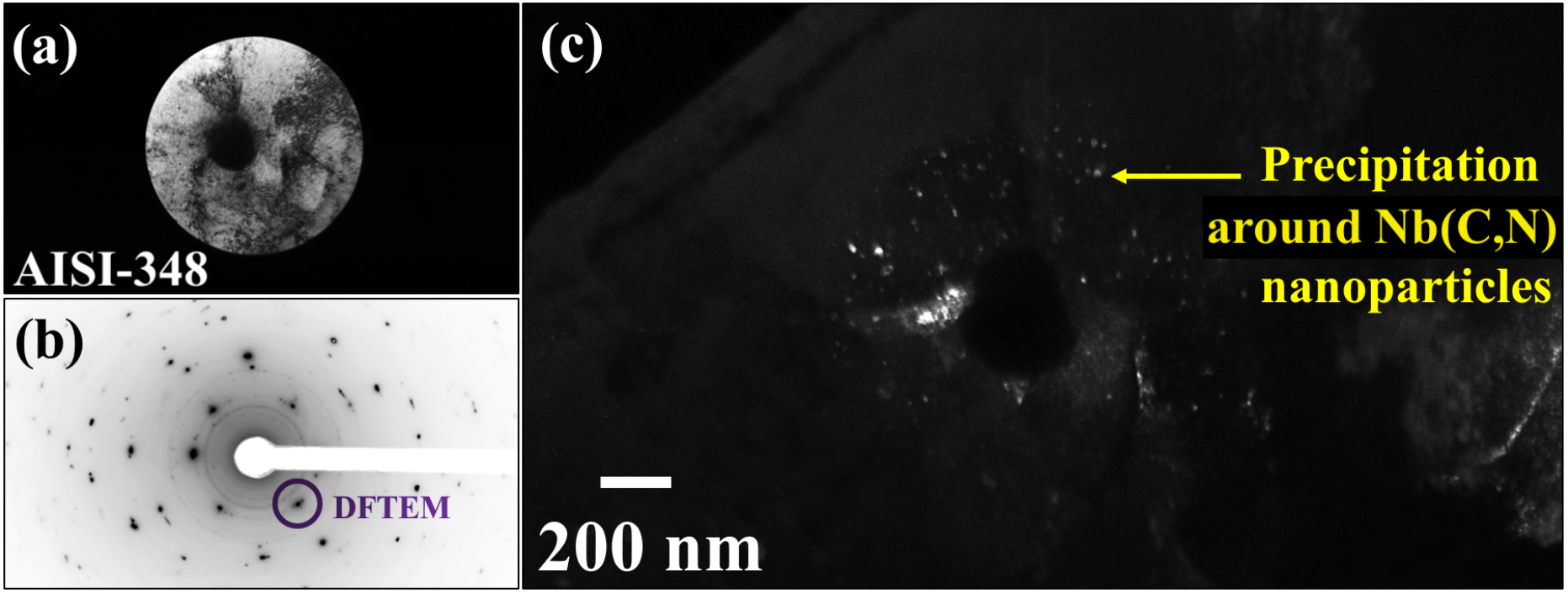

Figure 5.10: (a) The BFTEM micrograph shows the SAED aperture around a Nb(C,N) nanoparticle in the austenite matrix after heavy ion irradiation (134 keV Xe) to 4 dpa and subsequent annealing. (b) Shows the diffraction pattern corresponding to (a). DFTEM micrograph in (c) shows the presence of small crystallites around the Nb(C,N) particles resulting from the precipitation of secondary (nanometre-sized) phases.

5.6 Discussion

5.6.1 Sequential quantitative data on bubble sizes and areal densities

The set of light and heavy ion irradiations followed by thermal annealing at 673 K in both the FeCrMnNi HEA and the AISI-348 steel presented in the last section allowed the quantification of He and Xe bubble sizes (diameter) as a function of the dose and after both irradiation (to 4 dpa) and subsequent thermal annealing. The analysis presented in this section is focused on matrix bubbles. Interfaces were monitored only at 4 dpa and during thermal annealing after irradiation: these results will be presented in the next subsection.

Figures 5.11(a) and 5.11(b) show the evolution of He and Xe bubble sizes, respectively, as a function of dose. Between 100 and 150 bubbles were analysed for each case studied. Although the average size of the He bubbles is slightly larger for the irradiations in the AISI-348 steel than in the FeCrMnNi HEA, the effects of light ion irradiation in both alloys were very similar in terms of He bubble sizes when the statistical error is taken into consideration. He bubbles became noticeable within the austenite matrix of the AISI-348 steel at an earlier dose than in the FeCrMnNi HEA. After irradiation to 4 dpa, thermal annealing induces some growth of He bubbles in the matrix and the average sizes were effectively the same in both materials. With respect to the formation of Xe bubbles, they became noticeable firstly in the FeCrMnNi HEA and up to 4 dpa, the Xe bubbles were slightly smaller in the HEA. After annealing, the Xe bubbles were observed to grow in the matrix of both alloys (the bigger error in the AISI-348 steel can be attributed to a larger dispersion in the bubble sizes).

The quantitative data obtained with the light ion irradiations on the AISI-348 steel and the FeCrMnNi HEA reported in this chapter can be compared with a recent and similar work by Kalchenko *et al.* [445]. In their work, Kalchenko *et al.* [445] irradiated a 40Fe-20Cr-20Mn-20Ni (wt.%) HEA and an austenitic stainless steel grade Fe18Cr10NiTi with 20 keV He ions using an *ex situ* methodology under the same conditions. The maximum dose studied by these authors was 4.8 dpa. Post-irradiation characterisation and bubble size analysis were carried out in a TEM after 10 min of thermal annealing at 773 K. Their results are shown in figure 5.11(a). Their average size of He bubbles at 4.8 dpa in the 40Fe-20Cr-20Mn-20Ni HEA after 10 min of annealing at 773 K was smaller (0.9±0.3 nm) than in the case presented in this thesis. For the Fe18Cr10NiTi steel the average size under the same irradiation and annealing conditions was also smaller (1.6±0.3 nm) than for the AISI-348 steel studied in the present work. However, when the statistical errors

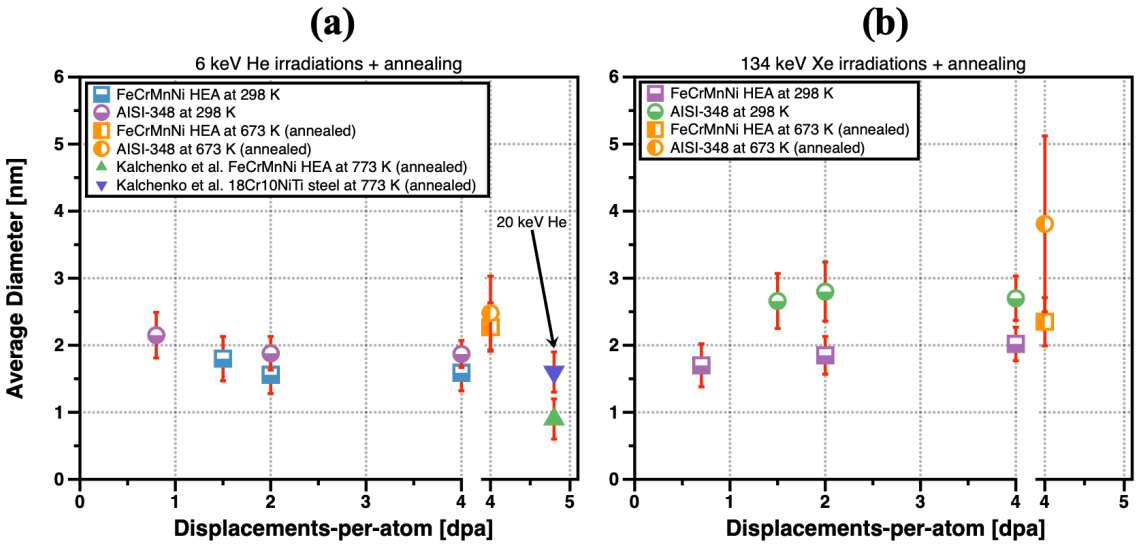

Figure 5.11: Average bubble sizes (diameter) as a function of dose and after irradiation and thermal annealing for (a) 6 keV He and (b) 134 keV Xe ion irradiations. Note: the data presented in graph (a) is from Kalchenko *et al.* [445].

are taken into consideration, the results of Kalchenko *et al.* and this present work are very similar and no firm conclusions can be made either based on the difference in the two irradiation methodologies or between the alloys under investigation. It is also worth emphasising that for the *ex situ* TEM ion irradiation methodology used by Kalchenko *et al.* [445], nothing can be said regarding He bubble sizes in the microstructure of these two alloys for doses lower than 4.8 dpa. However, it is interesting to note that lower He beam energies with the *in situ* TEM ion irradiation technique can reproduce quantitatively (within the statistical error) the results obtained independently by other authors when using the *ex situ* TEM ion irradiation methodology.

Similar quantitative data for areal densities (number of He or Xe bubbles per area) as a function of dose and after thermal annealing were obtained with the results from the experiments performed in this chapter. The results are shown in figures 5.12(a) and 5.12(b). Four different areas were analysed for each case studied. It is interesting that, upon nucleation and growth of inert gas bubbles, the areal densities are observed to decrease as can be seen when comparing the values from 4 dpa at 298 K with the 4 dpa at 673 K (after annealing). Such trend is observed for both He and Xe irradiations. Note that the He bubble sizes in the work by Kalchenko *et al.* were smaller at 4.8 dpa after 10 min of annealing at 773 K, but their areal densities were also larger than the values reported in this thesis by one order of magnitude.

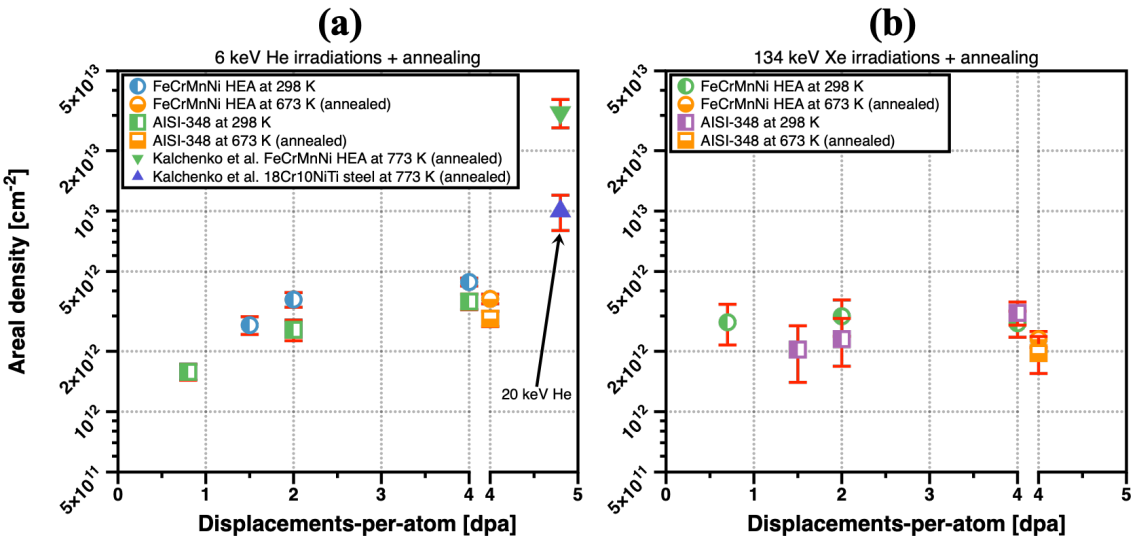

Figure 5.12: Average areal densities of bubbles as a function of dose and after irradiation and thermal annealing for (a) 6 keV He and (b) 134 keV Xe ion irradiations. Note: the data presented in graph (a) is from Kalchenko *et al.* [445].

5.6.2 Inert gas bubble size analysis: matrix phases, interfaces and thermal annealing

As both the average sizes and areal densities did not vary significantly up to 4 dpa before annealing, a more detailed investigation was carried at 4 dpa before and after annealing, with a focus on the bubble behaviour in the matrix phases and at the interfaces of both alloys under investigation. For the histograms reported in this section, the y-axis corresponds to the absolute number of bubbles.

From the BFTEM micrographs recorded after irradiation up to 4 dpa and subsequent annealing, it was possible to perform size (*i.e.* diameter) distribution statistical analyses for both He and Xe bubbles in the FeCrMnNi HEA and the austenitic stainless steel AISI-348. The study of the nucleation and evolution of inert gas bubbles in these two multicomponent alloys has been subdivided into two parts: He and Xe bubbles (i) in the matrix phase and (ii) decorated at interfaces that could be either grain boundaries or annealing twin interfaces.

The histograms of He bubble sizes in the matrix and at the interfaces in both alloys are shown in figures 5.13(a-b) and 5.14(a-b), respectively. The analysis shows that in the AISI-348 at 4 dpa and prior to annealing, He bubbles appear to be bigger than in the HEA. With respect to their average sizes at 4 dpa, quantitatively after subsequent extended annealing at 673 K, He bubbles grew in the matrix of both alloys by around 42% and 33% (in diameter) on average, respectively for the FeCrMnNi HEA and the AISI-348 steel. With respect to the He bubbles in these alloys at 4 dpa and after subsequent annealing, it can be concluded that they both have a very similar response to the light ion irradiation.

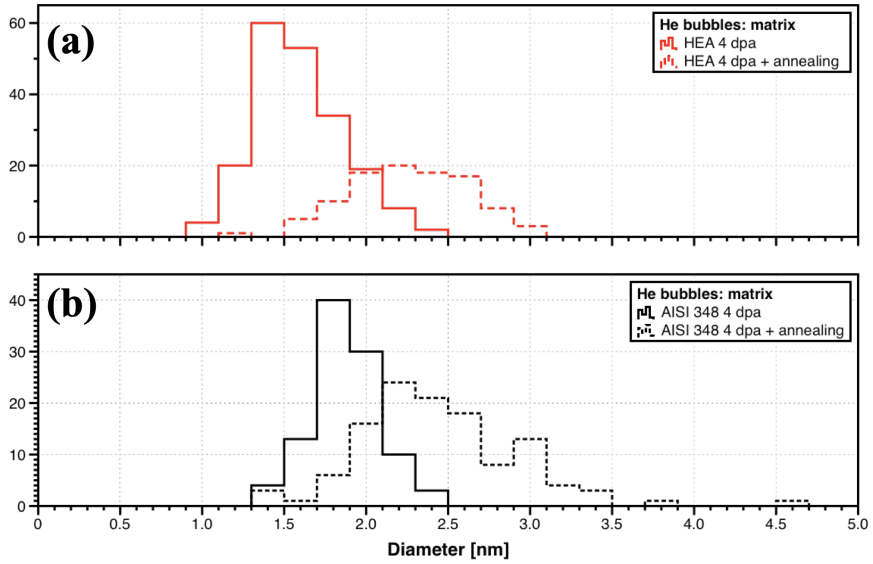

Figure 5.13: The size (diameter) distribution of He bubbles in the matrix of the (a) FeCrMnNi HEA and (b) AISI-348 after 4 dpa and subsequent annealing to 673 K.

For the light ion irradiations, results are different when the nucleation and growth of He bubbles are analysed at the interfaces of each alloy. At 4 dpa, the He bubble sizes are similar for both alloys, but after extended annealing at 673 K, the HEA exhibited considerable bubble growth as can be seen in the histogram in figure 5.14(a). On average the calculations indicate that for the HEA, the percentage of growth was around 139% compared with 50% (in diameter) for AISI-348.

Similarly, the histograms of Xe bubble sizes in the matrix and at the interfaces in both alloys are shown in figures 5.15(a–b) and 5.16(a–b), respectively.

The distributions of Xe bubbles in the matrix show that for the FeCrMnNi HEA, Xe bubbles exhibited a small growth after annealing whilst in the AISI-348 steel this growth was more pronounced. By analysing the distributions of Xe bubbles in the matrix, the trend reported for He bubbles in the matrix was also observed here: at 4 dpa and prior to annealing, Xe bubbles are relatively bigger in the steel when compared to the FeCrMnNi HEA (histograms in figure 5.15(a–b)). At 4 dpa, the average size of Xe bubbles has increased around 16% and 41% (in diameter), respectively, for the HEA and the AISI-348. At the interfaces, Xe bubbles were not found to grow significantly in either material at 4 dpa and after subsequent annealing as can be observed in the histograms in figure 5.16.

The results of the inert gas bubbles size analysis are summarised in figure 5.17. The red error bars in the plots indicate the standard deviation (σ) of the average diameter of the bubbles for each case studied.

Light and heavy ion irradiation followed by annealing of the FeCrMnNi HEA resulted in the nucleation and growth of inert gas bubbles in the matrix whereas, at the interfaces, only He bubbles were observed to grow significantly after annealing.

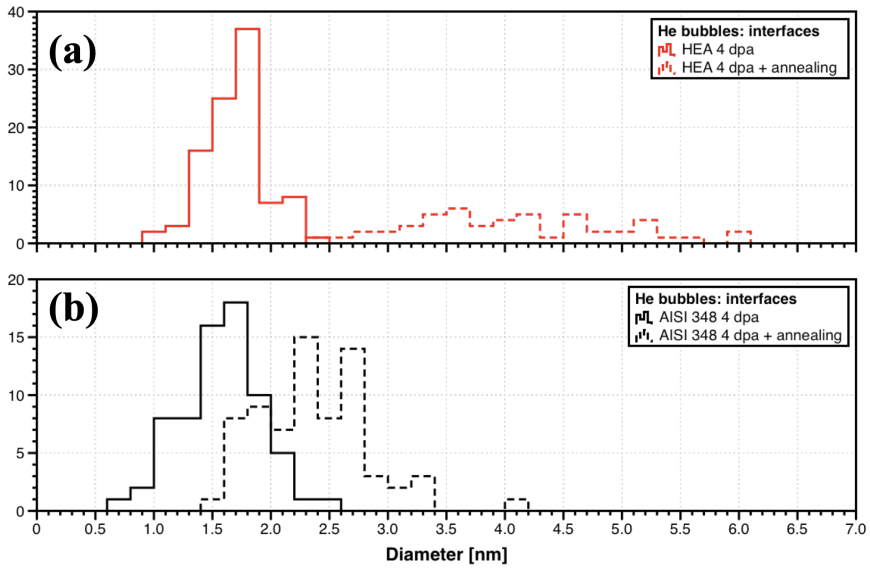

Figure 5.14: The size (diameter) distribution of He bubbles at interfaces in the (a) FeCrMnNi HEA and (b) AISI-348 after 4 dpa and subsequent annealing to 673 K.

In the case of AISI-348 irradiated and annealed under the same conditions, the results suggest that at 4 dpa both He and Xe bubbles in the matrix are bigger when compared with the HEA. In the steel, Xe bubbles grow considerably in the matrix after annealing. For both alloys, Xe bubbles at the interfaces were not found to grow neither after irradiation nor annealing.

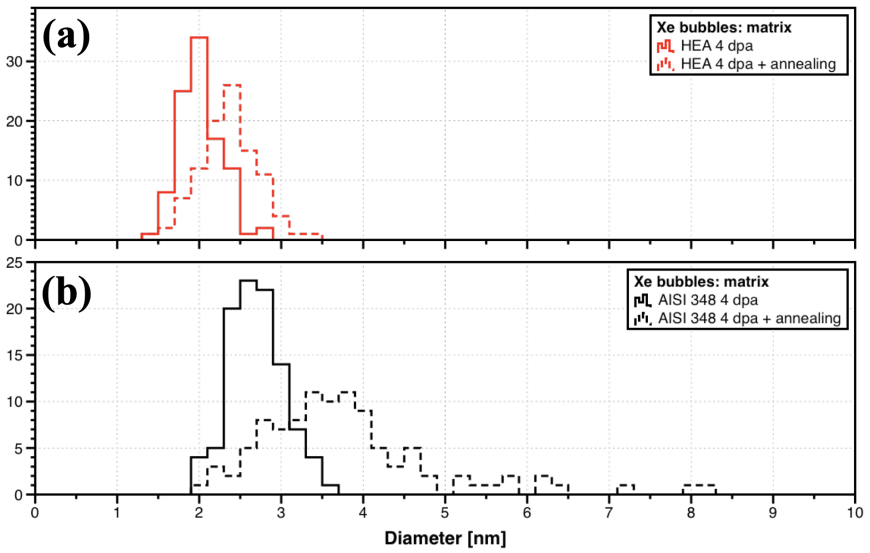

Figure 5.15: The size (diameter) distribution of Xe bubbles in the matrix of (a) the FeCrMnNi HEA and (b) AISI-348 steel after 4 dpa and subsequent annealing to 673 K.

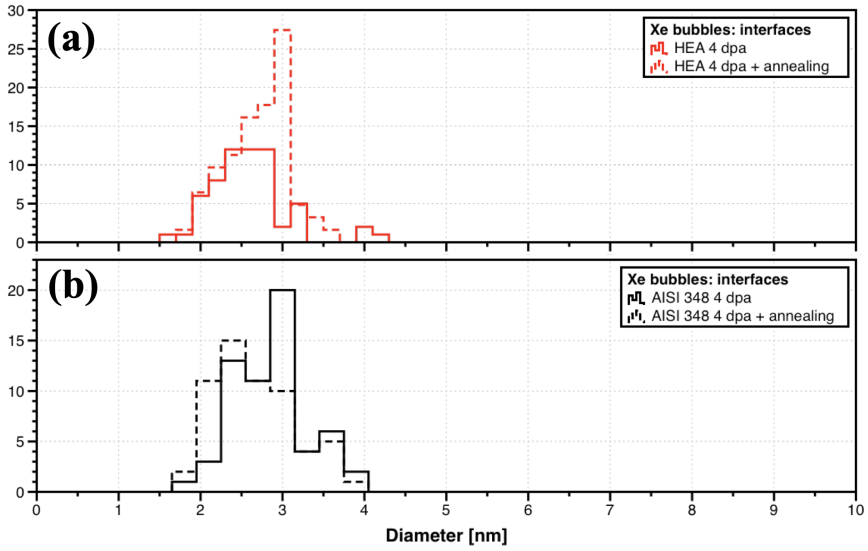

Figure 5.16: The size (diameter) distribution of Xe bubbles at interfaces of (a) the FeCrMnNi HEA and (b) AISI-348 steel after 4 dpa and subsequent annealing to a temperature of 673 K.

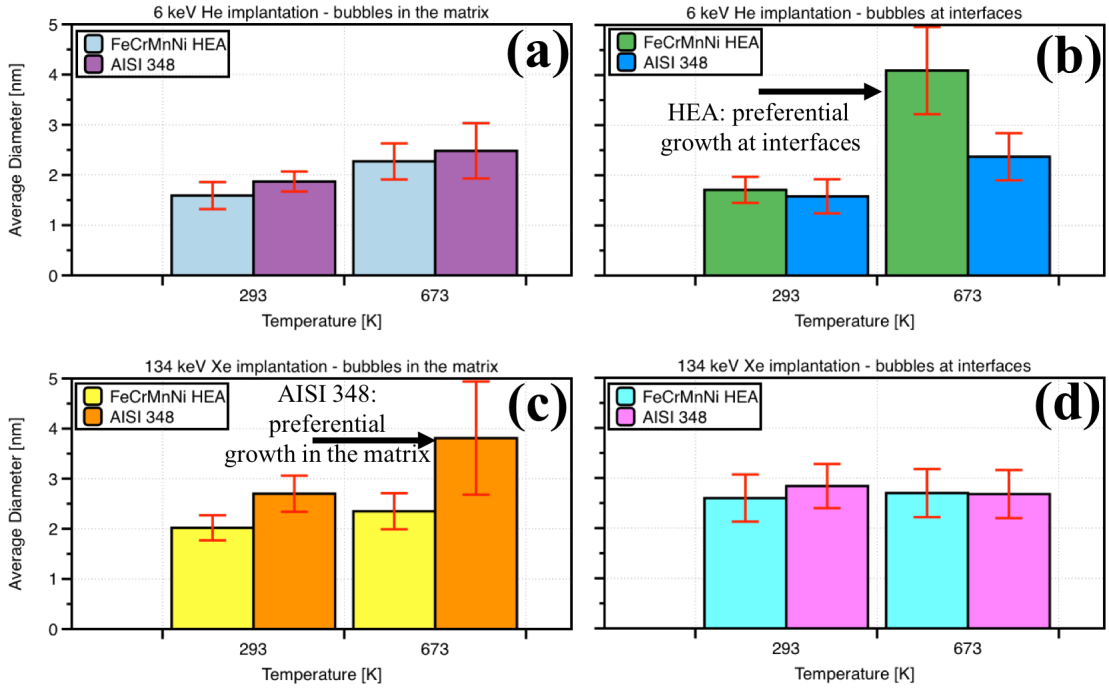

Figure 5.17: Trends resulting from the size analysis of He and Xe bubbles at interfaces and in the matrix for both the FeCrMnNi HEA and AISI-348 after irradiation up to 4 dpa with (a–b) He and (c–d) Xe including subsequent annealing to 673 K.

5.6.3 The relationship between inert gas bubbles nucleation and growth in the irradiated multicomponent metallic alloys

During atomic collisions with the crystal structures of the FeCrMnNi HEA and AISI-348 point defects will be generated: vacancies and interstitials (Frenkel pairs). Monte Carlo calculations with SRIM show that 6 keV He creates an average of 13 vacancies per ion collision whilst 134 keV Xe generates 907–910 vacancies per ion collision. As a result of the implantation of the inert gases and subsequent generation of point defects, inert gas bubbles will nucleate throughout the matrix of these materials as shown in the sections above.

The mechanism of inert gas bubble nucleation and growth in crystalline solids involves the kinetics of vacancies and interstitials at the atomic level. In a solid containing mobile vacancies, inert gas bubbles will grow via the continuous arrival of vacancies and inert gas atoms (interstitials). Similarly, the departure of vacancies (and interstitials) will lead the bubble to shrink. When both arrival and departure rates of vacancies reach a balance (*i.e.* a steady-state condition), the inert gas bubbles will neither grow nor shrink [22, 137, 446]. Thus, the study of inert gas bubbles in high-entropy alloys can be used to test the current hypothesis of reduced mobility of radiation-induced point defects.

The results reported here show that for He bubbles in the matrix, bubbles are marginally bigger in the AISI-348 compared with the FeCrMnNi HEA. Upon extended annealing, the He bubbles grow in the matrix of both materials, although in the case of the steel, the size distribution indicates that bubbles are larger than in the HEA matrix. This indicates that under the same irradiation conditions, in the stainless steel, vacancies are slightly more likely to diffuse and get trapped by the He bubbles. Additionally, the interaction between interstitials and bubbles is also more prone in the AISI-348 matrix which could also result in bigger bubble sizes. However, when the statistical error in measuring the size of bubbles is taken into account, light ion irradiations followed by subsequent annealing at 673 K in the matrices of both the AISI-348 and the FeCrMnNi lead to very similar nucleation and growth of He bubbles.

Regarding He bubbles at the interfaces, the growth upon annealing was notable in the HEA as shown in figure 5.17(b). This suggests that interfaces in the HEA microstructure – such as grain and twin boundaries – act as sinks for irradiation-induced point defects at moderate temperatures. The presence of annealing twins throughout the HEA microstructure is also expected to influence these observed results. From the comparison between the two pristine microstructures of the FeCrMnNi HEA and the AISI-348 presented in chapter 4, twins are likely prone to

occur in the former alloy as the equiatomic composition can decrease the stacking fault energy, thus contributing to twinning in this HEA.

At first glance the results in the HEA exhibit a discrepancy: He bubbles clearly have not grown in the matrix as much as at the interfaces. This suggests that vacancies have limited mobility in the matrix and that bubbles at interfaces had to incorporate vacancies from the interfaces (and possibly from the matrix near to the interface) in order to grow. These observations can be explored in terms of the intrinsic disordered atomic structure of a HEA.

In the bulk (matrix) of a highly concentrated alloy (like the FeCrMnNi HEA), the migration barriers for diffusion have been demonstrated to be higher than in pure metals and diluted alloys (such as the AISI-348) [447]. As a result, activation energies for either vacancies and interstitials diffusion under irradiation could be higher in these alloys. The trends observed in this work in the case of the HEA irradiations with 6 keV He, indicate that inert gas bubbles have not shown an equal growth rate in the matrix probably as a consequence of the complex defect energetics distribution caused by the disordered atomic solid solution. Recent reports from both computation and experiments have demonstrated that a "sluggish" diffusion property acts in order to enhance the recombinations of Frenkel defects leading to the observed superior radiation tolerance for these highly concentrated alloys [87, 340, 447, 448].

The complex energy landscape associated with the sluggish diffusion in highly concentrated alloys is affected by temperature according to Zhao *et al.* [447, 449]. At high temperatures, the sluggish diffusion property will cease. These authors also noted that the presence of interfaces will also affect such a property by inducing preferential diffusion of some chemical species at these sites. In this way, preferential diffusion will result in the diffusion of point defects at the interfaces and may induce chemical segregation processes, although in this work, segregation has not been observed for either light ion irradiations or heavy ion irradiation in the FeCrMnNi HEA. This preferential diffusion behaviour of point defects has also been reported for Fe-Cr alloys [450]. These facts may explain the preferential growth of He bubbles at the interfaces of the FeCrMnNi HEA upon annealing (figure 5.17(b)) in contrast with the results in the matrix.

More "aggressive" irradiations with 134 keV Xe ions have also confirmed these assumptions. As shown in figure 5.17(c), after irradiation up to 4 dpa, Xe bubbles are bigger in the steel and also grow more in this alloy upon annealing compared with the HEA. As noted before, a single ion collision between Xe and the microstructure of both alloys will create a large number of Frenkel defects: approximately 1000 vacancies per cascade. In the HEA due to the sluggish diffusion, there will be more recombination and annihilation than in the stainless steel or even fewer net vacancies

per cascade due to higher lattice potential energies: thus leading to a reduction in the population of defects that could contribute to the growth of inert gas bubbles. However, probably due to the reduced mobility of Xe atoms in solids, the growth of Xe bubbles has not been clearly observed in either interfaces or the matrix in either alloy. Regarding the heavy ion irradiation experiments, when the statistical error is taken into account, both alloys have a similar irradiation response.

Post-irradiation TEM examination of the AISI-348 after Xe irradiations have clearly given indications of phase separation (precipitation) as shown in figure 5.10. Precipitation has not been observed in the FeCrMnNi HEA under the same irradiation/annealing conditions indicating a possible connection between the thermodynamic state of the alloys under investigation with the effects of energetic particle irradiation, but this effect will be further explored in the next chapter.

5.7 Summary and conclusions

The irradiation response of an equiatomic alloy in comparison with its non-equiatomic alloy counterpart followed by subsequent annealing have been investigated. This has shown that the dynamics of nucleation and growth of inert gas bubbles (in the matrix) were possibly slightly delayed or suppressed in the FeCrMnNi high-entropy alloy case. However any such effect is within the error bars of the bubble size measurements. Therefore, considering the experimental limitations and the standard deviations in the average size of the bubbles, these experiments have demonstrated that the sluggish diffusion concept plays at most a very minor role in the evolution of the inert gas bubbles in the HEA under irradiation and annealing. Diffusion is likely to occur in the interfaces of the HEA when subjected to light ion irradiations. This may be strongly related with the presence of twins – more likely to occur with a higher density in the FeCrMnNi HEA than in the AISI-348 steel – that may act as sinks for irradiation-induced defects, thus affecting the kinetics of nucleation and growth of inert gas bubbles at the interfaces between twins and the random solid solution matrix. The experimental observations in this chapter agrees with previous reports in the literature where the sluggish diffusion effect significantly diminishes (i) upon increasing the (irradiation) temperature and (ii) at the interfaces [449].

As discussed above, the statistical error associated with the bubble sizes measurements can be considered as the limiting factor when trying to evidence the sluggish diffusion in HEAs under irradiation. However, defect population and availability along with the atomic mobilities of inert gases species in solids are factors that can be used to interpret the present results on AISI-348 and the FeCrMnNi HEA. The bubble size distributions as well as the analysis presented in figure 5.17 establish a baseline, *i.e.* (1) the light ion irradiations with 6 keV He leads to equivalent bubble

sizes in the matrices of both alloys, but prominent growth at the interfaces of the FeCrMnNi HEA; conversely (2) heavy ion irradiations with 134 keV Xe leads to equivalent bubble sizes at the interfaces of both alloys, but significant growth in the matrix of the austenitic stainless steel.

Xe irradiations will create two orders of magnitude more damage (vacancies per cascade) in each cascade than He irradiations and this fact will result in very different cascade morphologies. Given these considerations, He irradiations will likely result in the generation of mainly Frenkel pairs whereas the heavy ion collisions will lead directly to the generation of small defect clusters. Assuming that He is more prone to diffuse than Xe under the temperatures of the experiments [451, 452], He bubbles in the FeCrMnNi HEA will grow at the interfaces by He diffusion/trapping at these sites. Similarly, Xe may be more mobile in the steel matrix and will eventually interact with the generated small clusters resulting in larger matrix bubbles as observed. Therefore, under these considerations, the sluggish diffusion hypothesis could be used to explain the observed trend in the bubble sizes, but due to the statistical error in measuring the bubble sizes, the results shows little difference in radiation response of both alloys.

Heavy ion irradiations followed by subsequent annealing in the AISI-348 have shown evidence of phase decomposition/precipitation whilst in the HEA the random solid solution lattice was preserved without irradiation-induced phase separation. These facts suggest that there is a strong link between the high thermodynamic phase stability of the HEA (under the studied conditions) and the response to energetic particle irradiation when compared to a very similar non-equiatomic alloy, the austenitic stainless steel AISI-348, and these latter facts are the subject of study in the next chapter.

Chapter 6

Comparison of phase stability under irradiation of AISI-348 steel and FeCrMnNi HEA

6.1 Introduction and background

One particular core effect of high-entropy alloys is the expected high thermodynamic phase stability promoted – theoretically – by the maximisation of the configurational entropy at (close-to) equiatomic compositions. The high-entropy effect lowers the Gibbs free energy of the alloy system, thus allowing the solidification and growth of a single-phase microstructure with maximum retained stability, *i.e.* no phase transformation is expected to occur even at high temperatures or when the alloy is subjected to mechanical loading. In metallurgy, the synthesis of metallic alloys using the high-entropy concept diverges from the conventional terminal solid solution approach where minor alloying elements are chosen in a certain compositional space (not at equiatomic composition) to form a single or dual-phase alloy, *e.g.* the austenitic stainless steels and the Ni-based super-alloys. Therefore, in the context of nuclear technology, it is of paramount importance to investigate how the high-entropy effect and its associated high thermodynamic single-phase stability may be affected by exposure to energetic particle irradiation.

In the previous chapter, heavy ion irradiations (134 keV Xe^{+}) have shown indications of radiation-induced precipitation (RIP) in the austenitic stainless steel. This manifested itself in the form of small crystallites that were observed in both bright- and dark-field TEM preferentially in the vicinity of Nb(C,N) nanoparticles within the austenite matrix. Interestingly, such precipitation did not occur in the FeCrMnNi HEA under identical irradiation conditions. In order to investigate possible connections between high thermodynamic phase stability and radiation damage, this

present chapter is concerned with probing the single phase stability of the FeCrMnNi high-entropy alloy under heavy ion irradiation varying both the temperature and the incident ion energy.

Following the methodology introduced in the last chapter, the austenitic stainless steel AISI-348 was irradiated with low- and medium-energy Xe ions at similar conditions to those used for the HEA to allow a direct comparison. The expected possible phase instabilities were radiation-induced segregation (RIS), precipitation (RIP) and phase transformations (RIPT). In conventional TEM, these effects can be monitored by analysing diffraction patterns before and after irradiation. RIS, RIP and RIPT can also be studied using advanced analytical methods such as STEM-EDX in modern electron microscopes with field emission guns (FEGs). The development of impurity damage (*i.e.* inert gas bubbles) and displacement damage (*i.e.* black-spots, dislocation loops) will be qualitatively explored and reported where appropriate, but these defects are not the main focus of these experiments.

6.2 Low-energy heavy ion irradiation

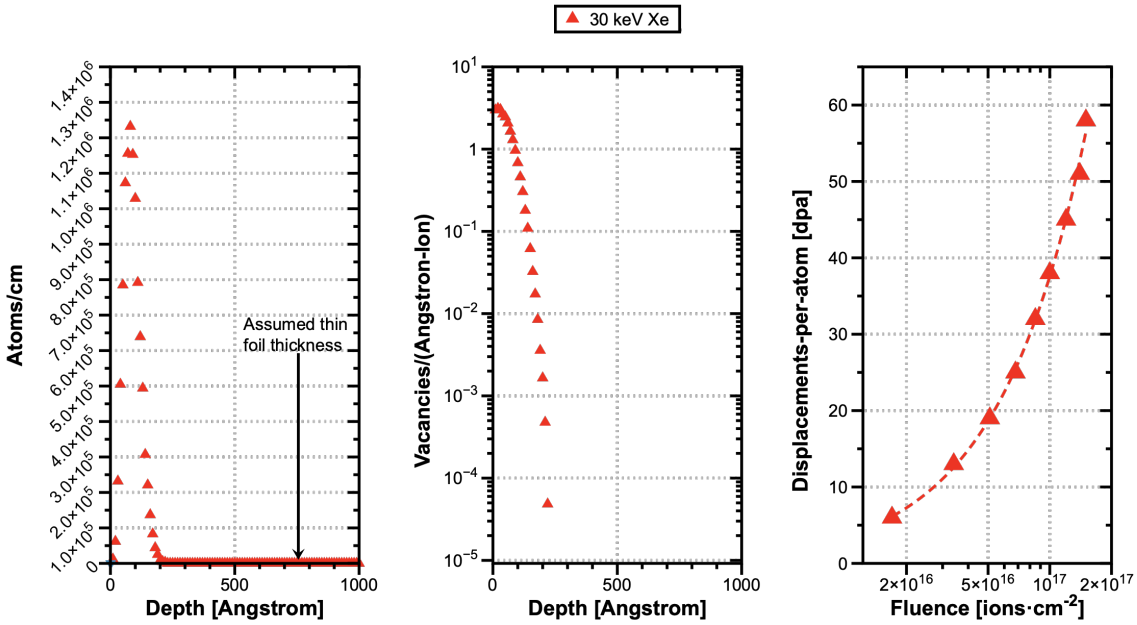

Figure 6.1: (a) The implantation depth, (b) the distributions of vacancies per Ångström-ion and (c) the fluence-to-dpa conversion for 30 keV Xe ions into the FeCrMnNi HEA and the AISI-348 steel calculated using the SRIM code. Calculations were carried out with 5000 ions in the "quick" calculation mode using the Kinchin-Pease model.

The first part of this chapter investigates the effects of 30 keV Xe irradiations in the AISI-348 steel and the FeCrMnNi HEA. These experimental conditions were

chosen because fast neutrons within a LWR will generate PKAs with energies ≈ 10 keV. The average PKA energy for 30 keV Xe ions in Fe is 11.7 keV (calculated using SRIM-2013 with 1000 ions). Thus low-energy heavy ion irradiations allow the simulation of neutron-induced cascades and average displacements similar to those in a nuclear reactor [453].

6.2.1 Design of the experiment

When using 30 keV Xe ions to carry out irradiations in the FeCrMnNi HEA and AISI-348, the longitudinal ion range of implantation is around 12 nm as shown in figure 6.1(a). As Xe is a heavy ion (Z = 54 and A = 131), the cascade damage consists of approximately circular-shaped regions (in 2-D projections) with radii less than 5 nm (the 2D projection of such a cascade is shown in figure 6.24 in section 6.3.2.3) indicating that single-ion impacts produce substantial displacement damage in localised lattice regions. Per ion collision, 30 keV Xe ions will cause on average 220 displacements in both alloys. The fluence-to-dpa conversion is exhibited in figure 6.1(c).

6.2.2 Low, moderate and high temperatures regimes

Heavy ion irradiations *in situ* within a TEM have been carried out in the temperature range of 293–1073 K. Firstly, the results are presented. A comprehensive discussion is then given at the end of this subsection.

6.2.2.1 Irradiations at 293 K

The microstructural evolution of the FeCrMnNi HEA and the AISI-348 at room temperature are presented in figure 6.2(a–c) and 6.2(d–f), respectively, up to a fluence of 2.8×10^{16} ions·cm^{-2} or 10 dpa. The insets in the figures are the diffraction patterns taken before the irradiations and after 10 dpa.

Xe bubbles were observed in both materials at a dose of around 5 dpa and in the case of the stainless steel, the austenite phase decomposed into small nanometre-sized precipitates starting at around 5 dpa. These precipitates grew in projected area for doses higher than 5 dpa as can be observed in the BFTEM figures 6.2(e) and 6.2(f): the yellow arrows in these micrographs are drawing the reader's attention to this observed growth. The radiation-induced precipitation has been detected primarily by observing the presence of the Debye-Scherrer rings in the diffraction pattern, as shown in the inset in figure 6.2(f), but the observation of the crystalline precipitates can also be seen in bright-field. In the TEM figures 6.2(b) and 6.2(c), the circle indicates that from 5 to 10 dpa, some black-spots were observed but were

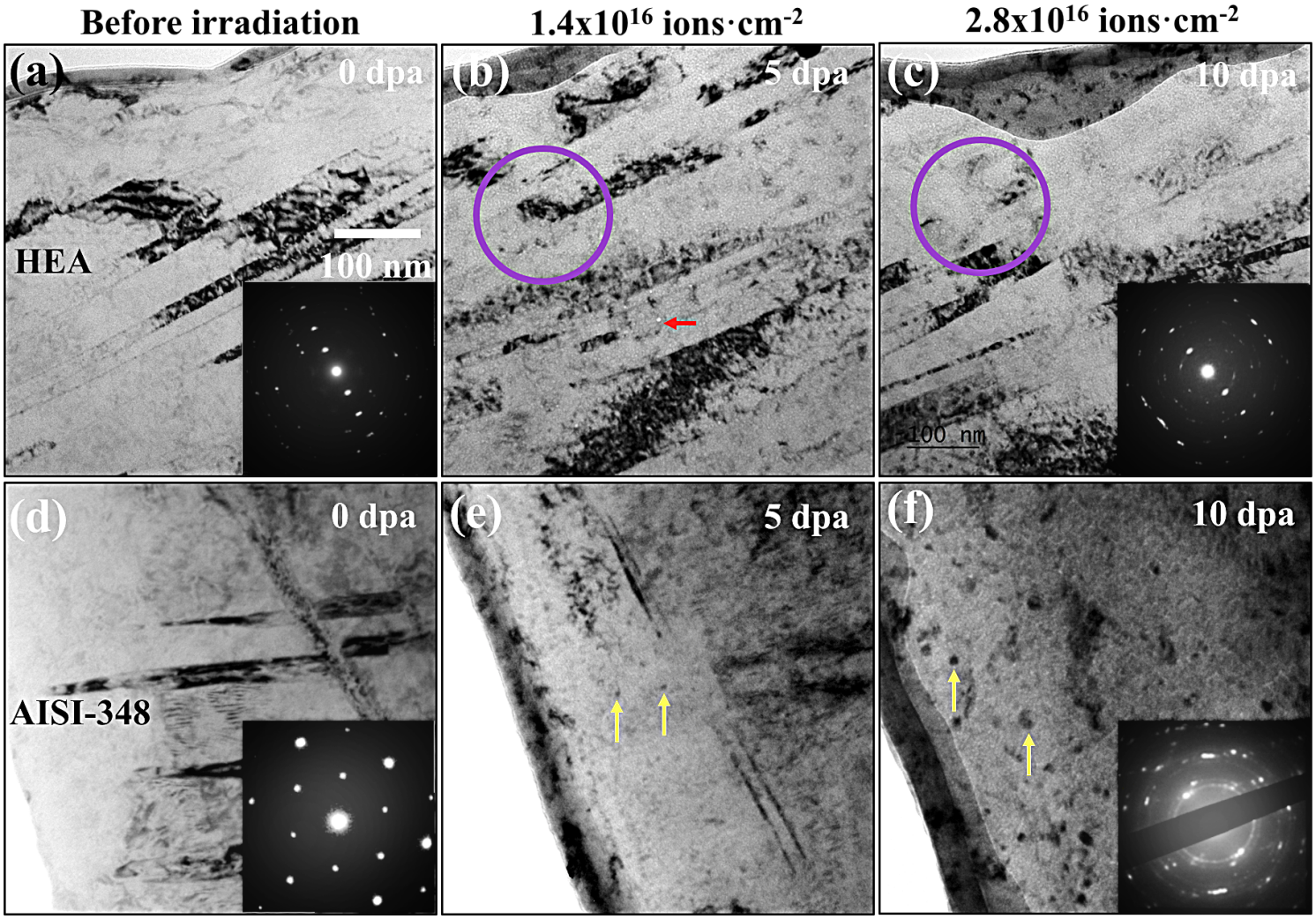

Figure 6.2: Microstructural evolution of the (a–c) FeCrMnNi HEA and (d–f) the AISI-348 steel under low-energy heavy ion irradiation at 293 K. Notes: scale bar in (a) applies to all micrographs in the figure. All micrographs were underfocused (≈1000 nm) and the contrast of micrographs (d–f) was slightly enhanced. The purple circles in figures (b–c) show the annihilation of black-dots in the FeCrMnNi HEA and the yellow arrows in figures (e–f) show the nucleation and evolution of precipitates in the AISI-348 steel.

absent at the higher dose, suggesting recombination/annihilation. The red arrow in figure 6.2(b) shows a bright Xe bubble at 5 dpa (in underfocus) that was annihilated upon increasing the dose.

At the end of the experiment, at a fluence of 5.7×10^{16} ions·cm^{-2} (21 dpa), precipitation was also observed around Nb(C,N) particles as shown in the BFTEM micrograph in figure 6.3(c). Apart from Xe bubbles – that have not grown significantly – the matrix of the FeCrMnNi HEA was free of precipitation at a dose of 21 dpa as shown in the micrographs in figures 6.3(a–b). In bright-field, annealing twins are observed with strong black contrast, but this condition was pre-existent at the beginning of the experiments as shown in figure 6.2(a).

6.2.2.2 Irradiations at 573 K

The microstructural evolution of the FeCrMnNi HEA and the AISI-348 steel under 30 keV Xe ion irradiation at 573 K is shown in figure 6.4. It should be noted that this is approximately the operating temperature of a commercial LWR.

In the high-entropy alloy matrix phase, Xe bubbles were observed at 8 dpa and had not grown significantly at 10 dpa as shown in the BFTEM micrographs in figures 6.4(b) and 6.4(c). Diffraction pattern insets presented in figures 6.4(a) and 6.4(c) indicate that the HEA has its random single-phase solid-solution preserved at 8 dpa. Conversely, significant microstructural alterations can be seen in the austenitic stainless steel as shown in figure 6.4(d–f). At 8 dpa, black-spots and Xe bubbles were observed throughout the austenite phase as shown in figure 6.4(e). At 10 dpa, the Xe bubbles were considerably bigger in the regions close to the edge of the FIB lamella as shown in the micrograph 6.4(f). Although the lamella slightly bent during the ion irradiation experiment, the diffraction pattern inset in figure 6.4(f) shows the presence of rings that were absent at the beginning of the experiment, which indicates that the austenite phase decomposed into precipitates under these experimental conditions at 573 K. These rings resemble an amorphous pattern, but this is more likely to be associated with the reduced size of precipitates (or even clusters) under the present irradiation conditions than with the amorphisation of the matrix and could even result from self-passivation (as the experiments are performed in a high vacuum level of $\approx1\times10^{-7}$ Pa.)

In the AISI-348 steel, matrix phase decomposition was also observed in a different area around 19 dpa as shown in figure 6.5(b) in which the DP (inset) now shows characteristic Debye-Scherrer rings. At a higher dose, the FeCrMnNi HEA was observed to be stable as shown in micrograph 6.5(a). Precipitates and black-spots were observed at 21 dpa in the AISI-348 steel and also remained stable during the irradiation to higher doses as assessed by an exploratory experiment the results of which are shown in figure 6.5(c–d): the precipitates were responsive to defocus and

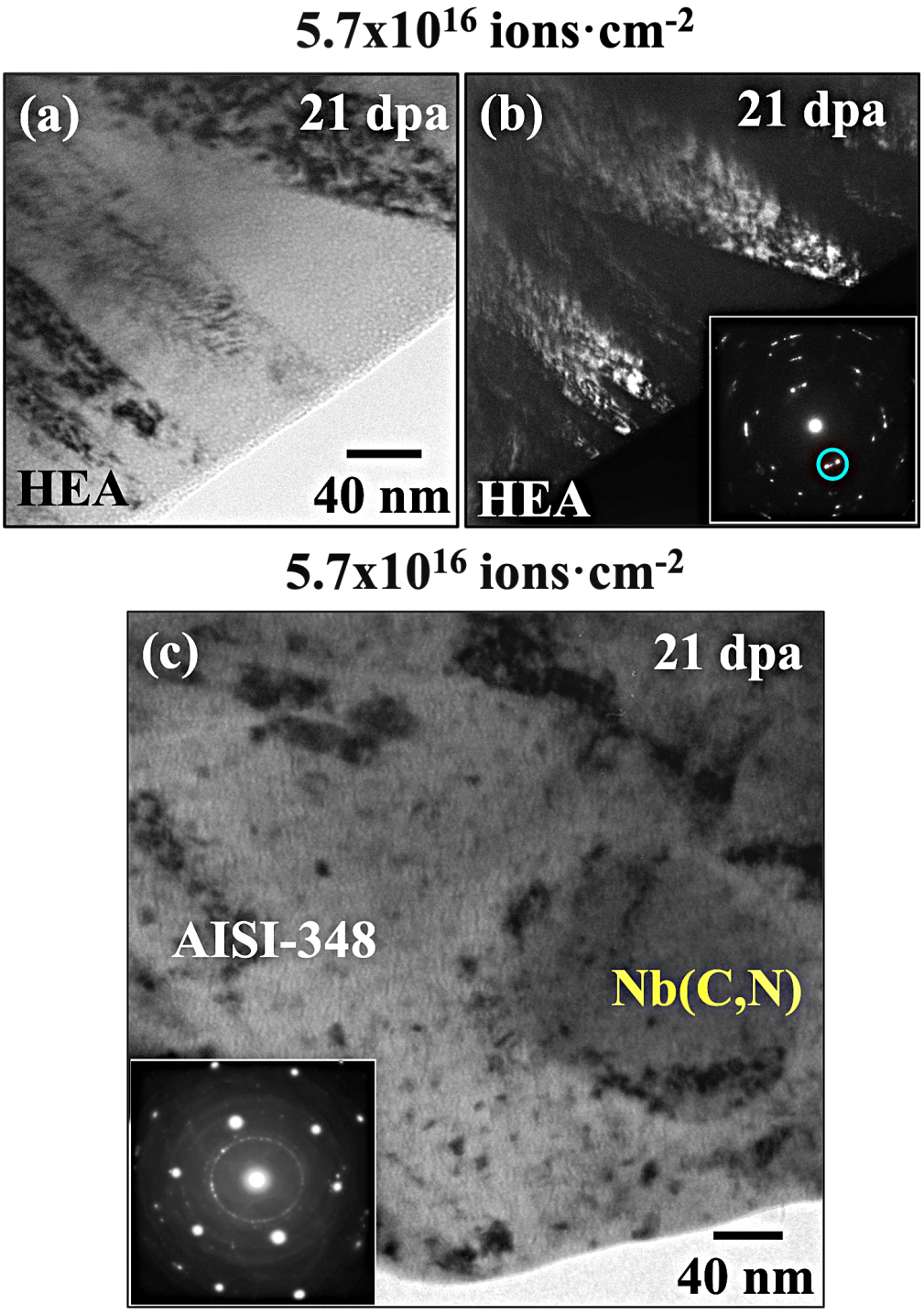

Figure 6.3: Low-energy heavy ion irradiation at 293 K to higher doses, 21 dpa, show that (c) precipitates are observed in the matrix phase of the AISI-348 whilst (a-b) the HEA matrix is still single-phase with the twins (satellite spots in the DP at (a) highlighted with a blue circle) which are better visualised in the DFTEM micrograph (b). Note: all micrographs were underfocused (≈1000 nm).

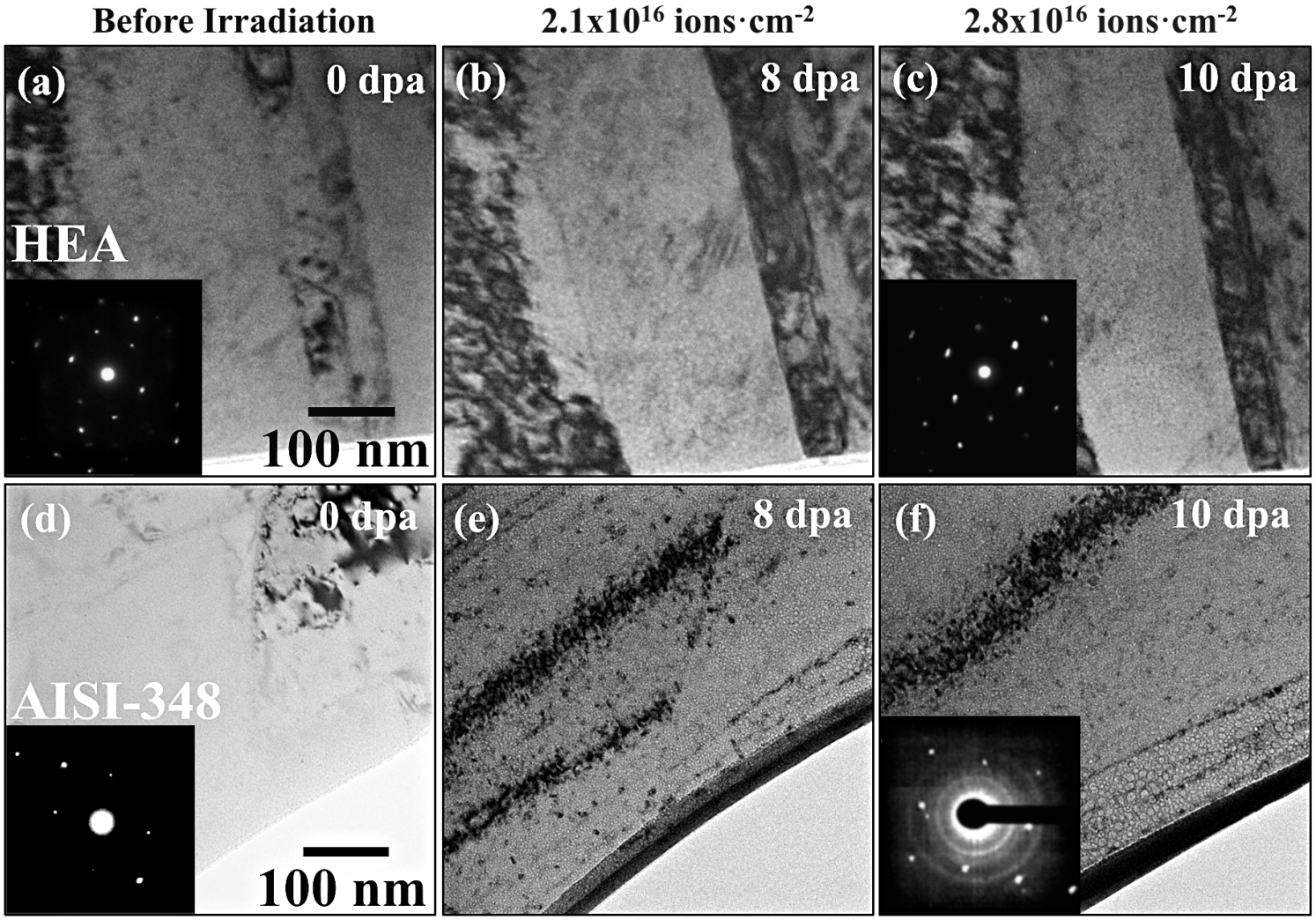

Figure 6.4: Microstructural evolution of (a–c) the FeCrMnNi HEA and (d–f) the AISI-348 under low-energy heavy ion irradiation at 573 K. Note: scale bar in (a) applies to all micrographs in the figure. Images are underfocused (≈1000 nm).

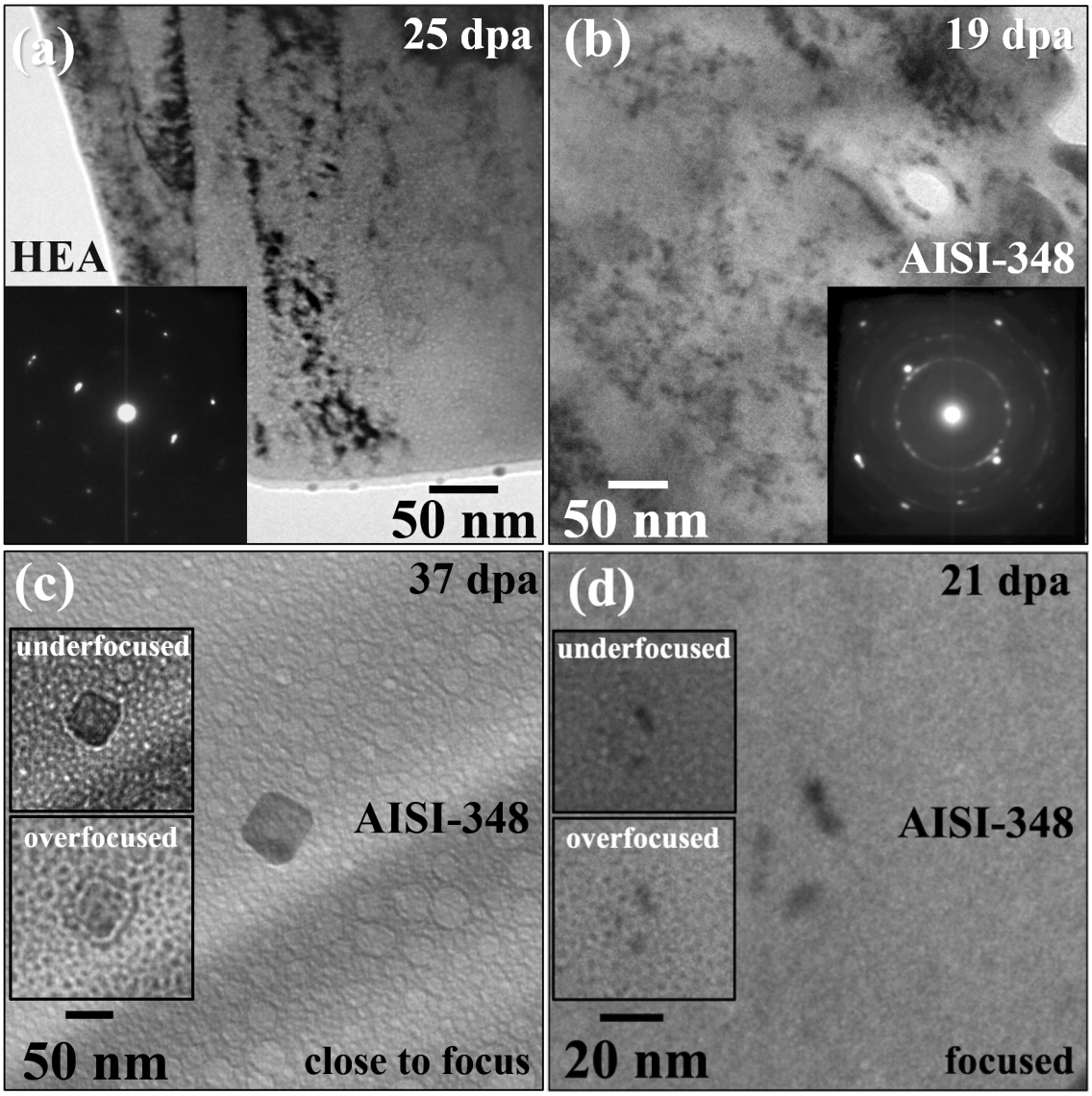

Figure 6.5: Low-energy heavy ion irradiations at 573 K, showing the microstructure of (a) the FeCrMnNi HEA with some Xe bubbles at higher fluences, 6.8×10^{16} ions·cm^{-2} (25 dpa) and (b) the AISI-348 steel showing that the austenite phase was decomposed at 5.1×10^{16} ions·cm^{-2} (19 dpa). (c) At a fluence of 1.0×10^{17} ions·cm^{-2} (37 dpa), bubble growth and precipitation are observed to occur in the AISI-348 steel and (d) black-spots evolve to a maximum size of 20 nm (at 21 dpa). The same was not observed to occur in the FeCrMnNi HEA. Note: (a–b) are underfocused to ≈1000 nm; the insets in (c) and (d) are defocused by ± 300 nm and ± 1000 nm, respectively.

generated Fresnel contrast as shown in the insets in the figure 6.5(c) whereas the contrast of black-spots did not change by defocusing the objective lens as shown in figure 6.5(d). This procedure has been used to distinguish the precipitates and black-spots at lower magnifications.

6.2.2.3 Irradiations at 873 K

Irradiations at 873 K were carried out in the FeCrMnNi HEA and the AISI-348 steel to the same doses and their microstructural evolution is exhibited in figure 6.6. Samples were held at 873 K for 30 minutes before irradiation and no microstructural changes were observed as a result of this thermal anneal. Radiation effects were detected and monitored *in situ* within the TEM from the very beginning of the irradiation experiment.

With respect to the FeCrMnNi HEA, Xe bubbles became noticeable at doses of around 2 dpa as shown in figure 6.6(b). Upon increasing the dose, craters were observed to form in the HEA as shown in figure 6.6(d) as a direct result of Xe bubble growth. Due to similarities in the TEM contrast from craters and bubbles, it was not possible to know whether contrast resulted from a region without Xe, a large Xe bubble or even an area with solute segregation assisted by irradiation. As shown in the inset diffraction patterns (figures 6.6a and 6.6d), taken before irradiation and at 10 dpa, the single-phase solid solution was observed to be decomposed as indicated by the presence of Debye-Scherrer rings.

Xe bubbles are noticeable in the AISI-348 also at doses around 2 dpa as can be seen in figure 6.6(d). For doses higher than 5 dpa, the nucleation and growth of Xe bubbles resulted in the formation of craters (or possibly radiation-induced segregation areas as mentioned in the paragraph above). It is worth noting that such craters were also observed in the FeCrMnNi HEA at around the same doses. By monitoring the diffraction pattern before (figure 6.6(e)) and after the irradiation (figure 6.6(h)), the formation of Debye-Scherrer rings can be seen at 10 dpa and suggests decomposition of the austenite matrix.

At higher doses, 15 dpa, microstructures of the AISI-348 steel and the FeCrMnNi HEA were also very similar. The presence of dark grey areas as exhibited in figure 6.7(a–d) indicates that radiation induced segregation has occurred during irradiation and this can be further confirmed by analysing the diffraction patterns inset in the figure 6.7(a) and (c): the austenite of the AISI-348 steel and the random solid solution of the FeCrMnNi HEA exhibited rings which indicate the presence of secondary phases, thus both initial microstructures are prone to decompose at doses higher than 10 dpa for irradiation temperatures of 873 K.

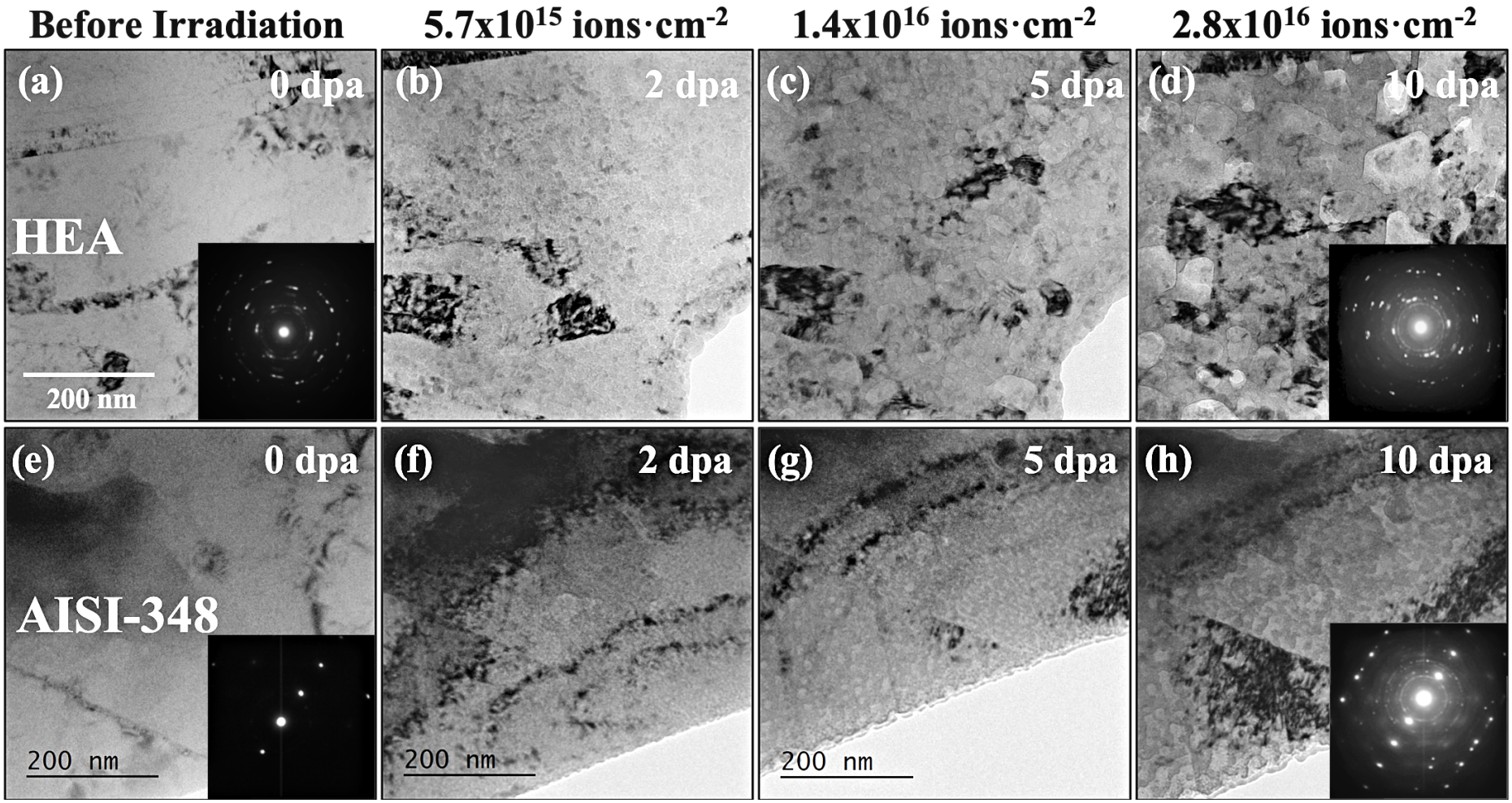

Figure 6.6: Microstructural evolution of (a–d) the FeCrMnNi HEA and (e–h) the AISI-348 steel under low-energy heavy ion irradiation at 873 K. Note: scale bar in (a) applies to all micrographs in the figure and all images are underfocused by ≈1000 nm.

6.2.2.4 Irradiations at 1073 K

At high temperatures, the FeCrMnNi HEA samples were observed to be destroyed within the TEM as can seen in figure 6.8. This effect starts at the regions close to the edge of the TEM lamella and it rapidly continues into the bulk of the specimen. The sample loses its electron-transparency after 10 minutes held at 1073 K. This effect has been observed to occur in all the TEM lamellae prepared from this alloy for irradiation at 1073 K. Due to this effect, it was impossible to assess the effects of radiation in this HEA at 1073 K. It must be said that such effect has been observed in our research group in other materials including refractory metals such as tungsten. However, to date, the cause of this effect remains unknown, although speculations

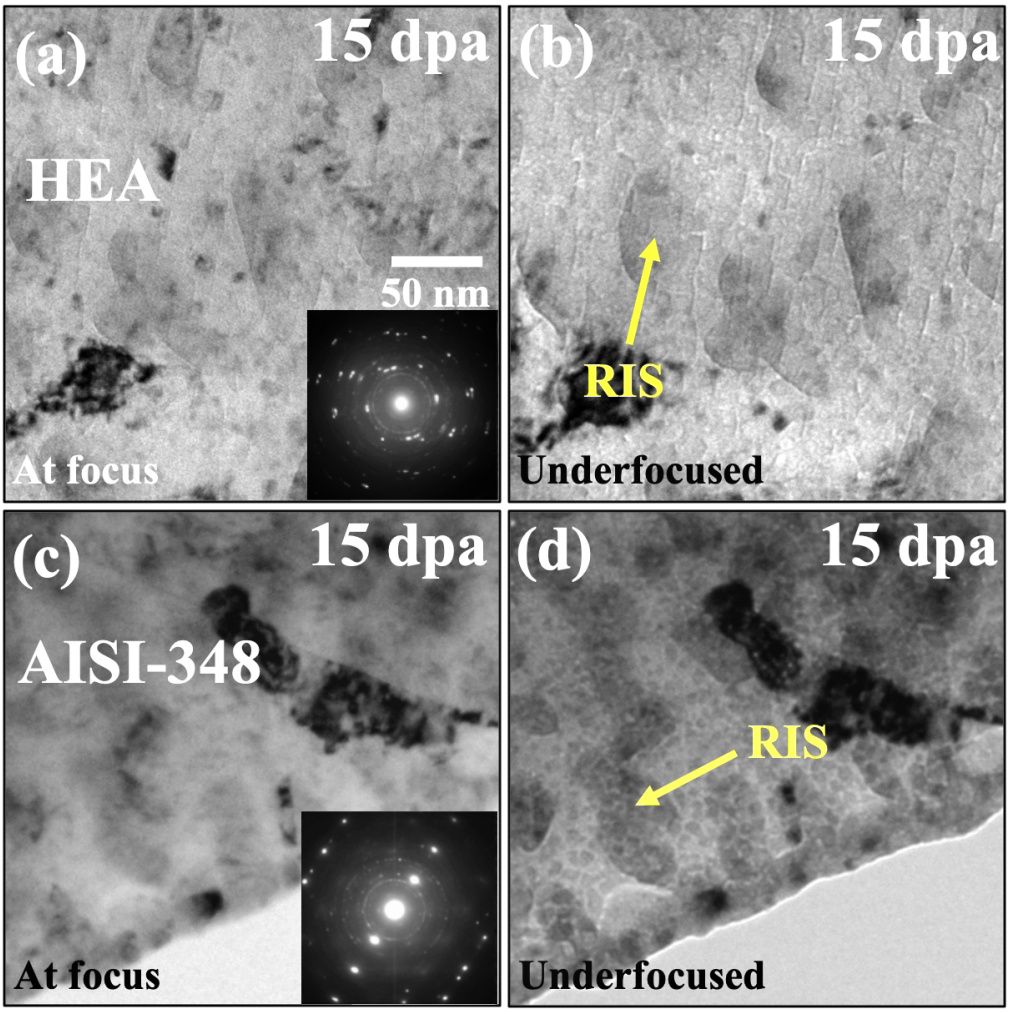

Figure 6.7: The microstructures of (a–b) the FeCrMnNi HEA and (c–d) the AISI-348 steel irradiated to 4.2×10^{16} ions·cm^{-2} (15 dpa) at 873 K. Dark grey zones have been observed to form in both alloys at these dose levels which suggests the occurrence of RIS and the formation of precipitates. Note: The underfocused micrographs (b) and (c) were taken with an underfocus of ≈1000 nm and 1600 nm, respectively, and the scale marker in (a) applies to all micrographs in the figure. The arrows indicate the areas of RIS.

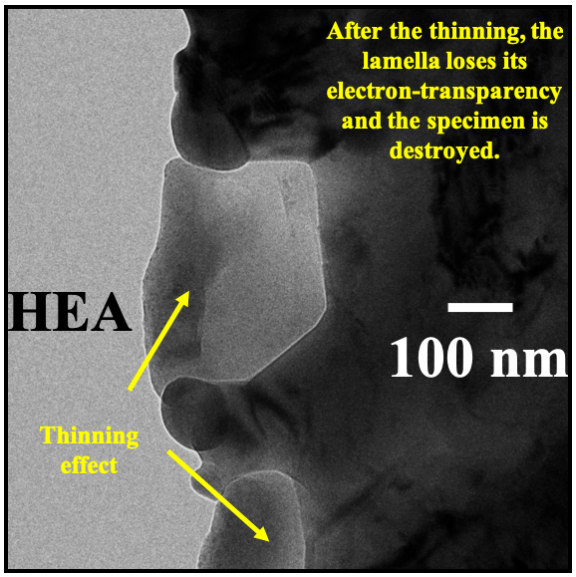

Figure 6.8: The microstructure of the FeCrMnNi HEA after annealing at 1073 K for 10 minutes.

lie in a thin film effect.

Conversely, the AISI-348 was held at 1073 K for approximately 30 minutes and before irradiation no changes were observed as exhibited in the figure 6.9(a). The microstructural evolution of the austenite phase under 30 keV Xe ion irradiation is shown in figure 6.9(b–d): at doses around 3 dpa, a new phase was observed to form under irradiation and its contrast was brighter than the austenite phase. The new phase grew as the dose increased and it ceased to grow if the ion beam was stopped.

Post-irradiation TEM characterisation has indicated that this new phase formed throughout the austenite matrix phase as shown in the BFTEM low-magnification micrograph in figure 6.10(a). Crystallographic indexing using data available in literature [454] with the experimental diffraction pattern obtained using the SAED aperture around this new phase as shown in figures 6.10(c-d), indicated that the new phase has a BCC crystal structure. At higher magnifications, Xe bubbles and nanometre-sized precipitates are also observed within the austenite matrix and in the newly formed phase as shown in figure 6.10(b). Additionally, the diffraction pattern shown in figure 6.10(d) has reflections that were shown later – in dark-field of a different orientation – to be from the precipitates (figure 6.17).

The quantitative data shown in figures 6.11(a) and 6.11(b) represent the average sizes (diameter) of this new phase and the average volumetric density as a function of the irradiation dose, respectively. The density reduced with increasing size of the phase. The results obtained with the austenitic stainless steel 348 are compared with data available in the literature for neutron-irradiated FeCrAl ferritic steels investigated after irradiation with atom probe tomography [455]. It can be seen that for neutron irradiations of a ferritic matrix, the sizes of the Cr-rich precipitates (which

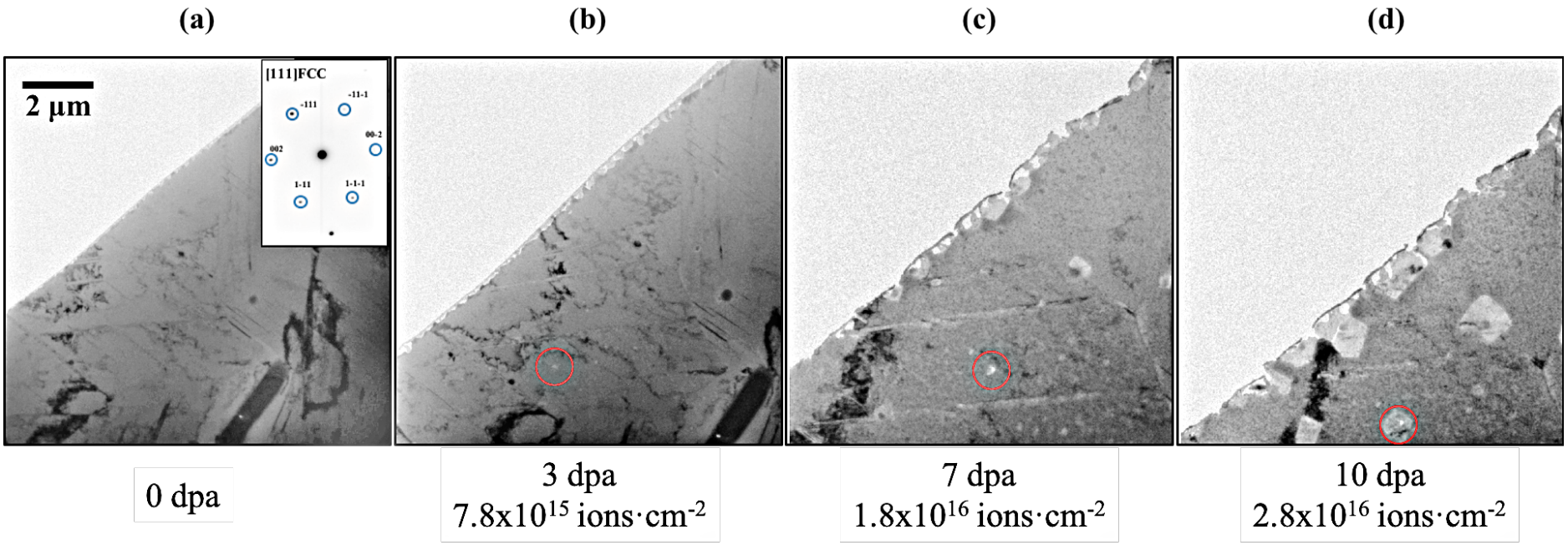

Figure 6.9: Low-magnification images of microstructural evolution of the austenite phase under 30 keV Xe irradiation at 1073 K. BFTEM micrograph shows (a) the microstructure after 30 minutes of annealing at 1073 K and (b–d) the subsequent microstructural evolution under irradiation up to 10 dpa. Note: the scale bar in (a) applies to all micrographs in the figure.

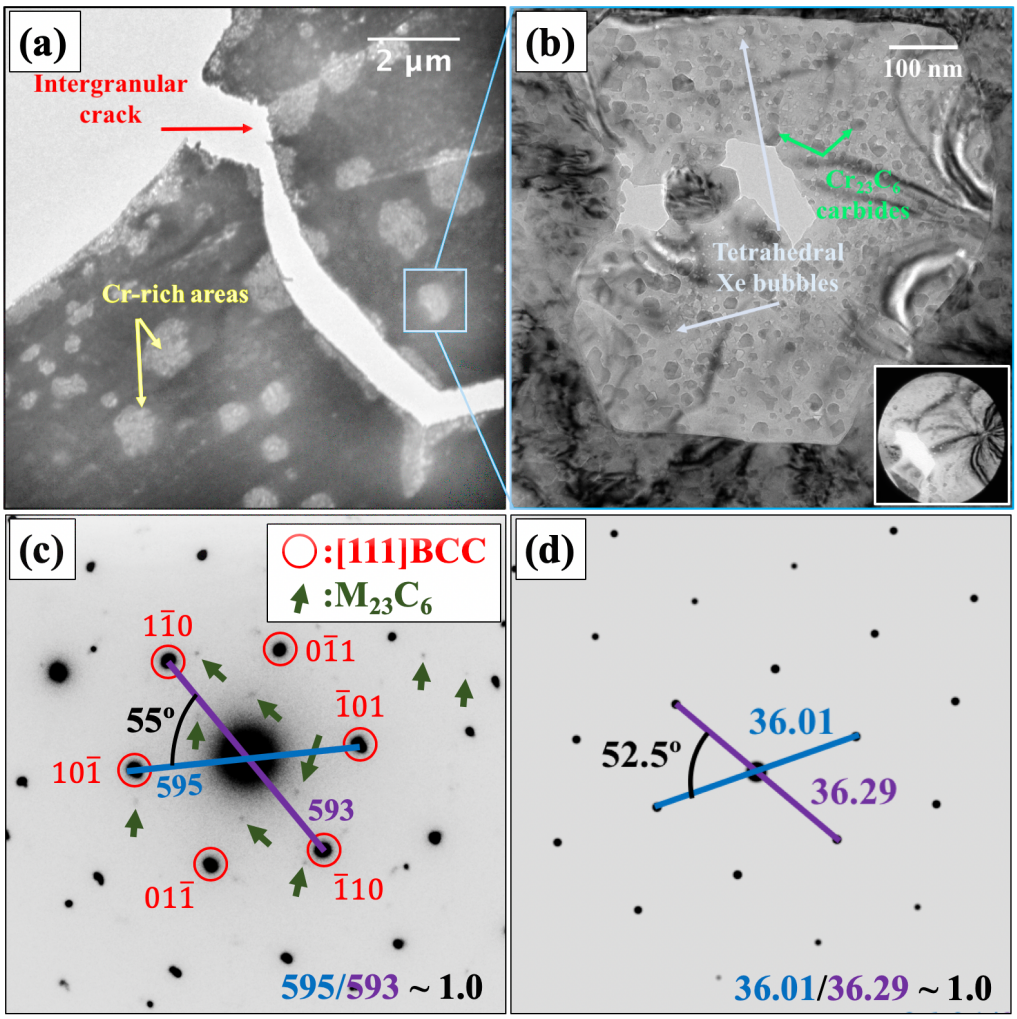

Figure 6.10: Post-irradiation screening of the AISI-348 steel after 1.3×10^{17} ions·cm^{-2} (46 dpa) at 1073 K: (a) and (b) are low and high-magnifications BFTEM micrographs, respectively, (c) selected-area diffraction pattern corresponding to the inset shown in (b) and (d) is the simulated DP from CrystalMaker with the Badjuk *et al.* dataset [454] used to index the new phase that formed under the present irradiation conditions.

will be later defined as α'-phase) are significantly smaller when compared with the heavy ion irradiations reported in this work for an austenitic steel. Similarly, the reduced sizes result into higher volumetric densities. In the case of the Fe-15Cr-Al, the size of the precipitates increased with the dose and a saturation trend for doses higher than 5 dpa was observed. Such increase in size resulted in a decrease in the volumetric densities upon increasing the dose. This trend was observed for the heavy ion irradiations of the AISI-348 steel, but not for the neutron irradiations of the Fe-10Cr-Al in which the sizes are directly proportional to the densities: Briggs *et al.* [455] suggested that for this latter case, the alloy with 10%-Cr is still in the nucleation and growth regime at around 7 dpa.

In order to further investigate the accelerated ageing, manifested by the forma-

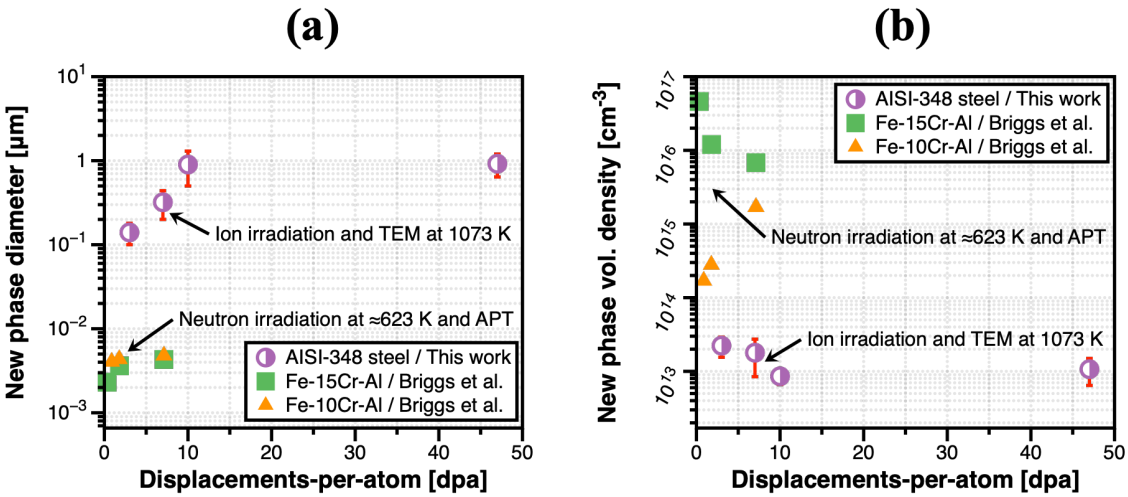

Figure 6.11: Quantitative data for the new BCC phase (α'-phase) that nucleated and grew in the AISI-348 steel matrix under 30 keV Xe ion irradiation at 1073 K showing: (a) the average diameter and (b) volumetric density. Note: results are compared with atom probe tomography data published by Briggs *et al.* [455] on neutron-irradiated FeCrAl alloys (composition in wt.%); error in sizes and density were not provided (or were to small to be detected in the plots) by Briggs *et al.* in their paper.

tion of nano-precipitates under irradiation, the same irradiation conditions reported above – *i.e.* 30 keV Xe at 1073 K – were used in a different experiment in a pristine sample monitored at a higher magnification. In the set of sequential *in situ* TEM ion irradiation micrographs shown in figure 6.12, the nucleation and growth of these nanometre-sized precipitates was observed. Monitoring an area closer to the edge of the TEM lamellae, the same experiment also shows a comparison between the microstructure of the AISI-348 prior to irradiation and after annealing for 20 min at 1073 K (figure 6.13(a)) with the same area after 17 dpa of 30 keV Xe ion irradiation (figure 6.13(b)).

Quantitative data extracted from the micrographs presented in figures 6.12 and 6.13 revealed that the size of the precipitates increased linearly with dose up to 55 nm at 7.3 dpa and remained constant around this value up to 17 dpa, but their volumetric density approached to saturation at doses around 5 dpa. These results are shown in figure 6.14(a-b). Such quantitative data is compared with data available in the literature for *ex situ* TEM ion irradiation using a 120 keV Ar beam at 823 K in the austenitic stainless steel HR3C (Fe-25Cr-20Ni in wt.% with smaller additions of Nb and N) reported in work performed by Jin *et al.* [456]. In the latter case, bulk specimens of HR3C steel were irradiated and post-irradiation characterisation at different doses revealed that the growth behaviour was approximately linear; however, the size of these nanometre-sized precipitates was smaller (≈10 nm at around 30 dpa) than in the AISI-348 case. With respect to the volumetric density

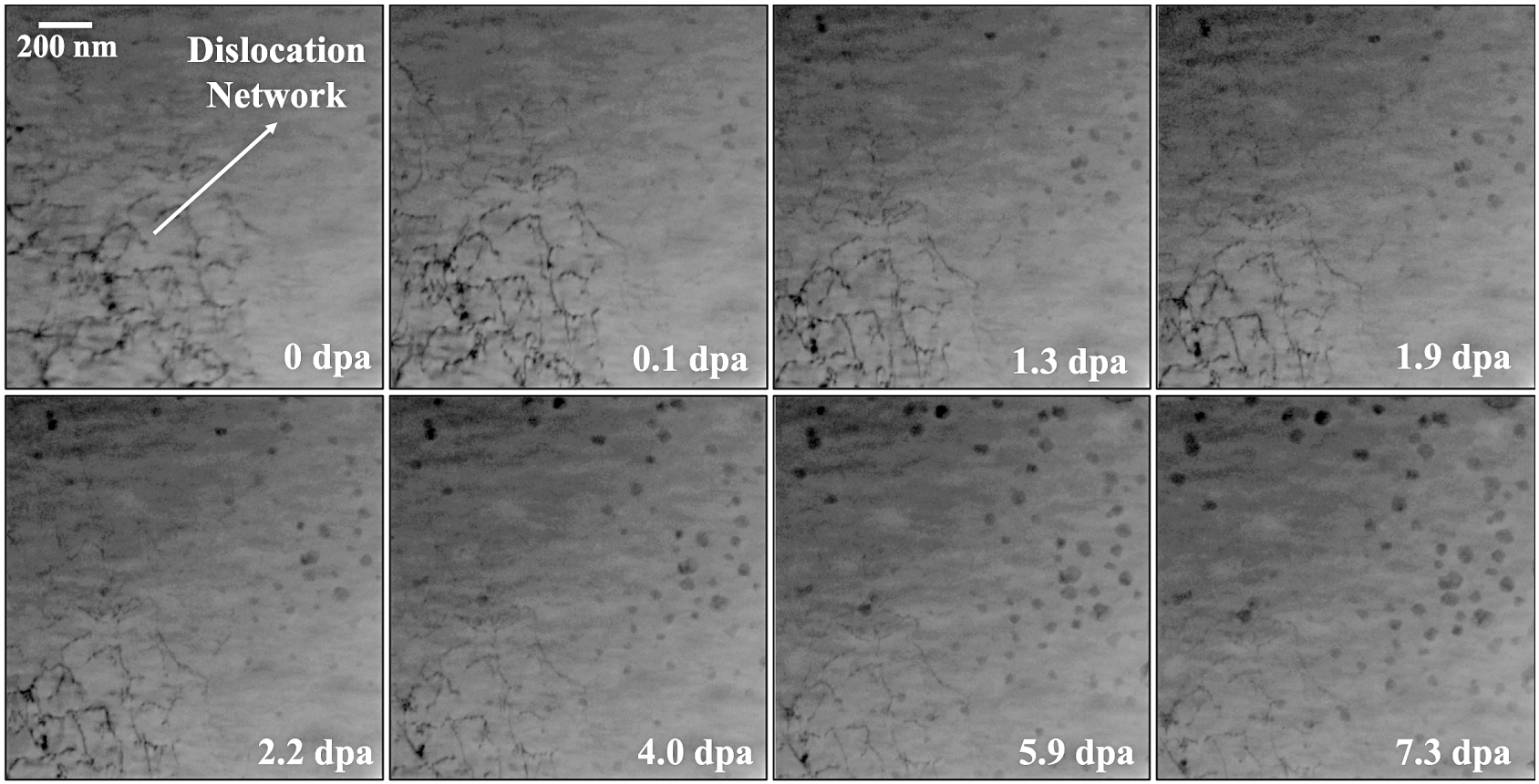

Figure 6.12: A set of sequential BFTEM micrographs showing the real-time evolution of nanometre-sized precipitates in the austenite matrix of the AISI-348 steel at 1073 K. Note: the scale bar in the micrograph at 0 dpa applies to all images in the figure.

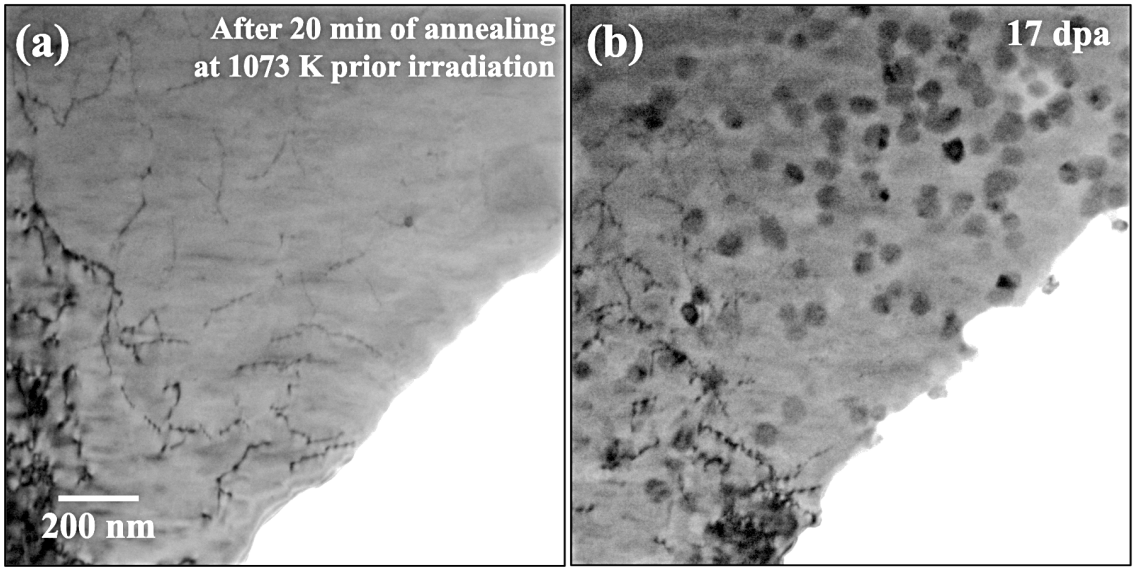

Figure 6.13: Formation of nanometre-sized precipitates in the AISI-348 steel before irradiation and after annealing at 1073 K (a) and after 30 keV Xe irradiation up to 17 dpa at 1073 K (b). Note: The scale bar in (a) also applies to (b).

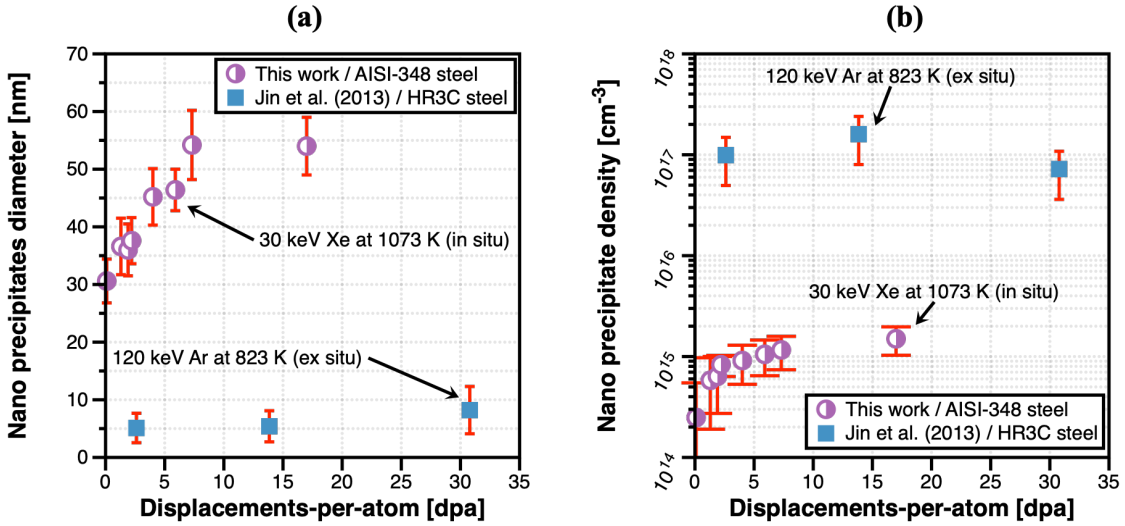

Figure 6.14: (a) Average precipitate diameter and (b) average volumetric density as a function of the irradiated dose for accelerated ageing due to heavy ion irradiation in two austenitic stainless steels: the AISI-348 steel (this work) monitored *in situ* within the TEM during irradiation and HR3C steel (Jin *et al.* [456]) investigated with ion irradiation followed by *ex situ* TEM.

of precipitates, the data obtained by Jin *et al.* [456] showed larger values (by two orders of magnitude) than the experiments reported in this thesis with 30 keV Xe ions in the AISI-348 steel. It should be noted that these authors have not reported the thickness of the TEM lamellae that they used to calculate the volumetric density of precipitates: in the case of the AISI-348, the thickness was ≈70 nm.

Although this is a comparison between two different austenitic stainless steels and two different irradiation techniques, the results indicate that in the case of irradiations conducted in electron-transparent lamellae *in situ* in the TEM, larger sizes of precipitates led to smaller volumetric densities whilst heavy ion irradiation in a bulk sample suggested that smaller sizes (below 10 nm) led to higher areal densities. Larger precipitate sizes observed in the AISI-348 steel at lower doses compared with the bulk HR3C steel can also suggest that the accelerating ageing effect may be faster in the former, possibly due to the irradiation conditions: higher irradiation temperature and heavier ions.

So far, the experiments using the *in situ* TEM heavy ion irradiation technique at 1073 K in the AISI-348 steel have revealed the formation of a new BCC phase and nanometre-sized precipitates. Analytical STEM-EDX characterisation was performed in order to qualitatively determine the composition of the new BCC phase as well as to assess the physical nature of the precipitates that were observed to form at 1073 K, and also during irradiation at all the temperatures studied in this chapter.

The set of STEM-EDX low-magnification micrographs presented in figure 6.15 show that the new BCC phase (figure 6.10(a–b)) is Cr-rich and Fe-depleted relative to the austenite matrix. It also shows that it has small additions of Ni, Mn and C. Therefore, this indicates that this could be the Cr-rich α'-phase that can form in austenitic stainless steels under specific conditions that will be later discussed.

At higher magnification and preferentially around the Nb(C,N) nanoparticles within the austenite phase, nanometre-sized precipitates are also observed as shown in figure 6.16. These spectral images show that such precipitates are primarily Cr- and Mn-rich. Carbon shows a build-up around the Nb(C,N) nanoparticle, but due to EDX limitations the degree of delineation could not easily be detected. When the irradiation temperature is lower than 1073 K, the precipitates do not grow significantly, thus the spots will tend form characteristic Debye-Scherrer diffraction rings. This makes it harder to carry out crystallographic identification as they may lead also to the formation of rings that resemble amorphous material due to their reduced sizes, like the diffraction pattern of the AISI-348 at 10 dpa during irradiations at 573 K as shown in figure 6.4(f).

The procedure that was used to characterise the nanometre-sized precipitates in this thesis is shown in figure 6.17(a–b). Upon growth under irradiation at higher

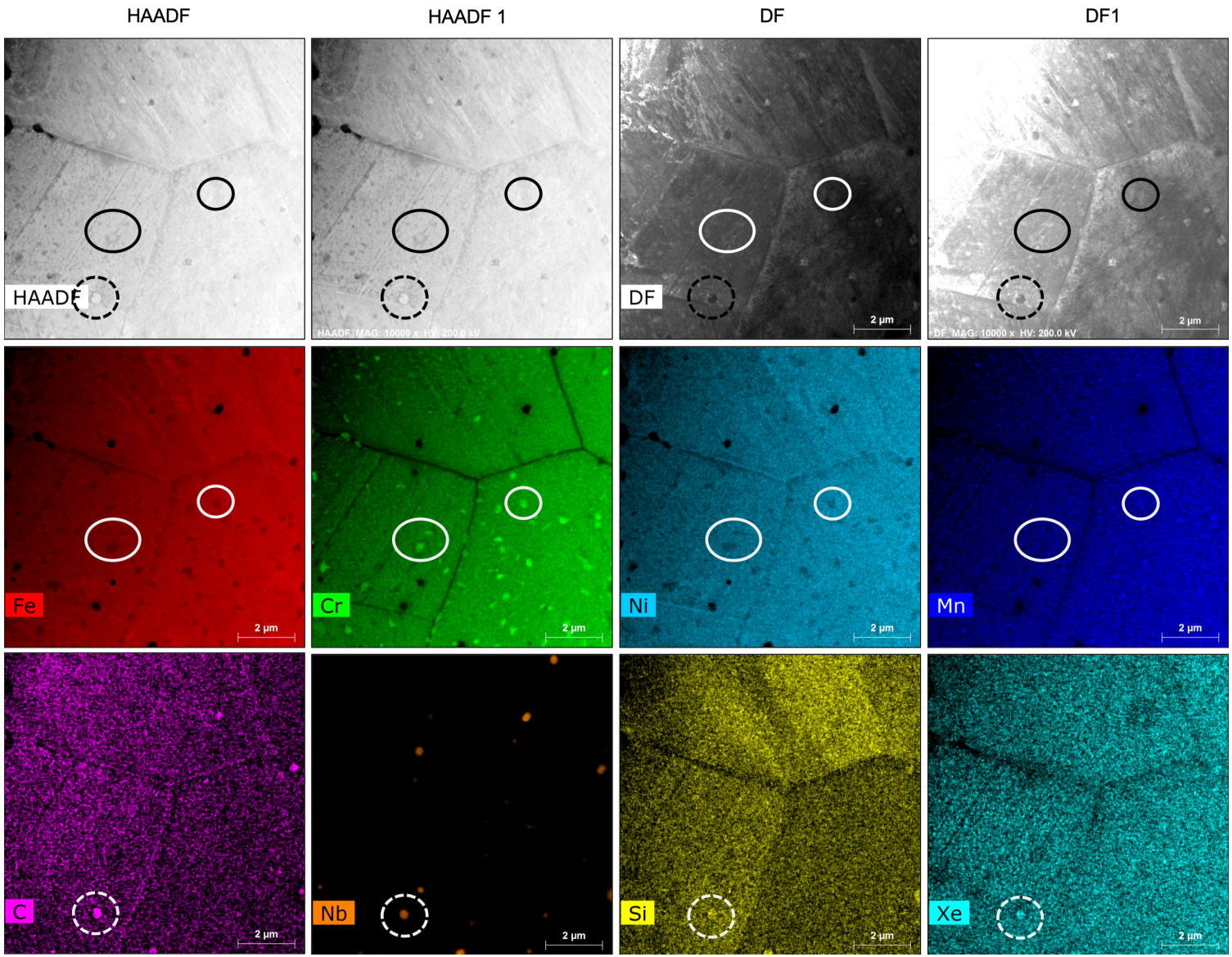

Figure 6.15: Low-magnification STEM-EDX mapping of the AISI-348 steel irradiated to 1.3×10^{17} ions·cm^{-2} (46 dpa) at 1073 K. Note: the solid circles show the α'-phase and the dashed circles show the Nb(C,N) nanoparticles.

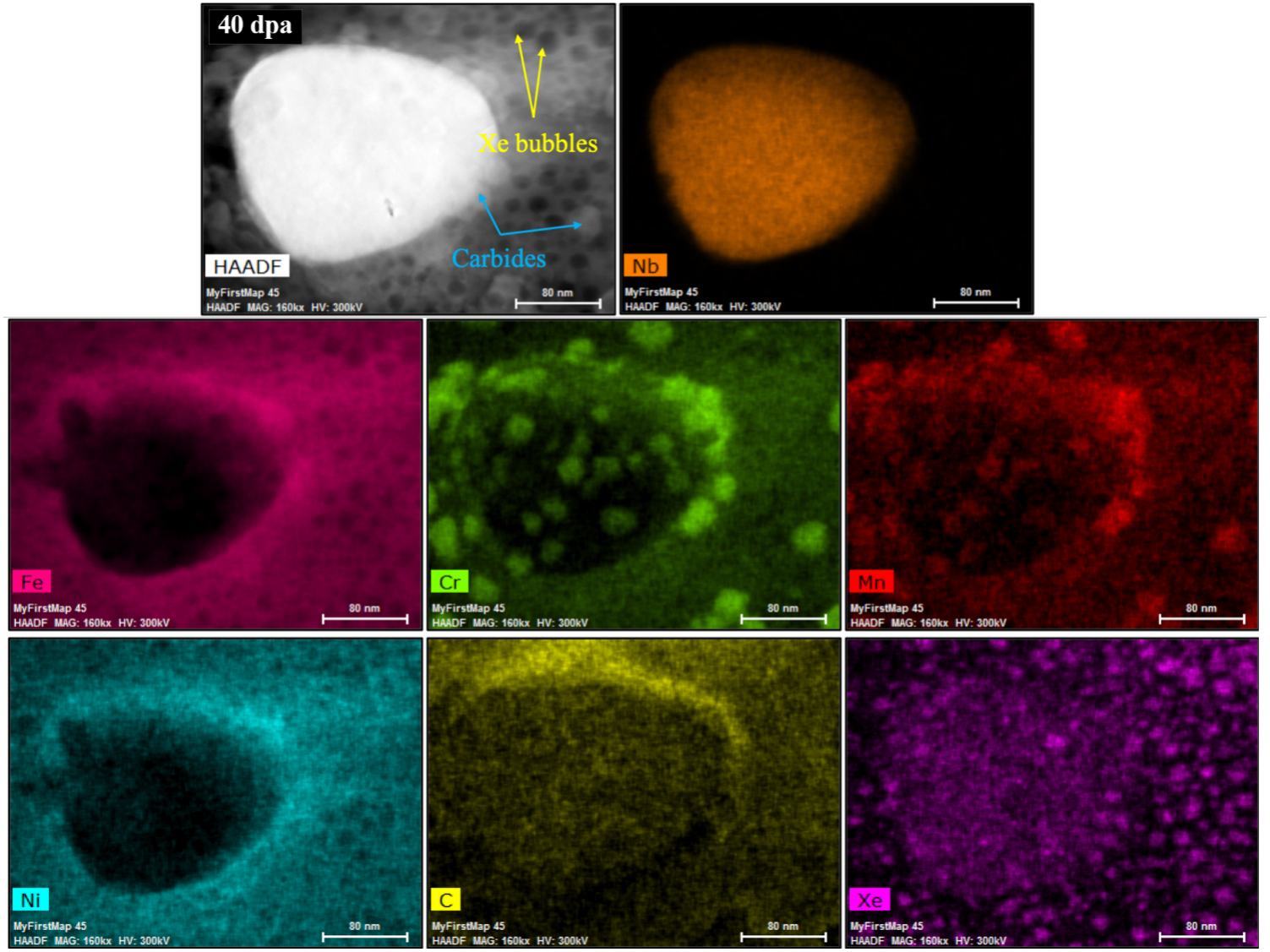

Figure 6.16: High-magnification STEM-EDX mapping of the AISI-348 irradiated to 1.1×10^{17} ions·cm^{-2} (40 dpa) at 1073 K. RIP occurs in the austenite matrix and also around the Nb(C,N) nanoparticles. The size of the precipitates is around 40 nm.

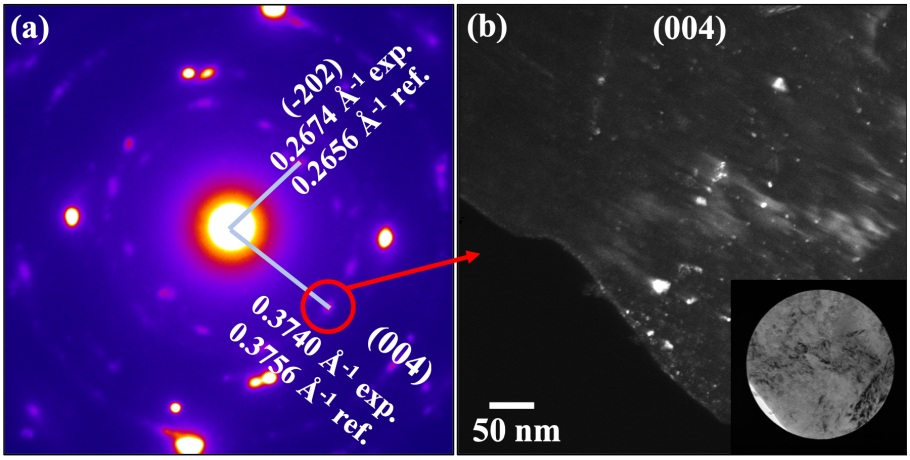

Figure 6.17: TEM characterisation of the $M_{23}C_6$ precipitates: the micrograph (a) is a selected-area diffraction pattern taken from the area shown in the inset in (b) which is a DFTEM micrograph using the (004) reflection. The fluence was around of 1.3×10^{17} ions·cm^{-2} (46 dpa).

temperatures, the spots are observed in the DP and can be clearly distinguished from the parent phase. As shown in figure 6.17(b), DFTEM is used to distinguish the reflections from the precipitates and the austenite. Upon the confirmation that a certain reflection in the DP belongs to the precipitates, the reciprocal space distances between this reflection and the transmitted beam are measured using ImageJ and the values compared with reference crystallographic data for $M_{23}C_6$ (known as the τ-carbide) [456, 457]. The deviation from the reference values is less than 0.18%. These precipitates were thus identified to be $M_{23}C_6$ where M is the major metal solute (Fe, Cr, Mn and/or Ni), in this case mainly Cr and Mn, and C the minor solute and their crystal structure is FCC. In combination with previous reports in the literature of austenitic stainless steel of this grade in which precipitation was identified through XRD measurements after 80 hours of thermal annealing in the austenite phase [32], the STEM-EDX and conventional TEM characterisations of the irradiated AISI-348 steel at the temperature of 1073 K indicated that such nano-precipitation is accelerated under the irradiation conditions studied in this section.

The technique of multivariate statistical analysis (MVSA) discussed in section 3.6.3 was used to provide some quantitative analysis of the STEM-EDX spectral images shown in figure 6.15, in particular to reveal more details on the α'-phase. As mentioned in section 3.6.3, the application of MVSA to refine data from STEM-EDX data is useful to reveal the presence of different phases in the elemental maps as well as to detect, differentiate and identify which elements are found in these phases. After the irradiation (46 dpa), the results in figure 6.18 indicate that MVSA detected the depletion of Cr in the γ-Fe phase as well as the fact that the α'-phase is not pure Cr as reported for FeCr and FeCrAl steels [458, 459]. In addition to

the identification of the Cr-rich α'-phase and the depletion of Cr in the γ-Fe phase, the MVSA results also detected the presence of pre-existing Nb(C,N) nano-particles. From the MVSA analysis and also the TEM and STEM/EDX data presented in this section, the presence of twins in the AISI-348 steel may contribute as nucleation sites for the formation of the Cr-rich α'-phase under irradiation – as such twins are sinks for diffusing crystalline defects (solutes and vacancies) – but the majority of these irradiation-induced phases nucleated within the γ-Fe phase.

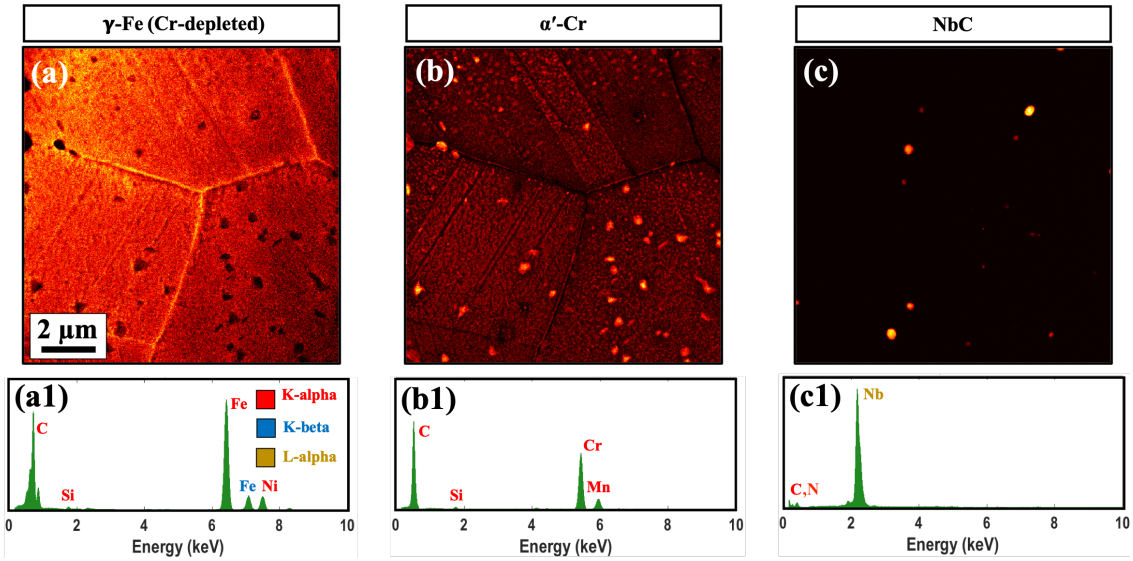

Figure 6.18: Post-irradiation MVSA analysis obtained from the STEM-EDX maps in figure 6.15 at 46 dpa. The amplitude map in (a) and its respective (a1) EDX spectrum represents the austenite phase depleted in Cr after irradiation. Similarly, the amplitude maps in (b) and (c) and their respective EDX spectra (b1) and (c1) show the Cr-rich α'-phase and the Nb(C,N) phase, the latter existing before irradiation.

Using the software ImageJ [460] it was possible to (roughly) estimate the Cr-rich α' and the τ-$M_{23}C_6$ phase fractions in terms of areas as shown in the set of micrographs in figure 6.19(a-d). This analysis results in an area fraction of 19.7% for the Cr-rich α' phase and 10.6% for the τ-$M_{23}C_6$ precipitates.

In summary, 30 keV Xe irradiation at 1073 K of the AISI-348 steel leads to the formation of a new phase, the Cr-rich α', and nanometre-sized τ-$M_{23}C_6$ precipitates. The formation of these phases under heavy ion irradiation as well as a detailed comparison of the results of low-energy heavy ion irradiation in the FeCrMnNi HEA and the AISI-348 steel will be discussed in the following subsection.

6.2.2.5 Discussion

6.2.2.5.1 Stability of the AISI-348 steel and the HEA matrix phases at low and moderate temperatures

Table 6.1 summarises the major radiation effects observed in the FeCrMnNi HEA

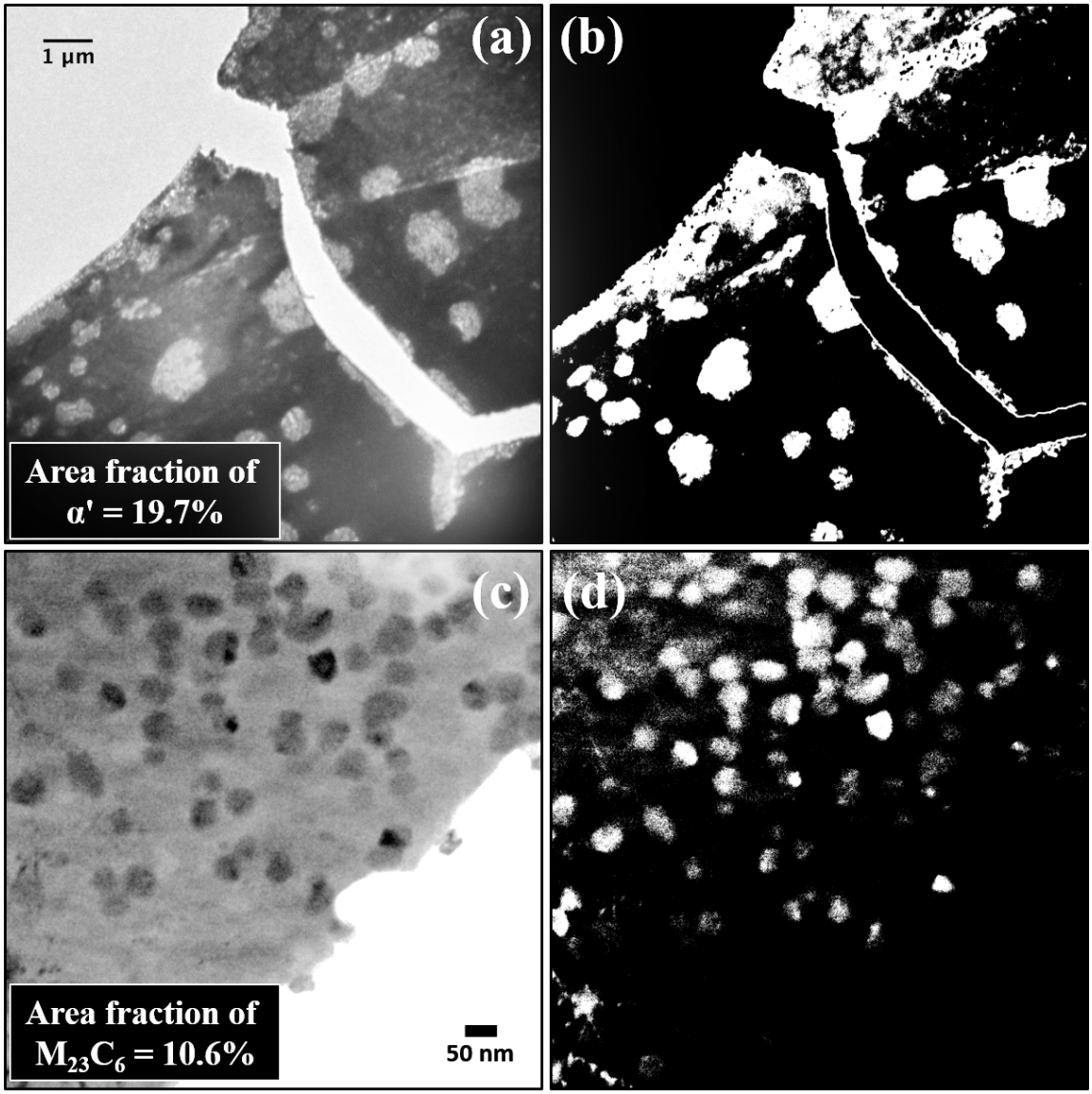

Figure 6.19: Estimation of area phase fractions for the (a-b) Cr-rich α' at 46 dpa and (c-d) τ-$M_{23}C_6$ precipitates at 17 dpa. Note: The micrographs (b) and (d) are the images treated (known as threshold images) with the ImageJ software to estimate the area phase fraction.

and in the AISI-348 steel when irradiated under similar conditions with low-energy heavy ions. At the lower temperatures of 298 and 573 K, the HEA matrix phase (the random solid solution) is retained after irradiation whereas the austenitic stainless steel suffers phase decomposition.

These results (and note that 573 K is close to the operational temperature of common LWRs) show that the FeCrMnNi HEA has superior radiation tolerance than its low-entropy counterpart, the austenitic stainless steel. Particularly, the retention of the matrix phase, *i.e.* the absence of precipitation and phase separation strongly indicates that the characteristic core-effects of high-entropy metallic alloys systems can be intrinsically related to a superior resistance to the deleterious effect of energetic particle exposure.

These experimental observations can be explained by using the concepts of phase stability from the thermodynamics of alloy systems. Regarding the FeCrMnNi HEA, the results from the last chapter were reproduced: at lower irradiation temperatures the high-entropy core effects manifest giving rise to higher phase stability under irradiation whilst precipitation was observed to occur in the AISI-348 steel under 134 keV Xe irradiation. This may be due to the sluggish diffusion of radiation-induced defects, thus reducing radiation damage effects, and providing better radiation resistance than the stainless steel. In this context such results indicate a link between thermodynamics of metallic alloys systems and radiation damage by showing that the elemental composition is a key parameter that can be possibly used to produce metallic alloys with superior radiation tolerance.

A dense collision cascade – as caused by the collision of 30 keV Xe ions with the FeCrMnNi HEA or the AISI-348 steel – can be understood as a fast phase transition with complex thermodynamics. The random lattice site occupancy, characteristic of HEAs and linked with the lattice distortion core-effect, has recently been associated with the creation of non-periodic fluctuations of the lattice potential resulting in modification of the atomic diffusion [461]. This will suppress defect generation during the collapse of the damage cascade. Immediately after the collapse of the cascade, the possible phase transition that the collisions could create in the microstructure of the HEA does not occur and the alloy is locally brought back to its initial state, *i.e.* the single-phase random solid solution. Recent interpretations in the literature suggest that this effect is similar to the magnetic frustration observed in ferromagnetic metallic systems [68], also similar to what happens in elemental metals.

In this way, in the low irradiation temperature regime (298–573 K), the direct comparison of the radiation effects in the HEA and its low-entropy counterpart (the steel) shows that the intrinsic properties of the HEA lattice are responsible for an enhancement of its radiation performance: *i.e.* a superior thermodynamic

Table 6.1: Low-energy heavy ion irradiation effects in the FeCrMnNi HEA and the AISI-348 (in the dose range 0-50 dpa)*.

$\mathbf{T}_{irr}$ **[K]**	**FeCrMnNi HEA**	**AISI-348**
298	- Stable matrix phase. - Xe bubbles: 2.9 nm.	- Matrix phase decomposed. - Xe bubbles: 2.1 nm.
573	- Stable matrix phase. - Black-spots. - Xe bubbles: 2.5 nm.	- Matrix phase decomposed - Black-spots - Xe bubbles: 3.4 nm in the matrix and 10-15 nm around Nb(C,N)/edges of sample.
873	- Matrix phase decomposed - Black-spots - Xe bubbles: 5-12 nm. - RIS.	- Matrix phase decomposed - Black-spots - Xe bubbles: 9-15 nm. - RIS.
1073	- Lamellae destroyed. - Experiments were not possible.	- RIS/RIP - Formation of the α' phase. - Precipitates were clearly defined. - Xe bubbles: tetragonal in the α' and spherical in the matrix.

*In this table, the average error in the bubbles-size measurements at 20 dpa is 10–15%.

stability will, therefore, result in an alloy microstructure that is capable of resisting the deleterious effect of energetic particle exposure when compared with another similar alloy of the same quaternary metallic system (Fe–Cr–Mn–Ni, but with non-equiatomic composition).

However, when the temperature increases to the range of 873–1073 K, the radiation effects in the two alloys become similar. At 873 K, the matrix phase of the FeCrMnNi HEA decomposed at doses around 10 dpa and as shown in figure 6.7, the alloys exhibited similar microstructures at doses around 15 dpa: dark zones observed in bright-field indicated the presence of precipitates as well as elemental segregated regions. At 1073 K the irradiation experiments could not be performed in the FeCrMnNi HEA due to the destruction (thickening) of the TEM lamellae during annealing (as shown in figure 6.8).

In the high temperature regime, this work research has shown that the high-entropy core effects play only a minor role in the radiation tolerance. As predicted by Zhang *et al.* [461] through *ab initio* calculations, the intrinsic diffusional characteristics of highly concentrated alloy systems diminishes at elevated temperatures. This has been confirmed in this present work by analysing the microstructure of the FeCrMnNi HEA under irradiation at the nanoscale *in situ* within the TEM. The differences between the behaviour at low and moderate temperatures with the irradiations at high temperatures support the conclusions of Zhang *et al.* [461]. The decrease of the attractive properties of HEA systems upon increasing the tempera-

ture can be viewed as a limiting factor for the application of these alloys in the next generation of nuclear reactors, which will generally operate at high temperatures ($T \geq$873 K).

Regarding the austenitic stainless steel, RIP was observed to occur at temperatures of 298, 573, 873 and 1073 K. In particular at 1073 K a new phase was observed to form during irradiation – the α' phase – which was characterised as having a BCC crystal structure with an enrichment of Cr and a depletion of Fe. These experimental results obtained with the AISI-348 deserve further attention and explanation.

6.2.2.5.2 Radiation-induced precipitation and formation of the α' phase and accelerated aging at high temperatures

Aiming at understanding the complex phase relationships in the AISI-348 steel under irradiation, a set of thermodynamic calculations with the software Thermo-calc® has been performed. These calculations are based on the CALPHAD method and the details on how such calculations are performed were provided in section 3.7. Additionally, it is well known that the CALPHAD method (used by Thermo-calc®) works with virtual phases [462] and, in this way, a solution is calculated even when the phase is not stable: in the case of the α', for example, a phase that is stable only at low temperatures.

The results from the thermodynamic calculation with Thermo-calc® are shown in figure 6.20. The phase diagram presented in figure 6.20(a) shows the phase molar fractions as a function of temperature. It can be seen that the α'-phase is stable up to around 800 K and it can be found in equilibrium with the austenite, the ferrite and other minority phases. In order to better resolve the temperature range where the α'-phase is observed to be stable, the phase digram has been enlarged in this region in figure 6.17(b). The elemental composition of the γ-Fe (austenite) and α'-phases is presented in figures 6.20(c) and 6.20(d), respectively, and it can be seen that these phases are distinguishable with respect to the Cr content and the crystal structure. However, the latter phase is not entirely pure Cr: the Fe content increases with temperature and the other major elements in the AISI-348 steel, *i.e.* Mn, Ni are also present in the α'. It is interesting that the calculated composition of the α' phase shows the presence of elements such as Mn (and small quantities of Si) which agrees with the MVSA quantification presented in figure 6.18: the phase observed experimentally also contain such elements to some extent. Another interesting observation from the calculated elemental composition of the austenite phase as a function of the temperature is the enrichment of Ni at very low temperatures. This phenomenon has already been reported to occur within the context of heat-affected zones of welded stainless steels [463].

The experimental observations of radiation-induced segregation leading to phase

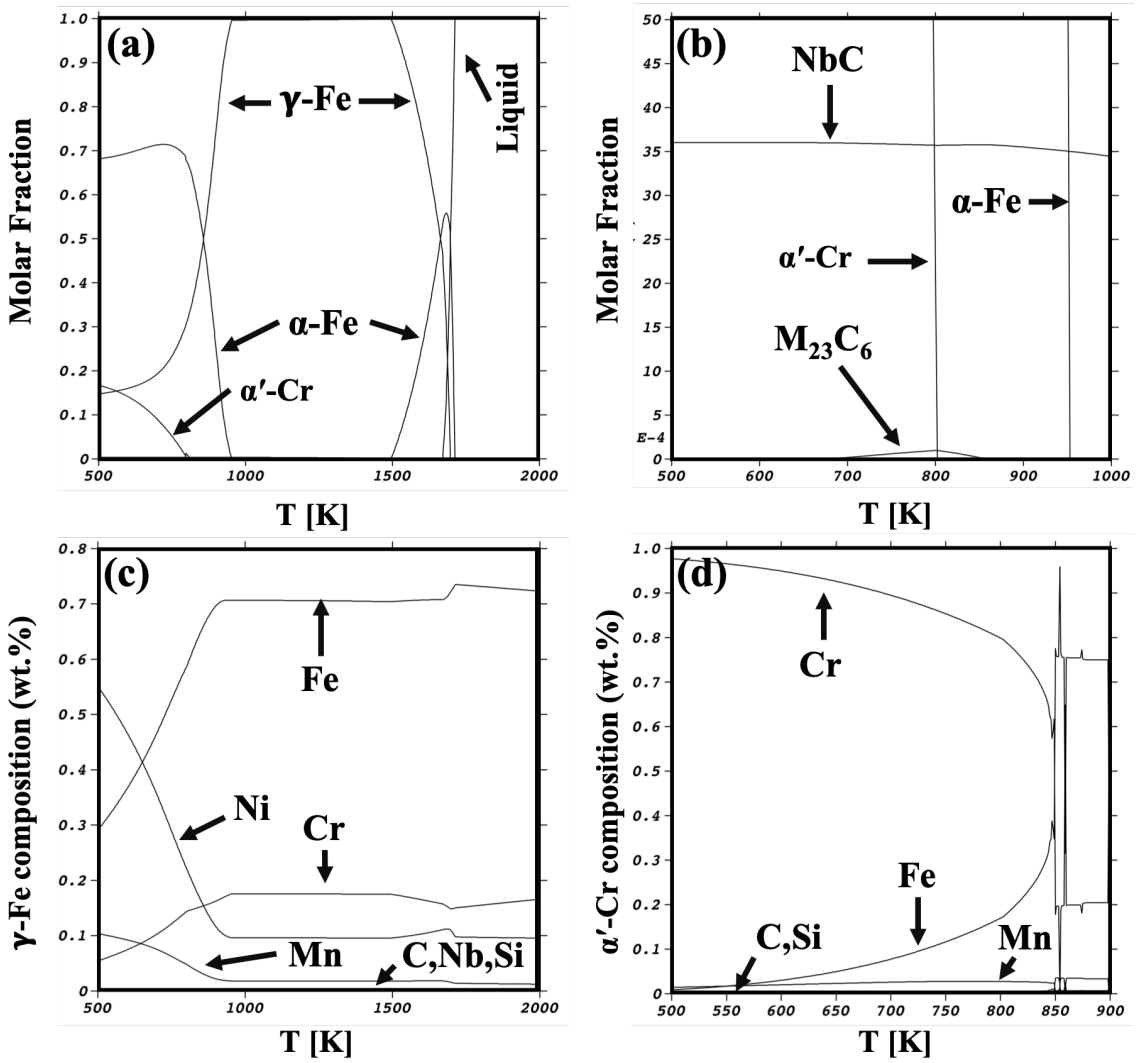

Figure 6.20: Equilibrium phase diagrams for the AISI-348 steel calculated using Thermo-calc® [415]. The molar fraction of the phases present in the steel system in the temperature range 500 to 2000 K is shown in (a) and (b) is a zoomed-region from the bottom part of the phase diagram (a) evidencing the presence of Nb(C,N) and $M_{23}C_6$ precipitates as minor phases. Elemental compositions of the γ-Fe (austenite, the matrix phase) and the Cr-rich α' phases are shown in (c) and (d), respectively.

formation (α'-phase) and precipitation ($M_{23}C_6$) during irradiation of the AISI-348 as shown in figure 6.19 in contrast with the retention of the high-entropy alloy matrix phase – albeit only at low and moderate temperatures – suggests a connection between the thermodynamics of metallic alloy systems and radiation damage resistance.

In a multicomponent alloy, energetic particle irradiation will generate Frenkel defects (vacancy-interstitial pairs) and whilst some additional recombination will occur on increasing the temperature, the heavy ion irradiation creates crystalline defects at supersaturated levels (when compared to equilibrium concentrations). As a result, the diffusion rate of the solutes will increase, thus affecting the alloy behaviour and its microstructure by promoting the nucleation and growth of secondary phases and precipitates. On the other hand, it is widely known that thermal treatments (or annealing) can induce the nucleation and growth of new phases and/or precipitation in stainless steels, and in particular in the 300-series, precipitation of $M_{23}C_6$ is expected to occur after 80–100 hours of annealing at 973 K [32, 39].

Irradiations at elevated temperatures will enhance atomic diffusion in austenitic stainless steels promoting the nucleation of phases and precipitation faster than in with elevated temperatures alone. As introduced in section 2.2.2.7, this phenomenon is known in the literature as RIS and it differs from the thermal process in terms of time-scale (faster kinetics of phase transformations) and the resulting elemental composition (phase inhomogeneities) of the phases or precipitates that form under irradiation.

The RIS effect has resulted in BCC Cr-rich α'-phase forming and growing within the γ-Fe matrix due to the continuous introduction of vacancies and interstitials by the ion collisions. As a result, the Gibbs free energy of the system will be lowered by the elimination of concentration gradients of displaced solute atoms. The results of the thermodynamic calculations show that both the α'-phase and the precipitates are observed in the equilibrium diagram which leads to an interesting conclusion: under irradiation, it is remarkable that the metastable austenite matrix decomposes into two phases that were predicted in the equilibrium phase diagrams from the thermodynamic calculations.

Clearly, the temperature range where the α'-phase is predicted to form under equilibrium is lower (stable up to 800 K) than the temperature at which its nucleation was observed under irradiation (1073 K). Such a discrepancy does not invalidate the detection of the α'-phase during irradiation, as the Thermo-calc calculations predict an equilibrium state and the sample under irradiation is evidently out of equilibrium. As discussed by Hack in his reference book [462], CALPHAD calculations are based on polynomial expansions of thermodynamic potentials, obtained by fitting to existing equilibrium properties at high temperatures. Herein, the re-

sults obtained with the Thermo-calc calculations are thus an extrapolation of these functions beyond the pressure, temperature and compositional ranges in which their parameters were fitted.

Given this discrepancy in the temperatures, it is surprising that two phases that were predicted to occur were observed in the experiments. It also worth noting that the MVSA detected elements in the α'-phase – such as Si and Mn – that were also predicted in results obtained with the Thermo-calc calculations. In addition, although the phase fractions roughly estimated with ImageJ in figure 6.19 represent areal phase fractions, the amount of α'-phase (around 20%) agrees well, for example, with the molar fraction calculated by Thermo-calc at 500 K (≈18%). The same cannot be said for the $M_{23}C_6$ precipitates which shows a much bigger areal phase fraction (around 10%) than the thermodynamic calculations that predict a molar fraction less than 0.05% (between 700–850 K).

These results lead to major conclusion regarding the irradiations in the AISI-348 steel at high temperatures: instead of bringing the austenite to a metastable state, the irradiation is leading the initial matrix phase to a thermodynamic state **closer** to the true calculated equilibrium, although observed at lower temperatures. Evidently, the full or complete thermodynamic equilibrium is not attained as the irradiation continuously introduces energy into the system and also the temperature and time are not sufficient to completely redistribute and solubilise the segregated solutes.

At lower and moderate temperatures, the same effect does not occur in the FeCrMnNi HEA, thus indicating that the lower Gibbs free energy state may have a direct relationship with the phase stability when these materials are exposed to energetic particle irradiation. Unfortunately due to an unsolved problem, electron-transparent lamellae of FeCrMnNi HEA were observed to be destroyed within the TEM when annealed at 1073 K prior the ion irradiation experiments. This has prevented heavy ion irradiation *in situ* TEM experiments with this alloy at this elevated temperatures. However, the irradiations at 873 K provide substantial evidence that the high-entropy core effects play a minor role in the phase stability of the alloy upon increasing the temperature.

6.3 Medium-energy heavy ion irradiation

Aiming at analysing the stability of the FeCrMnNi HEA under higher energy particle irradiation, heavy ion irradiations have been performed using 300 keV Xe ions at the MIAMI-2 facility. For these experiments, samples of the AISI-348 steel and the FeCrMnNi HEA were irradiated up to high doses (≈ 100 dpa) at low and moderate temperatures where the high-entropy alloy was observed to have better radiation

performance than its low-entropy counterpart, the austenitic stainless steel, in terms of thermodynamic phase stability. The objective of the set of experiments reported in this section is to study the effects of irradiation on the microstructure, with a particular focus on the phase-stability, monitored by assessing the diffraction pattern before and after irradiation.

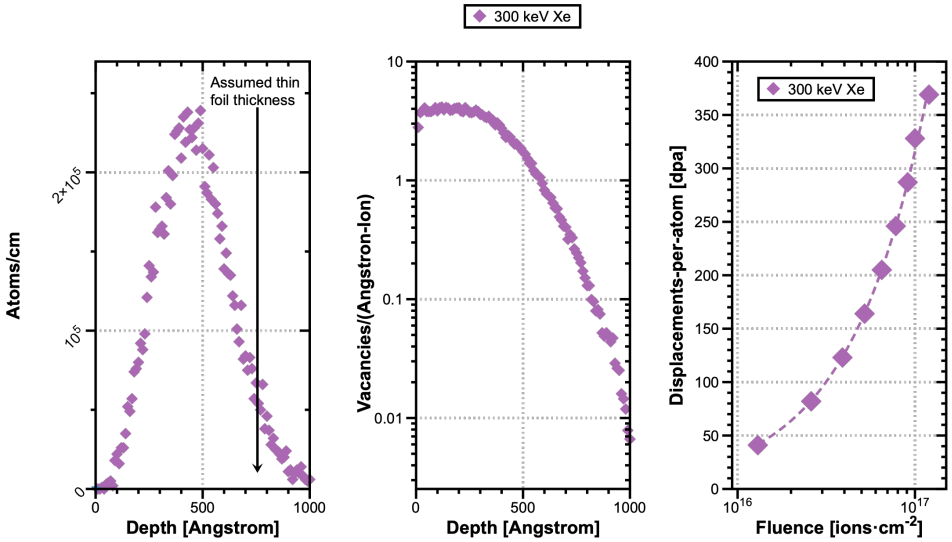

Figure 6.21: (a) The implantation profile, (b) the distributions of vacancies per Ångström-ion and (c) the fluence-to-dpa conversion for 300 keV Xe ions into the FeCrMnNi HEA and the AISI-348 steel calculated using the SRIM code. Calculations were carried out with 5000 ions in the "quick" calculation mode using the Kinchin-Pease model.

6.3.1 Design of the experiment

When using 300 keV Xe ions to carry out irradiation on the FeCrMnNi HEA and the AISI-348 steel, the longitudinal ion (peak) range is around 50 nm as shown in figure 6.21(a) and the distribution of vacancies per ion as a function of depth is shown in figure 6.21(b).

Using the methodology proposed by Stoller *et al.* [140], the number of displacements per ion collision was calculated using the phonons file from SRIM to be approximately 1900 for both materials (one order of magnitude higher than in the irradiations performed with 30 keV Xe ions in the previous section) and this allowed fluence-to-dpa conversion to be performed as shown in figure 6.21(c). In these present experiments, the alloys were irradiated to fluences of 3.9×10^{16} ions·cm^{-2} and 4.4×10^{16} ions·cm^{-2} corresponding to 123 and 140 dpa, respectively.

6.3.2 Low and moderate temperatures regimes

Samples were irradiated at room temperature (298 K) and at 573 K so as to represent the normal operational conditions of second generation light-water reactors. The results have been divided into subsections as follows.

6.3.2.1 Irradiations at 298 K

In the set of BFTEM micrographs presented in figure 6.22, the microstructures of the AISI-348 and FeCrMnNi HEA irradiated up to 3.9×10^{16} ions·cm^{-2} (123 dpa) are shown. The insets in these micrographs are the respective diffraction patterns and show that the austenite and the HEA have not suffered decomposition after the irradiation. Xe bubbles were observed to form in the matrix phase of both alloys. Additionally, black-spots were observed throughout the microstructure of both alloys. In figure 6.22(c), Xe bubbles were observed to have grown significantly at the interfaces of the Nb(C,N) nanoparticle within the austenite matrix, thus showing that they act as preferential sinks for point defects whereas in the FeCrMnNi HEA, very few large Xe bubbles were observed in the matrix phase as shown in figure 6.22(d).

6.3.2.2 Irradiations at 573 K

The microstructures of the AISI-348 and the FeCrMnNi HEA irradiated up to 4.4×10^{16} ions·cm^{-2} (140 dpa) at 573 K are shown in figure 6.23(a-b). At this temperature, the effects of medium-energy heavy ion irradiation were notably different in the two alloys. As can be seen in the BFTEM micrograph in figure 6.23(a), the Xe bubbles were considerably larger at 573 K when compared with the same irradiations at 298 K: an average diameter of around 25 nm. Additionally, the austenite phase decomposed into precipitates as observed in BF in the same figure (6.23(a)) and in the diffraction pattern by the presence of Debye-Scherrer rings.

In conclusion, under medium-energy heavy ion irradiation of the FeCrMnNi HEA at 573 K, small Xe bubbles are observed to form throughout the microstructure as shown in figure 6.23(b). However the single phase random solid solution was retained at 140 dpa as shown in the inset diffraction pattern. Damage clusters (black-spots) can be seen in the HEA and also in the AISI-348 steel in BF.

6.3.2.3 Discussion

The phase stability under irradiation of AISI-348 steel and FeCrMnNi HEA have been further investigated with medium-energy heavy ion irradiations. Following the same trends observed in the low-energy regime, in the temperature range of 298–573

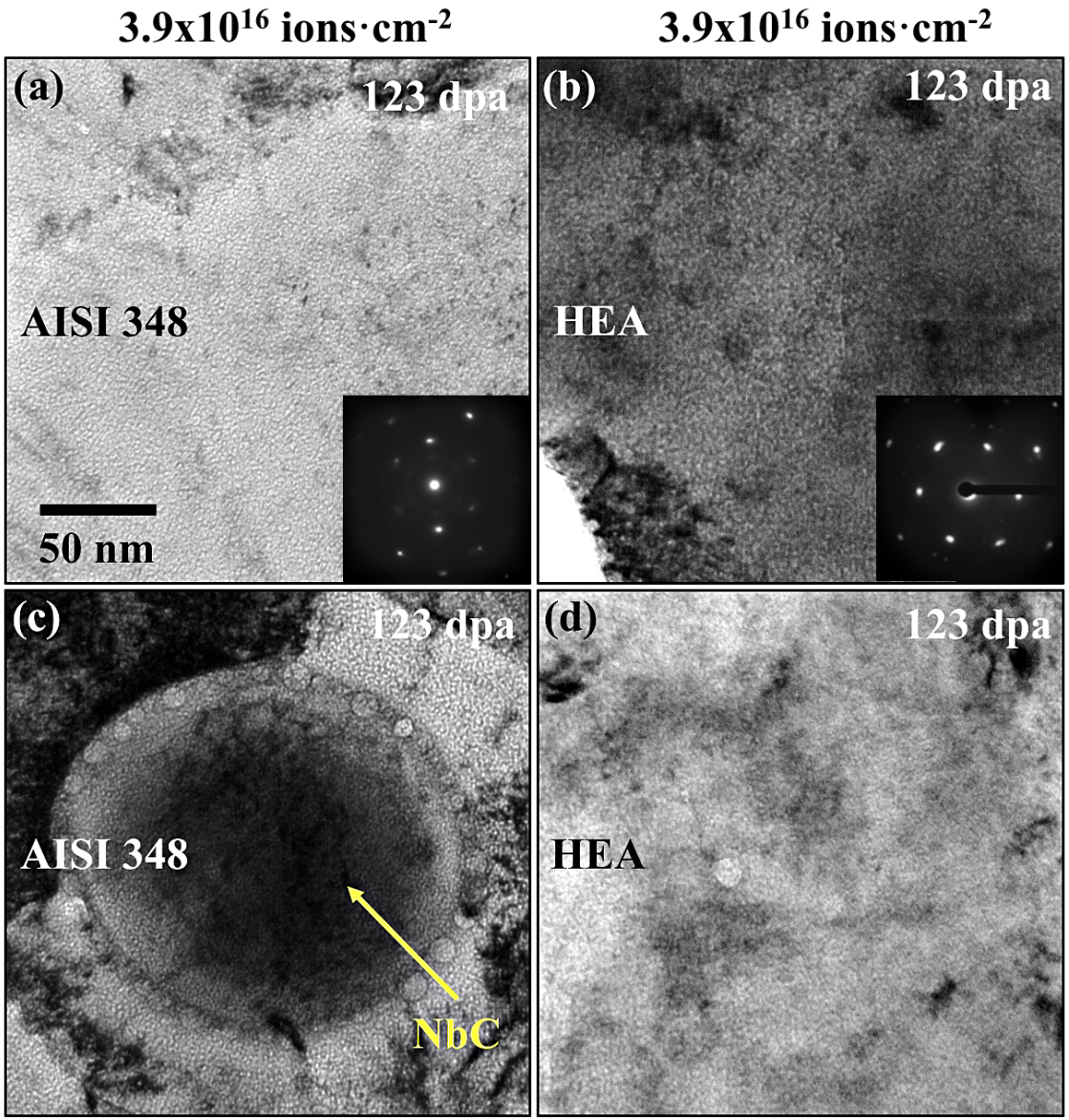

Figure 6.22: The microstructure of (a) the AISI-348 steel and (b) the FeCrMnNi HEA at a fluence of 3.9×10^{16} ions·cm^{-2} (123 dpa) at 298 K. The micrographs (c) and (d) were taken in other regions of the sample with (c) the Nb(C,N) nanoparticle where Xe bubbles are observed to grow at the interfaces. Note: the scale marker in (a) applies to all micrographs in the figure. All micrographs were taken at an underfocus of 1000 nm.

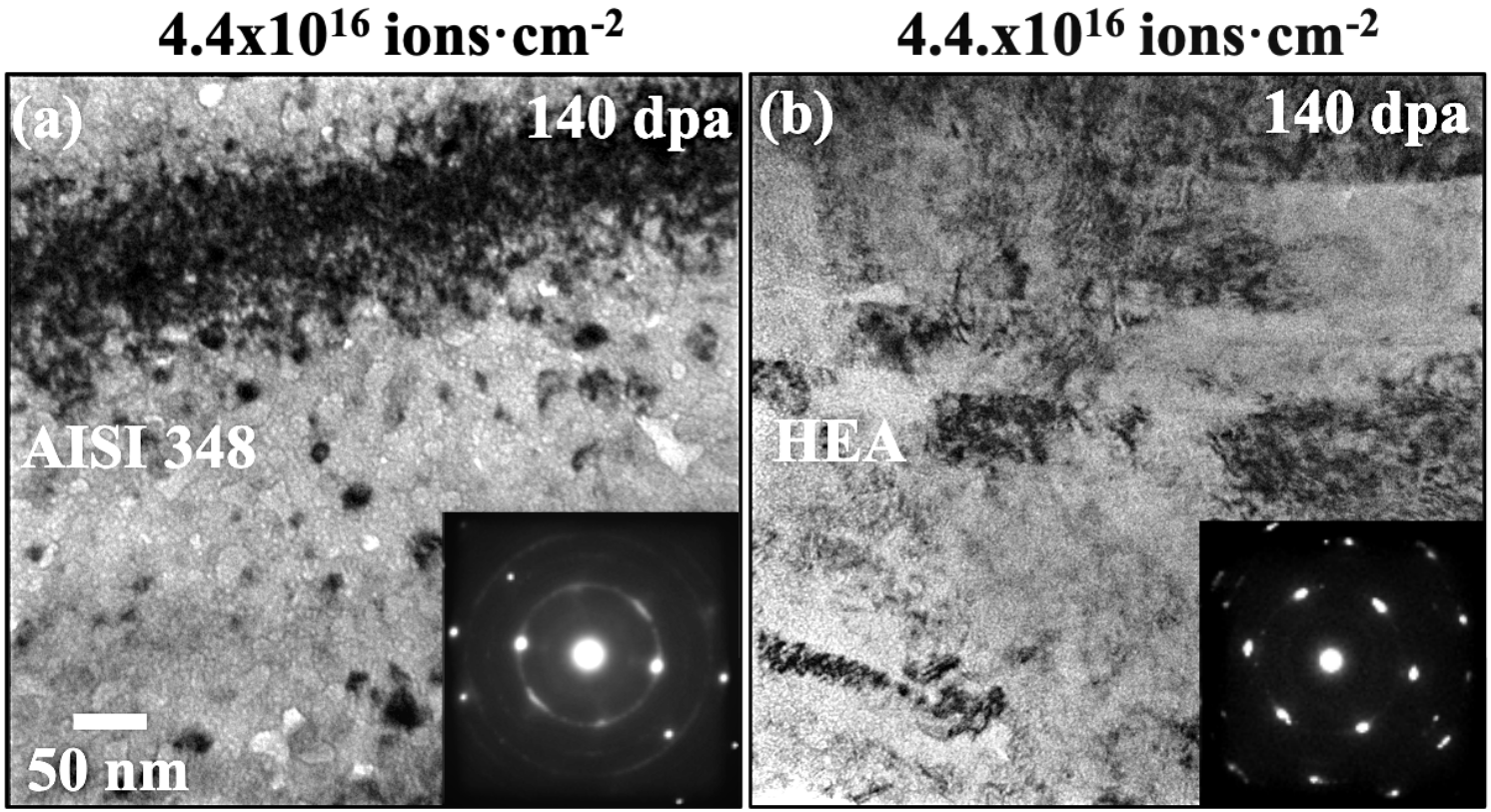

Figure 6.23: The microstructure of the (a) AISI-348 and the (b) FeCrMnNi HEA at a fluence of 4.4×10^{16} ions·cm^{-2} (140 dpa) at 573 K. Note: the scale marker in (a) also applies to (b). All micrographs were taken at an underfocus of 1000 nm.

K, the FeCrMnNi HEA was observed to possess higher relative radiation tolerance than the AISI-348. This is because the austenite phase has been observed to decompose into precipitates, but in the medium-energy irradiation, such decomposition only occurred at 573 K and not during room temperature irradiations.

In these studied temperature regimes, the differences between low-energy and medium-energy heavy ion irradiations can be discussed in terms of the shape of the collision cascades as shown in figure 6.24. Lower energy heavy ion irradiation energies generate dense cascades in which displacements, replacements and recombination will occur in a small volume of the sample ($\approx$ 100 nm^3) whereas in the case of 300 keV Xe irradiations, the cascades will extend to larger volumes (over two orders of magnitude higher or $\approx$ 64000 nm^3).

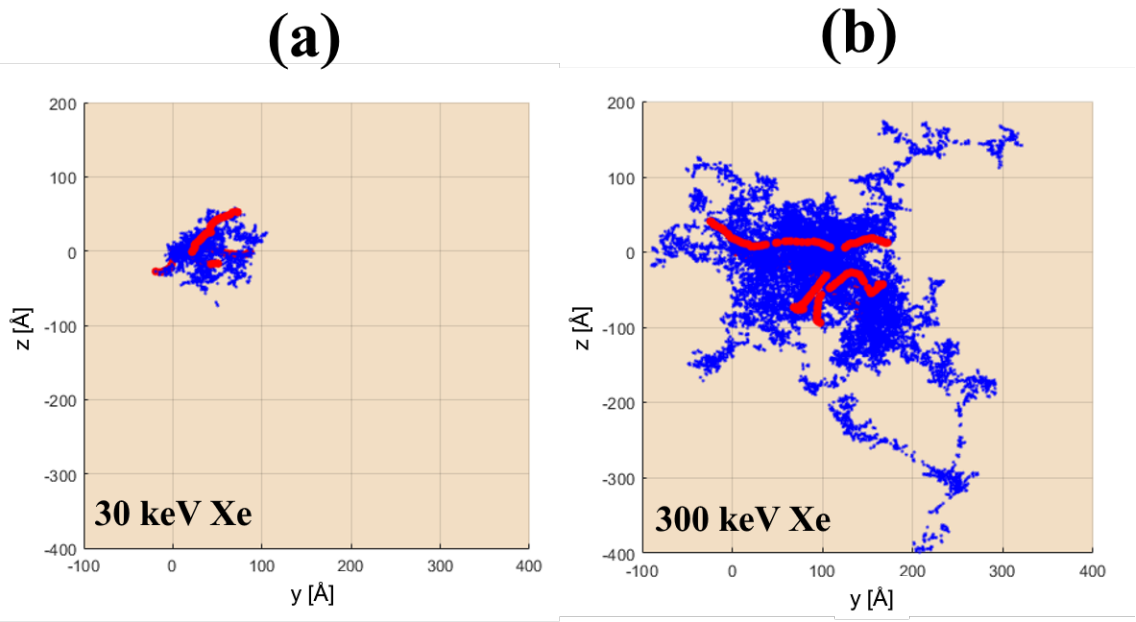

Figure 6.24: Collision cascades profile comparison between 30 and 300 keV Xe ions in the FeCrMnNi HEA (same applies for the AISI-348). The figures are displaying the transport of five Xe ions into the alloys. Note: blue dots represent the recoils and red dots are the PKAs.

The spatial spread of Frenkel pairs in the latter case – particularly with the tendency to form sub-cascades – will result in more efficient recombination of point defects that could suppress precipitation and/or clustering at lower temperatures. This experimental evidence is in agreement with molecular dynamics performed by Phythian *et al.* [464] on Fe and Cu with simulation energies from eV to keV. At higher temperatures, when atomic mobility of atoms is enhanced and due to the elemental segregation promoted by the atomic collisions, clustering, nucleation and growth of precipitates will occur in a similar manner to that observed it the low-energy heavy ion irradiations. Greater mobility can also result in more recom-

bination of point defects [191]. This can also be used to explain why the Xe bubbles have grown more in the AISI-348 steel than in the HEA as observed in the 300 keV Xe irradiations at 573 K: as in the HEA, diffusion is believed to be slower, local recombination is favoured whilst in the AISI-348 steel, Xe bubbles act as a sink for mobile defects, thus leading to an increase in their sizes.

Therefore, it has been experimentally demonstrated that for two metallic alloys within the quaternary FeCrMnNi system, high-entropy (or close to equiatomic composition) will generate a more radiation tolerant single-phase material than its low-entropy counterpart, the austenitic stainless steel. These results provide more compelling evidence of the relationship between thermodynamic phase stability and radiation tolerance.

6.4 Thermodynamics of alloys, degradation mechanisms and accelerated damage in MIAMI experiments

In this chapter, the comparison between the FeCrMnNi HEA and the AISI-348 steel under 30 keV Xe heavy ion irradiation revealed an overall trend in which the austenitic stainless steel decomposes into nanometre-sized precipitates (from 298 to 1073 K) and also in complex secondary phases (at 1073 K) whilst the random solid solution single-phase FeCrMnNi HEA was observed to be stable, although this stability was limited to the range from 298 to 573 K. At high temperatures, 873 and 1073 K, the radiation response of both alloys was very similar and decomposition was observed in both alloys at 873 K. Experiments at 1073 K were not performed with the FeCrMnNi HEA due to an unknown effect that caused the destruction of TEM lamellae during annealing at such temperature: this effect deserves further investigation as the melting point of this alloy is expected to be around 1673–1763 K. The results at 300 keV also confirm this trend to some extent, but the austenite was also observed to be stable at 298 K, but not at 573 K. The FeCrMnNi HEA was stable under 300 keV at all irradiation temperatures investigated in this work.

It is important to note that the major difference between the two alloys studied is the elemental composition. Both alloys have approximately the same grain sizes as studied in sections 4.2 and 4.3 in chapter 4. From the theory of thermodynamics of alloys, being closer to equiatomic composition in the case of the FeCrMnNi HEA enhances the thermodynamic stability of the whole system by lowering its Gibbs free energy: in the field of HEAs, this is known as a high-entropy core effect [55]. Thus, under the irradiation conditions and techniques used in this work, the results obtained and analysed throughout this chapter indicate a possible intrinsic rela-

tionship between the thermodynamic stability of a metallic alloy and its radiation resistance.

In materials science, if an alloy is not thermodynamically stable, secondary phases may form as a result of exposure to energetic particle irradiation. This is also a concern when a particular alloy is selected to be used in an environment where other degradation mechanisms may operate such as creep. In creep, the resistance that a certain alloy has to plastic deformation when under the action of loads at high temperatures can be weakened if this alloy experiences phase transformations during the process [248]. For example, the formation of the α'-phase in FeCrAl alloys under irradiation (as observed here for the AISI-348 steel) significantly increases its hardness (embrittlement) [455, 458], thus affecting the set of initial properties for which the alloy was designed: replacing Zr-based alloys in LWRs [465].

Some strategies to increase the thermodynamic stability of austenitic stainless steels are already known. This is often carried out, for example, by adding minor alloying elements such as Mn, Ni and Nb [32]. In the latter case, the additions of Nb to stabilise an austenitic steel will also contribute to the formation of Nb(C,N) which prevent the sensitisation of the austenite matrix, *i.e.* the formation of $M_{23}C_6$ carbides [417]. However, as investigated in this chapter, the AISI-348 steel which is Nb-stabilised, have shown a trend to form nanometre-sized precipitates under irradiation suggesting that the additions of Nb in this steel was found to not suppress RIS and RIP effects: in some cases, it was detected that $M_{23}C_6$ tend to precipitate in regions closer to the Nb(C,N) (as shown in figure 6.15). At the same time, the FeCrMnNi HEA has shown an increased irradiation resistance against phase decomposition. This leads to the conclusion that new strategies for materials design aiming at more thermodynamically stable metallic alloys could benefit from the considerations, ideas and hypothesis from the emerging field of high-entropy alloys. This would result not only in alloys with higher radiation resistance, but it has the potential to revolutionise the whole field of nuclear materials.

Another feature that may play a role in the radiation response of the FeCrMnNi HEA is the presence of twins throughout its microstructure. These twins can act as sinks for irradiation-induced defects, thus reducing the nucleation and growth of extended defects and also decreasing the damage accumulation within the HEA matrix phase. Some twins are also observed in the AISI-348 steel, but they are more likely to occur in the FeCrMnNi HEA: an increase of the content of alloying elements is often related with a decrease in the stacking fault formation energy which is intrinsically connected with the occurrence of twins [248]. In the case of the AISI-348 steel, the STEM-EDX assessment at 1073 K, for example, has shown that the nucleation of phases such as the alpha prime, occurs mainly within the grains. Whilst in the HEA such twins may play a significant role in the radiation

resistance, in the AISI-348 steel they are clearly not preventing either precipitation or phase transformation under irradiation. These findings provide motivation for further studies, as for example, the phenomenon of nanotwinning in HEAs has been recently related to a synergy of multiple deformation mechanisms that are responsible for superior mechanical performance when compared with existing structural alloys [346].

When the results on RIS and RIP obtained in the MIAMI facility are compared with *ex situ* heavy ion irradiation (in the case of the work by Jin *et al.* [456]) and neutron irradiation (the work on the α'-phase formation in FeCrAl alloys [455]), although the alloys under consideration were different in composition and sometimes also in crystal structure, it is clear that the dose rate is a major parameter in the radiation response of stainless steels. For the MIAMI irradiations reported in this chapter, the dose rate was around of 1.1×10^{-2} dpa·s^{-1} whilst for *ex situ* heavy ion irradiation and neutron irradiations, the dose rates reported by Jin *et al.* [456] and Briggs *et al.* [455] were $\approx 9.6\times10^{-3}$ and 8×10^{-7} dpa·s^{-1}, respectively. Due to the synergistic combination of high dose rates and high irradiation temperature – in particular the results at 1073 K with the AISI-348 steel – the average sizes of nanometre-sized precipitates and complex secondary phases such as the α'-phase are bigger than in the cases used for comparison. It is important to emphasise that such observations agrees with the RIS model proposed by Wiedersich-Okamoto-Lam-Bruemmer introduced and reviewed in section 2.2.2.7: high temperatures and dose rates inevitably result in an enhancement of the RIS effect. Dose rate is still, of course, a current and significant challenge when using ion beams to simulate radiation damage in nuclear reactors [319]. It is also impressive that such high dose rate do not promote phase decomposition in the FeCrMnNi HEA at least in the temperature range from 298 to 573 K.

Naturally, the investigations presented in this chapter also have some limitations that provide motivation for further work in the field. Due to the limited time availability of microscopes with STEM-EDX capabilities, only the AISI-348 steel that was irradiated at 1073 K was post-screened, revealing the presence of nanometre-sized precipitates of $M_{23}C_6$ type and the Cr-rich α'-phase. More studies could be carried out on the phase stability of both alloys investigated in this chapter, not only by monitoring the diffraction pattern evolution with the irradiation dose and temperature, but also by carrying out elemental mapping in field emission gun electron-microscopes with STEM-EDX capability. Atom probe tomography could also be used to reveal possible RIS and RIP effects at the atomic scale, for example, the formation of clusters caused by RIS and that evolve by RIP with irradiation time, temperature and dose.

6.5 Summary and conclusions

In this chapter, although the metallic alloys under investigation can be considered similar (apart from the content of the elemental composition), superior phase stability of the FeCrMnNi HEA has been evidenced when compared with the austenitic stainless steel AISI-348, but this is limited to irradiation temperatures in the range of 298–573 K. At higher temperatures, both alloys behaved similarly under irradiation: phase degradation due to the irradiation does occur in both metallic alloys and the high-entropy core effects were observed to play only a minor rule in the phase stability under irradiation. Another difference between the radiation response of the two alloys is the presence of a higher density of twins in the FeCrMnNi HEA. These twins can act as sinks for radiation-induced defects, reducing the population of defects in the matrix of the HEA, leading to a superior radiation tolerance when compared with the AISI-348. In addition, the effect of such twins may be more pronounced at lower temperatures as bulk diffusion takes over at higher temperature.

The investigation and results presented in this chapter suggest that new metallic alloys for nuclear reactors could be designed by tuning the elemental composition towards high-entropy, *i.e.* multicomponent alloys at equimolar compositions. Although an ideal equiatomic alloy would be economically unfeasible (mainly due to the availability and costs of some of the alloying elements), recent studies have indicated that thermodynamic stabilities close to those of the single-phase random solid solution alloy can be attained with somewhere between the dilute and the equimolar compositions (highly concentrated alloys). In this way, future work on computational thermodynamics will be of paramount importance to guide the experimental development of new metallic alloys using the HEA concept. Additionally, the comparison between the AISI-348 steel and the FeCrMnNi HEA was limited to the study of their radiation response using the *in situ* TEM ion irradiation technique. Corrosion and oxidation tests under reactor-like conditions and differences in the mechanical performance before and after irradiation are possible topics for further investigations.

Nevertheless, the phase stability of such new designed alloys should be higher at high temperatures: as showed in this present research work, at 873 K both FeCrMnNi HEA and the AISI-348 steel exhibited similar radiation effects including RIS and RIP. This is an indicative that, under the studied conditions, the HEA was not stable at this temperature, therefore, this could be a limiting factor for applications in high-temperature nuclear reactors (*e.g.* generation IV). The effect of thickening observed to occur in the FeCrMnNi HEA lamellae at 1073 K deserves further investigation. If the bulk produced alloy is not stable at high temperatures, this will be a strong limiting factor for future applications within the nuclear

technology, mainly in the high-temperature environments of innovative nuclear reactors. Additionally, this project has shown that the ion irradiation with *in situ* TEM methodology is a fast and reliable way to carry out radiation damage experiments in novel alloys before their consideration for tests in expensive experiments in MTRs.

Chapter 7

Synthesis, characterisation and radiation resistance of high-entropy alloy thin film coatings

7.1 Preface and motivations

In March 2011, the east coast of Japan was subjected to an intense earthquake of magnitude 9.0 on the Richter scale. As a consequence of this earthquake – for which the epicentre was beneath the sea – a tidal wave known as a tsunami was initiated and hit the city of Ōkuma located in the prefecture of Fukushima. On the coastal side of the city, the tsunami hit the Fukushima-Daiichi nuclear power plant complex which had at the time ten fully operational boiling-water reactors (BWRs) supplied and operated by the companies General Electric, Toshiba and Hitachi. Despite the tall and sturdy seawalls protecting the surroundings of the power complex, the tsunami caused significant damage to the BWRs by inducing water flooding and subsequent failure of the diesel generators that were responsible for the continuous flow of cooling water to the reactors' cores [466].

In the design of these BWRs, Zr alloys were had been as the nuclear fuel cladding material due to their superior mechanical strength, oxidation resistance and low thermal neutron cross section under the normal envelope of operational conditions. The flooding caused an event known as loss-of-coolant accident (LOCA) in the BWRs, triggered by the failure of the diesel generators and batteries, and this resulted in the anomalous rise of the temperature in-core leading to overheating of the fuel rods. Upon contact with water vapour and air at high temperatures, the element Zr undergoes a fast oxidation reaction that generates large quantities of hydrogen gas

(H_2) according to the chemical reaction: $Zr + 2H_2O \longrightarrow ZrO_2 + 2H_2$. The generation and accumulation of hydrogen gas in the Fukushima-Daiichi nuclear reactors caused several explosions resulting in loss of life and damage to the environment. This recent nuclear accident was categorised as the worst civilian nuclear accident since Chernobyl in 1986.

In the 7 years since the nuclear accident in Fukushima, the worldwide nuclear materials community has been performing several new joint investigations aimed at increasing the safety of operation of nuclear reactors especially under accident conditions. The research and development of new materials and alloys that are able to preserve their structural integrity without introducing additional safety issues for the installation under either normal and abnormal operation conditions has opened a new pathway in the field of materials sciences known as Accident Tolerant Fuels (or ATFs) [467]. In order to be considered a candidate as an ATF, a material should meet at least four major criteria: (i) resistance to high temperature oxidation, (ii) reduced activation, (iii) superior mechanical properties and (iv) improved radiation resistance/tolerance when compared with conventional nuclear materials [467]. In addition to these properties, candidate materials within the ATF programme should outperform conventional Zr alloys (currently in use worldwide) in both normal operational conditions and during transient and/or accident conditions such as LOCA.

7.2 Objectives and perspectives of the research reported in this chapter

Following the experimental evidence provided in this thesis on the possible enhanced phase stability under irradiation of high-entropy alloy systems, and particularly their ability to retain the matrix phase at low and intermediate irradiation temperatures, the major goal of the research reported in this chapter is to investigate the feasibility of depositing a high-entropy alloy thin film (HEATF) using the ion beam sputter-deposition technique. An initial investigation on the feasibility of sputter-depositing HEATFs on Si wafer substrates is firstly presented. Then, a detailed study of the deposition of the HEATF on Zircaloy-4^{TM} substrates is performed, including an in-depth electron microscopy characterisation. In addition to the characterisation of the thin film as-deposited on Zircaloy-4^{TM}, the radiation resistance of the HEATF is assessed by subjecting the system (HEATF/Zircaloy-4^{TM}) to heavy ion irradiation *in situ* within a TEM.

The main idea is that the presence of a hard and resistant thin film as a coating for Zr alloys in the Fukushima reactors would have prevented the occurrence of the nuclear accident caused by LOCA as these films would have acted as a physical bar-

rier between the environment and the nuclear fuel cladding alloy, thus preventing the oxidation reactions with water vapour at high temperatures. In fact, a recently completed multi-national research project led by United States – the ceramic coating for corrosion (C3) resistance of nuclear fuels – has already proposed titanium nitride (TiN) thin films as coatings for Zr alloys [468, 469]. For this reason, in the experiments reported in this chapter, the radiation response of the HEATF/Zircaloy-4^{TM} system is compared with the radiation response of TiN thin films under similar irradiation conditions. The experiments reported in this chapter are also aligned with the core objectives of a recent multi-national project co-funded by the European Commission – the H2020 project IL TROVATORE led by Prof. Konstantina Lambrinou (UoH) – that aims to identify, optimise and validate the most promising ATF cladding material concepts in an industrially-relevant environment, *i.e.* under neutron irradiation in PWR-like water.

Herein, the development of a HEATF on a Zircaloy-4^{TM} substrate and its radiation response are studied only in prototypic conditions targeting the PWR nominal operation conditions. To be considered an ATF material, the HEATF would have to be tested in a wide variety of other conditions that would go beyond the scope of this thesis. These would include, for example, testing the compatibility between the HEATF and the PWR's coolant in its operational state (*e.g.* pressurised water) or in its accident state (*e.g.* steam at high temperatures). In addition, new ATF materials need to be able to resist to a wide variety of degradation mechanisms that operate at the same time whilst in a reactor. The degradation mechanisms that may act synergistically are mainly – not exhaustively – radiation damage, corrosion and oxidation, inter-diffusion of species from the cladding to the coating (in the case of thin films used as protective barriers) and intense mechanical loads and axial forces arising from either swelling or internal pressure build-up in the fuel rods due to the progressive production of fission gases [470, 471].

In the research reported in this chapter, the technique of heavy ion irradiation *in situ* within a TEM has been used as a fast screening tool for assessing the radiation response of the developed HEATF. However, true accident tolerance as well as enhanced radiation resistance can only be demonstrated by means of dedicated neutron irradiation testing in an MTR. Therefore, the results reported in this chapter are only introducing new perspectives to be incorporated in the development of future candidate materials with enhanced radiation resistance within the scope of the ATF programme.

7.3 Synthesis and characterisation of the HEATF on Si substrates

In this section, the synthesis and characterisation of thin films in the quaternary system Fe–Cr–Mn–Ni deposited on Si wafer substrates will be reported. In this initial study, the Si wafer substrates were chosen due to their high degree of flatness, low price and high availability (especially when compared to expensive nuclear fuel cladding alloys, (*i.e.* Zr alloys) and also due to the fact that these substrates do not require any surface preparation prior to deposition. This section reports on the synthesis and characterisation of HEATFs in prototypic conditions. Upon the confirmation of the feasibility of depositing HEATF on Si substrates, the experimental conditions were recorded and the deposition on Zircaloy-4^{TM} substrates was carried out (section 7.4).

7.3.1 Deposition conditions and methodology

FeCrMnNi thin films were deposited using the ion beam sputter-deposition system described in section 3.1.4. This system is part of the surface coating and characterisation (SCC) laboratory located at the University of Huddersfield.

The thin films were deposited using Fe, Cr, Mn and Ni elemental targets with a purity of 99.95%. An Ar ion source with 1.25 keV accelerating voltage was used to induce sputtering of the elemental targets onto the substrate. The temperature of the substrate was monitored during the deposition and was in the range of 350–370 K. For all of the thin films produced the deposition conditions were the same and the total deposition time was 2 hours with the deposition pressure around 3×10^{-2} Pa. Two types of thin film were produced: an equiatomic thin film (the HEATF) and a non-equiatomic thin film (the NETF). In order to achieve the desired elemental composition, the sputtering targets were positioned in the deposition chamber and the equiatomic condition was accomplished after several trial and error attempts to position them such that equal deposition rates of each element were achieved.

To analytically characterise the thin films, an Oxford energy dispersive X-ray system in a FEI Quanta 3D FEG scanning electron microscope was used. The elemental quantification in this EDX system was performed with the ZAF standardless correction [407]. To reduce the uncertainties in the elemental quantification, different electron energies 30–15 keV and different site dependencies were analysed. Transmission electron microscopy was carried out in a JEOL 3010 TEM operating at 300 kV with a LaB_6 filament on samples produced using the focused ion-beam lift-out technique.

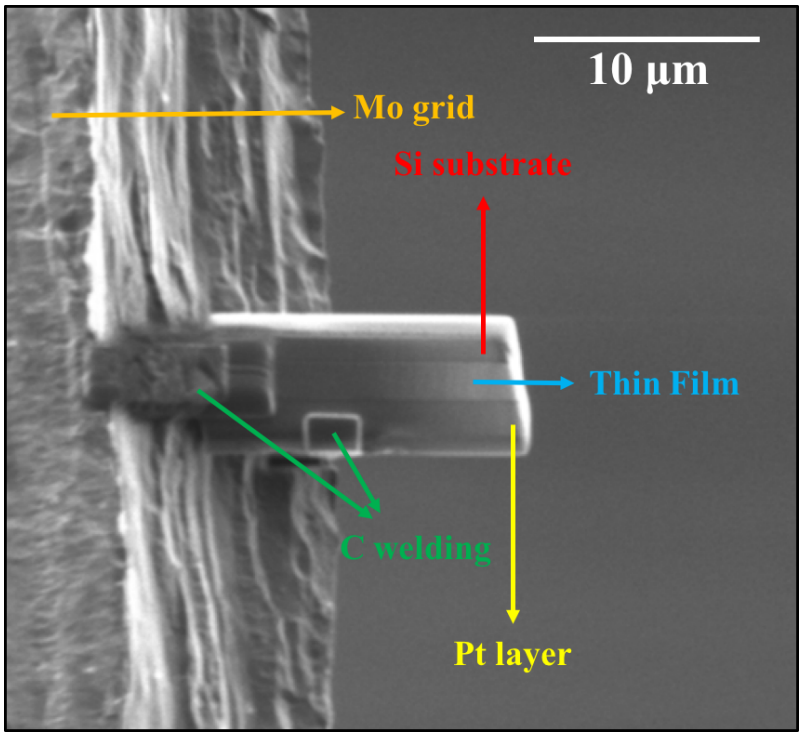

Figure 7.1: A HEATF lamella attached to a Mo TEM grid during the FIB sample preparation. Note: micrograph taken with SEM-BSE.

7.3.2 Results

The elemental composition of the HEATF and the NETF are presented in table 7.1 and the error in the ZAF quantification was less than 5%. Figure 7.1 shows an SEM backscattered electron (BSE) micrograph of a TEM lamella of the HEATF attached to a Mo grid during the FIB procedure. The lamella was attached to the Mo grid using carbon deposition. The multilayered structure of the sample can be observed: a protective top Pt layer, the FeCrMnNi HEATF and the silicon substrate. Comparing the composition of the FeCrMnNi HEATF with the bulk FeCrMnNi HEA composition presented in table 4.5 (section 4.3.2.1), it is possible to see that both alloys are very similar when the error in the composition is taken into consideration: only the Cr content is a bit lower in the bulk HEA to prevent the formation of secondary phases during heat-treatment after casting.

Table 7.1: The elemental composition of the FeCrMnNi HEATF measured by SEM-EDX.

Element	**NETF [wt.%]**	**HEATF [wt.%]**
Fe	14.6±0.7	23.7±1.1
Cr	21.7±1.1	22.9±1.3
Mn	39.3±2.0	25.8±1.2
Ni	24.4±1.2	27.6±1.4

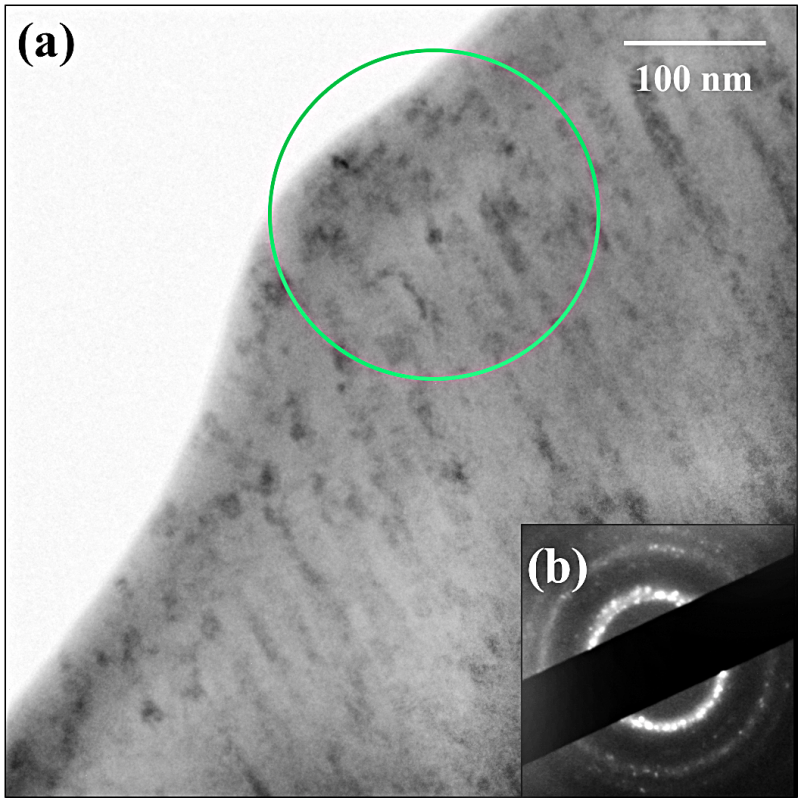

Figure 7.2: The NETF microstructure at the nanoscale. The circle in (a) represents the selected area corresponding to the diffraction pattern in (b).

Using the SEM-BSE cross-sectional micrographs, it was possible to measure the thickness of the thin films. The FeCrMnNi HEATF and the NETF thicknesses were 1.51±0.06 μm and 1.58±0.05 μm, respectively.

The microstructure of the NETF at the nanoscale is shown in micrograph 7.2(a). The film is composed of nanocrystallites with sizes around 5–30 nm. Selected-area diffraction gave a polycrystalline pattern as shown in figure 7.2(b). These nanocrystals gave rise to variation in diffraction contrast when tilting the specimen around the x-axis using a double-tilt TEM holder. In figure 7.3, several BFTEM micrographs taken within an x-tilt range of 0–10° confirmed that the microstructure of the NETF was entirely composed of nanocrystals approximately 40 nm in size. The methodology of tilting the specimen has allowed the identification of individual grains and figure 7.4(a) shows the grain pattern of the NETF. The DFTEM micrographs in figures 7.4(b) and 7.4(c) were taken, respectively, at 0 and 10° and show details of the nanograins throughout the microstructure at different orientations.

In contrast, the microstructure of the HEATF consists of bigger grains as shown in figure 7.5(a) and its respective diffraction pattern is shown in figure 7.5(b). DFTEM was used to better resolve the grains as shown in micrograph 7.5(b). Planar defects were also observed within the grains of the HEATF. Those appear to be crystalline in nature and are shown in the BFTEM micrographs 7.5(d-e).

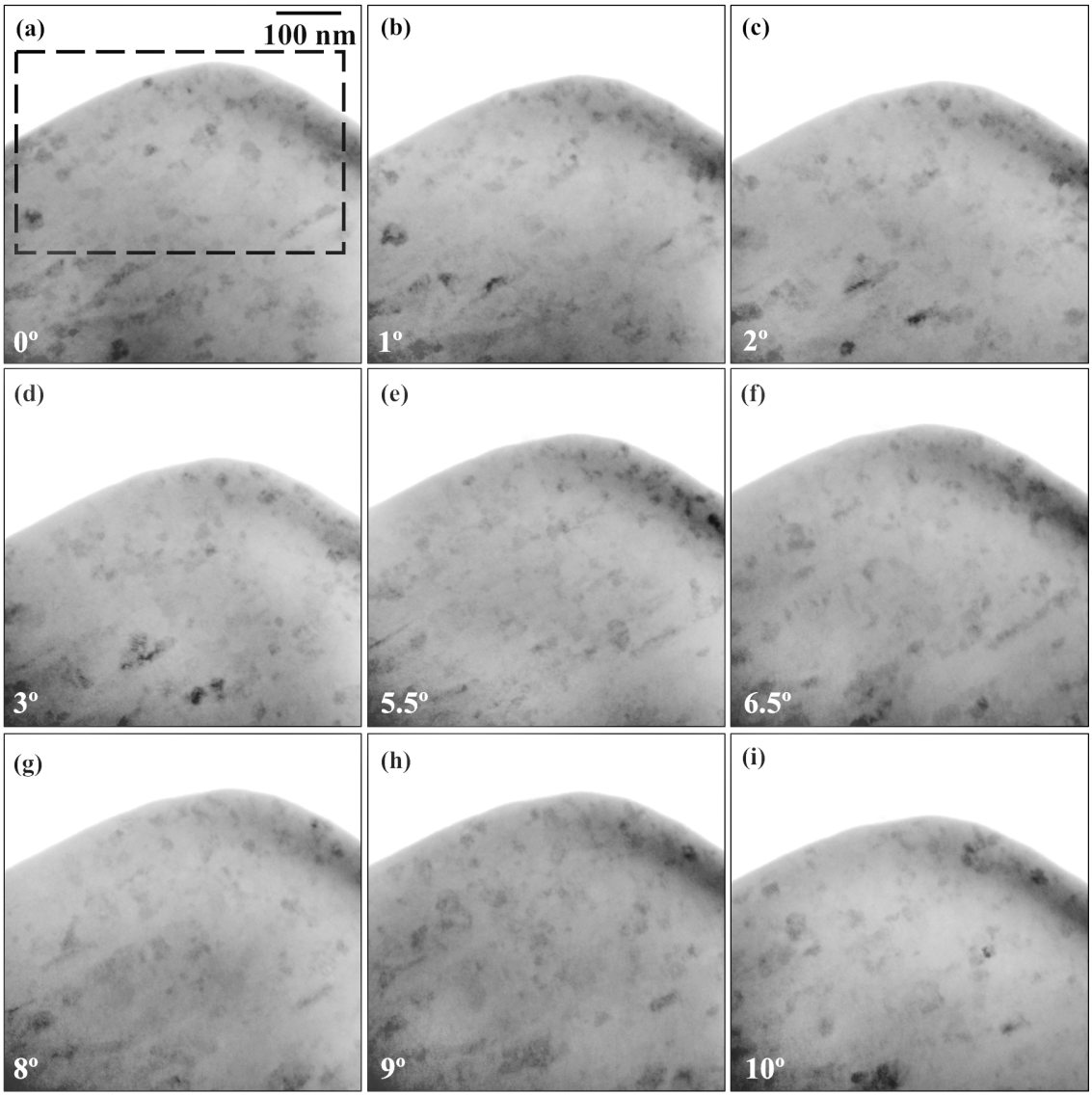

Figure 7.3: Several BFTEM micrographs showing the microstructure of the NETF from 0 to 10° x-axis tilt. Note: the dashed region in (a) represents the area analysed to compose image 7.4.

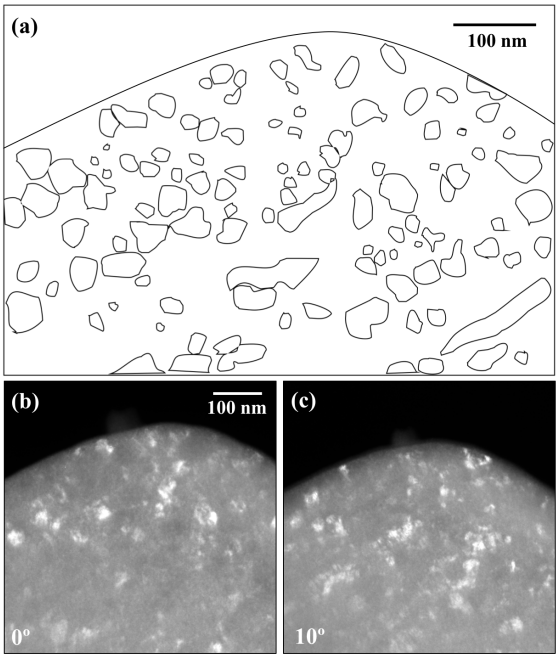

Figure 7.4: (a) The grain pattern of the NETF constructed from the BFTEM micrographs taken in the tilting range of 0–10°. The dark field TEM micrographs (b) and (c) show the microstructure of the NETFs at 0 and 10°, respectively.

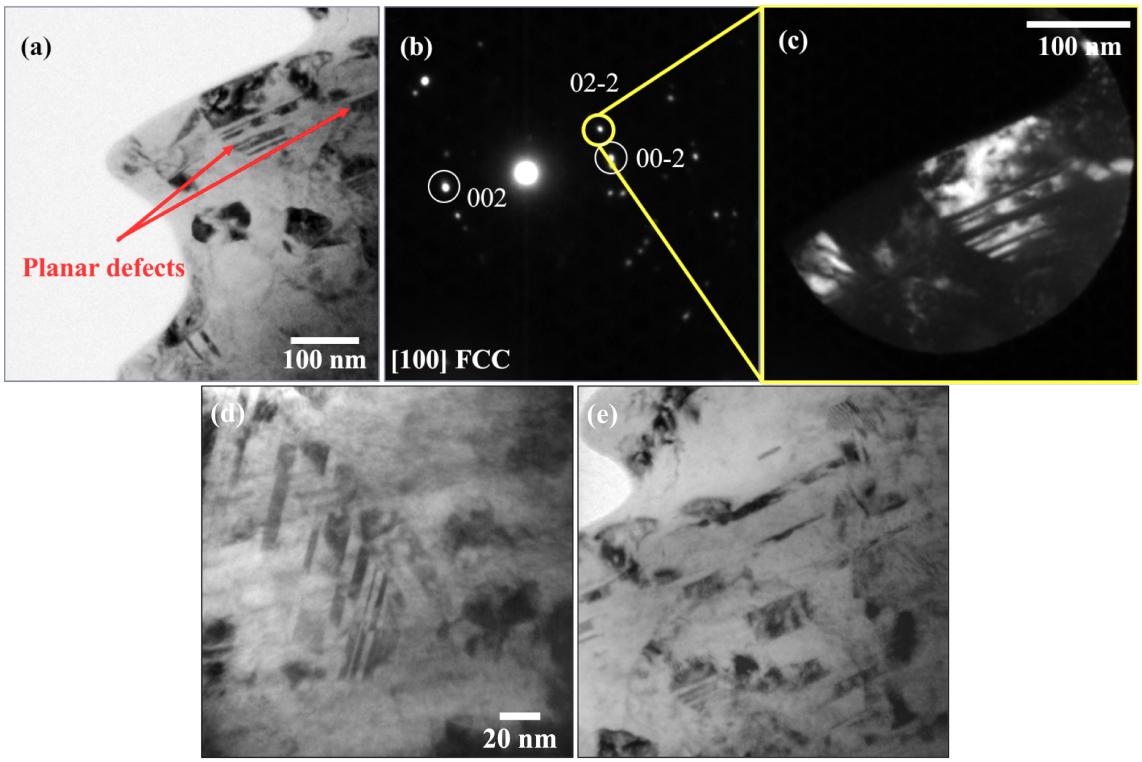

Figure 7.5: The microstructure of the HEATF showing (a) BFTEM micrograph and (b) the corresponding diffraction pattern. (c) The DFTEM micrograph showing the presence of larger grains when compared with the NETF (around 100 nm). The BFTEM micrographs (d-e) show the planar defects in the HEATF.

By means of crystallographic analysis using the software CrystalMaker and data available in the literature [384], the HEATF diffraction patterns were well indexed with the face-centred cubic (FCC) structure. From the conventional TEM characterisation it could be seen that the grain sizes in the HEATF were in the 50–250 nm range, therefore, they were clearly bigger than in the NETF despite the fact that all thin films produced in this work were deposited under the same conditions. A histogram of grain sizes for both NETF and HEATF is shown in figure 7.6.

When analysed at higher magnifications in the electron microscope, the underfocused BFTEM micrographs 7.7(a-b) revealed the presence of speckled Fresnel contrast resembling surface roughening in both the NETF and the HEATF.

7.3.3 Discussion

7.3.3.1 The nucleation and growth dynamics and the thermodynamics of HEATFs

The physical mechanisms for nucleation and growth of crystal nuclei in metallic alloys have been subjected to intense study in the past century and laid the foundation of modern metallurgy [472, 473]. Earliest theories were based on the fact that the nucleation and growth of liquid droplets and subsequent solidification of embryos in vapour-liquid environments assume that the Gibbs free energy of the system is a function of the radius r of spherical-shaped embryos [474],

$$\Delta G(r) = 4\pi r^2\sigma + \frac{4}{3}\pi r^3 \Delta G_v \tag{7.1}$$

where σ is the energy per area and ΔG_v the free energy per volume. Equation 7.1 express the fact that in the liquid-droplet model, the Gibbs free energy regulates the formation of an embryo through a trade-off between two components: surface and volumetric energies. The local maximum of the function $\Delta G(r)$ will occur when:

$$\frac{d\Delta G(r)}{dr} = 0 \rightarrow r^* = -\frac{2\sigma}{\Delta G_v} \tag{7.2}$$

where $r*$ is known as the critical radius for nucleation and indicates that embryos with radii $r < r^*$ will have a tendency to vanish whilst $r = r^*$ is the necessary condition for the formation of a small nucleus for nucleation and growth of crystals. The liquid-droplet model establishes a link between the thermodynamics of a certain metallic alloy system with the nucleation and growth of crystals.

Such considerations can be use to explain the observed experimental differences between the HEATF and the NETF from a microstructural perspective. As stated in section 2.1.1.2, the equiatomic condition of a high-entropy alloy is responsible for maximising the entropy (equation 2.4) which implies the minimisation of the Gibbs

free energy of the alloy system (equation 2.1).

The critical radius for nucleation can be correlated with the Gibbs free energy of a system which is affected by the elemental composition of the thin films. Equation 7.2 introduces an inversely proportional relationship between the Gibbs free energy per volume and the critical radius. When the microstructure of the HEATF and the NETF were analysed by TEM, it was clear that the former has bigger grains than the latter. Such experimental evidence corroborates the fact that lower Gibbs free energy will promote the nucleation of bigger embryos in an otherwise identical thermodynamic system (here Fe–Cr–Mn–Ni). As the NETF has, by definition, higher Gibbs free energy, it is expected that its critical radius for the nucleation of embryos will be smaller grains than in the HEATF. This is therefore an experimental confirmation that the high-entropy effect is influential in the dynamics of nucleation and growth of high-entropy alloy thin films and that the microstructure of such thin films can be engineered via IBSD at room temperature by the careful control of the elemental composition.

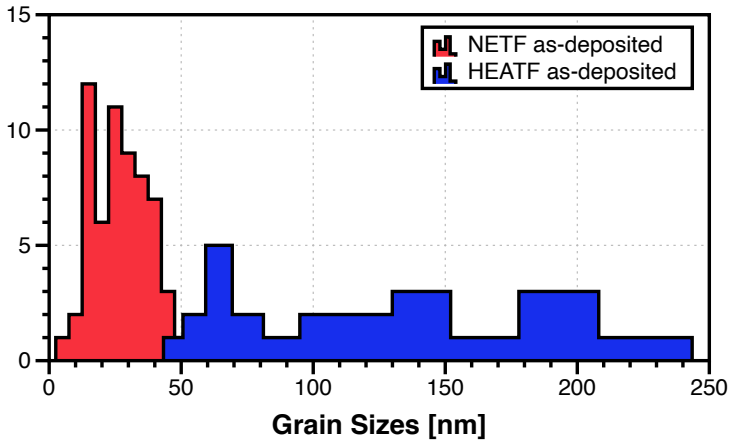

Figure 7.6: Histograms of the grain sizes measured from the microstructures of both NETF and HEATF as-deposited. The average grain size for the NETF and HEATF are 26.6±1.3 and 109.4±10.7 nm, respectively. The HEATF has bigger grains, but the dispersion of sizes is also larger than the NETF.

Two facts deserve further considerations. Nucleation and growth of crystals require atomic diffusion which is often achieved by high deposition temperatures. As reported herein, the temperature of the substrate during deposition was equal for both films and it was around 350 K. Assuming that the melting temperature of Si is 1685 K, the homologous deposition temperature was $0.21T_m$. Grain (re)crystallisation in thin solid films happens at homologous temperatures in the range of 0.3-0.5T_m as reported by Thornton [374]. Despite the fact that the deposition temperature for the HEATF and the NETF reported in this work is outside this range, it is well known in the thin solid films community that atomic diffusion can be promoted (and even enhanced) during deposition by the assistance of ion

bombardment of the growing film. In the case of the non-equiatomic film, nucleation but lack of growth is therefore likely to be a feature rather associated with its own non-equiatomic condition than the lack of atomic diffusion [475].

A second consideration is on the configurational entropy of both thin films. When equation 2.4 is used with the compositions given in table 7.1, the configurational entropies for the HEATF and the NETF are $1.32k_bN_a$ and $1.38k_bN_a$, respectively. This led to the conclusion that the configurational entropy has a small influence on the observed microstructural differences in the two films. This is in agreement with a recent publication where authors probed the entropy hypothesis in these alloy systems using the cluster variation method and concluded that competition between highly conflicting interactions (known in metallurgy as frustration) are the relevant factor for the stabilisation of random solid solutions [68]. This latter fact deserves further investigation aiming to confirm whether or not the configurational entropy is the major relevant thermodynamic factor causing microstructural differences in highly concentrated alloy systems when compared with terminal and intermediary diluted alloy systems.

7.3.3.2 Twinning and surface roughening

The underfocused micrographs 7.7(a) and 7.7(b) have also revealed that both thin films manifested speckled Fresnel contrast at high magnifications and this can be attributed to surface roughening. Ion beam sputter-deposition of thin films involves low energy ion implantation which can also introduce stresses in the films [476].

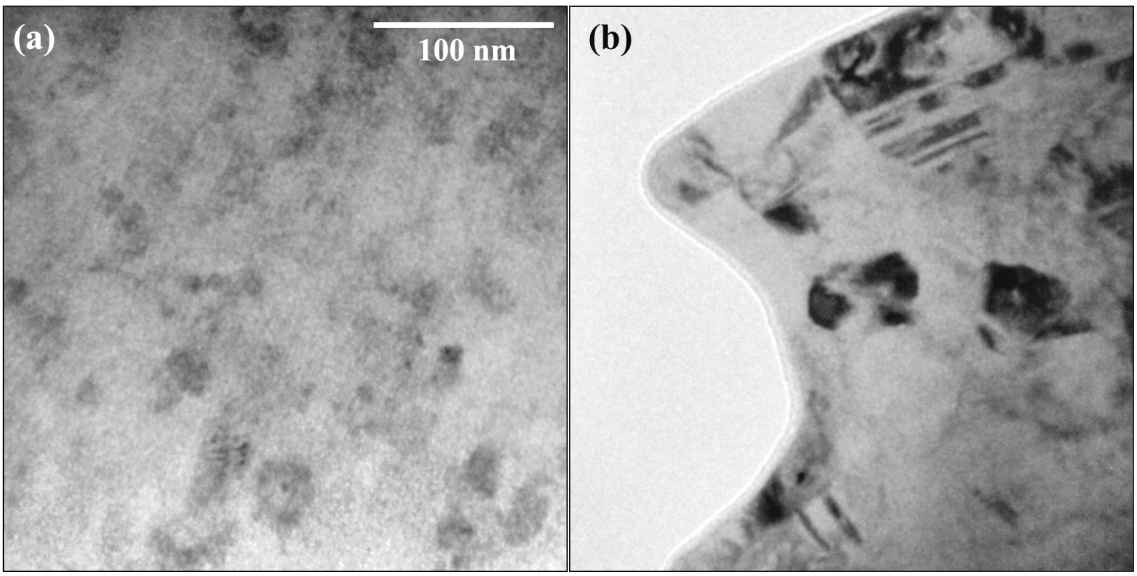

Figure 7.7: Speckled contrast in underfocused bright field TEM micrographs due to surface roughening in both (a) NETF and (b) HEATF. The micrographs were recorded with an objective lens underfocus of 0.95 μm. Note: the scale bar in (a) also applies to (b).

These residual stresses have been related to different types of deposition-related effects in thin films including epitaxy and phase transitions. Eventually, by the action of temperature and other deposition conditions, the residual stresses may be relieved resulting in the formation of stacking faults, cracks, dislocations, twinning and surface roughening.

Planar defects resembling twinning were observed in the HEATF and were absent in the NETF. It is worth emphasising that such twins have been also observed in the FeCrMnNi bulk HEA as shown in the figure 4.8. This type of defect has recently been subjected to intense research within the context of nanocrystalline materials [477–479]. The HEATF microstructure is a multicomponent random solid solution formed with metals in the system Fe–Cr–Mn–Ni. The combination of these different atomic species will result in a random solid solution with a crystal lattice containing atoms with different sizes. This atomic mismatch of the crystal lattice in a HEATF may indicate that planar defects can be formed in its microstructure as a result of internal mechanisms that reduce the elastic strain and the residual stresses caused by the mismatch in atomic sizes.

7.3.4 Conclusions

The viability of ion beam sputter-deposition of a high-entropy alloy thin film in the quaternary system Fe–Cr–Mn–Ni has been demonstrated. Two thin solid films were deposited on a Si substrate and the microstructural differences were analysed using conventional TEM. It has been shown that the high-entropy effect may be influential in the dynamics of nucleation and growth of nanocrystals and due to these effects, the grain size of the HEATF was bigger (around of 100–250 nm) than the NETF (around of 25 nm on average). The next stage of this research consists of depositing the HEATF onto Zircaloy-4^{TM} and assessing its radiation resistance using heavy ion irradiation *in situ* within a TEM.

7.4 Synthesis and characterisation of the HEATF on Zircaloy-4^{TM}

Zr alloys are of great importance for the technology of nuclear reactors. The element Zr has reduced thermal neutron absorption cross section (1.58±0.12 barn) giving rise to superior neutronics performance in LWRs [480]. Additionally, these alloys exhibit a whole set of suitable properties for application in extreme environments such as high corrosion resistance and good mechanical strength [25]. Despite these beneficial properties, the recent Fukushima-Daiichi nuclear disaster raised the issue

of the oxidation behaviour of Zr-based alloys at higher temperatures in contact with water vapour.

The ion beam sputter-deposition of a HEATF onto a Zircaloy-4^{TM} substrate is reported in this section. The HEATF is herein evaluated aiming at investigating this material as a possible future candidate for further research within the ATF programme.

7.4.1 Deposition and methods

Prior to the thin film deposition, the Zircaloy-4^{TM} substrate was mechanically polished using SiC papers with grits from 120 to 1200 μm aiming at to reduce its thickness and increase the surface flatness. Final polishing using diamond lapping films with diamond paste (down to 1 μm grit-size) was carried out for better surface finishing. The substrate was then electropolished at 233 K using an electrolyte of 10% $HClO_4$ and 90% CH_3OH (in vol.%) with 20 V applied using steel electrodes. Electropolishing was performed for up to 2 minutes and at the end, the surface was mirror-like. After the surface preparation of the substrate, the HEATF was deposited using the same conditions and methods reported in appendix A.

7.4.2 Characterisation at the mesoscale

The elemental composition of the Zircaloy-4^{TM} substrate was estimated via energy dispersive X-ray spectroscopy and is shown at table 7.2. The detection of a small amount of O suggests the presence of a Zr oxide layer on the top of the alloy. When freshly-polished Zr metallic surfaces are exposed to O (even at low temperatures) an oxide layer is formed and it behaves as a passivation layer that protects the material from further oxidation [321]. The formation energy of of Zr oxides are reported to have high negative values (thus low formation energy), of around -1000 kJ·mol^{-1} [481], and so, an oxide passivation layer readily forms on fresh-polished Zr surfaces and is impossible to avoid under normal circumstances. Regarding the elemental composition, it should be noted that commercial Zircaloy-4^{TM} has also Fe and Cr in solid solution at the levels of 0.22 and 0.12 wt.%, respectively, whose detection with the EDX system was not possible probably due to the experimental limitations of the instrument in detecting low-content elements.

Figure 7.8(a) shows the microstructure of Zircaloy-4^{TM} which is composed of needle-like grains characteristic of a Widmanstätten pattern. The grain size varies from 25 to 100 μm which agrees with previous observations of Zr-alloys [482]. As the grain microstructure was clearly revealed after eletropolishing, the preparation recipe used was adequate for such purposes. In addition, neither pitting or over-etching spots were observed after the electropolishing.

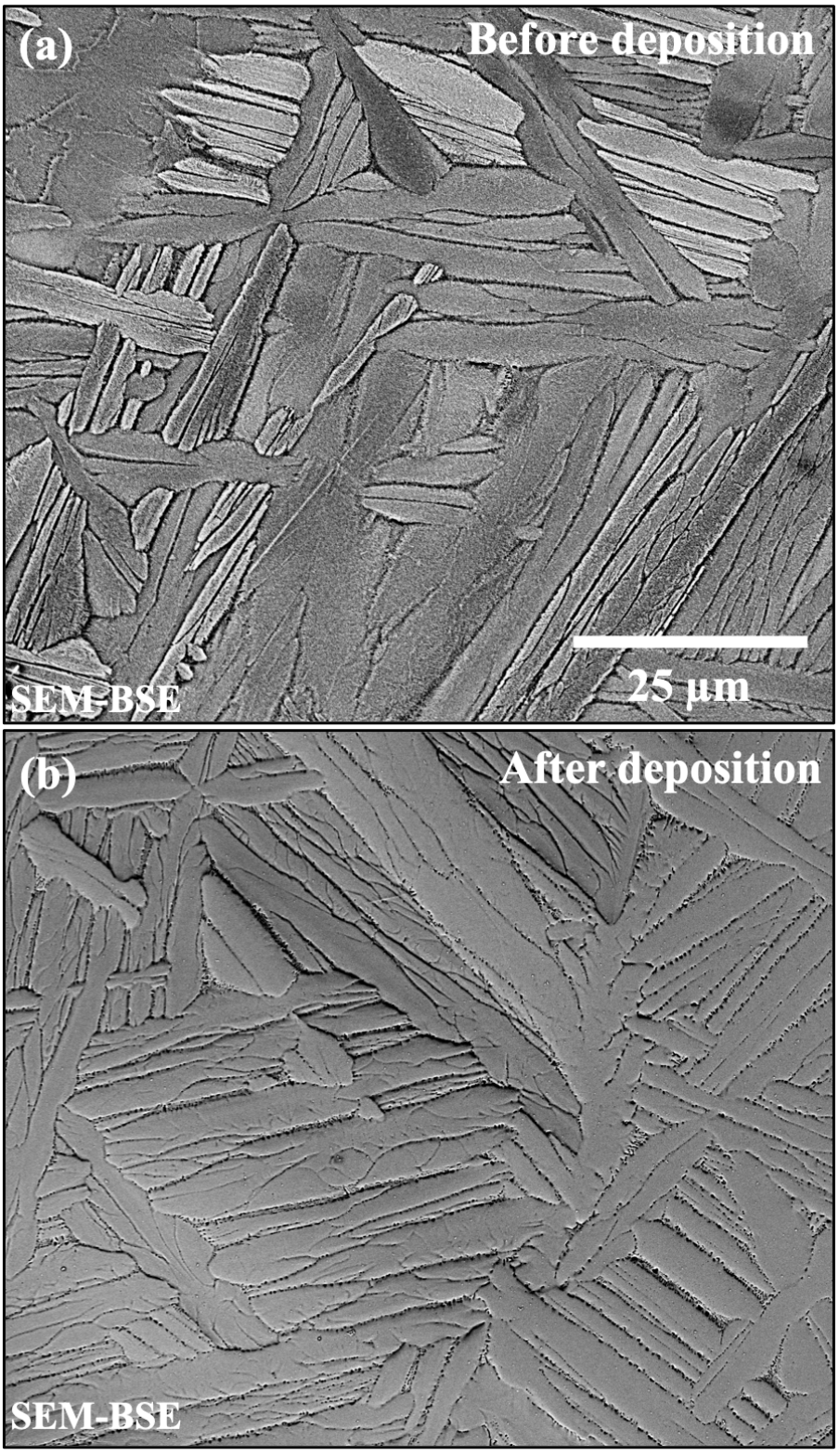

Figure 7.8: SEM-BSE micrographs showing (a) the microstructure of the Zircaloy-4^{TM} substrate before the deposition and (b) the FeCrMnNi HEATF after deposition on the Zircaloy-4^{TM} substrate. Small changes in the BSE contrast after deposition as shown in (b) are attributed to different crystallographic orientations of the substrate as shown in (a).

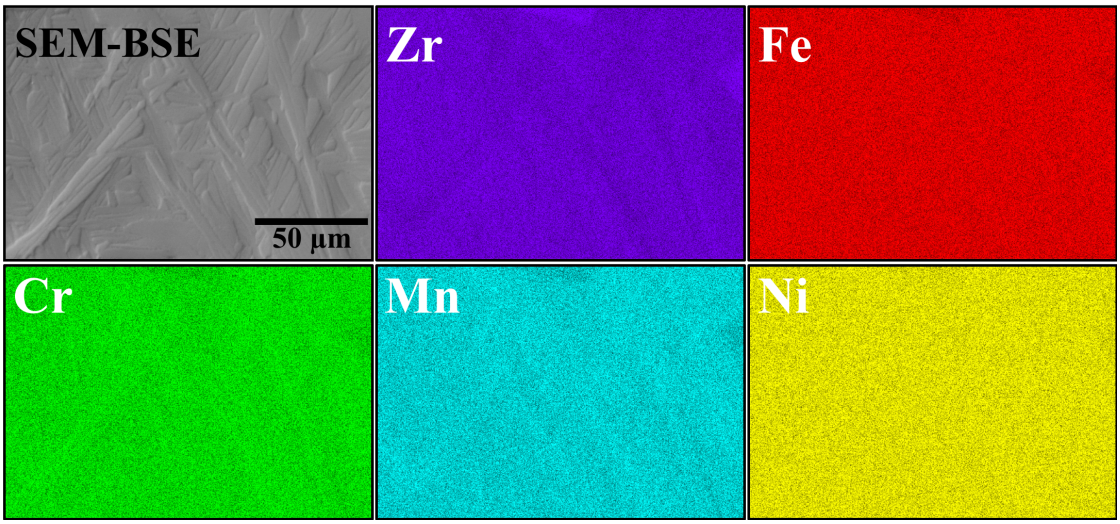

Figure 7.9: SEM-BSE elemental map of the FeCrMnNi HEATF as deposited on the Zircaloy-4^{TM} substrate. These elemental maps are showing uniformity in the distribution of coating elements on the substrate: no secondary phase was detected at this scale.

After deposition, the microstructure of the Zircaloy-4^{TM} had its grain pattern preserved as showed by the SEM figure 7.8(b), but the significant changes in the backscattered electron contrast indicates that the FeCrMnNi HEATF was deposited uniformly throughout the matrix as this SEM operational mode is sensitive to the elemental composition and the orientation of the grains. Such experimental evidence was further confirmed by the elemental maps exhibited in the set of micrographs 7.9.

The EDX spectrum of the HEATF deposited on Zircaloy-4^{TM} is shown in figure 7.10 and its quantification (table 7.3) indicates that the thin film was close to

Table 7.2: The elemental composition of the Zircaloy-4^{TM} prior to deposition as measured by SEM-EDX.

Element	**Zircaloy-4^{TM} [wt.%]**
O	3.5±0.2
Zr	95.3 ±4.8
Sn	1.2 ±0.1

Table 7.3: The elemental composition of the HEATF on Zircaloy-4^{TM} after deposition and measured by SEM-EDX.

Element	**HEATF [wt.%]**
Fe	25.3±0.5
Cr	23.4±0.5
Mn	24.3±0.5
Ni	27.0±0.6

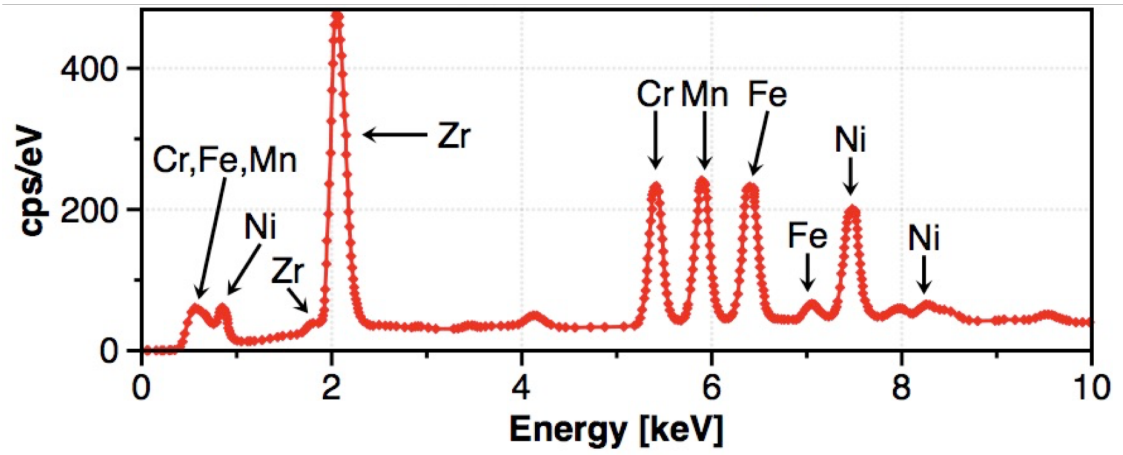

Figure 7.10: EDX spectrum of the FeCrMnNi HEATF as deposited on the Zircaloy-4^{TM} substrate. The elemental quantification is shown in table 7.3.

equiatomic. The measured composition of the FeCrMnNi HEATF on Zircaloy-4^{TM} was found to be similar to the FeCrMnNi HEATF deposited on Si presented in table 7.1 and also to the bulk FeCrMnNi HEA as shown in table 4.5 (section 4.3.2.1). By using the electron beam of the SEM with an energy of 30 keV, the Zircaloy-4^{TM} matrix was also detected through EDX as shown in the spectrum in figure 7.10.

7.4.3 Characterisation at the nanoscale

Three layers can be seen in figure 7.11(a) and they represent a multilayered microstructure at the nanoscale: the deposited FeCrMnNi HEATF, the Zr oxide layer and the Zircaloy-4^{TM} substrate. The underfocused BFTEM micrograph in figure 7.11(b) shows that porosity was present in the oxide layer. Surface roughening was observed in the FeCrMnNi HEATF as also shown in figure 7.11(b). The oxide layer was of irregular shape and size and its thickness was approximately 50–80 nm.

TEM characterisation of the interface of the HEATF and the Zircaloy-4^{TM} substrate indicated the presence of some amorphous material, possibly the oxide layer, as shown in the BFTEM micrograph in figure 7.12(a) and its respective diffraction pattern in figure 7.12(b). The grain-size of the FeCrMnNi HEATF was in the range 100–200 nm (similar to the results reported in appendix A for the HEATF deposited on the Si substrate). The presence of twins was also observed for the film deposited on the Zircaloy-4^{TM} substrate as evidenced by the BF and DFTEM figures 7.12(c–d).

7.4.4 Discussion

The microstructure of a sputter-deposited thin film is related to the temperature and pressure conditions during the deposition. According to models proposed by Movchan and Demchishin [375] and later amended by Thornton [373, 374], in thin

solid films deposited at low homologous temperatures (less than $0.3T_m$), the typical microstructure consists of columnar grains and voided grain boundaries [373–375]. This is clearly not the case for the FeCrMnNi HEATF studied in the present work. Assuming the FeCrMnNi melting point around of 1800 K (typically the melting temperature of ferrous alloys) [217, 483], the homologous temperature for the FeCrMnNi HEATF deposition on the Zircaloy-4^{TM} substrate was $\approx 0.2T_m$.

The differences in the HEATF microstructure from the previous models proposed by Movchan, Demchishin and Thornton were explored in the research reported in section 7.3 and in a publication by our group [376] where it was demonstrated that the high-entropy effect may affect the dynamics of nucleation and growth when (closer to) equiatomic elemental composition is achieved. By favouring the nucleation of bigger grains, the microstructure of the HEATF deposited on Zircaloy-4^{TM}

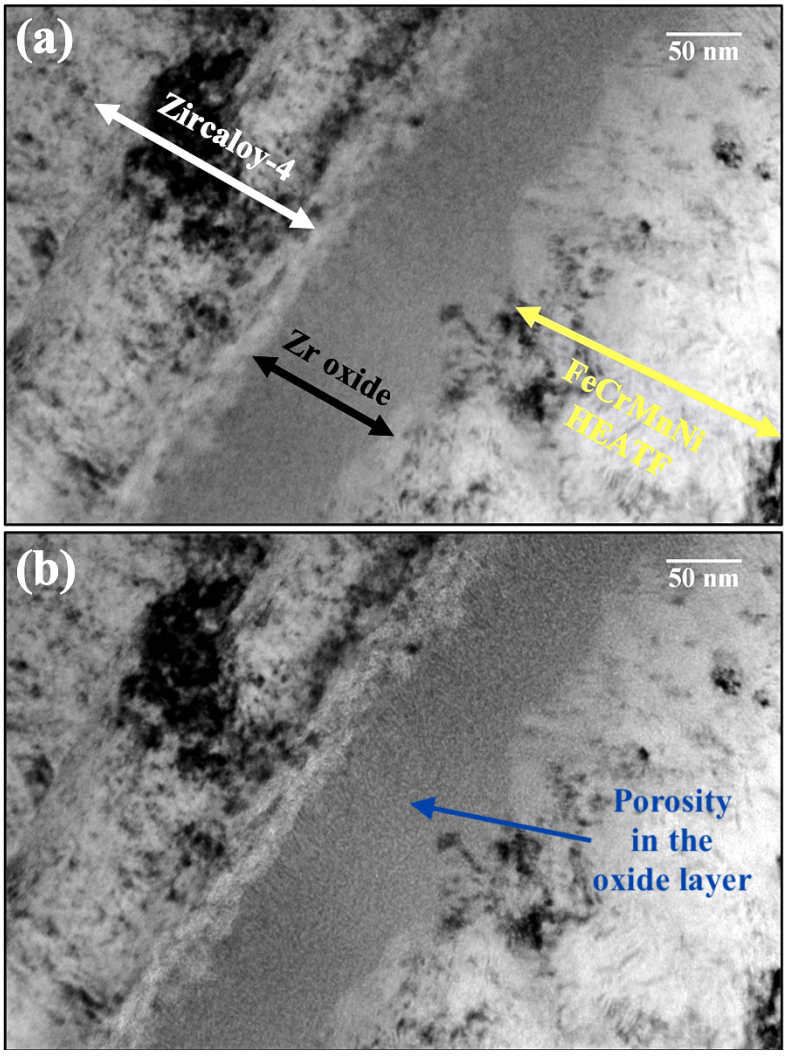

Figure 7.11: BFTEM micrographs of the FeCrMnNi HEATF deposited on Zircaloy-4^{TM} (a) at focus and (b) underfocused (1 μm) showing porosity in the oxide layer. The micrographs show the three-layer structure with the Zircaloy-4^{TM} substrate, the oxide layer and the FeCrMnNi HEATF.

resembles typical metallurgical grain boundaries closer to an equiaxed grain microstructure.

An oxide layer was observed between the Zircaloy-4^{TM} substrate and the FeCrMnNi HEATF. The formation of an oxide/passivation layer after the Zircaloy-4^{TM} electropolishing is favoured by the low formation energy for oxidation, particularly for metals like Zr, Ti, Ta, Nb and Cr. Attempts to avoid this oxidation by changing electropolishing and processing parameters were not successful. The impact of this oxide layer on the mechanical properties of this thin film is a motivation for future studies.

Surface roughening may be present in the microstructure of the thin film deposited on Zircaloy-4^{TM} as was detected in the thin films deposited on Si (figure

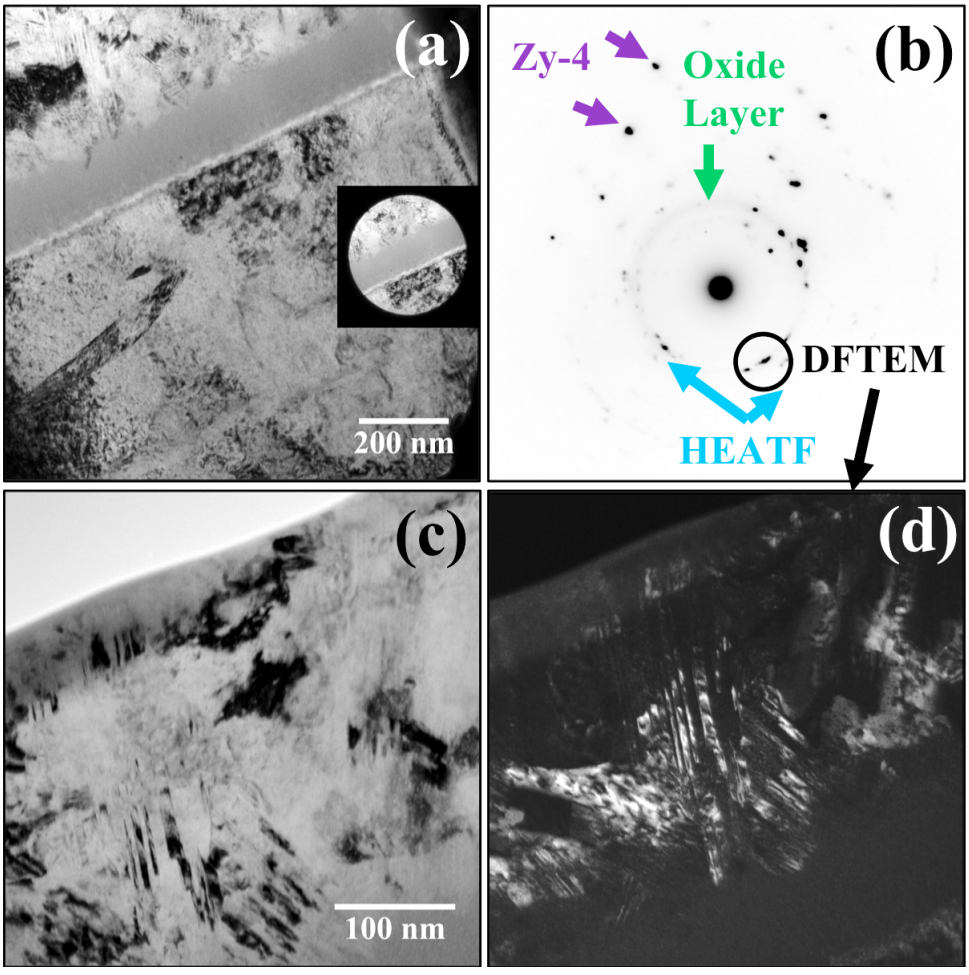

Figure 7.12: (a) BFTEM micrograph of the HEATF microstructure. (b) Diffraction pattern taken in the region of the interface between the HEATF and the Zircaloy-4^{TM} substrate as shown in the inset in (a). The diffraction pattern contains the Zircaloy-4^{TM} reflection spots, the HEATF reflection spots and the amorphous Zr oxide ring. The BFTEM and DFTEM micrographs (c) and (d), respectively, show the presence of planar defects in the thin film. Note: the underfocus degree in (a) and (c) was 1000 nm.

7.7). Additionally, porosity was observed in the oxide layer as can be seen in figure 7.11. The surface roughening phenomenon has been studied by several authors in the thin solid films community, including Lloyd [484] and Nakahara [485]. This effect can be attributed to the fact that IBSD of thin solid films is viewed as a low energy implantation process and the low mobility of solutes favours clustering of implanted interstitial species [486]. In this way, the speckled contrast observed in thin films at the nanoscale can be either surface roughening or porosity due to voids or Ar bubbles (Ar is used to generate plasma in the IBSD system as described in section 3.1.4). Whether or not they are bubbles is still a subject for further analytical characterisation using high-resolution aberration-corrected (S)TEM microscopes as the physical dimensions of these objects is around 1–2 nm.

Following the synthesis and characterisation of the FeCrMnNi HEATF deposited on the Zircaloy-4^{TM} substrates, cross-sectional samples were subjected to heavy ion irradiation in order to analyse their radiation response and this will be presented in the next section. Although we are proposing these HEATFs as new materials systems for investigation within the scope of the ATF programme, in the research reported in this thesis, only their radiation resistance *in situ* within a TEM was assessed under PWR nominal operation conditions. Further tests of corrosion and oxidation resistance, compatibility with reactor coolant materials, mechanical performance and response to neutron irradiation would have to be carried out before it could be considered for use in a nuclear reactor.

7.5 Radiation resistance of the HEATF deposited on Zircaloy-4^{TM}

In this section, the radiation resistance of the FeCrMnNi was assessed through the use of medium-energy heavy ion irradiations. According to English and Eyre [487], the methodology of using medium-energy heavy ion irradiations (E$\leq$200 keV) can be considered an efficient means of simulating neutron-induced radiation damage effects in alloys. These irradiation conditions also allowed the study of nucleation and growth of inert gas (Xe) bubbles within the HEATF microstructures.

7.5.1 The design of the experiment

As the samples were deposited on a Zircaloy-4^{TM} substrate, FIB milling was necessary in order to produce electron-transparent specimens for TEM *in situ* heavy ion irradiation. The cross-sectional FIB lift-out lamellae were irradiated using 134 keV Xe ions *in situ* in a TEM at 573 K in the MIAMI-2 facility. The calculated implantation and damage profiles for both the FeCrMnNi HEATF and the Zircaloy-4^{TM}

substrate are exhibited in figures 7.13(a) and 7.13(b). The choice for the medium-energy regime was made justified to get an approximately uniform implantation and damage profiles across the thin foil.

In these experiments, the analysis was focused on the FeCrMnNi HEATF microstructure rather than the Zircaloy-4^{TM} substrate. Fluence-to-dpa conversion was applied to the HEATF: 2.4×10^{15} ions·cm^{-2} and 1.5×10^{16} ions·cm^{-2} correspond to 2.6 dpa and 15.4 dpa, respectively. The latter dose was the maximum achieved at the end of the experiment. Post-irradiation TEM characterisation was performed using conventional TEM techniques and EFTEM. The results are compared with similar irradiations performed on a conventional functional thin film – titanium nitride (TiN) – recently proposed as an accident tolerant fuel coating for nuclear fuel cladding alloys by Alat *et al.* [468, 469].

7.5.2 Results and discussion

7.5.2.1 Microstructural response of the HEATF/Zircaloy-4^{TM} system under *in situ* TEM heavy ion irradiation

The cross-sectional microstructure of the HEATF, the oxide layer and the Zircaloy-4^{TM} before irradiation and after annealing at 573 K is shown in the BFTEM figure 7.14(a).

During irradiation at around of 2.6 and 6.2 dpa, the BFTEM micrographs in figure 7.14(b–c) exhibit formation of nanoclusters (whose appear with black contrast) preferentially in the oxide layer and in the Zircaloy-4^{TM} substrate, but were less noticeable in the microstructure of the HEATF. The underfocused figure 7.14(c)

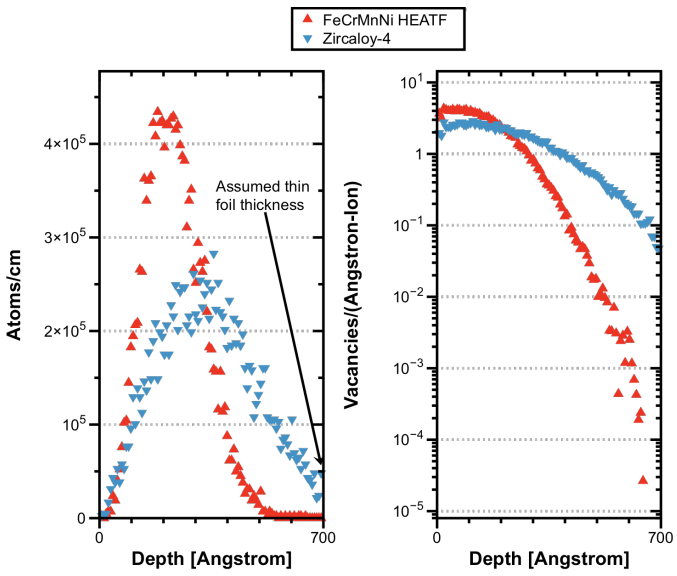

Figure 7.13: (a) The implantation and (b) damage profiles for the FeCrMnNi HEATF and the Zircaloy-4^{TM} for the 134 keV Xe ion irradiation.

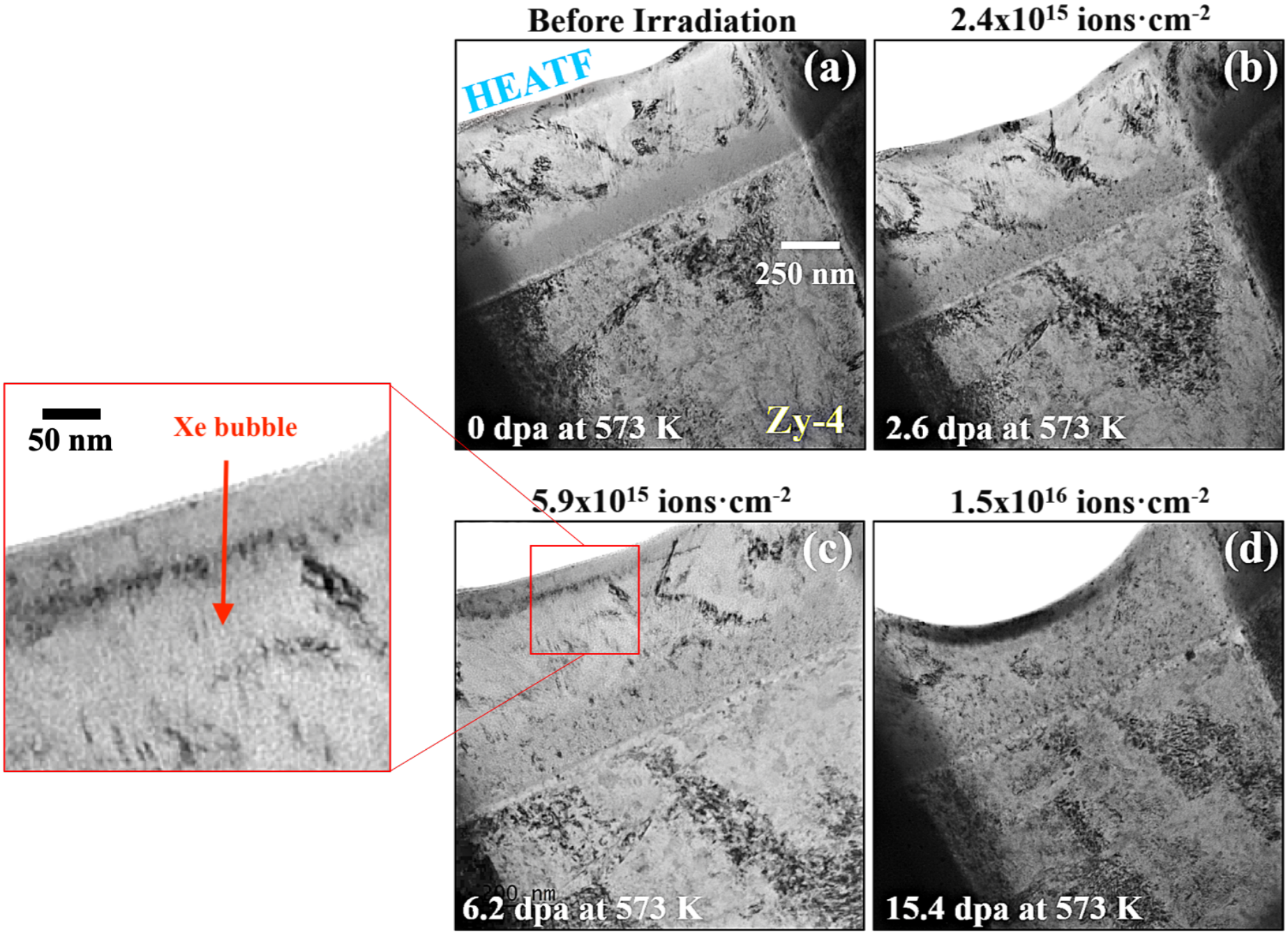

Figure 7.14: The microstructural evolution of the FeCrMnNi HEATF and the Zircaloy-4^{TM} substrate monitored *in situ* within the TEM from (a) 0 dpa to (d) 15.4 dpa. Note: all the micrographs in the figure are underfocused (1 μm) and the scale bar in (a) also applies to (b-d).

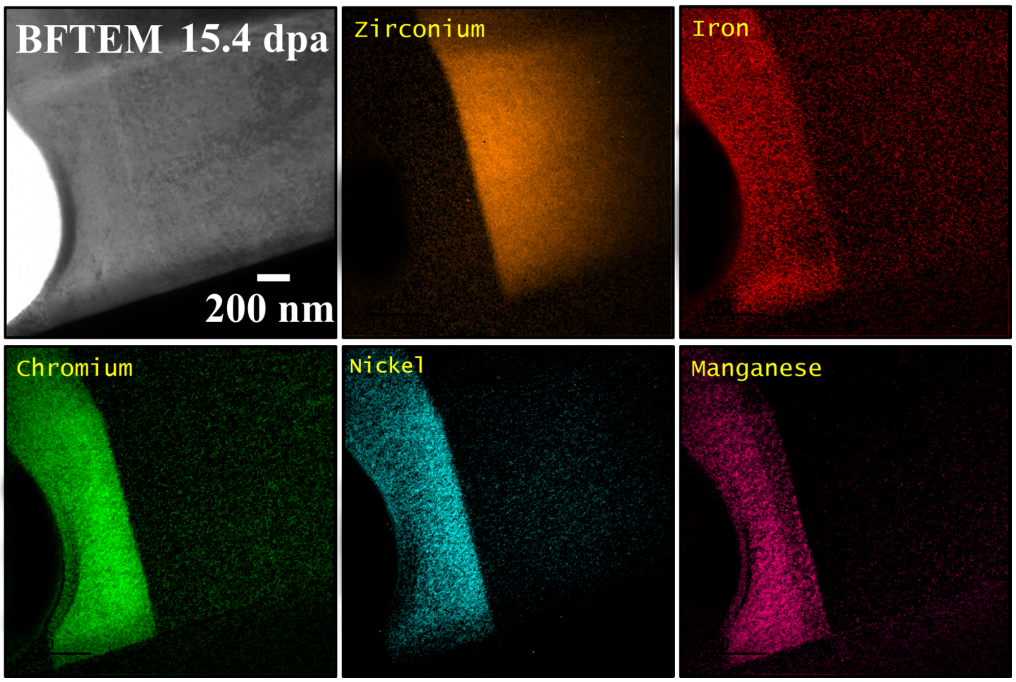

Figure 7.15: EFTEM micrographs of the post-irradiated FeCrMnNi HEATF deposited on the Zircaloy-4^{TM} substrate at the end of the irradiation experiment at 15.4 dpa.

revealed the presence of Xe nano-bubbles in the HEATF at 6.2 dpa (the Xe bubbles can be seen more clearly in the HEATF microstructure later in zoomed figures 7.18(b-c)). At the end of the experiment, it was observed that the thin film had experienced to ion-induced bending and sputtering with its morphology slightly changed. By the changes in the diffraction contrast of the oxide layer as shown in the set of figures 7.14(a–d), it can be noticed its size had significantly reduced. Displacement damage (black-spots) and Xe bubbles were observed in the HEATF at the end of the experiment at 15.4 dpa as shown in figure 7.14(d).

The analytical characterisation using the MIAMI-2 facility EFTEM capabilities is shown in figure 7.15. It can be seen that although the HEATF was subjected to high doses, there is no indication of radiation-induced solute segregation or phase transformation. Therefore, the thin film had its random solid solution preserved. However, Mn is observed to be depleted in the oxide layer region which was observed to shrink by the end of the experiment. The other elements, Fe, Cr and Ni have uniform signals in the region of the oxide. During the irradiations and at moderate temperatures (573 K), elemental migration to the oxide is a possibility. The reduction in the oxide layer thickness indicates that this migration may have occurred, although it has clearly not compromised the other areas of the thin film random solid solution.

7.5.2.2 Microstructural response of the TiN thin film under *in situ* TEM heavy ion irradiation

TEM cross-section lamellae were prepared (using the same FIB lift-out technique as for the HEATF) from a TiN thin film deposited on an Al-Si alloy for irradiations under the same conditions as those used for the FeCrMnNi HEATF, but with a slightly lower irradiation temperature (473 K) in order to minimise bulk diffusion from the substrate which has a low melting point. This material was provided by the University of São Paulo as part of a joint scientific collaboration and it was produced using the technique of magnetron-sputtering.

The microstructure of the TiN thin film before irradiation is shown in figure 7.16(a). During irradiation, as the dose increases, the grain boundaries of the TiN nanocrystals broaden. The size of Xe bubbles also significantly increased from 2.6 to 6.2 dpa as can be qualitatively seen in figure 7.16(b) and 7.16(c).

Analytical characterisation with EFTEM has identified Ti segregation along the grain boundaries as shown in the set of micrographs in figure 7.17. This segregation was further confirmed by means of STEM-EDX analysis performed in a FEI Talos F200X TEM at the Oak Ridge National Laboratory. These results indicates that such irradiation-induced segregation has been caused by two major factors followed by the dissociation of the TiN crystal under displacing irradiation: (i) the growth of Xe bubbles and (ii) the preferential migration of Ti displaced atoms towards the nanocrystal interfaces. During the irradiation-induced segregation, Xe bubbles would be able to incorporate displaced N atoms which can contribute to the pronounced growth from 2.6 to 6.2 dpa. Additionally, multivariate statistical analysis (MVSA) has revealed the presence of Ti within the Xe bubbles as shown in figure 7.17. Due to inherent difficulties of detecting N using the EDX technique, the lack of signal of N within the Xe bubbles is evident. However, if the TiN dissociates as indicated by the Ti segregation, monoatomic N atoms will have a tendency to recombine into molecular N gas (*i.e.* N_2) and also segregate into Xe bubbles, thus contributing for their growth.

Within the context of nuclear reactors, if TiN is applied as a coating material on the Zr alloys as proposed by Alat *et al.* [468], dissociation of the TiN followed by subsequent irradiation-induced segregation of Ti atoms along the grain boundaries and the nucleation and growth of inert gas bubbles due to transmutation reactions (mainly with N under neutron bombardment) will be likely to occur. These Ti-enriched grain boundaries could be then subjected to the same oxidation reaction as the Zr, for example, leading to the generation of H_2 gas: a fact that would need mitigation within the context of ATFs.

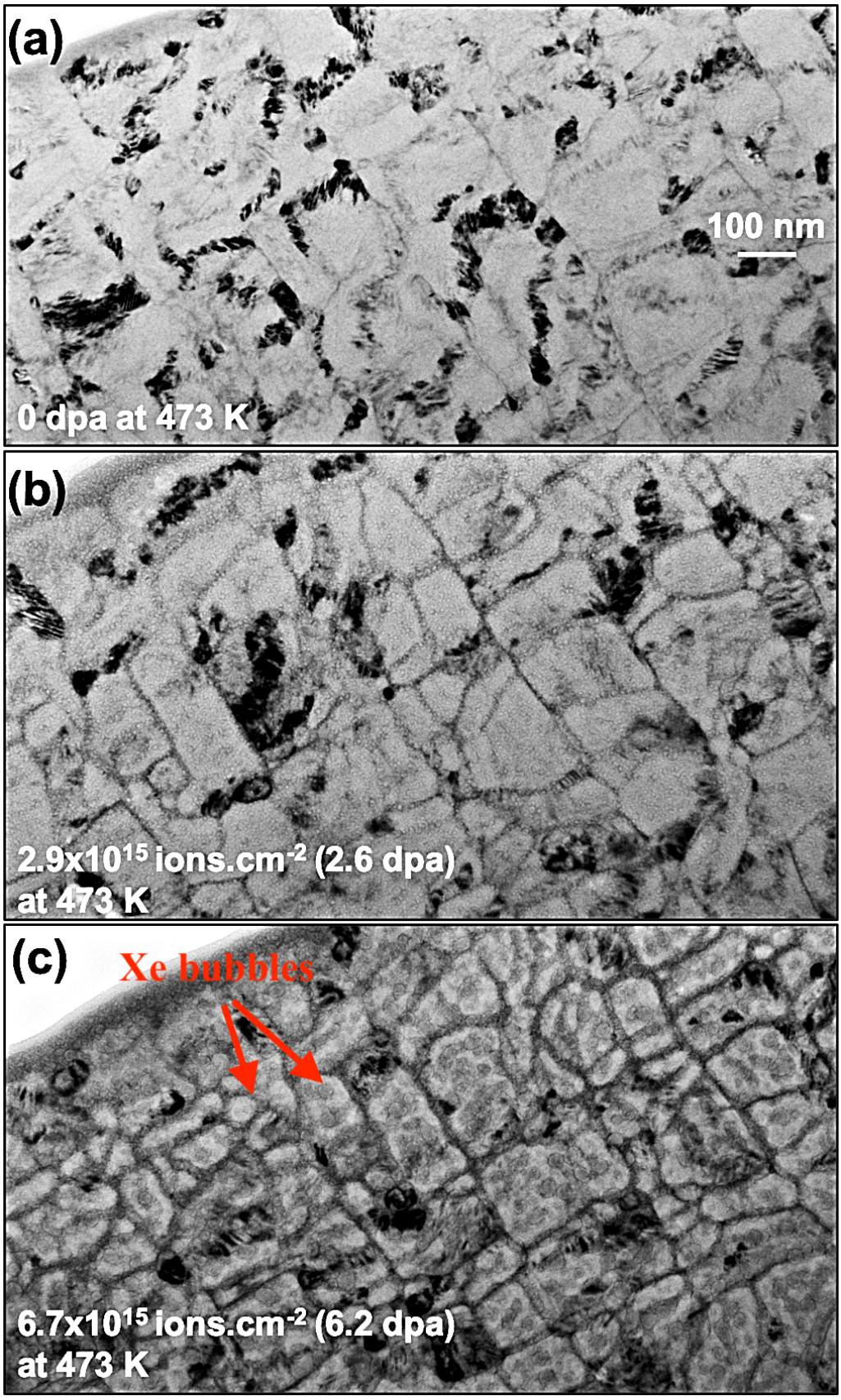

Figure 7.16: The microstructural evolution of the TiN thin film monitored *in situ* within the TEM and irradiated at similar conditions to the FeCrMnNi HEATF. Note: all micrographs in the figure are underfocused (≈ 1 μm) and the scale marker in (a) applies to all micrographs in the figure.

7.5.2.3 Quantitative comparison between the radiation response of HEATF and TiN coatings

A detailed comparative characterisation of the radiation response of TiN and HEATF coatings is shown in figure 7.18. The irradiations were carried out up to 6.2 dpa where significant modifications to the TiN microstructure were observed to occur. As investigated in section 7.5.2.2, the grain boundaries of the TiN crystals were observed to broaden due to Ti segregation as confirmed independently via two different analytical techniques: STEM-EDX and EFTEM. The same effect was not observed in the irradiations performed in the HEATF coatings. When comparing figures 7.18(b) with 7.18(e) and 7.18(c) with 7.18(f), one can qualitatively notice that the size of Xe bubbles has significantly increased from 2.6 to 6.2 dpa in the TiN microstructure whilst for similar irradiations performed in the HEATF coating,

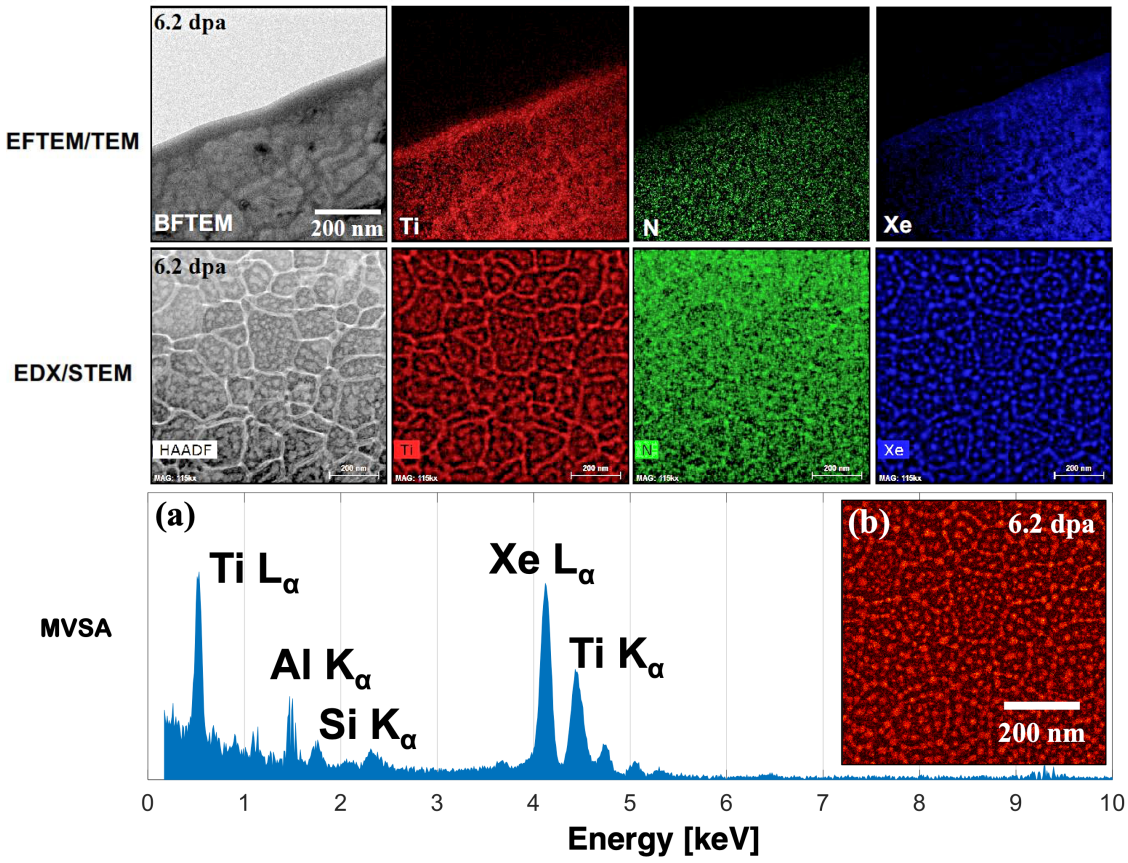

Figure 7.17: EFTEM micrographs of the TiN thin films irradiated to 6.2 dpa showing Ti segregation. Results were further confirmed by STEM-EDX analysis of the same irradiated lamella. The bottom figure is the multivariate statistical analysis (MVSA): (a) the EDX spectrum corresponding to the (b) spectral image. The spectral image (b) in combination with the EDX spectrum in (a) indicates the presence of Ti within Xe bubbles after 6.2 dpa of irradiation.

this "anomalous growth" effect was not observed. In order to better quantify the effects of heavy ion irradiations in such thin film coatings, a quantitative comparison between radiation response in both microstructures is performed in this section.

By measuring the size (diameter) of the Xe bubbles as a function of dose for both the TiN and the HEATF coatings, quantitative distributions of Xe bubbles sizes were obtained as a function of dose and the results are shown in figures 7.19(a-b) for both films. In the case of the TiN thin film, at 2.6 dpa, the average Xe bubble diameter was measured to be 4.1±0.2 nm whilst at 6.2 dpa, the average Xe bubble diameter was measured to be 25.2±0.5 nm: an average increase of around 600%. For the FeCrMnNi HEATF, at 2.6 dpa, the average Xe bubble diameter was measured to be 3.9±0.1 nm. At 6.2 dpa, the average Xe bubble diameter in the HEATF microstructure was measured to be 4.7±0.1 nm. For the quoted average sizes above, the error is the standard error of the mean. The Xe bubbles thus had only a small growth in the case of HEATF which is not statistically significant when the errors are taken into consideration. These results on average bubbles sizes as a function of the irradiation dose are also better appreciated in a form of a plot as shown in figure 7.20(a).

The areal densities of the Xe bubbles were also measured for both TiN and HEATF coatings. For this purpose, five different areas were analysed and the areal densities reported here represent average values of the five measurements carried out in different areas. The error reported on the average areal densities values is the standard error of the mean. This procedure was carried out as suggested by Harrison *et al.* [488]. The measured areal densities as a function of the irradiation dose for both TiN and HEATF are presented in figure 7.20(b). Whilst for the HEATF the areal density of Xe bubbles was constant upon increasing the irradiation dose (within the errors), in the case of the TiN, the areal density reduced by one order of magnitude from 2.6 to 6.2 dpa. This reduction is in agreement with the fact that the average Xe bubbles sizes increased 600% in the TiN microstructure over the same dose range: in order to grow, bubbles have to coalesce which implies in the reduction of the areal densities.

The quantitative comparison presented in this section corroborates the fact that the TiN thin film had undergone severe with radiation-induced segregation, possibly triggered by the "anomalous" growth of Xe bubbles (600% from 2.6 to 6.2 dpa). Such a radiation-induced segregation effect is possibly followed by the dissociation of TiN crystals which could release monoatomic N atoms that upon recombination into N_2 gas may contribute to the observed growth of the Xe bubbles with increasing the irradiation dose. In comparison, in the HEATF case, neither radiation-induced segregation nor "anomalous" growth of Xe bubbles were detected. Whether or not such N_2 really influences the kinetics of bubbles growth is a subject of further research.

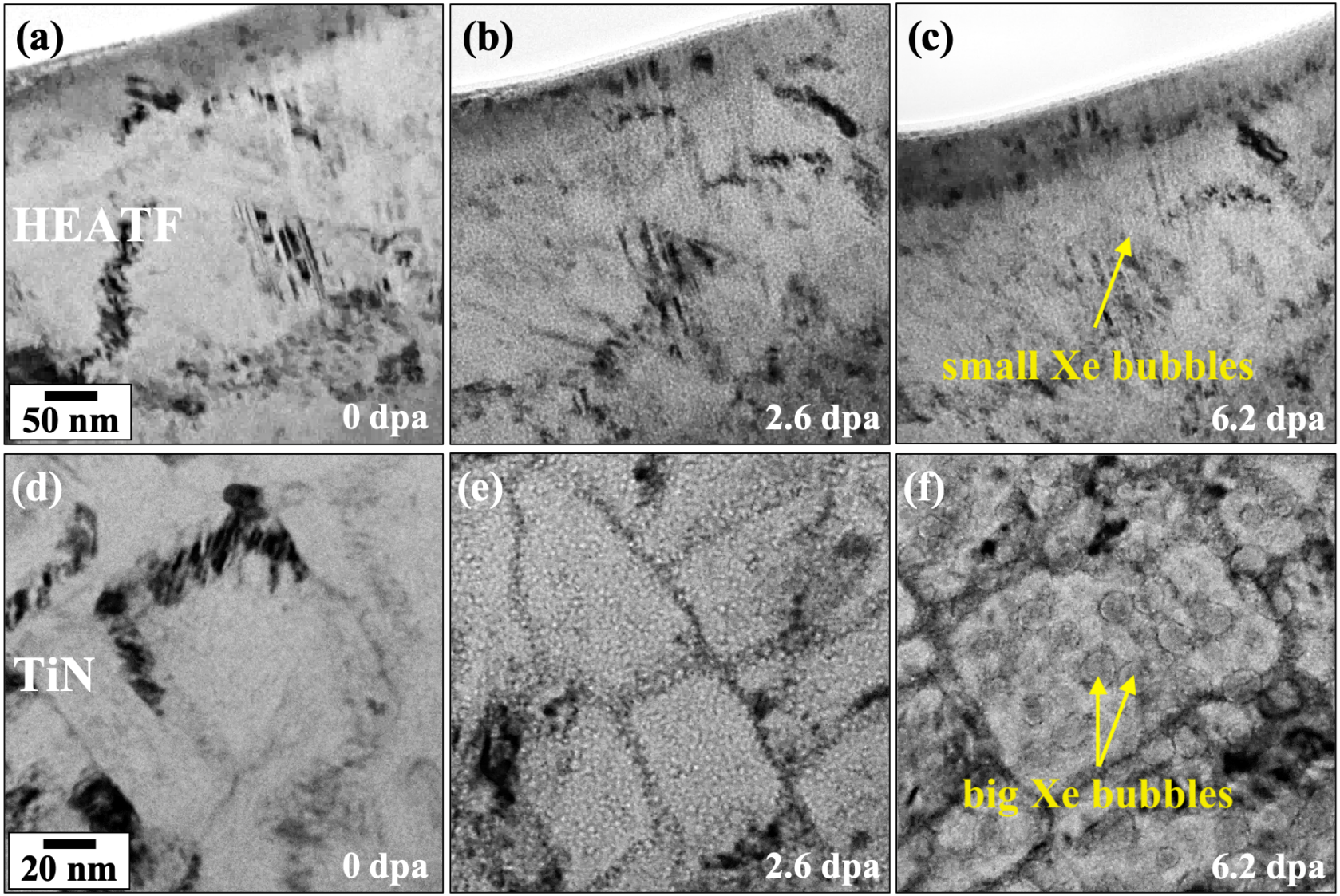

Figure 7.18: *In situ* TEM monitoring of Xe bubble nucleation and growth (a-c) in the HEATF and (d-f) in the TiN as a result of the heavy ion irradiations reported in this section. All micrographs in the figure were recorded with an objective lens underfocus of ≈ 1000 nm Note: scale bar in (a) also applies to (b-c) and the scale bar in (d) also applies to (e-f).

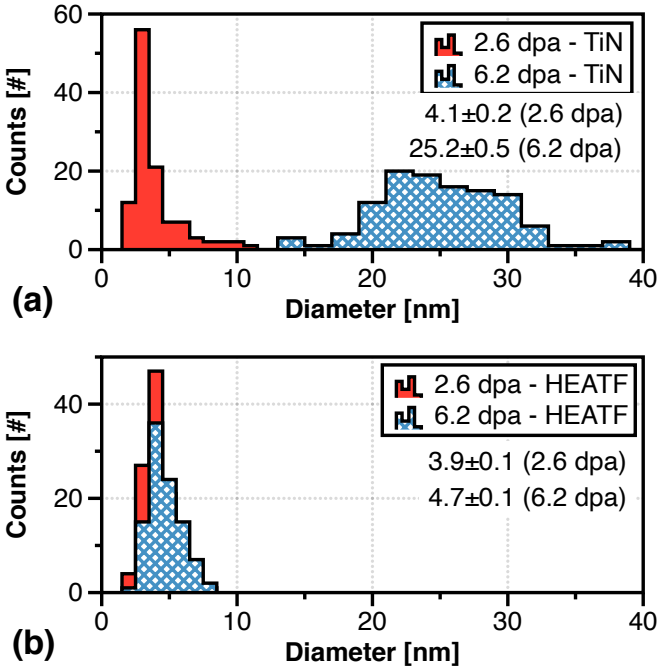

Figure 7.19: Histograms of sizes (diameter) of Xe bubbles as a function of the irradiated dose in (a) TiN and (b) HEATF coatings.

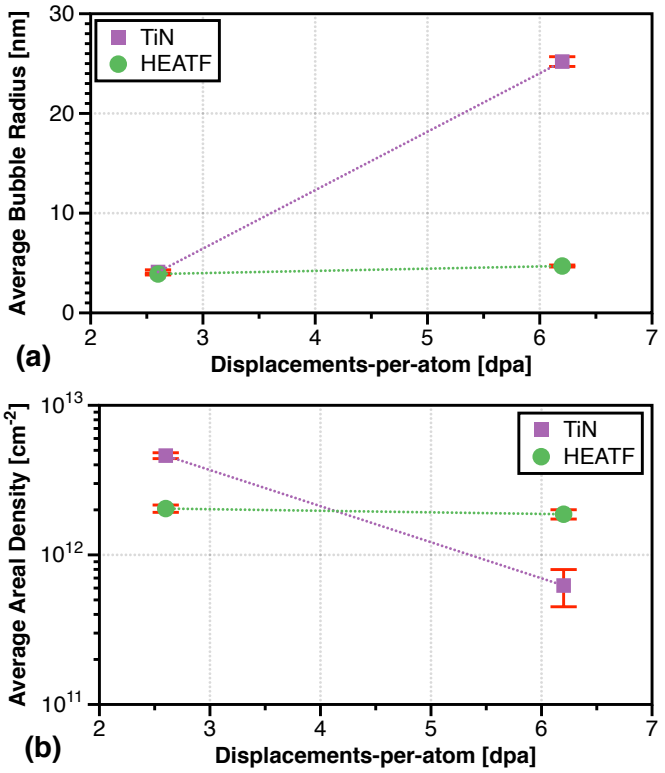

Figure 7.20: (a) Average Xe bubbles diameter and (b) average areal density of Xe bubbles as a function of the irradiation dose for TiN and HEATF coatings.

The considerations presented here suggest that, under the conditions studied in this work, TiN may be not the best solution for ATF systems as previously claimed on the basis of corrosion, oxidation and Zr-compatibility measurements [468, 469]. The present study also suggests a high radiation resistance potential for the HEATF coatings which could be further investigated within the scope of ATFs as only its *in situ* TEM heavy ion irradiation response was investigated in this work.

7.6 Conclusions and perspectives for HEATFs in the accident tolerant fuels technology

Equiatomic thin solid films from the metallic quaternary system Fe–Cr–Mn–Ni were successfully deposited on Si substrates and subsequently deposited with on Zircaloy-4^{TM} substrates. By assessing the radiation resistance of the HEATF using heavy ion irradiation with *in situ* TEM, after 15 dpa, the HEATF had its random solid solution preserved; irradiation-induced segregation and/or phase separation were not detected. Xe bubbles developed in the HEATF as a primary radiation effect, but quantitative measurements showed that such bubbles did not grow significantly upon increasing the irradiation dose. A comparison of the HEATF irradiations with a conventional ceramic thin film – TiN – has shown that the latter was clearly subjected to dissociation and elemental segregation possibly related with growth of around 600% in the average sizes Xe bubbles in the dose range from 2.6 to 6.2 dpa. These latter facts demonstrate that the TiN thin films may have limited applicability in the context of ATFs in nuclear applications.

The HEATFs were herein proposed as a potential materials for fuel cladding in the framework of the ATF programme, but only the radiation resistance aspect of these coatings was studied under PWR nominal operation conditions using the heavy ion irradiation *in situ* TEM methodology. Prior to their use in commercial nuclear reactors, additional testing is still required aiming at the investigation of their: (i) compatibility with the coolant in all its physical states (*e.g.* water and steam), (ii) mechanical properties before and after irradiation, and (iii) response to neutron irradiation.

It is well known that plasma vapour deposition of thin solid films is already a recognised commercial technique to produce coatings on a wide variety of materials in fields including the aerospace, automotive and semiconductor industries, optical components and sensors [489]. The development of HEATF on Zr-based alloys could open new alternatives to make LWRs technology safer and tolerant against possible accidents, but the effort to develop this technology is at an early stage of testing, as shown in this present chapter where their radiation response under *in situ* TEM

heavy ion irradiation was investigated.

Possibilities for further research include the design of new thin films resistant to both irradiation and corrosion that could be used also in innovative nuclear reactors operating at high temperatures (Generation-IV) as a protective barrier against aggressive coolants. Generation-IV heavy liquid metal (HLM)-cooled fast neutron reactors – *e.g.* lead-cooled fast reactors (LFRs) and lead-bismuth eutectic (LBE)-cooled fast reactors – pose a significant challenge in corrosion science due to the inherent corrosiveness of HLM coolants for structural and nuclear fuel cladding steels. It has been reported that austenitic stainless steels might experience selective leaching of alloying elements (such as Cr, Ni and Mn) within the reactor core resulting in steel ferritization due to the removal of austenite stabilisers [490–492]. Such significant material degradation could be mitigated by using a protective coating with excellent corrosion resistance in such environments. These facts emphasise the need for further research a the corrosion response of the HEATF developed in this research.

Future research on the topic of coatings for nuclear fuel claddings, irradiations aiming at comparing the microstructures of the FeCrMnNi HEATF and the FeCrMnNi HEA in its bulk form should be carried out aiming at evaluating the effects of grain sizes on both bubble formation and displacement damage accumulation. It must be emphasised that the HEATF is a nanocrystalline metallic thin film and recent research by our group [493] and others [494] has revealed an interesting relationship between nanocrystallinity and superior radiation tolerance within the scope of HEAs for nuclear applications.

Chapter 8

Neutron and heavy-ion irradiation effects on Ti-based MAX phases

8.1 Introduction and background

Similarly to the highly concentrated multicomponent alloys (including high entropy alloys), the MAX phases have also attracted the attention of the nuclear materials community as a new class of candidate materials for use in innovative designs of nuclear power reactors (Generations III+ and IV) in which operation at high temperatures and high neutron doses are major requirements. In particular, the properties of interest that make the MAX phases promising candidate materials for future reactor power plants are: good thermal conductivity; low thermal expansion; high resistance to chemical attack, oxidation and corrosion; and intermediate hardness between metals and conventional ceramics.

One particular aspect of the study of MAX phases is the intense debate on their thermodynamic stability at higher temperatures [105]: this is essentially the capability of these ternary compounds to preserve their nanolaminated single-phase structure at high temperatures and also under the action of external conditions such as corrosion and mechanical load. In order to be considered as candidate materials for the next fleet of innovative nuclear reactors, it is of paramount importance that the MAX phases also demonstrate superior phase stability under irradiation impact with energetic particles.

By analysing the ternary phase diagrams of the Ti–Si–C [441] and Ti–Al–C [439] systems available in the scientific literature calculated at the isothermal sections around 1273 K and at a pressure of 1 atm as shown in figure 8.1, it can be seen that, along with the known stoichiometric ternary carbide phases, *i.e.* Ti_3SiC_2 and Ti_2AlC, several other phases may form under the decomposition of these ternary phases: titanium silicides, titanium aluminides (known as intermetallic phases) and

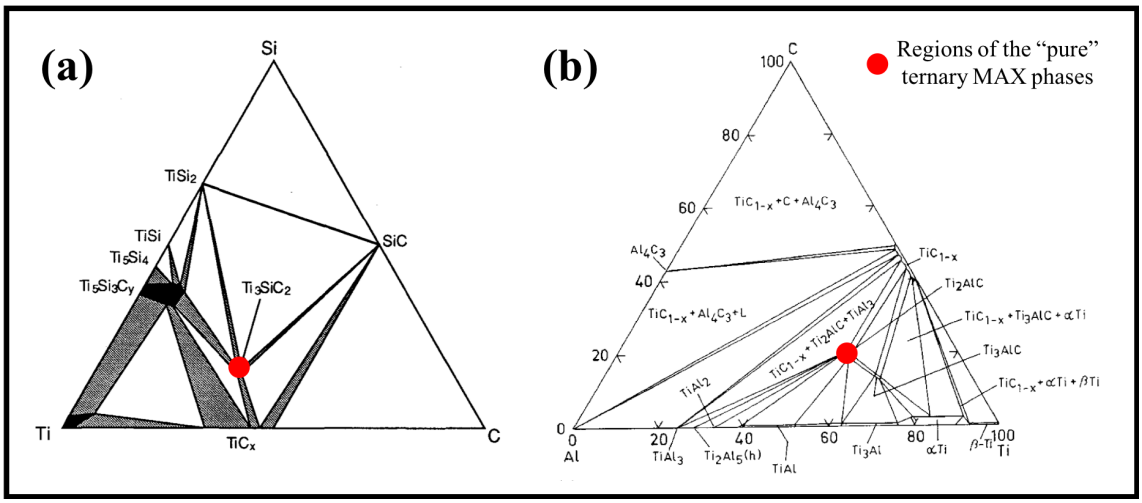

Figure 8.1: The ternary phase diagrams in the isothermal section of 1273 K and 1 atm for the systems (a) Ti–Si–C [441] (b) and Ti–Al–C [439]. (Adapted from references [441] and [439].)

TiC or SiC. The phase decomposition – which occurs when the MAX phase microstructure is exposed to high temperatures – involves the depletion or enrichment of at least one constituent.

The multiple aspects and reported results on the radiation tolerance of MAX phase compounds under neutron and ion irradiation were introduced in section 2.4.3. To date, the number of studies on the resistance of such MAX phases to neutron exposure is fairly limited. To date, three papers have been published which have explored the neutron radiation damage microstructure of Ti-based MAX phases up to around 3.6 dpa [354–356].

This chapter reports on a electron microscopy study of the radiation tolerance of two Ti-based MAX phases – Ti_3SiC_2 and Ti_2AlC – from a microstructural perspective. These MAX phases were irradiated with neutrons at the HFIR located at the Oak Ridge National Laboratory up to 2 and 10 dpa at 1273 K. This irradiation temperature is relevant as the Ti-based MAX phases are currently candidates to be used as structural materials for future nuclear fusion reactors [495]. Then, the same materials in a pristine condition were subjected to heavy ion irradiations *in situ* within a TEM at the MIAMI-2 facility up to 5 dpa at 1008 K in order to compare the results with the neutron irradiated MAX phases. The ion irradiation temperature was smaller than the neutron irradiation temperature due to a thermally-induced decomposition effect observed in electron-transparent Ti-based MAX phase samples under annealing within the TEM: this will be reported in detail in section 8.3.2.1. Similar ion irradiations carried out on pure α-Ti and α-Al as a comparison with these elemental metals which are constituents of the MAX phases. Evidence of phase decomposition when the MAX phases are subjected to thermal annealing at

high temperatures will also be presented.

This chapter contributes new data on the radiation tolerance and phase stability of the Ti-based MAX phases at high temperatures as well as suggesting possible further investigations on the effects of energetic particle irradiation on these materials. In the discussion, the current challenges in using MAX phase compounds within nuclear reactor technology will be addressed.

8.2 Neutron irradiation effects in Ti-based MAX phases at high temperatures

In this section, the neutron irradiation response of the Ti-based MAX phases at high temperatures is investigated. The results will be introduced along with some discussion. In the last subsection, a discussion of the applicability of these materials within the nuclear technology will be presented.

8.2.1 Materials and Methods

Ti-based MAX phases were irradiated at the HFIR to two dose levels: 2 and 10 dpa. The neutron fluencies corresponding to doses of 2 and 10 dpa at the HFIR were 2×10^{21} and 1×10^{22} n·cm^{-2}, respectively. The irradiation temperature was 1273 K. Both MAX phases, the Ti_2AlC and Ti_3SiC_2, were produced by the commercial company 3-ONE-2 LCC from Philadelphia (USA). The methods of bulk MAX phase synthesis were described in section 3.1.3.

Due to the fact that the bulk irradiated samples were radioactive, TEM samples were produced in controlled conditions using "hot" electron microscopes and focused ion beams in the Low Activation Materials and Development Analysis laboratory at Oak Ridge National Laboratory. Conventional lift-out FIB technique was used to produce the electron transparent foils from areas that were pre-coated with 2.25 μm thick Pt protective layers aimed at avoiding damage by the Ga ion beam. The Ti_2AlC and Ti_3SiC_2 irradiated at 2 dpa were designated 7A1 and 7S1, respectively. Similarly, the 10 dpa samples were designated 9A1 and 9S1. At the LAMDA laboratory, the bulk samples are stored in the radiological materials vault number PIG-4016. After sample preparation, the Mo grids with the TEM samples attached had no measurable radiological activity and were cleared by Radiation Control Technicians at ORNL to be used in non-radiological electron microscopy laboratories.

In this study, three TEM samples were produced for each irradiation case and twelve samples in total were screened. Post-irradiation analysis was carried out primarily in a JEOL JEM-2100F TEM operating at 200 kV with a Schottky Field-

Emission Gun at LAMBDA and subsequently in a Hitachi H-9500 TEM at the MIAMI-2 facility. Bright-field, dark-field and selected-area diffraction pattern techniques were used. Aiming at identifing the Burgers vectors of dislocation lines and loops, the two-beam method was used along with data available in the literature for dislocation behaviour in HCP systems [496, 497]. Crystallographic data from the scientific literature on both MAX phase materials were used to generate the crystal models that were applied to index experimental diffraction patterns [429, 430]. Figure 8.2(a) shows the atomic models of the crystal structures constructed in CrystalMaker for both the Ti_2AlC and Ti_3SiC_2 MAX phases. To compare the neutron irradiation effects with the pristine materials, eight samples of the Ti_3SiC_2 and seven samples of the Ti_2AlC were produced and studied within the TEM.

8.2.2 Results and discussion on the neutron irradiation response of Ti-based MAX phases

Due to the wide variety of neutron irradiation-induced defects observed in these Ti-based MAX phases, the results section has been subdivided by defect-type. Pristine

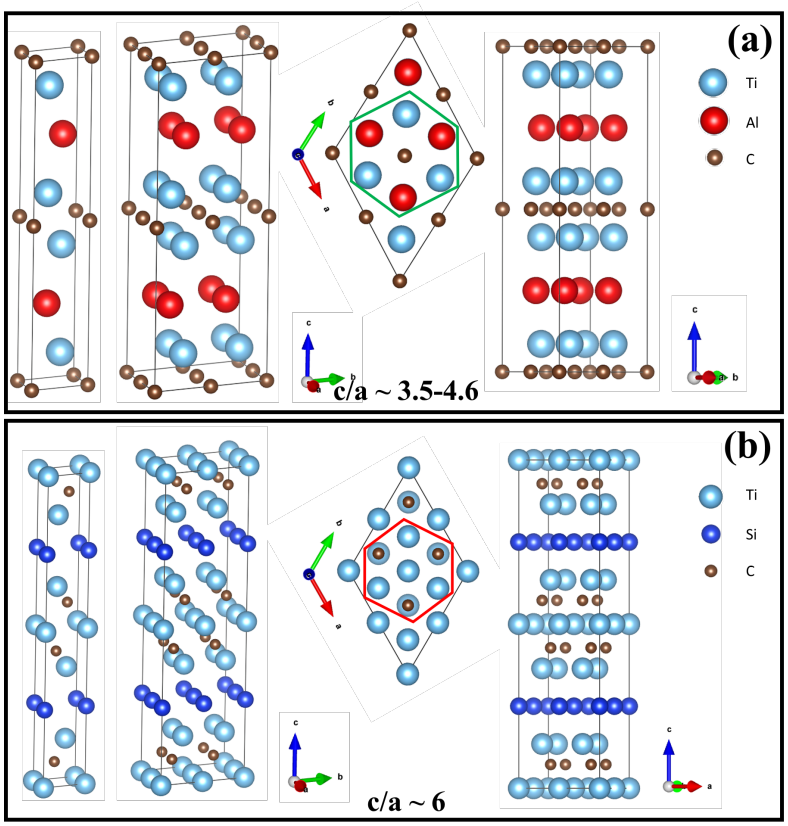

Figure 8.2: The crystal structures of (a) Ti_2AlC and (b) Ti_3SiC_2 visualised using CrystalMaker with data available in the literature [429, 430]. Both materials have a hexagonal-compact crystal structure. The laminated nature of the materials is clearly visible.

microstructures with pre-existing defects are shown aimed at distinguishing existing defects from the damage microstructures at 2 and 10 dpa.

8.2.2.1 Pre-existing defects in the pristine microstructures

The pristine microstructures of both MAX phases were already subjected to investigation in section 4.4.1.2 which revealed that both Ti_2AlC and Ti_3SiC_2 were relatively free of defects, however, as shown in the figures 8.3(a–b) some pristine samples have shown pre-existing defects which are detailed here for comparison with the neutron-irradiated microstructures.

The presence of secondary phases has been observed in Ti_3SiC_2 [431]. These phases are often reported in the literature as undesirable impurity inclusions in Ti_3SiC_2. The morphology of these impurity phases with respect to the MAX phase matrix was used to identify their nature: angular-shaped grains are SiC crystals whereas round-shaped grains are TiC [431]. These secondary phases were predicted by the calculated ternary phase diagrams in figure 8.2. According to Morgiel *et al.* [431], TiC is more prone to nucleate during reactive hot pressing within the ternary carbide matrix and the SiC grains are less frequently observed.

In the microstructure of the Ti_2AlC small black-spots and titanium hydride (TiH) precipitates have been observed in only one pristine specimen (out of 7) as shown in figure 8.3(a–b). With respect to black-spots, their formation may be attributable to surface damage introduced by the polishing steps during the FIB procedure. Although these defects have only been detected in one out of seven pristine samples, their location within the matrix was limited to some grains and can be observed only at very high magnifications.

The formation of hydrides in Ti_2AlC, to date has not been reported in the scientific literature. A possible mechanism for hydride formation within Ti-based MAX phases may involve the incorporation of hydrogen during sample preparation. The sources of hydrogen could be either the colloidal silica solution with water that was used as an abrasive solution during the mechanical polishing step or even the residual hydrogen within the FIB. Additionally, the FIB lamellae are subjected to shear stresses during the polishing stages, thus possibly contributing to some atomic rearrangement which with hydrogen incorporation would allow the necessary conditions for TiH nucleation and growth: the conditions for the activation of a (near) martensitic mechanism as reported by Ding *et al.* [498]. Nevertheless, the possible formation of TiH within Ti_2AlC indicates that this ternary carbide is not as thermally and mechanically stable as assumed by Barsoum [105]. In order to form TiH by a (near) martensitic mechanism, the Ti_2AlC matrix has to be, by definition, mechanically unstable [32, 499–501]. TiH has not been observed in either the neutron-irradiated specimens nor in the pristine specimens of Ti_3SiC_2.

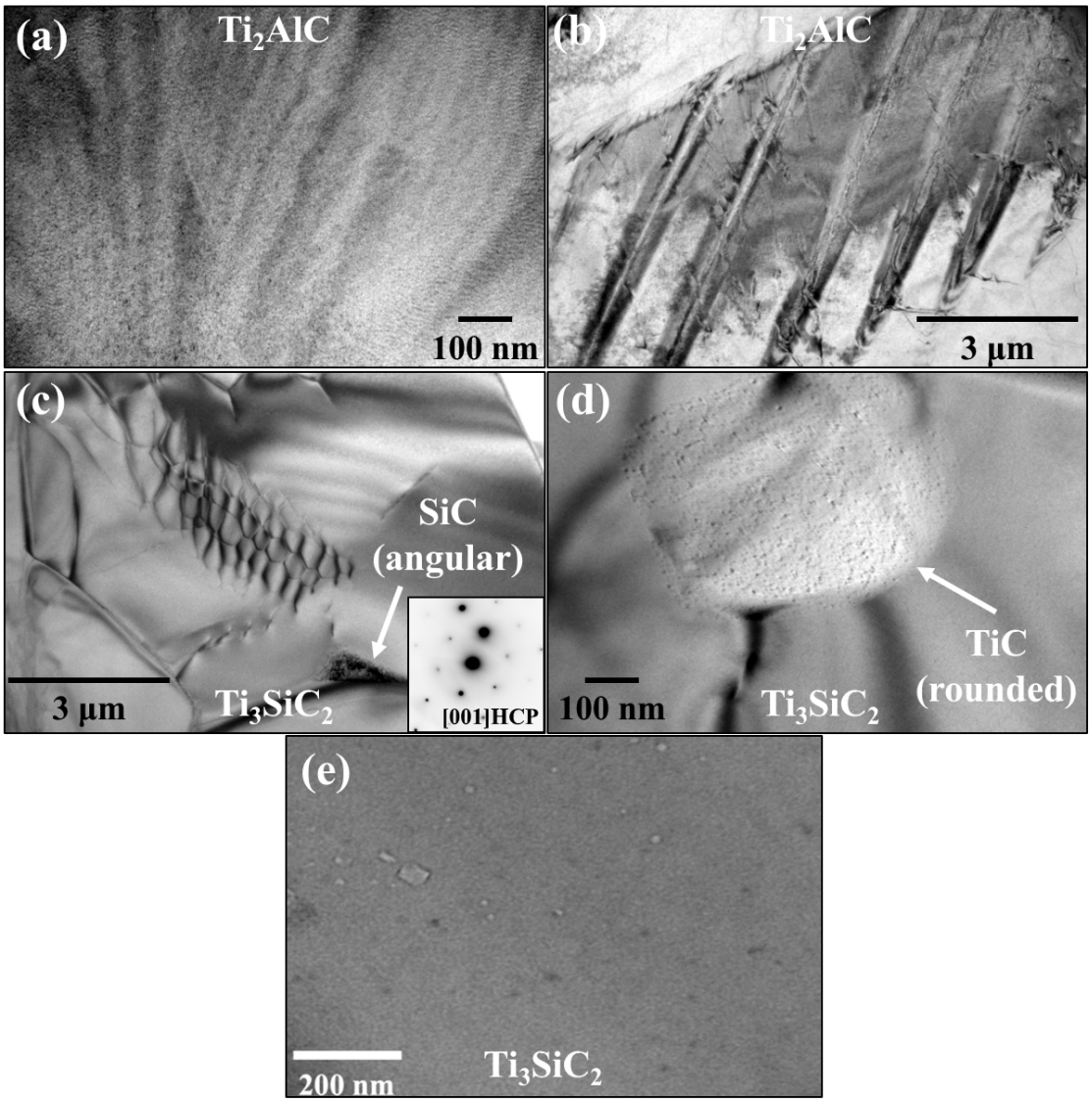

Figure 8.3: BFTEM micrographs of the pristine Ti-based MAX phases recorded at room temperature showing (a) the presence of some black-spots and (b) artefacts resembling TiH in the Ti_2AlC; (c) a dislocation network viewed at the basal zone axis in the Ti_3SiC_2 and (d) black-spots concentrated in a secondary phase. The micrograph (e) shows pre-existing cavities in one Ti_3SiC_2 grain. Note: micrograph (e) has been recorded with the objective lens underfocused by $\approx$ 1000 nm whilst micrographs (a–d) are in focus.

Dislocation lines and ordered dislocation networks were observed in two out of eight pristine Ti_3SiC_2 specimens as shown in figure 8.3(c). These defects are seen to form preferentially along the [0001] basal zone axis. FIB damage in the form of black-spots was absent in the matrix of the Ti_3SiC_2, but was observed within the (Si,Ti)C inclusions as can be seen in figure 8.3(d). The dislocation lines appear to be generated at the grain boundaries. At high temperatures during the RHP, these dislocation lines are mobile and can interact to form an ordered dislocation network suggesting that this type of defect is characteristic of grain growth and stress accommodation during the synthesis of the material. Figure 8.3(e) shows pre-existing cavities in the Ti_3SiC_2, but these defects were observed in only one pristine sample.

8.2.2.2 Black-spots

The damage microstructure of the Ti_2AlC in the BFTEM micrograph shown in figure 8.4(a) exhibits the presence of black-spots (vacancy/interstitial clusters or small loops) at 2 dpa. Their average sizes (diameter) were measured in ImageJ and were around 5.0 nm at both 2 and 10 dpa in average. DFTEM has been used to distinguish the contrast of these defects from that of other features. Comparing 2 to 10 dpa, the areal density of black-spots was observed to be greater at the higher dose (in all screened samples) as shown in figure 8.4(b–c). For the Ti_2AlC, the measured areal densities of black-spots at 2 and 10 dpa were $4.4\pm0.4\times10^{11}$ and $9.6\pm0.5\times10^{11}$ cm^{-2}, respectively. The fact that the black-spot density increases as a function of the irradiation dose may indicate that low recovery of radiation-induced defects has occurred in the matrix phase of the Ti_2AlC.

These present results are in disagreement with two previous works which reported the dynamic recovery of Frenkel defects under irradiation in a very similar MAX phase, Ti_3AlC_2, that was irradiated at 968 K with neutrons at lower doses (0.1 dpa) [354] and in the Ti_2AlC with heavy ion irradiations at high temperatures [502]. Such differences with previous work suggests that, in the present work, the point defects generated by the collisions of neutrons with the Ti_2AlC phase matrix are in fact increasing from 2 to 10 dpa and accumulating in this MAX phase. However, the diffraction patterns recorded at 2 and 10 dpa have shown that the matrix phase has neither suffered decomposition nor amorphisation (insets in figure 8.4(a) and 8.4(c)).

In the case of Ti_3SiC_2, black-spot damage was concentrated preferentially within the secondary phases. Figure 8.4(d) shows the Ti_3SiC_2 free of black-spot damage at 2 dpa while the TiC inclusions exhibited an accumulation of these defects. Black-spots were observed close to grain boundaries in the Ti_3SiC_2 matrix at 2 dpa as shown in figure 8.4(e). At 10 dpa, black-spots were observed only in the secondary

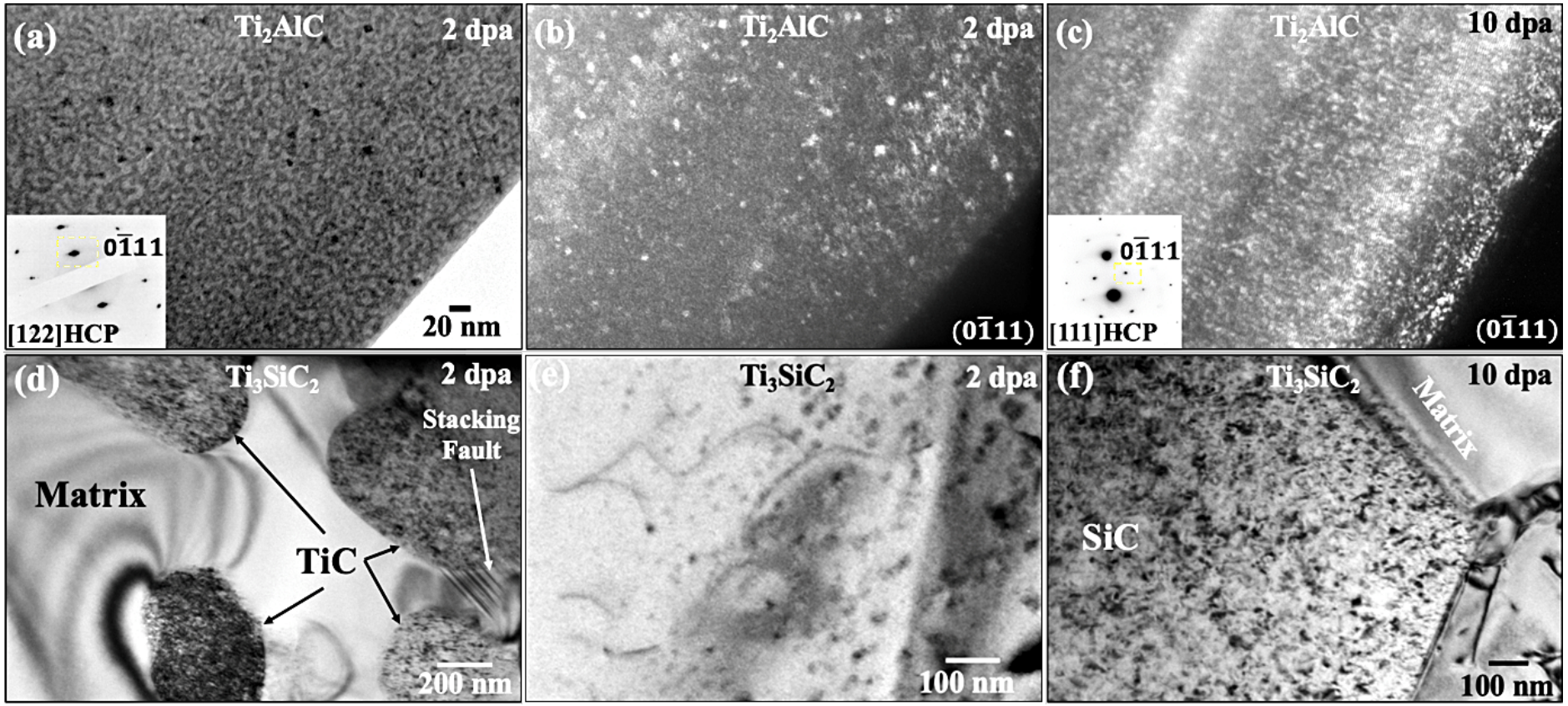

Figure 8.4: (a) A BFTEM micrograph of the Ti_2AlC at 2 dpa showing black-spot damage and (b–c) DFTEM micrographs at 2 and 10 dpa, respectively, showing the evolution of the black-spots as a function of the dose. The areal density of black-spots has increased on going from 2 to 10 dpa. (d) and (f) BFTEM micrographs of Ti_3SiC_2 at 2 and 10 dpa, respectively, showing that black-spot damage is preferentially concentrated within the secondary particles (SiC and TiC). (e) Black-spot damage in the Ti_3SiC_2 close to grain-boundaries of the matrix phase (seen only at 2 dpa). Note: the scale marker in (a) also applies to (b–c).

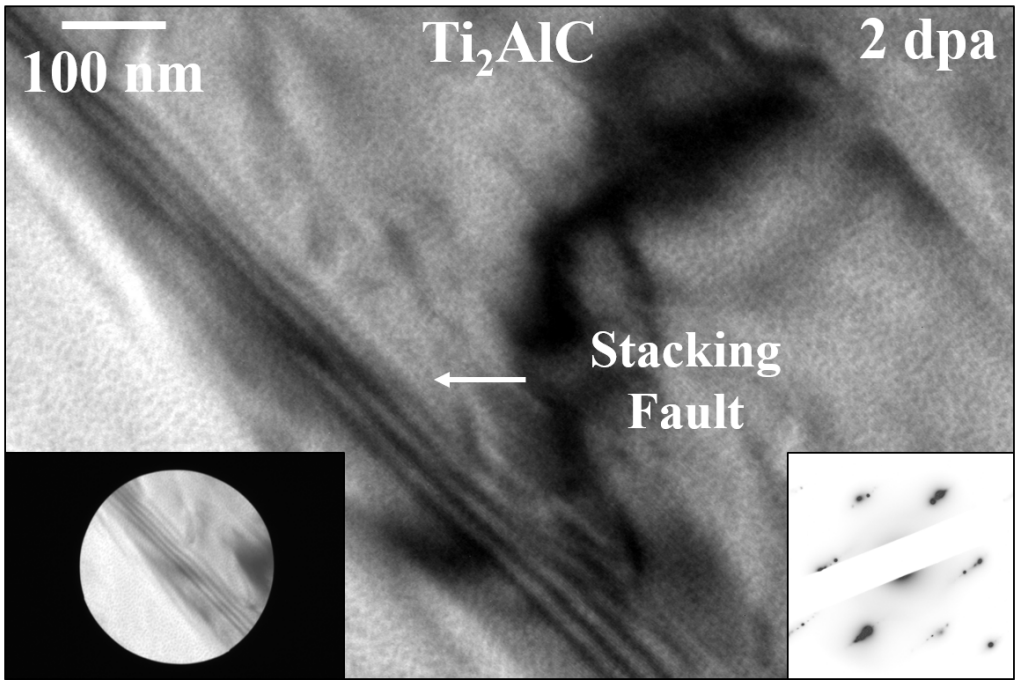

Figure 8.5: Long stacking faults observed parallel to the [0001] zone axis in Ti_3AlC_2 neutron irradiated to 2 dpa at 1273 K.

phases as shown in the figure 8.4(f). Regarding these defects in the matrix, no direct relationship between dose and areal density could be obtained with any of the samples screened. These trends on generation and accumulation of black-spot damage within the secondary phases rather than in the Ti_3SiC_2 matrix phase were reported for the same MAX phase irradiated with neutrons at lower doses and lower irradiation temperatures [355]. The understanding of the mechanism of radiation tolerance of the Ti_3SiC_2 will be the subject of further discussion at the end of this section.

8.2.2.3 Stacking faults

Stacking faults were observed at the interfaces of the (Ti,Si)C in the 2 dpa samples of the Ti_3SiC_2 as shown in figure 8.4(d). Similarly, bigger stacking faults were observed in the Ti_2AlC at 2 dpa as shown in figure 8.5. These defects were characterised by analysing the diffraction pattern with the SAED aperture placed around the defect as suggested by Williams and Carter [383]: when at the zone axis (the [0001] shown as an inset in figure 8.5), the reflections split into satellite spots.

The removal of A-layers in the stacking sequence of the MAX phase is a proposed cause to explain the existence of these two-dimensional radiation-induced defects in the Ti_3SiC_2 [503]. The formation of stacking faults within the Ti_3AlC_2 irradiated at around 1000 K up to 3.2 dpa has been confirmed by Tallman *et al* [356]. In the current work, stacking faults have not been observed in the pristine samples nor in

either of the two Ti-based MAX phases irradiated to 10 dpa, although they were looked for.

Compact crystal structures, such as the hexagonal compact and the face-centred cubic, favour the formation of two-dimensional crystal defects such as stacking faults [248, 504]. The formation of stacking faults in both MAX phases at 2 dpa suggests that these materials are of low stacking fault energy (SFE). These defects are defined as an interruption of the atomic stacking sequence of the HCP MAX phase. The absence of stacking faults at 10 dpa is an interesting observation and may indicate that: (i) some degree of atomic rearrangement/recombination does occur in these MAX phases at higher doses and irradiation temperatures that is large enough to promote annihilation of such defects, and/or (ii) different irradiation-induced processes such as local composition alterations and irradiation-induced elemental segregation which may take place at 10 dpa, thus changing (increasing) the stacking fault energy in these Ti-based MAX phases. Regarding the latter, the formation of stacking faults is strongly affected by the local elemental composition. While alloying usually decreases the stacking fault energy, segregation (either due to irradiation or synthesis routes) tends to increase it, thus reducing the probability of the formation of such extended defects [248, 504].

8.2.2.4 Cavities

Cavities were observed in both MAX phases at 2 and 10 dpa by means of defocusing the objective lens of the TEM (Fresnel contrast). In the case of the Ti_2AlC, the BFTEM micrographs in figure 8.6(a–b) show the presence of voids with diameters around 40 nm. At higher magnifications, figure 8.6(c), small voids were also observed in the Ti_2AlC and they could be distinguished from black-spots defects by changing the Fresnel contrast. In this MAX phase, cavities were observed preferentially within the matrix, but not along the grain boundaries. In the Ti_3SiC_2, the BFTEM micrographs in figure 8.6(d–e) show the presence of voids at 2 and 10 dpa in the matrix and along the grain boundaries, respectively.

The occurrence of irradiation-induced voids in Ti-based MAX phases at 1008 K and up to 3.4 dpa has been reported in a single paper [356]. These authors reported the observation of voids preferentially at the grain boundaries, but not in the bulk matrix phase which led the conclusion that accumulation of vacancies with subsequent void nucleation and growth was not observed in the matrix due to a certain degree of dynamic recovery of Frenkel defects. As vacancies and interstitials are mobile at 1008 K, the nucleation and growth of cavities along the grain boundaries will be favoured as they will act as sinks for irradiation-induced defects: *i.e.* there will be a tendency for accumulation at the interfaces where extended defects (like voids) are prone to form.

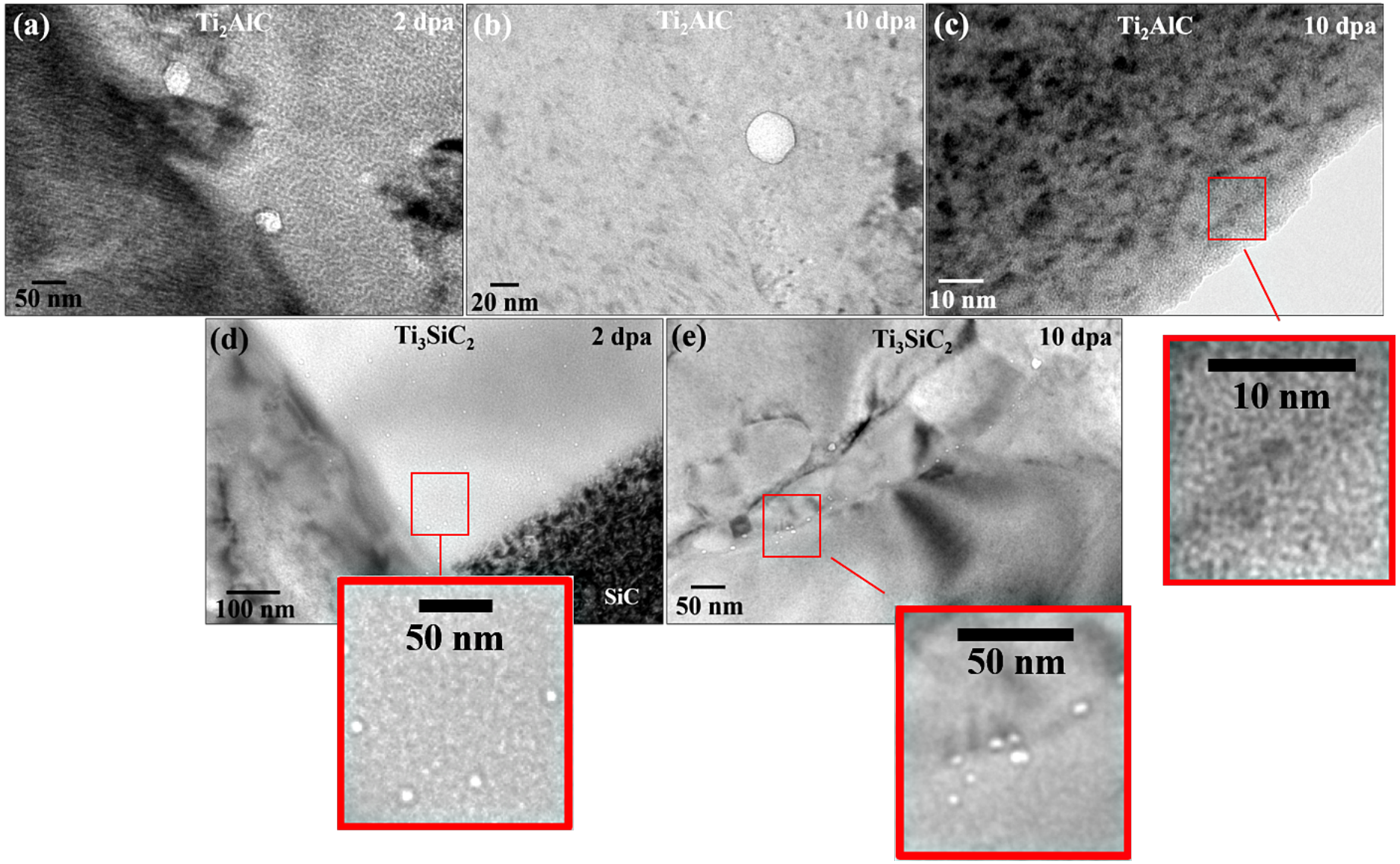

Figure 8.6: BFTEM micrographs showing cavities in Ti_2AlC at (a) 2 dpa and (b) 10 dpa. (c) Ti_2AlC at higher magnification showing the presence of small voids and black-spots. Ti_3SiC_2 at (d) 2 dpa and (e) 10 dpa showing voids in the matrix and along grain boundaries. Note: the defocus for (a–d) was 300 nm and for (e) was 1000 nm.

For this work where the Ti-based MAX phases were irradiated with neutrons at 1273 K, cavities were observed at doses as low as 2 dpa, but the results present some inconsistencies. Large and dispersed cavities were observed in the Ti_2AlC at 2 dpa, but at higher doses, 10 dpa, a large number of small cavities was observed which were only visible at higher magnifications. At lower doses, dynamic recovery of irradiation-induced defects may occur thus limiting the nucleation and growth of cavities, but as the dose increases, this effect would appear to have diminished. Possible causes of this reduction are the degradation of the matrix phase as well as the saturation of point defects.

In the Ti_3SiC_2 MAX phase, voids were observed in the matrix at 2 dpa, but only along grain boundaries at 10 dpa. In this specific case, recombination of point defects seems to play a major rule, although at higher doses, accumulation of defects at sinks can be linked with the observation of voids at these sites. In this way, recombination appears to be an intrinsic property of the bulk matrix, but not in regions closer to interfaces such as grain boundaries. The large cavities in both materials, could be pre-existing cavities that have grown under irradiation as such defects were observed in the pristine Ti_3SiC_2, for example.

8.2.2.5 Dislocation loops, lines and networks

In all MAX phase samples analysed in this work, dislocation lines, loops and networks were observed. As shown in the set of BFTEM micrographs in figure 8.7, dislocation loops were identified in both MAX phases at 2 and 10 dpa via the two-beam method. The figure shows the microstructures of the Ti_2AlC and the Ti_3SiC_2 at 2 and 10 dpa under two bright-field conditions: one where the most excited reflection allows the observation of the dislocation loops ($\vec{b} \cdot \vec{g} \neq 0$) and the other one where the excited reflection shows no contrast at the dislocation positions ($\vec{b} \cdot \vec{g} = 0$).

In the set of BFTEM micrographs in figure 8.7, dislocation loops are observed in the Ti_2AlC at 2 dpa (a–b) and 10 dpa (e–f) and in the Ti_3SiC_2 at 2 dpa (c–d) and 10 dpa (g–h). The areal density of dislocation loops was observed to decrease on going from 2 to 10 dpa in the Ti_2AlC, but not in the Ti_3SiC_2. Note that these trends have been observed in all samples analysed (> 3) increasing the confidence that they are statistically representative.

Using the two-beam method within the TEM in combination with reference data from the literature on dislocation loops and crystallography of HCP systems [496, 504], it was possible to determine the direction of the Burgers vectors for the identified dislocation loops in these neutron-irradiated Ti-based MAX phases. Tilting the specimens around the specific zone axis exhibited as insets in the micrographs in figure 8.7, two Burgers vectors were matched with the conditions shown figure 8.7 (*i.e.* $\vec{b} \cdot \vec{g} = 0$ and $\vec{b} \cdot \vec{g} \geq 1$): $\vec{b} = \frac{1}{3}[\bar{1}\bar{1}20]$ and $\vec{b} = \frac{1}{3}[2\bar{1}\bar{1}0]$. High-resolution TEM

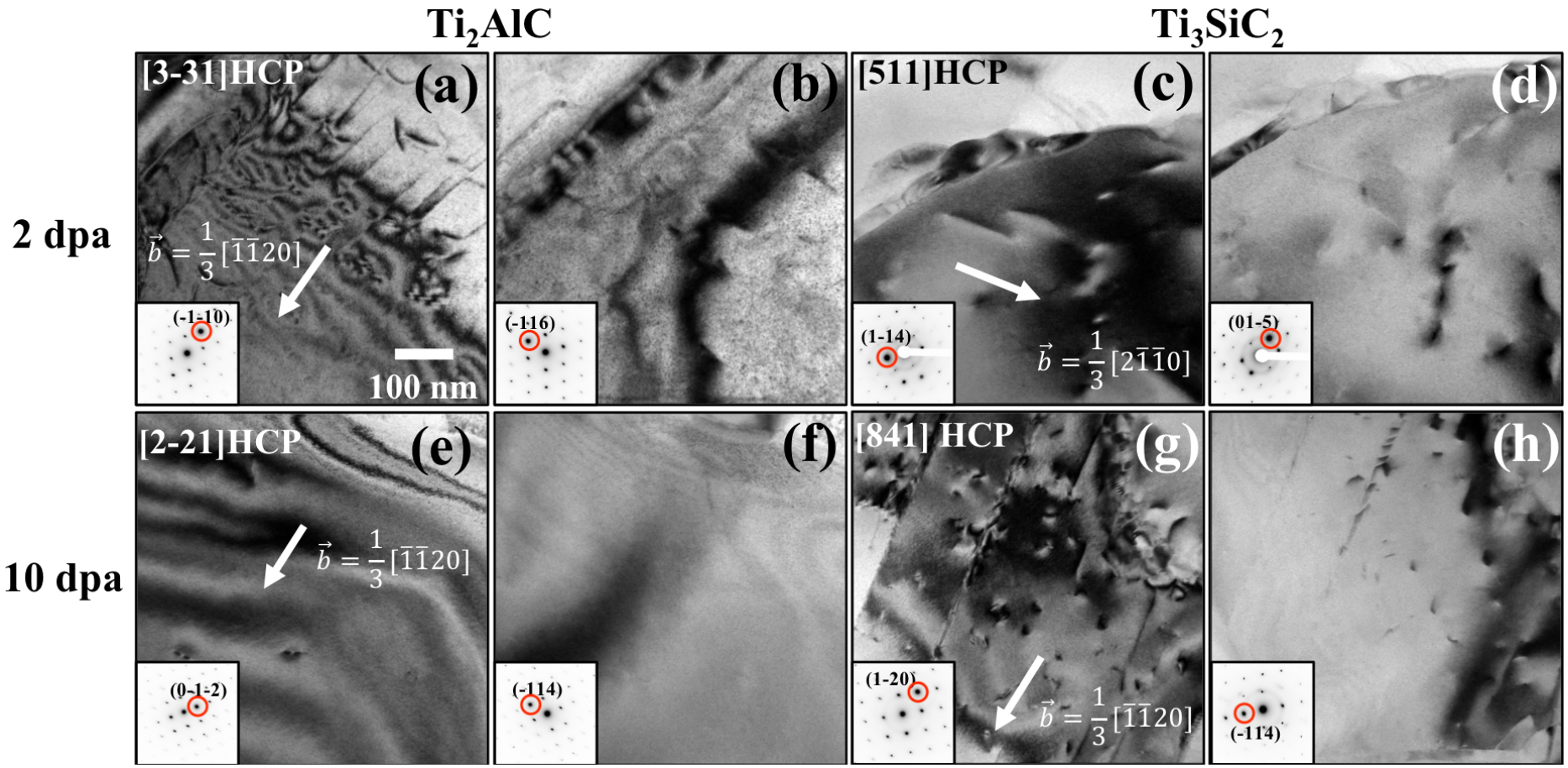

Figure 8.7: (a-b) Dislocation loops observed in the Ti_2AlC at 2 dpa and (e–f) at 10 dpa; (c–d) in the Ti_3SiC_2 at 2 dpa and (g–h) at 10 dpa. The Burgers vector analysis indicated that these are <a> loops constrained within basal planes. Note: the scale marker displayed in (a) applies to all micrographs in the figure.

was used to investigate the nature of some loops as shown in figure 8.8(a–b). The presence of an extra-plane of atoms (represented by the red circle in image 8.8(b)) categorises such defects as possibly interstitial loops of the <a> type. The average sizes and the areal density of these dislocation loops are shown in the table 8.1.

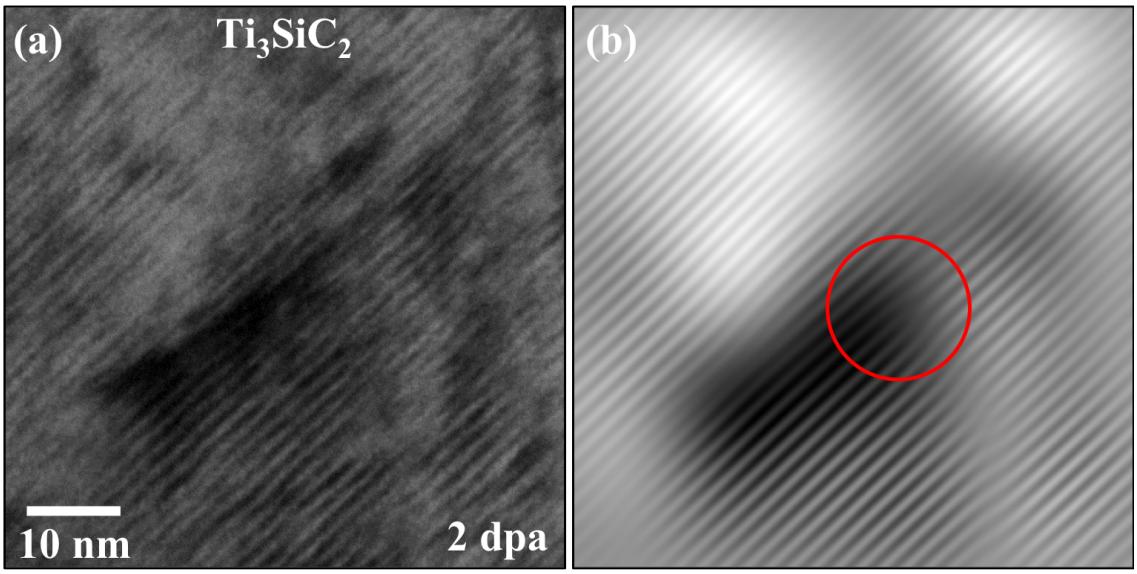

Figure 8.8: (a) A high-resolution TEM micrograph of a dislocation loop in neutron irradiated Ti_3SiC_2 at 2 dpa and (b) a Fourier filtered image from the micrograph (a) showing the interstitial nature of the loop. The micrograph in (a) was taken at focus, without an objective aperture and looking down the $[\bar{1}2\bar{1}0]$ direction. Note: the scale marker in (a) also applies to (b).

The Burgers vectors $\vec{b} = \frac{1}{3}[\bar{1}\bar{1}20]$ and $\vec{b} = \frac{1}{3}[2\bar{1}\bar{1}0]$ have been considered as representative of perfect dislocation loops constrained in the basal plane of the HCP crystal system and this plane is their preferential direction for gliding. However, Aubry *et al.* have studied the nature of such dislocation loops in HCP systems and conclude that loops with these Burgers vectors can also be constrained in one prismatic and at least two pyramidal directions [496]. The slip direction and glide systems for <a> and <c> loops in HCP crystals are defined by the crystallographic ratio c/a. According to previous reported data from Meyers *et al.*, Teutonico *et al.* and Aubry *et al.* [248, 496, 504, 505], glide in the basal plane preferentially occurs when the c/a ratio is higher than 1.633 and, conversely, prismatic and pyramidal slip are preferred when c/a <1.633. Unit cell analysis of both 321 and 211 MAX phases showed that these ratios are ≈6 and 3.5–4.6, respectively [108]. Therefore, such analysis indicates that the identified <a> loops are highly likely to be perfect basal loops gliding along the (0001) planes. It is should be noted that such loops have not been observed in neutron-irradiated Ti-based MAX phases: only <c> loops were identified, but at lower doses and lower irradiation temperatures [356].

TEM observation along the basal zone axis have revealed the presence of complex

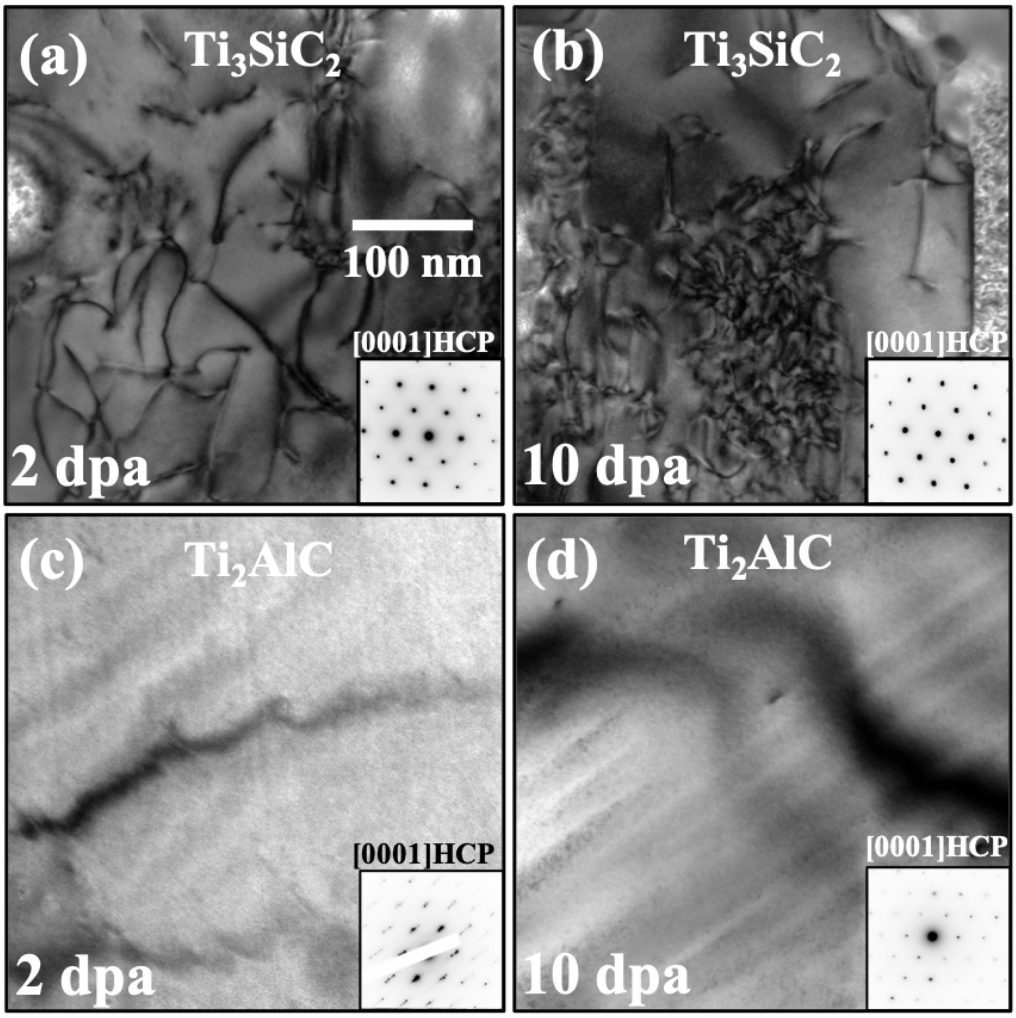

Figure 8.9: BFTEM micrograph taken along the basal zone axis [0001] (a) Ti_3SiC_2 at 2 dpa; (b) Ti_3SiC_2 at 10 dpa; (c) Ti_2AlC at 2 dpa; and (d) Ti_2AlC at 10 dpa. Note: the scale marker in (a) applies to all micrographs in the figure.

dislocation networks in Ti_3SiC_2 at 2 dpa (figure 8.9(a)) and 10 dpa (8.9(b)). For these cases, the dislocation lines appear to emanate from the interfaces to the centres of the MAX phase grains (or emanate from the centre of the MAX phase grains and stopping at the interfaces). This may be an indication that these dislocations possess some mobility during irradiation at 1273 K. Both areal density and entanglement complexity of these dislocations increase on going from 2 to 10 dpa. Such dislocation networks were not observed in the Ti_2AlC at any doses or along different zone axes (figures 8.9(c-d)).

Tallman *et al.* studied the formation of dislocation loops in neutron-irradiated Ti-based MAX phases up to 0.14 dpa at around 1000 K, but only identified <c> loops with a Burgers vector of $\vec{b} = \frac{1}{2}[0001]$ [356]. In the same work, the authors reported a direct relationship between dose and size for both materials. The areal density was also bigger in the Ti_3AlC_2 when compared with the Ti_3SiC_2. In the present work, the areal density of dislocation loops was lower at 10 dpa than at 2

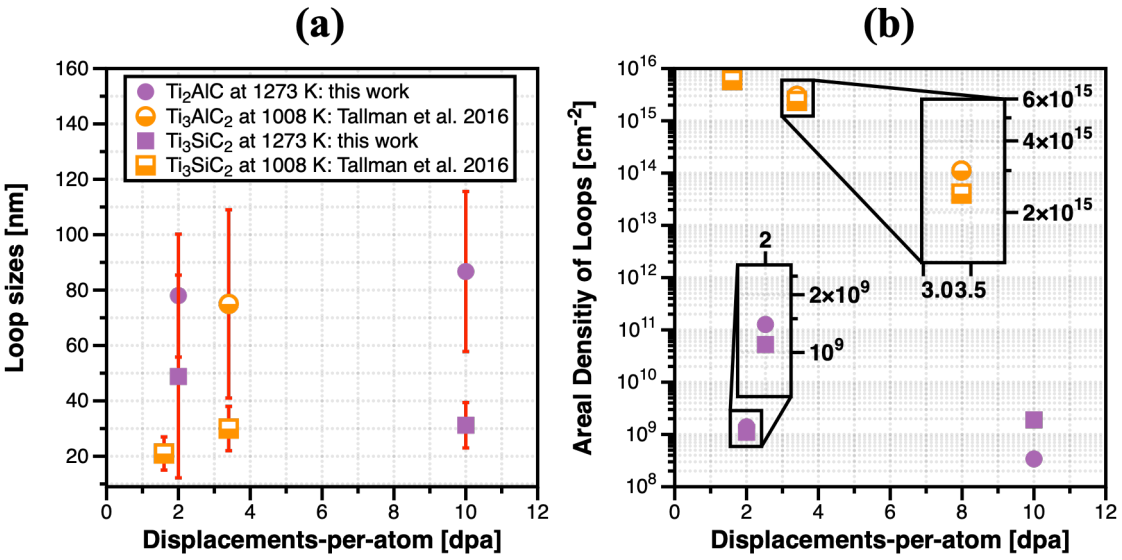

Figure 8.10: Quantitative data for dislocation loops obtained from this work in both the Ti_2AlC and the Ti_3SiC_2 at 2 and 10 dpa neutron-irradiated at 1273 K and from data available in the literature reported by Tallman *et al.* [356] for both Ti_3SiC_2 and Ti_3AlC_2 at 1.6 and 3.4 dpa neutron-irradiated at 1008 K: (a) loop sizes and (b) areal densities.

dpa for the Ti_2AlC and this was the trend for all samples analysed. Comparison between the quantitative data provided by this work and Tallman *et al.* [356] is shown in figures 8.10(a) and 8.10(b).

Dislocation loops, lines and networks have been reported here at 2 and 10 dpa for 321 and 211 Ti-based MAX phases irradiated at 1273 K. These types of irradiation-induced defects are considered local perturbations (strain fields) of the crystal lattice [248]. Annihilation and interaction of dislocations have been observed during irradiations at high temperatures due to the enhanced mobility promoted by thermal energy and this is also true for some ceramic compounds that have fewer slip systems than common metals [248]. The comparison of 2 and 10 dpa samples suggests that both MAX phases had a reduced number of dislocations at higher doses, perhaps indicating some degree of recovery. The careful dislocation analysis have also shown that <a> loops can form in these materials and they were identified to be constrained within the basal planes in contrast to Tallman *et al.* who observed that <c> loops with $\vec{b} = \frac{1}{2}[0001]$ were formed, but at lower doses and temperatures. Whether the dislocation loops within Ti-based MAX phases evolves from <c> to <a> types as reported to occur for HCP crystals [497, 506] remains to be determined in future work.

Due to the active influence of dislocation networks acting as sinks for point defects, the presence of these complex defects in Ti_3SiC_2 at 2 and 10 dpa suggests that they impact the lattice in a positive way: inhibiting swelling processes and

Table 8.1: Areal density and average size of dislocation loops obtained in this work.

MAX Phase	**Loop Size [nm]**		**Areal Density [cm^{-2}]**	
	2 dpa	10 dpa	2 dpa	10 dpa
Ti_3SiC_2	48.8 ± 36.6	31.2 ± 8.3	1.1×10^9	1.9×10^9
Ti_2AlC	78.0 ± 22.2	86.7 ± 28.9	1.4×10^9	3.4×10^8

amorphisation (although this latter is not a concern at 1273 K) as well as reducing the population of vacancies and interstitials that could agglomerate into other defects such as voids and bubbles. Hence, the presence of dense dislocation networks as a result of neutron irradiation suggests that the elastic and plastic properties of these materials may change significantly due to irradiation, thus reducing their applicability in environments that require resistance to mechanical stresses.

8.2.2.6 Phase instabilities, recrystallisation and precipitation

Irradiation-induced phases have been identified in both Ti-based MAX phases in the 10 dpa samples. Figure 8.11(a–c) shows the presence of needle-like precipitates within the matrix phase of the Ti_2AlC MAX phase at 10 dpa. The precipitates were visible in bright-field only when viewed along specific zone axes: along the [0001] zone axis, such precipitates were not observed in bright-field. This indicates the existence of orientation relationships between the matrix phase and the precipitates. DFTEM has been used to better resolve the morphology of the precipitates whose sizes were in the range 20–300 nm. As shown in the diffraction pattern inset in figure 8.11(b), these precipitates have generated some satellite spots (although with very low intensity), but not rings suggesting that they can be coherent with the matrix [248]. Similar phase instabilities have been observed in Ti_3SiC_2 at 10 dpa as presented in figure 8.11(d–f). As can be seen in the BFTEM and DFTEM micrographs in figures 8.11(d) and 8.11(e), such phase instabilities were small grains with sizes varying from 5 to 100 nm. The use of the SAED aperture was indicated that such sub-grains are smaller crystals randomly oriented. Additionally, precipitation along the grain boundaries was observed in the Ti_3SiC_2 at 10 dpa as shown in the figure 8.11(f).

Lin *et al.* [507] observed the formation of structures following the sequence Ti_2AlC–TiC–Ti_2AlC in the synthesis of the Ti_2AlC at high temperatures. The TiC particles shared crystallographic properties with the MAX phase matrix phase, although they differed in size, morphology (platelet-like) and were inhomogeneously distributed within the matrix. A possible non-equilibrium thermodynamical state may occur during neutron irradiation at high temperatures in which the Ti_2AlC MAX phase decomposes into TiC given that collisional processes may selective enhance C diffusion thus perturbing the existing matrix phase. Upon displacing C

atoms from solid solution, the neutron irradiation will then assist the precipitation of TiC. It is worth noting that the solubility of C in the Ti–Al system is limited [508]. Therefore, if C segregates it is highly likely that will recombine with either Ti or Al to form precipitates. Conversely, the possibility of the formation of titanium aluminide phases cannot be discarded as such intermetallics are well known for their high thermodynamic stability [507].

Secondary phases have been reported in the Ti_3SiC_2 matrix as a result of high energy ion irradiation at 523 K [349]. XRD revealed that TiC started to nucleate at doses as low as 2.8 dpa. Increasing the dose to 10.3 dpa, the phase content of the TiC also increased. According to the authors, the combination of displaced lattice atoms, fast diffusion at moderate to high temperatures and cascade events during irradiation allowed the precipitation of new phases in the Ti_3SiC_2. The fact that Ti, Si, Al and C redistribute and nucleate secondary phases under irradiation at high doses suggests that further studies by means of both simulations and experiments are needed in order to assess the thermodynamic stability of both Ti_3SiC_2 and Ti_2AlC when exposed to displacing irradiation. Similarly to the Ti_2AlC, the formation of titanium silicide intermetallic phases could not be ruled out due to the energetics from the thermodynamics of intermetallics.

8.2.3 Discussion of the effects of neutron irradiation on the Ti-based MAX phases and directions for future work

For the two different MAX phases analysed here at two different neutron doses at the same irradiation temperature, the strong presence of black-spots and cavities in the Ti_2AlC matrix indicates that in terms of displacement damage, this MAX phase has an overall lower performance than the Ti_3SiC_2. The presence of pre-existing TiC and SiC grains in the latter suggests that their interfaces may act as sinks for irradiation induced defects, thus increasing the radiation tolerance of the matrix phase. Whether or not such radiation tolerance is due to fast diffusion of defects along the A-layers – as suggested by Middleburgh *et al.* [357] – is a subject for future computational and experimental work. With regard to the dislocation loops, <a> loops formed as a result of neutron irradiation at high temperatures and high doses and was reported here, to the best of our knowledge, for the first time. In all samples studied in this work, amorphisation was not observed in line with expectations for irradiations at high temperatures. Evidence of irradiation-induced phase decomposition was found in both MAX phases, but the morphology of the phases and their relationship with the matrix phase were found to be different. This latter fact strongly suggests that these nanolaminated materials may not be of superior thermodynamic stability at high temperatures and doses despite previous

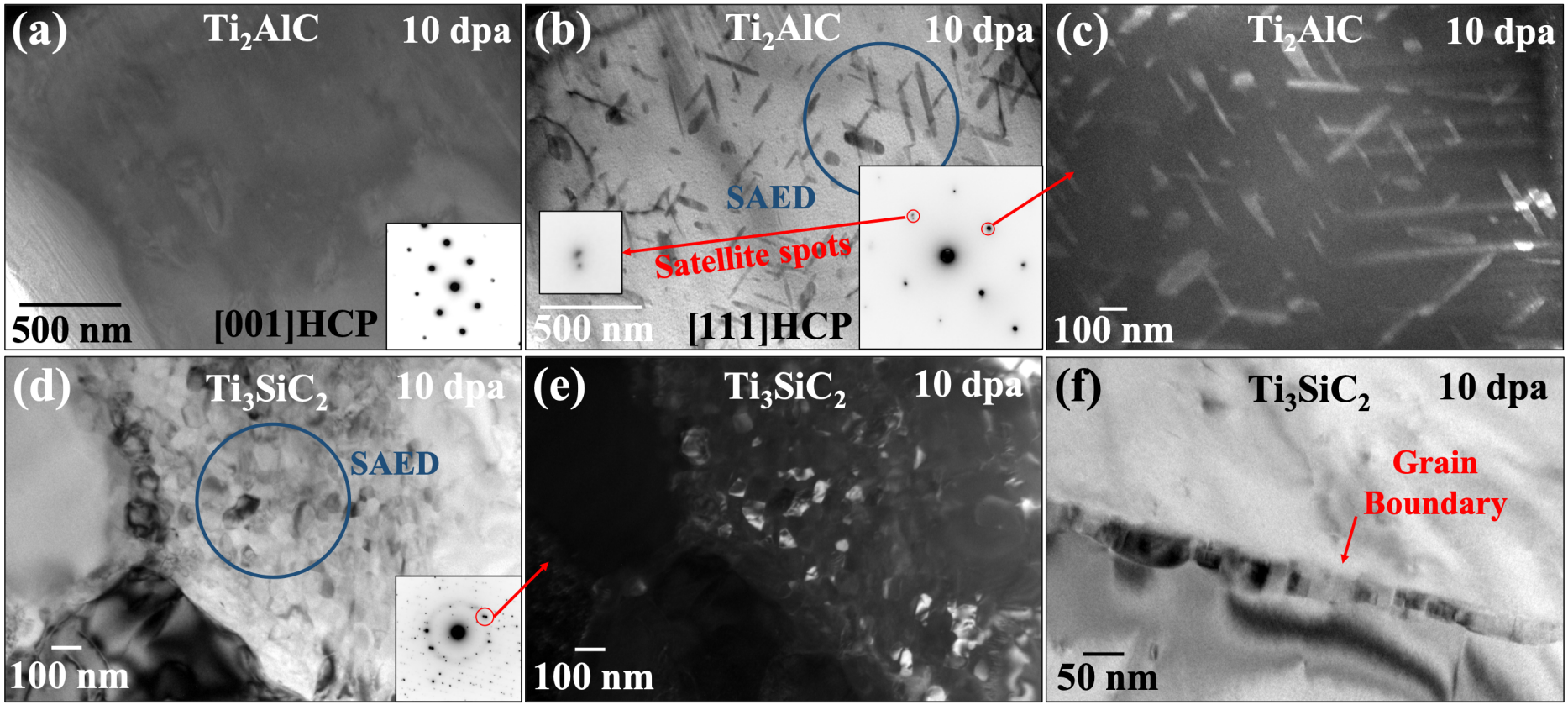

Figure 8.11: The microstructure of (a–c) Ti_2AlC and (d–f) Ti_3SiC_2 at 10 dpa where irradiation-induced phases have been detected. Note: the yellow arrows in the inset in (b) show the spots where a satellite spot (from the precipitates) was observed.

reports to the contrary [107, 110].

Recent investigations on the irradiation behaviour of MAX phases have categorised these materials as potential candidates for the next generation of structural materials for innovative nuclear reactors [495]. If the aim is to apply MAX phases as structural materials, for example, in Molten-Salt Reactors (MSR), they will need to demonstrate the ability to operate in a temperature range of 973–1273 K and retain their structural integrity (i.e. phase stability and retention of useful physical and chemical properties with reduced microstructural modifications) up to maximum doses of 200 dpa [21]. However, to date, the microstructural modifications as well as alteration of properties under neutron irradiation have been largely unexplored. The existing dataset is limited to low doses (< 4 dpa) and moderate temperatures ranges, although the present work extends this dataset to 10 dpa at 1273 K and demonstrates some microstructural changes. Recent work (including ion irradiation) have shown that in MAX phases, a wide variety of alterations and defects do develop down at the atomic level and physical properties do change under energetic particle exposure [348, 349, 352–356, 509]. These are all limiting factors for the application of MAX phases within nuclear technology, but this research field is only at its early stage.

The results from the current TEM study indicate that with respect to the neutron-irradiated Ti-based MAX phases at high temperatures a complex chain of radiation-induced defects form in both MAX phases including secondary phases. In this way, as well as introducing new data for this field of research, this TEM characterisation work has identified topics which should be addressed for nuclear applications for Ti-based MAX phases: (i) the relationship of dislocation loops and networks with the elasto-plastic performance of the irradiated MAX phases compared with pristine material; (ii) an analytical characterisation of the phase instabilities and segregation that were reported here; and (iii) the influence of A-layers on the radiation tolerance of MAX phases.

8.3 Heavy-ion irradiation effects at high temperatures

Following the electron-microscopy characterisation of the neutron-irradiated Ti-based MAX phases at Oak Ridge National Laboratory, experimental efforts were made to reproduce the damage microstructures using heavy ion irradiation *in situ* within a TEM at the University of Huddersfield. In this section, a heavy ion irradiation study of the radiation resistance of the Ti_2AlC and Ti_3SiC_2 is presented. An *in situ* TEM annealing study was also performed aimed at investigating the phase

stability of both MAX phases at 1273 K. Results are discussed by comparing the irradiations with two pure metals, Ti and Al constituents of the ternary carbides.

8.3.1 Materials and methods

Samples of the Ti_2AlC and Ti_3SiC_2 were subjected to heavy ion irradiation *in situ* within a TEM at the MIAMI-2 facility. The ion beam was set to 700 keV Kr^{+2} via mass/charge selection and both irradiation and damage profiles are shown in figure 8.12. A maximum of 1% at.% of Kr was implanted into the MAX phase lamellae according to SRIM calculations.

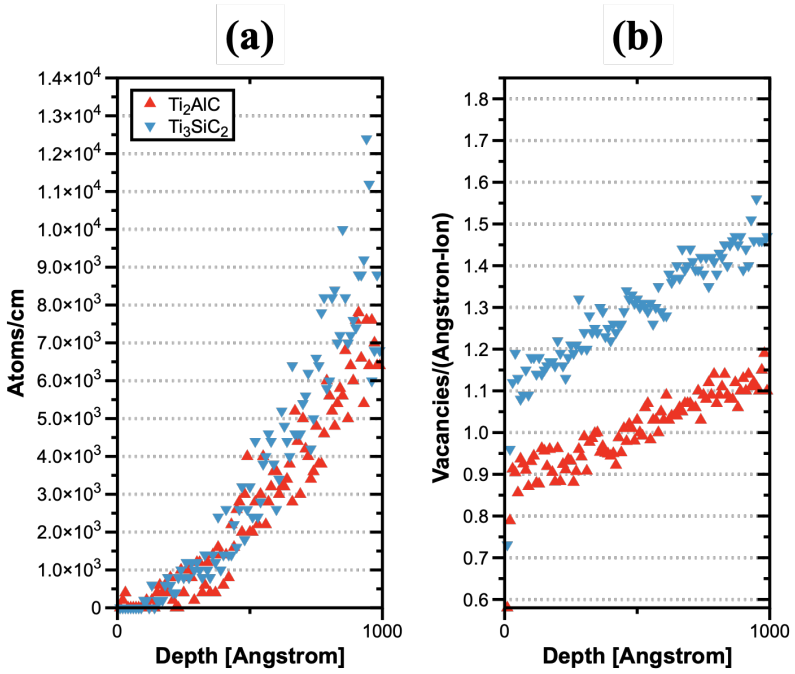

Figure 8.12: (a) The implantation and (b) damage profiles for 700 keV Kr ions into Ti_2AlC and Ti_3SiC_2, calculated from SRIM [148].

As the neutron-irradiated MAX phases were irradiated in HFIR at 1273 K, a first study (section 8.3.2.1) with the aim of assessing their phase stability was conducted and revealed that the matrix phases undergo decomposition at this temperature which made it impossible to carry out a direct comparison between neutron and ion irradiations at these temperatures. For this investigation, a double-tilt heating holder was used with the TEM lamellae produced via FIB milling. The temperature ramp was 60 K·min^{-1}. This heating holder has an accuracy of ±5 K according to the manufacturer (Gatan). The irradiation temperature was then set to 1008 K for the MAX phases during heavy ion irradiation and this was chosen to match previous neutron irradiations carried out by Tallman *et al.* [355, 356] (up to 3.4 dpa at 1008 K).

In addition, the α-Ti and α-Al pure metals were irradiated with the same ion beam parameters, but at 1143 and 558 K so as to match approximately the homologous temperature of the MAX phases irradiations. With respect to the Ti-based MAX phases, it has been reported that although they do not have a melting temperature, the dissociation of the matrix phase into a Ti-based carbide plus a liquid phase is expected to occur at around 1673 K [105, 369]. Therefore, the irradiation temperatures for pure Ti and Al were close to the homologous temperature of $0.60T_m$ assuming 1673 K as the probable melting point of the Ti-based MAX phases, but this is an approximation.

Fluence-to-dpa calculations were performed using the outputs from the SRIM code and the procedure suggested by Stoller *et al.* [140]. The Ti_2AlC and the Ti_3SiC_2 atomic densities were calculated to be 7.33×10^{22} and 8.30×10^{22} atoms·cm^{-3}. 700 keV Kr^{+2} generates 894 and 1440 displacements per ion on average for the Ti_2AlC and the Ti_3SiC_2, respectively. The implantation and damage profiles are shown in figures 8.12(a–b). For the fluence-to-dpa calculations it was assumed that the damage is averaged over a thickness of 100 nm for all irradiated lamellae. The Ti_2AlC was irradiated up to 4.1×10^{15} ions·cm^{-2} and the Ti_3SiC_2 up to 2.9×10^{15} ions·cm^{-2}, both cases corresponding to a maximum dose of 5 dpa.

8.3.2 Results

The results section has been subdivided into three subsections: (i) the *in situ* TEM annealing of the MAX phases aiming at assessing their thermodynamic stability at high temperatures; (ii) a comparison of the irradiation of the Ti-based MAX phases and the pure Ti and Al metals; (iii) a comparison between the results obtained with heavy ion irradiation and neutron irradiation.

8.3.2.1 MAX phase decomposition upon thermal annealing at 1273 K

The microstructure of Ti_3SiC_2 before and during annealing at around 1073 K is exhibited in the BFTEM figures 8.13(a–b).

At room temperature, the pristine microstructures were observed to be free of defects and secondary phases. However, upon increasing the temperature, small rounded precipitates were observed to form. The samples were held at 1273 K for 2 hours and BFTEM characterisation in the Ti_3SiC_2 revealed that these precipitates resulted in Debye-Scherrer rings in the diffraction pattern as can be seen in the inset in figure 8.13(b), taken during annealing. Similar results were obtained for the Ti_2AlC as shown in figure 8.13(c–d). For the Ti_2AlC, extra-spots in the DP are observed (rather than Debye-Scherrer rings) after annealing as shown in the inset in micrograph 8.13(d). In the case of the Ti_2AlC, the matrix phase decomposition

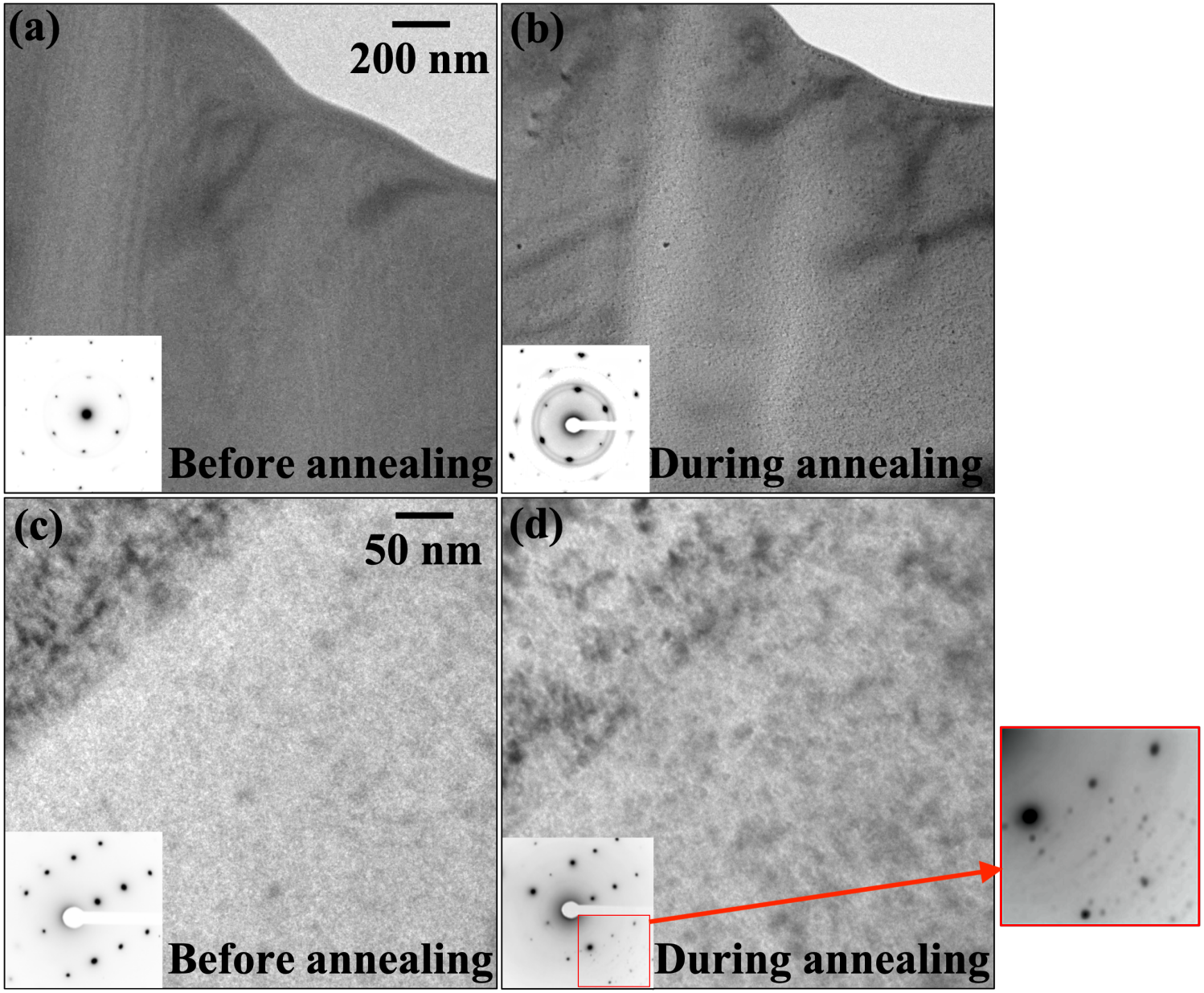

Figure 8.13: The microstructure of the Ti_3SiC_2 (a) before and (b) during *in situ* TEM annealing at around 1073 K. The microstructure of Ti_2AlC (c) before and (d) during *in situ* TEM annealing at around 1273 K. Note: scale bar in (a) also applies to (b) and scale bar in (c) also applies to (d).

starts to occur at around 1173 K whilst in the Ti_3SiC_2, this effect starts around 973 K. In the Ti_3SiC_2, by placing the objective aperture on these diffraction rings, DFTEM revealed the precipitates were indeed responsible for the Debye-Scherrer rings in the diffraction pattern (figure 8.14-2). At the end of the annealing experiment, these precipitates reached a maximum size in the range of 30–40 nm. For the Ti_2AlC case, the decomposition manifested without noticeable formation of Debye-Scherrer rings, but caused extra-spots in the diffraction patterns. Neither disordering nor amorphisation was observed during these experiments, as the g-reflections of the matrix have not diminished and no amorphous rings were observed in the DPs.

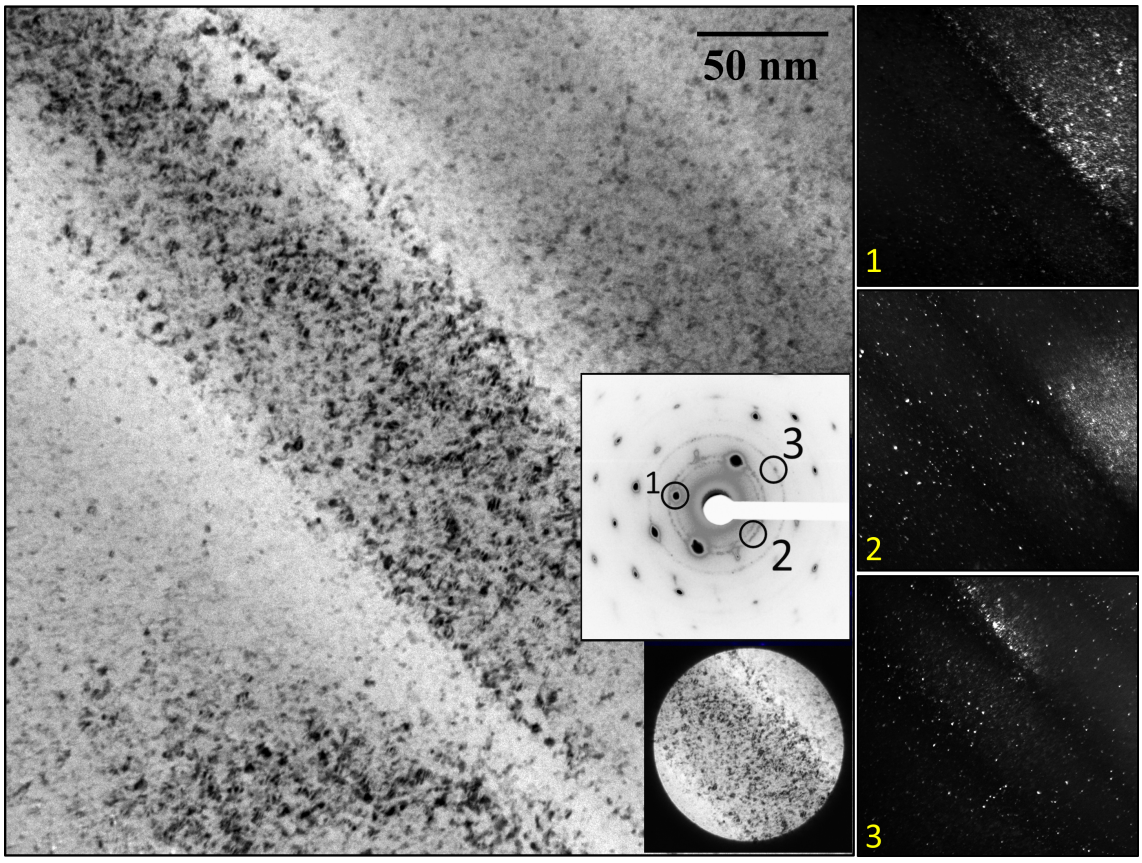

Figure 8.14: BFTEM and DFTEM characterisation of the Ti_3SiC_2 after 2 hours of *in situ* TEM annealing at 1273 K. DFTEM micrograph 1 shows pre-existing defects in the Ti_3SiC_2 whereas micrographs 2-3 show the presence of secondary phases after annealing.

After the *in situ* TEM annealing experiment, EFTEM was used to assess qualitatively the elemental composition of the precipitates. As shown in the composite RGB image and the BFTEM micrograph in figure 8.15, these precipitates were found to be Ti- and C-depleted, but enriched with Si. The identification of Si-rich zones following the annealing of the Ti_3SiC_2 suggests that due to atomic diffusion at high temperatures, the MAX phase matrix decomposes into titanium silicide intermetal-

lic phases (titanium aluminides in the case of the Ti_2AlC). According to the ternary diagrams presented figure 8.1(a–b), these intermetallic phases are predicted to form at a temperature of 1273 K [439, 441].

Some conclusions can be made based on the observation of the MAX phase matrix decomposition during the *in situ* TEM annealing experiments. As the temperature increases from room temperature to 1273 K, the concentration of equilibrium vacancies (and other defects) will increase exponentially (*i.e.* with the temperature). The excess of mobile defects, their possible agglomeration and the existence of surfaces are factors that govern the nucleation of precipitates (secondary phases) by means of increasing the Gibbs free energy of the material [33].

For simplicity, one can represent the MAX phase matrix by the symbol α and the Al or Si supersaturated precipitates by the symbol β. The nucleation of secondary phases at high temperatures is a process mediated by atomic diffusion.

The model to describe the heterogeneous nucleation of supersaturated secondary phases in solids involves three major considerations (regarding the Gibbs free energy of the system): (i) the formation of the β precipitates will result in a volume reduction $-V\Delta G_v$ and in an energy increase promoted by the misfit between the α/β phases represented by $V\Delta G_s$; (ii) an increase of the free energy caused by the creation of new interfaces (A), *i.e.* $A\gamma$; and (iii) a reduction of the free energy caused by the annihilation of defects followed by the nucleation of embryos that will result in an energy release of ΔG_d. Under these considerations, the total Gibbs free energy for heterogeneous nucleation (ΔG_{het}) can be expressed by [33]:

$$\Delta G_{het} = -V(\Delta G_v - \Delta G_s) + A\gamma - \Delta G_d \tag{8.1}$$

Equation 8.1 shows that upon the annihilation of defects and formation of embryonic sites, the overall Gibbs free energy of the system could be reduced, thus favouring the nucleation of β precipitates. The exponential increase of the concentration of vacancies upon increasing the temperature results in a significant increase in the atomic diffusion rates, therefore, causing a speed-up of the nucleation processes of secondary phases.

As evidenced by the formation of the Debye-Scherrer rings in the diffraction pattern upon annealing as shown in figure 8.13, where the matrix phase diffraction spots remained unchanged, and in combination with the observation of an interlayer between the Pt cover and the Ti_3SiC_2 bulk in the neutron-irradiated MAX phases at 1273 K, as shown in figure 8.16 from cross-section TEM lamellae analysis, the secondary phase formation (or matrix phase decomposition) occurs at the surface and not within the bulk matrix which reinforces the hypothesis of a mechanism of heterogeneous nucleation mediated by point defects at high temperatures. The

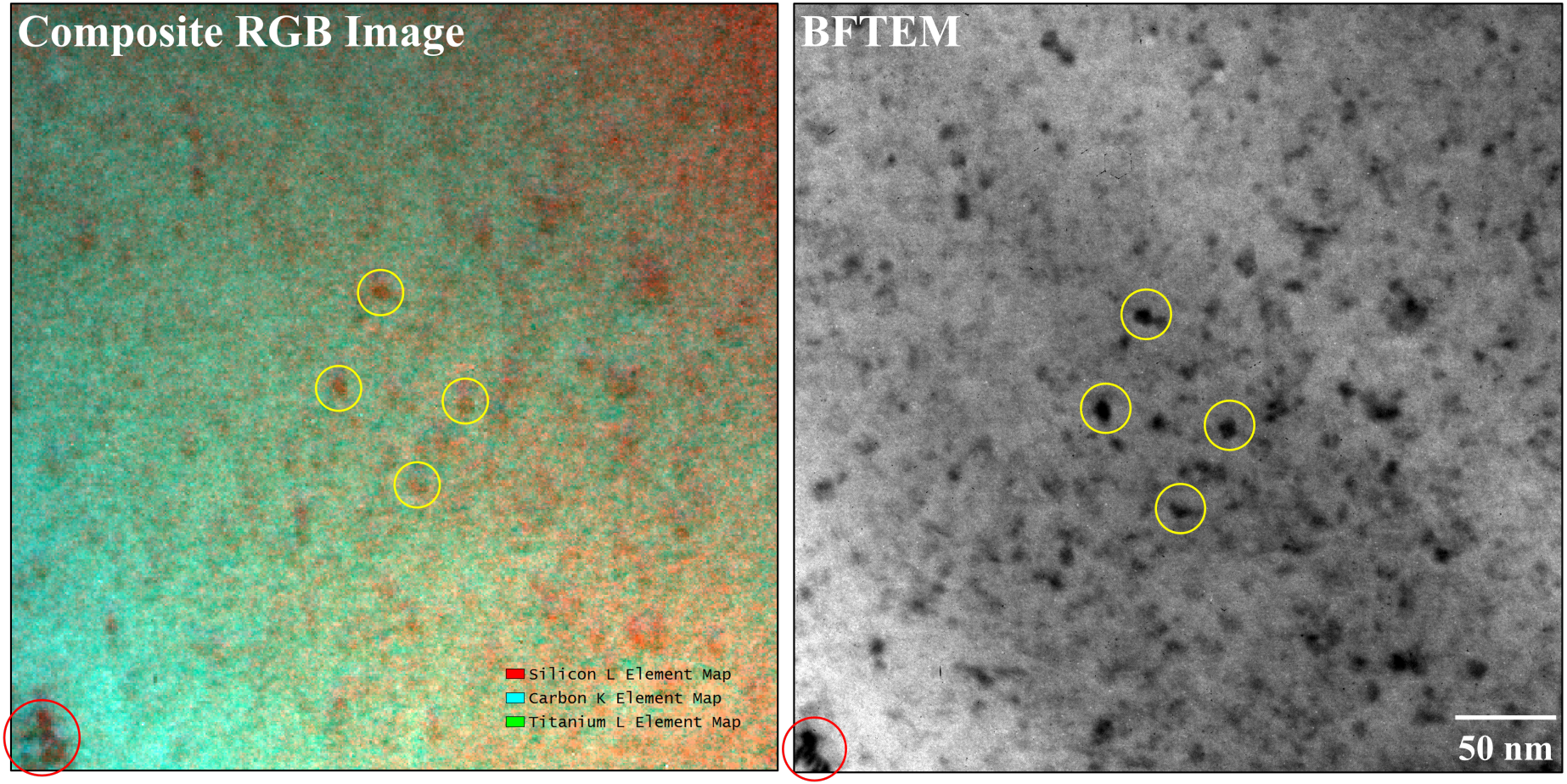

Figure 8.15: EFTEM characterisation of the Ti_3SiC_2 matrix phase decomposition after *in situ* TEM annealing for 2 hours at 1273 K showing small embryos that nucleated upon annealing and the EFTEM analysis indicated they are enriched in Si.

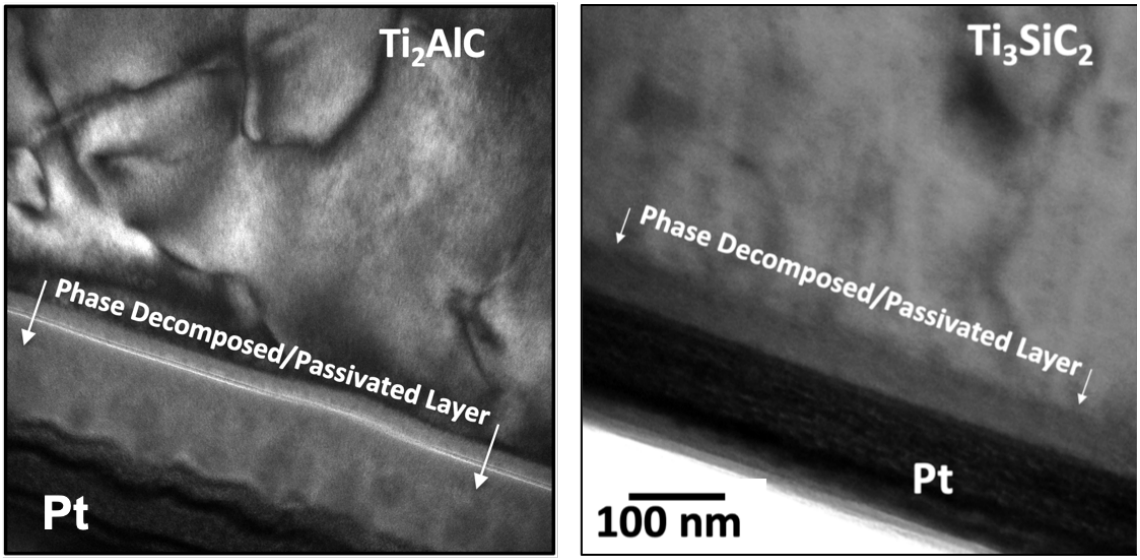

Figure 8.16: BFTEM images of cross-section specimens of (left) Ti_2AlC and (right) Ti_3SiC_2 after neutron irradiation to 2 dpa at 1273 K. The decomposition layer can be clearly seen in both materials.

question remains whether this decomposition at the surfaces is a form of passivation behaviour.

The radii of the Debye-Scherrer rings in the diffraction pattern inset in the BFTEM micrograph at the figure 8.14 were used to determine the reciprocal lattice spacing of the phase formed as a result of thermal annealing. By this it was possible to measure the reciprocal d-spacing between the transmitted electron beam and the first order reflections: 4.56±0.18 nm. Comparing the results with experimental X-ray diffraction data from Jeitschko [510] for similar reflections, 4.78 nm, the formed phase may be the $TiSi_2$ as predicted in the ternary diagram of the Ti–Si–C system (figure 8.1(a)) and detected by the EFTEM analysis in 8.15. It is important to emphasise that all the crystallographic information regarding the other possible intermetallic phases within this ternary system – *i.e.* Ti_5Si_4, $Ti_5Si_3C_y$ and TiSi – were tested, but did not match the experimental results. The depletion of carbon in the regions where the intermetallic phase is formed suggests that the pre-existence of O in the MAX phases, either in the form of an oxide layer at the surfaces or as impurities, can be a factor of major influence as segregated C atoms may combine with O to form carbon monoxide (CO) and then, escape from the solid solution, promoting the formation of titanium silicides [511].

Nevertheless, a decomposition or passivation layer was observed after 2 dpa of neutron irradiation at 1273 K as shown in figure 8.16. In order to carry out such neutron irradiations, the bulk Ti-based MAX phase samples remained in the HFIR for years at high temperature. Naturally, this brings the question of whether the decomposition layers observed in the bulk Ti-based MAX phases after neutron irra-

diation at 2 dpa are the same as those observed in the present work during thermal annealing within the TEM without any irradiation. To answer this question, different analytical methods should be used – such as XRD and STEM-EDX – in both neutron irradiated bulk specimens (requiring the use of radiological laboratories) and thermal annealed TEM lamellae specimens which goes beyond the scope of this thesis. In addition, the decomposition layer observed in the neutron irradiated samples at 2 dpa and during TEM annealing are not related to the radiation-induced precipitation observed in section 8.2.2.6, as in this latter case, the precipitation was observed only at 10 dpa and not at the surface.

8.3.2.2 Comparison of the MAX phases results with the Ti and Al under heavy ion irradiation

The effects of 700 keV Kr ion irradiation on the microstructure of Ti and Al and in the Ti_2AlC and Ti_3SiC_2 MAX phases are shown in the set of underfocused BFTEM micrographs in figure 8.17 (defocus degree of around 1000 nm). For all the irradiations, the irradiation temperature was chosen to give an homologous temperature of around $0.60T_m$. The microstructures of these four materials were monitored *in situ* within the TEM and the irradiations stopped at around 5 dpa.

The types of radiation damage that were observed in the Ti for irradiation doses as low as 1 dpa were black-spots and cavities. As the irradiation dose was increased from 1 to 5 dpa, damage accumulated and saturation within the Ti grains was observed before the final dose of 5 dpa. Similarly, radiation damage was observed in the Al, but in this case, dislocation loops were observed to form at doses of around 1.4 dpa and became mobile upon increasing the dose. Cavities were observed to form throughout the Al at doses of around 2.7 dpa. These cavities in pure Ti and Al are shown in further detail in the BFTEM micrographs in figure 8.18.

Interestingly, radiation damage effects were not observed in either of the Ti-based MAX phases under the conditions studied. The evolution of the matrix phases of the Ti_2AlC and Ti_3SiC_2 from 0 to 5 dpa at 1008 K are shown in figure 8.17. Black-spots related to the phase decomposition due to thermal annealing (as reported in section 8.3.2.1) are visible in both Ti-based MAX phases before irradiation at 1008 K. Strikingly and in contrast to the metals, dislocation loops, black-spots, voids, stacking faults and amorphisation were not observed to occur in these materials under the studied irradiation conditions. The diffraction patterns of the MAX phases before and after irradiation up to 5 dpa are presented in figure 8.19: it can be noticed that Debye-Scherrer rings due to the phase decomposition layer are visible in the Ti_3SiC_2 diffraction pattern.

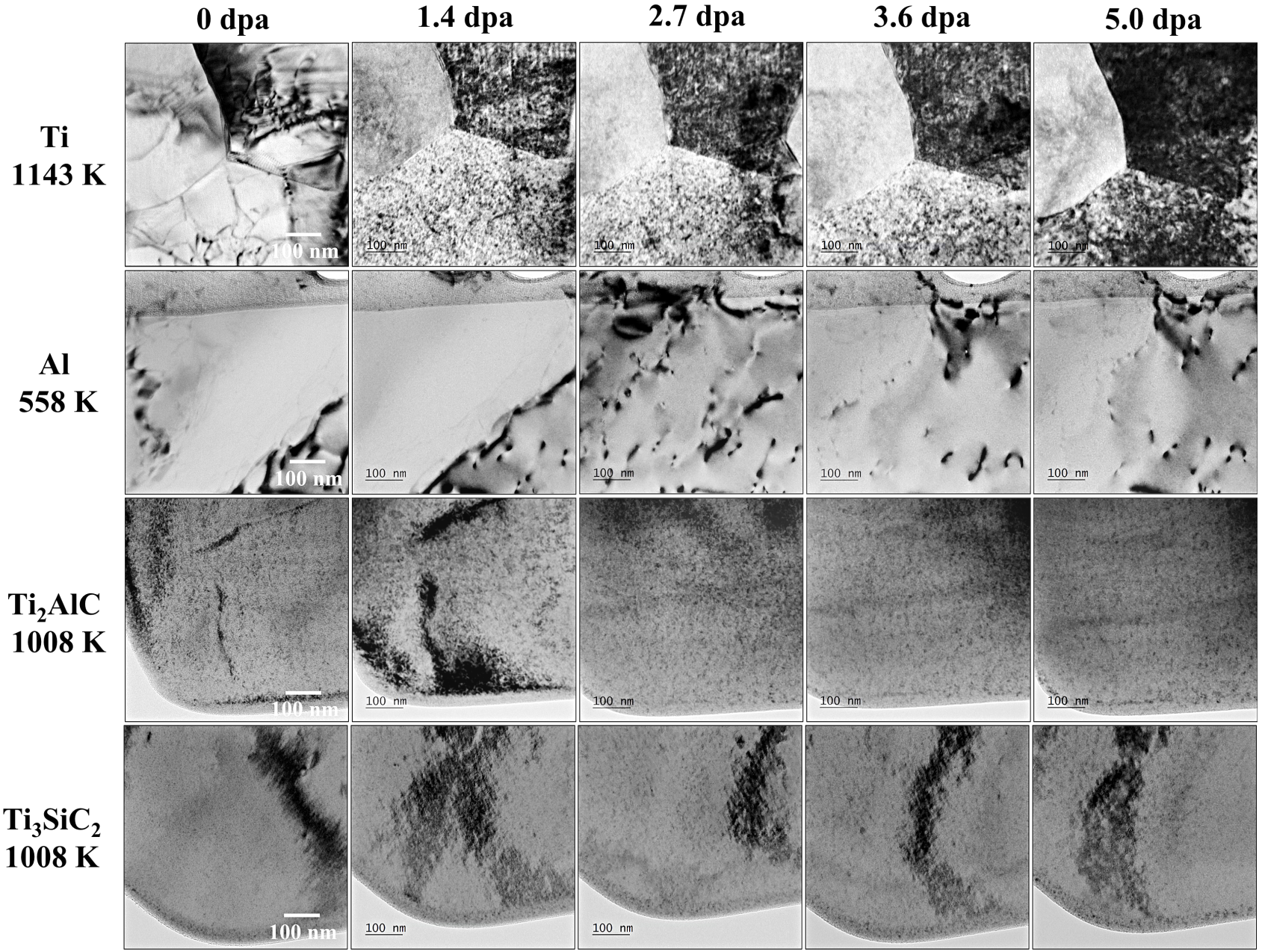

Figure 8.17: Comparison of heavy ion irradiation of Ti, Al, Ti_2AlC and Ti_3SiC_2.

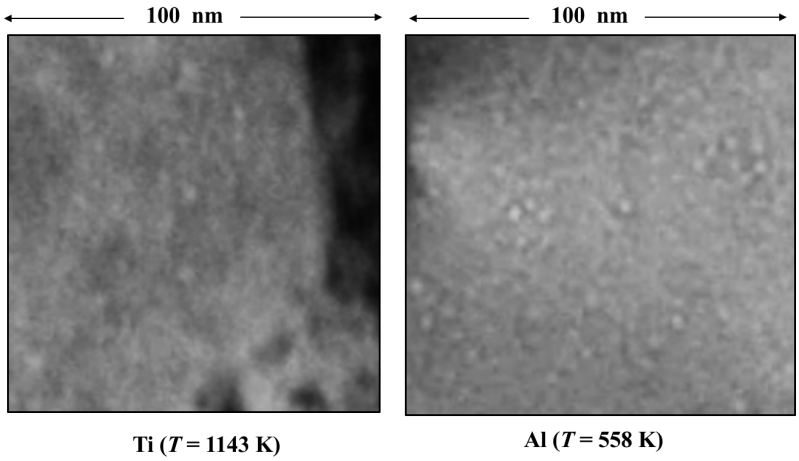

Figure 8.18: Cavities observed in the pure Ti and Al at around 1 and 2.7 dpa, respectively.

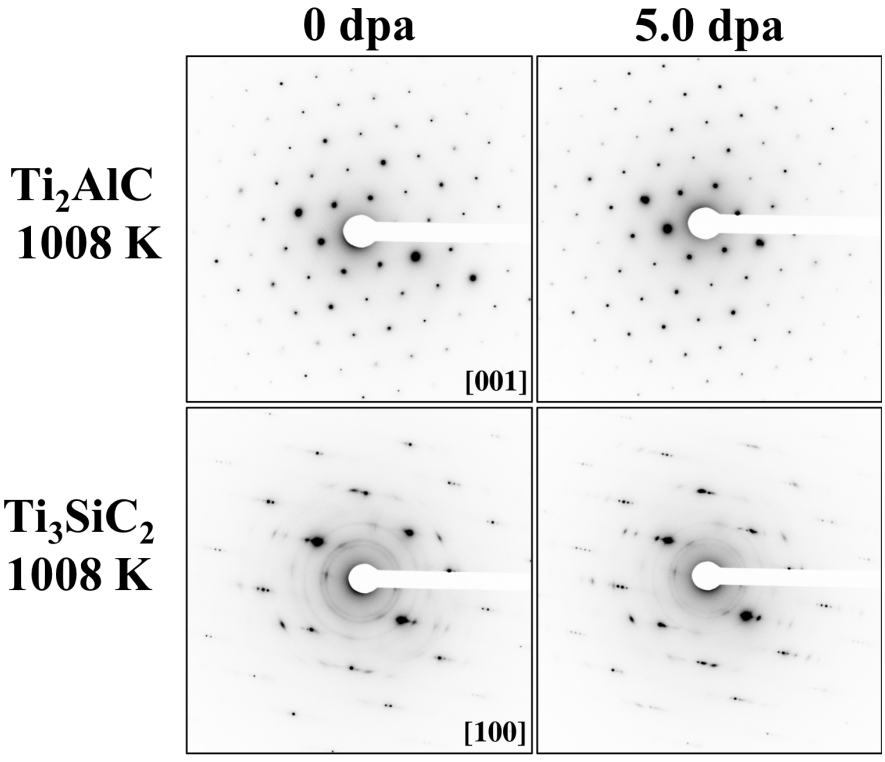

Figure 8.19: Diffraction patterns of the Ti-based MAX phases before and after heavy ion irradiation up to 5 dpa. No significant alterations were observed.

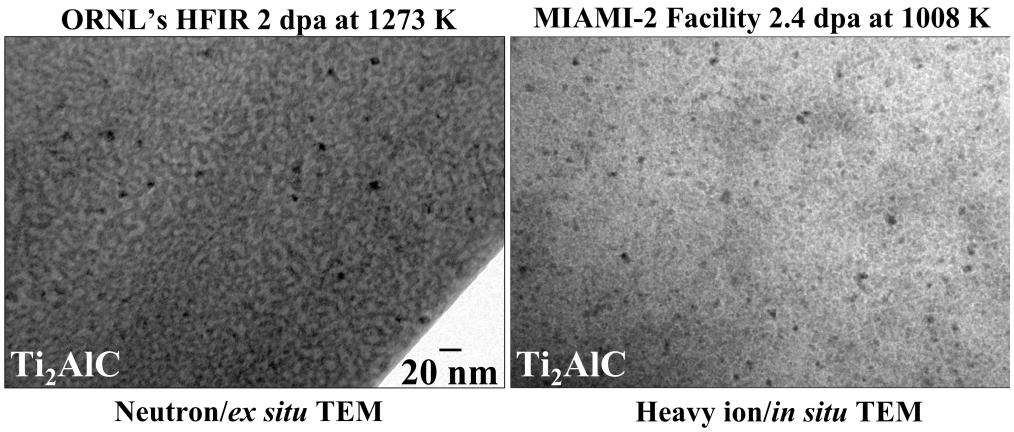

Figure 8.20: A single experimental case where a direct comparison with the neutron- and heavy-ion irradiated Ti_2AlC exhibited led similar damage microstructures.

8.3.2.3 Neutron and heavy ion irradiated MAX phases

In a single experiment (out of 17), the damage microstructure of the Ti_2AlC irradiated with the heavy ions at 1008 K up to 2.4 dpa was similar with the neutron irradiated Ti_2AlC up to 2 dpa at 1273 K. The BFTEM micrographs in figure 8.20 show both the ion and neutron irradiated damage microstructures where black-spots are observed in the first case and the precipitates in the latter (*i.e.* the decomposition layer). Due to the lack of reproducibility, this experiment was an isolated event rather than a recurrent experimental observation.

Although these experimental observations were not reproduced in additional identical heavy ion irradiation experiments, it can be noted that the black-spot contrast in the neutron-irradiated specimen is similar to that in the decomposed intermetallic layer: this indicates that analytical electron-microscopy techniques at high magnifications are needed to distinguish different microstructural features. Conventional TEM can be also used as the black-spots do not introduce rings into the diffraction pattern as do the nanometre-sized precipitates, but a combination of conventional and analytical TEM would clarify appropriately such features.

It is clear that Frenkel defects are being generated within the MAX phases during the irradiation. Additionally, the displacement cascades generated by the collision with a 700 keV Kr ion in these materials will also induce atomic mixing of the M, A and X layers. However, as reported by Middleburgh *et al.* in the Ti_3SiC_2 [357], at the temperature of the experiments herein reported, interstitials are mobile, but the lowest energy barrier for migration is in the Si layer (A-layer): Si, C and Ti interstitials have migration energies of 0.02, 0.45 and 0.99 eV, respectively. With regard to vacancies, the Si vacancy is mobile at the temperature of these experiments, but C and Ti vacancies are not. For the latter case the vacancy migration energies are for Si, C and Ti: 0.61 (2D migration), 4.13 (in the X-layer, 4.71 eV otherwise) and

3.51 eV (between A-layers), respectively. The energetics of MAX phases indicates that in the A-layers, diffusion occurs much more readily than in the other layers. This suggests that radiation damage should develop and accumulate in these MAX phases as observed in the neutron irradiated case. But, the lack of extended radiation damage effects in the heavy ion irradiation case – *i.e.* lack of clustering of interstitials or voids/bubbles – seems somewhat counterintuitive.

8.3.3 Discussion: contribution of this research and future directions

All the previous works and their contributions to the field were described in detail in the literature review chapter. The research presented in this thesis regarding the neutron irradiation resistance of Ti-based MAX phases at high temperatures and doses up to 10 dpa is the first report under such conditions. The justification for these studies is that such MAX phase compounds are potential materials for use in the next generation of nuclear reactors (mainly generations III+ and IV) where operation at high temperatures is a major requirement.

In the work presented here, Ti_2AlC and Ti_3SiC_2 were investigated at two different neutron irradiation doses: 2 and 10 dpa. TEM revealed the development of an intricate and complex chain of defects in both materials, but due to the formation of black-spots and cavities in the Ti_2AlC, Ti_3SiC_2 was found to possess (slightly) better radiation tolerance. Two major aspects of this general trend can be noticed: the presence of secondary phases (Ti,Si)C and the occurrence of dense dislocation network in the Ti_3SiC_2 may act as sinks for radiation-induced point defects, thus protecting the matrix phase from the accumulation of damage.

Additional defects were also observed in the neutron irradiated materials: stacking faults at 2 dpa, but not at 10 dpa; cavities within the matrix of both Ti_2AlC and Ti_3SiC_2 at 2 dpa, but at 10 dpa these were observed only along the grain boundaries of the latter whereas in the matrix for the former; and perfect basal dislocation loops at 2 and 10 dpa for both materials in contrast to recent reports where only <c> loops were observed although at lower irradiation doses and temperatures.

Nevertheless, at 10 dpa, both MAX phases showed evidence of irradiation-assisted segregation and phase decomposition. Phase decomposition has also been observed in these MAX phases under *in situ* TEM annealing as forming a passivation layer on the surfaces of the TEM lamellae. These facts suggest that the thermodynamic stability of both Ti-based MAX phases investigated in this work at higher temperatures deserves further investigation prior to considering their use in future high-temperature nuclear reactors.

Direct comparison with heavy ion irradiation *in situ* within a TEM revealed

that the MAX phases exhibit no radiation damage for irradiations up to 5 dpa, in contrast with the neutron irradiation results. As a limiting factor for heavy ion irradiation *in situ* within a TEM, the escape of Frenkel pairs through the surfaces of the TEM lamellae during irradiation may be a cause for the lack of observable radiation damage. However, damage build-up was clearly observed in the Ti and Al irradiations. Whether or not the fast diffusion through the A-layers is a major component behind the irradiation tolerance of these materials is a subject for future investigations.

Following the trend in the scientific literature on the potential use of MAX phases in nuclear technology, specifically in the design of new and innovative nuclear reactors as structural materials, the MAX phases do exhibit superior radiation tolerance when compared with conventional ceramics. For example, if the aim is to use such materials in molten-salt fast reactors, the requirement will be substantial radiation tolerance, oxidation resistance and high thermodynamic phase stability within the temperature range of 973–1273 K and doses up to 200 dpa [21]. Although the present work shows evidence of phase decomposition and significant radiation damage build-up in these materials (under neutron irradiation), the overall dataset on the effects of energetic particle irradiation the microstructure of such materials is largely unexplored and further research is needed prior to policy-maker and/or future engineering decisions.

8.4 Conclusions

The conclusions of this research on the neutron irradiation response of the Ti-based MAX phases can be summarised as follows:

- Black-spots were observed the Ti_2AlC as a primary form of irradiation-induced damage whilst, in the Ti_3SiC_2, the black-spot damage was seen only in the secondary (Ti,Si)C particles at 2 and 10 dpa and close to grain-boundaries in the matrix at 2 dpa.

- Cavities were observed in both MAX phases at 2 dpa, but only along the grain boundaries for the Ti_3SiC_2 at 10 dpa. Pre-existing cavities were observed only in the Ti_3SiC_2 in one out of eight pristine samples studied, suggesting that the large cavities observed in both materials at 2 and 10 dpa are pre-existing defects that have grown.

- Perfect basal dislocation loops have been observed in both materials at 2 and 10 dpa. Dislocation analysis via the two-beam method revealed the interstitial nature of such <a> loops. Complex disordered dislocation networks were observed in the Ti_3SiC_2 at 2 and 10 dpa along the basal direction (*i.e.* [0001]).

- Phase instabilities were observed at 10 dpa suggesting that the MAX phases had undergone irradiation-induced segregation and precipitation.
- At 2 dpa stacking faults were observed in both MAX phases. This type of defect was not observed at 10 dpa. This latter fact is consistent with the evidence presented on radiation-induced segregation as changes in the local composition of both MAX phases would probably result in an increase of the energy formation of stacking faults [248], thus mitigating their formation at higher doses.

Regarding the heavy ion irradiation of the Ti-based MAX phases *in situ* within the TEM, extended defects were not observed at 1008 K up to 5 dpa whereas similar irradiations with the pure element counterparts resulted in intense generation of cavities and dislocation loops. *In situ* TEM high temperature annealing with subsequent analytical characterisation has revealed that these Ti-based MAX phases undergo surface phase decomposition to a possible intermetallic phase suggesting that the thermodynamic stability of the Ti-based MAX phases may be not as high as previously thought, but these facts are yet to be confirmed also in bulk specimens. Further research is needed to define the conditions under which ion irradiation can simulate the effects of neutron irradiation in these MAX phases.

Chapter 9

Summary and Conclusions

The progress of nuclear energy by means of the design, development and operation of future innovative and more efficient new generations of nuclear power plants is heavily dependent on the materials sciences. It is clear that the current materials challenges in this area are problems of extreme complexity and new nuclear materials will have to demonstrate superior resistance to thermal and mechanical stresses, and excellent performance against oxidation and corrosion mechanisms. These are of particular importance at high temperatures if nuclear accidents such as LOCA are to be avoided. In addition to all the suitable physical and chemical properties that such new materials are expected to possess in order to allow their application within nuclear reactors as structural materials, they must also be able to resist damage due to energetic particle irradiation.

The application of ion beams to simulate the damage caused by neutrons in nuclear reactors has proven to be an useful methodology to tackle such materials challenges since the dawn of the atomic age. Despite the notable physical differences between charged and neutral energetic particles, ion beams that allow fast pre-screening of prospective nuclear materials even when the comparisons between neutron and ion damage is not straightforward. This is due to the fact that if a new material is tested under a certain set of conditions with energetic ions and it shows poor resistance to irradiation, the need for expensive long timescale experiments in Materials Test Reactors can be reduced.

As a general guide to define whether a potential nuclear material possesses superior radiation tolerance, comparisons of their performance must be made with existing materials. Within the wide range of conventional nuclear materials, zirconium- and iron-based alloys are among the most widely used structural materials worldwide. In the current research, radiation damage effects in novel highly-concentrated multicomponent alloys known as high-entropy alloys and novel Ti-based ternary carbides known as MAX phases were investigated in a wide variety of conditions and their radiation responses have been compared with conventional nuclear mate-

rials such as AISI-348 steel and TiN. Additionally, the ion irradiation with *in situ* TEM technique was used throughout this work as the main methodology and under these experimental conditions, the radiation response of the materials was monitored in real-time. The main insights and outcomes obtained using this approach are summarised in the following section.

9.1 Summary

The relationship between the effects of energetic particle irradiation and the microstructure of materials has been reported in this thesis. The focus was on innovative metallic alloys and the MAX phases as prominent possible candidates for future nuclear reactors. As the high-entropy alloys and the MAX phases are materials with different physico-chemical nature, *i.e.* a metallic alloy and ternary ceramic carbides, the concepts of thermodynamics of materials and radiation damage were used to explore the response of such materials to irradiation.

The materials investigated in this work were characterised after synthesis and before irradiation using conventional and analytical electron microscopy techniques as presented in chapter 4. Following this detailed characterisation, the radiation response of the two similar metallic alloys – FeCrMnNi HEA and AISI-348 steel – was studied in chapter 5 under similar conditions with light and heavy ions aiming to probe whether the high-entropy effects such as sluggish diffusion can contribute to a superior radiation tolerance of the HEA compared with its low-entropy counterpart, the stainless steel. A second study was reported in chapter 6 to address the phase stability of the FeCrMnNi HEA and the austenitic stainless steel when subjected to low- and medium-energy, heavy ion irradiation. It was discovered that the radiation resistance of a metallic alloy is intrinsically related to its thermodynamic stability, particularly in preventing the formation of secondary phases (including precipitation) which is a phenomenon known to degrade the mechanical behaviour and corrosion/oxidation resistance of nuclear materials.

Chapter 7 explored the synthesis and characterisation of high-entropy alloy thin films from the quaternary system FeCrMnNi that were produced using the technique of ion beam sputter-deposition. After demonstrating the feasibility of depositing equiatomic thin films on Si substrates, the FeCrMnNi high-entropy alloy thin film was successfully deposited on Zircaloy-4^{TM} substrates and its radiation tolerance was studied using heavy-ion irradiation *in situ* within a TEM. For comparison, similar irradiations were performed on magnetron-sputtered thin films of titanium nitride, a material that has been recently proposed as a hard coating for accident tolerant fuels.

The neutron and ion irradiation responses of novel Ti-based MAX phases were

studied in chapter 8. A comprehensive electron microscopy post-irradiation characterisation of neutron-irradiated specimens at 1273 K at doses of 2 and 10 dpa was carried out and the results provide a new data set for these materials regarding their radiation response and stability in neutron environments. The thermal stability of the MAX phases under annealing as well as their radiation response to heavy-ion irradiation were also investigated.

9.2 Conclusions

The results indicate that the high-entropy alloy possesses higher radiation tolerance than its low-entropy counterpart, the AISI-348 steel; however, this was confined to moderate temperatures. The experiments performed on these metallic alloys provide new datasets for the scientific literature on high-entropy alloys which are the subject of recent intense debate and investigation aimed at their application in future nuclear technologies.

The sluggish-diffusion concept was studied in chapter 4. The results obtained with light and heavy ion irradiation of both alloys showed a statistical trend indicating a superior radiation tolerance of the FeCrMnNi HEA specifically that the nucleation of inert gas bubbles is reduced in high-entropy metallic systems, however, when the statistical error in measuring the bubbles sizes is taken into account, both alloys have shown similar results with respect to the nucleation and growth of inert gas bubbles.

The phase stability of the metallic alloys was investigated in chapter 5. At low and moderate temperature regimes, radiation-induced precipitation was observed to occur in the AISI-348 steel whereas in the FeCrMnNi HEA, the random solid solution was observed to remain unchanged. At higher temperatures, the radiation effects on both metallic alloys were observed to be similar. Phase transformations at 1073 K were identified in the AISI-348 steel under low-energy heavy ion irradiation and thermodynamic calculations using the software ThermoCalc indicated that the austenite matrix phase is metastable. As a result of the introduction of point defects in excess (*i.e.* higher than equilibrium concentrations) these irradiation-induced phase transformations indicate that the austenitic stainless steel is driven towards thermodynamic equilibrium. Although irradiation experiments could not be performed in the FeCrMnNi HEA at 1073 K due to an unknown and unsolved apparent "melting" effect of the TEM lamellae, the phase instabilities were detected in the stainless steel at all the irradiation temperatures which emphasises an interesting result: that the radiation damage tolerance is intrinsically related to thermodynamic stability. Analogies with creep and heat-affected zones in welding were used to reflect on the results.

Based on the results regarding the superior radiation tolerance of the bulk FeCrMnNi HEA, thin films based on the high-entropy alloy concept were synthesised and characterised as presented in chapter 7. The feasibility of depositing such thin films on Zircaloy-4^{TM} substrates was investigated. It was demonstrated that these HEATFs possess higher radiation tolerance than TiN thin films when irradiated with heavy-ions in reactor-like conditions. It is worth emphasising that the TiN was recently considered as a hard coating candidate for zirconium-based alloys. However the results of this current research show that radiation-induced segregation takes place whereas this was not the case in the HEATF. In the near future, the experimental development reported in this thesis may offer the possibility of designing new accident tolerant fuel concepts based on high-entropy alloy coatings, as the synthesis and production of bulk HEAs for nuclear application faces challenges regarding the limited availability and price of some alloying elements such as Cr and Ni.

In chapter 8, a detailed and comprehensive study of the neutron radiation resistance of Ti-based MAX phases was carried out. This study provides a new dataset of irradiation data regarding these novel materials as – for the first time – their microstructures following irradiation in a materials test reactor have been assessed at 2 and 10 dpa at an irradiation temperature of 1273 K. An intricate and complex chain of radiation effects including dislocation loops, lines and networks, cavities, stacking faults and black-dots was observed as well as phase decomposition (at 10 dpa). The latter observation suggests that the radiation stability of these materials is not as high as expected from previous publications. Attempts to simulate the neutron damage using heavy ion irradiation *in situ* within a TEM were not successful: possibly due to the influence of the electronic stopping power (when using 700 keV Kr ions) in inducing recovery of point defects. This suggests that for these MAX phases, the emulation of neutron damage should be carried out with ion beams conditions configured to induce collisions within the nuclear stopping range. In addition, the thermal stability of the MAX phases was studied using TEM. It was observed that a passivation layer starts to form at temperatures around 1073 K. Mainly composed of nanocrystals, this layer impaired the analysis of defects during the heavy ion irradiation experiments, limiting the attempts of comparing the neutron and ion irradiated microstructures.

9.3 Recommendations for further research work

The possibility of designing new metallic alloys by tuning the elemental composition in order to achieve superior radiation tolerance and high thermodynamic phase stability provides an opportunity that could contribute to the advancement of future nuclear technologies by harnessing the high-entropy core effects. New alloys could

be produced using these principles which could replace existing conventional nuclear materials in the near future. However, studies are needed to define whether strict equiatomic compositions are the best solution for this purpose or whether if the close to equimolar approach would actually deliver better properties and radiation tolerance. For this, prior to the development of new alloys, computational thermodynamics calculations can be used as a preliminary tool as they provide fast and reliable answers for such purposes. It is also clear that the element Ni, used in the FeCrMnNi HEA investigated in this thesis, should be replaced by another element that possesses reduced activation in neutron-irradiation environments. The replacement should be selected in order to maintain the corrosion and oxidation behaviours of such new highly-concentrated alloys as the element Ni is known to improve such properties in metallic alloys.

Another fact that deserves further attention is the radiation response of these alloys at high temperatures using *in situ* TEM ion irradiation. In this work, it was found that electron-transparent samples of the FeCrMnNi HEA are observed to be destroyed at temperatures around of 1073 K. This effect has also been observed with other metals in our research group. The physical mechanisms that induce this processes within the TEM below the normal melting point are still unknown and as a result, irradiation experiments at high temperatures were not possible. Another aspect that deserves attention is the fact that the radiation damage experiments performed throughout this work used the ion irradiation *in situ* TEM methodology. In order to confirm the results on the possible superior radiation tolerance of highly concentrated alloy systems, *ex situ* ion and neutron irradiation experiments are also needed.

As bulk HEAs could be an expensive alternative to the present nuclear fuel cladding alloys, the development of HEATFs as cheaper coatings for Zr-based alloys is a possible solution that was explored, developed and characterised in this thesis, but only targeting the nominal operation of PWRs. Further studies should be carried out on the radiation response of HEATF under extreme conditions (such as LOCA). Studies aiming at investigating the mechanical properties, corrosion and oxidation resistances (thus compatibility with the reactor's coolant) and tribological properties of such new thin films will be needed prior to their consideration for testing in MTRs. Comparative studies exploring the effects of irradiation on bulk HEAs and HEATFs are also needed as recent work in the literature indicate a superior radiation tolerance of HEATFs due to their reduced grain sizes (*i.e.* nano-crystallinity) [493, 494].

The radiation resistance of MAX phases under neutron and ion irradiation was also studied as they have been recently considered as possible ceramic materials for the next generation of nuclear reactors. Following the electron microscopy analysis of neutron irradiation induced defects, new studies are needed to address whether it

is possible to simulate neutron damage using ion irradiation. Further experiments are also required to determine the thermal stability of these materials at high temperatures as the MAX phase matrix decomposition may significantly impair the application of these ceramic compounds for future nuclear reactors, although the formation of self-passivating surface layer at high temperatures could be considered a good property of such materials for applications in extreme environments. Studies that investigate the relationship between the irradiation temperature and dose required for possible amorphisation of these materials are also needed.

Bibliography

[1] T. Veblen. *The place of science in modern civilization*. Routledge, 2017 (cit. on p. 1).

[2] I. Ursu. *Physics and technology of nuclear materials*. Elsevier, 2015 (cit. on pp. 1, 2).

[3] O. Camara, I. Hanif, M. Tunes, R. Harrison, G. Greaves, S. Donnelly, and J. Hinks. "Effects of temperature on the ion-induced bending of germanium and silicon nanowires". In: *Materials Research Express* 4.7 (2017), p. 075056 (cit. on p. 1).

[4] W. E. Frazier, E. W. Lee, M. E. Donnellan, and J. J. Thompson. "Advanced lightweight alloys for aerospace applications". In: *JOM* 41.5 (1989), pp. 22–26 (cit. on p. 1).

[5] M. Wegener. "Metamaterials beyond optics". In: *Science* 342.6161 (2013), pp. 939–940 (cit. on p. 1).

[6] R. Valiev. "Nanostructuring of metals by severe plastic deformation for advanced properties". In: *Nature Materials* 3.8 (2004), p. 511 (cit. on p. 1).

[7] S. Vepřek. "The search for novel, superhard materials". In: *Journal of Vacuum Science & Technology A: Vacuum, Surfaces, and Films* 17.5 (1999), pp. 2401–2420 (cit. on p. 1).

[8] S. Stankovich, D. A. Dikin, G. H. Dommett, K. M. Kohlhaas, E. J. Zimney, E. A. Stach, R. D. Piner, S. T. Nguyen, and R. S. Ruoff. "Graphene-based composite materials". In: *Nature* 442.7100 (2006), p. 282 (cit. on p. 1).

[9] M. H. Gass, U. Bangert, A. L. Bleloch, P. Wang, R. R. Nair, and A. Geim. "Free-standing graphene at atomic resolution". In: *Nature nanotechnology* 3.11 (2008), p. 676 (cit. on p. 1).

[10] M. Asif and T. Muneer. "Energy supply, its demand and security issues for developed and emerging economies". In: *Renewable and Sustainable Energy Reviews* 11.7 (2007), pp. 1388–1413 (cit. on p. 2).

[11] D. Helm, J. Wardlaw, and B. Caldecott. *Delivering a 21st century infrastructure for Britain*. Policy Exchange London, UK, 2009 (cit. on p. 2).

[12] N. Panwar, S. Kaushik, and S. Kothari. "Role of renewable energy sources in environmental protection: a review". In: *Renewable and Sustainable Energy Reviews* 15.3 (2011), pp. 1513–1524 (cit. on p. 2).

[13] M. Dresselhaus and I. Thomas. "Alternative energy technologies". In: *Nature* 414.6861 (2001), p. 332 (cit. on p. 3).

[14] N. Chowdhury. *Is nuclear energy renewable energy?* Accessed on 04.03.2018. Available at `https://tinyurl.com/matthesis2`. Stanford Physics Department, 2012 (cit. on p. 3).

[15] A. M. Weinberg and R. P. Hammond. "Limits to the Use of Energy: The limit to population set by energy is extremely large, provided that the breeder reactor is developed or that controlled fusion becomes feasible". In: *American Scientist* 58.4 (1970), pp. 412–418 (cit. on p. 3).

[16] Nuclear Companies and Stocks. *Nuclear Energy Efficiency vs Fossil Fuels (Oil,Gas) in Power Load Factors, Energy Density and Waste*. Accessed on 04.03.2018. Available at `https://tinyurl.com/mattthesis1`. 2011 (cit. on p. 3).

[17] IAEA. *Safety Standard Series: External Events Excluding Earthquakes in the Design of Nuclear Power Plants, International Atomic Energy Agency, Safety Guide No.* Tech. rep. NS-G-1.5, Vienna, 2003 (cit. on p. 3).

[18] A. Robertas, A. Juozas, M. Andrea, D. Finnicim, M. Carelli, B. Petrovic, and C. Kling. "External events analysis and probabilistic risk assessment application for iris plant design". In: *The 13th international conference on nuclear engineering abstracts*. 2005 (cit. on p. 3).

[19] M. Tunes, C. de Oliveira, and C. Schoen. "Multi-objective optimization of a compact pressurized water nuclear reactor computational model for biological shielding design using innovative materials". In: *Nuclear Engineering and Design* 313 (2017), pp. 20–28 (cit. on p. 3).

[20] P. Yvon and F. Carré. "Structural materials challenges for advanced reactor systems". In: *Journal of Nuclear Materials* 385.2 (2009), pp. 217–222 (cit. on p. 3).

[21] S. Zinkle and G. Was. "Materials challenges in nuclear energy". In: *Acta Materialia* 61.3 (2013), pp. 735–758 (cit. on pp. 3, 5, 252, 265).

[22] M. W. Thompson. *Defects and radiation damage in metals*. Cambridge University Press, 1974 (cit. on pp. 5, 26–29, 31, 37, 38, 40, 43, 44, 60, 160).

[23] I. Cook. "Materials research for fusion energy". In: *Nature Materials* 5.2 (2006), pp. 77–80 (cit. on pp. 5, 6).

[24] P. Hosemann and J. Vujić. “Material issues for current and advanced nuclear reactor designs”. In: *Contemporary Materials* 1.5 (2014), pp. 10–25 (cit. on p. 5).

[25] H. Rickover, L. Geiger, and B. Lustman. *History of the development of zirconium alloys for use in nuclear reactors*. Tech. rep. Washington, DC: Energy Research and Development Administration, Washington, D.C. (USA). Div. of Naval Reactors, 1975 (cit. on pp. 5, 214).

[26] M. T. Simnad. “A brief history of power reactor fuels”. In: *Journal of Nuclear Materials* 100.1-3 (1981), pp. 93–107 (cit. on pp. 5, 6, 62).

[27] S. Zinkle. “Advanced irradiation-resistant materials for Generation IV nuclear reactors”. In: *Structural Materials for Generation IV Nuclear Reactors*. Ed. by P. Yvon. Woodhead Publishing, 2017, pp. 569–594. ISBN: 978-0-08-100906-2 (cit. on p. 5).

[28] L. TerraPower. “Traveling-wave reactors: a truly sustainable and full-scale resource for global energy needs”. In: *Proceeding of ICAPP*. Vol. 2010. 2010 (cit. on p. 5).

[29] M. A. Tunes, F. T. Degasperi, C. L. Rodrigues, T. F. Silva, M. H. Tabacniks, N. Added, and C. G. Schön. “Radiation damage research at LAMFI: Laboratory of Materials and Ion Beams”. In: *Revista Brasileira de Aplicações de Vácuo* 35.3 (2017), pp. 111–116 (cit. on pp. 5, 60).

[30] R. W. Cahn and P. Haasen. *Physical metallurgy. vol. 1*. North-Holland, 1996 (cit. on pp. 7–9, 11, 78).

[31] F. Mazzolani. *Aluminium alloy structures*. CRC Press, 1994 (cit. on p. 7).

[32] H. Bhadeshia and R. Honeycombe. *Steels: microstructure and properties*. Butterworth-Heinemann, 2017 (cit. on pp. 8–10, 12, 13, 62, 77, 78, 116, 119, 120, 126, 139, 184, 191, 199, 237).

[33] D. A. Porter, K. E. Easterling, and M. Sherif. *Phase transformations in metals and alloys*. CRC press, 2009 (cit. on pp. 8, 10, 15–17, 257).

[34] I. Gurrappa and D. V. Reddy. “Characterisation of titanium alloy, IMI-834 for corrosion resistance under different environmental conditions”. In: *Journal of Alloys and Compounds* 390.1 (2005), pp. 270–274 (cit. on p. 8).

[35] G. Welsch, R. Boyer, and E. Collings. *Materials properties handbook: titanium alloys*. ASM international, 1993 (cit. on p. 8).

[36] Y. Lee, A. Dahle, and D. StJohn. “The role of solute in grain refinement of magnesium”. In: *Metallurgical and Materials Transactions A* 31.11 (2000), pp. 2895–2906 (cit. on p. 8).

[37] W. H. Wang. “Roles of minor additions in formation and properties of bulk metallic glasses”. In: *Progress in Materials Science* 52.4 (2007), pp. 540–596 (cit. on p. 8).

[38] B. Stoughton. *The metallurgy of iron and steel*. McGraw-Hill publishing company, 1908 (cit. on p. 8).

[39] L. Scheer. *Was ist Stahl: Einführung in die Stahlkunde für jedermann*. Springer, 1938 (cit. on pp. 8–12, 77, 120, 126, 139, 191).

[40] R. Elliott. *Cast iron technology*. Butterworth-Heinemann, 1988 (cit. on p. 8).

[41] H. T. Angus. *Cast iron: physical and engineering properties*. Elsevier, 2013 (cit. on p. 8).

[42] W. Garrison Jr. “Steels: classifications”. In: *Encyclopedia of materials: science and technology*. Ed. by K. J. Buschow, R. W. Cahn, M. C. Flemings, B. Ilschner, E. J. Kramer, S. Mahajan, and P. Veyssière. Second Edition. Oxford: Elsevier, 2001, pp. 8840–8843 (cit. on p. 8).

[43] F. B. Pickering. *Physical metallurgy and the design of steels*. Applied Science Publishers, 1978 (cit. on pp. 9, 10, 12, 62).

[44] R. Hudd. “Sheet steel: low carbon”. In: *Encyclopedia of materials: science and technology*. Ed. by K. J. Buschow, R. W. Cahn, M. C. Flemings, B. Ilschner, E. J. Kramer, S. Mahajan, and P. Veyssiere. Second Edition. Oxford: Elsevier, 2001, pp. 8456–8461 (cit. on p. 9).

[45] J. Svoboda. “Low-alloy steels”. In: *ASM Handbook*. 15 (1988), pp. 715–721 (cit. on p. 9).

[46] R. Kuziak, R. Kawalla, and S. Waengler. “Advanced high strength steels for automotive industry”. In: *Archives of Civil and Mechanical Engineering* 8.2 (2008), pp. 103–117 (cit. on p. 9).

[47] W. Hume-Rothery, R. E. Smallman, and C. W. Haworth. *The structure of metals amd alloys*. The Institute of Metals, 1969 (cit. on pp. 9, 15).

[48] B. Weiss and R. Stickler. “Phase instabilities during high temperature exposure of 316 austenitic stainless steel”. In: *Metallurgical Transactions* 3.4 (1972), pp. 851–866 (cit. on p. 10).

[49] N. Shulumba, O. Hellman, Z. Raza, B. Alling, J. Barrirero, F. Mücklich, I. A. Abrikosov, and M. Odén. “Lattice vibrations change the solid solubility of an alloy at high temperatures”. In: *Physical review letters* 117.20 (2016), p. 205502 (cit. on p. 11).

[50] G. Speich, V. Demarest, and R. Miller. “Formation of austenite during intercritical annealing of dual-phase steels”. In: *Metallurgical and Materials Transactions A* 12.8 (1981), pp. 1419–1428 (cit. on p. 11).

[51] M. Hillert, K. Nilsson, and L. Torndahl. “Effect of alloying elements on the formation of austenite and dissolution of cementite”. In: *The Journal of the Iron and Steel Institute* 209.1 (1971), pp. 49–66 (cit. on p. 11).

[52] G. Molinder. “A quantitative study of the formation of austenite and the solution of cementite at different austenitizing temperatures for a 1.27% carbon steel”. In: *Acta Metallurgica* 4.6 (1956), pp. 565–571 (cit. on p. 11).

[53] T. Sourmail. “Precipitation in creep resistant austenitic stainless steels”. In: *Materials Science and Technology* 17.1 (2001), pp. 1–14 (cit. on pp. 11, 12, 77).

[54] J. R. Davis et al. *Stainless steels*. ASM international, 1994 (cit. on p. 11).

[55] B. Murty, J.-W. Yeh, and S. Ranganathan. *High-entropy alloys*. Butterworth-Heinemann, 2014 (cit. on pp. 13–15, 18–21, 128, 198).

[56] F. C. Achard. *Recherches sur les propriétés des alliages métalliques. Par Mr Achard*. Imprimé chez George Jacques Decker & Fils, 1788 (cit. on p. 13).

[57] B. Cantor, I. Chang, P. Knight, and A. Vincent. “Microstructural development in equiatomic multicomponent alloys”. In: *Materials Science and Engineering: A* 375 (2004), pp. 213–218 (cit. on p. 14).

[58] B. Cantor, K. Kim, and P. J. Warren. “Novel multicomponent amorphous alloys”. In: *Materials Science Forum*. Vol. 386. Trans Tech Publ. 2002, pp. 27–32 (cit. on pp. 14, 17).

[59] B. Cantor. “Multicomponent and high entropy alloys”. In: *Entropy* 16.9 (2014), pp. 4749–4768 (cit. on pp. 14, 18).

[60] B. Cantor. “Stable and metastable multicomponent alloys”. In: *Annales de Chimie*. Vol. 32-3. Lavoisier. 2007, pp. 245–256 (cit. on p. 14).

[61] J.-W. Yeh, S.-K. Chen, S.-J. Lin, J.-Y. Gan, T.-S. Chin, T.-T. Shun, C.-H. Tsau, and S.-Y. Chang. “Nanostructured High-Entropy Alloys with Multiple Principal Elements: Novel Alloy Design Concepts and Outcomes”. In: *Advanced Engineering Materials* 6.5 (2004), pp. 299–303 (cit. on pp. 14, 17, 18).

[62] J. W. Yeh, Y. L. Chen, S. J. Lin, and S. K. Chen. “High-entropy alloys–a new era of exploitation”. In: *Materials Science Forum*. Vol. 560. Trans Tech Publ. 2007, pp. 1–9 (cit. on p. 14).

[63] J.-W. Yeh. “Alloy design strategies and future trends in high-entropy alloys”. In: *JOM* 65.12 (2013), pp. 1759–1771 (cit. on pp. 14, 18).

[64] S. Ranganathan. “Alloyed pleasures: Multimetallic cocktails”. In: *Current Science* 85.5 (2003), pp. 1404–1406 (cit. on pp. 14, 20).

[65] J. Basu and S. Ranganathan. “Bulk metallic glasses: A new class of engineering materials”. In: *Sadhana* 28.3-4 (2003), pp. 783–798 (cit. on p. 14).

[66] T. Saito, T. Furuta, J.-H. Hwang, S. Kuramoto, K. Nishino, N. Suzuki, R. Chen, A. Yamada, K. Ito, Y. Seno, et al. “Multifunctional alloys obtained via a dislocation-free plastic deformation mechanism”. In: *Science* 300.5618 (2003), pp. 464–467 (cit. on p. 14).

[67] C.-J. Tong, M.-R. Chen, J.-W. Yeh, S.-J. Lin, S.-K. Chen, T.-T. Shun, and S.-Y. Chang. “Mechanical performance of the Al x CoCrCuFeNi high-entropy alloy system with multiprincipal elements”. In: *Metallurgical and Materials Transactions A* 36.5 (2005), pp. 1263–1271 (cit. on p. 14).

[68] C. G. Schön, T. Duong, Y. Wang, and R. Arróyave. “Probing the entropy hypothesis in highly concentrated alloys”. In: *Acta Materialia* 148 (2018), pp. 263–279 (cit. on pp. 15, 20, 21, 187, 213).

[69] C. G. Schön, T. Duong, Y. Wang, and R. Arróyave. “A proof of concept: thermodynamics of aluminum–transition metal highly concentrated alloys”. In: *Journal of Alloys and Compounds* 781 (2019), pp. 595–605 (cit. on pp. 15, 20, 21).

[70] M. Widom, W. P. Huhn, S. Maiti, and W. Steurer. “Hybrid Monte Carlo and molecular dynamics simulation of a refractory metal high entropy alloy”. In: *Metallurgical and Materials Transactions A* 45.1 (2014), pp. 196–200 (cit. on p. 15).

[71] Z. Liu, Y. Lei, C. Gray, and G. Wang. “Examination of solid-solution phase formation rules for high entropy alloys from atomistic Monte Carlo simulations”. In: *JOM* 67.10 (2015), pp. 2364–2374 (cit. on p. 15).

[72] L. Xie, P. Brault, A.-L. Thomann, X. Yang, Y. Zhang, and G. Shang. “Molecular dynamics simulation of Al–Co–Cr–Cu–Fe–Ni high entropy alloy thin film growth”. In: *Intermetallics* 68 (2016), pp. 78–86 (cit. on p. 15).

[73] J. Li, Q. Fang, B. Liu, Y. Liu, and Y. Liu. “Mechanical behaviors of AlCrFeCuNi high-entropy alloys under uniaxial tension via molecular dynamics simulation”. In: *RSC Advances* 6.80 (2016), pp. 76409–76419 (cit. on p. 15).

[74] D. Xiao, P. Zhou, W. Wu, H. Diao, M. Gao, M. Song, and P. Liaw. "Microstructure, mechanical and corrosion behaviors of AlCoCuFeNi-(Cr, Ti) high entropy alloys". In: *Materials & Design* 116 (2017), pp. 438–447 (cit. on p. 15).

[75] F. Granberg, K. Nordlund, M. W. Ullah, K. Jin, C. Lu, H. Bei, L. M. Wang, F. Djurabekova, W. J. Weber, and Y. Zhang. "Mechanism of radiation damage reduction in equiatomic multicomponent single phase alloys". In: *Phys. Rev. Lett.* 116.April (2016), p. 135504 (cit. on pp. 15, 66, 140).

[76] Y. Zhang and Y. J. Zhou. "Solid solution formation criteria for high entropy alloys". In: *Materials Science Forum*. Vol. 561. Trans Tech Publ. 2007, pp. 1337–1339 (cit. on pp. 15, 17).

[77] R. DeHoff. *Thermodynamics in materials science*. CRC Press, 2006 (cit. on p. 18).

[78] H.-T. Hsueh, W.-J. Shen, M.-H. Tsai, and J.-W. Yeh. "Effect of nitrogen content and substrate bias on mechanical and corrosion properties of high-entropy films (AlCrSiTiZr) 100- xNx". In: *Surface and Coatings Technology* 206.19-20 (2012), pp. 4106–4112 (cit. on p. 18).

[79] K.-H. Cheng, C.-H. Lai, S.-J. Lin, and J.-W. Yeh. "Structural and mechanical properties of multi-element (AlCrMoTaTiZr) Nx coatings by reactive magnetron sputtering". In: *Thin Solid Films* 519.10 (2011), pp. 3185–3190 (cit. on p. 18).

[80] B. Fultz. "Vibrational thermodynamics of materials". In: *Progress in Materials Science* 55.4 (2010), pp. 247–352 (cit. on p. 18).

[81] R. A. Swalin and J. Arents. "Thermodynamics of solids". In: *Journal of The Electrochemical Society* 109.12 (1962), pp. 308C–308C (cit. on p. 18).

[82] A. Takeuchi and A. Inoue. "Calculations of mixing enthalpy and mismatch entropy for ternary amorphous alloys". In: *Materials Transactions, JIM* 41.11 (2000), pp. 1372–1378 (cit. on p. 19).

[83] F. R. Boer. *Cohesion in metals: transition metal alloys*. Vol. 1. North Holland, 1988 (cit. on p. 19).

[84] J.-W. Yeh. "Physical metallurgy of high-entropy alloys". In: *JOM* 67.10 (2015), pp. 2254–2261 (cit. on p. 20).

[85] F. Otto, A. Dlouhy, C. Somsen, H. Bei, G. Eggeler, and E. P. George. "The influences of temperature and microstructure on the tensile properties of a CoCrFeMnNi high-entropy alloy". In: *Acta Materialia* 61.15 (2013), pp. 5743–5755 (cit. on p. 20).

[86] M.-H. Tsai, J.-W. Yeh, and J.-Y. Gan. "Diffusion barrier properties of AlMoNbSiTaTiVZr high-entropy alloy layer between copper and silicon". In: *Thin Solid Films* 516.16 (2008), pp. 5527–5530 (cit. on p. 20).

[87] Y. Zhang, G. M. Stocks, K. Jin, C. Lu, H. Bei, B. C. Sales, L. Wang, L. K. Béland, R. E. Stoller, G. D. Samolyuk, et al. "Influence of chemical disorder on energy dissipation and defect evolution in concentrated solid solution alloys". In: *Nature Communications* 6 (2015), p. 8736 (cit. on pp. 20, 140, 161).

[88] K.-Y. Tsai, M.-H. Tsai, and J.-W. Yeh. "Sluggish diffusion in Co–Cr–Fe–Mn–Ni high-entropy alloys". In: *Acta Materialia* 61.13 (2013), pp. 4887–4897. ISSN: 1359-6454 (cit. on p. 20).

[89] K.-Y. Tsai, M.-H. Tsai, and J.-W. Yeh. "Reply to comments on "Sluggish diffusion in Co-Cr-Fe-Mn-Ni high-entropy alloys" by K.Y. Tsai, M.H. Tsai and J.W. Yeh, Acta Materialia 61 (2013) 4887-4897". In: *Scripta Materialia* 135 (2017), pp. 158–159 (cit. on p. 20).

[90] A. Paul. "Comments on "Sluggish diffusion in Co–Cr–Fe–Mn–Ni high-entropy alloys" by K.Y. Tsai, M.H. Tsai and J.W. Yeh, Acta Materialia 61 (2013) 4887–4897". In: *Scripta Materialia* 135 (2017), pp. 153–157 (cit. on p. 20).

[91] Y. Jien-Wei. "Recent progress in high entropy alloys". In: *Annales de Chimie Science des Materiaux* 31.6 (2006), pp. 633–648 (cit. on p. 21).

[92] C. Varvenne and W. A. Curtin. "Strengthening of high entropy alloys by dilute solute additions: CoCrFeNiAlx and CoCrFeNiMnAlx alloys". In: *Scripta Materialia* 138 (2017), pp. 92–95 (cit. on p. 21).

[93] G. Toulouse. *Frustration and disorder new problems in statistical mechanics spin glasses in a historical perspective*. Heidelberg Colloquium on Spin Glasses, Springer, 1983, pp. 2–17 (cit. on p. 21).

[94] G. Toulouse. "The frustration model". In: *Modern trends in the theory of condensed matter*. Springer, 1980, pp. 195–203 (cit. on p. 21).

[95] S. Kirkpatrick. "Frustration and ground-state degeneracy in spin glasses". In: *Physical Review B* 16.10 (1977), p. 4630 (cit. on p. 21).

[96] G. Toulouse, S. Dehaene, and J.-P. Changeux. "Spin glass model of learning by selection". In: *Proceedings of the National Academy of Sciences* 83.6 (1986), pp. 1695–1698 (cit. on p. 21).

[97] S. Diaz, S. De Brion, G. Chouteau, B. Canals, V. Simonet, and P. Strobel. "Magnetic frustration in the spinel compounds GeCo2O4 and GeNi2O4". In: *Physical Review B* 74.9 (2006), p. 092404 (cit. on p. 21).

[98] R. Moessner and A. P. Ramirez. "Geometrical frustration". In: *Physics Today* 59.2 (2006), pp. 24–29 (cit. on p. 21).

[99] C. C. Koch. *Nanostructured materials: processing, properties and applications*. William Andrew, 2006 (cit. on p. 22).

[100] W. Jeitschko, H. Nowotny, and F. Benesovsky. "Kohlenstoffhaltige ternäre Verbindungen (H-phase)". In: *Monatshefte für Chemie* 94.4 (1963), pp. 672–676 (cit. on p. 22).

[101] W. Jeitschko, H. Nowotny, and F. Benesovsky. "Kohlenstoffhaltige ternäre Verbindungen (V-Ge-C, Nb-Ga-C, Ta-Ga-C, Ta-Ge-C, Cr-Ga-C und Cr-Ge-C)". In: *Monatshefte für Chemie* 94.5 (1963), pp. 844–850 (cit. on p. 22).

[102] W. Jeitschko, H. Nowotny, and F. Benesovsky. "Die H-Phasen: Ti2CdC, Ti2GaC, Ti2GaN, Ti2InN, Zr2InN und Nb2GaC". In: *Monatshefte für Chemie* 95.1 (1964), pp. 178–179 (cit. on p. 22).

[103] W. Jeitschko, H. Nowotny, and F. Benesovsky. "Die H-Phasen Ti2TlC, Ti2PbC, Nb2InC, Nb2SnC und Ta2GaC". In: *Monatshefte für Chemie* 95.2 (1964), pp. 431–435 (cit. on p. 22).

[104] V. H. Nowotny. "Strukturchemie einiger verbindungen der übergangsmetalle mit den elementen C, Si, Ge, Sn". In: *Progress in Solid State Chemistry* 5 (1971), pp. 27–70 (cit. on p. 22).

[105] M. W. Barsoum. "The MN+1AXN phases: A new class of solids: Thermodynamically stable nanolaminates". In: *Progress in Solid State Chemistry* 28.1 (2000), pp. 201–281 (cit. on pp. 22, 23, 233, 237, 254).

[106] W. Jeitschko and H. Nowotny. "Die Kristallstruktur von Ti3SiC2 — ein neuer Komplexcarbid-Typ". In: *Monatshefte für Chemie* 98.2 (1967), pp. 329–337 (cit. on p. 22).

[107] M. W. Barsoum and T. El-Raghy. "The MAX phases: unique new carbide and nitride materials: ternary ceramics turn out to be surprisingly soft and machinable, yet also heat-tolerant, strong and lightweight". In: *American Scientist* 89.4 (2001), pp. 334–343 (cit. on pp. 22, 252).

[108] M. W. Barsoum. *MAX phases: properties of machinable ternary carbides and nitrides*. John Wiley & Sons, 2013 (cit. on pp. 22, 23, 246).

[109] M. W. Barsoum and M. Radovic. *Mechanical properties of the MAX phases*. Elsevier, 2001 (cit. on pp. 23, 24).

[110] M. W. Barsoum and M. Radovic. "Elastic and Mechanical Properties of the MAX Phases". In: *Annual Review of Materials Research* 41.1 (2011), pp. 195–227 (cit. on pp. 23–26, 139, 252).

[111] M. Romeo and R. Escamilla. “Pressure effect on the structural, elastic and electronic properties of Nb2AC (A=S and In) phases; ab initio study”. In: *Computational Materials Science* 81 (2014), pp. 184–190 (cit. on p. 23).

[112] Y. Zhou, Z. Sun, X. Wang, and S. Chen. “Ab initio geometry optimization and ground state properties of layered ternary carbides Ti3MC2 (M = Al, Si and Ge)”. In: *Journal of Physics Condensed Matter* 13.44 (2001), pp. 10001–10010 (cit. on p. 24).

[113] C. Lue, J. Lin, and B. Xie. “NMR study of the ternary carbides M2AlC (M=Ti,V,Cr)”. In: *Physical Review B* 73.3 (2006), p. 035125 (cit. on p. 24).

[114] Z. Sun and Y. Zhou. “Ab initio calculation of titanium silicon carbide”. In: *Physical Review B* 60.3 (1999), pp. 1441–1443 (cit. on p. 24).

[115] G. Hug and E. Fries. “Full-potential electronic structure of Ti2AlC and Ti2AlN”. In: *Physical Review B* 65.11 (2002), p. 113104 (cit. on p. 24).

[116] G. Hug, M. Jaouen, and M. W. Barsoum. “X-ray absorption spectroscopy, EELS, and full-potential augmented plane wave study of the electronic structure of Ti 2 Al C , Ti 2 Al N , Nb 2 Al C , and (Ti 0.5 Nb 0.5) 2 Al C”. In: *Physical Review B* 71.2 (2005), p. 024105 (cit. on p. 24).

[117] N. Medvedeva and D. Novikov. “Electronic properties of-based solid solutions”. In: *Physical Review B - Condensed Matter and Materials Physics* 58.24 (1998), pp. 16042–16050 (cit. on p. 24).

[118] Y. Kuroda, I. Low, M. Barsoum, and T. El-Raghy. “Indentation responses, wear and damage characteristics of hot-isostatically-pressed Ti3SiC2”. In: *Journal of the Australasian Ceramic Society* 37.1 (2001), pp. 95–102 (cit. on p. 24).

[119] L. Farber. “Transmission electron microscopy study of a low-angle boundary in plastically deformed Ti3SiC2”. In: *Philosophical Magazine Letters* 79.4 (1999), pp. 163–170 (cit. on p. 24).

[120] B. Kooi, R. Poppen, N. Carvalho, J. T. M. De Hosson, and M. Barsoum. “Ti3SiC2: A damage tolerant ceramic studied with nano-indentations and transmission electron microscopy”. In: *Acta Materialia* 51.10 (2003), pp. 2859–2872 (cit. on p. 24).

[121] M. Radovic, M. Barsoum, A. Ganguly, T. Zhen, P. Finkel, S. Kalidindi, and E. Lara-Curzio. “On the elastic properties and mechanical damping of Ti3SiC2, Ti3GeC2, Ti3Si0. 5Al0. 5C2 and Ti2AlC in the 300–1573 K temperature range”. In: *Acta Materialia* 54.10 (2006), pp. 2757–2767 (cit. on p. 24).

[122] M. Radovic, M. Barsoum, T. El-Raghy, S. M. Wiederhorn, and W. E. Luecke. "Effect of temperature, strain rate and grain size on the mechanical response of Ti3SiC2 in tension". In: *Acta Materialia* 50.6 (2002), pp. 1297–1306 (cit. on p. 25).

[123] F. Frank and A. Stroh. "On the theory of kinking". In: *Proceedings of the Physical Society. Section B* 65.10 (1952), p. 811 (cit. on p. 25).

[124] A. Zhou, S. Basu, and M. Barsoum. "Kinking nonlinear elasticity, damping and microyielding of hexagonal close-packed metals". In: *Acta Materialia* 56.1 (2008), pp. 60–67 (cit. on p. 25).

[125] M. Barsoum and T. El-Raghy. "Room-temperature ductile carbides". In: *Metallurgical and Materials Transactions A* 30.2 (1999), pp. 363–369 (cit. on p. 26).

[126] G. E. Dieter and D. J. Bacon. *Mechanical metallurgy*. Vol. 3. McGraw-hill New York, 1986 (cit. on p. 26).

[127] M. Barsoum, T. El-Raghy, and M. Ali. "Processing and characterization of Ti 2 AlC, Ti 2 AlN, and Ti 2 AlC 0.5 N 0.5". In: *Metallurgical and Materials Transactions A* 31.7 (2000), pp. 1857–1865 (cit. on p. 26).

[128] D. Wan, F. Meng, Y. Zhou, Y. Bao, and J. Chen. "Effect of grain size, notch width, and testing temperature on the fracture toughness of Ti3Si (Al) C2 and Ti3AlC2 using the chevron-notched beam (CNB) method". In: *Journal of the European Ceramic Society* 28.3 (2008), pp. 663–669 (cit. on p. 26).

[129] W. Tian, Z. Sun, H. Hashimoto, and Y. Du. "Compressive deformation behavior of ternary compound Cr 2 AlC". In: *Journal of Materials Science* 44.1 (2009), pp. 102–107 (cit. on p. 26).

[130] M. Radovic, M. Barsoum, T. El-Raghy, J. Seidensticker, and S. Wiederhorn. "Tensile properties of Ti3SiC2 in the 25–1300 C temperature range". In: *Acta Materialia* 48.2 (2000), pp. 453–459 (cit. on p. 26).

[131] K. Lambrinou, T. Lapauw, B. Tunca, and J. Vleugels. "MAX Phase Materials for Nuclear Applications". In: *Developments in Strategic Ceramic Materials II*. John Wiley and Sons, Ltd, 2017. Chap. 21, pp. 223–233 (cit. on p. 26).

[132] T. Lapauw, B. Tunca, T. Cabioch, J. Lu, Persson, K. Lambrinou, and J. Vleugels. "Synthesis of MAX phases in the Hf–Al–C system". In: *Inorganic Chemistry* 55.21 (2016), pp. 10922–10927 (cit. on p. 26).

[133] B. Tunca, T. Lapauw, O. M. Karakulina, M. Batuk, T. Cabioch, J. Hadermann, R. Delville, K. Lambrinou, and J. Vleugels. "Synthesis of MAX phases in the Zr-Ti-Al-C system". In: *Inorganic Chemistry* 56.6 (2017), pp. 3489–3498 (cit. on p. 26).

[134] T. Lapauw, K. Lambrinou, T. Cabioch, J. Halim, J. Lu, A. Pesach, O. Rivin, O. Ozeri, E. Caspi, L. Hultman, et al. "Synthesis of the new MAX phase Zr2AlC". In: *Journal of the European Ceramic Society* 36.8 (2016), pp. 1847–1853 (cit. on p. 26).

[135] T. Lapauw, J. Halim, J. Lu, T. Cabioch, L. Hultman, M. W. Barsoum, K. Lambrinou, and J. Vleugels. "Synthesis of the novel Zr3AlC2 MAX phase". In: *Journal of the European Ceramic Society* 36.3 (2016), pp. 943–947 (cit. on p. 26).

[136] T. Lapauw, B. Tunca, D. Potashnikov, A. Pesach, O. Ozeri, J. Vleugels, and K. Lambrinou. "The double solid solution (Zr, Nb) 2 (Al, Sn) C MAX phase: a steric stability approach". In: *Scientific Reports* 8.1 (2018), p. 12801 (cit. on p. 26).

[137] S. E. Donnelly and R. C. Birtcher. "Ion-induced spike effects on metal surfaces". In: *Philosophical Magazine A - Physics of Condensed Matter Structure Defects and Mechanical Properties* 79.1 (1999), pp. 133–145 (cit. on pp. 27, 36, 37, 40, 160).

[138] R. Birtcher and S. Donnelly. "Plastic flow induced by single ion impacts on gold". In: *MRS Online Proceedings Library Archive* 439 (1996) (cit. on p. 27).

[139] A. E521. "Standard Practice for Neutron Radiation Damage Simulation by Charged-Particle". In: *Annual Book of ASTM Standards* 12.02.Reapproved (2009), pp. 1–21 (cit. on pp. 28, 38, 105).

[140] R. E. Stoller, M. B. Toloczko, G. S. Was, A. G. Certain, S. Dwaraknath, and F. A. Garner. "On the use of SRIM for computing radiation damage exposure". In: *Nuclear instruments and methods in physics research section B: beam interactions with materials and atoms* 310 (2013), pp. 75–80 (cit. on pp. 28, 31, 35, 104, 105, 193, 254).

[141] N. Bohr. "II. On the theory of the decrease of velocity of moving electrified particles on passing through matter". In: *The London, Edinburgh, and Dublin Philosophical Magazine and Journal of Science* 25.145 (1913), pp. 10–31 (cit. on p. 28).

[142] N. Bohr. "LX. On the decrease of velocity of swiftly moving electrified particles in passing through matter". In: *The London, Edinburgh, and Dublin Philosophical Magazine and Journal of Science* 30.178 (1915), pp. 581–612 (cit. on p. 28).

[143] J. Lindhard, M. Scharff, and H. E. Schiøtt. *Range concepts and heavy ion ranges*. Munksgaard Copenhagen, 1963 (cit. on p. 29).

[144] W. Busza and A. S. Goldhaber. "Nuclear stopping power". In: *Physics Letters B* 139.4 (1984), pp. 235–238 (cit. on p. 29).

[145] J. F. Ziegler. "The stopping and range of ions in solids". In: *Ion Implantation Science and Technology (Second Edition)*. Elsevier, 1988, pp. 3–61 (cit. on pp. 29, 35, 104).

[146] L. C. Northcliffe and R. F. Schilling. "Range and stopping-power tables for heavy ions". In: *Atomic Data and Nuclear Data Tables* 7.3-4 (1970), pp. 233–463 (cit. on p. 29).

[147] Wikipedia. *Stopping power (particle radiation) — Wikipedia, The Free Encyclopedia*. [Online; accessed 19-March-2018]. 2018 (cit. on p. 29).

[148] J. F. Ziegler, M. D. Ziegler, and J. P. Biersack. "SRIM–The stopping and range of ions in matter (2010)". In: *Nuclear Instruments and Methods in Physics Research Section B: Beam Interactions with Materials and Atoms* 268.11-12 (2010), pp. 1818–1823 (cit. on pp. 30, 31, 35, 104, 105, 253).

[149] H. Trinkaus and B. Singh. "Helium accumulation in metals during irradiation – where do we stand?" In: *Journal of Nuclear Materials* 323.2-3 (2003), pp. 229–242 (cit. on p. 30).

[150] M. Behar, C. D. Denton, R. C. Fadanelli, I. Abril, E. Cantero, R. Garcia-Molina, and L. Nagamine. "Experimental and theoretical determination of the stopping power of ZrO2 films for protons and alpha particles". In: *European Physical Journal D* 59 (2010), pp. 209–213 (cit. on p. 30).

[151] L. Northcliffe and R. Schilling. "Range and stopping-power tables for heavy ions". In: *Atomic Data and Nuclear Data Tables* 7.3 (1970), pp. 233–463 (cit. on p. 30).

[152] H. H. Andersen. "Accelerators and Stopping Power Experiments". In: *Interaction of Charged Particles with Solids and Surfaces*. Boston, MA: Springer US, 1991, pp. 145–192. ISBN: 978-1-4684-8026-9 (cit. on p. 30).

[153] N. Metropolis and S. Ulam. "The monte carlo method". In: *Journal of the American Statistical Association* 44.247 (1949), pp. 335–341 (cit. on pp. 30, 104).

[154] T. Kakavand, M. Mirzaii, M. Eslami, and S. Valizadeh. "Cyclotron production of 52Mn and Monte Carlo benchmarking". In: *Journal of Radioanalytical and Nuclear Chemistry* 304.2 (2015), pp. 669–674 (cit. on p. 31).

[155] C. Golnik, D. Bemmerer, W. Enghardt, F. Fiedler, F. Hueso-González, G. Pausch, K. Römer, H. Rohling, S. Schöne, L. Wagner, et al. "Tests of a Compton imaging prototype in a monoenergetic 4.44 MeV photon field—a benchmark setup for prompt gamma-ray imaging devices". In: *Journal of Instrumentation* 11.06 (2016), P06009 (cit. on p. 31).

[156] V. McLane. *Neutron cross sections*. Vol. 2. Elsevier, 2012 (cit. on p. 31).

[157] D. J. Hughes. *Neutron cross sections*. Vol. 2. Elsevier, 2016 (cit. on p. 31).

[158] J. J. Duderstadt. *Nuclear reactor analysis*. Wiley, 1976 (cit. on p. 31).

[159] J. A. Brinkman. "On the nature of radiation damage in metals". In: *Journal of Applied Physics* 25.8 (1954), pp. 961–970 (cit. on pp. 31, 36, 37, 39).

[160] G. Kinchin and R. Pease. "The displacement of atoms in solids by radiation". In: *Reports on Progress in Physics* 18.1 (1955), p. 1 (cit. on pp. 31, 33, 34, 36, 105).

[161] R. Coltman, C. Klabunde, and J. Redman. "Survey of thermal-neutron damage in pure metals". In: *Physical Review* 156.3 (1967), p. 715 (cit. on p. 31).

[162] A. Santamarina, D. Bernard, P. Blaise, M. Coste, A. Courcelle, T. Huynh, C. Jouanne, P. Leconte, O. Litaize, S. Mengelle, et al. "The JEFF-3.1. 1 nuclear data library". In: *JEFF report* 22.10.2 (2009), p. 2 (cit. on pp. 32, 33).

[163] U. N. S. C. on the Effects of Atomic Radiation. *Ionizing radiation: sources and biological effects. Report to the general assembly*. NATO, 1982 (cit. on p. 33).

[164] M. Gilbert, S. Dudarev, S. Zheng, L. Packer, and J.-C. Sublet. "An integrated model for materials in a fusion power plant: transmutation, gas production, and helium embrittlement under neutron irradiation". In: *Nuclear Fusion* 52.8 (2012), p. 083019 (cit. on p. 33).

[165] D. Kramer, H. Brager, C. Rhodes, and A. Pard. "Helium embrittlement in type 304 stainless steel". In: *Journal of Nuclear Materials* 25.2 (1968), pp. 121–131 (cit. on pp. 33, 43).

[166] E. Kovacs and A. Keresztes. "Effect of gamma and UV-B/C radiation on plant cells". In: *Micron* 33.2 (2002), pp. 199–210 (cit. on p. 33).

[167] M. Tunes, C. de Oliveira, and C. Schön. "Multi-objective optimization of a compact pressurized water nuclear reactor computational model for biological shielding design using innovative materials". In: *Nuclear Engineering and Design* 313 (2017), pp. 20–28 (cit. on p. 33).

[168] B. Campbell and A. Mainwood. "Radiation damage of diamond by electron and gamma irradiation". In: *Physica Status Solidi A* 181.1 (2000), pp. 99–108 (cit. on p. 33).

[169] A. G. Sabnis. "Characterization of Annealing of Co60 Gamma-Ray Damage at the Si/Si02 Interface". In: *IEEE Transactions on Nuclear Science* 30.6 (1983), pp. 4094–4099 (cit. on p. 33).

[170] P. Sigmund. "On the number of atoms displaced by implanted ions or energetic recoil atoms". In: *Applied Physics Letters* 14.3 (1969), pp. 114–117 (cit. on p. 34).

[171] B. Watt. "Energy spectrum of neutrons from thermal fission of U 235". In: *Physical Review* 87.6 (1952), p. 1037 (cit. on p. 34).

[172] M. Burton. "Radiation chemistry." In: *The Journal of Physical Chemistry* 51.2 (1947), pp. 611–625 (cit. on p. 34).

[173] K. Nordlund, S. J. Zinkle, A. E. Sand, F. Granberg, R. S. Averback, R. Stoller, T. Suzudo, L. Malerba, F. Banhart, W. J. Weber, et al. "Improving atomic displacement and replacement calculations with physically realistic damage models". In: *Nature Communications* 9.1 (2018), p. 1084 (cit. on pp. 34, 35).

[174] M. T. Robinson and I. M. Torrens. "Computer simulation of atomic-displacement cascades in solids in the binary-collision approximation". In: *Physical Review B* 9.12 (1974), p. 5008 (cit. on p. 35).

[175] M. Norgett, M. Robinson, and I. Torrens. "A proposed method of calculating displacement dose rates". In: *Nuclear engineering and design* 33.1 (1975), pp. 50–54 (cit. on p. 35).

[176] S. Ishino. "Effect of Cascade as Fundamental Research on Radiation Damage of Core Component Materials". In: *Journal of Nuclear Science and Technology* 26.1 (1989), pp. 137–142 (cit. on p. 36).

[177] R. Sizmann. "The effect of radiation upon diffusion in metals". In: *Journal of Nuclear Materials* 69-70.C (1978), pp. 386–412 (cit. on pp. 36, 47).

[178] H. Sakaida, N. Sekimura, and S. Ishino. "In-situ observation of cascade damage in nickel and copper under heavy ion irradiation". In: *Journal of Nuclear Materials* 179-181.2 (1991), pp. 928–930 (cit. on p. 36).

[179] S. Ishino, H. Kawanishi, K. Fukuya, and T. Muroga. “In situ studies of the effects of ion beams on materials using the electron microscope ion beam interface”. In: *IEEE Transactions on Nuclear Science* 30.2 (1983), pp. 1255–1258 (cit. on p. 36).

[180] D. Seidman, R. Averback, and K. Benedek. “Displacement cascades. Dynamics and atomic structure”. In: *Physica Status Solidi B* 144.1 (1987), pp. 85–104 (cit. on p. 36).

[181] R. S. Averback and D. N. Seidman. “Energetic displacement cascades and their roles in radiation effects”. In: *Materials Science Forum*. Vol. 15. Trans Tech Publ. 1987, pp. 963–984 (cit. on p. 36).

[182] K. Merkle, L. Singer, and R. Hart. “Fission-Fragment Damage in Gold Films”. In: *Journal of Applied Physics* 34.9 (1963), pp. 2800–2804 (cit. on p. 36).

[183] C. Becquart and B. Wirth. “1.14 - Kinetic Monte Carlo Simulations of Irradiation Effects”. In: *Comprehensive Nuclear Materials*. Ed. by R. J. Konings. Elsevier, 2012, pp. 393–410 (cit. on p. 36).

[184] T. Muroga, K. Hirooka, and S. Ishino. “Effects of radiation on materials”. In: *ASTM STP* 870 (1984), pp. 407–418 (cit. on p. 36).

[185] F. Seitz. “The effects of irradiation on metals”. In: *Reviews of Modern Physics* 34.4 (1962), p. 656 (cit. on p. 37).

[186] USNRC. *Standard review plan for the review of safety analysis reports for nuclear power plants*. US Nuclear Regulatory Commission, Office of Nuclear Reactor Regulation, 1981 (cit. on p. 37).

[187] A. Hughes and J. Caley. “The effects of neutron irradiation at elevated temperatures on the tensile properties of some austenitic stainless steels”. In: *Journal of Nuclear Materials* 10.1 (1963), pp. 60–62 (cit. on p. 38).

[188] R. Barnes. “Embrittlement of stainless steels and nickel-based alloys at high temperature induced by neutron radiation”. In: *Nature* 206.4991 (1965), p. 1307 (cit. on p. 38).

[189] I. I. Balachov, E. Shcherbakov, A. Kozlov, I. Portnykh, and F. Garner. “Influence of radiation-induced voids and bubbles on physical properties of austenitic structural alloys”. In: *Journal of Nuclear Materials* 329-333 (2004). Proceedings of the 11th International Conference on Fusion Reactor Materials (ICFRM-11), pp. 617–620 (cit. on p. 38).

[190] L. Fournier, B. Sencer, G. Was, E. Simonen, and S. Bruemmer. "The influence of oversized solute additions on radiation-induced changes and post-irradiation intergranular stress corrosion cracking behavior in high-purity 316 stainless steels". In: *Journal of Nuclear Materials* 321.2-3 (2003), pp. 192–209 (cit. on p. 38).

[191] P. Shewmon. *Diffusion in solids*. Springer, 2016 (cit. on pp. 38, 48, 198).

[192] A. Le Claire. "On the theory of impurity diffusion in metals". In: *Philosophical Magazine* 7.73 (1962), pp. 141–167 (cit. on p. 38).

[193] H.-E. Schaefer. "Investigation of thermal equilibrium vacancies in metals by positron annihilation". In: *Physica Status Solidi A* 102.1 (1987), pp. 47–65 (cit. on p. 38).

[194] G. Kuczynski. "Measurement of self-diffusion of silver without radioactive tracers". In: *Journal of Applied Physics* 21.7 (1950), pp. 632–635 (cit. on p. 38).

[195] J. Askill. *Tracer diffusion data for metals, alloys, and simple oxides*. Springer Science & Business Media, 2012 (cit. on p. 38).

[196] D. Gugan. "The annealing of deformed sodium". In: *Philosophical Magazine* 13.123 (1966), pp. 533–540 (cit. on p. 38).

[197] C. Baker and A. Kelly. "Energy to form and to move vacant lattice sites in graphite". In: *Nature (London)* 193.4812 (1962) (cit. on p. 38).

[198] A. Sosin. "Atomistic interpretation of radiation effects in metals". In: *Materials in Nuclear Applications*. ASTM International, 1960 (cit. on p. 38).

[199] J. W. Corbett and L. C. Ianniello. *Radiation-induced voids in metals: proceedings*. Vol. 1971. US Atomic Energy Commission, Office of Information Services;[available from National Technical Information Service, Springfield, Va.], 1972 (cit. on p. 38).

[200] D. Olander. "Nuclear fuels–present and future". In: *Journal of Nuclear Materials* 389.1 (2009), pp. 1–22 (cit. on p. 38).

[201] W. Schilling. "Self-interstitial atoms in metals". In: *Journal of Nuclear Materials* 69 (1978), pp. 465–489 (cit. on p. 39).

[202] R. A. Johnson and E. Brown. "Point defects in copper". In: *Physical Review* 127.2 (1962), p. 446 (cit. on p. 39).

[203] B. Wirth, G. Odette, D. Maroudas, and G. Lucas. "Energetics of formation and migration of self-interstitials and self-interstitial clusters in α-iron". In: *Journal of Nuclear Materials* 244.3 (1997), pp. 185–194 (cit. on p. 39).

[204] K. Nordlund, M. Ghaly, R. Averback, M. Caturla, T. D. de La Rubia, and J. Tarus. "Defect production in collision cascades in elemental semiconductors and fcc metals". In: *Physical Review B* 57.13 (1998), p. 7556 (cit. on p. 39).

[205] R. E. Stoller. "The role of cascade energy and temperature in primary defect formation in iron". In: *Journal of Nuclear Materials* 276.1 (2000), pp. 22–32 (cit. on p. 39).

[206] S. Wooding, L. Howe, F. Gao, A. Calder, and D. Bacon. "A molecular dynamics study of high-energy displacement cascades in α-zirconium". In: *Journal of Nuclear Materials* 254.2-3 (1998), pp. 191–204 (cit. on p. 39).

[207] M. Biget, F. Maury, P. Vajda, A. son, and P. Lucasson. "Production and mutual annihilation of Frenkel pairs in low temperature irradiated zirconium". In: *Radiation Effects* 7.3-4 (1971), pp. 223–229 (cit. on p. 40).

[208] C. Ewels, R. Telling, A. El-Barbary, M. Heggie, and P. Briddon. "Metastable Frenkel pair defect in graphite: source of Wigner energy?" In: *Physical review letters* 91.2 (2003), p. 025505 (cit. on p. 40).

[209] A. Monti and E. Savino. "Frenkel pair stability in a hexagonal close packed lattice". In: *Physica Status Solidi B* 92.1 (1979) (cit. on p. 40).

[210] V. Emtsev, T. Mashovets, and V. Mikhnovich. "Frenkel pairs in germanium and silicon". In: *Soviet Physics-Semiconductors* 26.1 (1992), pp. 12–25 (cit. on p. 40).

[211] P. G. Lucasson and R. M. Walker. "Production and recovery of electron-induced radiation damage in a number of metals". In: *Physical Review Letters* 127 (2 1962), pp. 485–500 (cit. on p. 40).

[212] E. Gaganidze, C. Petersen, E. Materna-Morris, C. Dethloff, O. Weiß, J. Aktaa, A. Povstyanko, A. Fedoseev, O. Makarov, and V. Prokhorov. "Mechanical properties and TEM examination of RAFM steels irradiated up to 70 dpa in BOR-60". In: *Journal of Nuclear Materials* 417.1-3 (2011), pp. 93–98 (cit. on p. 40).

[213] G. Greaves. "A Transmission Electron Microscopy Study of Inert Gases in Silicon and Iron". PhD thesis. University of Salford, 2012 (cit. on p. 40).

[214] S. Donnelly. "The density and pressure of helium in bubbles in implanted metals: a critical review". In: *Radiation Effects* 90.1-2 (1985), pp. 1–47 (cit. on pp. 40, 41, 57).

[215] W. Jäger, R. Manzke, H. Trinkaus, R. Zeller, J. Fink, and G. Crecelius. "The density and pressure of helium in bubbles in metals". In: *Radiation effects* 78.1-4 (1983), pp. 315–325 (cit. on p. 40).

[216] D. Mitchell, S. Donnelly, and J. Evans. “A transmission electron microscopy study of xenon bubbles in ion-implanted tin”. In: *Philosophical Magazine A* 61.4 (1990), pp. 531–542 (cit. on p. 41).

[217] M. A. Tunes, R. W. Harrison, G. Greaves, J. Hinks, and S. Donnelly. “Effect of He implantation on the microstructure of zircaloy-4 studied using in situ TEM”. In: *Journal of Nuclear Materials* 493 (2017), pp. 230–238 (cit. on pp. 41, 142, 219).

[218] J. Rife, S. Donnelly, A. Lucas, J. Gilles, and J. Ritsko. “Optical absorption and electron-energy-loss spectra of helium microbubbles in aluminum”. In: *Physical Review Letters* 46.18 (1981), p. 1220 (cit. on p. 42).

[219] P. F. P. Fichtner, J. Kaschny, R. A. Yankov, A. Mücklich, U. Kreißig, and W. Skorupa. “Overpressurized bubbles versus voids formed in helium implanted and annealed silicon”. In: *Applied physics letters* 70.6 (1997), pp. 732–734 (cit. on p. 42).

[220] R. Barnes. “A theory of swelling and gas release for reactor materials”. In: *Journal of Nuclear Materials* 11.2 (1964), pp. 135–148 (cit. on p. 42).

[221] G. Greenwood, A. Foreman, and D. Rimmer. “The role of vacancies and dislocations in the nucleation and growth of gas bubbles in irradiated fissile material”. In: *Journal of Nuclear Materials* 1.4 (1959), pp. 305–324 (cit. on p. 42).

[222] P. B. Hirsch, A. Howie, and M. J. Whelan. “A kinematical theory of diffraction contrast of electron transmission microscope images of dislocations and other defects”. In: *Philosophical Transactions of the Royal Society A: Mathematical, Physical and Engineering Sciences* 252.1017 (1960), pp. 499–529 (cit. on pp. 43, 44).

[223] J. Silcox and P. Hirsch. “Dislocation loops in neutron-irradiated copper”. In: *Philosophical Magazine* 4.48 (1959), pp. 1356–1374 (cit. on pp. 43, 44).

[224] K. Westmacott, D. Hull, and R. Barnes. “Dislocation sources in quenched aluminium-based alloys”. In: *Philosophical Magazine* 4.45 (1959), pp. 1089–1092 (cit. on pp. 43, 44).

[225] R. Smallman and K. Westmacott. “Stacking faults in face-centred cubic metals and alloys”. In: *Philosophical magazine* 2.17 (1957), pp. 669–683 (cit. on pp. 43, 47).

[226] P. Hirsch. “Direct observations of moving dislocations: reflections on the thirtieth anniversary of the first recorded observations of moving dislocations by transmission electron microscopy”. In: *Materials Science and Engineering* 84 (1986), pp. 1–10 (cit. on pp. 43, 44, 60).

[227] R. Smallman and K. Westmacott. “Structure of quenched and irradiated metals”. In: *Journal of Applied Physics* 30.5 (1959), pp. 603–616 (cit. on p. 44).

[228] G. Carpenter and D. Northwood. “The contribution of dislocation loops to radiation growth and creep of Zircaloy-2”. In: *Journal of Nuclear Materials* 56.3 (1975), pp. 260–266 (cit. on p. 44).

[229] M. Makin. “Electron displacement damage in copper and aluminium in a high voltage electron microscope”. In: *Philosophical Magazine* 18.153 (1968), pp. 637–653 (cit. on p. 44).

[230] R. C. Rau and R. L. Ladd. “Radiation damage in vanadium”. In: *Journal of Nuclear Materials* 30.3 (1969), pp. 297–302 (cit. on p. 44).

[231] S. J. Zinkle and K. Farrell. “Void swelling and defect cluster formation in reactor-irradiated copper”. In: *Journal of Nuclear Materials* 168.3 (1989), pp. 262–267 (cit. on p. 44).

[232] A. Whapham and B. Sheldon. “Radiation damage in uranium dioxide”. In: *Philosophical Magazine* 12.120 (1965), pp. 1179–1192 (cit. on p. 44).

[233] M. Kirk, I. Robertson, M. Jenkins, C. English, T. Black, and J. Vetrano. “The collapse of defect cascades to dislocation loops”. In: *Journal of Nuclear Materials* 149.1 (1987), pp. 21–28 (cit. on p. 44).

[234] R. Konings. *Comprehensive nuclear materials*. Elsevier, 2011 (cit. on p. 44).

[235] M. Makin and S. Manthorpe. “The annealing of neutron irradiation hardening in copper crystals”. In: *Philosophical Magazine* 10.106 (1964), pp. 579–594 (cit. on p. 44).

[236] T. Blewitt. *Radiation damage in solids*. Billington, 1962 (cit. on p. 44).

[237] J. Diehl, C. Leitz, and W. Schilling. “Hardening of copper single crystals by neutron irradiation at low temperatures”. In: *Physics Letters* 4.4 (1963), pp. 236–238 (cit. on p. 45).

[238] A. Seeger. “2nd UN Conference on Peaceful Uses of Atomic Energy”. In: *United Nations, New York* 6 (1958), p. 250 (cit. on p. 45).

[239] A. Seeger. “Kristallplastizität”. In: *Kristallphysik II/Crystal Physics II*. Springer, 1958, pp. 1–210 (cit. on p. 45).

[240] J. Gibson, A. N. Goland, M. Milgram, and G. Vineyard. “Dynamics of radiation damage”. In: *Physical Review* 120.4 (1960), p. 1229 (cit. on p. 45).

[241] M. Makin, A. Whapham, and F. Minter. “Dislocation loops and hardening in neutron irradiated copper”. In: *Philosophical Magazine* 6.63 (1961), pp. 465–468 (cit. on p. 45).

[242] F. Garner, M. Hamilton, N. Panayotou, and G. Johnson. "The microstructural origins of yield strength changes in AISI 316 during fission or fusion irradiation". In: *Journal of Nuclear Materials* 104 (1981), pp. 803–807 (cit. on pp. 45, 46).

[243] F. Garner. "Radiation Damage in Austenitic Steels". In: *Comprehensive Nuclear Materials*. 1. Elsevier, 2012, pp. 33–95. ISBN: 9780080560335 (cit. on pp. 45, 46, 56, 57, 59, 60, 65).

[244] M. Makin and F. Minter. "The mechanical properties of irradiated niobium". In: *Acta Metallurgica* 7.6 (1959), pp. 361–366 (cit. on p. 46).

[245] R. Klueh and D. Alexander. *Neutron irradiation effects on the ductile-brittle transition of ferritic/martensitic steels*. Tech. rep. Oak Ridge National Lab., TN (United States), 1997 (cit. on p. 46).

[246] A. Wronski and A. Johnson. "A hardening effect associated with stage III recovery in neutron irradiated molybdenum". In: *Philosophical Magazine* 8.90 (1963), pp. 1067–1070 (cit. on p. 46).

[247] J. Samuels and S. Roberts. "The brittle–ductile transition in silicon. I. Experiments". In: *Proceedings of the Royal Society of London. A. Mathematical and Physical Sciences* 421.1860 (1989), pp. 1–23 (cit. on pp. 46, 47).

[248] K. K. Chawla and M. Meyers. *Mechanical behavior of materials*. Prentice Hall Upper Saddle River, 1999 (cit. on pp. 47, 95, 199, 242, 246, 248, 249, 266).

[249] M. Coates, A. Kumar, and S. Roberts. "Crack initiation in the brittle fracture of ferritic steels". In: *Fatigue & Fracture of Engineering Materials & Structures* 29.9-10 (2006), pp. 661–671 (cit. on p. 47).

[250] S. Roberts. "Modelling brittle-ductile transitions". In: *Multiscale Phenomena in Plasticity: From Experiments to Phenomenology, Modelling and Materials Engineering*. Springer, 2000, pp. 349–364 (cit. on p. 47).

[251] B. D. Wirth. "How does radiation damage materials?" In: *Science* 318.5852 (2007), pp. 923–924 (cit. on p. 47).

[252] G. Odette, M. Alinger, and B. Wirth. "Recent developments in irradiation-resistant steels". In: *Annu. Rev. Mater. Res.* 38 (2008), pp. 471–503 (cit. on p. 47).

[253] B. Uberuaga, R. Hoagland, A. Voter, and S. Valone. "Direct transformation of vacancy voids to stacking fault tetrahedra". In: *Physical review letters* 99.13 (2007), p. 135501 (cit. on p. 47).

[254] D. J. Bacon, Y. N. Osetsky, R. Stoller, and R. E. Voskoboinikov. "MD description of damage production in displacement cascades in copper and α-iron". In: *Journal of Nuclear Materials* 323.2-3 (2003), pp. 152–162 (cit. on p. 47).

[255] X.-M. Bai, A. F. Voter, R. G. Hoagland, M. Nastasi, and B. P. Uberuaga. "Efficient annealing of radiation damage near grain boundaries via interstitial emission". In: *Science* 327.5973 (2010), pp. 1631–1634 (cit. on p. 47).

[256] D. McLean. *Mechanical properties of metals*. Krieger Pub Co, 1977 (cit. on p. 47).

[257] K. Kamada. "Effects of Annealing and Irradiation on the Stacking-Fault Energy of Cu–Al Solid Solutions". In: *Journal of Applied Physics* 39.3 (1968), pp. 1824–1828 (cit. on p. 47).

[258] T. Byun and N. Hashimoto. "Strain localization in irradiated materials". In: *Nuclear Engineering and technology* 38.7 (2006), pp. 619–638 (cit. on p. 47).

[259] R. Faulkner, S. Song, D. Meade, and C. Goodwin. "Radiation-induced grain boundary segregation". In: *Materials science forum*. Vol. 294. Trans Tech Publ. 1999, pp. 67–74 (cit. on p. 47).

[260] E. Kenik, T. Inazumi, and G. Bell. "Radiation-induced grain boundary segregation and sensitization of a neutron-irradiated austenitic stainless steel". In: *Journal of Nuclear Materials* 183.3 (1991), pp. 145–153 (cit. on p. 47).

[261] R. Carter, D. Damcott, M. Atzmon, G. Was, S. M. Bruemmer, and E. Kenik. "Quantitative analysis of radiation-induced grain-boundary segregation measurements". In: *Journal of Nuclear Materials* 211.1 (1994), pp. 70–84 (cit. on p. 47).

[262] R. W. Balluffi, S. M. Allen, and W. C. Carter. "Diffusion in Multicomponent Systems". In: *Kinetics of Materials*. Hoboken, NJ, USA: John Wiley & Sons, Inc., 2005, pp. 131–144 (cit. on p. 47).

[263] T. H. Blewitt and R. R. Coltman. "The Effect of Neutron Irradiation on Metallic Diffusion". In: *Physical Review* 85.2 (1952), p. 384 (cit. on p. 47).

[264] Y. Adda, M. Beyeler, and G. Brebec. "Radiation effects on solid state diffusion". In: *Thin Solid Films* 25.1 (1975), pp. 107–156 (cit. on p. 47).

[265] T. R. Anthony. "Solute segregation and stresses generated around growing voids in metals". In: *Radiation-induced voids in metals*. Ed. by J.W. Cobertt and L.C. Ianniello. Vol. 15. USAEC CONF-710601, 1971, pp. 630–646 (cit. on p. 47).

[266] P. Okamoto, S. Harkness, and J. Laidler. “Solute segregation to voids during electron irradiation”. In: *Transactions of the American Nuclear Society* 16 (1973), pp. 1317–1330 (cit. on p. 47).

[267] P. R. Okamoto and H. Wiedersich. “Segregation of alloying elements to free surfaces during irradiation”. In: *Journal of Nuclear Materials* 53.C (1974), pp. 336–345 (cit. on p. 47).

[268] V. Sethi and P. Okamoto. *Radiation-induced segregation in complex alloys*. Tech. rep. Argonne National Laboratory, 1980 (cit. on p. 47).

[269] A. Marwick. “Segregation in irradiated alloys: the inverse Kirkendall effect and the effect of constitution on void swelling”. In: *Journal of Physics F: Metal Physics* 8.9 (1978), p. 1849 (cit. on pp. 47, 59).

[270] S. Watanabe, Y. Takamatsu, N. Sakaguchi, and H. Takahashi. “Sink effect of grain boundary on radiation-induced segregation in austenitic stainless steel”. In: *Journal of Nuclear Materials* 283 (2000), pp. 152–156 (cit. on p. 47).

[271] P. Okamoto and L. Rehn. “Radiation-induced segregation in binary and ternary alloys”. In: *Journal of Nuclear Materials* 83.1 (1979), pp. 2–23 (cit. on pp. 47, 48, 59).

[272] S. M. Bruemmer, L. A. Charlot, J. S. Vetrano, and E. P. Simonen. “Radiation-induced grain boundary segregation in austenitic stainless steels”. In: *MRS Proceedings* 373 (1994), p. 119 (cit. on p. 48).

[273] H. Wiedersich, P. Okamoto, and N. Q. Lam. “A theory of radiation-induced segregation in concentrated alloys”. In: *Journal of Nuclear Materials* 83.1 (1979), pp. 98–108 (cit. on p. 48).

[274] A. Gusak and K. Tu. “Interaction between the Kirkendall effect and the inverse Kirkendall effect in nanoscale particles”. In: *Acta Materialia* 57.11 (2009), pp. 3367–3373 (cit. on p. 48).

[275] J. Perks, A. Marwick, and C. English. *A computer code to calculate radiation-induced segregation in concentrated ternary alloys AERE R 12121*. 1986 (cit. on p. 48).

[276] T. R. Allen and G. Was. “Modeling radiation-induced segregation in austenitic Fe–Cr–Ni alloys”. In: *Acta Materialia* 46.10 (1998), pp. 3679–3691 (cit. on p. 48).

[277] J. P. Wharry, Z. Jiao, and G. S. Was. “Application of the inverse Kirkendall model of radiation-induced segregation to ferritic–martensitic alloys”. In: *Journal of Nuclear Materials* 425.1-3 (2012), pp. 117–124 (cit. on p. 48).

[278] Editorial. “Materials Testing Reactor”. In: *Physics Today* 5.6 (1952), pp. 27–28 (cit. on p. 49).

[279] H. Ullmaier and W. Schilling. “Radiation damage in metallic reactor materials”. In: *Physics of modern materials. Characterization of materials, defects and mechanical properties*. 1980 (cit. on p. 49).

[280] G. Was, Z. Jiao, E. Getto, K. Sun, A. Monterrosa, S. Maloy, O. Anderoglu, B. Sencer, and M. Hackett. “Emulation of reactor irradiation damage using ion beams”. In: *Scripta Materialia* 88 (2014), pp. 33–36 (cit. on pp. 49–52).

[281] A. Izhutov, I. Y. Zhemkov, and Y. V. Naboishchikov. “Potential Capabilities of Operating Reactor BOR-60 and Reactor MBIR under Construction to Perform Experiments on Transmutation of Minor Actinides (IAEA-CN245-103)”. In: *IAEA Conferences* (2017) (cit. on p. 49).

[282] G. Was and R. S. Averback. “Radiation damage using ion beams”. In: *Comprehensive Nuclear Materials*. Elsevier Ltd, 2012, pp. 195–221 (cit. on pp. 49–52).

[283] L. K. Mansur. “Void swelling in metals and alloys under irradiation: an assessment of the theory”. In: *Nuclear Technology* 40.1 (1978), pp. 5–34 (cit. on p. 51).

[284] L. Mansur. “Correlation of neutron and heavy-ion damage: II. The predicted temperature shift if swelling with changes in radiation dose rate”. In: *Journal of Nuclear Materials* 78.1 (1978), pp. 156–160 (cit. on p. 51).

[285] N. Packan, K. Farrell, and J. Stiegler. “Correlation of neutron and heavy-ion damage: I. The influence of dose rate and injected helium on swelling in pure nickel”. In: *Journal of Nuclear Materials* 78.1 (1978), pp. 143–155 (cit. on p. 51).

[286] G. S. Was and T. Allen. “Intercomparison of microchemical evolution under various types of particle irradiation”. In: *Journal of nuclear materials* 205 (1993), pp. 332–338 (cit. on pp. 52, 53).

[287] B. Mironov, H. Freeman, A. Brown, F. Hage, A. Scott, A. Westwood, J.-P. Da Costa, P. Weisbecker, and R. Brydson. “Electron irradiation of nuclear graphite studied by transmission electron microscopy and electron energy loss spectroscopy”. In: *Carbon* 83 (2015), pp. 106–117 (cit. on p. 52).

[288] P. Wang and G. S. Was. “Oxidation of Zircaloy-4 during in situ proton irradiation and corrosion in PWR primary water”. In: *Journal of Materials Research* 30.9 (2015), pp. 1335–1348 (cit. on p. 52).

[289] G. E. Lucas. “The evolution of mechanical property change in irradiated austenitic stainless steels”. In: *Journal of Nuclear Materials* 206.2-3 (1993), pp. 287–305 (cit. on p. 56).

[290] J. Noden, C. Knights, and M. Thomas. “Growth of austenitic stainless steels oxidised in carbon and oxygen bearing gases”. In: *British Corrosion Journal* 3.1 (1968), pp. 47–55 (cit. on p. 56).

[291] H. Jirkova, B. Masek, M. F.-X. Wagner, D. Langmajerova, L. Kucerova, R. Treml, and D. Kiener. “Influence of metastable retained austenite on macro and micromechanical properties of steel processed by the Q&P process”. In: *Journal of Alloys and Compounds* 615 (2014), S163–S168 (cit. on p. 56).

[292] C. Dimitrov, M. Tenti, and O. Dimitrov. “Resistivity recovery in austenitic Fe-Cr-Ni alloys neutron irradiated at 23K”. In: *Journal of Physics F: Metal Physics* 11.4 (1981), p. 753 (cit. on p. 57).

[293] E. A. Kenik and J. T. Busby. “Radiation-induced degradation of stainless steel light water reactor internals”. In: *Materials Science and Engineering: R: Reports* 73.7-8 (2012), pp. 67–83 (cit. on p. 57).

[294] S. Zinkle, P. Maziasz, and R. Stoller. “Dose dependence of the microstructural evolution in neutron-irradiated austenitic stainless steel”. In: *Journal of Nuclear Materials* 206.2-3 (1993), pp. 266–286 (cit. on p. 57).

[295] F. A. Garner and L. Greenwood. “Survey of recent developments concerning the understanding of radiation effects on stainless steels used in the LWR power industry”. In: *11th International Conference on Environmental Degradation of Materials in Nuclear Power Systems–Water Reactors*. 2003, pp. 887–909 (cit. on p. 57).

[296] H. Heinisch, M. Hamilton, W. Sommer, and P. Ferguson. “Tensile property changes of metals irradiated to low doses with fission, fusion and spallation neutrons”. In: *Journal of Nuclear Materials* 191 (1992), pp. 1177–1182 (cit. on p. 57).

[297] F. Garner and L. Greenwood. “Neutron irradiation effects in fusion or spallation structural materials: some recent insights related to neutron spectra”. In: *Radiation effects and defects in solids* 144.1-4 (1998), pp. 251–286 (cit. on p. 57).

[298] R. K. Nanstad, M. L. Hamilton, F. A. Garner, and A. S. Kumar. “Effects of radiation on materials: 18th international symposium”. In: *ASTM*. American Society for Testing & Materials. 1999 (cit. on p. 57).

[299] D. Edwards, F. Garner, and L. Greenwood. "The influence of transmutation, void swelling, and flux/spectra uncertainties on the electrical properties of copper and copper alloys". In: *Journal of Nuclear Materials* 212 (1994), pp. 404–409 (cit. on p. 57).

[300] F. Garner, M. B. Toloczko, L. R. Greenwood, C. R. Eiholzer, M. Paxton, and R. J. Puigh. "Swelling, irradiation creep and growth of pure rhenium irradiated with fast neutrons at 1030–1330 C". In: *Journal of Nuclear Materials* 283 (2000), pp. 380–385 (cit. on p. 57).

[301] F. Garner, D. Edwards, S. Bruemmer, S. Porollo, Y. V. Konobeev, V. Neustroev, V. Shamardin, and A. Kozlov. "Recent developments concerning potential void swelling of PWR internals constructed from austenitic stainless steels". In: *Proceedings, Fontevraud* 5 (2002) (cit. on pp. 58, 59).

[302] H. Brager, F. Garner, D. Gelles, and M. Hamilton. "Development of reduced activation alloys for fusion service". In: *Journal of Nuclear Materials* 133 (1985), pp. 907–911 (cit. on pp. 58, 59).

[303] P. Maziasz. "Formation and stability of radiation-induced phases in neutron-irradiated austenitic and ferritic steels". In: *Journal of Nuclear Materials* 169 (1989), pp. 95–115 (cit. on pp. 58–60).

[304] L. Mansur, E. Lee, P. Maziasz, and A. Rowcliffe. "Control of helium effects in irradiated materials based on theory and experiment". In: *Journal of Nuclear Materials* 141 (1986), pp. 633–646 (cit. on p. 57).

[305] F. A. Garner, B. M. Oliver, L. R. Greenwood, D. J. Edwards, S. M. Bruemmer, and M. L. Grossbeck. "Generation and retention of helium and hydrogen in austenitic steels irradiated in a variety of LWR and test reactor spectral environments". In: *10th International Conference on Environmental Degradation of Materials in Nuclear Power Systems–Water Reactors*. 2001 (cit. on p. 57).

[306] M. Griffiths. "The effect of irradiation on Ni-containing components in CANDU reactor cores: a review". In: *Nuclear Review* 2.1 (2014), pp. 1–16 (cit. on p. 57).

[307] G. Was and J. Busby. "Role of irradiated microstructure and microchemistry in irradiation-assisted stress corrosion cracking". In: *Philosophical Magazine* 85.4-7 (2005), pp. 443–465 (cit. on p. 57).

[308] K. C. Russell. "Phase stability under irradiation". In: *Progress in Materials Science* 28.3-4 (1984), pp. 229–434 (cit. on p. 57).

[309] A. Marwick, R. Piller, and P. Sivell. “Mechanisms of radiation-induced segregation in dilute nickel alloys”. In: *Journal of Nuclear Materials* 83.1 (1979), pp. 35–41 (cit. on p. 59).

[310] A. Rowcliffe and M. Grossbeck. “The response of austenitic steels to radiation damage”. In: *Journal of Nuclear Materials* 122.1 (1984), pp. 181–190 (cit. on p. 59).

[311] S. Zinkle and L. Snead. “Opportunities and limitations for ion beams in radiation effects studies: Bridging critical gaps between charged particle and neutron irradiations”. In: *Scripta Materialia* 143 (2018), pp. 154–160 (cit. on p. 60).

[312] A. Etienne, M. Hernández-Mayoral, C. Genevois, B. Radiguet, and P. Pareige. “Dislocation loop evolution under ion irradiation in austenitic stainless steels”. In: *Journal of Nuclear Materials* 400.1 (2010), pp. 56–63 (cit. on p. 60).

[313] S. Jublot-Leclerc, X. Li, L. Legras, M.-L. Lescoat, F. Fortuna, and A. Gentils. “Microstructure of Au-ion irradiated 316L and FeNiCr austenitic stainless steels”. In: *Journal of Nuclear Materials* 480 (2016), pp. 436–446 (cit. on p. 60).

[314] B. Rouxel, C. Bisor, Y. De Carlan, A. Courcelle, and A. Legris. “Influence of the austenitic stainless steel microstructure on the void swelling under ion irradiation”. In: *EPJ Nuclear Sciences & Technologies* 2 (2016), p. 30 (cit. on p. 60).

[315] A. Etienne, B. Radiguet, N. Cunningham, G. Odette, and P. Pareige. “Atomic scale investigation of radiation-induced segregation in austenitic stainless steels”. In: *Journal of Nuclear Materials* 406.2 (2010), pp. 244–250 (cit. on p. 61).

[316] K. Nakata and I. Masaoka. “Solute segregation along non-migrated and migrated grain boundaries during electron irradiation in austenitic stainless steels”. In: *Journal of Nuclear Materials* 150.2 (1987), pp. 186–193 (cit. on p. 61).

[317] N. Shigenaka, S. Ono, Y. Isobe, T. Hashimoto, H. Fujimori, and S. Uchida. “Effect of zirconium addition to austenitic stainless steels on suppression of radiation induced chromium segregation at grain boundaries under ion irradiation”. In: *Journal of Nuclear Science and Technology* 33.7 (1996), pp. 577–581 (cit. on p. 61).

[318] T. Allen, J. Busby, G. Was, and E. Kenik. “On the mechanism of radiation-induced segregation in austenitic Fe–Cr–Ni alloys”. In: *Journal of Nuclear Materials* 255.1 (1998), pp. 44–58 (cit. on p. 61).

[319] G. Was, J. Busby, T. Allen, E. Kenik, A. Jensson, S. Bruemmer, J. Gan, A. Edwards, P. Scott, and P. Andreson. "Emulation of neutron irradiation effects with protons: validation of principle". In: *Journal of nuclear materials* 300.2-3 (2002), pp. 198–216 (cit. on pp. 61, 200).

[320] J. Berling and T. Slot. "Effect of Temperature and Strain Rate on Low-Cycle Fatigue Resistance of AISI 304, 316, and 348 Stainless Steels". In: *Fatigue at High Temperature*. 100 Barr Harbor Drive, PO Box C700, West Conshohocken, PA 19428-2959: ASTM International, 1969, pp. 3–3–28 (cit. on p. 61).

[321] I. Bespalov, M. Datler, S. Buhr, W. Drachsel, G. Rupprechter, and Y. Suchorski. "Initial stages of oxide formation on the Zr surface at low oxygen pressure: An in situ FIM and XPS study". In: *Ultramicroscopy* 159 (2015), pp. 147–151 (cit. on pp. 62, 215).

[322] L. Thomas and J. Beeston. "The microstructure of neutron irradiated type-348 stainless steel and its relation to creep and hardening". In: *Journal of Nuclear Materials* 107.2-3 (1982), pp. 159–167 (cit. on pp. 63–65).

[323] Allegheny Ludlum Corporation. *Stainless Steels Types 321, 347 and 348*. 2017 (cit. on p. 62).

[324] A. Abe, C. Giovedi, D. de Souza Gomes, and A. Teixeira Silva. "Revisiting Stainless Steel as PWR Fuel Rod Cladding after Fukushima Daiichi Accident". In: *Journal of Energy and Power Engineering* 8 (2014), pp. 973–980 (cit. on p. 64).

[325] F. A. Garner, L. R. Greenwood, and R. E. Mizia. *Assessment of XM-19 as a Substitute for AISI 348 in ATR Service*. Tech. rep. November. Idaho National Laboratory, 2007 (cit. on pp. 64, 65, 117).

[326] J. E. Irvin and A. L. Bernent. "Nature of Radiation Damage to Engineering Properties of Various Stainless Steel Alloys". In: *Effects of Radiation on Structural Metals*. 100 Barr Harbor Drive, PO Box C700, West Conshohocken, PA 19428-2959: ASTM International, 1967, pp. 278–278–50 (cit. on p. 64).

[327] J. J. Holmes, R. E. Robbins, and A. J. Lovell. "Post-irradiation tensile behavior of 300 series stainless steels". In: *Irradiation Effects in Structural Alloys for Thermal and Fast Reactors*. 100 Barr Harbor Drive, PO Box C700, West Conshohocken, PA 19428-2959: ASTM International, 1969, pp. 371–371–19 (cit. on p. 64).

[328] J. E. Irvin, A. L. Bement, and R. G. Hoagland. "The combined effects of temperature and irradiation on the mechanical properties of austenitic stainless steels". In: *Flow and Fracture of Metals and Alloys in Nuclear Environments*. 100 Barr Harbor Drive, PO Box C700, West Conshohocken, PA 19428-2959: ASTM International, 1965, pp. 236–236–15 (cit. on p. 64).

[329] J. Beeston. "Mechanical and physical properties of irradiated type 348 stainless steel". In: *Effects of Radiation on Materials*. ASTM International, 1981 (cit. on p. 64).

[330] F. Garner, B. M. Oliver, and L. R. Greenwood. "The dependence of helium generation rate on nickel content of Fe–Cr–Ni alloys irradiated to high dpa levels in EBR-II". In: *Journal of Nuclear Materials* 258 (1998), pp. 1740–1744 (cit. on p. 65).

[331] F. Garner. "Irradiation performance of cladding and structural steels in liquid metal reactors". In: *Materials Science and Technology*. Weinheim, Germany: Wiley-VCH Verlag GmbH & Co. KGaA, 2006. ISBN: 9783527603978 (cit. on p. 65).

[332] H. J. Ryu. "Tungsten-based High Entropy Alloys and Composites for Plasma Facing Materials". In: *Plasma-Wall Interaction for Irradiated Tungsten and Tungsten Alloys in Fusion Devices*. Ed. by IAEA. 2015 (cit. on p. 65).

[333] T. Egami, W. Guo, P. D. Rack, and T. Nagase. "Irradiation Resistance of Multicomponent Alloys". In: *Metallurgical and Materials Transactions A* 45.1 (2014), pp. 180–183 (cit. on p. 65).

[334] T. Nagase, S. Anada, P. D. Rack, J. H. Noh, H. Yasuda, H. Mori, and T. Egami. "MeV electron-irradiation-induced structural change in the bcc phase of Zr–Hf–Nb alloy with an approximately equiatomic ratio". In: *Intermetallics* 38 (2013), pp. 70–79 (cit. on pp. 65, 68).

[335] T. Nagase, P. D. Rack, J. H. Noh, and T. Egami. "In-situ TEM observation of structural changes in nano-crystalline CoCrCuFeNi multicomponent high-entropy alloy (HEA) under fast electron irradiation by high voltage electron microscopy (HVEM)". In: *Intermetallics* 59 (2015), pp. 32–42 (cit. on pp. 65, 68).

[336] N. A. P. K. Kumar, K. J. Leonard, H. Bei, T. S. Byun, Y. Zhang, S. J. Zinkle, H. B. K. J. Leonard, T. S. Byun, Y. Zhang, and S. J. Zinkle. "Ion Irradiation effects on high-entropy alloy". In: *Fusion Reactor Materials Program* 54 (2013), pp. 145–153 (cit. on p. 66).

[337] C. Li, A. P. K. K. Nimishakavi, H. Bei, Y. Zhang, B. Wirth, and S. Zinkle. "Evaluation of Radiation Effects in FeMnNiCr High Entropy Alloy". In: *Microstructural Processes in Irradiated Materials at 2015 TMS Annual Meeting and Exhibition*. 2015 (cit. on p. 66).

[338] N. K. Kumar, C. Li, K. Leonard, H. Bei, and S. Zinkle. "Microstructural stability and mechanical behavior of FeNiMnCr high entropy alloy under ion irradiation". In: *Acta Materialia* 113 (2016), pp. 230–244 (cit. on pp. 66, 68, 78, 127, 128, 130, 139).

[339] C. Li, X. Hu, T. Yang, N. K. Kumar, B. D. Wirth, and S. J. Zinkle. "Neutron irradiation response of a Co-free high entropy alloy". In: *Journal of Nuclear Materials* 527 (2019), p. 151838 (cit. on pp. 66–68).

[340] C. Lu, L. Niu, N. Chen, K. Jin, T. Yang, P. Xiu, Y. Zhang, F. Gao, H. Bei, S. Shi, M.-R. He, I. M. Robertson, W. J. Weber, and L. Wang. "Enhancing radiation tolerance by controlling defect mobility and migration pathways in multicomponent single-phase alloys". In: *Nature Communications* 7 (2016), p. 13564 (cit. on pp. 67, 68, 140, 161).

[341] D. Chen, Y. Tong, H. Li, J. Wang, Y. Zhao, A. Hu, and J. Kai. "Helium accumulation and bubble formation in FeCoNiCr alloy under high fluence He+ implantation". In: *Journal of Nuclear Materials* 501 (2018), pp. 208–216 (cit. on p. 67).

[342] S. Q. Xia, X. Yang, T. F. Yang, S. Liu, and Y. Zhang. "Irradiation Resistance in AlxCoCrFeNi High Entropy Alloys". In: *JOM* 67.10 (2015), pp. 2340–2344 (cit. on p. 67).

[343] T. Yang, S. Xia, W. Guo, R. Hu, J. D. Poplawsky, G. Sha, Y. Fang, Z. Yan, C. Wang, C. Li, Y. Zhang, S. J. Zinkle, and Y. Wang. "Effects of temperature on the irradiation responses of Al0.1CoCrFeNi high entropy alloy". In: *Scripta Materialia* 144 (2018), pp. 31–35 (cit. on pp. 67, 68).

[344] S.-q. Xia, Z. Wang, T.-f. Yang, and Y. Zhang. "Irradiation behavior in high entropy alloys". In: *Journal of Iron and Steel Research International* 22.10 (2015), pp. 879–884 (cit. on p. 67).

[345] C. Lu, T. Yang, K. Jin, N. Gao, P. Xiu, Y. Zhang, F. Gao, H. Bei, W. J. Weber, K. Sun, et al. "Radiation-induced segregation on defect clusters in single-phase concentrated solid-solution alloys". In: *Acta Materialia* 127 (2017), pp. 98–107 (cit. on p. 68).

[346] Z. J. Zhang, M. M. Mao, J. Wang, B. Gludovatz, Z. Zhang, S. X. Mao, E. P. George, Q. Yu, and R. O. Ritchie. "Nanoscale origins of the damage tolerance of the high-entropy alloy CrMnFeCoNi". In: *Nature Communications* 6.1 (2015), p. 10143 (cit. on pp. 68, 200).

[347] R. Harrison, G. Greaves, H. Le, H. Bei, Y. Zhang, and S. Donnelly. "Chemical effects on He bubble superlattice formation in high entropy alloys". In: *Current Opinion in Solid State and Materials Science* 23.4 (2019), p. 100762 (cit. on p. 68).

[348] K. R. Whittle, M. G. Blackford, R. D. Aughterson, S. Moricca, G. R. Lumpkin, D. P. Riley, and N. J. Zaluzec. "Radiation tolerance of Mn+1AXnphases, Ti3AlC2and Ti3SiC2". In: *Acta Materialia* 58.13 (2010), pp. 4362–4368 (cit. on pp. 69, 70, 252).

[349] L. Zhang, Q. Qi, L. Shi, D. O'Connor, B. King, E. Kisi, and D. Venkatachalam. "Damage tolerance of Ti3SiC2 to high energy iodine irradiation". In: *Applied Surface Science* 258.17 (2012), pp. 6281–6287 (cit. on pp. 69, 70, 250, 252).

[350] L. F. Marion and I. Monnet. "Saturation of irradiation damage in (Ti,Zr)3(Si,Al)C2 compounds". In: *Journal of Nuclear Materials* 433.1-3 (2013), pp. 534–537 (cit. on pp. 69, 70).

[351] X. Liu, M. Le Flem, J.-L. Béchade, F. Onimus, T. Cozzika, and I. Monnet. "XRD investigation of ion irradiated Ti3Si0.90Al0.10C2". In: *Nuclear Instruments and Methods in Physics Research Section B: Beam Interactions with Materials and Atoms* 268.5 (2010), pp. 506–512 (cit. on pp. 69, 70).

[352] J. Nappé, I. Monnet, P. Grosseau, F. Audubert, B. Guilhot, M. Beauvy, M. Benabdesselam, and L. Thomé. "Structural changes induced by heavy ion irradiation in titanium silicon carbide". In: *Journal of Nuclear Materials* 409.1 (2011), pp. 53–61 (cit. on pp. 70, 252).

[353] D. W. Clark, S. J. Zinkle, M. K. Patel, and C. M. Parish. "High temperature ion irradiation effects in MAX phase ceramics". In: *Acta Materialia* 105 (2016), pp. 130–146 (cit. on pp. 70, 79, 252).

[354] D. J. Tallman, E. N. Hoffman, E. N. Caspi, B. L. Garcia-Diaz, G. Kohse, R. L. Sindelar, and M. W. Barsoum. "Effect of neutron irradiation on select MAX phases". In: *Acta Materialia* 85 (2015), pp. 132–143 (cit. on pp. 71, 234, 239, 252).

[355] D. J. Tallman, L. He, B. L. Garcia-Diaz, E. N. Hoffman, G. Kohse, R. L. Sindelar, and M. W. Barsoum. "Effect of neutron irradiation on defect evolution in Ti3SiC2 and Ti2AlC". In: *Journal of Nuclear Materials* 468 (2016), pp. 194–206 (cit. on pp. 71, 234, 241, 252, 253).

[356] D. J. Tallman, L. He, J. Gan, E. N. Caspi, E. N. Hoffman, and M. W. Barsoum. "Effects of neutron irradiation of Ti3SiC2 and Ti3AlC2 in the 121–1085 C temperature range". In: *Journal of Nuclear Materials* 484 (2017), pp. 120–134 (cit. on pp. 71, 234, 241, 242, 246–248, 252, 253).

[357] S. C. Middleburgh, G. R. Lumpkin, and D. Riley. "Accommodation, accumulation, and migration of defects in Ti3SiC2 and Ti3Al2 MAX phases". In: *Journal of the American Ceramic Society* 96.10 (2013), pp. 3196–3201 (cit. on pp. 71, 250, 263).

[358] M. Kangilaski. *Report on the Effects of Neutron Radiation on Structural Materials*. Battelle Memorial Institute, Columbus Laboratories, Radiation Effects ..., 1967 (cit. on p. 77).

[359] A. Metals and F. Group. *STAINLESS STEEL 348*. Nov. 2019. URL: `www.steelforge.com/stainless-steel-348/` (cit. on pp. 78, 117).

[360] A. Stansfield. *The electric furnace: its evolution, theory and practice*. Hill Publishing Company, 1907 (cit. on p. 78).

[361] D. R. M. Rae. "Plasma Arc Process Systems, Reactors, and Applications". In: *Plasma chemistry and plasma processing* 9.1 (1989) (cit. on p. 78).

[362] C. Chang and J. Szekely. "Plasma applications in metals processing". In: *JOM* 34.2 (1982), pp. 57–64 (cit. on p. 78).

[363] S. Ye. *Plasma arc furnaces in A-to-Z guide to thermodynamics, heat and mass transfer, and fluids engineering*. Begellhouse, 1983 (cit. on p. 78).

[364] I. B. Cutler, C. Bradshaw, C. J. Christesen, and E. P. Hyatt. "Sintering of alumina at temperatures of 1673 K and Below". In: *Journal of the American Ceramic Society* 40.4 (1957), pp. 134–139 (cit. on p. 79).

[365] D. Lipusz, A. Isztli, and L. A. Gomze. "Influence of sintering time on properties of alumina-based ceramic composite". In: *Materials Science Forum*. Vol. 812. Trans Tech Publ. 2015, pp. 143–147 (cit. on p. 79).

[366] A. Chaklader and R. Cook. "Kinetics of reactive hot-pressing of clays and hydroxides". In: *Bulletin of the American Ceramic Society* 47.8 (1968), p. 712 (cit. on p. 79).

[367] A. Chaklader and L. McKenzie. "Reactive Hot Pressing of Clays". In: *Bulletin of the American Ceramic Society* 43.12 (1964), pp. 892–93 (cit. on p. 79).

[368] A. Chaklader. “Reactive Hot Pressing: a New Ceramic Process”. In: *Nature* 206.4982 (1965), p. 392 (cit. on p. 79).

[369] M. W. Barsoum and T. El-Raghy. “Synthesis and characterization of a remarkable ceramic: Ti3SiC2”. In: *Journal of the American Ceramic Society* 79.7 (1996), pp. 1953–1956 (cit. on pp. 79, 254).

[370] W. Zhang, N. Travitzky, C. Hu, Y. Zhou, and P. Greil. “Reactive hot pressing and properties of Nb2AlC”. In: *Journal of the American Ceramic Society* 92.10 (2009), pp. 2396–2399 (cit. on p. 79).

[371] Y. Zhou, F. Meng, and J. Zhang. “New MAX-Phase Compounds in the V–Cr–Al–C System”. In: *Journal of the American Ceramic Society* 91.4 (2008), pp. 1357–1360 (cit. on p. 79).

[372] I. Salama, T. El-Raghy, and M. Barsoum. “Synthesis and mechanical properties of Nb2AlC and (Ti, Nb) 2AlC”. In: *Journal of Alloys and Compounds* 347.1-2 (2002), pp. 271–278 (cit. on p. 79).

[373] J. A. Thornton. “High Rate Thick Film Growth”. In: *Annual Review of Materials Science* 7.1 (1977), pp. 239–260 (cit. on pp. 79, 218, 219).

[374] J. A. Thornton. “The microstructure of sputter-deposited coatings”. In: *Journal of Vacuum Science & Technology A: Vacuum, Surfaces, and Films* 4.6 (1986), pp. 3059–3065 (cit. on pp. 79, 80, 212, 218, 219).

[375] B. Movchan and A. Demchishin. “Structure and properties of thick condensates OF nickel, titanium, tungsten, aluminium oxides, and zirconium oxides in vacuum.” In: *Fiz. Metal. Metalloved.* 28 (1969), pp. 653–60 (cit. on pp. 79, 218, 219).

[376] M. A. Tunes, V. M. Vishnyakov, and S. E. Donnelly. “Synthesis and characterisation of high-entropy alloy thin films as candidates for coating nuclear fuel cladding alloys”. In: *Thin Solid Films* 649 (2018), pp. 115–120 (cit. on pp. 80, 219).

[377] P. A. Jacquet. “Electrolytic and chemical polishing”. In: *Metallurgical Reviews* 1.1 (1956), pp. 157–238 (cit. on p. 81).

[378] D. Northwood, R. Gilbert, L. Bahen, P. Kelly, R. Blake, A. Jostsons, P. Madden, D. Faulkner, W. Bell, and R. Adamson. “Characterization of neutron irradiation damage in zirconium alloys—an international “round-robin” experiment”. In: *Journal of Nuclear Materials* 79.2 (1979), pp. 379–394 (cit. on p. 82).

[379] L. A. Giannuzzi et al. *Introduction to focused ion beams: instrumentation, theory, techniques and practice*. Springer Science & Business Media, 2004 (cit. on p. 82).

[380] L. Giannuzzi and F. Stevie. "A review of focused ion beam milling techniques for TEM specimen preparation". In: *Micron* 30.3 (1999), pp. 197–204 (cit. on p. 82).

[381] T. J. Renk, P. P. Provencio, A. Shlapakovski, A. Petrov, K. Yatsui, W. Jiang, H. Suematsu, et al. "Materials modification using intense ion beams". In: *Proceedings of the IEEE* 92.7 (2004), pp. 1057–1081 (cit. on p. 84).

[382] L. Reimer. *Transmission electron microscopy: physics of image formation and microanalysis Springer Series in Optical Sciences*. Berlin: Springer, 2013 (cit. on pp. 84–86).

[383] D. B. Williams and C. B. Carter. *The transmission electron microscope*. Springer, 1996, pp. 3–17 (cit. on pp. 84–87, 90, 92, 93, 95, 241).

[384] B. Fultz and J. M. Howe. *Transmission electron microscopy and diffractometry of materials*. Springer Science & Business Media, 2012 (cit. on pp. 85–87, 89, 92, 96, 211).

[385] O. W. Richardson. "Thermionic phenomena and the laws which govern them". In: *Nobel Lecture* 12 (1929), p. 1929 (cit. on pp. 85, 86).

[386] A. Crewe, D. Eggenberger, J. Wall, and L. Welter. "Electron gun using a field emission source". In: *Review of Scientific Instruments* 39.4 (1968), pp. 576–583 (cit. on p. 86).

[387] J. A. Hinks. "Radiation Damage in Copper Indium Selenide". PhD thesis. University of Salford, 2007 (cit. on pp. 91–93, 95).

[388] F. Krumeich. *Introduction into the transmission and scanning transmission electron microscopy*. First Edition. http://www.microscopy.ethz.ch/downloads/TEM.pdf, 2018 (cit. on p. 94).

[389] D. G. Stroppa, L. F. Zagonel, L. A. Montoro, E. R. Leite, and A. J. Ramirez. "High-Resolution Scanning Transmission Electron Microscopy (HRSTEM) Techniques: High-Resolution Imaging and Spectroscopy Side by Side". In: *ChemPhysChem* 13.2 (2012), pp. 437–443 (cit. on p. 96).

[390] D. Pashley and A. Presland. "Ion damage to metal films inside an electron microscope". In: *Philosophical Magazine* 6.68 (1961), pp. 1003–1012 (cit. on p. 97).

[391] J. Parsons and L. Howe. "Measurement of the ion flux emanating from oxide coated emission filaments in a Siemens electron microscope". In: *Journal of Scientific Instruments* 41.12 (1964), p. 773 (cit. on p. 97).

[392] J. Hinks. "A review of transmission electron microscopes with in situ ion irradiation". In: *Nuclear Instruments and Methods in Physics Research Section B: Beam Interactions with Materials and Atoms* 267.23 (2009), pp. 3652–3662 (cit. on p. 97).

[393] J. Hinks, J. Van Den Berg, and S. Donnelly. "MIAMI: Microscope and ion accelerator for materials investigations". In: *Journal of Vacuum Science & Technology A: Vacuum, Surfaces, and Films* 29.2 (2011), p. 021003 (cit. on pp. 97–100).

[394] P. Thackery, R. Nelson, and H. Sansom. *A combined heavy ion accelerator-electron microscope for the direct observation of radiation effects*. UK Atomic Energy Authority Research Group, 1968 (cit. on p. 97).

[395] Danfysik. *Model 921 A: High Current Ion Source System*. Danfysik Corporation. 2018 (cit. on p. 102).

[396] I. Hanif. "Ion Irradiation Modification of Silicon Nanowires". PhD thesis. University of Huddersfield, 2017 (cit. on pp. 104, 105).

[397] Wikipedia. *High Flux Isotope Reactor*. Accessed on 29.19.2019. Available at `https://en.wikipedia.org/wiki/High_Flux_Isotope_Reactor`. 2019 (cit. on pp. 106, 107).

[398] N. Xoubi and R. Primm III. *Modeling of the high flux isotope reactor cycle 400*. Tech. rep. 2005 (cit. on p. 107).

[399] S. Hogle and G. Ivan Maldonado. "Modeling of the High Flux Isotope Reactor Cycle 400 with KENO-VI". In: *Transactions of the American Nuclear Society* 104 (2011), p. 915 (cit. on p. 107).

[400] G. Bowden and R. Knight. *Specifications for high flux isotope reactor fuel elements HFIR-FE-3*. Tech. rep. Oak Ridge National Lab., TN (USA), 1984 (cit. on p. 107).

[401] D. C. Joy. "Scanning electron microscopy". In: *Materials Science and Technology* (2006) (cit. on pp. 108, 109).

[402] R. Wiesendanger. *Scanning probe microscopy and spectroscopy: methods and applications*. Cambridge University Press, 1994 (cit. on p. 108).

[403] J. I. Goldstein, D. E. Newbury, J. R. Michael, N. W. Ritchie, J. H. J. Scott, and D. C. Joy. *Scanning electron microscopy and X-ray microanalysis*. Springer, 2017 (cit. on p. 108).

[404] S. Wright, D. Dingley, and D. Field. *Determining deformation, recovery and recrystallization fractions from Orientation Imaging Microscopy (OIM) data*. Tech. rep. San Francisco Press, Inc., San Francisco, CA (United States), 1996 (cit. on p. 109).

[405] J. Sutliff and B. Bewlay. *Orientation imaging of a Nb-Ti-Si directionally solidified in-situ composite*. Tech. rep. San Francisco Press, Inc., San Francisco, CA (United States), 1996 (cit. on p. 109).

[406] R. Van Grieken and A. Markowicz. *Handbook of X-ray Spectrometry*. CRC Press, 2001 (cit. on p. 109).

[407] J. Trincavelli, S. Limandri, and R. Bonetto. "Standardless quantification methods in electron probe microanalysis". In: *Spectrochimica Acta Part B: Atomic Spectroscopy* 101 (2014), pp. 76–85 (cit. on pp. 109, 125, 206).

[408] M. Burke, M. Watanabe, D. Williams, and J. Hyde. "Quantitative characterization of nanoprecipitates in irradiated low-alloy steels: advances in the application of FEG-STEM quantitative microanalysis to real materials". In: *Journal of Materials Science* 41.14 (2006), pp. 4512–4522 (cit. on pp. 110–112).

[409] M. Watanabe, D. Ackland, A. Burrows, C. Kiely, D. Williams, O. Krivanek, N. Dellby, M. Murfitt, and Z. Szilagyi. "Improvements in the X-ray analytical capabilities of a scanning transmission electron microscope by spherical-aberration correction". In: *Microscopy and Microanalysis* 12.6 (2006), pp. 515–526 (cit. on p. 110).

[410] J. Titchmarsh. "EDX spectrum modelling and multivariate analysis of sub-nanometer segregation". In: *Micron* 30.2 (1999), pp. 159–171 (cit. on p. 110).

[411] J. M. Titchmarsh and S. Dumbill. "Multivariate Statistical analysis of FEG-STEM EDX spectra". In: *Journal of Microscopy* 184.3 (1996), pp. 195–207 (cit. on p. 110).

[412] M. Aronova, Y. Kim, G. Zhang, and R. Leapman. "Quantification and thickness correction of EFTEM phosphorus maps". In: *Ultramicroscopy* 107.2-3 (2007), pp. 232–244 (cit. on p. 113).

[413] H. Zhang, R. Egerton, and M. Malac. "EELS Investigation of the Formulas for Inelastic Mean Free Path". In: *Microscopy and Microanalysis* 17.S2 (2011), pp. 1466–1467 (cit. on p. 114).

[414] N. Saunders and A. P. Miodownik. *CALPHAD (calculation of phase diagrams): a comprehensive guide*. Vol. 1. Elsevier, 1998 (cit. on p. 115).

[415] J.-O. Andersson, T. Helander, L. Höglund, P. Shi, and B. Sundman. "Thermo-Calc & DICTRA, computational tools for materials science". In: *Calphad* 26.2 (2002), pp. 273–312 (cit. on pp. 115, 190).

[416] FOPIL. *Portfolio of products.* [Online; accessed 19-March-2018 `http://www.fopil.com.br/produtos.php?produtos=1`]. 2018 (cit. on p. 117).

[417] A. Padilha, R. Plaut, and P. Rios. "Stainless steels heat treatment (Chapter 12)". In: *Steel Heat Treatment. CRC Press: Boca Raton* (2007) (cit. on pp. 117, 199).

[418] P. Rowlands, A. Whittaker, A. Hoaksey, J. Garrett, and L. Popple. "The oxidation performance of Magnox and advanced gas-cooled reactor steels in high pressure CO 2". In: *Nucl. Energy* 25.5 (1986), pp. 267–275 (cit. on p. 117).

[419] E. L. Brown and A. J. Deardo. "On the origin of equiaxed austenite grains that result from the hot rolling of steel". In: *Metallurgical Transactions A* 12.1 (1981), pp. 39–47 (cit. on p. 118).

[420] C. Sellars and J. Whiteman. "Recrystallization and grain growth in hot rolling". In: *Metal Science* 13.April (1978), pp. 187–194 (cit. on p. 118).

[421] A. Jivkov, N. Stevens, and T. Marrow. "A two-dimensional mesoscale model for intergranular stress corrosion crack propagation". In: *Acta Materialia* 54.13 (2006), pp. 3493–3501 (cit. on p. 119).

[422] H.-G. Lambers, S. Tschumak, H. J. Maier, and D. Canadinc. "Role of Austenitization and Pre-Deformation on the Kinetics of the Isothermal Bainitic Transformation". In: *Metallurgical and Materials Transactions A* 40.6 (2009), pp. 1355–1366 (cit. on p. 119).

[423] Y. Zeng, X. Cai, and M. Koslowski. "Effects of the stacking fault energy fluctuations on the strengthening of alloys". In: *Acta Materialia* (2018). ISSN: 1359-6454 (cit. on pp. 119, 128).

[424] K. Schulz and J. Papp. *Niobium and Tantalum: Indispensable Twins.* US Department of the Interior, US Geological Survey, 2014 (cit. on p. 120).

[425] J. M. Silcock and W. J. Tunstall. "Partial dislocations associated with NbC precipitation in austenitic stainless steels". In: *Philosophical Magazine* 10.105 (1964), pp. 361–389 (cit. on p. 120).

[426] M. G. D. V. Cuppari and S. F. Santos. "Physical properties of the NbC carbide". In: *Metals* 6.10 (2016), p. 250 (cit. on p. 125).

[427] C. Kempter, E. Storms, and R. Fries. “Lattice dimensions of NbC as a function of stoichiometry”. In: *The Journal of Chemical Physics* 33.6 (1960), pp. 1873–1874 (cit. on p. 125).

[428] A. Gusev. “Disorder and Long-Range Order in Non-Stoichiometric Interstitial Compounds Transition Metal Carbides, Nitrides, and Oxides”. In: *Physica status solidi (b)* 163.1 (1991), pp. 17–54 (cit. on p. 125).

[429] E. Kisi, J. Crossley, S. Myhra, and M. Barsoum. “Structure and crystal chemistry of Ti3SiC2”. In: *Journal of Physics and Chemistry of Solids* 59.9 (1998), pp. 1437–1443 (cit. on pp. 132, 236).

[430] T. Cabioc’h, P. Eklund, V. Mauchamp, and M. Jaouen. “Structural investigation of substoichiometry and solid solution effects in Ti2Al (Cx, N1- x) y compounds”. In: *Journal of the European Ceramic Society* 32.8 (2012), pp. 1803–1811 (cit. on pp. 132, 236).

[431] J. Morgiel, J. Lis, and R. Pampuch. “Microstructure of Ti3SiC2 based ceramics”. In: *Mater. Lett.* 27.June (1996), pp. 85–89 (cit. on pp. 132, 133, 139, 237).

[432] W. J. Wakelkamp, F. J. van Loo, and R. Metselaar. “Phase relations in the TiSiC system”. In: *Journal of the European Ceramic Society* 8.3 (1991), pp. 135–139 (cit. on pp. 133, 136).

[433] Racault.C and Langlais.F. “On the chemical vapour deposition of Ti3SiC2 from TiCl4-SiCl4-CH4-H2 gas mixtures Partl A thermodynamic approach”. In: *Journal of Materials Science* 29 (1994), pp. 5023–5040 (cit. on pp. 133, 136).

[434] J. Emmerlich, D. Music, P. Eklund, O. Wilhelmsson, U. Jansson, J. M. Schneider, H. Högberg, and L. Hultman. “Thermal stability of Ti3SiC2 thin films”. In: *Acta Materialia* 55.4 (2007), pp. 1479–1488 (cit. on pp. 133, 136).

[435] D. Green. “Stress-Induced Microcracking at Second-Phase Inclusions”. In: *Journal of the American Ceramic Society* 64.3 (1981), pp. 138–141 (cit. on p. 133).

[436] V. Tvergaard and J. W. Hutchinson. “Microcracking in ceramics induced by thermal expansion or elastic anisotropy”. In: *Journal of the American Ceramic Society* 71.3 (1988), pp. 157–166 (cit. on p. 133).

[437] C. Soong, P. Woo, and D. Hoyle. “Contamination cleaning of TEM/SEM samples with the ZONE cleaner”. In: *Microscopy Today* 20.6 (2012), pp. 44–48 (cit. on p. 134).

[438] P. A. Burr, D. Horlait, and W. E. Lee. “Experimental and DFT investigation of (Cr, Ti)3AlC2 MAX phases stability”. In: *Materials Research Letters* 5.3 (2017), pp. 144–157 (cit. on pp. 134, 135).

[439] D. Bandyopadhyay, R. Sharma, and N. Chakraborti. “The Ti-Al-C system (titanium-aluminum-carbon)”. In: *Journal of Phase Equilibria and Diffusion* 21.2 (2000), p. 195 (cit. on pp. 136, 233, 234, 257).

[440] N. Stoloff, C. Liu, and S. Deevi. “Emerging applications of intermetallics”. In: *Intermetallics* 8.9-11 (2000), pp. 1313–1320 (cit. on p. 136).

[441] S. Sambasivan and W. T. Petuskey. “Phase relationships in the Ti-Si-C system at high pressures”. In: *Journal of Materials Research* 7.6 (1992), pp. 1473–1479 (cit. on pp. 136, 233, 234, 257).

[442] J. P. Palmquist, S. Li, P. O. Persson, J. Emmerlich, O. Wilhelmsson, H. Högberg, M. I. Katsnelson, B. Johansson, R. Ahuja, O. Eriksson, L. Hultman, and U. Jansson. “Mn+1AXn phases in the Ti-Si-C system studied by thin-film synthesis and ab initio calculations”. In: *Physical Review B - Condensed Matter and Materials Physics* 70.16 (2004), pp. 1–13 (cit. on p. 136).

[443] D. Miracle and O. Senkov. “A critical review of high entropy alloys and related concepts”. In: *Acta Materialia* 122 (2017), pp. 448–511 (cit. on p. 140).

[444] R. W. Harrison, G. Greaves, J. Hinks, and S. Donnelly. “Engineering self-organising helium bubble lattices in tungsten”. In: *Scientific Reports* 7.1 (2017), p. 7724 (cit. on p. 142).

[445] A. Kalchenko, S. Karpov, I. Kopanets, M. Tikhonovsky, and G. Tolstolutskaya. “Comparative study of helium bubble formation in CrFeNiMn high-entropy alloy and 18Cr10NiTi steel after irradiation and post-irradiation annealing”. In: *Problems of atomic science and technology* 5.123 (2019) (cit. on pp. 154–156).

[446] S. Donnelly. “Nanobubbles in ion-implanted solids”. In: *Manipulation, Manufacturing and Measurement on the Nanoscale (3M-NANO), 2014 International Conference on*. IEEE. 2014, pp. 18–22 (cit. on p. 160).

[447] S. Zhao, Y. Osetsky, and Y. Zhang. “Preferential diffusion in concentrated solid solution alloys: NiFe, NiCo and NiCoCr”. In: *Acta Materialia* 128 (2017), pp. 391–399 (cit. on p. 161).

[448] K. Jin, C. Lu, L. Wang, J. Qu, W. Weber, Y. Zhang, and H. Bei. “Effects of compositional complexity on the ion-irradiation induced swelling and hardening in Ni-containing equiatomic alloys”. In: *Scripta Materialia* 119 (2016), pp. 65–70 (cit. on p. 161).

[449] S. Zhao, W. J. Weber, and Y. Zhang. "Unique challenges for modeling defect dynamics in concentrated solid-solution alloys". In: *JOM* 69.11 (2017), pp. 2084–2091 (cit. on pp. 161, 162).

[450] D. Terentyev, P. Olsson, T. Klaver, and L. Malerba. "On the migration and trapping of single self-interstitial atoms in dilute and concentrated Fe–Cr alloys: Atomistic study and comparison with resistivity recovery experiments". In: *Computational Materials Science* 43.4 (2008), pp. 1183–1192 (cit. on p. 161).

[451] J. Winkelmann. "Diffusion of xenon". In: *Gases in Gases, Liquids and their Mixtures*. Springer, 2007, pp. 152–155 (cit. on p. 163).

[452] D. L. Morrison, T. S. Elleman, and D. N. Sunderman. "Diffusion of Xenon in Ceramic Oxides". In: *Journal of Applied Physics* 35.5 (1964), pp. 1616–1622 (cit. on p. 163).

[453] C. A. English. "Low-dose neutron irradiation damage in FCC and BCC metals". In: *Journal of Nuclear Materials* 108-109.C (1982), pp. 104–123 (cit. on p. 166).

[454] T. Badjuk, G. Kushma, and O. Rybajlo. "Temperature and concentration depencence of the unit cell dimensions of Fe-Cr solid solutions". In: *Izvestiya Vysshikh Uchebnykh Zavedenii, Chernaya Metallurgiya* 17 (1974), pp. 126–128 (cit. on pp. 175, 177).

[455] S. A. Briggs, P. D. Edmondson, K. C. Littrell, Y. Yamamoto, R. H. Howard, C. R. Daily, K. A. Terrani, K. Sridharan, and K. G. Field. "A combined APT and SANS investigation of alpha-prime phase precipitation in neutron-irradiated model FeCrAl alloys". In: *Acta Materialia* 129 (2017), pp. 217–228 (cit. on pp. 175, 177, 178, 199, 200).

[456] S. Jin, L. Guo, F. Luo, Z. Yao, S. Ma, and R. Tang. "Ion irradiation-induced precipitation of Cr23C6 at dislocation loops in austenitic steel". In: *Scripta Materialia* 68.2 (2013), pp. 138–141 (cit. on pp. 178, 180, 181, 184, 200).

[457] H. Yakel. "Atom distributions in tau-carbide phases: Fe and Cr distributions in (Cr23- xFex) C6 with x= 0, 0.74, 1.70, 4.13 and 7.36". In: *Acta Crystallographica Section B* 43.3 (1987), pp. 230–238 (cit. on p. 184).

[458] P. D. Edmondson, S. A. Briggs, Y. Yamamoto, R. H. Howard, K. Sridharan, K. A. Terrani, and K. G. Field. "Irradiation-enhanced alpha-prime precipitation in model FeCrAl alloys". In: *Scripta Materialia* 116 (2016), pp. 112–116 (cit. on pp. 184, 199).

[459] R. Harrison, A. Carruthers, J. Hinks, M. Burke, and S. Donnelly. "Cascade size and dose rate effects on alpha-prime precipitation in ion-irradiated Fe14Cr alloy". In: *Scripta Materialia* 172 (2019), pp. 33–37 (cit. on p. 184).

[460] T. Ferreira and W. Rasband. "ImageJ user guide". In: *ImageJ-Fiji* 1 (2012), pp. 155–161 (cit. on p. 185).

[461] Y. Zhang, S. Zhao, W. J. Weber, K. Nordlund, F. Granberg, and F. Djurabekova. "Atomic-level heterogeneity and defect dynamics in concentrated solid-solution alloys". In: *Current Opinion in Solid State and Materials Science* 21.5 (2017), pp. 221–237 (cit. on pp. 187, 188).

[462] K. Hack. *The SGTE casebook: thermodynamics at work*. Elsevier, 2008 (cit. on pp. 189, 191).

[463] E. A. de Pauli, C. G. Schön, and S. D. Brandi. "Multicomponent Phase Diagram of Lean Duplex Stainless Steel UNS S82441 and Its Application to Evaluate the Microstructure in the Heat Affected Zone". In: *Journal of Phase Equilibria and Diffusion* 38.3 (2017), pp. 332–342 (cit. on p. 189).

[464] W. Phythian, R. Stoller, A. Foreman, A. Calder, and D. Bacon. "A comparison of displacement cascades in copper and iron by molecular dynamics and its application to microstructural evolution". In: *Journal of nuclear materials* 223.3 (1995), pp. 245–261 (cit. on p. 197).

[465] K. A. Terrani. "Accident tolerant fuel cladding development: Promise, status, and challenges". In: *Journal of Nuclear Materials* 501 (2018), pp. 13–30 (cit. on p. 199).

[466] P. D. Edmondson. "Comment on the nuclear materials and energy special issue on Fukushima Daiichi 5 years on—Impact, implications, and innovations". In: *Nuclear Materials and Energy* 10 (2017), p. 17 (cit. on p. 203).

[467] S. J. Zinkle, K. A. Terrani, J. C. Gehin, L. J. Ott, and L. L. Snead. "Accident tolerant fuels for LWRs: A perspective". In: *Journal of Nuclear Materials* 448.1-3 (2014), pp. 374–379 (cit. on p. 204).

[468] E. Alat, A. T. Motta, R. J. Comstock, J. M. Partezana, and D. E. Wolfe. "Multilayer (TiN, TiAlN) ceramic coatings for nuclear fuel cladding". In: *Journal of Nuclear Materials* 478 (2016), pp. 236–244 (cit. on pp. 205, 222, 225, 231).

[469] E. Alat, A. T. Motta, R. J. Comstock, J. M. Partezana, and D. E. Wolfe. "Ceramic coating for corrosion (c3) resistance of nuclear fuel cladding". In: *Surface and Coatings Technology* 281 (2015), pp. 133–143 (cit. on pp. 205, 222, 231).

[470] R. B. Rebak. “Versatile oxide films protect FeCrAl alloys under normal operation and accident conditions in light water power reactors”. In: *JOM* 70.2 (2018), pp. 176–185 (cit. on p. 205).

[471] I. Charit. “Accident tolerant nuclear fuels and cladding materials”. In: *JOM* 70.2 (2018), pp. 173–175 (cit. on p. 205).

[472] R. Becker and W. Döring. “Kinetische behandlung der keimbildung in übersättigten dämpfen”. In: *Annalen der Physik* 416.8 (1935), pp. 719–752 (cit. on p. 211).

[473] M. Volmer and A. Weber. “Keimbildung in übersättigten Gebilden”. In: *Zeitschrift für physikalische Chemie* 119.1 (1926), pp. 277–301 (cit. on p. 211).

[474] J. H. Hollomon and D. Turnbull. “Nucleation”. In: *Progress in Metal Physics* 4 (1953), pp. 333–388 (cit. on p. 211).

[475] M. Birkholz, B. Selle, W. Fuhs, S. Christiansen, H. Strunk, and R. Reich. “Amorphous-crystalline phase transition during the growth of thin films: The case of microcrystalline silicon”. In: *Physical Review B* 64.8 (2001), p. 085402 (cit. on p. 213).

[476] A. Roitburd. “Equilibrium structure of epitaxial layers”. In: *Physica Status Solidi A* 37.1 (1976), pp. 329–339 (cit. on p. 213).

[477] D. Jang. “Nano-sized Nanocrystalline and Nano-twinned Metals”. In: *Encyclopedia of Nanotechnology*. Springer, 2012, pp. 1739–1747 (cit. on p. 214).

[478] J. R. Greer. “Nanotwinned metals: It’s all about imperfections”. In: *Nature Materials* 12.8 (2013), p. 689 (cit. on p. 214).

[479] Q. An, W. A. Goddard III, K. Y. Xie, G.-d. Sim, K. J. Hemker, T. Munhollon, M. F. Toksoy, and R. A. Haber. “Superstrength through nanotwinning”. In: *Nano letters* 16.12 (2016), pp. 7573–7579 (cit. on p. 214).

[480] H. Pomerance. “Thermal neutron capture cross sections”. In: *Physical Review* 88.2 (1952), p. 412 (cit. on p. 214).

[481] D. R. H. Jones and M. F. Ashby. *Engineering materials 1*. Butterworth-Heinemann, 2012 (cit. on p. 215).

[482] A. H. Committee. *Metals handbook*. Vol. 2. American society for Metals, 1973 (cit. on p. 215).

[483] W. Dienst, P. Hofmann, and D. K. Kerwin-Peck. “Chemical interactions between UO2 and zircaloy-4 from 1000 to 2000 C”. In: *Nuclear Technology* 65.1 (1984), pp. 109–124 (cit. on p. 219).

[484] J. Lloyd and S. Nakahara. “Voids in thin as-deposited gold films prepared by vapor deposition”. In: *Journal of Vacuum Science and Technology* 14.1 (1977), pp. 655–659 (cit. on p. 221).

[485] S. Nakahara. "Microporosity induced by nucleation and growth processes in crystalline and non-crystalline films". In: *Thin Solid Films* 45.3 (1977), pp. 421–432 (cit. on p. 221).

[486] H. Leamy and A. Dirks. "Microstructure and magnetism in amorphous rare-earth–transition-metal thin films. I. Microstructure". In: *Journal of Applied Physics* 49.6 (1978), pp. 3430–3438 (cit. on p. 221).

[487] C. A. English and B. L. Eyre. "Heavy-ion damage in Alpha-Fe". In: *Nature* 260 (1976), pp. 619–21 (cit. on p. 221).

[488] R. W. Harrison, G. Greaves, J. Hinks, and S. Donnelly. "A study of the effect of helium concentration and displacement damage on the microstructure of helium ion irradiated tungsten". In: *Journal of Nuclear Materials* 495 (2017), pp. 492–503 (cit. on p. 228).

[489] P. Capezzuto and A. Madan. *Plasma deposition of amorphous silicon-based materials*. Elsevier, 1995 (cit. on p. 231).

[490] K. Lambrinou, E. Charalampopoulou, T. Van der Donck, R. Delville, and D. Schryvers. "Dissolution corrosion of 316L austenitic stainless steels in contact with static liquid lead-bismuth eutectic (LBE) at 500C". In: *Journal of Nuclear Materials* 490 (2017), pp. 9–27 (cit. on p. 232).

[491] O. Klok, K. Lambrinou, S. Gavrilov, E. Stergar, T. Van der Donck, S. Huang, B. Tunca, and I. De Graeve. "Influence of plastic deformation on dissolution corrosion of type 316L austenitic stainless steel in static, oxygen-poor liquid lead-bismuth eutectic at 500C". In: *Corrosion* 73.9 (2017), pp. 1078–1090 (cit. on p. 232).

[492] E. Charalampopoulou, N. Cautaerts, T. Van der Donck, D. Schryvers, K. Lambrinou, and R. Delville. "Orientation relationship of the austenite-to-ferrite transformation in austenitic stainless steels due to dissolution corrosion in contact with liquid Pb-Bi eutectic". In: *Scripta Materialia* 167 (2019), pp. 66–70 (cit. on p. 232).

[493] Y. Zhang, M. A. Tunes, M. L. Crespillo, F. Zhang, W. L. Boldman, P. D. Rack, L. Jiang, C. Xu, G. Greaves, S. E. Donnelly, L. Wang, and W. J. Weber. "Thermal stability and irradiation response of nanocrystalline CoCr-CuFeNi high-entropy alloy". In: *Nanotechnology* 30.29 (2019), p. 294004 (cit. on pp. 232, 271).

[494] O. El-Atwani, E. Esquivel, E. Aydogan, E. Martinez, J. Baldwin, M. Li, B. P. Uberuaga, and S. A. Maloy. "Unprecedented irradiation resistance of nanocrystalline tungsten with equiaxed nanocrystalline grains to dislocation

loop accumulation". In: *Acta Materialia* 165 (2019), pp. 118–128 (cit. on pp. 232, 271).

[495] W. E. Lee, E. Giorgi, R. Harrison, A. Maitre, and O. Rapaud. "Nuclear Applications for Ultra-High Temperature Ceramics and MAX Phases". In: *Ultra-High Temperature Ceramics: Materials for Extreme Environment Applications* (2014), pp. 391–415 (cit. on pp. 234, 252).

[496] S. Aubry, M. Rhee, G. Hommes, V. V. Bulatov, and A. Arsenlis. "Dislocation dynamics in hexagonal close-packed crystals". In: *Journal of the Mechanics and Physics of Solids* 94 (2016), pp. 105–126 (cit. on pp. 236, 244, 246).

[497] S. I. Golubov, A. Barashev, and R. E. Stoller. *On the origin of radiation growth of hcp crystals*. Tech. rep. November 2011. 2012 (cit. on pp. 236, 248).

[498] R. Ding and I. P. Jones. "In situ hydride formation in titanium during focused ion milling". In: *Journal of Electron Microscopy* 60.1 (2011), pp. 1–9 (cit. on p. 237).

[499] Z. Nishiyama. *Martensitic transformation*. Elsevier, 2012 (cit. on p. 237).

[500] J. Bowles and J. Mackenzie. "The crystallography of martensite transformations I". In: *Acta Metallurgica* 2.1 (1954), pp. 129–137 (cit. on p. 237).

[501] H. Bhadeshia. "Martensite and bainite in steels: transformation mechanism & mechanical properties". In: *Le Journal de Physique IV* 7.C5 (1997), pp. C5–367 (cit. on p. 237).

[502] S. Liu, T. Yang, J. Zhang, Z. Yan, Y. Lu, D. Han, C. Wang, Y. Fang, and Y. Wang. "Thermal effects in ion irradiated Ti2AlC and Ti3SiC2". In: *Nuclear Instruments and Methods in Physics Research Section B: Beam Interactions with Materials and Atoms* (2017) (cit. on p. 239).

[503] L. Farber, M. W. Barsoum, A. Zavaliangos, T. El-Raghy, and I. Levin. "Dislocations and Stacking Faults in Ti3SiC2". In: *Journal of the American Ceramic Society* 81.6 (2005), pp. 1677–1681 (cit. on p. 241).

[504] M. A. Meyers. *Dynamic behavior of materials*. John wiley & sons, 1994 (cit. on pp. 242, 244, 246).

[505] L. Teutonico. "Dislocations in hexagonal crystals". In: *Materials Science and Engineering* 6.1 (1970), pp. 27–47 (cit. on p. 246).

[506] D. Bhattacharyya, E. Cerreta, R. McCabe, M. Niewczas, G. Gray III, A. Misra, and C. Tome. "Origin of dislocations within tensile and compressive twins in pure textured Zr". In: *Acta Materialia* 57.2 (2009), pp. 305–315 (cit. on p. 248).

[507] Z. J. Lin, M. J. Zhuo, Y. C. Zhou, M. S. Li, and J. Y. Wang. “Microstructural characterization of layered ternary Ti2AlC”. In: *Acta Materialia* 54.4 (2006), pp. 1009–1015 (cit. on pp. 249, 250).

[508] P. Gouma, M. Mills, and Y.-W. Kim. “Characterization of the precipitation process in a TiAl-based alloy with carbon and silicon additions”. In: *Philosophical Magazine Letters* 78.1 (1998), pp. 59–66 (cit. on p. 250).

[509] M. K. Patel, D. J. Tallman, J. A. Valdez, J. Aguiar, O. Anderoglu, M. Tang, J. Griggs, E. Fu, Y. Wang, and M. W. Barsoum. “Effect of helium irradiation on Ti3AlC2 at 500 C”. In: *Scripta Materialia* 77 (2014), pp. 1–4 (cit. on p. 252).

[510] W. Jeitschko. “Refinement of the crystal structure of TiSi2 and some comments on bonding in TiSi2 and related compounds”. In: *Acta Crystallographica Section B: Structural Crystallography and Crystal Chemistry* 33.7 (1977), pp. 2347–2348 (cit. on p. 259).

[511] W. J. J. Wakelkamp. *Diffusion and phase relations in the systems Ti-Si-C and Ti-Si-N*. Technische Universiteit Eindhoven, 2013 (cit. on p. 259).